

Pierre-Marie Robitaille
Lawrence J. Berliner

BIOLOGICAL MAGNETIC RESONANCE 26

Ultra High Field Magnetic Resonance Imaging

INCLUDES



CD-ROM



Springer

Ultra High Field Magnetic Resonance Imaging

Volume 26

A Continuation Order Plan is available for this series. A continuation order will bring delivery of each new volume immediately upon publication. Volumes are billed only upon actual shipment. For further information please contact the publisher.

Pierre-Marie Robitaille
Lawrence Berliner

Ultra High Field Magnetic Resonance Imaging

Volume 26

 **Springer**

Pierre-Marie Robitaille
Department of Radiology
The Ohio State University Medical
Center
130 Means Hall, 1654 Upham Drive
Columbus, Ohio 43210
robitaille.1@osu.edu

Lawrence Berliner
Department of Chemistry &
Biochemistry
University of Denver
2190 E. Iliff Avenue
F. W. Olin Hall, Room 202
Denver, CO 80208
USA
berliner@du.edu

Library of Congress Control Number: 2006928051

ISBN-10: 0-387-34231-1
ISBN-13: 978-0387-34231-3

Printed on acid-free paper.

© 2006 Springer Science+Business Media, LLC

All rights reserved. This work may not be translated or copied in whole or in part without the written permission of the publisher (Springer Science+Business Media, LLC, 233 Spring Street, New York, NY 10013, USA), except for brief excerpts in connection with reviews or scholarly analysis. Use in connection with any form of information storage and retrieval, electronic adaptation, computer software, or by similar or dissimilar methodology now known or hereafter developed is forbidden.

The use in this publication of trade names, trademarks, service marks, and similar terms, even if they are not identified as such, is not to be taken as an expression of opinion as to whether or not they are subject to proprietary rights.

Printed in the United States of America. (MVY)

9 8 7 6 5 4 3 2 1

springer.com

to Patricia Anne

CONTRIBUTORS

Gregor Adriany, PhD (chap. 10)
Center for Magnetic Resonance Research
University of Minnesota
2021 Sixth Street SE
Minneapolis, MN 55455-3007, USA
(612) 626-2001
gregor@cmrr.umn.edu

Can Akgün, PhD (chap. 10)
Center for Magnetic Resonance Research
University of Minnesota
2021 Sixth Street SE
Minneapolis, MN 55455-3007, USA
(612) 626-2001
akgun@cmrr.umn.edu

Peter Andersen, PhD (chap. 10)
Center for Magnetic Resonance Research
University of Minnesota
2021 Sixth Street SE
Minneapolis, MN 55455-3007
(612) 626-2001
peter@cmrr.umn.edu

Lawrence J. Berliner, PhD (editor/preface)
Department of Chemistry & Biochemistry
University of Denver
2190 East Iliff Avenue, Olin 202
Denver, CO 80208-2436, USA
(303) 871-2436, 2435
berliner@du.edu

John Bird, PhD (chap. 2)
Magnex Scientific Ltd.
The Magnet Technology Center
6 Mead Road, Oxford Industrial Park
Yarnton, Oxfordshire OX5 1QU, UK
011 44-1-865-853-870
john.bird@magnex.com

Wei Chen, PhD (chap. 10)
Center for Magnetic Resonance Research
University of Minnesota
2021 Sixth Street SE
Minneapolis, MN 55455-3007, USA
(612) 626-2001
wei@cmrr.umn.edu

Gregory Christoforidis, MD (chap. 13)
Department of Radiology
The Ohio State University
627 Means Hall, 1654 Upham Drive
Columbus, OH 43210, USA
(614) 293-8315
christoforidis-2@medctr.osu.edu

Christopher M. Collins, PhD (chap. 8)
Department of Radiology
Pennsylvania State University
NMR/MRI Building, H066
500 University Drive
Hershey, PA 17033, USA
(717) 531-7402
cmcollins@psu.edu

Bruce Fischl, PhD (chap. 11)
Department of Radiology, MGH
149 Thirteenth Street, Room 2301
Charlestown, MA 02129, USA
(617) 726-4897
fischl@nmr.mgh.harvard.edu

Michael Garwood, PhD (chap. 10)
Center for Magnetic Resonance Research
University of Minnesota
2021 Sixth Street SE
Minneapolis, MN 55455-3007, USA
(612) 626-2001
gar@cmrr.umn.edu

Rolf Gruetter, PhD (chaps. 10, 12)
EPFL SB IPMC LIFMET
PH D2 455 (Batiment H), Station 3
CH-1015 Lausanne, Switzerland
011 44 21 693 4467
rolf.gruetter@epfl.ch

Pierre-Gilles Henry, PhD (chaps. 10, 12)
Center for Magnetic Resonance Research
University of Minnesota
2021 Sixth Street SE
Minneapolis, MN 55455-3007, USA
(612) 626-2001
henry@cmrr.umn.edu

Darren Houlden, BSc,CPhys, MInstP
(chap. 2)
Magnex Scientific Ltd.
The Magnet Technology Center
6 Mead Road, Oxford Industrial Park
Yarnton, Oxfordshire, OX5 1QU, UK
011 44-1-865-853-827
darren.houlden@magnex.com

Tamer S. Ibrahim, PhD (chap. 7)
The University of Oklahoma
School of Electrical and Computer
Engineering
202 West Boyd Street
Norman, Oklahoma 73019-1023, USA
(412) 383-6946
ibrahim@ou.edu

Douglas A.C. Kelley, PhD (chap. 3)
Global Applied Science Laboratory
General Electric Healthcare Technologies
UCSF QB3 Institute
1700 4th Street Room 102E
San Francisco, CA 94158, USA
(415) 514-4416
douglas.kelley@med.ge.com

Nick Kerley, PhD (chap. 2)
Magnex Scientific Ltd.
The Magnet Technology Center
6 Mead Road, Oxford Industrial Park
Yarnton, Oxfordshire, OX5 1QU, UK
011 44-1-865-853-821
nick.kerley@magnex.com

Paul C. Lauterbur, PhD (foreword)
Department of Chemistry
University of Illinois
A512 Chemical & Life Sciences Lab
600 S. Mathews Avenue
Urbana, IL 61801, USA
(217) 244-0600
pcl@uiuc.edu

Hongxia Lei, PhD (chap. 12)
EPFL SB IPMC LIFMET
PH D2 455 (Batiment H), Station 3
CH-1015 Lausanne, Switzerland
011 44 21 693 4467
hongxia.lei@epfl.ch

Silvia Mangia, PhD (chap. 12)
Center for Magnetic Resonance Research
University of Minnesota
2021 Sixth Street SE
Minneapolis, MN 55455-3007, USA
(612) 626-2001
mangia@cmrr.umn.edu

Malgorzata Marjanska, PhD (chap. 10)
Center for Magnetic Resonance Research
University of Minnesota
2021 Sixth Street SE
Minneapolis, MN 55455-3007, USA
(612) 626-2001
gosia@cmrr.umn.edu

Steen Moeller, PhD (chap. 10)
Center for Magnetic Resonance Research
University of Minnesota
2021 Sixth Street SE
Minneapolis, MN 55455-3007, USA
(612) 626-2001
moeller@cmrr.umn.edu

Pierre-François Van de Moortele, PhD
(chap. 10)
Center for Magnetic Resonance Research
University of Minnesota
2021 Sixth Street SE
Minneapolis, MN 55455-3007, USA
(612) 626-2001
pfdm@cmrr.umn.edu

Vera Novak, MD, PhD (chap. 13)
Beth Israel Deaconess Medical Center
Division of Gerontology
110 Francis Street LMOB, Suite 1B
Boston, MA 20015, USA
(617) 632-8680
vnovak@bidmc.harvard.edu

Gülin Öz, PhD (chap. 12)
Center for Magnetic Resonance Research
University of Minnesota
2021 Sixth Street SE
Minneapolis, MN 55455-3007, USA
(612) 626-2001
gulin@cmrr.umn.edu

Simon Pittard, PhD (chap. 2)
Magnex Scientific Ltd.
The Magnet Technology Center
6 Mead Road, Oxford Industrial Park
Yarnton, Oxfordshire, OX5 1QU, UK
011 44-1-865-853-858
simon.pittard@magnex.com

Klaas Prüssmann, PhD (chap. 10)
Institute for Biomedical Engineering
Gloriastrasse-35
CH- 8092 Zurich, Switzerland
011 41-1-632-6696
pruessmann@biomed.ee.ethz.ch

Andreas Potthast, PhD (chap. 4)
Siemens Medical Solutions Inc.
CSG R&D Collaborations
MGH NMR Center
149 13th Street, Suite 2301
Cambridge, MA 02129-2060, USA
(617) 726-9343
Andreas.Potthast@siemens.com

David Rayner, PhD (chap. 2)
Magnex Scientific Ltd.
The Magnet Technology Center
6 Mead Road, Oxford Industrial Park
Yarnton, Oxfordshire, OX5 1QU, UK
011 44-1-865-853-822
david.rayner@magnex.com

Pierre-Marie L. Robitaille, PhD
(editor/preface/chap. 1)
Department of Radiology
The Ohio State University
130 Means Hall, 1654 Upham Drive
Columbus, Ohio 43210, USA
(614) 293- 3046
robitaille.1@osu.edu

Bruce R. Rosen, MD, PhD (chap. 11)
Department of Radiology, MGH
149 Thirteenth Street, Room 2301
Charlestown, MA 02129, USA
(617) 726-5122
bruce@nmr.mgh.harvard.edu

Franz Schmitt, PhD (chap. 4)
Siemens Medical Solutions, MREF
Development Field Generating Units
Coordination 7T
Allee am Roethelheimpark 2
91052 Erlangen, Germany
011 49 9131 84 7426
franz.schmitt@siemens.com

David Simkin, PhD (chap. 2)
Magnex Scientific Ltd.
The Magnet Technology Center
6 Mead Road, Oxford Industrial Park
Yarnton, Oxfordshire, OX5 1QU, UK
011 44-1-865-853-881
david.simkin@magnex.com

Michael B. Smith, PhD (chap. 9)
Department of Radiology
Pennsylvania State University
NMR/MRI Building, H066
500 University Drive
Hershey, PA 17033, USA
(717) 531-6075
mbsmith@psu.edu

Bernd Stoeckel, PhD (chap. 4)
Siemens Medical Solutions USA
660 First Avenue
New York, NY 10016, USA
(917) 584-2356
Bernd.Stoeckel@siemens.com

Melissa Terpstra, PhD (chap. 12)
 Center for Magnetic Resonance Research
 University of Minnesota
 2021 Sixth Street SE
 Minneapolis, MN 55455-3007, USA
 (612) 626-2001
 melissa@cmrr.umn.edu

Keith Thulborn, PhD (chap. 5)
 Center for Magnetic Resonance
 Research
 University of Illinois at Chicago
 Room 1A, 1801 West Taylor Street
 Chicago, Illinois 60612, USA
 (312) 355-3755
 kthulbor@uic.edu

Ivan Tkac, PhD (chap. 10, 12)
 Center for Magnetic Resonance
 Research
 University of Minnesota
 2021 Sixth Street SE
 Minneapolis, MN 55455-3007, USA
 (612) 626-2001
 ivan@cmrr.umn.edu

Christina Triantafyllou, PhD (chap. 4)
 Department of Radiology, MGH
 Building 149, Room 2301, 13th Street
 Charlestown, MA 02129, USA
 (617) 726-2933
 christin@nmr.mgh.harvard.edu

Kâmil Uğurbil, PhD (chap. 10)
 Center for Magnetic Resonance Research
 University of Minnesota
 2021 Sixth Street SE
 Minneapolis, MN 55455-3007, USA
 (612) 626-2001
 kamil@cmrr.umn.edu

J. Thomas Vaughn, PhD (chaps. 6, 10)
 Center for Magnetic Resonance
 Research
 University of Minnesota
 2021 Sixth Street SE
 Minneapolis, MN 55455-3007, USA
 (612) 626-2001
 tommy@cmrr.umn.edu

Lawrence L Wald, PhD (chaps. 4, 11)
 Department of Radiology, MGH
 Building 149, Room 2301, 13th Street
 Charlestown, MA 02129, USA
 (617) 724-9706
 wald@nmr.mgh.harvard.edu

Jianli Wang, PhD (chap. 9)
 Department of Radiology
 Pennsylvania State University
 NMR/MRI Building, H066
 500 University Drive
 Hershey, PA 17033-0850, USA
 (717) 531-8044
 jlwang@psu.edu

Florian Wiesinger, PhD (chap. 10)
 Center for Magnetic Resonance
 Research
 University of Minnesota
 2021 Sixth Street SE
 Minneapolis, MN 55455-3007, USA
 (612) 626-2001
 florian@cmrr.umn.edu

Christopher J. Wiggins, PhD (chap. 4)
 Department of Radiology, MGH
 Building 149t, Room 2301, 13th Street
 Charlestown, MA 02129, USA
 (617) 726-4060
 wiggins@nmr.mgh.harvard.edu

Graham Wiggins, D.Phil (chap. 4)
 Department of Radiology, MGH
 Building 149, Room 2301, 13th Street
 Charlestown, MA 02129, USA
 (617) 726-4060
 gwiggins@nmr.mgh.harvard.edu

Essa Yacoub, PhD (chap. 10)
 Center for Magnetic Resonance
 Research
 University of Minnesota
 2021 Sixth Street SE
 Minneapolis, MN 55455-3007, USA
 (612) 626-2001
 yacoub@cmrr.umn.edu

Qing X. Yang, PhD (chap. 9)
Department of Radiology
Pennsylvania State University
NMR/MRI Building, H066
500 University Drive
Hershey, PA 17033-0850, USA
(717) 531-5856
gyang@psu.edu

Xiao-Hong Zhu, PhD (chap. 10)
Center for Magnetic Resonance Research
University of Minnesota
2021 Sixth Street SE
Minneapolis, MN 55455-3007, USA
(612) 626-2001
zhu@cmrr.unm.edu

FOREWORD

From the early examples of what was to be called MRI, extending the technique to higher fields than those of less than 0.1 T used in the first large-volume instruments was a goal, but the way there was unclear. The practical success of large superconducting magnets was a surprise, and the astonishment continued as they developed fields from 0.3 T to 0.6 T to 1.5 T, and even more, up to the now common 3T systems, and a few 4T machines, and now to about 100 times the fields used in the first medium- and large-bore devices.

In the early machines, low radiofrequencies of 4 MHz or so meant that RF coil designs were simple (even inexperienced undergraduates could design and build such circuits with little knowledge of more than DC electrical circuits), and the forces on gradient coils were small. The effects of magnetic susceptibility inhomogeneity in and around the object being imaged were negligible, and RF penetration depths were not a problem for human-scale samples. Everything began to change as higher fields and higher frequencies came into use, and the earlier idyllic simplicities began to seem quaint. The trend continued, however, driven by the increased signal-to-noise ratios and the resultant higher resolutions and speed available, and sophisticated engineering became more and more essential, not only for magnets but for gradient systems and radiofrequency transmitters and receivers, but also for better software for modeling and correcting distortions. Experts who had said, and even written, that frequencies above 10 MHz would never be practical watched in amazement as scientists and engineers pushed instrument performances to ever-higher levels at ever-increasing magnetic field strengths, as this volume demonstrates.

Also demonstrated here is a changing emphasis, from instrumentation to the early stages of concentrating on the unique applications that UHFMRI (or should we call it UHPMRI, P for performance) can bring to the science of magnetic resonance imaging. We are beginning to see the dramatically enhanced possibilities inherent in what were once viewed only as problems, especially magnetic susceptibility effects, but also higher frequencies and the effects of tissue conductivity on the transmission of RF signals. I believe that it is these trends that will characterize the next decade of this field, coupled, paradoxically, with the emerging field of ultra low field MRI. The wide middle range will continue to dominate most clinical practice for many years to come, but new growth is visible everywhere else.

Paul C. Lauterbur
June 2, 2005

PREFACE

This volume of Biological Magnetic Resonance is dedicated to recent progress in the development of Ultra High Field Magnetic Resonance Imaging (UHFMRI). The list of contributors arises from many of the most prominent UHFMRI sites, both in the United States and Europe. Consequently, this work represents a wonderful compendium of ideas and results. The images contained within these pages are stunning.

The presentation opens with a historical perspective by Pierre-Marie Robitaille. Following the introduction, the contents can be divided into three broad sections: (1) System integration and magnet design (chapters 2–5), (2) Radiofrequency (RF) coil design and theoretical aspects (chapters 6–9), and (3) Experimental findings (chapters 10–13). Interestingly, virtually all chapters touch (at least briefly) on the principle of reciprocity and signal to noise in UHFMRI. Of particular note, however, in this regard is chapter 7. In this chapter, Ibrahim reiterates his recently published mathematical findings that the excitation of the spins cannot be explained using the standard form of the principle of reciprocity. This is due to the asymmetry in the permeability tensor of the transverse magnetization. This theoretical conclusion is certain to have important consequences in magnetic resonance. In addition to discussions focused on signal and noise, several chapters address dielectric resonances including most notably contributions by Robitaille (chapter 1), Ibrahim (chap. 7), Collins (chap. 8) and Uğurbil et al. (chap. 10). The same interest is also maintained throughout the work relative to RF power requirements.

The section on System Integration and Magnet Design begins with chapter 2, wherein John Bird and his colleagues at Magnex Scientific detail much of the engineering aspects of UHF magnet construction. Then follows Douglas Kelley from General Electric (chapter 3), who provides an overview of system integration. For those who have not yet participated in the assembly of such a system, this chapter may act as a handy guide. Franz Schmitt and the group at Siemens then present a chapter on the design of a clinical UHFMRI system. The images and approaches contained therein are both superb and educational. Finally, in chapter 5, Keith Thulborn provides an excellent overview of the challenges involved in integrating a 9.4T human scanner. The chapter is of note particularly for site preparation and is highly recommended reading for everyone at that stage of the process. In addition, sodium images of a non-human primate are presented at 9.4 T that hint at the promise of great things to come at this field strength.

The next three chapters address the important problem of RF coil design, both practically and theoretically. As such, the section on RF Coils and Theoretical Aspects is led most appropriately by Thomas Vaughn, the primary force behind the growth and use of the TEM resonator. In chapter 6, Dr. Vaughn focuses on the theoretical and experimental aspects of RF coil design at UHF frequencies with particular emphasis on this coil. The chapter is particularly noteworthy for the head and body images it provides. Chapter 7 highlights much of the theoretical work done by the RF group at OSU. Written by Dr. Ibrahim, the chapter contains a wealth of theoretical results with the FDTD method and excellent descriptions of RF coil/head interactions in UHFMRI. As stated above, this chapter is unique in the manner in which it addresses the principle of reciprocity. It also presents computational findings from Dr. Ibrahim and the OSU group relative to anticipated RF power findings in MRI. A similar approach to understanding RF coils is presented in chapter 8 by Christopher Collins. In fact, it is interesting to compare chapters 7 and 8 due to the similarity of approaches. The theoretical section finishes with chapter 9, in which Qing Yang and his colleagues address magnetic susceptibility. The chapter is of note not only for its extensive and detailed treatment of the subject matter, but also for the outstanding images it contains. Corrections for susceptibility effects promise to become an ever more important aspect of work at UHF, and this chapter is required reading for anyone interested in the topic.

The section on Experimental findings opens with a contribution from the Center for Magnetic Resonance Research at the University of Minnesota. This chapter sets much of the tone for the future of UHFMRI and is noteworthy for the awesome assembly of results it presents. The chapter includes not only theoretical discussions but also an excellent presentation of functional MRI at high fields. Then follows chapter 11 and the work of Lawrence Wald and his colleagues at Massachusetts General Hospital. The power of UHFMRI in obtaining high-resolution images is well demonstrated in this chapter, and the authors have done a superb job of capturing all its important aspects. This also promises to be one of the key areas of MRI research in the future, and Wald et al. clearly illuminate the path. Some of the images contained in chapter 11 are simply stunning. The experimental section then presents a chapter (12) by Rolf Gruetter and his colleagues on clinical spectroscopy. Clearly, human scanners with frequencies of 300 MHz will have distinct advantages in chemical shift dispersion relative to 1.5 or even 3T instruments. Gruetter's chapter is noteworthy for the detailed manner in which he addresses the spectroscopic problem. Finally, the volume closes with a chapter by Vera Novak and Greg Christoforidis on the clinical promise of UHFMRI (chapter 13). The images contained therein were obtained at 8 Tesla and call upon us all to bring UHFMRI to the clinical setting as soon as possible. In this regard, these investigators are to be commended for undertaking the arduous task of examining clinical subjects at UHF and of outlining for all to see the tremendous value of these scanners.

In closing, it is our hope that, whether you are a novice or an expert in MRI, you will gain not only insight but also pleasure in reading the pages that are about to follow. We are at the dawn of a new era in magnetic resonance, and it is our hope that this work will help spur us all forward in making UHFMRI a clinically important modality.

Pierre-Marie L. Robitaille
Columbus, Ohio

Lawrence J. Berliner
Denver, Colorado

CONTENTS

Chapter 1

Ultra High Field Magnetic Resonance Imaging: A Historical Perspective

Pierre-Marie L. Robitaille

1. Introduction	1
2. Ultra High Field MRI	2
3. Conclusion	7

Chapter 2

Design Considerations for Ultra High Field MRI Magnet Systems

*John Bird, Darren Houlden, Nick Kerley, David Rayner,
David Simkin, and Simon Pittard*

1. Introduction	19
2. The Evolution of High Field MRI	19
3. Magnet Design Strategies	11
4. Cryostats	27
5. Shielding	30
6. Shimming	32
7. MRI above 9.4 Tesla	37
8. The Future of MRI	40
9. Conclusions	42

Chapter 3

Hardware Considerations in Ultra High Field MRI: An Overview of System Integration

Douglas A. C. Kelley

1. Introduction	45
2. Motivation for UHFMRI	46
3. Magnets for UHFMRI	47

4. Gradient Coils and Drivers	50
5. RF Coils and Coil Interfaces	51
6. Design Characteristics and Considerations	53
7. Conclusions	55

Chapter 4

Aspects of Clinical Imaging at 7 T

Franz Schmitt, Andreas Potthast, Bernd Stoeckel, Christina Triantafyllou, Christopher J. Wiggins, Graham Wiggins, and Lawrence L. Wald

1. Introduction	59
2. General System Configuration of a 7T Clinical MRI System	62
3. Challenges of Clinical Imaging at 7 T	83
4. Clinical Scanning on 7 T	87
5. Summary	96

Chapter 5

The Challenges of Integrating a 9.4T MR Scanner for Human Brain Imaging

Keith R. Thulborn

1. Introduction	105
2. Choice of Magnetic Field Strength	106
3. Site Planning	107
4. Results	123

Chapter 6

Ultra High Field MRI:High-Frequency Coils

J. Thomas Vaughan

1. Introduction	127
2. RF Coil Losses	128
3. Efficient Coil Design	132
4. Volume Coils	142
5. Conclusion	156

Chapter 7

A Perspective into Ultra High Field MRI RF Coils*Tamer S. Ibrahim*

1. Introduction	163
2. The Approach to RF Coil Design: Now and Then	164
3. RF Coil Simulator Using the FDTD Method	167
4. RF Power Requirements in MRI	174
5. The Road to Clinically Useful Images	178
6. Concluding Remarks	202

Chapter 8

Radiofrequency Field Calculations for High Field MRI*Christopher M. Collins*

1. Introduction	209
2. Electromagnetic Properties of Tissue as Functions of B_1 Frequency	210
3. Numerical RF Field Calculations: The FDTD Method	212
4. Relating Field Calculation Results to MRI	222
5. Results of RF Field Calculations for High Field MRI	233

Chapter 9

Magnetic Susceptibility Effects in High Field MRI*Qing X. Yang, Michael B. Smith,
and Jianli Wang*

1. Introduction	249
2. Magnetic Susceptibility	250
3. T_2^* Contrast at High Magnetic Field	251
4. Magnetic Susceptibility Effect: A Blessing and Curse for High Field MRI	253
5. Characterization of Magnetic Susceptibility-Induced Field Distortion	254
6. Magnetic Field Inhomogeneity Artifacts and Reduction	258
7. Image Blurring and Geometric Distortion Artifacts in Rapid Imaging and Correction	270
8. Final Remarks	280

Chapter 10

High Magnetic Fields for Imaging Cerebral Morphology, Function, and Biochemistry

Kâmil Uğurbil, Gregor Adriany, Can Akgün, Peter Andersen, Wei Chen, Michael Garwood, Rolf Gruetter, Pierre-Gilles Henry, Malgorzata Marjanska, Steen Moeller, Pierre-François Van de Moortele, Klaas Prüssmann, Ivan Tkac, J. Thomas Vaughan, Florian Wiesinger, Essa Yacoub, and Xiao-Hong Zhu

1. Introduction	285
2. Signal-to-Noise Ratio	287
3. Image Intensity and B_1 Nonuniformities at High Magnetic Fields	291
4. Morphological Imaging of Brain Tissue	295
5. Functional and Physiological Imaging in the Brain	300
6. Parallel Imaging	321
7. Imaging Using Low-Gyromagnetic Nuclei	322
8. Spectroscopy at High Magnetic Fields	325
9. Conclusion	331

Chapter 11

High-Resolution and Microscopic Imaging at High Field

Lawrence L. Wald, Bruce Fischl, Bruce R. Rosen

1. Introduction	343
2. MR Instrumentation for Microimaging	344
3. Myelin-Based Microimaging Cortical Lamina	352
4. Microimaging in the ex-vivo Human Brain	360
5. Conclusions	366

Chapter 12

In-vivo NMR Spectroscopy of the Brain at High Fields

Rolf Gruetter, Pierre-Gilles Henry, Hongxia Lei, Silvia Mangia, Gülin Öz, Melissa Terpstra, and Ivan Tkac

1. Introduction	373
2. General Sensitivity Considerations	374
3. RF Considerations	376
4. In-vivo ^{13}C NMR Spectroscopy	380
5. In-vivo ^1H NMR Spectroscopy	384

6. Insights from High Field NMR Spectroscopy Studies of the Brain	388
7. Outlook.....	400

Chapter 13

Clinical Promise: Clinical Imaging at Ultra High Field

Vera Novak and Gregory Christoforidis

1. Introduction	411
2. High-Resolution Anatomical Imaging.....	412
3. Cerebrovascular Small-Vessel Disease	416
4. Stroke Imaging	419
5. Tumor Imaging.....	423
6. Functional MRI and Spectroscopy	430
7. Safety and Limitations	431
8. Conclusions	432
 Contents of Previous Volumes	 439
Index	463

ULTRA HIGH FIELD MAGNETIC RESONANCE IMAGING: A HISTORICAL PERSPECTIVE

Pierre-Marie L. Robitaille

Department of Radiology, The Ohio State University

1. INTRODUCTION

As one recalls the 1970s and some of the first steps in magnetic resonance imaging [1–4], it is easy to discern the great strides that have been made in this discipline over the past 30 years [5–7]. Early coarse and grainy results [4] have given way to exquisite anatomical and functional images [5–7]. The availability of MRI is now synonymous with quality of medical care, even within the rural hospital setting, and the 1.5 Tesla scanner has become a workhorse of the modern radiological exam. With the exception of CT, and this primarily in the abdomen, no other radiological modality can compete with MRI, not only in terms of the breadth of exams currently possible, but also in the future promise of the technique. Indeed, it seems that every year new clinical applications join the arsenal of MRI exams. Soon, it is anticipated that MRI will be able to fully scan the entire body [8] in great detail, including the most difficult thoracic [9–17] and abdominal locations [18–22]. Technical advancements forged and tested in the research laboratories of the world [23–40] continue to add to the versatility and power of MRI scanners. Nonetheless, what is perhaps most fascinating relative to the evolution of MRI is the seemingly untapped potential that remains. The spawning of new techniques may well open up tremendous venues for MRI in the coming decades. Thus, the clinical horizon is imperceptible. One is left only with the realization that future progress may well surpass all contributions to date.

In fact, it is clear that many aspects of MRI are, if not in their infancy, at least in their childhood. These include interventional MRI [41–44], MR spectroscopy, in-vivo EPR [45], ultra low field MRI [46], and, of course, ultra high field MRI. In addition, future discoveries in probes, molecular targeting, pharmaceutical monitoring, and contrast enhancement methods are sure to further amplify the unimaginable promise of magnetic resonance [47–56]. In the past 10 years, a revolution has slowly begun to take place in image acquisition techniques with the introduction of phased arrays [23] and partially parallel imaging techniques [24–27, 35]. The power of these new approaches has proven so phenomenal that their advent,

for now, far surpasses in importance the push toward higher fields. Indeed, technology-based improvements in imaging are far from reaching a plateau. As such, if MRI as a discipline suffers from a single affliction, it is in a lack of resources to fully pursue all of these avenues.

2. ULTRA HIGH FIELD MRI

It is anticipated that, by the beginning of 2008, at least 30 UHFMRI systems will dot the globe. Less than eight years will have elapsed from the construction of the first UHFMRI magnet [57] and the first two UHFMRI systems [58–61]. Industrial concerns are investing significant financial and human resources toward the clinical development of this modality. As a result, virtually all new UHFMRI systems are now being produced by the major MRI vendors: Siemens, GE, and Phillips. UHFMRI is being rushed into the clinical arena in a manner clearly distinct from the long and arduous experimental stage surrounding the world's 4 Tesla systems.

Almost from the inception of UHFMRI, the 7 Tesla magnet has been destined to play a dominant role in clinical investigation [60,61]. With its 90-cm bore size, the aforementioned system results in a clinical instrument that is clearly superior to an 8 Tesla/80-cm magnet [57–59]. This is true both in terms of patient comfort and potential gradient performance. In the end, a small concession in field strength (3 rather than 4, 7 rather than 8) is made for the promise of greater bore size, and perhaps, lower production costs. The 8T system, like the 4T system, seems destined to play a purely experimental role in the development of MRI. Clinical practice will take place at 3 and 7 T.

2.1. From Concept to Reality

2.1.1. Theoretical Arguments

In retrospect, it seems like the decision to advance toward Ultra High Fields was nothing but logical. After all, the Boltzmann equation has always provided sufficient impetus for increasing field strength, at least in NMR. However, the situation in MRI was not all that clear in the late 1990s. Almost since the inception of MRI as a technique, skepticism has surrounded the increase to higher fields. This was especially true for the first UHFMRI systems. For much of the scientific community, there was real concern relative to the feasibility of such an adventure. In fact, this position made ample sense given that early warnings had always existed about RF penetration problems [62,63], RF power requirements [64–67], susceptibility artifacts, and insurmountable dielectric resonance phenomena [63,68]. Toft had advanced the notion that dielectric resonances should not play a dominant role in human MRI [69]. Yet confusion on this issue still prevailed. Concerns were uttered that fundamental dielectric resonances would produce signal voids in the

head that could not be overcome. Moreover, even if a system could be built, RF power requirements should render the low flip angle gradient echo methods the only feasible imaging sequences. Indeed, it seemed that sufficient physical limitations existed to stop any move much beyond 4 Tesla, where RF power, susceptibility, and dielectric resonances were already being advanced as significant issues [62–69]. Beyond these physical difficulties, there awaited the technical challenge of producing a UHFMRI magnet. There was also real doubt that a suitable RF coil could ever be constructed. Such was the theoretical atmosphere that surrounded the birth of Ultra High Field MRI.

2.1.2. *Experimental Results*

At the same time, sufficient progress had been made at 4 T to invite inquiry into higher field strengths [68,70–92]. It is true that the early 4 Tesla images (late 1980s and early 1990s) were plagued by inhomogeneity and poor contrast [68,70–72]. In large measure this was a manifestation of the suboptimal performance of the birdcage coil at these fields. As a result, considerable investment was made in the development of RF coils more apt to acquire suitable images at 4 T. Soon Roeschmann, while working at Phillips, introduced the use of the TEM resonator [78]. Further advancements in this design were brought forth by Vaughn [79,80] and improvements in both sensitivity and homogeneity were marked. Still today, the TEM resonator holds a prominent place in high-field imaging at 4 T, and this resonator would be responsible for acquiring the first results at UHF frequencies [93].

In conjunction with progress in RF coils, improvements were also made in image acquisition. Thus, although the initial 4T images lacked contrast, this was soundly reversed in the early 1990s when Garwood and Ugurbil acquired the first MDEFT images at this field strength using an experimental SISCO system in California. For whatever reason, the presentation of these results was delayed until publication of a more extensive work [74], yet private viewing left no doubt in anyone's mind as to what could be accomplished at high fields. The first BOLD-based human fMRI paper soon followed [75], along with a group of simply spectacular results in fMRI at high field [94,95]. Without question, the advantage of high fields in fMRI has now been firmly established. Excellent human body imaging has been demonstrated at 4 T [96], and while UHF systems already existed at the time these last results were published, they nonetheless point the way to what will be possible at 7, 8, and 9.4 T [97–100].

Beyond imaging, high fields also held tremendous promise for spectroscopy. As such, Vaughn further modified the TEM resonator to enable double-tuned $^{31}\text{P}/^1\text{H}$ and $^{13}\text{C}/^1\text{H}$ studies. This allowed ^{31}P spectroscopic imaging [81,82] and measurements of the TCA cycle using ^{13}C glucose infusions [83]. While early work at 4 T was largely single voxel, multi-voxel methods revealed that significant improvements in SNR [84,85] and spectral resolution were attainable at this field strength [86,87]. Despite perceived technical hurdles relative to decreasing T_2^* and increasing B_0 and B_1 inhomogeneity at 4 T, the problems were surmountable. The

expected increases in SNR and spectral resolution would ultimately be realized. High-resolution spectroscopic images would reveal significant metabolite heterogeneity in gray and white matter [85,101]. Eventually, Hetherington et al. generated the first statistical maps of metabolic abnormalities [88,102]. The clinical utility of high-field spectroscopy was slowly being demonstrated, and this continued beyond the arrival of the first UHFMRI systems [89,90,103–107]. Very-high-resolution spectroscopy was established [105], and the world's first transmurally resolved phosphorus spectrum was obtained from the human heart [76]. Scientific reports began to demonstrate definite improvements in ^1H NMR studies of the human brain. Importantly, it was demonstrated that the ^1H glucose peak could be accurately resolved and thus enable unambiguous quantification of tissue glucose [77]. Improvements in resolution demonstrated that PCr could be resolved from Cr in the human brain spectrum [105]. This further strengthened arguments in favor of increased chemical shift dispersion at higher fields.

Thus, while daunting theoretical arguments flourished, experimental findings suggested that indeed there was great promise much beyond 4 T. In part, the animal scanners were responsible for this confidence. Concerns remained particularly relative to the RF power requirements at Ultra High Field. Indeed, the B_0^2 dependence of RF power had been well documented by comparing RF power requirements at 1.5, 3, and 4 T [65]. Unfortunately, there was a paucity of data in the MR community relative to actual power requirements. The issue was further complicated by the use of various RF coil designs and Q values. Yet, if RF power requirements were indeed daunting, perhaps other spin excitation methods would come to be developed. In any case, it was clear that if there was a limit to human MRI imaging in the immediate future it would lie somewhere between 4 and 8 T. The goal, in essence, was to find that field strength. If an image could not be produced at 8 T, perhaps it could at 7, 6, or even 5 T. It was certain that each of these fields could be reached using an 8 Tesla magnet and four fully broad-banded transceiver channels. Concerns remained, but the promise contained within the Boltzmann equation continued to be the decisive factor.

2.2. Early Ultra High Field Results

Eventually, and with the construction of a suitable magnet [57], some of the experimental and theoretical anxiety began to dissipate. Rapid acquisition of the first UHF image was to dispel much of the remaining doubt [58]. RF power and dielectric resonance concerns lingered [108–109] but were countered [110–111]. As more studies began to confirm the promise and power of UHFMRI [60,112–121], doubt began to fade. With the advent of the first high-resolution 8 Tesla images [122] and the early functional and spectroscopic studies [61,101,123–128], clinical usefulness became unquestionable [112–128]. Human studies at 7 Tesla have now demonstrated clear improvements in detectability, reproducibility, and specificity of fMRI at ultra high fields [123–128]. These results are beginning to be

echoed [129]. With the advent of proper RF coil excitation, UHFMRI is slowly beginning to produce images of consistently excellent quality.

2.2.1. Dielectric Resonances

As clinically important images began to appear [118–122], the physical issues that had so held back the advancement of MRI seemed to lose importance. Most agree with the initial statements [110–111] that dielectric resonances play no important role in human UHFMRI [130–132]. However, it is somewhat surprising to see how many years it took to resolve the issue. True dielectric resonance would have spelled the downfall of any move to higher fields. Dielectric resonances, as fundamental entities, cannot be compensated for simply by changes in RF excitation or RF coil design. They remain a manifestation of the sample itself, including its geometry. As such, it was critical to the success of UHFMRI that no fundamental dielectric resonances exist in MRI. Early on in the history of UHFMRI the inhomogeneity seen on UHF images was properly ascribed to RF coil/sample interactions [93], and virtually every group now recognizes that dielectric resonances are without much consequence in human MRI [see Chapters 7, 8 and 10]. Nonetheless, few can appreciate the challenge that the presence of fundamental dielectric resonances could have posed for those seeking ever higher fields in the late 1990s.

2.2.2. RF Penetration

As for RF penetration, the issue appears without much interest. The subject became somewhat resolved when the center of the human head became readily visible in the first 8 T image [58]. Nonetheless, the fact that it is possible to image so deep within the human head at UHF frequencies without any evidence of RF penetration problems should give some of us cause to ponder [117]. As highlighted by Professor Lauterbur in the Foreword, how often had this issue been advanced prior to the advent of UHFMRI as a fatal flaw in any dream about higher fields?

2.2.3. RF Power Requirements and Noise Power

Given anticipated B_0^2 behavior for RF power requirements, it was little wonder that the first UHFMRI system was equipped with enough RF power to deliver a 10-kW RF pulse at 340 MHz. In retrospect, it is now clear that many of the pre-UHFMRI concerns were overstated [62–67]. RARE and MDEFT images [113–114] have now been acquired that were previously considered impossible at UHF frequencies. Some of these sequences had recourse to adiabatic excitations previously thought to be impractical [108]. RF power requirements are lower than what had been expected [58], and the surest demonstration of this fact is the explosive move to higher fields. The B_0^2 relationship [64–65] simply does not hold beyond 4 T in MRI, as stated early on [58]. Nonetheless, the behavior of RF power as a function of field strength has yet to be defined fully. Measurements at 7 T suggest that RF power increases linearly from 4 to 7 T [61]. However, 8T results [58] and FDTD calculations [133–134] suggest that RF power must drop eventually with

field strength. To believe otherwise ignores thermodynamic principles [135–136]. In this regard, the low RF power requirements of an 800-MHz high-resolution spectrometer should be considered.

Ultimately, RF power requirements are also related to noise power [137]. Consequently, knowledge of RF power profiles will enable the MRI scientist to move beyond the Nyquist equation and simple analytical expressions in an understanding of noise power in MRI [58,137].

Whatever the outcome, it is clear that given the advent of 9.4T systems and the drive toward 11.7 T, RF power requirements will no longer present the insurmountable challenge imagined prior to the advent of UHFMRI [58]. Nonetheless, considering the importance of quantifying RF power requirements as a function of field strength, it is surprising how little effort is currently being made in obtaining such measurements in MRI while properly considering corrections for RF coil performance.

2.3. RF Coils

The excellence of all UHFMRI results depends ultimately on RF coil performance. From the early days of UHFMRI, it was realized that understanding RF coil/head interaction was key to obtaining a homogeneous image [93]. In this respect, computational approaches remain central to the development of this field. Nonetheless, the early UHF results were at a disadvantage since they were not guided by computational results. This is because initial computational work completely ignored the RF coil/head interaction. Typically, the field map of the RF coil was calculated. The field was obtained and the head inserted into the field without any consideration for changes caused on the coil itself. As such, the early computational results shed little light on the problem. It was only with a proper understanding of the RF coil/head interaction that progress began to be made [138]. Soon it was demonstrated that the RF field within the head could be optimized by the manner in which the head was excited [139]. This theoretical work has now been elegantly demonstrated experimentally [140–142]. Phased-array methods [143–145] that can readily invoke such B_1 optimization concepts are also emerging. These approaches depend on the incorporation of multiple transceivers [59]. Such “ B_1 shimming” [139–145] promises to be the cornerstone of UHFMRI in the future. Wald et. al. [146] provide additional insight into these problems through a direct comparison of TEM, birdcage, and phased-array methods at ultra high fields.

2.4. Safety

It appears that UHFMRI continues to provide a clinically safe diagnostic technique. Indeed, an extensive review of the literature confirms the innocuous nature of these approaches [147]. At the same time, since the advent of UHFMRI [147–153], there has been significant effort expended in understanding MR safety at Ultra High Fields. Physiological monitoring [148] and psychological measures

[150] point to the relative safety of UHFMRI. Exposure of rodents to ultra high fields for extended periods revealed no subchronic effects [153]. Nonetheless, perhaps it is prudent to move away from macroscopic measures of high-field safety or gross physiological changes [148] to more important microscopic measures at the cellular level. Thus, recent isolated cell experiments are cause for some caution [154]. The finding that ultra high fields can cause substantial, and at times non-reversible [above 10 Tesla], changes in the cellular cytoskeleton was somewhat unexpected, even though B_0 interactions with large macromolecular assemblies had been considered [147]. As such, much more studies of this nature may be warranted in conjunction with the push to still higher fields. It may be appropriate to further document any potential effects of Ultra High Fields on the cellular cytoskeleton. Furthermore, it may be advisable to augment similar studies to include not only isolated cells but also whole organs and animals. In the meantime, prudence dictates that clinical exposure to Ultra High Fields be appropriately limited. As a scientific community, it is also important to have the courage to push science forward. MRI remains, by far, the most powerful imaging modality, especially relative to its apparent lack of significant biological effects.

2.5. Clinical Results

Beyond the tremendous push toward fMRI [123–129], there has been a concerted effort to obtain clinical results at ultra high fields [119–120,122,155–161]. In large measure, the early results were centered on presenting an overview of neuroradiological imaging at ultra high fields [119–120,122]. However, since then, projects have materialized with a clear emphasis on clinical medicine [see Chapters 11 and 13]. In addition to truly impressive ex vivo findings [162], there have been concerted efforts toward an understanding of findings in stroke in vivo [158–159]. Studies of human glioblastomas, both in vivo and ex vivo, have also appeared [160–161]. Finally, there has been a focus on improving initial high-resolution results. The roadmap that has been drawn up is extremely promising [see Chapter 11]. Within the next decade, UHFMRI is certain to make increased contributions to the clinical practice of radiology. In fact, now that many of the early technical hurdles have been all but eliminated, the time is right for a pronounced initiative in the clinical application of UHFMRI.

3. CONCLUSION

Human progress does not arise by accident. Someone must first dream, and then work toward realization of that dream. This is true in all aspects of human life, whether scientific or political. Yet dreams are seldom realized in isolation. Others must rally toward the goal. Ultra High Field MRI has now entered a phase where its further dissemination will depend on the efforts of countless individuals around the globe. Once more, progress will hinge on the unique synergy found in the MRI community between scientist, engineer, and clinician. Given this situation, the fu-

ture for UHFMRI is indeed very bright and a complete anatomical, physiological, and metabolic exam may well be within the grasp of this modality. Many dreams remain unfulfilled, especially in the minds of the new generation with respect to MRI. Realizing these new dreams will require daring, the determination to succeed, and the self-confidence to take yet another step into the unknown.

4. REFERENCES

1. Lauterbur PC. 1973. Image formation by induced local interactions: example employing nuclear magnetic resonance. *Nature* **242**:190–191.
2. Mansfield P, Maudsley AA. 1977. Medical imaging by NMR. *Br J Radiol* **50**:188.
3. Mansfield P. 1977. Multi-plane image formation using NMR spin echoes. *J Phys C* **10**:L55.
4. Mansfield P, Morris PG. 1982. *NMR imaging in biomedicine*. New York: Academic Press.
5. Stark D, Bradley WG. 1999. *Magnetic resonance imaging*. St. Louis: Mosby.
6. Runge VM, Nitz WR, Schmeets SH, Faulkner WH, Desai NK. 2005. *The physics of clinical MR taught through images*. New York: Thieme Medical Publishers.
7. Buxton, Richard B. 2002. Introduction to functional magnetic resonance imaging: principles and techniques. Cambridge: Cambridge UP.
8. Lauenstein TC, Gochde SC, Herborn CU, Goyen M, Oberhoff C, Debatin JF, Ruehm SG, Barkhausen J. 2004. Whole-body MR imaging: evaluation of patients for metastases. *Radiology* **233**:139–148.
9. Leiner T, Katsimaglis G, Yeh EN, Kissinger KV, van Yperen G, Eggers H, Manning WJ, Botnar RM. 2005. Correction for heart rate variability improves coronary magnetic resonance angiography. *J Magn Reson Imaging* **22**:577–582.
10. Kim WY, Danias PG, Stuber M, Flamm SD, Plein S, Nagel E, Langerak SE, Weber OM, Pedersen EM, Schmidt M, Botnar RM, Manning WJ. 2001. Coronary magnetic resonance angiography for the detection of coronary stenosis. *N Engl J Med* **345**:1863–1869.
11. Weber OM, Martin AJ, Higgins CB. 2003. Whole-heart steady-state free precession coronary artery magnetic resonance angiography. *Magn Reson Med* **50**:1223–1228.
12. Katoh M, Stuber M, Buecker A, Gunther RW, Spuentrup E. 2005. Spin-labeling coronary MR angiography with steady state free precession and radial k-space sampling: initial results in healthy volunteers. *Radiology* **236**:1047–1052.
13. Sakuma H, Ichikawa Y, Suzawa N, Hirano T, Makino K, Koyama N, van Cauteren M, Takeda K. 2005. Assessment of coronary arteries with total study time of less than 30 minutes by whole heart coronary MR angiography. *Radiology* **237**:316–321.
14. Deitrich O, Losert C, Attendberger U, Fasol U, Peller M, Nikolaou K, Reiser MF, Schoenberg SO. 2005. Fast oxygen-enhanced multislice imaging of the lung using parallel acquisition techniques. *Magn Reson Med* **53**:1317–1325.
15. Wild JM, Fischele S, Woodhouse N, Paley MNJ, Kasuboski L, van Beek EJR. 2005. 3D volume-localized pO₂ measurement in the human lung with ³He MRI. *Magn Reson Med* **53**:1055–1064.
16. Moeller HE, Chen XJ, Saan B, Hagspiel KD, Johnson GA, Altes TA, de Lange EE, Kauczor HU. 2002. MRI of the lungs using hyperpolarized noble gases. *Magn Reson Med* **47**:1029–1051.

17. Finck C, Puderback M, Bock M, Lodemann KP, Zuna I, Schmahl A, Delorme S, Kauczor HU. 2004. Regional lung perfusion: assessment with partially parallel three-dimensional MR imaging. *Radiology* **231**(1):175–184.
18. Ryeom HK, Che BH, Kim JY, Kwon S, Ko CW, Kim HM, Lee SB, Kang DS. 2005. Biliary afresia: feasibility of mangafodipir trisodium-enhanced MR cholangiography for evaluation. *Radiology* **235**:250–258.
19. Ward J, Sheridan MB, Guthrie JA, Davies MH, Millson CE, Lodge JPA, Pollard SG, Prasad KR, Toogood GJ, Robinson PJ. 2004. Bile duct structures after hepatobiliary surgery: assessment with MR cholangiography. *Radiology* **231**:101–108.
20. Zuo CS, Seoane PR, Hu J, Harnish PP, Rofsky NM. 2004. MR imaging of the stomach: Potential use for mangafodipir trisodium: a study in swine. *Radiology* **232**:160–163.
21. Bielen DJLE, Bosmans HTC, DeWever LLI, Maes F, Tejpar S, Vanbeckevoort D, Marchal GJF. 2005. Clinical validation of high resolution fast spin-echo MR colonography after colon distention with air. *J Magn Reson Imaging* **22**:400–405.
22. Ajaj W, Debatin JF, Lauenstein T. 2003. Dark lumen magnetic resonance colonography: comparison with conventional colonoscopy for the detection of colorectal pathology. *Gut* **52**:1738–1743.
23. Roemer PB, Edelstein WA, Hayes CE, Souza SP, Mueller OM. 1990. The NMR phased array. *Magn Reson Med* **16**:192–225.
24. Kelton JR, Magin RL, Wright SM. 1989. An algorithm for rapid image acquisition using multiple receiver coils. *Proc Soc Magn Reson Med* 1172.
25. Ra JB, Rim CY. 1993. Fast imaging using subencoding data sets from multiple detectors. *Magn Reson Med* **30**:142–145.
26. Carlson JW, Minemura T. 1993. Image time reduction through multiple receiver coil data acquisition and image reconstruction. *Magn Reson Med* **29**:681–687.
27. McDougall MP, Wright SM. 2005. 64-channel array coil for single echo acquisition magnetic resonance imaging. *Magn Reson Med* **54**:386–392.
28. Hayes CE, Edelstein WA, Schenck JR, Mueller OM, Eash M. 1985. An efficient, highly homogeneous radiofrequency coil for whole-body NMR imaging at 1.5 T. *J Magn Reson* **63**:6222–628.
29. Roemer PB, Edelstein WA. 1986. Shelf-shielder gradient coils. *Proc Soc Magn Reson Med* 1067.
30. Mansfield P, Chapman B. 1986. Active magnetic screening of coils for static and time dependent magnetic field generation in NMR imaging. *J Phys E: Sci Instrum* **19**:541–546.
31. Stehling MK, Turner R, Mansfield P. 1991. Echo planar imaging: magnetic resonance imaging in a fraction of a second. *Science* **254**: 43–50.
32. Henning J, Nauwerth A, Friedburg H. 1986. Rare imaging: a fast imaging method for clinical MR. *Magn Reson Med* **3**:823–833.
33. Haase A, Frahm J, Matthaei D, Hanicke W, Merboldt KD. 1986. FLASH imaging: rapid NMR imaging using low flip angles. *J Magn Reson* **67**:258–266.
34. Sodickson DK, Manning WJ. 1997. Simultaneous acquisition of spatial harmonics [SMASH]: fast imaging with radiofrequency coils arrays. *Magn Reson Med* **38**:591–603.
35. Pruessmann KP, Weiger M, Scheidegger MB, Boesiger P. 1999. SENSE: Sensitivity encoding for fast MRI. *Magn Reson Med* **42**:952–962.
36. Bassler PJ, Mattiello J, LeBihan D. 1994. Estimation of the effective self diffusion tensor from the NMR spin-echo. *J Magn Reson B* **103**:247–254.

37. Basser PJ, Mattiello J, LeBihan D. 1994. MR diffusion tensor spectroscopy and imaging. *Biophys J* **66**: 259–267.
38. Vangelderden P, Devleeschouwer MHM, Despres D, Pekar J, VanZijl PCM, Moonen CTW. 1994. Water diffusion and acute stroke. *Magn Reson Med* **31**(2):154–163.
39. LeBihan D. 2003. Looking into the functional architecture of the brain with diffusion MRI. *Nature Rev Neurosci* **4**(6):469–480.
40. Wakana S, Jiang H, Nagae-Poetscher LM, van Zijl P, Mori S. 2004. Fiber tract-based atlas of human white matter anatomy. *Radiology* **230**:77–87.
41. Jolesz FA. 2005. Future perspective for intraoperative MRI. *Neurosurg Clin North Am* **16**(1):201.
42. Nimsky C, Ganslandt O, von Keller B, Romstock J, Fahlbush D. 2004. Intraoperative high-field strength MR imaging: implementation and experience in 200 patients. *Radiology* **233**:67–78.
43. Bradley WG. 2002. Achieving gross total resection of brain tumors: intraoperative MR can make a big difference. *Am J Neuroradiol* **23**:348–349.
44. JS Levine. 1999. Interventional MR imaging: concepts, systems, and applications in neuroradiology. *Am J Neuroradiol* **20**:735–748.
45. Gallez B, Swartz H. 2004. In vivo EPR: when, how and why? *NMR Biomed* **17**(5):223–225.
46. Tseng CH, Wong GP, Pomeroy VP, Mair RW, Hinton DP, Hoffman D, Stoner RE, Hersman FW, Cory DG, Walsworth RL. 1998. Low-field MRI of laser polarized noble gas. *Phys Rev Let* **81**(17):3785–3788.
47. Bhattacharya P, Harris K, Lin A, Mansson M, Norton VA, Perman WH, Weitekamp DP, Ross BD. 2005. Ultra fast steady state free precession imaging of hyperpolarized ^{13}C in-vivo. *MAGMA* **5**(5). In press.
48. Gilles RJ. 2002. In vivo molecular imaging. *J Cell Biochem* **39**(Suppl):231–238.
49. Herschman HR. 2003. Molecular imaging: looking at problems, seeing solutions. *Science* **302**:605–608.
50. Schmieder AH, Winter PM, Caruthers SD, Harris TD, Williams TA, Allen JS, Lacy EK, Zhang H, Scott MJ, Hu G, Robertson JD, Wickline SA, Lanza GM. 2005. Molecular MR imaging of melanoma angiogenesis with $\alpha_v\beta_3$ -targeted paramagnetic nanoparticles. *Magn Reson Med* **53**:621–627.
51. Butte JW, Ben-Hur T, Miller BR, Mizrachi-Kol R, Einstein O, Reinhartz E, Zywicke HA, Douglas T, Frank JA. 2003. MR microscopy of magnetically labeled neurospheres transplanted in the Lewis EAE rat brain. *Magn Reson Med* **50**:201–205.
52. Weissleder R, Moore A, Mahood U, Bhorade R, Benveniste H, Chiocca AE, Basilion JP. 2000. In-vivo magnetic resonance imaging of transgene expression. *Nat Med* **6**:351–355.
53. Louie AY, Huber MM, Ahrens ET, Rothbacher U, Moats R, Jacobs RE, Fraser SE, Meade TJ. 2000. In vivo visualization of gene expression using magnetic resonance imaging. *Nat Biotechnol* **18**:321–325.
54. Natanzon A, Aletras AH, Hsu Ly, Arai AE. 2005. Determining canine myocardial area at risk with manganese-enhanced MR imaging. *Radiology* **236**:859–866.
55. Ward J, Robinson PJ, Guthrie A, Downing S, Wilson D, Lodge JPA, Prasad KR, Toogood GJ, Wyatt JI. 2005. Liver metastases in candidates for hepatic resection: comparison of helical CT and gadolinium and SIPO-enhanced MR imaging. *Radiology* **237**:170–180.

56. Li W, Tutton S, Vu AT, Pierchal L, Li BSY, Lewis JM, Pravad PV, Edelman RR. 2005. First pass contrast enhanced magnetic resonance angiography in humans using ferumoxytol, a novel Ultrasmall Superparamagnetic Iron Oxide [USPIO]-based blood pool agent. *J Magn Reson Imaging* **21**:46–52.
57. Warner R, Pittard S, Feenan PJ, Goldi F, Abduljalil AM and Robitaille PML. 1998. Design and manufacture of the world's first whole body MRI magnet operating at a field strength above 7.0 Tesla: initial findings. *Proc Int Soc Magn Reson Med* 254.
58. Robitaille PML, Abduljalil AM, Kangarlu A, Zhang X, Yu Y, Burgess R, Bair S, Noa P, Yang L, Zhu H, Palmer B, Jiang Z, Chakeres DM, Spigos D. 1998. Human magnetic resonance imaging at eight tesla. *NMR Biomed* **11**:263–265.
59. Robitaille PML, Warner R, Jagadeesh J, Abduljalil AM, Kangarlu A, Burgess RE, Yu Y, Yang L, Zhu H, Jiang Z, Bailey RE, Chung W, Somawiharja Y, Feynan P, Rayner D. 1999. Design and assembly of an 8 tesla whole body MRI scanner. *J Comput Assist Tomog* **23**:808–820.
60. Yacoub, E, Shmuel A, Pfeuffer J, Van de Moortele PF, Adriany G, Anderson P, Vaughan JT, Merkle H, Ugurbil K, Hu X. 2001. Imaging human brain function in humans at 7 Tesla. *Magn Reson Med* **45**(4):588–94.
61. Vaughan JT, Garwood M, Collins CM, Liu W, DelaBarre L, Adriany G, Anderson P, Merkle H, Goebel R, Smith MB, Ugurbil K. 2001. 7T vs. 4T: RF power, homogeneity, and signal-to-noise comparison in head images. *Magn Reson Med* **46**(1):24–30.
62. Hoult DI, Lauterbur PC. 1979. The sensitivity of the zeugmatographic experiment involving humans. *J Magn Reson* **34**:425–33.
63. Roschmann P. 1987. Radiofrequency penetration and absorption in the human body — limitations to high field in whole-body nuclear magnetic resonance imaging. *Med Phys* **14**(6):922–931.
64. Bottomley PA, Edelstein WA. 1981. Power deposition in whole-body NMR imaging. *Med Phys* **8**:510–512.
65. Wen H, Denison TJ, Singerman RW, Balaban RS. 1997. The intrinsic signal-to-noise ratio in human cardiac imaging at 1.5, 3 and 4T. *J Magn Reson* **125**(1):65–71.
66. Chen CN, Sank VJ, Cohen SM, Hoult DI. 1986. The field dependence of NMR imaging, I: laboratory assessment of signal to noise ratio and power deposition. *Magn Reson Med* **3**:722–9.
67. Hoult DI, Chen CN, Sank VJ. 1986. The field dependence of NMR imaging, II: arguments concerning an optimal field strength. *Magn Reson Med* **3**:730–46.
68. Bomsdorf H, Helzel T, Kunz D, Roschmann P, Tschendel O, Wieland J. 1988. Spectroscopy and imaging with a 4 Tesla whole-body MR system. *NMR Biomed* **1**:151–158.
69. Toft PS. 1994. Standing waves in uniform water samples. *J Magn Reson* **B104**:143–147.
70. Barfuss H, Fisher H, Hentschel D, Ladebeck R, Vetter J. 1988. Whole-body MR imaging and spectroscopy with a 4T system. *Radiology* **169**:811–816.
71. Barfuss H, Fischer H, Hentschel D. 1990. In-vivo magnetic resonance of human with a 4T whole-body magnet. *NMR Biomed* **1**:31–45.
72. Bomsdorf H, Roschmann P, Wieland J. 1991. Sensitivity enhancement in whole-body natural abundance C-13 spectroscopy using C-13/H-1 double resonance techniques at 4 Tesla. *Magn Reson Med* **22**(1):10–22.
73. Wen H, Chesnick AS, Balaban RS. 1994. The design and test of a new volume coil for high field imaging. *Magn Reson Med* **32**(4):492–498.

74. Ugurbil K, Garwood M, Ellermann J, Hendrich K, Hinke R, Hu X, Kim SG, Menon R, Merkle H, Ogawa S, Salmi R. 1993. Imaging at high magnetic fields: initial experiences at 4 T. *Magn Reson Q* **9**(4):259–277.
75. Ogawa S, Tank DW, Menon R, Ellermann JM, Kim SG, Merkle H, Ugurbil K. 1992. Intrinsic signal changes accompanying sensory stimulation: functional brain mapping with magnetic resonance imaging. *Proc Natl Acad Sci USA* **89**(13):5951–5955.
76. Menon RS, Hendrich K, Hu X, Ugurbil K. 1992. ³¹P NMR spectroscopy of the human heart at 4 T: detection of substantially uncontaminated cardiac spectra and differentiation of subepicardium and subendocardium. *Magn Reson Med* **26**(2):368–376.
77. Gruetter R, Garwood M, Ugurbil K, Seaquist ER. 1996. Observation of resolved glucose signals in ¹H NMR spectra of the human brain at 4 Tesla. *Magn Reson Med* **36**(1):1–6.
78. Roschmann PKH. 1988. High-frequency coil system for a magnetic resonance imaging apparatus. US Patent 4,746,866.
79. Vaughan JT, Hetherington HP, Otu J, Pan JW, Pohost GM. 1994. High frequency volume coils for clinical NMR imaging and spectroscopy. *Magn Reson Med* **32**:206–218.
80. Vaughan J, Hetherington HP, Harrison J, Otu J, Pan J, Noa P, Pohost G. 1994. High frequency coils for clinical nuclear magnetic resonance imaging and spectroscopy. *Phys Med* **9**:147–153.
81. Twieg DB, Hetherington HP, Ponder SL, den Hollander JA, Pohost GM. 1994. Spatial resolution in ³¹P metabolite imaging of the human brain at 4.1 T. *J Magn Reson B* **104**:53.
82. Chu W-J, Hetherington HP, Kuzniecky RI, Vaughan JT, Twieg DB, Hugg JW, Elgavish GA. 1996. Is the intracellular pH different from normal in the epileptic focus of temporal lobe epilepsy patients? A ³¹P NMR study. *Neurology* **47**:756–760.
83. Pan JW, Mason GF, Vaughan JT, Chu W-J, Zhang YT, Hetherington HP. 1997. ¹³C editing of human brain glutamate by J-refocused coherence transfer spectroscopy at 4.1 T. *Magn Reson Med* **37**:355–358.
84. Hetherington HP, Pan JW, Mason GF, Ponder SL, Twieg DB, Deutsch G, Mountz J, Pohost G. 1994. 2D spectroscopic imaging of the human brain at 4T. *Magn Reson Med* **32**:530–534.
85. Hetherington HP, Mason GF, Pan JW, Pohost GM. 1994. Evaluation of cerebral gray and white matter metabolite differences by spectroscopic imaging at 4.1 T. *Magn Reson Med* **32**:565–571.
86. Mason G, Pan JW, Ponder SL, Twieg DB, Pohost GM, Hetherington HP. 1994. Detection of brain glutamate and glutamine in spectroscopic images at 4.1 T. *Magn Reson Med* **32**:142–145.
87. Pan JW, Mason GF, Pohost GM, Hetherington HP. 1996. Spectroscopic imaging of human brain glutamate by water suppressed J-refocused coherence transfer at 4.1 T. *Magn Reson Med* **36**:7–12.
88. Hetherington HP, Pan JW, Mason GF, Adams D, Vaughn JM, Twieg DB, Pohost GM. 1996. Quantitative ¹H spectroscopic imaging of human brain at 4.1 T using image segmentation. *Magn Reson Med* **36**:21–29.
89. Hetherington HP, Kuzniecky R, JW Pan, JT Vaughan, DB Twieg, GM Pohost. 1995. Application of high field spectroscopic imaging in the evaluation of temporal lobe epilepsy at 4.1 T. *Magn Reson Imag* **13**:1175–1180.

90. Hetherington HP, Kuzniecky R, Pan JW, Mason GF, Vaughan JT, Harris C, Morawetz H, Pohost GM. 1995. ^1H spectroscopic imaging in temporal lobe epilepsy at 4.1 T. *Ann Neurol* **38**:396–404.
91. Kuzniecky RI, Hetherington HP, Pan JW, Hugg JW, Palmer C, Gilliam F, Faught E, Morawetz R. 1997. Proton spectroscopic imaging in patients with malformations of cortical development and epilepsy. *Neurology* **48**:1018–1024.
92. Hugg JW, Kuzniecky RI, Gilliam FG, Morawetz RB, Faught RE, Hetherington HP. 1996. Normalization of contralateral metabolic function following temporal lobectomy demonstrated by ^1H MRSI. *Ann Neurol* **40**:236–239.
93. Robitaille PML. 1999. Black-body and transverse electromagnetic [TEM] resonators operating at 340 MHz: volume RF coils for UHFMRI. *J Comput Assist Tomog* **23**:879–890.
94. Lee S-P, Silva AC, Ugurbil K, Kim SG. 1999. Diffusion weighted spin echo fMRI at 9.4 T: microvascular/tissue contribution to BOLD signal changes. *Magn Reson Med* **42**(5):919–928.
95. Duong TQ, Kim DS, Ugurbil K, Kim SG. 2001. Localized cerebral blood flow response at submillimeter columnar resolution. *Proc Natl Acad Sci USA* **98**(19):10904–10909.
96. Vaughan JT, Adriany G, Snyder CJ, Tian J, Thiel T, Bolinger L, Liu H, DelaBarre L, Ugurbil K. 2004. Efficient high-frequency body coil for high-field MRI. *Magn Reson Med* **52**(4):851–859.
97. Shmuel A, Yacoub E, Pfeuffer J, Van de Moortele PF, Adriany G, Hu X, Ugurbil K. 2002. Sustained negative BOLD, blood flow and oxygen consumption response and its coupling to the positive response in the human brain. *Neuron* **36**(6):1195–1210.
98. Formisano E, Kim DS, Di Salle F, van de Moortele PF, Ugurbil K, Goebel R. 2003. Mirror-symmetric tonotopic maps in human primary auditory cortex. *Neuron* **40**(4):859–869.
99. Olman C, Ronen I, Ugurbil K, Kim DS. 2003. Retinotopic mapping in cat visual cortex using high-field functional magnetic resonance imaging. *J Neurosci Methods* **131**(1–2):161–170.
100. Olman CA, Ugurbil K, Schrater P, Kersten D. 2004. BOLD fMRI and psychophysical measurements of contrast response to broadband images. *Vision Res* **44**(7):669–683.
101. Mason GF, Chu W-J, Vaughan JT, Ponder SL, Twieg DB, Adams D, Hetherington HP. 1998. Evaluation of ^{31}P Metabolite differences in human cerebral gray and white matter. *Magn Reson Med* **39**:346–353.
102. Pan JW, Twieg DB, Hetherington HP. 1998. Quantitative spectroscopic imaging of the human brain at 4.1 T. *Magn Reson Med* **40**:363–369.
103. Kuzniecky RI, Hugg JW, Hetherington HP, Butterworth E, Bilir E, Faught E, Gilliam F. 1998. Relative utility of ^1H spectroscopic imaging and hippocampal volumetry in the lateralization of mesial temporal lobe epilepsy. *Neurology* **51**(1):66–71.
104. Chu WJ, Kuzniecky RI, Hugg JW, Khalil BA, Gilliam F, Faught E, Hetherington HP. 2000. Evaluation of temporal lobe epilepsy using ^1H spectroscopic imaging segmentation at 4.1 T. *Magn Reson Med* **43**:359–367.
105. Gruetter R, Weisdorf SA, Rajanayagan V, Terpstra M, Merkle H, Truwit CL, Garwood M, Nyberg SL, Ugurbil K. 1998. Resolution improvements in in vivo ^1H NMR spectra with increased magnetic field strength. *J Magn Reson* **135**(1):260–264.
106. Cho YK, Merkle H, Zhang J, Tsekos NV, Bache RJ, Ugurbil K. 2001. Noninvasive measurements of transmural myocardial metabolites using 3D ^{31}P NMR spectroscopy. *Am J Physiol* **280**(1):H489–497.

107. Chu WJ, Hetherington HP, Kuzniecky RI, Simor T, Mason GF, Elgavish GA. 1998. Lateralization of human temporal lobe epilepsy by ^{31}P NMR spectroscopic imaging at 4.1 T. *Neurology* **51**:472–479.
108. LeRoy-Willig A. 1999. Does RF brain heating decrease at 8 T? *NMR Biomed* **12**(2):115.
109. Roschmann P. 1999. Comments on "Human magnetic resonance imaging at 8 tesla." *NMR Biomed* **12**(5):315–317.
110. Robitaille PML. 1999. Response to "Does RF brain heating decrease at 8 T." *NMR Biomed* **12**:256.
111. Robitaille PML. 1999. On RF power and dielectric resonances in UHFMRI. *NMR Biomed* **12**:318–319.
112. Burgess RE, Yu Y, Abduljalil AM, Kangarlu A, Robitaille P-ML. 1999. High signal to noise FLASH imaging at 8 Tesla. *Magn Reson Imag* **17**:1099–1103.
113. Kangarlu A, Abduljalil AM, Norris DG, Schwartzbauer C, Robitaille P-ML. 1999. Human rapid acquisition with relaxation enhancement imaging at 8 T without specific absorption rate violation. *MAGMA* **9**:81–84.
114. Norris DG, Kangarlu A, Schwartzbauer C, Abduljalil AM, Christoforidis G, Robitaille P-ML. 1999. MDEFT Imaging of the human brain at 8 Tesla. *MAGMA* **9**:92–96.
115. Abduljalil AM, Robitaille P-ML. 1999. Macroscopic susceptibility in ultra high field MRI. *J Comput Assist Tomog* **23**:832–841.
116. Abduljalil AM, Kangarlu A, Yu Y, Robitaille P-ML. 1999. Macroscopic susceptibility in ultra high field MRI, II: acquisition of spin echo images from the human head. *J Comput Assist Tomog* **23**:842–844.
117. Robitaille P-ML, Kangarlu A, Abduljalil AM. 1999. RF penetration in ultra high field magnetic resonance imaging [UHF MRI]: challenges in visualizing details within the center of the human brain. *J Comput Assist Tomog* **23**:845–849.
118. Burgess RE, Yu Y, Christoforidis GA, Bourekas EC, Chakeres DW, Spigos DG, Kangarlu A, Abduljalil AM, Robitaille P-ML. 1999. Human leptomeningeal and cortical vascular anatomy of the cerebral cortex at 8 Tesla. *J Comput Assist Tomogr* **23**:850–856.
119. Christoforidis GA, Bourekas EC, Baujan M, Abduljalil AM, Kangarlu A, Spigos DW, Chakeres DW, Robitaille P-ML. 1999. High resolution MRI of the deep brain vascular anatomy at 8 Tesla: susceptibility based enhancement of the venous structures. *J Comput Assist Tomogr* **23**:857–866.
120. Bourekas EC, Christoforidis GA, Abduljalil AM, Kangarlu A, Spigos DG, Chakeres DW, Robitaille P-ML. 1999. High resolution MRI of the deep gray nuclei at 8 Tesla. *J Comput Assist Tomogr* **23**:867–874.
121. Kangarlu A, Abduljalil AM, Robitaille P-ML. 1999. T_1 and T_2 weighted imaging at 8 tesla. *J Comput Assist Tomogr* **23**:875–878.
122. Robitaille P-ML, Abduljalil AM, Kangarlu A. 2000. Ultra high resolution imaging of the human head at 8 tesla: 2K x 2K for Y2K. *J Comp Assist Tomogr* **24**:2–7.
123. Yacoub E, Shmuel A, Pfeuffer J, Van De Moortele PF, Adriany G, Andersen P, Vaughan JT, Merkle H, Ugurbil K, Hu X. 2001. Imaging brain function in humans at 7 Tesla. *Magn Reson Med* **45**(4):588–594.
124. Yacoub E, Shmuel A, Pfeuffer J, Van De Moortele PF, Adriany G, Ugurbil K, Hu X. 2001. Investigation of the initial dip in fMRI at 7 Tesla. *NMR Biomed* **14**(7–8):408–412.

125. Duong TQ, Yacoub E, Adriany G, Hu X, Ugurbil K, Vaughan JT, Merkle H, Kim SG. 2002. High-resolution, spin-echo BOLD, and CBF fMRI at 4 and 7 T. *Magn Reson Med* **48**(4):589–593.
126. Pfeuffer J, Adriany G, Shmuel A, Yacoub E, Van De Moortele PF, Hu X, Ugurbil K. 2002. Perfusion-based high-resolution functional imaging in the human brain at 7 Tesla. *Magn Reson Med* **47**(5):903–911.
127. Pfeuffer J, van de Moortele PF, Yacoub E, Shmuel A, Adriany G, Andersen P, Merkle H, Garwood M, Ugurbil K, Hu X. 2002. Zoomed functional imaging in the human brain at 7 Tesla with simultaneous high spatial and high temporal resolution. *Neuroimage* **17**(1):272–286.
128. Yacoub E, Van De Moortele PF, Shmuel A, Ugurbil K. 2005. Signal and noise characteristics of Hahn SE and GE BOLD fMRI at 7 T in humans. *Neuroimage* **24**(3):738–750.
129. Triantafyllou C, Hoge RD, Krueger G, Wiggins CJ, Potthast A, Wiggins GC, Wald LL. 2005. Comparison of physiological noise at 1.5 T, 3T and 7T and optimization of fMRI acquisition parameters. *Neuroimage* **26**(1):243–250.
130. Kangarlu A, Baertlein BA, Lee R, Ibrahim T, Yang L, Abduljalil AM, Robitaille P-ML. 1999. Dielectric resonance phenomena in ultra high field magnetic resonance imaging. *J Comput Assist Tomogr* **23**:821–831.
131. Ibrahim TS, Lee R, Abduljalil AM, Baertlein BA, Robitaille PML. 2001. Dielectric resonances and B_1 field inhomogeneity in UHFMRI: computational analysis and experimental findings. *Magn Reson Imag* **19**:219–226.
132. Collins CM, Liu WZ, Schreiber W, Yang QX, Smith MB. 2005. Central brightening due to constructive interference, with, without and despite dielectric resonances. *J Magn Reson Imaging* **21**(2):192–196.
133. Ibrahim TS, Lee R, Baertlein BA, Robitaille PML. 2001. On the frequency dependence of electromagnetic power deposition in the human head: MRI from 3 to 11 T. *42nd Exp Nucl Magn Reson Conf*, 220.
134. Ibrahim TS. 2004. A numerical analysis of radio-frequency power requirements in magnetic resonance imaging experiment. *IEEE Trans Micro Theor Tech* **52**(8):1999–2003.
135. Planck M. 1901. Ueber das gesetz der energieverteilung in normalspectrum. *Ann Phys* **4**:553–563.
136. Robitaille PML. 2003. On the validity of Kirchhoff's law of thermal emission. *IEEE Trans Plasma Sci* **31**(6):1263–1267.
137. Robitaille PML. 2004. The reverse of the Planckian experiment. *Proc Am Phys Soc*, March Meeting pp. Y35–12. www.aps.org/meet/MAR04/baps/abs/S9150012.html.
138. Ibrahim TS, Abduljalil AM, Lee R, Baertlein BA, Robitaille P-ML. 2001. Analysis of B_1 field profiles and SAR values for multi-strut transverse electromagnetic RF coils in high field MRI applications. *Phys Med Biol* **46**:2545–2555.
139. Ibrahim TS, Lee R, Robitaille P-ML. 2001. Effect of RF coil excitation on field inhomogeneity at ultra high fields: a field optimized TEM resonator. *Magn Reson Imag* **19**:1339–1347.
140. Van de Moortele P-F, Adriany G, Akgun C, Moeller S, Ritter J, Vaughan JT, Ugurbil K. 2005. B_1 Phase spatial patterns at 7 tesla: impact on B_1 inhomogeneities with a head transceive transmission line array coil. *Proc Int Soc Magn Reson Med* **13**:2748.
141. Van de Moortele P-F, Adriany G, Akgun C, Moeller S, Ritter J, Collin C, Smith MB, Vaughan JT, Ugurbil K. 2005. B_1 phase spatial patterns at 7 tesla. *Magn Reson Med*. In press.

142. Vaughan JT, DelaBarre L, Snyder C, Adriany G, Collins CM, Van de Moortele P-F, Moeller S, Ritter J, Strupp J, Andersen P, Tian J, Smith MB, Ugurbil K. 2005. RF image optimization at 7 and 9.4 T. *Proc Int Soc Magn Reson Med* **13**:953.
143. Wiggins GC, Potthast A, Triantafyllou C, Wiggins CJ, Wald LL. 2005. Eight-channel phased array coil and detunable TEM volume coil for 7 T brain imaging. *Magn Reson Med* **54**(1):235–240.
144. Adriany G, Van de Moortele PF, Wiesinger F, Moeller S, Strupp JP, Andersen P, Snyder C, Zhang X, Chen W, Pruessmann KP, Boesiger P, Vaughan T, Ugurbil K. 2005. Transmit and receive transmission line arrays for 7 tesla parallel imaging. *Magn Reson Med* **53**(2):434–445.
145. Adriany G, Ritter J, Van deMoortele P-F, Moeller S, Snyder C, Voje B, Vaughan T, Ugurbil K. 2005. A geometrically adjustable 16 channel transceive transmission line array for 7 tesla. In press.
146. Wald LL, Wiggins GC, Potthast A, Wiggins CJ, Triantafyllou C. 2005. Design considerations and coil comparisons for 7 T brain imaging. *Appl Magn Reson* **29**(1):19–37.
147. Kangarlu A, Robitaille P-ML. 2000. Biological effects and health implications in magnetic resonance imaging. *Concepts Magn Reson* **12**(5):321–359.
148. Kangarlu A, Burgess RE, Zhu H, Nakayama T, Hamlin RL, Abduljalil AM, Robitaille P-ML. 1999. Cognitive, cardiac and physiological safety studies in ultra high field magnetic resonance imaging. *J Magn Reson Imaging* **17**:1407–1416.
149. Schenk JF. 2000. Safety of strong, static magnetic fields. *J Magn Reson Imaging* **12**:2–19.
150. Chakeres DW, Bornstein R, Kangarlu A. 2003. Radomized comparison of cognitive function in humans at 0 and 8 Tesla. *J Magn Reson Imaging* **18**(3):342–345.
151. Shellock FG, Cruz JV. 2004. MR procedures: biological effects, safety and patient care. *Radiology* **232**:635–652.
152. Denegre JM, Valles JM, Lin K, Jordan WB, Mowry KL. 1998. Cleavage planes in frog eggs are altered by strong magnetic fields. *Proc Natl Acad Sci USA* **95**:14729–14732.
153. High WB, Sikora J, Ugurbil K, Garwood M. 2000. Subchronic in vivo effects of a high static magnetic field (9.4 T) in rats. *J Magn Reson Imaging* **12**(1):122–139.
154. Valiron O, Peris L, Rikken G, Schweitzer A, Saoudi Y, Remy C, Job D. 2005. Cellular disorders induced by high magnetic fields. *J Magn Reson Imaging* **22**:334–335.
155. Chan S. 2002. The clinical relevance and scientific potential of ultra high field strength MR Imaging. *J Am Neuroradiol* **23**(9):1441–1442.
156. Novak P, Novak V, Kangarlu A, Abduljalil AM, Chakeres DW, Robitaille P-ML. 2001. High resolution MRI of the brainstem at 8 T. *J Comput Assist Tomogr* **25**(2):242–246.
157. Novak V, Abduljalil A, Kangarlu A, Slivka A, Bourekas E, Novak P, Chakeres D, Robitaille P-ML. 2001. Intracranial ossifications and microangiopathy at 8 Tesla MRI. *Magn Reson Imag* **19**(8):1133–1139.
158. Novak V, Kangarlu A, Abduljalil A, Novak P, Slivka A, Chakeres D, Robitaille P-ML. 2001. Ultra high field MRI at 8 tesla of subacute hemorrhagic stroke. *J Comput Assist Tomogr* **25**(3):431–436.
159. Novak V, Abduljalil AM, Novak P, Robitaille P-ML. 2005. High resolution ultra high field MRI of stroke. *Magn Reson Imaging* **23**(4):539–548.
160. Christoforidis GA, Grecula JC, Newton HB, Kangarlu A, Abduljalil AM, Schmalbrock P, Chakeres DW. 2002. Visualization of microvasculature in glioblastoma multiforme with 8T high-spatial-resolution MR imaging. *Am J Neuroradiol* **23**(9):1553–1556.

161. Christoforidis GA, Kangarlu A, Abduljalil AM, Schmalbrock P, Chaudry A, Yates A, Chakeres DW. 2004. Susceptibility based imaging of glioblastoma microvascularity at 8 T: correlation of MR imaging and Postmortem Pathology. *Am J Neuroradiol* **25**(5): 756–760.
162. Augustinack JC, van der Kouwe AJW, Blackwell ML, Salat DH, Wiggins CJ, Frosch MP, Wiggins GC, Potthast A, Wald LL, Fischl BR. 2005. Detection of entorhinal layer II using 7 tesla magnetic resonance imaging. *Ann Neurol* **57**(4):489–494.

DESIGN CONSIDERATIONS FOR ULTRA HIGH FIELD MRI MAGNET SYSTEMS

John Bird, Darren Houlden, Nick Kerley, David Rayner,
David Simkin and Simon Pittard
Magnex Scientific Ltd, Oxford, UK

1. INTRODUCTION

Magnetic field strength has always been an important parameter to consider for Magnetic Resonance Imaging (MRI). It is generally agreed that the Signal to Noise Ratio (SNR) is approximately proportional to magnetic field strength [1,2], although other more subtle effects, such as chemical shift dispersion and susceptibility, also scale with field strength and can cause problems for good anatomical imaging. However, it is no surprise to learn that the engineering challenges presented by the commercial construction of higher field MRI systems are formidable. This chapter is an opportunity to introduce these to a wider audience.

2. THE EVOLUTION OF HIGH FIELD MRI

From the introduction of the first clinical MRI systems to the present day, magnets operating at a field of 1.5 Tesla (T) remain the system of first choice for routine imaging. However, the late 1980s saw the development of in-vivo spectroscopic applications on animal models at 200 (4.7 T) and 300 MHz (7.05 T). Although it proved possible to implement these advanced techniques on standard 1.5T scanners, the advantages of the higher fields became clear.

In 1990 the world's first whole body 4T magnet was manufactured by Oxford Magnet Technology (OMT, now Siemens Magnet Technology) and installed as part of a Phillips medical system at the University of Alabama (Birmingham, USA). Two other 4T systems were installed shortly after — a Siemens medical system at the University of Minnesota (Minneapolis, USA), and General Electric Medical Systems (GEMS) at the National Institute for Health (NIH) in Bethesda, Maryland, USA. Siemens manufactured their own magnet while GEMS subcontracted theirs to OMT.

These early sites struggled with multiple engineering problems and had to pursue significant technological developments before useful images could be obtained. For these reasons high field systems would remain in the research environment for many years.

There was a change of focus in the early 1990s back toward 3T systems following the development of actively shielded gradient coils. These reduced inductive coupling with the main magnet and permitted designs with a smaller bore (800 mm), making the system much more compact. In addition to the magnets being significantly less expensive to manufacture than 4T magnets and relatively easy to site, the system engineering problems were much more manageable. In 1991 Magnex Scientific Ltd. (Magnex) installed the world's first 3T "clinical" research system at the Henry Ford Hospital in Detroit, Michigan, USA.

Meanwhile real-time imaging using a technique known as Echo Planar Imaging (EPI) had been pioneered at Nottingham University by Professor Sir Peter Mansfield and colleagues [3]. This imaging technique generates a complete image in a single Free Induction Decay (FID), resulting in relatively poor SNRs. It was clear that EPI would benefit from the additional signal strength that a high field magnet would offer. In the late 1980s, Rzedzian and Pykett founded ANMR Inc. to commercialize EPI. The ANMR system utilized a resonant gradient system (Echospeed™ [4]) and a compact 3T/800-mm magnet manufactured by Magnex. In partnership with GEMS the ANMR, 3T Echospeed systems started to be installed during early 1994. The first system was installed at the University of Pittsburgh Medical Center, closely followed by sites at the University of California at Los Angeles (Figure 1) and the University of Florida in Gainesville.

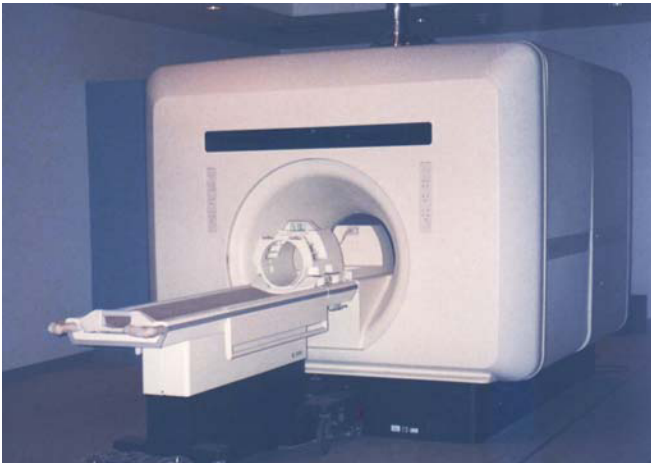


Figure 1. The first-generation 3T GE Signa™ clinical research scanner. See the attached CD for the color version.

The interest in high field systems gathered significant momentum with the implementation at 4 T of functional imaging (fMRI) using the Blood Oxygen Level-Dependent (BOLD) effect by Seiji Ogawa et. al. [19] at the University of Minnesota (Minneapolis, USA). Ogawa was able to image brain activity (function) by the variation in signal strength brought about by local susceptibility changes from blood oxygen levels.

By 1997 the number of high field whole-body magnets (3 T or above) installed worldwide numbered less than forty, and almost thirty of these systems were based around 3T magnet systems, with a further ten at 4 T. The majority of these systems were being operated as pure clinical research systems.

By 1998 GEMS had begun to deliver a second-generation 3T Signa™ that was close to being a routine clinical product using standard gradients developed for the 1.5T Signa™ platform. The second generation product used a larger bore (940-mm) actively shielded 3T magnet developed by Magnex and a fully featured Signa™ clinical console. Although 3 T was becoming a routine clinical field strength, it was not until 1999 that the 3T system was formally FDA certified, eight years after the first 3T magnet was installed in a clinical research site.

In 1996 Professor Pierre-Marie Robitaille at Ohio State University (Columbus, USA) commissioned an 8T/800-mm bore magnet to be manufactured by Magnex [5], to be delivered in late 1997. About a year later, a similarly designed 7T/900-mm magnet was delivered to Professor Kamil Ugurbil at the University of Minnesota (Minneapolis, USA). The differences in field strength and bore size reflected the uncertainty of the relative importance of these two parameters. The group at Minnesota had compromised on field strength to be able to accommodate a higher-power Room Temperature (RT) shim and gradient system.

In 1998 and 1999 the Ohio State group published a number of images with spectacular resolution taken at 8T [5]. Meanwhile, the Minnesota group started to use the 7T magnet to obtain enhanced spectroscopic and functional images of the brain [6,7].

Between 2000 and 2003 a further three 7T systems were installed, one at Massachusetts General Hospital (MGH) in Boston (USA), a second at the National Institutes for Health (NIH) in Bethesda (USA), and a third at Niigata University (Japan).

These ultra high field magnets also opened up the possibility of imaging nuclei other than the hydrogen nucleus. This was of particular interest to Professor Keith Thulborn's group at the University of Illinois in Chicago (UIC). In 1999 work started on a 9.4T/800-mm magnet for UIC with the primary application of sodium imaging. This magnet was delivered and installed by GEMS in the spring of 2004.

Over the last few years, 3T has become a routine clinical field strength, with systems being available from all the major MR vendors. These systems are now incorporating third-generation magnet designs that are shorter, lighter, and easier to site. Many high field clinical research sites are now focusing on 7T, with systems being offered by the major imaging vendors (Figure 2).

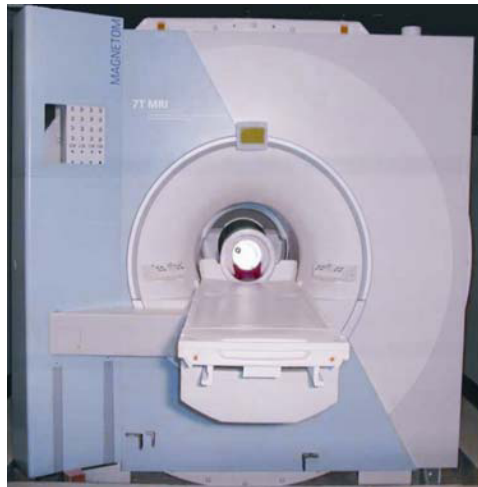


Figure 2. The Siemens 7T Magnetom™ scanner installed at the MGR NMR center. See the attached CD for the color version.

Beyond 7T there are research groups focusing on 9.4T and even higher field strength systems. Already design work is underway for a next-generation whole-body sized 500-MHz (11.74T) magnet. These 11.74T magnets will have to incorporate sub-4.2K operating techniques to enhance the performance of the superconducting wires used. This technology has been proven to date in mid-bore magnets (300–400 mm) at the National High Field Magnet Laboratory at the University of Florida and other sites such as the NIH, and is described later in this chapter.

3. MAGNET DESIGN STRATEGIES

The design of a superconducting MRI magnet involves a complex iterative process in which a balance has to be made between often the conflicting demands of size (bore), homogeneity requirements, management of mechanical stress, stability, and cost. For clarity we will describe these issues separately, but it must be emphasized that they are highly interactive. We describe these factors as they apply particularly to the large MRI magnets — 7T/900 mm, 8T/800 mm, and 9.4T/650 mm — although all design features have evolved from experience gained with smaller-bore (animal imaging) systems.

3.1. Geometrical Issues

For imaging purposes the magnet is required to have extremely high homogeneity over the imaging volume. For whole-body magnets this zone of homogeneity

is typically defined by a 45-cm diameter volume and may require that the field be uniform over this volume to small fractions of parts per million. It is impractical and uneconomic to attempt to achieve this directly due to manufacturing and winding tolerances. A good design will allow corrections at all stages of manufacture.

In a standard design the magnet coils are circular and wound on cylindrical aluminum formers, usually in recessed slots, then potted, generally with epoxy resin. An excellent overall ultra high field MRI design is the compensated solenoid as shown in Figure 3.

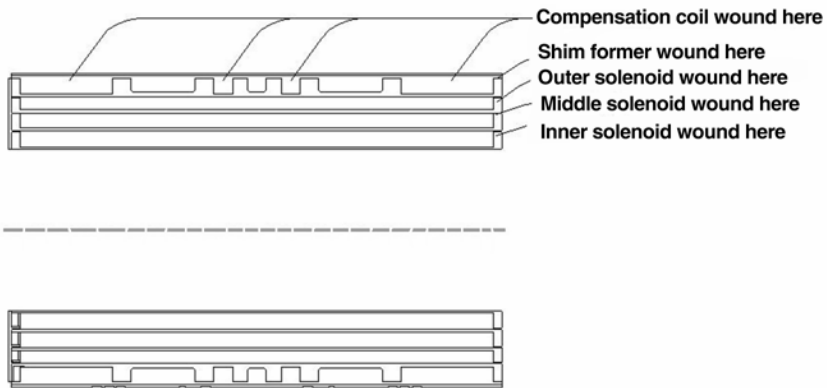


Figure 3. The compensated solenoid magnet configuration.

The smaller compensation windings consist of four coils whose function is to “compensate” for the major homogeneity errors introduced during winding. The design of Figure 3 allows second, fourth, and sixth orders to be controlled by small adjustment to the compensation coils during magnet manufacture and has proved capable of producing homogeneities of better than 5 ppm over the zone of homogeneity. A theoretical field profile is shown in Figure 4.

After winding, magnet homogeneity must be improved by at least an order of magnitude. This is achieved by additional subsidiary windings known as shims. Their design and operation are discussed in detail later in this chapter.

3.2. Mechanical Issues

The construction of a large MRI system requires consideration of large forces and stresses arising in different ways. The first and largest are the mechanical forces and stresses on the conductors and magnet formers when the magnet is energized.

The forces between the windings are taken through the formers. The compensated coil design approach benefits from the fact that the peak stresses and forces

within the coil set appear in the solenoidal windings, where they can be properly reacted and supported, rather than in the smaller compensating coils. It is necessary to employ powerful Finite-Element Method (FEM) calculations in order to properly reveal overall stress patterns in the magnet structure. Figure 5 shows the result of one FEM calculation showing that the highest stress areas are at the ends of the main coils with relatively low stresses on the compensation coils. Nevertheless, the forces on the outermost compensation coils are still of the order 1000–2000 tons, so the design of the compensation formers must be mechanically integrated into the main coil structure.

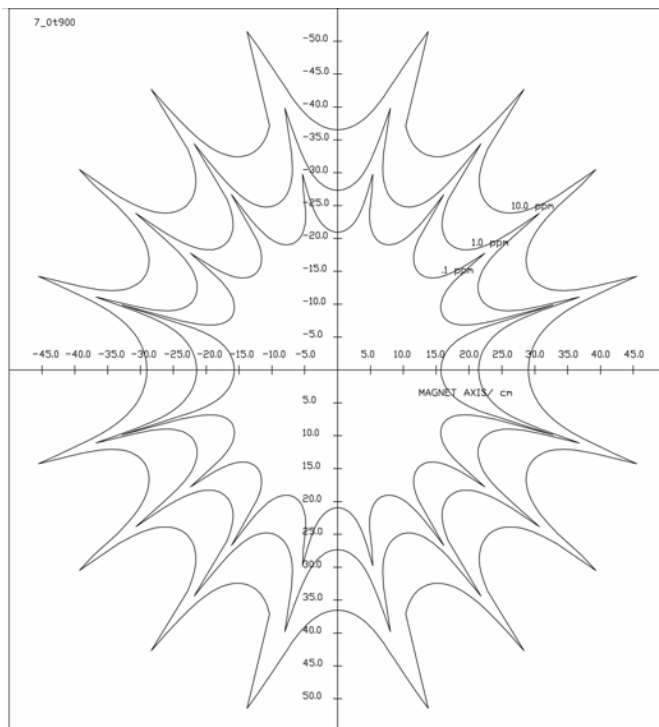


Figure 4. Theoretical field contours of a 7T/900-mm bore magnet viewed from a point transverse to the magnet axis.

In addition we must also consider the stresses induced by the actual winding of the magnet and those that will result from differential contraction as the magnet is cooled from room temperature to the working temperature. These can also be examined by FEM techniques. In the case of copper stabilized conductors wound on aluminum formers, cool-down shrinkage results in the copper coil being free of the former at 4.2 K since the copper contracts less than the aluminum. With long sole-

noids, however, the axial stress will be positive and care must be taken to ensure the structural integrity of the end flanges of the former. This condition may be relieved during energization as the solenoidal coils experience a force toward the magnet center.

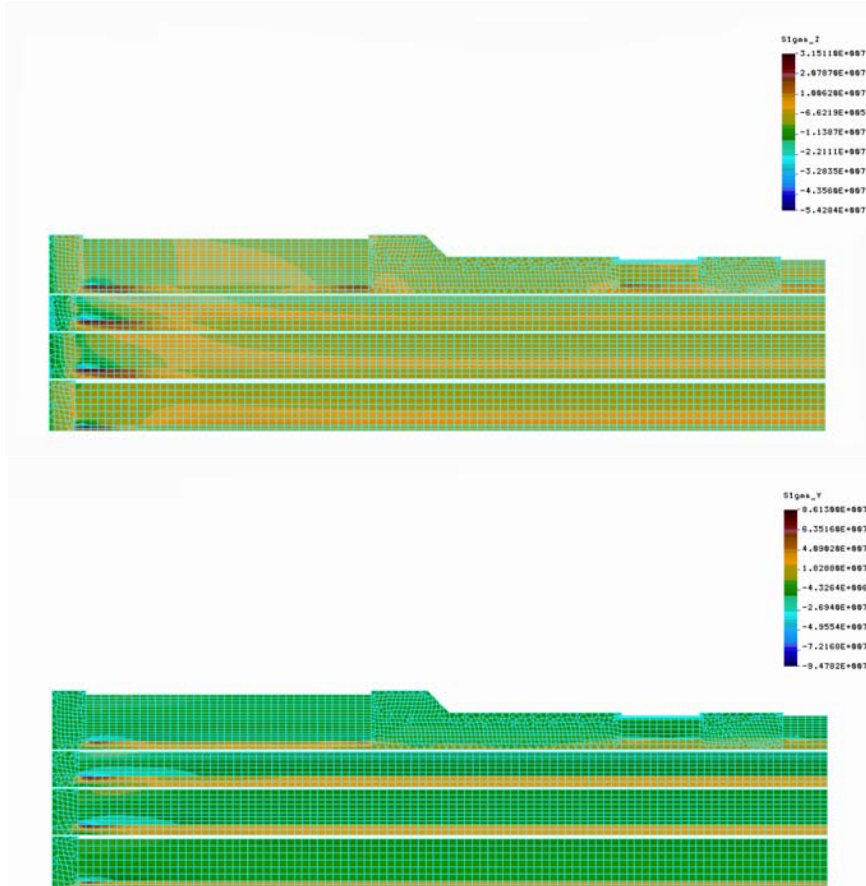


Figure 5. FEM calculation of hoop stress (only a quarter of the magnet is shown). See the attached CD for the color version.

Forces due to gravity and external fields need to be considered when designing the magnet suspension. These will be discussed later.

3.3. Conductors

The development of superconducting magnets over the last 40 years has in many respects followed the evolution of superconducting wire over the same pe-

riod (8). The vast majority of magnets continue to be wound with NbTi, which is the most economic wire commercially available. Its use is limited to fields at or below about 9.4 T, and we will discuss later the options available to reach higher fields. NbTi wire is available in many forms — circular cross-section, rectangular cross-section, and “wire-in channel” (WIC). All forms are available in many sizes; the larger (and more expensive) the wire the greater is the current-carrying capacity.

The most efficient magnet design requires making a selection from this wide choice. Most designs use more than one type of wire within the magnet, as the highest field appears only in a small proportion of the total volume of conductor, normally those turns near the magnet bore, and falls off rapidly with radius. Variations in field between 9.6 and 2.0 Tesla are typically seen. Use of the more expensive wire can therefore be restricted to the high field regions. This use of a variety of conductors according to the magnetic field experienced by each is known as wire grading.

For whole-body MRI magnets the particularly large forces and stresses in the high field regions make WIC wire the preferred option (Figure 6). This class of conductor has a relatively high copper-to-superconductor ratio, and so is mechanically better able to support the magnetic stresses. The WIC approach is particularly flexible in that the dimensions of the copper channel can be modified independently of the superconducting wire; likewise, the superconductor can be modified within the same overall cross-section. This flexibility allows the stress and current-carrying properties of the wire to be separated and results in economically viable designs.

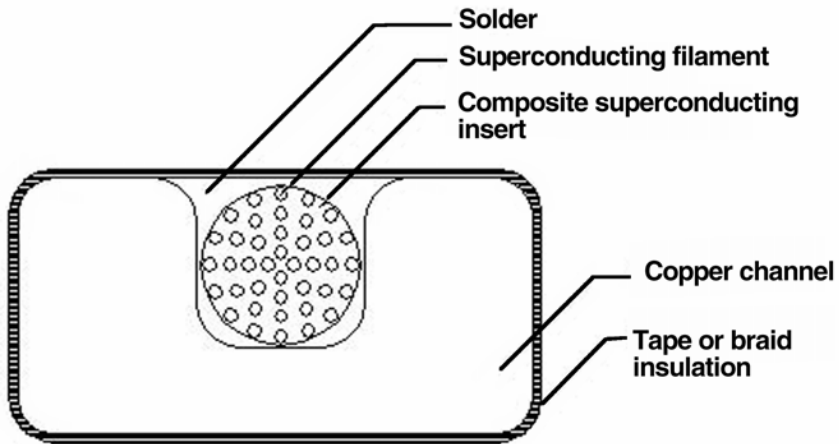


Figure 6. Schematic cross-section of WIC composite superconductor.

3.4. Mode of Operation

Magnets are normally operated in “persistent” mode, in which the windings are shorted by a superconducting “switch.” This, in principle, is a short length of superconductor in series with, but separated from, the main magnet, connected to the magnet power supply, and surrounded by a small heater. During energization the switch heater is used to ensure that the switch is in its normal state and so is of high resistance. When the desired current is reached the heater is turned off and the switch becomes superconducting with the current continuing to circulate. The current in the power supply may then be ramped to zero, the power supply disconnected, and current leads removed.

A superconducting circuit will retain the current flowing indefinitely, but in a real magnet circuit there are likely to be many joints between lengths of superconducting wire. Only if these are constructed with great care (ultra low resistance) will the field decay at an acceptable rate for MRI scanning (better than 0.015 ppm/hr).

3.5. Energy Management

MRI magnets store large quantities of energy — for the whole body 7–9T systems the energy stored is about 80 MJ. It is essential that this energy be dissipated safely in the unlikely event that the magnet ceases to be superconducting, an occurrence known as a quench.

In a quench, the current flowing in the magnet can drop from, say, 200 amps to 0 within a few tens of seconds, and since the magnet inductance can be over 1000 H there is the possibility of generating voltages in excess of 10 kV. As well as being dangerous to personnel, this can damage magnet windings.

The procedure taken to manage this energy release is first to divide the magnet into a number of much smaller sections so that the voltage generated is at a safe level, then to protect each section with a suitable resistor–diode network capable of handling the voltages and temperatures generated. The magnet sections should ideally have similar inductances and not couple strongly with each other.

The resistor–diode network is mounted at the top of the helium reservoir and the heat generated in the circuit is safely discharged into cold helium gas (or liquid) which boils off rapidly.

4. CRYOSTATS

4.1. Fundamentals

The function of a conventional cryostat is to support the magnet and immerse it in a reservoir of liquid helium at 4.2 K and then to thermally isolate this from room temperature. A cross-section of a typical cryostat is shown in Figure 7, and a photograph of a 7T/900-mm bore system during test in Figure 8.

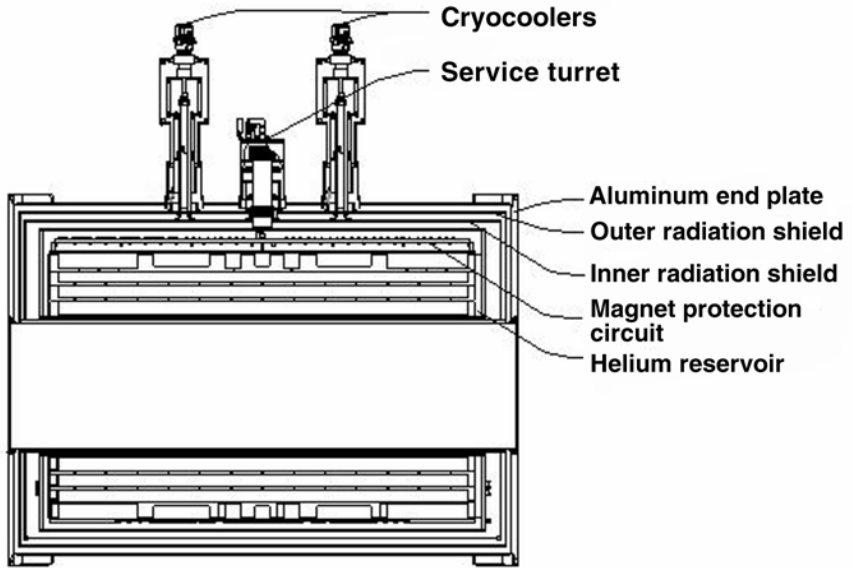


Figure 7. Cross-section of an 8T/800-mm bore magnet and cryostat.



Figure 8. A 7T/900-mm bore magnet system in test. See the attached CD for the color version.

The principal means of thermal isolation is the vacuum in the outer casing of the cryostat. This casing has to support the difference between atmospheric pressure outside and zero pressure inside but also allow for an internal pressure of several atmospheres, which might occur in the event of the cryogen being trapped inside and boiling off. The cryostat is therefore constructed from welded stainless steel and must be certified as a pressure vessel. The magnet axis is sometimes offset below the cryostat centerline to increase the volume of liquid available in the reservoir between refills. The room temperature bore tube is also normally constructed from stainless steel.

Radiation from room temperature is intercepted with aluminum radiation shields that completely surround the helium reservoir. Radiation effects are further minimized by wrapping multilayers of thin aluminized Mylar (called “superinsulation”) around the shields. Filling of the cryostat with liquid helium and electrical access to the magnet and shims is made possible via a service turret on the very top of the cryostat (Figure 8).

The magnet windings and formers have to be supported against gravitational loads. These are largest during transport and especially important if the system is designed to be mobile, but we also must consider the loads experienced during manufacture, when the magnet and helium vessel are rotated from vertical to horizontal.

In normal operation the magnet windings and coil formers and the helium surrounding them have to be supported through the vacuum space to the outer cryostat casing. This presents a contradiction since the suspension should be as slender as possible to minimize conduction losses while it should be as rugged as possible to support the mechanical forces. Suspensions are now typically made from fiberglass rods, relatively small in diameter and as long as possible.

4.2. Closed Cycle Coolers

A typical whole-body MRI system will contain 1800 liters of liquid helium and will require refilling after 500 liters has boiled off. Until the 1990s refilling would have been necessary about every month. More recently, it has become normal to use cryorefrigerators based on the Gifford-McMahon principle to significantly reduce helium boil-off.

The most recent developments include fitting the cryostat with one or more two-stage refrigerators in which each stage is thermally linked to one of the radiation shields. With two coolers (each providing 100 W at 80 K and 5 W at 20 K) it is possible to cool the outer shield to 70–80 K and the inner to 30–40 K. Helium boil-off rates can then be low enough to give a 1–2 year refill interval as long as diligent maintenance of the cooler systems and their chilled water supplies is carried out.

Of course, this is bought at the cost of considerable engineering skill in order to allow the coolers to function efficiently and reliably. They normally function

only in fields below about 0.08 T and must therefore be positioned high above the magnet in order for the stray field to be low enough. Careful design will position the coolers outside any passive shield (see below) so that servicing can, as far as possible, be independent of magnet operation.

5. SHIELDING

The field of a magnet extends in all directions and is invisible; the stray (fringe) field for a high field MRI magnet can be as large as 0.0005 T (5 gauss) several meters from the magnet center. This particular field value is large enough to present a hazard to anyone wearing a pacemaker. Fields in the range 1–100 gauss affect instrumentation such as computers and x-ray machines to varying extents. There is, therefore, a considerable practical benefit if the stray field can be minimized or shielded.

We have already referred to “active” shielded magnets. These are manufactured with an extra, reverse energized coil outside the main magnet that acts to cancel some of the stray field. Unfortunately, for larger-bore ultra high field systems the extra cost, volume, and weight of active shielded designs is considered too high and in systems for clinical imaging only passive shielding has been used.

One common form of passive shield puts the MRI magnet in the center of a room made entirely of annealed low-carbon steel with joints internally welded. Such a room might contain 200–500 tons of steel and can reduce the extent of the 5-gauss contour by a factor two (Figure 9). Such a shield requires careful mechanical and magnetic design to minimize the amount of steel required. Figure 10 shows the shielded room for a 9.4T system under construction.

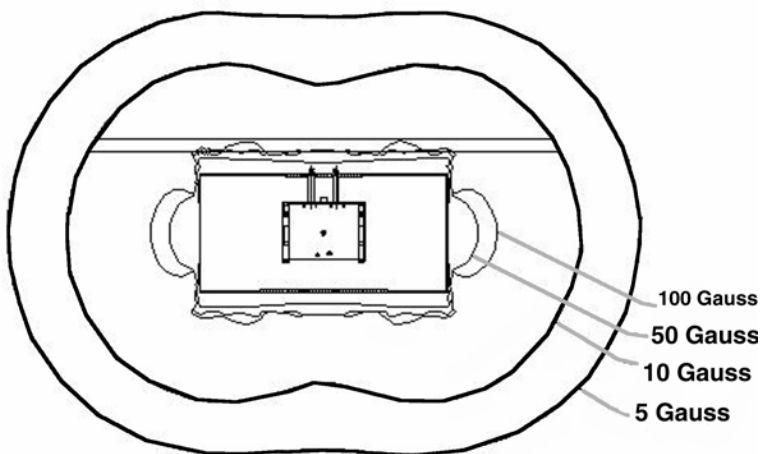


Figure 9. Stray field contours for a shielded 8T/800-mm bore magnet.



Figure 10. Shielding installation for a 9.4T/650-mm bore magnet.

We must next consider two consequential engineering challenges. First there will be magnetic forces between the magnet and shield, and if these are not well controlled the magnet, which has the lower mass, will try to move against its suspension system. The best way to avoid this is to balance the forces by ensuring that the shield is as symmetrical as possible and that the center of the shield and the center of the magnet coincide (which means that the shield will pass under floor level). The larger the room, the smaller the forces and the more tolerant the system will be to any slight force asymmetry. Sometimes, however, the shield has to be designed to fit relatively close to the magnet, and the forces can be large enough to cause internal damage to the magnet system if uncontrolled. In these cases, strain gauges are incorporated into the magnet suspension structure to enable them to be monitored during energization and the magnet position within the shield adjusted, if necessary, using jacking devices.

A second challenge relates to changes in the magnet homogeneity brought about by the shielding. If these are sufficiently small, the adjustments can be made using the shims, as described below. In more severe cases the magnet and its shield must be designed together and backed up with extra or strengthened superconducting shims.

6. SHIMMING

We have described how the magnet is designed to achieve its target homogeneity. The final homogeneity required for good-quality images requires an additional level of control and correction and is known as shimming. The extent to which shimming is necessary depends not only on the magnet design but is influenced by environmental site distortions and any shielding used to reduce the stray field.

Shimming can be performed in three ways. Each has merits and drawbacks, so they are usually used in combination.

6.1. Superconducting Shims

These are active shims typically located on a glass-reinforced or aluminum former inside the cryostat but with a larger diameter than the magnet. Each shim is designed to provide a pure spherical harmonic contribution to the main field so that they can be individually and systematically set to give the required correction.

Z , Z^2 , and Z^3 are the labels given to the first-, second-, and third-order axial shims (Z being the magnet principal axis). These are geometrically simple and easy to wind (also usually using WIC).

Similar labels X , Y , ZX , ZY , X^2-Y^2 , XY , Z^2X , Z^2Y , $Z(X^2-Y^2)$, ZXY are geometric shorthand for first-, second-, and third-order transverse shims that have increasingly complex geometry (and winding challenges).

Shims may be energized using a suitable multichannel power supply following a harmonic analysis of the raw magnet data and the individual shim strengths before being put into persistent mode along with the magnet. As with all superconducting coil systems, there is normally some long-term drift, but as this is typically below 0.01 ppm/hr it is not important in the timescales of an MRI scan.

6.2. Passive Shims

Most manufacturers of MRI magnets use passive shims, sometimes to the exclusion of active shimming, to correct magnet inhomogeneities. Passive shims consist of arrays of mild steel plates of precise geometry and magnetic properties that are fitted into slots or trays inside the magnet bore. Figure 11 shows a typical arrangement. Passive shimming can give excellent results but there exists the possibility of field drift due to temperature changes in the individual shim pieces.

Consider the case of a typical 9.4T/650-mm bore magnet shimmed completely with steel pieces. The mass of steel needed is slightly in excess of 1.8 kg, which, considering the size of the system, is not substantial. However, the effect of a 1°C change in temperature is a change in the central field by -0.9 ppm. This may be correctable if the central field drift is considered as linear during the scan duration. However, associated with the drift are other homogeneity orders that the passive shims are required to correct. In this example a drift of +4.3 Hz in Z , -0.9 Hz in Z^2 , and -2.0 Hz in X would also be produced by the 1°C change.

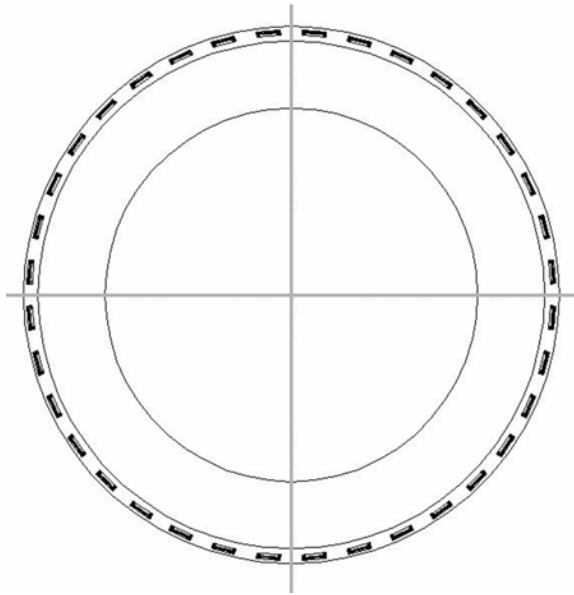


Figure 11. Schematic cross-section of an MRI magnet bore showing the gradient coils (hatched) surrounded by a shim tube with 36 shim trays.

Controlling the temperature of the shim pieces is therefore crucial in high field magnets, where the main shimming is performed using passive shims. If fitted to the gradient the passive shims can be subject to substantial temperature changes caused by pulsing in the gradients, and imaging experiments should only be started when the gradient has reached its equilibrium temperature. The thermal equilibrium is changed by air convection within the bore of the gradient, and it is only the thermal mass of the system that prevents temperature changes from being seen by the shim pieces. Putting the shims in a separate shim tube allows thermal separation between the shims and the warm gradients, but this is insufficient to prevent the shim pieces from warming up over a period of time.

Shim pieces can be fitted in the cryostats of the superconducting magnet. This gives a very stable temperature region but requires that the magnet be deenergized during shimming to allow the passive shims to be fitted. Any touches between the cryostat bore tubes will cause increased cryogen boil-off, which will not be seen until the system is cooled.

It is possible to change the shim material from mild steel to other materials that show lower temperature variation of magnetic properties. In the region around 293 K cobalt has a quarter the thermal variation of magnetic properties compared to mild steel. However, this only reduces the drift issues rather than removing them completely.

Sharing the shimming requirements between active (superconducting) and passive shims confers the benefit of reducing the overall mass of passive shim material required. For the 9.4T/650-mm magnet considered earlier, the mass of steel required can be reduced to about 0.15 kg. For this magnet the passive shims are fitted in a separate shim tube with 24 shim trays on a radius of 320 mm, and allow correction up to sixth order. Dummy shim pieces were used to pack the trays and prevent movement of the shim pieces during pulse sequences. The field drift predicted is $-0.15 \text{ Hz}/^\circ\text{C}$, and the largest remaining homogeneity drift is $-0.32 \text{ Hz}/^\circ\text{C}$. This is much closer to the homogeneity stability required during the scan than the previous case, where only passive shims were used in the design. It should be noted that the improvement in the drift is not as great as may be anticipated from the reduction in mass of the steel. This is due to the different fields experienced at each passive shim location. In the optimization of the homogeneity with passive shims the effect on the central magnetic field is not considered, as this can be adjusted independently. However, the effect of the shims on the central field cannot be entirely ignored as thermal changes will contribute to central field drift.

6.3. Room Temperature (RT) Shims

These are constructed from conventional copper conductors, located inside the magnet bore driven by another multichannel power supply. Using RT shims it is possible to actively shim using *in-vivo* results. This technique is known as slice shimming and relies on controlling the current in the RT shims as the image is being acquired. Optimum shim values are set for each 2D slice in the scan to improve the homogeneity compensation locally rather than globally [9]. This technique requires computer control of the shim current power supply, a standard feature in modern imaging consoles. However, careful consideration of the RT shim design is necessary when shimming during a scan. The rise time of the shim currents creates eddy currents in surrounding conducting structures, similar to the main gradient coils. These eddy currents oppose the rise of the current and so reduce the speed at which the current change can be applied. RT shims also interact with one another unless carefully designed, and these interactions make the creation of mathematical algorithms for optimizing the shim currents more difficult. However, as the spherical harmonics generated by RT shims cannot compensate the local homogeneity structures seen, further research is needed to create non-spherically harmonic shims specific to the structures.

6.3.1. *In-Vivo* Passive Shims

Our description of shimming issues has so far related to the “bare” magnet, in isolation from the MRI experiment. As soon as a patient or other specimen is introduced into the magnet bore, the region of homogeneity is disturbed and we may be required to perform *in-vivo* shimming.

The move to higher magnetic fields is driven by the theoretical improvement in (SNR) for MRI scans taken at higher fields, as discussed in the introduction to

this chapter. However, this move to higher fields comes at the cost of adding extra factors that can deteriorate the image quality. The foremost of these is the increased effect of changes in the sample susceptibility on the quality of the image. These effects are most severe in areas where there are air–tissue transitions as the water in the tissues has a negative susceptibility, and the oxygen in the air has a slightly positive susceptibility. Susceptibility effects are directly proportional to the central field of the magnet and give blurring and distortion of the image or in the extreme case can cause signal dropout.

Active RT shims usually cannot compensate all the spherical harmonics seen in local regions. This is either because high harmonics are generated or the amplitudes of the harmonics are large. It is difficult to design high-order RT shims with high strength, and so passive shims are often used based on the in-vivo results. On the other hand, with RT shims the currents can be changed between patients; with in-vivo passive shims custom inserts are needed for each patient. The passive shim pieces have been manufactured using photocopier toner mixed in a resin to give the small corrections needed. The variation of toner concentration in the resin and the size of the pieces create a wide range of correction options. In the case of head images these pieces may be fixed to a plate held in the patient’s mouth [10] or fitted onto a mask on the patient’s face. These solutions are not easy on the patient. This use of passive shims to correct for patient susceptibility is best used alongside the dynamic (active) shims for optimal results.

Some regions of the body have specific susceptibility problems, and can be corrected by targeted techniques. The changes in susceptibility at the front lobe of the brain produce a harmonic correction that appears almost completely in the Z axis, which is aligned with the axis of the head. This inhomogeneity can be corrected using RT coils held in the mouth and driven by small currents. These coils, like the oral passive shims, are uncomfortable for the patient. Recently coils external to the head have been used successfully to correct for the Z-field component produced [11]. The correct current to be used in the mouth coil is determined by taking scans with small positive and negative currents in the coil, and then finding the optimum coil current by a least squares fitting approach. Optimizing the homogeneity with the mouth coil requires simple changes to the currents in the coil, whereas the oral passive shims must be removed and refitted between shim runs. In practice this makes the mouth coil more acceptable to the patient.

6.4. Gradient Coils and Acoustic Noise

Generally the design constraints on gradients are gradient efficiency (strength), coil inductance (controlling rise time), and the region of uniformity (controlling the size of the imaging volume). These constraints remain at ultra high field, but the additional issue of acoustic noise now becomes paramount. In severe cases the acoustic noise from the gradient can be sufficient to damage the patient’s hearing unless precautions are taken. The noise arises due to vibrations caused by the Lorentz forces developed on the current-carrying wires within the high static mag-

netic field of the main magnet. As the gradient currents are modulated at audio frequencies, audio frequency sounds are produced. Many methods have been considered to reduce the acoustic noise generated by the gradient to a minimum, and several patents exist relative to these issues.

The gradient coils are typically constructed from wound wires or etched copper plates, bonded onto fiberglass formers and potted with epoxy resin. The main gradient coil is also fitted with an outer layer that acts as an active gradient shield. Fixing the main coil and the outer layers together into one piece with a turned central cylinder reduces the audio noise produced by the coil assembly. The currents in the shield and the main coils are in opposition to each other, so that their respective forces tend to cancel out when the shields and coils are coupled together by the stiff cylinder between them (see Figure 12).

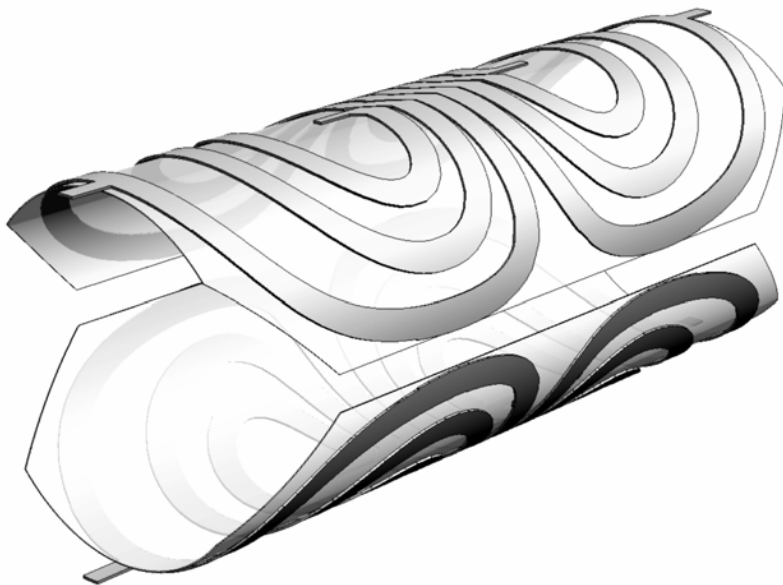


Figure 12. A typical gradient plate layout.

A large proportion of the acoustic noise is produced by coupling with the magnet structure. In standard field systems the gradient is designed to rest on rubber supports at the resonant nodes of the gradient structure. At high field some manufacturers use a vacuum-sealed gradient coil assembly, and mount the gradient coil and vacuum vessel directly on the floor so that it is mechanically decoupled from the magnet [12].

Some researchers have proposed that an important source of noise generation is the eddy currents produced in the magnet structure. The introduction of a separate copper shield outside the gradient can prevent the eddy currents from propagating into the magnet, and so reduce the noise generated [13]. Another method of reducing noise is to design gradients based on “torque free” current sections [14,15]. These have coaxial return paths and offer reduced acoustic noise as the forces within them are locally balanced. It adds an extra constraint to the gradient at the design stage, but does not significantly alter the overall gradient structure.

The rise time of the gradient is important as fast gradient echo sequences are used to gain the most from the high field. However, there is a limit to the gradient rise time as there are physiological effects produced on the patient by the electric fields generated by changes in the magnetic field. Gradient pulses can produce nerve stimulation and cause tingling sensations [16].

The EPI pulse sequence is particularly sensitive to the central field uniformity due to accumulation of phase errors during the scan, and the long duration of the read sequence. In EPI the phase encode has a longer sampling time than the read direction so distortion mainly occurs in the phase encode direction.

The preferred method of gaining the optimum from the move to ultra high field MRI is to use parallel imaging approaches, such as SENSE (SENSitivity Encoding). Parallel imaging uses multiple coil arrays around the subject to increase the imaging speed without the need to have faster gradient switching. This technique takes full advantage of the SNR gained by moving to ultra high field as the technique naturally lowers the SNR.

7. MRI ABOVE 9.4 TESLA

Although 9.3952 T is a memorable proton NMR frequency (400 MHz), it also represents something of a “natural barrier” since it is close to the maximum persistent field readily achievable with Niobium Titanium superconductor at 4.2 K.

To understand why the wire performance is limiting and what the technology options are available to reach higher fields, we need to introduce the concept of a critical field.

Superconducting wire loses its superconductive properties and becomes resistive if exposed to magnetic fields greater than its critical field (B_c). The total magnetic field that the wire is exposed to consists of any background field plus the self-generated magnetic field from the current in the wire. For a typical wire used in a 9.4T magnet, Figure 13 shows the relationship between the wire’s maximum current-carrying capacity (critical current I_c) and the maximum background field (B_{op}). For a magnet to be stable the operating current needs to be comfortably below these critical parameters of the wire. Figure 13 indicates that the maximum field at which the wire can be superconducting is 10.4T.

This is at zero current capacity and is known as the critical field. Different methods of manufacture can affect this value to a small degree. It is clear from this data that a 9.4T magnet is operating near to the limits of the wire.

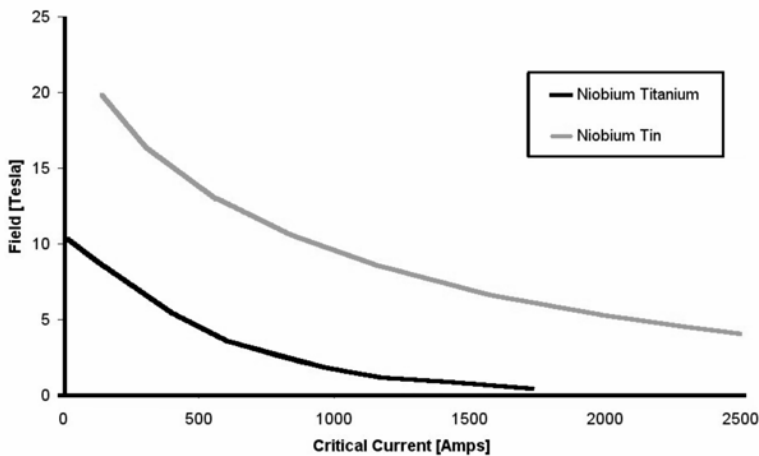


Figure 13. Variation of field with critical current for NbTi and Nb₃Sn.

If we wish to breach the 9.4T “barrier,” then two strategies are available. Both are mature technologies and are used to manufacture ultra high field NMR magnets for chemical analysis.

7.1. Superconductor

The first approach is to find an alternative to NbTi with a higher critical field. Many promising superconducting materials were discovered during the 1960s, and a number of these might have proved suitable [8]. However, for a number of technical and manufacturing reasons only NbTi and Niobium-Tin (Nb₃Sn) superconducting alloys have been developed to the point of routine production and are available on a reliable and predictable commercial basis today. Nevertheless, the critical field for Nb₃Sn at 4.2 K [17] is attractively high (about 22T, somewhat dependant on tertiary elemental doping and state of anneal).

The whole subject of technical superconductors is outside the scope of this chapter, but suffice it to say that NbTi can easily be wound into coils because it is quite a flexible and tough material. Conversely, Nb₃Sn is not; it is an extremely brittle and expensive superconductor. A strain of only about 1% causes irreversible damage to its superconducting properties. Consequently it is necessary to wind Nb₃Sn coils with the superconductor in an unreacted “green state” before the Nb₃Sn is actually formed. The coil is then heat treated at around 700°C to form the Nb₃Sn in-situ. Not only does this require the use of heat-resisting materials during manufacture of the coil, but handling of the coil has to be executed extremely carefully. Once an Nb₃Sn coil has been reacted, it can never be unwound or reused. All the associated processes of production such as making superconducting joints are

also nonreversible, so the associated technical and commercial risk with this material is much higher than with NbTi.

Because of the special materials and handling requirements, an Nb₃Sn coil is typically at least one order of magnitude more expensive to produce than an NbTi coil of similar size. To minimize the cost of ultra high field magnets, only the region in the windings where the conditions exceed the performance of NbTi is it replaced by Nb₃Sn.

7.2. Temperature

Our discussions so far have assumed that the magnet is immersed in a bath of liquid helium at atmospheric pressure (boiling at 4.2 K) and maintained by the cryostat. However, if the temperature of the helium and magnet can be further reduced, examination of Figure 14 shows how the critical field of NbTi increases, ultimately to a theoretical limit of over 14 T at absolute zero.

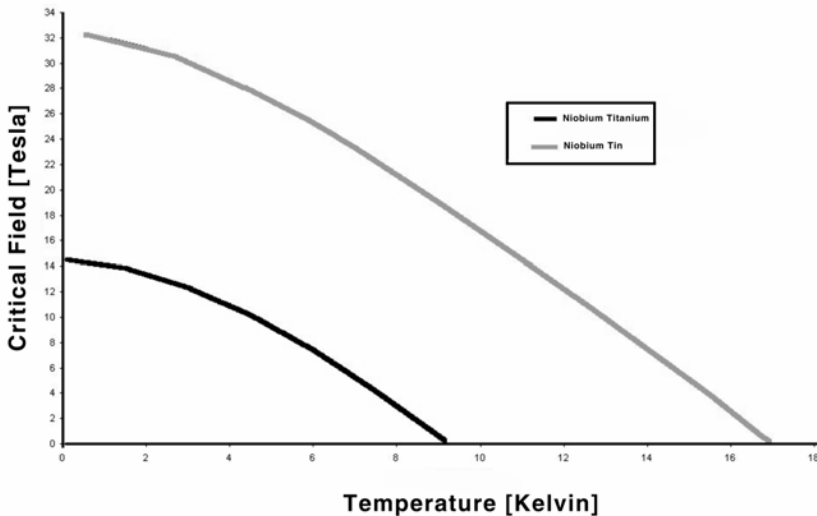


Figure 14. Variation of critical field with temperature for NbTi and Nb₃Sn.

The simplest way to cool a large volume of liquid is to pump directly on the bath to reduce the liquid vapor pressure and hence temperature.

In practice there are physical, technical and commercial limits to the lowest temperature that can be achieved for a magnet that may weigh as much as 25000 kg. The effectiveness of a pump falls off as the pressure (and mass flow rate) de-

creases, while the change of state of helium to superfluid helium (2.2 K and 52 mbar) is accompanied by a significant enthalpy change. We can conclude that the optimum temperature for a pumped magnet system is just above 2.2 K (typically 2.5 K), at which temperature the critical field of NbTi is about 13.3 T. In practical terms this extends the viability of NbTi wire to at least 11.74 T (500 MHz).

From a manufacturer's point of view there are many technological issues to resolve in order to keep 2.5-K operation reliable, simple and safe. The first obstacle is to manufacture all the components, including the safety features, to be helium leak-tight (better than 10^{-8} mbar·l·s⁻¹) as the helium reservoir is now below atmospheric pressure. Any ingress of air into a sub-4.2K cryogenic system will freeze and if not monitored and cleared has the potential of causing a major failure. These components also need to cope with frequent large temperature changes, typically from 90 K to room temperature.

To reduce the vapor pressure, the systems are supplied with a continuously running pumping station. If the pumps are stopped, the helium bath will start to warm up. However, by minimizing the heat leak into the helium reservoir and with the large thermal mass of the magnet the warm-up rate can be very slow. With several days at hand, power failures or even pump failures can be resolved before there is any risk to the magnet.

With the helium reservoir below atmospheric pressure a different technique is required for cryogen filling. A valved section of the helium transfer siphon remains in the service turret at all times. A second section of the siphon is precooled before being linked. The valve is opened and the vacuum in the reservoir draws the liquid from the storage dewar.

As there are more critical parameters to monitor on a sub-4.2K superconducting magnet, monitoring systems have been developed. These have the ability to raise alarms if any of the magnet parameters are outside the normal operating range.

8. THE FUTURE OF MRI

8.1. Higher Magnetic Fields

Virtually all clinical imaging today is performed with magnets made from NbTi superconductor. The most common field strengths are in the range 1 to 4 T, but for fMRI research and other specialized applications of imaging (of both humans and animals) significantly higher fields are used. The maximum magnetic field strengths have mostly been limited to 8 T [5] for humans, but for animals ≤ 9.4 T or in a few instances 11.74 T has been used.

We have seen that 9.4 T represents an upper limit to the persistent field readily achievable with NbTi superconductor operating at 4.2 K. Also the task of building magnets becomes technically much more difficult as the fields increase and higher field magnets become increasingly larger and heavier and consequently more expensive to build and operate. The stray fields (5-gauss line) either spread more or become more difficult to constrain — either by active shield coils or passive iron

shielding — so there are significantly larger infrastructure costs such as requirements for space and use of liquid helium.

Some recent animal imaging research magnets with warm bores in the range 210 to 400 mm do operate at 11.74 T. These are operated using NbTi in liquid helium at a reduced pressure and temperature of about 2.5 K. 11.74 T is the realistic limit for NbTi superconducting magnets even at reduced temperatures.

To reach fields higher than this, other superconducting materials must be used and a number of these are in principle suitable. Most of the research on low-temperature (Type II) superconductors was done in the 1960s [8], and many promising superconducting materials were discovered. But for a number of technical and production reasons, only NbTi and niobium–tin (Nb_3Sn) superconducting alloys have been developed to the point of routine production and available on a reliable and predictable commercial basis today.

To operate an MRI magnet significantly above 11.74 T inevitably requires the use of Nb_3Sn wire. In these cases the quantity of Nb_3Sn wire required can be significantly reduced using pumped magnet technology. For example, at 4.2 K a 14.1 T magnet would require an Nb_3Sn section to produce 4.7 T of the central field. In a pumped magnet the Nb_3Sn is only required to contribute 2.3 T to the central field. In terms of Nb_3Sn wire usage, this is a 75% reduction. The maximum field that can be achieved begins to be determined by other factors such as engineering design (stress, energy management) and reality situations, including acceptable technical and associated commercial risks that include timescales and costs.

8.2. Liquid Helium and Refrigeration

Helium is the only liquid refrigerant that can be used to operate MRI systems — it is the life blood of MRI superconducting magnets. However, liquid helium is a finite resource and largely associated with the production of oil and gas. A point to note with helium gas is that once released into the atmosphere it is eventually lost into space as its thermal velocity exceeds the earth's escape velocity.

Fortunately there have been some spectacular advances in the last decade in closed-cycle low-temperature refrigeration. Early Gifford-McMahon cryocoolers such as the Leybold model RGD5100 provided 5 and 100 W of cooling capacity at the 20 and 80 K stages. These are routinely used for cooling two radiation shields to minimize the consumption of liquid helium of an MRI system to a few liters per day. During the 1990s the design and technology of closed-cycle refrigeration advanced considerably. Cryocoolers such as the Sumitomo RGD408D are able to produce 1 W at 4.2 K and 35 W at 35 K, which has opened up the availability of MRI magnets with low or zero helium consumption.

The current generation of Pulse Tube Refrigerators (PTR) is now able to produce similar levels of refrigeration but with vibration levels typically 100 times lower. A second advantage of a PTR is that there are no cold moving parts and service intervals are long — typically more than 20,000 hours. Although in principle the helium consumption problem has been reduced, it will never be totally

eliminated. All of these low-temperature refrigerators must operate in fields of less than about 500 gauss because they use conventional electric motors. They have to be moved sufficiently far away from the stray field of the magnet and may also require local motor shields using iron as necessary.

The use of very high power gradient coils and certain demanding imaging sequences (such as EPI) can generate additional heating inside magnets, which can substantially increase helium consumption. Although various complex mechanisms such as eddy currents and shield vibrations come into play in generating this heat, it is anticipated that improved design of gradient coils will reduce this.

9. CONCLUSIONS

The construction of very high field clinical and animal imaging magnets is a special technology within the capabilities of just a handful of companies around the world. The technology of such magnets is a remarkable combination of quantum mechanics and heavy engineering that has steadily evolved over more than three decades. It requires superconducting coils to store many tens of MJ of energy in the magnetic field and also to restrain bulk body forces of hundreds of tons while at the same time ensuring that local energy releases of no more than a few microjoules (for example, through coil movements or cracking during magnet energization) occur at any one time and place in the coils.

Higher fields will certainly come into play for research purposes. Whole-body magnets up to 11.74 T are being planned and small-bore animal imaging magnets up to 17 T are also under debate, although both these magnets are getting close to the limits of what is technically possible today.

The demand for ultra high field MRI systems in the future will depend on how MRI science evolves and what clinical benefits arise. There is no doubt that if clinicians ever request MRI in fields higher than 16 or 17 T then construction will present formidable engineering challenges.

Finally, we should not forget that little is really known about the effects of exposure of animals and humans to high magnetic fields. There is much anecdotal evidence of temporary effects that people have experienced such as giddiness or “seeing stars” usually when moving or turning their head in fields well in excess of 2 T [18]. Human exposure to high fields will only be allowed if the perceived benefits outweigh the potential hazards.

10. ACKNOWLEDGMENTS

The photograph in Figure 1 by kind permission of Professor Mark S. Cohen, University of California at Los Angeles. The photograph in Figure 2 by kind permission of Dr Lawrence L. Wald, Massachusetts General Hospital.

11. REFERENCES

1. Hoult DI, Richards RE. 1976. The signal-to-noise ratio of the nuclear magnetic resonance experiment. *J Magn Reson* **24**:71–83.
2. Edelstein WA, Glover GH, Hardy CJ, Redington RW. 1986. The intrinsic signal-to-noise ratio in NMR imaging. *Magn Reson Med* **3**(4):604–618.
3. Stehling MK, Turner R, Mansfield P. 1991. Echo planar imaging: magnetic resonance imaging in a fraction of a second. *Science* **254**:43–50.
4. Pykett IL, Rzedzian RR. 1987. Instant Images of the body by magnetic resonance. *Magn Reson Med* **5**(6):563–571.
5. Ogawa S, Tank DW, Menon R, Ellermann JM, Kim SG, Merkle H, Ugurbil K. 1992. Intrinsic signal changes accompanying sensory stimulation — functional brain mapping with magnetic resonance imaging. *Proc Natl Acad Sci USA* **89**(13), 5951–5955.
6. Robitaille P-ML, Warner R, Jagadeesh J, Abduljalil AM, Kangarlu A, Burgess R, Yang YYL, Zhu H, Jiang Z, Bailey RE, Chung W, Somawiharja Y, Feenan P, Rayner DL. 1999. Design and assembly of an 8 Tesla whole-body MR scanner. *J Comput Assist Tomogr* **23**(6):808–820.
7. Tkac I, Andersen P, Adriany G, Merkle H, Ugurbil K, Gruetter R. 2001. In-vivo ^1H NMR spectroscopy of the human brain at 7T. *Magn Reson Med* **46**(3):451–456.
8. Pfeuffer J, Adriany G, Shmuel A, Yacoub E, Van De Moortele PF, Hu X, Ugurbil K. 2002. Perfusion-based high-resolution functional imaging in the human brain at 7T. *Magn Reson Med* **47**(5):903–911.
9. Wilson MN. 1998. *Superconducting magnets*. Oxford: Oxford UP.
10. de Graaf RA, Brown PB, McIntyre S, Rothman DL, Nixon TW. 2003. Dynamic shim updating (DSU) for multislice signal acquisition. *Magn Reson Med* **49**(3):409–416.
11. Roorchansingh V, Jesmanowicz A, Hyde JS. 2004. Magnetic field homogeneity improvement in the lower frontal lobe by combined resistive and passive shims with a user-defined mask. *Proc Int Soc Magn Reson Med* 1650.
12. Wong EC, Mazaheri Y. 2004. Shimming of the inferior frontal cortex using an external local shim coil. *Proc Int Soc Magn Reson Med* 520.
13. Katsunuma A, Takamori H, Sakakura Y, Hamamura Y, Ogo Y, Katayama R. 2002. Quiet MRI with novel acoustic noise reduction. *Magn Reson Mat Phys Biol Med* **13**:139–144.
14. Edelstein WA, Hedeem RA, Mallozzi RP, El Hamamsy SA, Ackermann RA, Havens TJ. 2002. Making MRI quieter. *Magn Reson Imag* **20**:155–163.
15. Bowtell RW, Peters A. 1999. Analytic approach to the design of transverse gradient coils with co-axial return paths. *Magn Reson Med* **41**:600–608.
16. Abduljalil AM, Aletras AH, Robitaille P-ML. 1997. Torque free asymmetric gradient coils for echo planar imaging. *Magn Reson Med* **31**:450–453.
17. Hidalgo-Tobon SS, Bencsik M, Bowtell RW. 2004. Reduction of peripheral nerve stimulation via the use of combined gradient and uniform field coils. *Proc Int Soc Magn Reson Med* **11**:659.
18. Asner FM. 1999. *High-field superconducting magnets*. Oxford: Oxford UP.
19. *Restrictions on exposure to static and time-varying electromagnetic fields*. 1995. National Radiological Protection Board, Chilton, Didcot, Oxon.

**HARDWARE CONSIDERATIONS IN
ULTRA HIGH FIELD MRI:
AN OVERVIEW OF SYSTEM INTEGRATION**

Douglas A. C. Kelley, PhD

GE Healthcare Technologies

Ultra high field MRI systems present a number of unique challenges to the system designer and integrator beyond simply scaling up the performance of a lower field system. The primary areas of concern are the magnet, gradient coils and drivers, and RF coils and coil interface. The art of system integration lies in identifying sufficiently clear performance targets for each of the subsystems and ensuring that those targets are met in a way that preserves the overall performance of the system. The following discussion identifies for each of these areas the key performance requirements that are changed at higher field strengths, methods to address those requirements, and how those methods affect the rest of the system. As this is an area of ongoing research and development, many of the specific solutions presented here are likely to be superseded in the future, but the general approach to the problem should remain valid. While a complete description of every aspect of system design and integration of UHFMRI systems is beyond the scope of this chapter, the following is intended to provide practical guidance in addressing the more common problems in siting or operating a UHFMRI system.

1. INTRODUCTION

The focus of this chapter is on system integration, which may be defined as the art of aligning the performance capabilities of available system components with the performance expectations of the users, altering and extending those capabilities as needed. A difficulty arises in that these alterations have both intended and unintended consequences, and users' expectations frequently place potential modifications in conflict.

An example of such a conflict is the bore diameter. To minimize the discomfort of experimental subjects it is highly desirable to increase the available bore diameter as much as possible. However, increasing the bore diameter weakens the

gradients as the fifth power of the radius (for a shielded gradient coil), creating a conflict with the need for stronger gradients at higher field strengths to overcome the increased chemical shift dispersion and patient-induced static field distortions due to differences in diamagnetic susceptibility between tissue and air. Addressing this conflict remains an area of active research [1].

One can list the characteristics of each of the subsystems that a system integrator must address, keeping in mind that these parameters are far from sufficient to specify a design for each of these components.

2. MOTIVATION FOR UHFMRI

Since the 1980s, one clear trend in the development of magnetic resonance imaging systems for human research applications has been the drive to higher and higher field strengths, from the first 1.5T and 2T systems in the early 1980s, to the first 4T systems [2–4] in the late 1980s, and the 8T [5], 7T, and 9.4T systems of the 1990s and the current decade. While the drive for higher field strength mirrors that of analytical NMR, focused on increasing chemical shift range and enhanced signal from nuclei with low gyromagnetic ratios, much of the focus to date in UHFMRI for humans has been on increasing sensitivity for proton imaging applications, allowing anatomical imaging with higher spatial resolution, and using the higher sensitivity to examine dynamic and functional aspects (including blood oxygenation level-dependent contrast (BOLD) and other measures of brain activity). Significant advances will certainly be made in spectroscopy applications (^1H as well as low gamma nuclei), including the use of hyperpolarized materials, but the main focus over the last few years has been imaging applications.

In designing a 7T system, then, one must envision a clinical MR system with a greatly expanded performance envelope, and herein lies the greatest practical difficulty — while clinical MR systems are certainly large in number, developing a new system requires significant levels of effort, particularly to provide for the support infrastructure needed to bring the product to the market successfully. The limited number of sites able to make use of such a system, combined with the high material costs for the components and the technical complexity of the development, make the commercial aspects of these systems extremely difficult to manage, and will continue to be key practical limitations to their adoption for clinical use for many years to come.

The primary motivation for UHFMRI, then, is increasing sensitivity and using that higher sensitivity for improved spatial or temporal resolution. Sensitivity is typically quantified in terms of the signal-to-noise ratio. There is an extensive literature devoted to comparison of signal-to-noise ratios across field strengths [6–8], which may be summarized as follows:

- For a given volume of thermally polarized material, the maximum signal increases quadratically with field strength, one factor arising from the Curie susceptibility and one factor from Lenz's law of in-

duction (by the Principle of Reciprocity, this factor includes the RF magnetic field per unit current of the receiver coil).

- Broadband noise (as distinct from discrete image artifacts or image distortions), sometimes called “intrinsic noise,” is generated by conduction currents in the tissue and increases slightly more than linearly in voltage with frequency, the deviation from linear increase arising due to the variation in conductivity with frequency observed for human tissue (for a derivation of this dependence, please see [8], establishing the linear noise voltage dependence on operating frequency and square root dependence on conductivity, and [9], establishing the roughly square root frequency dependence of tissue conductivity).
- Optimal sensitivity is dependent upon RF coil design, and so comparisons between field strengths must also take into account comparisons between coil configurations.
- Relaxation times are also dependent upon field strength, with T_1 generally increasing with field strength and T_2 generally decreasing, and so the available magnetization for a particular pulse sequence with a particular set of timings can be significantly different at different field strengths.
- RF coil sensitivity (the induction part of the signal) generally varies significantly with position, and so the overall sensitivity will not be uniform.
- Methods which produce uniform image intensity necessarily produce nonuniform image noise [10,11].

While one can simply state that the goal of moving to higher field is to increase the sensitivity, based on these observations, the signal-to-noise ratio by itself provides a poor metric for whether this goal has been achieved.

3. MAGNETS FOR UHFMRI

Superconducting magnets [12,13] are an enabling technology for UHFMRI. The focus in the clinical MRI market on producing compact, stable, high current magnets with improved cryogenic performance has led to advances in superconducting joint technology, superconductor processing, and cryogenic design without which the cost of 7T and higher field strength magnets would be prohibitive and the robustness of the designs unacceptable. These component and process technologies are generally trade secrets held by the various manufacturers, and so the magnet is typically a purchased item, for which the system integrator can specify some of the performance parameters but the rest of the magnet is essentially a black box.

The typical features of a UHFMRI magnet are revealed in a description of the 8T magnet installed at Ohio State University in 1998 [5]. The magnet is a truncated multilayer solenoid with additional compensation coils for the large Z2 and Z4

terms produced by the truncation of the solenoid. Clinical magnets typically use six shorter solenoidal coils offset along the Z-axis to optimize the use of superconductors [14]; the solenoid results in lower magnetic forces between coil elements and a lower peak magnetic field on the conductor (which allows higher current densities and avoids the use of low-temperature cryostats or more exotic superconducting materials). Surrounding the primary windings and compensation coils are the superconducting shim coils and the superconducting joints and switches.

Among the factors to consider in a magnet for UHFMRI are shielding, cryogenic maintenance, and homogeneity. Most clinical magnets incorporate active shielding, where a second set of windings is added in opposition to the primary windings to reduce the field outside the magnet and so minimize the area required for the MRI suite. These shield windings, while decreasing the field outside the magnet, also lower the desired field within the magnet, and so the primary windings of a shielded magnet are necessarily stronger than an unshielded magnet. This approach is not practical with current technology due to the forces that would result on the correction coil former and the peak magnetic field to which the windings would be exposed.

The typical solution to this problem has been to use a magnetically shielded room, essentially a big steel box. Due to its high magnetic permeability, the steel concentrates the magnetic field and provides true shielding both of the environment from the magnet and the magnet from the environment. The mass of steel required is typically several hundred metric tons. Two designs are common — a rectangular box that is simpler to construct but requires the floor plates to be buried up to 1.5 m below the floor level, and an octagonal box that has a lower total mass but is more difficult to construct [15].

Cryogenic performance affects the stability of the magnet as well as the operational costs. Liquid helium is required to maintain the temperature of the superconducting wire and so allow it to remain in the superconducting state. The components of the magnet vessel external to the helium can act as an evacuated dewar to minimize heat transfer to the helium can. Given the mass of material within the helium can (the magnet formers and windings themselves, which weigh roughly 20 metric tons for a 7T 90-cm magnet and 36 metric tons for a 9.4T 80-cm magnet), a substantial suspension mechanism is required, and a significant set of design problems is related to stiffening and strengthening this suspension while minimizing its thermal conductivity. A benefit of the larger cold mass is that once it gets cold it requires a significant amount of heat to raise its temperature. A further set of problems arises from the larger size of the helium can compared to lower field magnets — thermal radiation is a significant heat transfer mechanism even in a vacuum, and the power transferred increases with surface area.

The typical method of blocking heat transfer is through the use of radiation shields — reflective metallic baffles maintained at constant intermediate temperatures between the outer vacuum vessel at 300 K and the helium can at 4 K. The temperature of these baffles is maintained through the use of cryogenic refrigerators, typically based on the Gifford-McMahon cycle. Commercially available units typically have two stages at 80 and 20 K. Common practice in clinical magnets has

been to move to helium recondensers to significantly reduce helium boil-off and the need to replenish the helium periodically, but to date no UHF magnets have incorporated this technology. Maintaining the operation of these refrigerators is an important practical problem — failure of the shield coolers will not produce an immediate increase in helium consumption (due to the large cold mass) but over time will produce a significant increase in consumption that must be addressed as soon as possible, given the high cost of recommissioning the magnet in the event of a quench. The incorporation of automated magnet monitoring with remote monitoring capabilities is thus essential.

The final area of consideration is maintaining magnet homogeneity. Three sources must be considered — the magnet itself, whether by design or by defect in materials or construction; the shield room, and any asymmetries resulting from its construction or the placement of the magnet within the shield; and the subject, where variations in tissue type and density result in significant variations in diamagnetic susceptibility, producing magnetic field distortions. The first two effects are static and are generally of fairly low order, and are generally corrected with a combination of superconducting shim coils mentioned previously, and passive shims, small pieces of ferromagnetic material placed typically within the bore of the magnet. While the first approach is more costly and poses a number of design problems, it is to be preferred for UHFMRI magnets for the following reason. The magnetic permeability of ferromagnetic materials is typically temperature dependent, and the temperature within the bore of the magnet generally cannot be controlled too well in close proximity to the gradient coil due to the heat produced by the coil in normal operation. Consequently, over the course of an imaging session, the center frequency and the homogeneity can vary substantially due to these temperature changes, producing artifacts in the images.

The third source poses a number of problems, because not only can the local perturbations be of spatially high order and essentially uncorrectable by external magnetic field coils, but due to motion of the subject the perturbation can be dynamic in nature. Typically additional coil windings to correct for second- and third-order perturbations produced by the subject are provided, with first-order perturbations corrected by DC offsets in the gradient coils. Care must be taken in the design of these coils to minimize a number of effects:

- currents induced by magnetic coupling to the gradient windings
- currents induced by electrical noise from the gradient drivers
- currents induced by vibration of the coil former (and hence the shim windings) in the static field

The first effect can only be corrected by coil design and appropriate manufacturing process control. While a conventional gradient design will produce minimal even-order fields due to its symmetry, asymmetric designs typically used for head-only gradient coils can produce fields of arbitrary spatial order. The second effect requires appropriate filtration in the shim driver, to ensure that the amplifier and coil present a large impedance at the higher frequencies (typically tens of kilohertz)

at which this noise is generated. Unfortunately, rolling off the gain of the amplifier at these frequencies also reduces the available slew rate for the shim currents.

Another interesting approach to correct for the high-order variations produced by the subject involves the use of pyrolytic graphite [16], which has a higher diamagnetic susceptibility than water. Appropriate placement and shaping of pads of this material can produce significant improvements in the field strength, although the design of the inserts is largely empirical, and this approach may even exacerbate the problem of dynamic perturbations due to motion.

4. GRADIENT COILS AND DRIVERS

One key difference between MRI and analytical NMR is that, whereas the fundamental measure of resolution in NMR (chemical shift) scales with field strength, the fundamental measure of resolution in MRI (spatial extent) is unchanged with field strength. Two of the primary sources of artifact, however, increase linearly in amplitude with field strength — chemical shift and susceptibility variations. Most imaging reconstruction techniques ascribe phase evolution solely to position encoding, and so at higher field strengths the gradient area per unit time must increase linearly to overcome the increasing effects of chemical shift and susceptibility variations.

Constructing a gradient coil requires solving two classes of problems — the electromagnetic problem, on which much has been published [17], and an extremely complicated mechanical engineering problem, on which little has been published. In the author's experience, roughly 15% of the effort in implementing a new gradient coil centers on the electromagnetic problem. The following paragraphs are intended to shed some light on the remainder.

Increasing the gradient area per unit time generally means increasing both peak slew rate and peak amplitude. Amplitude is limited by the maximum current we can drive. The slew rate is limited by the voltage one can apply to the gradient coil.

Electrical current affects the gradient coil in two particular ways that impact the overall performance of the system. First, Joule heating of the gradient conductors increases the temperature of the gradient coil. While almost all modern gradient coils incorporate a water-cooling mechanism to carry this heat away, the structural materials used in the gradient coil (generally fiberglass and various types of epoxy) are necessarily poor thermal conductors — good thermal conductors are also usually good electrical conductors, and placing a good electrical conductor in such close proximity to the gradient coil windings would produce additional eddy current distortions of the gradient waveforms. Getting the heat to the coolant remains a significant problem.

Second, Lorentz forces on the gradient windings increase with field strength and current. These Lorentz forces produce bulk vibration of the gradient coil as well as acoustic noise. Bulk vibration of the coil generally leads to vibration of the sample, producing motion artifacts, and also produces a time-varying static field

perturbation due to the magnetic susceptibility of the coil itself. In addition, a vibrating conductor in a magnetic field produces an electromotive force, which will appear to the gradient amplifier as additional (frequency dependent) load resistance.

Acoustic noise represents a significant limitation on system performance, and has received much attention in recent years on clinical MR systems. Determining appropriate scaling laws for sound pressure levels in the magnet bore with field strength is extremely difficult due to the inevitable changes in magnet bore and gradient coil geometry. In practice, one must build and install the coil, take all possible steps to minimize the radiated acoustic noise from the gradient (through the use of vibration isolation and acoustic damping materials), and test whether protocols of interest exceed safe operating guidelines when subjects where hearing protection, such as the FDA Significant Risk Criteria or the IEC 60601-2-33 standards. In general one must also consider occupational exposure of system operators and other support personnel. Should the protocols exceed the limits, one has no choice but to modify the protocol (such as timing changes to avoid mechanical resonances, waveform shape modifications such as the use of sinusoidal rather than trapezoidal waveform transitions, or reduction in duty cycle).

The primary limit on applied voltage is electrical breakdown between conductive elements. Particularly near sharp edges in the conductor pattern, voltages of several kilovolts can be present between conductive elements in the coil or the leads and cooling manifolds. The presence of even a small air bubble can provide a pathway for discharge, which generally leads to the formation of a carbon track that shorts out the two conductive elements. Prior to breakdown, local voltage stresses can produce microdischarges that emit RF signals which can be picked up by the receiver (so-called “white pixels”). One should note, however, that most such microdischarges originate from metallic components in intermittent contact.

5. RF COILS AND COIL INTERFACES

Much discussion has taken place over the last 15 years regarding the design of RF coils for ultra high field systems. Hoult provides a treatment of the physics of RF interactions with lossy dielectrics, but the complexity of human tissue generally precludes the use of analytical techniques [6]. Several groups have developed methods based on finite-difference time domain (FDTD) calculations, which have become an essential tool in evaluating RF coil designs [18]. Unfortunately, however, the practical application of these calculations has been hampered by the need for special computing hardware and by the difficulties in producing quantitatively predictive results as to required input power for a particular load. Two general conclusions have nonetheless become clear:

- While volume resonators of various designs (such as a birdcage or a TEM) can certainly be made to function at 300 MHz and higher, they cannot produce a uniform excitation field due to ohmic and displacement current flow within the tissue. Numerical simulations using the

Finite-Difference Time Domain method and related methods have indicated that different configurations of drive currents may produce a more uniform excitation pattern than could be achieved with the eigenmodes of the resonant structure [19].

- Small surface coils acting as receivers retain their sensitivity advantages [20] over volume resonators.

One key aspect of phased array design [10], whether for enhanced sensitivity or parallel imaging, is minimizing the coupling between array elements. As noted early on, there are three elements of this coupling: inductive coupling, capacitive coupling, and coupling through the sample.

Inductive coupling is traditionally minimized by overlapping nearest neighboring coil elements to reduce mutual inductance, and by using a low-input impedance preamplifier with an impedance transformer to present a high impedance to the coil and so suppress current flow on the coil, which will similarly reduce coupled current flow on nearby elements. Overlapping the coil elements places significant constraints on the design, particularly for parallel imaging applications. The intrinsic sensitivity of a given element decreases with size, up to the point where the noise from the sample becomes comparable to the Johnson noise from the coil itself. Since the sample noise voltage increases slightly more than linearly with frequency (due to the frequency dependence of the noise power and the frequency dependence of tissue conductivity), the minimum coil size therefore decreases with frequency. Given the overlap requirement, the maximum field of view of the array is then constrained for a fixed number of receiver channels.

Solutions to this problem are currently under development by a number of groups. First, the number of receiver channels can be increased, provided the data throughput can be sustained, which often requires significant hardware and software changes beyond simply the addition of further receivers. Second, more generic coil arrangements can be utilized provided some additional means is provided to suppress currents from neighboring elements, such as that described by Zhang [21].

A further problem concerns the reliance on low-input impedance preamplifiers. As the number of channels grows, the physical space available for these preamplifiers decreases, and direct coupling between preamplifiers, protection switches, and other RF components outside the coil can become a significant problem as well.

Much consideration has properly been given to specific absorption rate limits (the power deposition rate in tissue). The IEC guidelines as well as the US Food and Drug Administration guidelines limit both the spatial average and the spatial peak SAR. At lower frequencies the power deposition distribution is fairly uniform, and so the two limits tend to be simply related. A further advantage of this condition is that one need only measure the total RF power delivered to the sample and estimate the mass of tissue within the field of view of the transmitter coil to produce an accurate estimate of the peak and average SAR. Further, given the sensitivity benefits of array coils, it has become common practice in clinical MR system to

rely predominantly on a single large-volume transmitter for most applications, with dedicated receiver arrays for each anatomical region.

For ultra high field systems this arrangement is likely to continue to prove unworkable due to the inability of a large-volume transmitter coil to produce a uniform excitation within an extended region of tissue (as well as the increasing inefficiency of such a coil, requiring a larger and significantly more costly power amplifier). Due to RF field inhomogeneity, the relation between the spatial peak and spatial average SAR is generally not so simple, and FDTD calculations indicate that significant changes in power requirements and field distribution can result from simple changes in the placement of the coil relative to the sample — the implication of this result is that variations are to be expected for different samples. While methods exist to map the RF magnetic field *in vivo*, no practical method has yet been demonstrated to map the RF electric field, and so a direct measurement of the SAR is not possible.

6. DESIGN CHARACTERISTICS AND CONSIDERATIONS

What follows is an attempt to provide a list of system characteristics to consider in developing or specifying an ultra high field MR system. While a complete description of each of these attributes is beyond the scope of the present article, the author hopes that this list will provide some impetus for further investigations by the reader.

Magnet

Field strength, Bore diameter, Cryostat length, Homogeneous volume, Homogeneity, Stability, Cryogen consumption, Shielding requirements, Sensitivity to environmental perturbations, Bore tube construction.

Gradient coil

Inner bore diameter, Outer bore diameter, Strength, Operating field of view, Maximum pixel shift (integral nonlinearity), Maximum voxel volume change (differential nonlinearity), Inductance (vs. frequency), Resistance (vs. frequency), Withstanding voltage, Weight, Mounting, Thermal capacity, Cooling mechanism, Rigidity modulus (vs. frequency), Lead construction.

Embedded resistive shim coils

Number of channels, Strength (per channel), Inductance (per channel), Resistance (per channel), Coupling to gradients, Coupling to other shims, Coupling to magnet, Cooling mechanism, Thermal capacity, Lead construction.

Embedded passive shims

Mounting mechanism, Thermal coefficient, Cooling mechanism, Extraction force, Electrical insulation, Capacity.

Gradient drivers

Peak drive current, Peak drive voltage, Output impedance (vs. frequency), Noise spectrum vs. load impedance, Amplitude stability (vs. frequency), Maximum current duty cycle, Current gain vs. frequency, Digital input resolution, Waveform update rate, Small signal bandwidth, Control interface, Allowable load impedance, Load compensation tunability.

Resistive shim drivers

Number of channels, Peak drive current, Peak drive voltage, Output impedance (vs. frequency), Output noise spectrum vs. load impedance, Amplitude stability, Noise rejection, Control interface, Allowable load impedance.

RF transmitter

Number of channels, Peak output power, Maximum pulse duration, Noise figure (blanked or unblanked), Maximum operating frequency, Minimum operating frequency, Gain vs. frequency, Amplitude stability vs. frequency, Phase stability vs. frequency, Dynamic gain linearity, Minimum blanking interval, Crosstalk (for multichannel transmitters), Maximum operating duty cycle, Waveform digital resolution, Maximum waveform bandwidth, Waveform digital update rate.

RF receiver

Number of channels, Gain, Dynamic gain linearity, Maximum bandwidth, Minimum bandwidth, Bandwidth adjustability, Phase noise, Amplitude stability, Channel crosstalk, Data throughput rate, Maximum data vector length.

RF coils and coil interface

Transmitter interface, Number of transmitter channels, Detuning driver voltage, Detuning driver current, Detuning driver switching time, Detuning driver fault detection mechanism, Connector type, Connector withstanding voltage, Connector power limit vs. load impedance, RF power sensor type, RF power monitor integration time, RF power monitor configuration control, Blanking mechanism, Blanking time, Output impedance.

Receiver interface

Number of receiver channels, Number of coil connections, Number of channels per connector, Detuning driver voltage, Detuning driver current, Detuning driver switching time, Detuning driver fault detection mechanism, Connector type, Input impedance, Gain, Noise figure, Spur-free dynamic range.

Transmitter coils

Inner diameter, Field of view, phantom load, B1 field strength per watt of input power (vs. location), Shielding mechanism, Tuning mechanism, Number of drive ports, Maximum duty cycle, Low frequency shield cutoff.

Spectrometer

Number of waveform generators, Digital resolution, Update rate, Buffer depth, Refill duration, Reconstruction engine, Data throughput, On-line data storage capacity, Network throughput, Programming environment, Scalability.

Patient handling

Physical dimensions, Positioning accuracy, Positioning reproducibility, Physiological monitoring, Noise rejection, Trigger control, Recording capabilities, Number and type of sources, Vibration isolation, Illumination and ventilation.

Application software

Library of existing pulse sequences, Development environment, Visualization capabilities, Database capabilities, Data transfer mechanisms.

7. CONCLUSIONS

Hardware development for ultra high field MR systems will remain an active area of scientific and engineering investigation for many years to come, both for its own sake and because the solutions to these problems will help improve lower field clinical MR systems as well. The potential of ultra high field MR technology to lead to advances in basic physiology and pathology will certainly result in improved diagnostic procedures at lower field strengths, particularly when coupled to novel contrast agents, including hyperpolarized materials [22,23]. While magnet technology will remain an important part of ultra high field MR system development, gradient and RF technology will continue to gate the development of new applications.

8. REFERENCES

1. Kimmlingen R, Eberlein E, Gebhardt M, Hartinger B, Ladebeck R, Lazar R, Reese T, Riegler J, Schmitt F, Sorensen GA, Wedeen V, Wald LL. 2005. An easy to exchange high performance head gradient insert for a 3T whole body MRI system: first results. *Proc Int Soc Magn Reson Med* 1630.
2. Bomsdorf H, Helzel T, Kunz D, Roschmann P, Tschendel O, Wieland J. 1988. Spectroscopy and imaging with a 4 Telsa whole-body MR system. *NMR Biomed* 1:151–158.
3. Barfuss H, Fisher H, Hentschel D, Ladebeck R, Vetter J. 1988. Whole-body MR imaging and spectroscopy with a 4-T system. *Radiology* 169:811–816.
4. Schenck JF, Dumoulin CL, Redington RW, Kressel HY, Elliott RT, McDougall IL. 1992. Human exposure to 4.0-Tesla magnetic fields in a whole-body scanner. *Med Phys* 19(4):1089–98.
5. Robitaille PML, Warner R, Jagadeesh J, Abduljalil AM, Kangarlu A, Burgess RE, Yu Y, Yang L, Zhu H, Jiang Z, Bailey RE, Chung W, Somawiharja Y, Feynan P, Rayner D. 1999. Design and assembly of an 8 tesla whole body MRI scanner. *J Comput Assist Tomogr* 23:808–820.
6. Hoult DI. 2000. Sensitivity and power deposition in a high field imaging experiment. *J Magn Reson Imag* 12(1):46–67.
7. Vaughan JT, Garwood M, Collins CM, Liu W, DelaBarre L, Adriany G, Anderson P, Merkle H, Goebel R, Smith MB, Ugurbil K. 2001. 7T vs. 4T: RF power, homogeneity, and signal-to-noise comparison in head images. *Magn Reson Med* 46(1):24–30.
8. Edelstein WA, Glover GH, Hardy CJ, Redington RW. 1986. The intrinsic signal-to-noise ratio in NMR imaging. *Magn Reson Med* 3(4):604–18.9.
9. Durney CM, Iskander MF. 1986. *Radiofrequency radiation dosimetry handbook*. Salt Lake City: U Utah P.
10. Roemer PB, Edelstein WA, Hayes CE, Souza SP, Mueller OM. 1990. The NMR phased array. *Magn Reson Med* 16:192–225.
11. Pruessmann KP, Weiger M, Scheidegger MB, Boesiger P. 1999. SENSE: sensitivity encoding for fast MRI. *Magn Reson Med* 42:952–962.
12. Wilson MN. 1983. *Superconducting magnets*. Oxford: Clarendon Press.
13. Iwasa Y. 1994. *Case studies in superconducting magnets*. New York: Plenum Press.
14. Montgomery DB. 1969. *Solenoid magnet design*. New York: Wiley-Interscience.
15. Pearson R. 2004. Personal communication.
16. Wilson JL, Jenkinson M, Jezzard P. 2002. Optimization of static field homogeneity in human brain using diamagnetic passive shims. *Magn Reson Med* 48(5):906–914.
17. Jin JM. 1999. *Electromagnetic analysis and design in magnetic resonance imaging*. Boca Raton, FL: CRC Press.
18. Strilka RJ, Li SZ, Martin JT, Collins CM, Smith MB. 1998. A numerical study of radiofrequency deposition in a spherical phantom using surface coils. *Magn Reson Imag* 16(7):787–798.
19. Ibrahim TL, Baertlein B, Abduljalil A, Zhu H, Robitaille PML. 2001. Effect of RF coil excitation on field inhomogeneity at ultra high fields: a field optimized TEM resonator. *Magn Reson Imag* 19(10):1339–1347.
20. Edelstein WA, Schenk JF, Hart HR, Hardy CJ, Foster TH, Bottomley PA. 1985. Surface coil magnetic resonance imaging. *JAMA* 253(6):828.
21. Zhang X, Webb A. 2004. Design of a capacitively decoupled transmit/receive NMR phased array for high field microscopy at 14.1 T. *J Magn Reson* 170(1):149–155.

22. Ardenkjaer-Larsen JH, Fridlund B, Gram A, Hansson L, Lerche MH, Servin R, Thangning M, Golman K. 2003. Increase in signal-to-noise ratio of >10,000 times in liquid-state NMR. *Proc Natl Acad Sci USA* 100(18):10158–10163.
23. Golman K, Ardenkjaer-Larsen JH, Svensson J, Axelsson O, Hansson G, Hansson L, Johannesson H, Leunbach I, Mansson S, Petersson JS, Pettersson G, Servin R, Wisstrand LG. 2002. ^{13}C -angiography. *Acad Radiol* 9:S507–510.

ASPECTS OF CLINICAL IMAGING AT 7 T

Franz Schmitt¹, Andreas Potthast¹, Bernd Stoeckel³,
Christina Triantafyllou², Christopher J. Wiggins²,
Graham Wiggins², and Lawrence L. Wald²

¹ *Siemens Medical Solution, Dept. MREF, Erlangen, Germany*

² *Massachusetts General Hospital Martinos Center,
Charlestown, MA, USA*

³ *Siemens Medical Solution, Malvern, PA, USA*

The intrinsic improvements in signal-to-noise ratio, spectral dispersion, and susceptibility contrast with increasing static magnetic field strength, B_0 , has spurred the development of MR technology from its very first application to clinical imaging. With maturing magnet, RF, and gradient technology, the clinical community has seen the static magnetic field of clinical systems increase from 0.2 to 1.5 to 3.0 T. Today, the "high field" label for human MR research describes initial experiences with 7, 8, and 9.4T systems. While currently primarily research instruments, this technology is bound to cross the boundary into the clinical diagnostic arena as key technical issues are solved and the methodology proves itself for addressing clinical issues. In this chapter we discuss the particular advantages and disadvantages of ultra high field systems for clinical imaging as well as some of the immediate technological challenges that must be solved to derive the full benefit of the extraordinary sensitivity of these systems, which has been glimpsed from their research use.

1. INTRODUCTION

When looking back to the history of clinical MRI we see a strong effort to find the cutting edge of useful MRI with respect to magnetic field strength. The first clinical systems in 1983 started at 0.35 and 0.5 T and were followed immediately by the development of 1.0 and 1.5 T in the mid to late 1980s. The latter field strengths have been the focus of MRI over the last 20 years. Although higher field strengths, such as 4 T [1,2], systems have been tested in the late 1980s and early 90s, it is only in the late 90s and early 2000s that even 3 T made it into the clinical arena.

Over the last 5 years, 3 T has become an important clinical field strength. All major vendors now deliver and focus strongly on 3T whole-body systems. Others also deliver dedicated head systems at 3 T [3]. Currently a strong majority of about 14000 systems operate at 1.5 T. About 400 clinical 3T systems are installed, and the numbers are increasing steadily with maturing 3T technology.

Since the signal-to-noise ratio (SNR) increases approximately with magnet field strength [4], going to higher magnetic fields in MRI has always been a driving force for improving the capabilities of MRI. For example, SNR-starved techniques such as fMRI [5] and diffusion tensor imaging (DTI) [6] strongly benefit from increases in field strength. Newer developments for speeding up imaging time, such as SENSE [7], SMASH [8], and GRAPPA [9], also benefit from the increase in SNR at higher field strength because of their intrinsic tradeoff of SNR versus imaging speed. In addition, MR spectroscopists always looked for higher field strength to enhance sensitivity and because spectral dispersion increases with magnetic field strength.

So overall there was, and still is, a push to go to higher field strength in order to explore its benefits for clinical and research imaging. In the late 80s and early 90s the first visionary push was made to seek funding for whole-body MRI systems up to 10 T [10]. However, it took until 1998 for the first 8T system to finally be built and installed at Ohio State University [11], followed by the first 7T magnet at the Center for Magnetic Research at the University of Minnesota in 1999 [12]. The second 7T system was then installed at MGH in 2001 and has been operating since early 2002. Recent installations at 7 T are now operating at the National Institutes of Health (NIH) in Bethesda, MD, the Institute for Neurobiology (IFN) in Magdeburg, Germany, and New York University (NYU) in New York City. Other sites are currently under construction, includes ones at Niigata University (Japan), Stanford University, the University of California at San Francisco, and the University of Nottingham (England). Ambitious, even higher field strengths are currently being explored that allow human subject access. At the University of Illinois (Chicago) a 9.4T/650-mm system is under test. The Center for Magnetic Resonance Research at the University of Minnesota also has a 9.4T/650-cm bore system operating since the end of 2004 [13]. An 11.7T system for human use is in discussion and planning in France [14]. However, 7 T seems to have become a quasi-standard at the moment, because affordable magnets are available with 900-mm warm bores. This allows the standard clinical gradient coils to be inserted. Demand for 7 T is rising worldwide. We estimate that the number of 7T scanners that will be delivered in the next five years will be approximately the same as the number of 3T systems that were installed in the 90s before the commercializing wave of clinical 3T scanners arrived.

All these UHF systems are used to explore MR imaging and spectroscopy applications for research and clinical use. T_1 becomes longer with increasing field [15]. This offers some advantage for MR angiography as the background tissue can be suppressed more easily. It was one of the main clinical wins for going to 3 T. T_2 does not change with magnetic field strength. However, T_2^* becomes shorter with increasing field strength due to increased macroscopic and microscopic susceptibil-

ity effects in the larger static field. Because T_2^* effects associated with blood oxygenation changes also become larger at higher field, there is a clear advantage for BOLD imaging, for example. Since tissue T_2^* also shortens at higher field, the optimum echo time for the BOLD experiment shortens for increasing B_0 field. The undesirable increases in macroscopic susceptibility effects pose more restrictions on fast gradient recalled echo (GRE) imaging applications as the susceptibility artifacts can become more prominent especially in the region of air–bone–tissue interfaces. Echo Planar Imaging (EPI) [16] therefore requires higher gradient performance in order to achieve shorter data acquisition time. For example, to achieve equal EPI distortion artifacts at 7 T compared to 3 T, theoretically the EPI readout train has to be shortened 7/3-fold, requiring increased gradient strength and slew rate.

Although the contrast and sensitivity gains are compelling, there are many technical issues to be solved. The most dominant issues are related to the increase in specific absorption rate (SAR), which theoretically increases with ω_b^2 at least up to 3 T [17,18]. Also, dielectric effects, first described by Röschmann et al. [19], although already visible at 1.5 and 3 T, are becoming dominant at 7 T and above and create significant image and contrast homogeneity challenges. Since the B_1 field distribution is altered on both the transmit and receive sides, this may affect the flip angle distribution across the image and therefore the T_1 contrast in T_1 -weighted imaging.

Vibration due to fast gradient switching is the source of acoustic noise. It also poses higher demands on how gradient and RF structures are mounted inside the magnet as the forces on the entire magnet and coil assembly are increasing. Acoustic noise at high fields scales with the magnetic field strength. All 7 and 8T systems can work close to or above the 140-dB level if no acoustic noise insulation and damping is performed and when driven at full gradient performance. This extreme level would prohibit human use, even with earplugs and earmuff use [20]. Reducing acoustic noise is therefore an important engineering issue at ultra high field. Other issues such as changes in the impedance of the gradient coil (GC) due to the forces on the gradient coil assembly have to be considered as well. In-vivo shimming for high field human scanners is more demanding due to the intrinsic field dependence of susceptibility. For spectroscopy significantly higher shim strength seems to be especially required.

Keeping in mind that 3 T in the 90s is now maturing as a clinical field strength, one may extrapolate the same for 7 T and ask how a 7T clinical system would look in the future. What would be the technical solutions to the RF and acoustic noise challenges mentioned above? What is the proper strategy to allow clinical T_1 -, T_2 -, and T_2^* -weighted imaging at 7 T and what can be achieved today? This is what we will explore in the present chapter.

2. GENERAL SYSTEM CONFIGURATION OF A 7T CLINICAL MRI SYSTEM

A hypothetical 7T clinical system is not different from a clinical 1.5 or 3T scanner with respect to system topology and configuration (see Figure 1). However, there are some differences in design and construction of certain components and an overall desire to utilize the highest performance subsystems to mitigate some of the relaxation and susceptibility challenges of ultra high field. Clearly, the magnet and base frequency of the RF system require alteration to “upgrade” a 1.5 or 3T system for use at 7 T. Other components such as the gradient and shim system can be specially designed for 7 T, but in general the same specifications that produce optimum performance at 3 T are needed at 7 T. Therefore, in practice one takes the highest-performance whole-body gradient set currently available, perhaps augmenting it with specially optimized insert gradients or increased acoustic shielding. The same is true for shimming, as a well-designed 7T MRI system require higher shim fields, necessitating increased shim efficiency or supply current. Additionally, the higher susceptibility effects at ultra high field have motivated the possible use of higher spatial order shim sets. The system’s software (SW) topology is also unchanged when compared to a clinical MRI system.

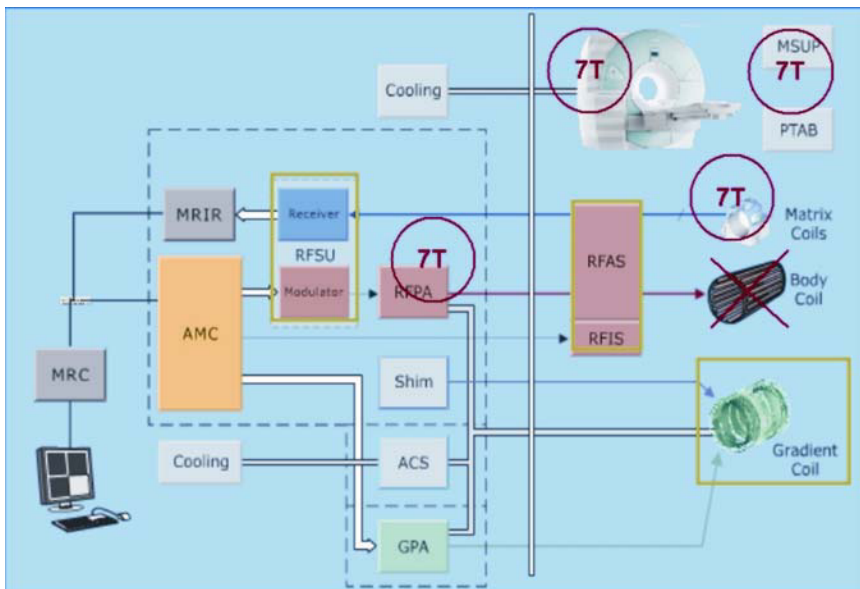


Figure 1. MRI system overview of the Siemens 7T MRI scanner. Green box: minor changes to standard system. In red circles: major changes needed to adapt to 7 T. See attached CD for color version.

2.1. Magnet

The magnet is the key element of an MRI system. Several issues have to be considered when designing and siting an ultra high field magnet such as a 7T/900-mm diameter magnet. As the magnet field strength, uniformity, and fringe field footprint are related to the amount of superconducting wire, it is generally expected that a 7T magnet is significantly larger and more expensive than a 1.5 or 3T magnet. In addition, the forces on the winding structures at ultra high field will demand an increase in the size of a UHF magnet in order to avoid collapsing of the magnet and additional quench protection is needed to safely dissipate the increased stored energy of the magnet. For further literature we refer to the Chapter 2 in the present volume.

2.1.1. Whole-Body Magnets

Overall, UHF whole-body magnets will be big and expensive. At present there is only a single vendor for 7T whole-body magnets, Varian Instruments, formerly known as MAGNEX Scientific. To date, typical sizes are 2.4 m in outer diameter, 900 mm inner bore, and 3.4 meter in length. Thus the clinical 7T magnet is quite large compared to short-bore clinical systems at 1.5 T, which over the last decade have been reduced to 1.2 m in length and 2 m in outer diameter. In addition to the physical bulk of the large magnet, we have to deal with increased demands from its larger magnetic footprint. This is especially problematic since current 7T designs are not self-shielded to reduce the fringe field [21]. The <5-gauss zone is considered the safe zone for uncontrolled access in an hospital environment. In this region, cardiac pacemakers and other forms of life support are considered safe to use. As floor space is expensive in a clinical environment, the 5-gauss fringe field area has to be kept as small as possible (see chapter 2, on magnets). Therefore passive magnetic shielding is required, which involves significant amounts of iron and its accompanying expense and construction effort. For 7T systems, depending on the degree of shielding, typically between 200 and 400 metric tons of iron are needed. That again poses a demand on the building structure and likely prevents a 7T system from being sited anywhere but on the ground floor.

2.1.2. Head-Only Magnet

One way to reduce both magnet expense and siting issues is to consider a self-shielded head-only magnet. For 7 T this would considerably shrink the magnet weight and size, perhaps a justifiable route as whole-body imaging at fields of 7 T and above is in its infancy, while neurological applications offer many more accessible clinical applications in the near future.

If full advantage is to be taken of the head-only magnet for easier siting in a clinical environment, a self-shielded magnet is required. The fringe field of such a magnet is then comparable to what can be achieved with a typical 3T whole-body magnet. In addition to reducing siting costs, building such a magnet will incur less cost as the superconducting wire length is considerably shorter and the overall

geometric size is significantly smaller. One matter of concern may be the steep fringe field of the short and compact self-shielded magnet. Physiological effects have been observed at 7 T, primarily while the human subject is moved into the magnet, and these effects might be more pronounced. Moving the human subject even more slowly into the magnet might help here. More research on this topic is required.

2.2. RF System

In this section we describe the basic configuration of the RF system with a focus on the changes needed to adapt a clinical system for 7T use.

The RF system of an MR scanner performs two main tasks. The first task is to transmit (TX) a high-power RF pulse (typically in the kW range) with well-defined frequency, amplitude, and phase into the TX coil in order to expose the human body with the needed B_1 excitation field. The transmit path is considered in two sections — the low power pulse generation section and the high power section — including the RF power amplifier and the downstream components such as transmit receive switches and power monitoring equipment. The second task is to receive (RX) the MR signal from the RX coils, amplify the signal, and down-convert it before A/D conversion. We refer to this signal path as the small-signal low-noise branch.

As the RF chain is frequency dependent, virtually all components in the TX and RX chain have to be reevaluated and matched to the higher frequency of 300 MHz, corresponding to the proton Larmor frequency at 7 T, and the frequencies for multi-nuclei MRS resonating at lower frequencies. In addition, they each have additional gain and dynamic range considerations.

2.2.1. RF Small-Signal Components

The trend toward utilizing the increased SNR of dedicated receive arrays and the accelerated encoding schemes enabled by parallel detection motivates the development of a clinical 7T system with a large number of receive channels, for example, 32 fully integrated high bandwidth receivers as found on state-of-the-art 1.5 and 3T clinical systems [22]. The RF system also needs to generate the lower frequencies needed for multi-nuclear spectroscopy. Most importantly for a clinical system, the receivers, synthesizers, and modulators need to be fully incorporated into the service software tools, allowing the service engineer to properly diagnose malfunctions.

TX

With the exception of the increased operating frequency, the small-signal components of the transmit chain do not have significantly different needs from lower field clinical units. Since spectroscopy and imaging of low-gamma nuclei is an appealing application for UHF instruments, a second modulator and TX channel can be added, which can be used for multi-nuclei experiments to perform, e.g.,

proton decoupling for ^{31}P experiments, i.e., transmitting at proton frequency while receiving at ^{31}P frequency.

The one additional need that is currently in the exploratory stage is the potential for multiple independent transmit channels for achieving transmit SENSE. While currently in the early research stage, this promising technology might be useful for accelerating transmit pulses with spatially varying amplitude and phases that could be helpful in overcoming dielectric center brightening, which dominates the 7T brain transmit profile (see 2.2.4, B_1 Shimming).

RX

MR signals are amplified by low-noise preamplifiers (noise figure <0.8 dB) integrated into the receive coil. Then the signals pass through a second stage of RF amplification. The goal of the initial amplification step is to amplify the signal and detect body noise to a level such that the additional noise from the receiver is insignificant. A difficulty specific to UHF is that the MR signal and body noise detected at the coil is significantly stronger than at lower fields. In general, the MR signal scales as B_0^2 and the noise as B_0 ; thus a 7T system can expect almost 22-fold higher signal levels compared to 1.5 T. Thus the UHF system requires less analog gain to satisfy the input power demands of the receiver (defined here as the demodulator and analog to digital converter (ADC)). Therefore it is more difficult to satisfy the receive chain criteria that the initial low-noise amplification gain be sufficient to amplify the signal and body noise to a level well above the noise floor of the receiver. The higher sensitivity of the UHF system also requires increased dynamic range of the receiver, currently limited by the receiver to 18-bit. Nonetheless, current experience with 3D whole-head scans suggests that this is sufficient, at least for head imaging.

2.2.2. High-Power Chain (RFPA to RF Coil)

Solid-state RF power amplifiers at 300 MHz with a peak RF power output in the multi-kW range and with the needed linearity and unconditional stability against oscillation were not available until the desire for ultra high field MR systems motivated their development.

Existing RF power amplifier (RFPA) systems are comprised of multiple solid-state final stages combined to achieve 7-kW peak power at the output that seems to be sufficient for head imaging only. If, however, higher power levels are needed, for example, for whole-body imaging, tube amplifiers will be the choice, as a solid-state amplifier with a power output on the order of 30 kW and higher will not be affordable and so unlikely to be available commercially. So far, UHF imaging experience is almost exclusively limited to head and extremity imaging, although whole-body imaging at 7 T has been demonstrated just recently by Vaughan et al. [23]. In order to approach whole-body imaging one therefore has to go different routes to use the available low-power RFPAs and combine them to achieve higher power output. Since the B_1 excitation inhomogeneity is already a problem in head

applications, it is likely to be an even greater problem for whole-body applications. B_1 shimming and TX SENSE [24] will be important for future 7T systems (see §2.2.3). This topology allows the TX path to be split into several low-power TX lines and therefore takes advantage of multiple sets of lowerpower RFPA.

A second RFPA can be optionally connected to allow decoupling MR spectroscopy experiments. Usually, the second RFPA supports MR frequencies below the ^1H frequency, except ^{19}F , while the primary RFPA is broadband and provides the entire frequency band from 40 to 305 MHz, and therefore covers all important multi-nuclei spectroscopy frequencies at 7 T (^{19}F , ^{31}P , ^7Li , ^{23}Na , ^{13}C , ^{17}O). The frequency range of the second RFPA offers more vendor choices.. For example, at 7 T this corresponds well to a standard 3T broadband RFPA covering the range of 40 to 130 MHz

2.2.3. RF Power Requirement

When assuming a sinusoidal changing B_1 field, $B_1(t) = B_1 \sin(\omega_0 t)$, the driving current, $I(t)$, is therefore proportional to B_1 and the calculated power, P , is deduced as $P \sim I^2$, which is proportional to ω_0^2 . This is the assumption behind the $P \sim \omega_0^2$ rule widely used for MR power estimation. Therefore the RF power required to produce a particular RF pulse of a given flip angle α and duration τ scales theoretically with ω_0^2 as long as dielectric effects can be neglected:

$$P \propto \sigma \cdot B_1^2 \cdot \omega_0^2 \int r_{\perp}^2 dV \propto \omega_0^2. \quad (1)$$

Following the ω_0^2 rule, one would expect to end up with an excessive RF power requirements for 7 T of

$$P_{7\text{T}} = P_{1.5\text{T}} \cdot \left(\frac{7\text{T}}{1.5\text{T}} \right)^2 = P_{1.5\text{T}} \cdot 21.7. \quad (2)$$

This theory, however, neglects the wavelength effects that start to appear when the RF wavelength in the dielectric head becomes comparable to the size of the head. In this case (which appears to become significant for frequencies above 200 MHz), a full numerical solution of Maxwell's equations is needed inside a head model that incorporates the tissue dielectric and conductive properties. A simple description of the power needed to achieve a given flip angle with a clinically relevant pulse shape is complicated by the fact that the B_1 distribution in the head is spatially inhomogeneous even in a transmit coil that is very homogeneous for a low dielectric constant sample. Thus different power requirements are needed in different locations within the head. Head model-based calculations of the power needed for excitation using a volume head coil suggest that the required power increases roughly supralinearly with field at low field (1.5 to 3 T) and more linearly above 3 T, with different slopes depending on whether the criteria is a 90° excitation in the center of the head or chosen to maximize the average slice image amplitude [18]. Other head-model simulations show signs of the needed RF

power leveling off with increasing field strength or even decreasing with field for UHF [25].

2.2.4. B_1 Shimming

Recently, a technique for RF shimming or B_1 shimming has been contemplated [26–28]. The idea behind that is to compensate RF inhomogeneity by using multiple independent transmit channels with distinctive spatial distributions. When employing B_1 shimming, therefore, a parallel array of RF power amplifiers, on the order of 8 to 32 units, would be required. The power requirements would be somewhat smaller when compared to the conventional technique. It is not clear at the moment what the power requirements will be. The individual channels would allow different amplitude and phase settings by, for example, passive attenuators and phase shifters on the small-signal side. A general solution, however, would provide independent freely programmable TX channels allowing to change amplitude, phase, and pulse shape individually (see Figure 2). This latter digital control of each excitation pulse waveform opens the possibility of shaped excitations that may overcome the B_1 inhomogeneities and susceptibility-induced phase shifts. Such spatially shaped pulses will likely benefit from transmit SENSE acceleration methods. Parallel transmit arrays could therefore solve the demand for higher RF peak power for whole-body applications, e.g., 16 times 4 kW would get us beyond the 35 kW that is already currently available on a clinical 3T scanner. The SAR limit for the human body, however, may limit this to a lower value anyway.

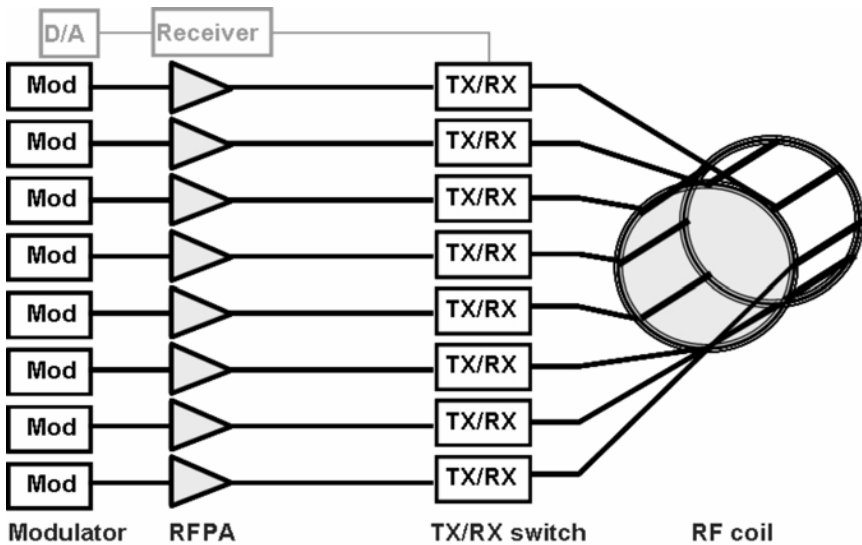


Figure 2. Schematic setup for B_1 shimming and TX sense at ultra high fields. Instead of using one RFPA only, the entire TX line is split into several TX channels, allowing freely programmable amplitude, phase, and pulse shapes per channel.

Being able to control B_1 profiles across the volume of interest (VOI) allows RX-based parallel imaging techniques to be extended [7–9] to the TX side. A technique, called transmit SENSE, recently introduced by Katscher and Zhu [29,30] uses a multiple TX coil topology for shortening excessively long spatial-spectral RF pulses. With such a technique, SAR monitoring is becoming very complex and will be subject to further research.

2.2.5. SAR Monitoring

SAR monitoring at 7 T is identical to the standard MR scanners at lower field strengths. Since SAR cannot be measured directly, the transmitted RF power is monitored and thereby limited to a certain maximum level. Forward and reflected RF power to and from the TX coil has to be considered as well. If we also take into account cable losses, internal coil losses, and the unloaded/loaded ratio of the coil, we can determine the total RF power deposition. However, the B_1 field distribution inside the body, altered by dielectric effects and RF eddy currents, has to be modeled with finite-difference time-domain (FDTD)-RF field simulation software and understood before applied in vivo. Careful modeling of the B_1 field and power distribution inside of, e.g., a head at 7 T, is mandatory. Thus SAR at 7T can be even more limiting for MR imaging than simple estimation based on the increased MR frequency suggests.

2.2.6. RF Coils

RF coils are the most exciting and challenging pieces of 7T instrumentation [31,32]. Exciting, because the rise of 7 T spawned many small RF companies to conquer the 300-MHz challenges, and new RF coil concepts are being developed at a quick pace. Challenging, because the B_1 RF inhomogeneities are problematic for clinical imaging. It is also not a simple task to build a phantom that resembles the human head well enough and reflects the RF properties of a human head as well. Therefore the final proof of a good-quality RF coil at 7 T is only given when in-vivo imaging is performed. Figures 3 and 4 demonstrate this situation. Figure 3 shows sagittal, coronal, and axial slices of a spherical phantom. Intensity brightening and signal voids are visible. Figure 4 compares MR images of two different phantom assemblies and solutions with a human head, imaged under the same sequence and protocol conditions. The upper row shows the loaded head phantom without internal structures and a permittivity ϵ of 49. The middle row has internal structures resembling the inner ear and an ϵ of 79 (for further information see Tropp et al. [33]). Clearly different signal profiles can be seen for different values of ϵ , and internal structures demonstrate the dielectric effects nicely. The lower row shows a coronal and an axial human head scan. The signal profile matches with the middle phantom image row quite well, suggesting that this phantom is more or less suitable for testing RF coils, but never will fully substitute for in-vivo testing as signal intensity patterns reflect flip-angle variation and therefore B_1 distribution. However, SAR cannot be estimated from the intensity variation patterns in these phantoms.

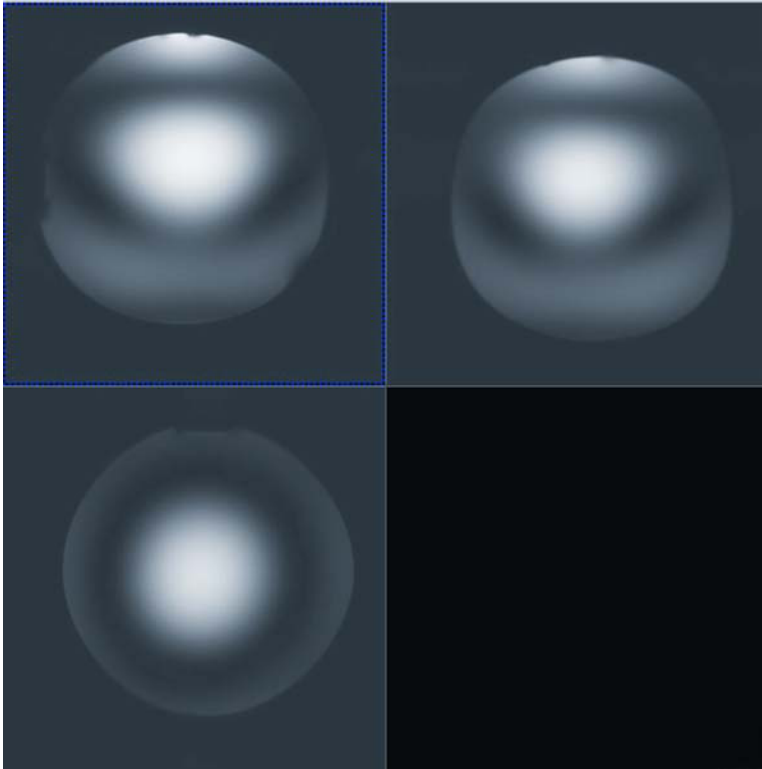


Figure 3. Dielectric effects in phantom images at 7 T. TE/TR = 4/100 ms, FL2D = 60°, BW = 300, FOV = 220 x 220; sagittal slice (top left), coronal slice (top right), axial slice (lower left).

Two major routes for RF coils at UHF are already visible today. A circularly polarized (CP) transmit/receive (TX/RX) head coil will be the initial workhorse for 7T scanners. Figure 5 shows nine slices of axial, sagittal, and coronal excitation of a human head, acquired with a low flip angle 2D GRE sequence used for scout imaging acquired with a CP birdcage head coil. Good volume coverage is given. Image brightening in the center caused by dielectric effects is visible. As multiple receive coils are standard in every clinical scanner now, it will be used heavily at 7 T as well. Figure 6 shows a comparison of a CP TX/RX coil with an 8-channel RX coil. Slice excitation was performed with the same TX coil. The same anatomical slice was selected for both sessions. At the left the TEM [34,35] TX/RX result is shown. Center brightening is visible. On the right, the 8-channel RX coil was used for data reception. This image appears brighter in the periphery, the high sensitivity near the surface coil elements compensating partly for the dielectric effects shown on the left. A profile comparison of a TX/RX TEM coil with an 8-channel

RX array coil is shown in Figure 7. SNR is significantly improved as can be seen by these graphs, even in the center of the head, which may be partly attributed to the smaller size of the 8-channel array coil, which is wrapped closely around the head inside the TEM coil used for TX in this comparison.

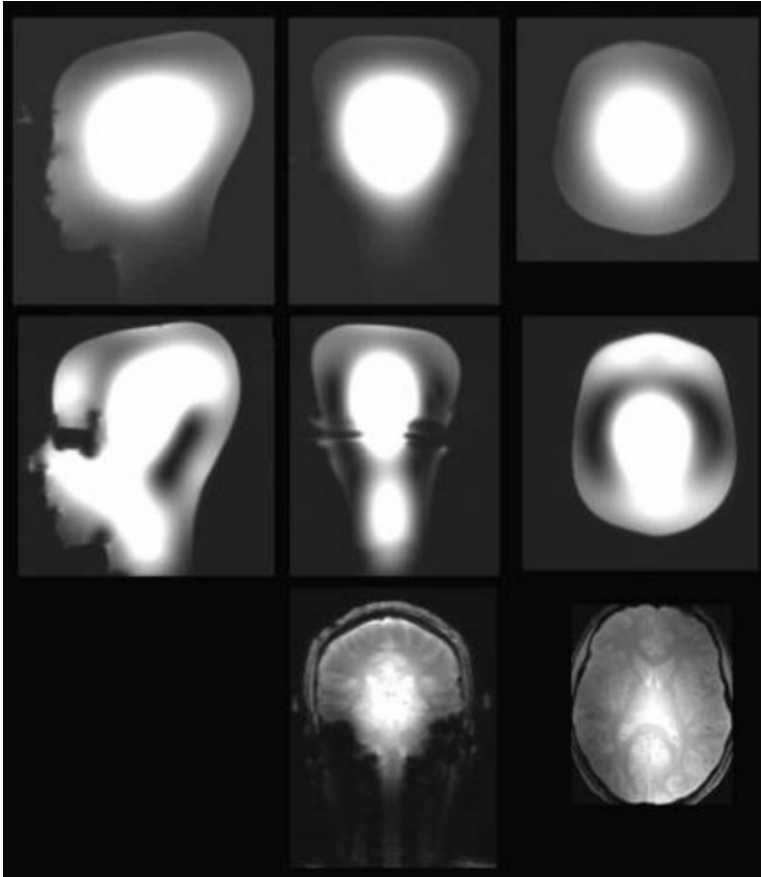


Figure 4. MR images of head-shaped phantoms acquired with the same type of RF coil. Different permittivities ϵ are set for the phantom images. Upper row: 70% isopropanol alcohol, 30% H₂O, 0.9% NaCl; $\epsilon = 49$. Middle row: NaCl loaded H₂O phantom with sinus and ear canals; $\epsilon = 78$; Lower row: coronal and axial slice through a human head. All images are acquired with TE/TR/flip angle of 5.5/40/10°.

As mentioned above, 16 to 32 receive channels are state of the art on 7T systems now. Therefore 32-element receive coils such as the helmet coil introduced by Wald and Wiggins [36] and the cardiac array coil introduced by Wintersperger et al. [37] and Hardy et al. [38] will be available in the near future. SNR improvements

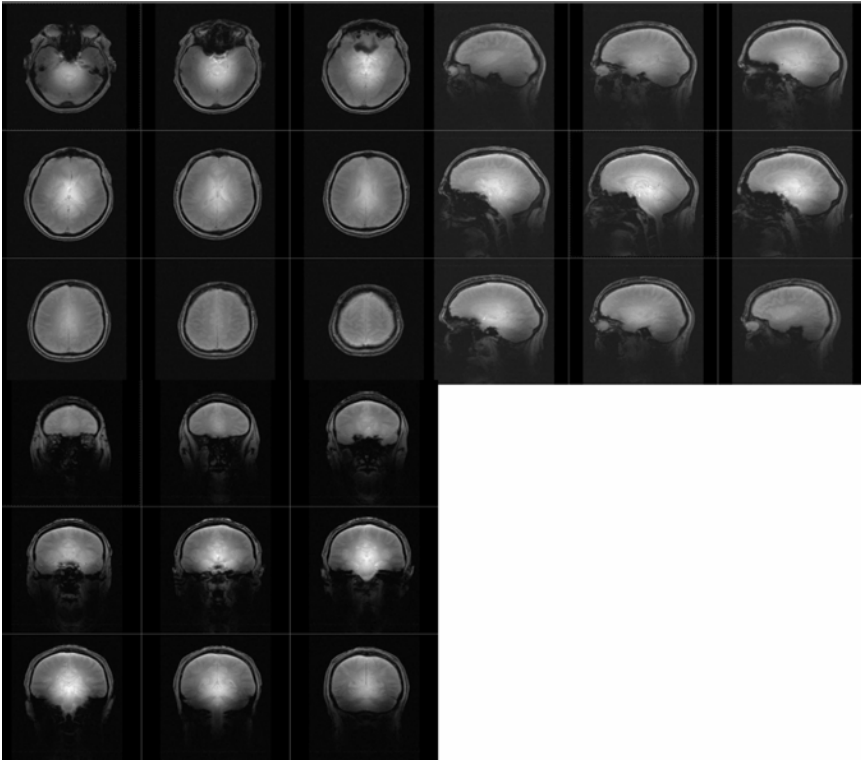


Figure 5. Low flip angle multi-slice GRE sequence in axial, coronal, and sagittal orientations. Data are acquired with a CP TX/RX birdcage coil. Flip angle = 20° , TE/TR = 3.3/113 ms, BW = 530 Hz/pxl, sl = 5 mm, = FOV = 228 x 280 with rectangular FOV.

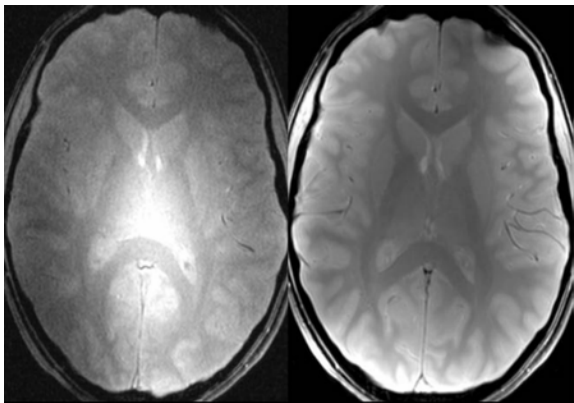


Figure 6. PD-weighted GRE images: TR = 200, TE = 3.92, flip = 20, 256 x 256 matrix, 200-mm FOV, TA = 29 sec. Left: acquired with a TEM-TX/RX coil. Right: same slice, but TEM TX and 8-channel RX coil.

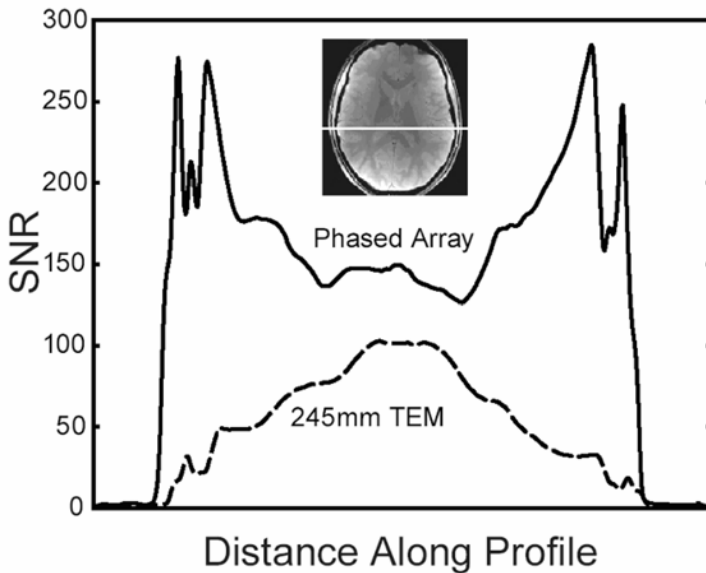


Figure 7. RF profiles: TEM TX/RX coils vs. array coil. SNR is plotted for a TX/RX TEM coils and the 8-channel RX coil array.

possible with such a coil type are significant and are on the order of 2–3 in the human cortex. Therefore we are certain that increasing numbers of RF coil vendors will provide RF coils with high channel numbers up to 32 and more, if system topology permits. First results with up to 90 channels [39] suggest that there is still a benefit with such high numbers of channels at higher fields such as 7 T.

2.3. Gradients

As mentioned above, in principle there is no need to have a specially suited gradient coil for a 7T clinical system, provided that the engineering of the gradient coil is done in a way that it can withstand the forces inside the magnet and incorporates all possible interaction with the environment inside an MR scanner, in particular with respect to acoustic noise and vibration [40]. This is generally assumed with state-of-the-art gradients in use for clinical MRI systems. Due to the shortening of T_2^* , however, faster and stronger gradients are advantageous. Especially for echo planar imaging (EPI) related MRI, such as functional MRI (fMRI), perfusion- and diffusion-weighted imaging (DTI [6], DSI [41]), the increase in SNR can be traded for higher readout bandwidth in order to minimize signal voids and image distortions caused by local susceptibility changes of interfaces between air, bones, and human tissue.

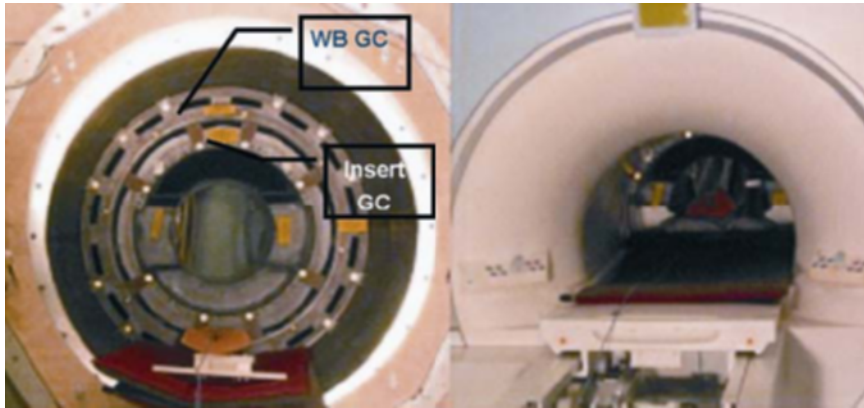


Figure 8. Gradient coils for 7 T. Left: nested whole-body gradient coil and nested insert head gradient coil. Middle: with covers. See attached CD for color version.

Whole-body gradient coils can only marginally be boosted up to higher performance. The interaction of the switched magnetic gradient fields with human tissue can cause peripheral nerve stimulation (PNS) [42–44] and therefore limit the use of the whole-body gradient performance. When considering that the main use of MRI at high field is either human head imaging or animal scanning, one can therefore consider a head or small-bore gradient insert. This allows a significant boost in gradient performance. An insert gradient coil is currently available that performs up to 100 mT/m at a slew rate of 800 T/m/s, which is more than a factor of 2 improvement in performance when compared to whole-body gradients [45]. Figure 8 shows this gradient in situ on the Massachusetts General Hospital Martinos Center’s 7T system. The head insert coil is nested inside the whole-body gradient coil, which allows both coils to be used individually. An electrical switch is provided to switch from the head insert to the whole-body gradient coil [46]. The switchover time is about 10 minutes. However, if whole-body imaging will be pursued the coil has to be removed, which will take about 1 day and is therefore not meant for clinical day-to-day use. If eventually whole-body imaging at 7T is required, the insert coil can be exchanged similar to the setting demonstrated by Kimmlingen et al. [45]. By means of a crane positioned at the rear end of the magnet the coil can be wheeled in and out of the magnet while being connected permanently via a Y switch to the GPA. The whole-body gradient coil is connected to the other side of the Y switch.

The use of a standard whole-body gradient coil has some advantages, too. Patient comfort has to be named first. Compared to head insert coils they provide much wider patient access and are therefore better tolerated by patients. Additionally, standard patient tables can be used. Only minor modification to the geometry is needed as the 7T magnet is typically longer, but the inner bore size is the same as on clinical 1.5 and 3T MRI magnets. Also, due to the lack of a whole-body RF

coil more flexibility is available to counteract acoustic noise, as it is possible to insert more dampening and noise insulation material into the space between the gradient coil and the patient bore tube.

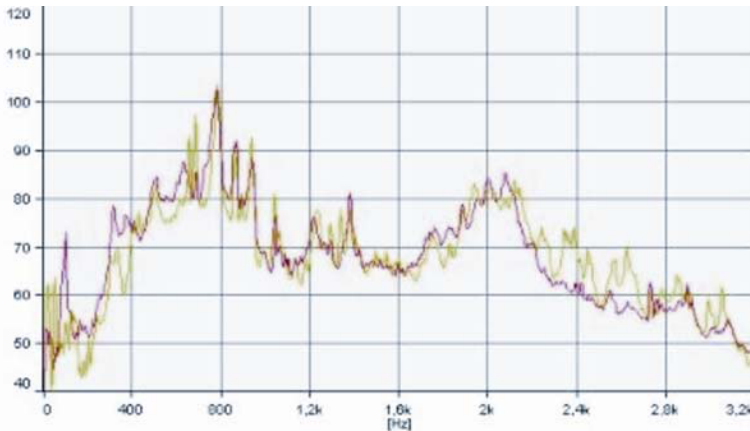


Figure 9. Acoustic noise spectra of same gradient coil in 1.5 and 7T magnets. Acoustic noise spectra of a whole body X gradient over a frequency range from 0 to 3.2 kHz. For comparison the spectra of the same gradient coil is shown for 1.5T (green) measured at 5 mT/m and 7 T (red), measured at 1 mT/m. See attached CD for color version.

In general, however, one can state for a plain gradient coil without covers and noise attenuation applied that the larger whole-body gradient coil is louder than a smaller-insert gradient coil when driven with the same sequence parameters. A whole-body coil is less stiff, is bigger, and has more weight when compared to the insert coil; therefore, its first eigenmodes of vibration will typically appear in the frequency range below 1 kHz, whereas for insert coils the eigenmodes are closer to the 2 kHz range and are thus easier to be avoided by sequence design and counteracted passively. Figure 9 shows an acoustic noise spectrum comparison of the same type of whole-body gradient coil in 1.5 and 7T magnets. A white noise gradient signal was used [47,48], and scaled to 5 and 1 mT/m for the 1.5 and 7T field strength, respectively. Good agreement of the acoustic noise spectra is visible, indicating that acoustic noise spectra of one particular gradient coil design behaves the same when placed into 1.5 and 7T magnetic fields, except that it is louder at 7 Tesla.

Another topic is the fold-over artifact, also known as the third arm artifact [49]. In general magnet homogeneity, gradient linearity, and RF coil homogeneity are matched to avoid those fold-over artifacts. This is not necessarily the case for small-bore gradient coils, such as insert coils, when placed into a whole-body, large FOV 7T magnet. Here, the shorter linearity region in combination with the large magnet homogeneity volume and the unwanted RF excitation outside the

gradient linearity volume can cause fold-over artifacts that are hard to fight when using the same quadrature coil for transmit (TX) and receive (RX) (for more information, refer to §2.3.2 and [31]).

2.3.1. Gradients in $B_0 > 1.5 T$

It is generally known that gradients interact with the main magnetic field it is exposed to. One very obvious issue is the Lorentz force and its effect on acoustic noise. The Lorentz force, \mathbf{F} , a vector entity, describes the force on a wire carrying a current, \mathbf{I} , exposed to the magnet field \mathbf{B}_0 :

$$\mathbf{F} \sim \mathbf{B}_0 \times \mathbf{I}_0 . \quad (3)$$

Equation (3) indicates that the force increases linearly with magnetic field B_0 . Therefore, when compared to a 1.5T clinical magnet of identical geometry, forces are 4.6 times stronger at 7 T. That imposes some mechanical stress and vibration onto the gradient assembly. Like any other mechanical structure, gradient coils do have vibration eigenmodes [40] as well, which means that if the coil oscillates it reaches high mechanical vibration amplitudes at these specific mode frequencies.

The first relevant eigenmode frequencies appear at about 800 and 1800 Hz for a typical whole-body gradient coil and for a typical head insert gradient coil of 360 mm inner diameter, respectively. At these modes the vibration and its associated acoustic noise amplitudes can reach about 20 dB more than the background. The mode distribution is mainly defined by the geometric shape of the gradient coil (cylinder) and its stiffness and mass.

Gradient coils are commonly embedded in epoxy resin, which yields optimum stiffness and mass. Therefore, further improvements in acoustic noise are not expected without using completely new and expensive materials, such as proposed by Stringer et al. [50] using ceramic formers. Proof of principle, however, has not yet been demonstrated.

A gradient coil is vibrating while pulsed and is therefore generating acoustic noise. Acoustic noise is measured as sound pressure level, SPL, in units of dB, and is a logarithmic measure. The ideal expected increase in SPL can be calculated as

$$20 \log \left(\frac{7 T}{1.5 T} \right) = 13.4 \text{ dB} . \quad (4)$$

Therefore, when comparing acoustic noise of a 7T system with a 1.5T system and assuming that an exactly identical geometrical setup (magnet and gradient) is used, the total acoustic noise increase would be 13.4 dB. Considering that MRI scanners at 1.5 and 3T already produce significant acoustic noise, it is therefore of even more concern at 7 T.

It is necessary to remain within certain regulatory limits. The allowed acoustic noise level without ear protection measured at the position of the ear [20] is set to 99 dB(A). The peak acoustic noise level has to stay below 140 dB. That means that

ear protection has to achieve 99 dB(A), which is considered the comfort level for patient scanning.

As mentioned above, we have currently reached an optimum with respect to vibration and noise of the gradient coil structure. Therefore, what remains is passive noise damping, noise insulation, and encapsulation as well as sequence and protocol design to reach the comfort level of 99 dB(A). Depending on the size of the gradient coil, i.e., whole-body or head-insert gradient coil, room for damping and insulation material is precious real estate inside the magnet. Whole-body gradient coils typically allow better acoustic noise damping and encapsulation possibilities as the space between the patient bore (in clinical 1.5 and 3T systems, this is the body RF coil) and the gradient coil is used. Overall, however, one can achieve a quite comfortable situation, as can be seen from Figure 10, which shows some typical sequence acoustic noise levels reached in our 7T systems when filling the room between the patient bore and gradient coil noise dampening and insulation materials.

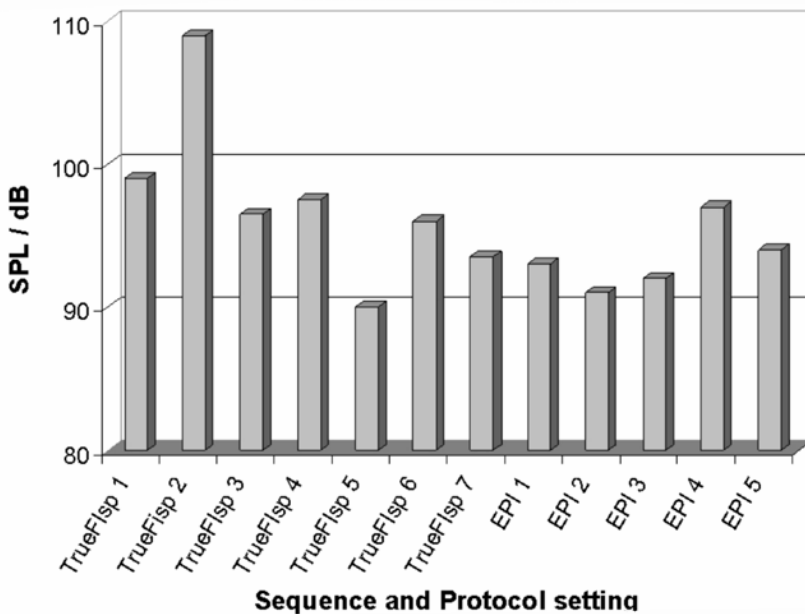


Figure 10. Noise level of clinical and technical sequences measured on our 7T whole-body system using a whole-body gradient coil.

For head-insert gradients the situation is different as its inner dimensions of typically 360 mm can prohibit space for acoustic noise damping and encapsulation.

Head gradient designs are being developed with an inner diameter of 400 mm to allow space for a noise encapsulation. Nevertheless, the situation is not entirely hopeless. Fortunately, the first eigen-mode frequency increases to about 1.8 kHz with smaller coil structures, and overall the coil assembly becomes stiffer. For standard clinical sequences, there is thus no danger of exciting the eigenmodes directly, and it is only the higher harmonics of a pulse sequence that can excite these modes.

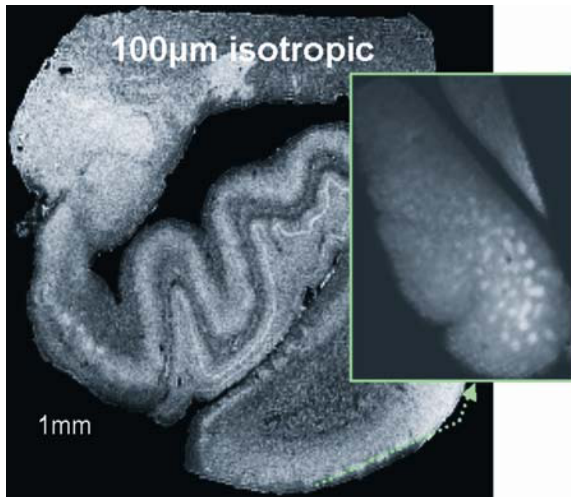


Figure 11. Image of medial temporal lobe (left) acquired at 7 T with 100- μm isotropic voxels (TR = 20, TE = 7.8, flip angle = 5, 10, 15, 20, 25°, FOV = 52 x 52 mm; 512 x 512 matrix, 256 slices). Right: oblique slice through layer II of EC showing the layer II islands as brighter regions. Layers in the CA fields of the hippocampus and the dentate gyrus are clearly visible. See attached CD for color version.

One may ask the question why one would want to use an insert coil inside a very homogeneous magnet that then causes the fold-in artifacts described in the section below? The answer lies in the improved SNR at UHF. High-resolution MRI is commonly used at UHF in order to explore unseen anatomical details in human tissue. While the requested high-resolution gradient amplitudes are no longer feasible with conventional whole-body gradient systems; high-performance insert-gradient coils are helpful for achieving additional gradient strength and slew rate. Figure 11 shows a very-high-resolution GRE scan taken from an ex-vivo sample of human medial temporal lobe. Even the small accumulation of the entorhinal cortex islands [51], which resembles a collection of about 50–100 cells, is visible aside from the layered structure of the cortex itself.

2.3.2. Short-Bore Gradients in a Long-Bore Magnet

Head-insert gradient coils have a much shorter linearity volume and therefore are suitable to reach higher gradient performance as peripheral nerve stimulation (PNS) thresholds are significantly higher and higher peak gradient strength is also more easily reachable as the performance follows a $1/r^5$ rule [52], with r being the radius of the gradient coil. That is the main advantage of using this type of gradient coil, i.e., higher performance. However, this comes at a price. First, the space available for the patient is rather confined. Second, when placed into a long and homogenous magnetic field, it can cause wraparound artifacts, also known as back-folding or third arm artifacts. This is shown in Figure 12. On the left it shows a coronal image acquired on a whole-body gradient coil with a 14-cm short TEM coil. The shoulders are clearly visible. This shoulder signal is well inside the linearity region of the whole-body gradient and therefore the region of interest, i.e., the brain can be imaged without problems. When using a head-insert gradient in combination with the same TEM coil (right), the shoulder signal now is folded back into the image FOV as an unwanted spurious signal artifact, even in the center of the image. Figure 13 illustrates this aspect schematically. This fold-over artifact is not present when we use the same type of head-insert gradient coil in our 3T whole-body system [46], which has a similar B_0 magnet homogeneity as our 7T magnet. At 3 T the TX B_1 field does not extend as far out of the RF coil as it does at 7 T.

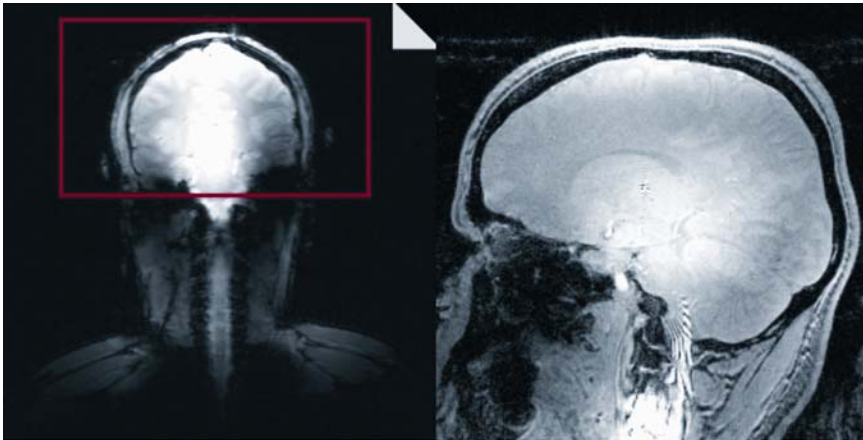


Figure 12. Left: coronal cut through a human head, acquired on a whole-body gradient coil with an end-capped TEM coil (27-cm diameter and 14 cm long, dimensions shown in red). Although the coil is short, signal is received from the chest and shoulder regions. Right: sagittal MR image acquired with the same RF coil on a head insert gradient coil. Fold in artifacts are visible even in the center of the image. See attached CD for color version.

There are ways to counteract this fold-over artifact. An RF blanket can be used to prevent RF penetration of the shoulder and chest or a special jacket that has small shim iron pieces sewn into it to destroy locally B_0 magnet homogeneity. Also, using more receiver coils with smaller sensitivity volumes, such as with the 8-channel array coil discussed above, significantly reduces this artifact [31].

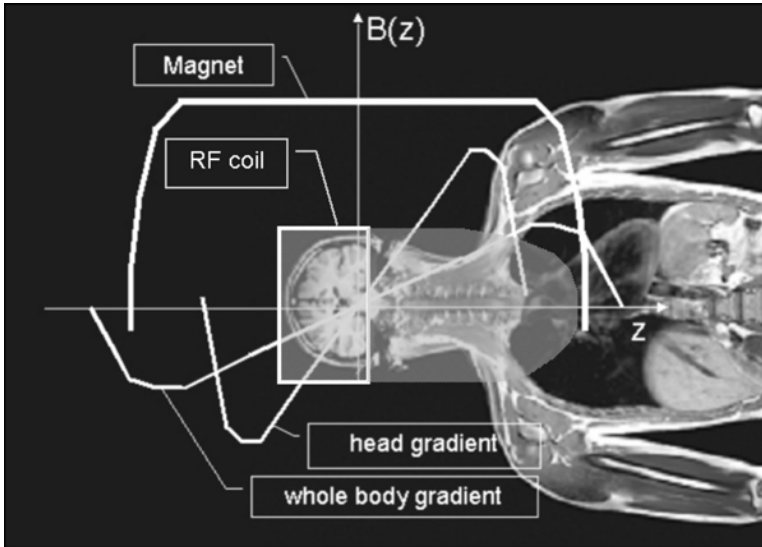


Figure 13. Interaction between magnet homogeneity, linearity volume of a gradient coil (long and short), and RF TX and RX profiles.

2.2.3. Interaction between Magnet and Gradients

The impedance of a gradient coil reflects the power needed to drive this coil. The power, P , is given by the resistance, R , and the current, I , driven through the coil:

$$P = R \cdot I^2. \quad (5)$$

A rather smooth frequency dependence of the resistance and inductance is expected, as can be seen in the upper graph of Figure 14a, which shows the resistance of the gradient coil measured at $B_0 = 0$ T. This smooth resistance curve is also measured in 1.5T MR systems. However, the behavior becomes different at higher fields of 3 T, and especially at 7 T, as shown in Figure 14b,c. This effect was reported by Rohan et al. in 1999 [53]. As mentioned in §2.3.1, gradient coils do vibrate when current is pulsed through them. This vibration causes a deflection of the

conducting wire pattern in the magnetic field of the magnet and therefore an EMF is induced, which is opposed to the driving voltage provided by the gradient power amplifier (GPA). This EMF can be measured and is visible to the GPA. The changes follow a B_0^2 -rule, as can be seen from the graphs of Figure 14b,c. The peaks at about 2 kHz are understood and correspond to the eigenmodes of the gradient coil assembly. Obviously, the peaks spread with increased magnetic field.

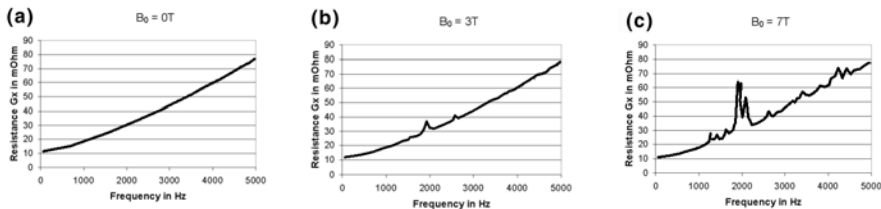


Figure 14. Gradient coil resistance vs. frequency shown for the same type of head insert design: (a) resistance outside magnetic field, (b) inside 3T magnet, (c) inside 7T magnet.

It should be noted that the driving current, I , has to represent the gradient pulse sequence and so has a certain frequency spectrum. Therefore, operation of the GPA can be problematic, as load matching relies on a smooth resistance curves. Especially when considering EPI in the 1–2 kHz range, increased $N/2$ ghosting can be an issue. In fact, it is becoming evident that $N/2$ ghosting is increasing with magnetic fields, even when the same gradient coil is used. The rationale behind it is that vibration causes a deflection of the gradient coil, which distorts the desired gradient magnetic field and introduces a very tiny, additional and unwanted, time-dependent gradient magnetic field. The ideal description of the gradient magnetic field is given by $B_{G_x} = b_0 + G_x \cdot x$ (pulse sequence timing is neglected here), where b_0 describes the offset of the gradient field and G_x is the gradient strength (in this case, of an x gradient). Introducing the vibration caused time dependence, and this is then described as

$$B_{G_x}(t) = b_0(t) + g(t) \cdot G_x \cdot x + \text{nonlinear terms} , \quad (6)$$

where $g(t)$ is the time dependence created by the vibration. For convenience, we neglect higher-order nonlinear terms. Both terms, $b_0(t)$ and $g(t)$, are in general addressable on clinical MRI scanners. The time-dependent $b_0(t)$ term modulates the offset of the gradient field and can be compensated by the digital B_0 term compensation. The term $g(t)$ can cause delays of the played-out gradient waveform and can be minimized by gradient regulator adjustment and gradient delay correction.

2.4. Shim

Whole-body magnets at 1.5 and 3 T come with a homogeneity of about 5 ppm over 40–50 cm DSV typically. Similar values are common at 7 T as well. In absolute terms, however, magnets become more and more inhomogeneous with increasing field strength. If the homogeneity is kept at, let's say, 5 ppm for 1.5 and 7 T magnets, then the absolute inhomogeneity, ΔB_0 , is increasing linearly with B_0 . For example, 1 ppm corresponds to 63 and 298 Hz at 1.5 and 7 T, respectively. When assuming that the gradient strength, G , is kept constant, this can lead to significantly higher image distortions, Δx , which are given by

$$\Delta x = \frac{\Delta B_0}{G}. \quad (7)$$

Another even more important aspect at ultra high field is magnetic susceptibility, χ , [54,55]. A magnet coil produces a magnetic field H_0 to which the physiological sample, i.e., a human body, is exposed. As the human body has certain magnetic properties, i.e., susceptibility, the more important characteristic is the magnetic flux B_0 , which incorporates these tissue magnetic properties as shown in this equation:

$$\mathbf{B}_0 = \mu_0 \cdot (1 + \chi) \cdot \mathbf{H}_0. \quad (8)$$

It is obvious that local inhomogeneity, ΔB_0 , from the nasal sinus regions as shown in Figure 15 also increases linearly with the external magnetic field H_0 . Considering a tissue interface with susceptibility χ_1 and χ_2 , a local field inhomogeneity $\Delta B_0 = (\chi_1 - \chi_2) B_0$ is caused that results in a phase difference over time and therefore has to be considered when programming MRI pulse sequences:

$$\Delta \Phi \propto \gamma \cdot \Delta B_0 \cdot t. \quad (9)$$

Signal voids due to phase cancellation (eq. (9)) and local image distortions (eq. (7)) are therefore a common susceptibility related issue.

Local inhomogeneities caused by susceptibility are hard to compensate, as these are high spatial orders of change. Several ideas have been proposed to shim these local effects. One approach, termed ferrosimming [56], uses small passive shims tailored to the shimmed subject. Another approach uses intra-oral diamagnetic passive shim material [57] or even small shim coils placed inside the gum [58]. Overall they seem to help, but so far no elegant solution has been found.

In conventional scanners only resistive global shim coils are installed. It is the task of these shim fields to compensate these local inhomogeneities as much as possible. The question is: up to what degree does one have to provide shim coefficients and what would be the required shim sensitivity? About a decade ago it was quite common for clinical systems to shim with the linear shim terms only. Insufficient fat saturation in MRI forced the vendors to reintroduce higher-order shim terms for clinical MRI again. Second-order shims (A20, A21, B21, A22, B22) are

common now (for further information on shim nomenclature, we suggest Gruetter et al. [59]). From small-bore NMR spectrometers and animal systems running at high field it is known that higher-order shim sets are required. Typically up to 4th order and sometimes up to 6th order are in use for a magnet field strength of 7 T and higher. So the question remains, what is needed for 7T human MR scanners, in particular up to what degree should the shim fields be increased?

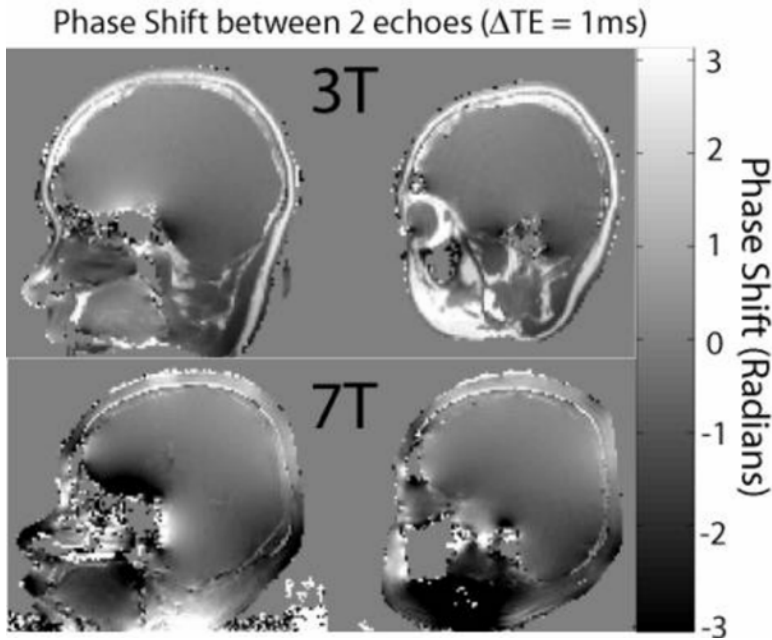


Figure 15. Sagittal field maps through a mid-sagittal plane and temporal lobe (inner ear region) of a human brain. Top row shows results taken at 3 T and the bottom row taken at 7 T.

There are two ways to increase the total shim fields produced by shim coils: (a) increasing the shim sensitivity (i.e., more coil windings), or (b) increasing the total current flowing through the shim coils. Provided one remains at the same geometry, increasing shim sensitivity will also increase the inductance of a particular shim coil and therefore increase potential coupling when gradients are pulsed. On the other hand, increasing shim currents will increase the resistive power losses in the shim coil and therefore increase the load on the cooling system. Hence a thorough design is required in order to avoid either insufficient shimming in humans or excessive coupling and heating. Compared to our Siemens 1.5T MRI systems, we have decided to go both ways. We quadrupled the second-order shim sensitivity and in addition doubled the total allowed shim currents, resulting in an eightfold increase in shim field strength. We believe that second-order shim coils of this sen-

sitivity and total current are sufficient for shimming human heads for MRI and MRS (SVS and CSI). However, we are aware that there is a debate about this topic in the research community. One side argues that second order is good enough, and that, as with smaller voxels, the high-order terms can be expressed in good approximation as a second-order series expansion. The other side votes for higher-order shimming and argues, for instance, that the head itself has some third-order symmetry.

As the changes in local B_0 homogeneity are increasing with B_0 , it seems to be interesting to explore another new hot topic in shimming, i.e., dynamic shimming [60,61]. Here the idea is to set up a system architecture that allows to dynamically change and set shim currents, for example, for each slice in a multi-slice experiment. Overall this involves a major change in system architecture. First, shim power supplies, typically designed to provide static currents, have to be redesigned for quickly changing currents. Second, when changing shim currents quickly, eddy currents can be induced, which renders this idea worthless if not counteracted. In the end, this would require eddy current compensation as it is used for the gradients. Self-shielded shim coils, similar to actively shielded gradient coils, seems to be advisable, although unshielded shim coils can be used as well; however, eddy current compensation would then be mandatory. This increases the design demands inside the gradient coil, where resistive shim coils are located and space is a precious commodity. Third, the MR system has to be able to change shim currents on the fly, similar to playing out gradient pulse waveforms. Overall implanting dynamic shims as described above would create a more complex system architecture than is the state of the art at the moment.

3. CHALLENGES OF CLINICAL IMAGING AT 7T

Approaching higher field strength in MRI is an adventure. This became clear after the major manufacturers decided to provide clinical scanners at 3 T. The promises of high fields are only partly fulfilled. The clear winner in going up to 3 T is musculoskeletal imaging and neuroimaging of the brain in general. There the theoretical twofold SNR improvement is considered to be proven. However, when looking at body imaging in general the difficulties become clear. Although image quality is typically better than at 1.5 T, it is hard to achieve the twofold increase in SNR in general.

Another issue is driven by SAR. Slice coverage can be limited when compared to 1.5 T. This holds true especially for sequence types such as TSE, HASTE, and TrueFISP [62], which employ a chain of RF pulses. However, at 7 T things get worse. It is known since 1989 from imaging using whole-body magnets at 4 T that dielectric effects become dominant [2,19]. This virtually has halted activity in high field whole-body imaging for more than a decade. Eventually the market settled at 3 T, which seems to be a convenient compromise to gain enough SNR, and the challenges of dielectric effects are tractable.

Another demanding aspect is safety at ultra high fields. The forces on ferromagnetic objects as well as on the human body itself have to be taken seriously. These aspects of UHF imaging will be considered in the following section.

3.1. SAR

At least up to about 250 MHz, the required RF power seems to follow an ω_0^2 rule. FDTD simulations [18] suggest that for frequencies above 250 MHz RF power increases only linearly when the 90° condition is adjusted to a small ROI in the center of the image plane. Ibrahim et al. [25], however, performed a different FDTD simulation of the human head, suggesting that the power required to produce a 90° pulse even drops at frequencies above 280 MHz. Experimental findings from T. Vaughan et al. [12] showed that the RF power required for 7 T is about a factor of 1.8 and 2.0 higher than needed for 4 T, for an ROI in the center and in the periphery of the brain, respectively.

In the worst case, if the ω_0^2 rule would apply, a 21.7-fold increase in RF power would be needed when compared to 1.5 T. As the findings of Collins, Ibrahim, and Vaughan suggest, a slower increase in RF power is likely. If this holds true, some relief for clinical imaging can be expected. However, the impact on SAR for some image sequences such as TSE sequences are significant. At 3 T SAR is already limiting the available slice coverage and at 7 T it will be even more severe. In order to overcome that limitation, one therefore has to concatenate slices, which will prolong overall scan time. Alternatively, one can prolong the RF pulse train, or one can reduce the flip angle for TSE, HASTE, and TrueFISP-type imaging. Both, however, sacrifice SNR and/or image contrast and will increase, for example, fat/water artifacts across the slice profile. Parallel imaging techniques can be applied, trading off some SNR vs. SAR. The Hyper-Echo technique introduced by Hennig et al. [63] and the prescribed signal evolution (PSE) technique introduced by Mugler et al. [64] have also been shown to significantly reduce SAR.

3.2. Dielectric Effects

The source of dielectric effects arises from interaction of the RF B_1 fields with the dielectric properties of the body, such as the permittivity, ϵ , and conductivity, σ , of the human tissue. The wave nature of the RF electromagnetic field and the dielectric and conductive boundaries of the body can no longer be neglected [65,66]. Effects from the wavelike nature of the RF fields significantly alter the desired B_1 homogeneity for clinical imaging. Because of that, RF coil designers are facing various challenges when building coils for UHF imaging. With a typical permittivity of about 60, the effective half wavelength dimension inside the human body shrinks to about 10 cm at 300 MHz, which corresponds to a fraction of a human head. Therefore, depending on the local dielectric properties of human tissue, the head can act as an RF resonator and can create standing wave patterns. As a result, the RF coil antenna structure is no longer solely defining the RF field distribution inside the human subject. It is convenient to consider this entire situation as inter-

ference of electromagnetic waves. While constructive interference, i.e., dielectric resonance, increases B_1 field strength in the center of the image, destructive interference, i.e., RF eddy currents and skin-depth effects, cause B_1 field strength reduction, mostly seen in the periphery of the images. On top of these phenomena are RF penetration effects caused by shielding of the penetrating waves by induced RF eddy currents in the conductive sample.

These varying MR signal patterns can be complex and depend upon the local distribution of the electrical and dielectric properties of the individual human tissue. The center brightening effect becomes very obvious in the spherical phantom images shown in Figure 3, filled with the typical phantom solution used for 1.5T MR imaging.

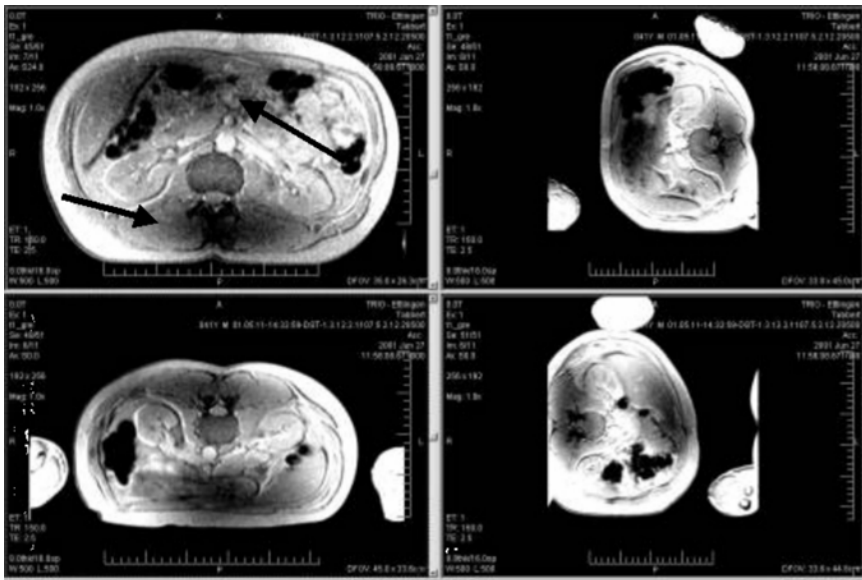


Figure 16. Upper left: axial cut, supine position. Upper right: axial cut, subject lying on left side. Lower left: prone position. Lower right: axial cut, subject lying on right side. Obviously, the dark bands (signal voids due to RF eddy currents) (see arrows) are bound to the human anatomy and not to the B profile of the RF coil. Image provided courtesy of Melanie Schmitt.

These effects can already be seen at 3 T when imaging the spine (Figure 16). It is related to the electric and dielectric properties of the bone, and the muscle interface, especially when imaging slim muscular patients. Four scans of the same subject and the same sequence and protocol settings have been acquired. The volunteer was asked to lay in a supine position, on the left side, prone, and on the right side, respectively. Signal darkening at the vertebral body and the abdomen (see arrow) is following rotation of the volunteer.

Overall, however, the problems are bearable at 3 T, and there are mitigating factors to counter it by using saline bags and/or oscillating RF coils [67]. Although achieving homogeneous B_1 fields in the body at 7 T is a true challenge, human body imaging at 7 T has been demonstrated recently [13]. Applying the known state-of-the-art RF technology will not suffice for clinical needs. Inventions such as RF shimming and transmit arrays may help in this regard (see §2.2.3).

3.3. Safety Aspects

Patient comfort is important at all field strengths, and even more for 7 T, as some physiological effects scale with magnetic field strength. Hydrodynamic effects can cause disturbing sensations when the human subject is moved into the magnet [68]. Some people experience dizziness and nausea due to the dB/dt exposure while passing through the strong fringe field gradients (dB/dr). In our system we usually limit this to about 1 m in 10–15 seconds. Motorized patient table drives will be common in the future for clinical MRI at 7 T in order to minimize these effects while passing through the magnet fringe field gradient. Varying the speed of the patient table while moving the subject through the fringe field seems obvious in order to minimize patient discomfort. The effect of dizziness and nausea is transient, and anecdotal reports seem to suggest that subjects can become acclimatized to these sensations. However, this has to be taken seriously, and further investigations are needed to fully understand these effects.

Some scanned subjects report a metallic taste on the tongue. This can be induced while speaking inside the magnet, but it is transient and will go away when the patient is moved out of the magnet (author's experience). Other subjects report the metallic taste while being moved into the magnet.

We estimate that about 500 subjects have been scanned on the four operating 7 and 8T magnets in the United States. No severe side effects have been reported so far. Further studies are required and will reveal the potential side effects, if they exist.

3.3.1. Magnetic Forces

The greatest danger from a 7T magnet comes from flying objects. Due to the nonlinear nature of magnetic fringe fields, it is easy to underestimate the strength of a magnetic field like that at 7 T [69]. Even more care has to be taken to ensure that no one enters the exam room with magnetic objects, especially during the time a subject is being scanned in the magnet. Metal detectors may help with this aspect. However, they are not foolproof, as workers can gradually become complacent. Therefore, it is advisable to allow access to the 7T magnet only for authorized and well-trained personnel.

The force onto a current conducting wire, described in §2.3.1, is proportional to the product of the magnetic field strength B_0 and the current I . However, when considering the forces on magnetic materials the situation becomes more complex.

For saturated ferromagnetic objects the force is proportional to the gradient of the magnetic field and can be described as

$$F \propto \frac{dB_0}{dr} . \quad (10)$$

It is interesting to note that at the center of the magnet, where the B_0 field is homogenous, there is no force.

For non-saturated diamagnetic and paramagnetic materials, such as the human body, the force is proportional to the product of B_0 and the field gradient:

$$F \propto B_0 \cdot \frac{dB_0}{dr} . \quad (11)$$

The forces on dia- and paramagnetic materials are significantly smaller [69]. Diamagnetic objects will be repelled from the magnet while paramagnetic parts will be attracted to the magnet. An experiment undertaken at the high field lab at the University of Nijmegen (Netherlands) [70,71] demonstrated that the diamagnetic forces experienced in the fringe field gradient of a 16T superconducting magnet can levitate a frog. If we consider a field gradient of 16 T over a range of 0.1 m, the diamagnetic force can be estimated from eq. (11). This results in a total force of 2560 T²/m. If we now consider the situation at a 7T whole-body magnet and assume that the fringe field gradient is about 7 T/1.5 m, we can then calculate the diamagnetic force experienced by a human subject as 33 T²/m, which is about 1% of what was experienced in the 16T frog experiment. So from that perspective it is expected to be safe — we are not flying yet, and will never do so at 7 T.

4. CLINICAL SCANNING ON 7 T

Software-wise, a 7T scanner is no different from a 1.5T clinical scanner. The same software structure is used. On the sequence side, however, it is advisable to rethink all sequences, especially those that impose significant SAR and require high peak RF power. One way to counteract this is by prolonging the duration of the SAR-relevant RF pulses. The idea behind this is best understood when considering what defines a flip angle, α , and the RF power to achieve this flip angle. The flip angle is calculated by the time integral over the $B_1(t)$ amplitude of the RF pulse:

$$\alpha = \gamma \cdot \int_{T_p} B_1(t) dt . \quad (12)$$

In geometric terms it corresponds to the area under the $B_1(t)$ envelope. SAR on the other hand is described as RF power, expressed as $\int_{T_p} B_1^2(t) dt$, divided by the human body mass:

$$SAR \propto \frac{\int B_1^2(t) dt}{\text{body mass}}. \quad (13)$$

This is demonstrated best with a rectangular RF pulse of amplitude B_1 played out for a time, T (see also Figure 17). Then the flip angle of pulse 1 is proportional to $B_1 T$. When now the duration is doubled to $2T$, the amplitude can be reduced to $B_1/2$ and still the same flip angle α results. On the other hand, the SAR is proportional to $B_1^2 T$ for pulse 1 and $B_1^2 T/2$ for pulse 2.

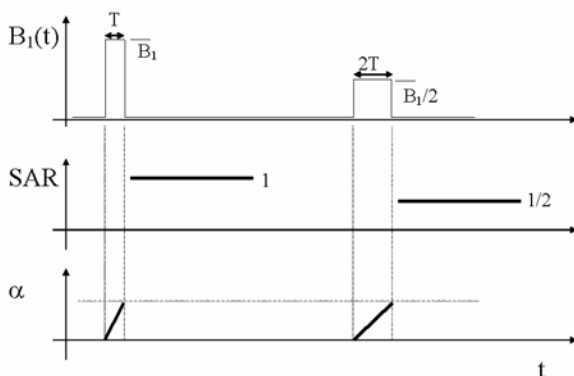


Figure 17. Relation of RF pulse duration to SAR.

Some experience exists on T_1 - and T_2 -weighted imaging at very high fields [72]. In particular, the Ohio State University group demonstrated initial results in the human brain with a human-scale 8T experimental MR system [73–75]. We refer the reader to these publications. In further text we will describe our experience with clinical-type MRI scanning.

4.1. T_1 -Weighted Imaging

T_1 -weighted imaging is a challenge as it is hard to reach a homogenous B_1 field across the image plane and along the slices. If the transmitted B_1 field changes over the image plane, the flip angle varies with it. That may result in different T_1 weighting, and thereby varying image contrast, for example, in imaging of gray and white matter, especially when using the same coil for TX and RX, such as birdcage or TEM coils [34]. One way to minimize B_1 inhomogeneity is to use different coils for TX and RX.

Two-dimensional spin echo (SE) T_1 -weighted imaging is becoming more problematic with increasing magnetic field strength. This is evident already at 3 T. Typically, the T_1 contrast in 2D SE imaging — still the standard in clinical brain

imaging — is rather low. It is considered sufficient, however, for pre- and post-contrast agent scans as the contrast changes are dominated by the contrast agent itself and not really depending on the intrinsic T_1 contrast. The reason for the lower T_1 contrast at higher field lies in the prolongation of T_1 in physiological samples [15]. Figure 18 shows a comparison study undertaken at 1.5 and 3 T. The same spin echo sequence parameters have been taken in order to demonstrate that effect. Automatic slice alignment was applied [76,77], guaranteeing exactly the same anatomical slice positioning as can be seen by these figures. In general the gray/white contrast is diminishing with increased B_0 . Gray/white contrast will be even lower at 7 T for 2D SE-type MR imaging.

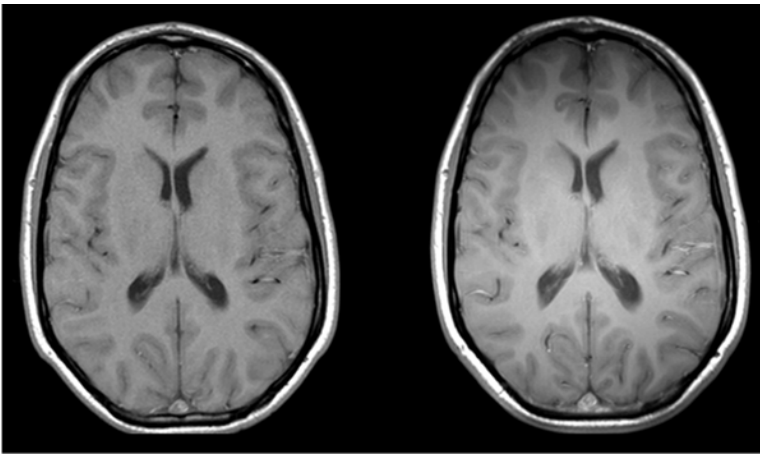


Figure 18. Comparison T_1 -weighted SE imaging at 1.5 and 3.0 T at exactly the same slice positions using AutoAlign. For further information, please see text.

The best T_1 contrast for human brain imaging is gained with 3D T_1 -weighted imaging techniques such as Magnetization-Prepared Rapid Gradient-Echo Imaging (MPRAGE) [78] and gradient recalled echo (GRE) imaging techniques such as 3D FLASH sequences. While 3D FLASH imaging suffers from the B_1 inhomogeneity commonly seen at 7 T, but there are ways to overcome that with MPRAGE. After an adiabatic nonselective inversion pulse, the data are acquired with an ultra fast Turbo-FLASH sequence. Gray/white contrast is gained by adjusting the inversion time. The use of the adiabatic inversion pulse is advantageous for UHF imaging as it overcomes the intrinsic B_1 inhomogeneity, as can be seen from Figure 19a–c. When MPRAGE is acquired with an 8-channel receive coil, excellent T_1 contrast and SNR across the whole brain results. In this case the scan time was about 9 minutes and the voxel size was $0.85 \times 0.85 \times 1 \text{ mm}^3$. For 3D T_1 -weighted imaging at 3 T, for example, the same scan time is applied, but lower spatial resolution and SNR results. Figure 19d shows image brightening in the sinus region, mimicking a

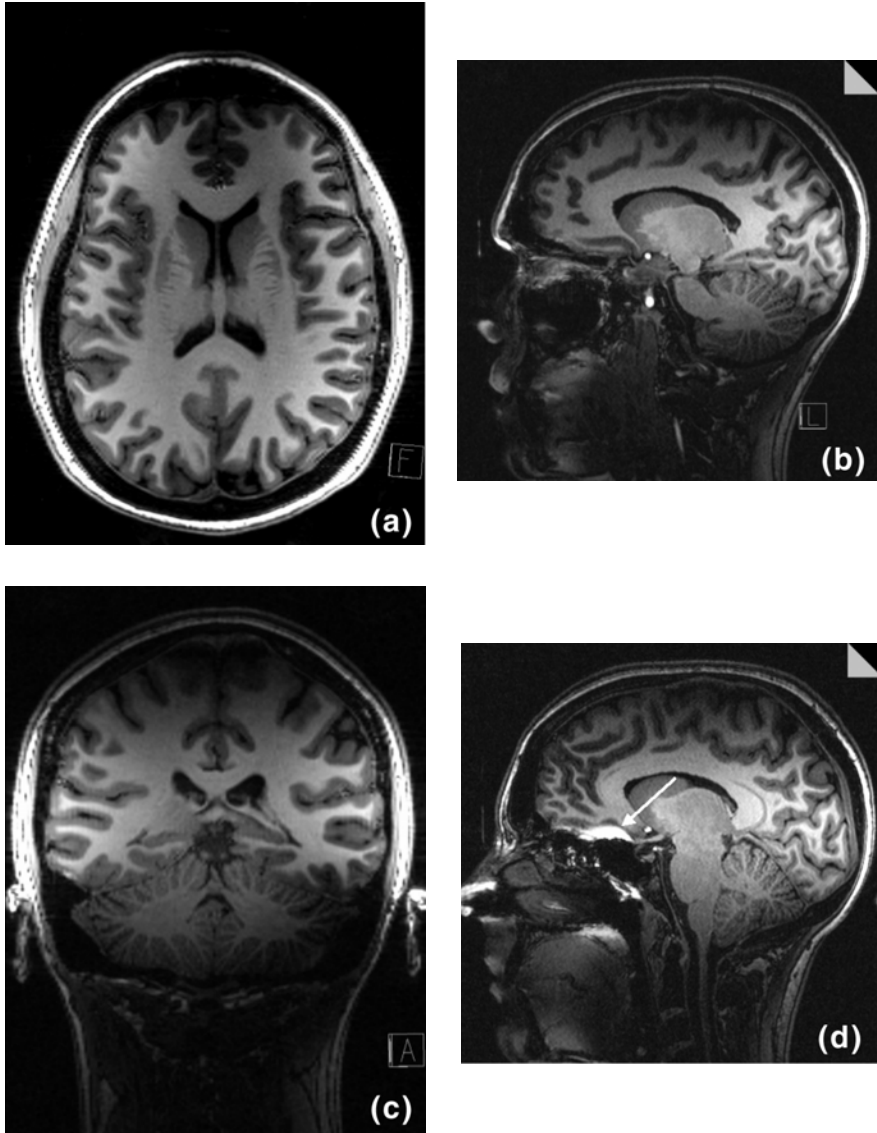


Figure 19. Reformatted whole-brain MPRAGE data set: FOV = 220 x 220, matrix = 256 x 256 x 160, pixel size = 0.85 x 0.85 x 1 mm³, acquisition time = 9:34 min; adiabatic inversion pulse, without B_1 normalization, acquired with an 8-channel receive array in sagittal orientation. Multiplanar reconstruction in (a) axial, (b) sagittal, and (c) coronal orientations. (D) Brightening in sinus region (see arrow) is caused by low-bandwidth adiabatic inversion pulse (for further information, please see text).

susceptibility artifact that is known from T_2^* -weighted imaging. However, as the echo time is only 3 ms, it cannot be caused by TE alone. In fact, it is a matter of the bandwidth of the adiabatic inversion pulse: if that bandwidth is too low it cannot invert spins in that sinus region of high B_0 inhomogeneity (due to susceptibility-induced field offsets). The result is obtained with MPRAGE using adiabatic inversion pulses, and susceptibility is coded into T_1 contrast.

4.2. Arterial Spin Labeling

MR Imaging can be sensitized to inflowing blood spins if these spins have a different magnetization state compared to that of stationary tissue. The technique to achieve this is commonly called arterial spin labeling (ASL), introduced by Detre et al. as continuous ASL (CASL) [79,80], refined by Edelman et al. as EPICSTAR [81,82] and Wong et al. as PICORE [83] and QUIPSS [84]. The inflowing blood exchanges with the tissue water and therefore changes tissue magnetization. Based on this effect, perfusion-weighted images can be generated by subtracting labeled and unlabeled inflowing blood signal images.

Due to a lack of SNR and transit-time constraints imposed by the shorter T_1 of blood at lower field strength, ASL use has been limited in the clinical arena at lower fields. However, ultra high fields seem to promise more utilization of these methods as they benefit strongly from the prolonged T_1 relaxation time of blood. Typically a pair of images is acquired, one labeled and the other unlabeled. The strength of the ASL signal changes, ΔS , as a function of the time, t , is dependent on the T_{1B} of blood and can be described as

$$\Delta S(t) \propto B_0 \cdot e^{-\frac{t}{T_{1B}}} . \quad (14)$$

As T_{1B} prolongs with increasing magnetic field, longer data acquisition times after the tagging pulses can be utilized, and the overall ASL SNR increases as well. This technique can be applied to achieve quantitative blood flow measurements or even for fMRI of brain activation. Figure 20 shows a functional MRI finger tapping comparison of BOLD and ASL. The same areas of the cortex are activated and demonstrated with both techniques. It is expected that ASL techniques will become an important field of research at UHF.

4.3. Time of Flight MR Angiography

The prolonged T_1 at UHF is an advantage for T_1 -weighted imaging in general, as per TR more M_z magnetization is available for repetitive excitation. This longer T_1 is particularly an advantage for time of flight (TOF) MR angiography [85] compared to imaging at lower field strength. Signal strength of the inflowing blood signal is similar to the ASL situation described above. Also, the non-blood background signal is lower and more homogeneous if the same TR is kept in comparison to low field MRI. Therefore, crisper vessel trees are expected when using the

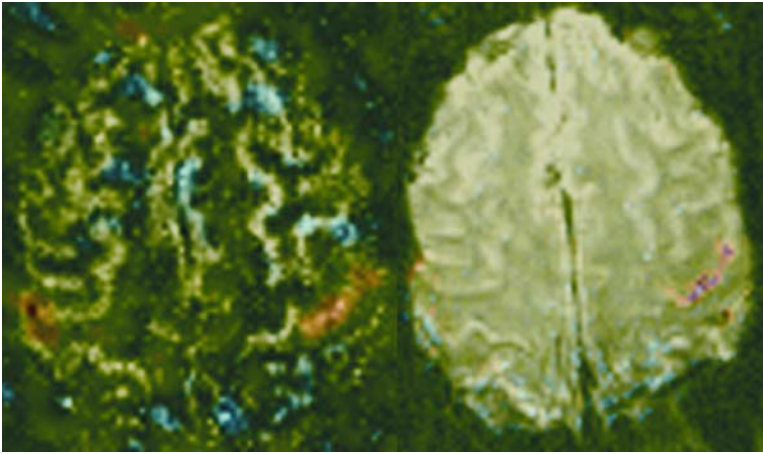


Figure 20. Comparison of finger-tapping fMRI experiment. ASL is shown on left; BOLD is shown on the right. See attached CD for color version.



Figure 21. Axial TOF vessel tree image acquired at 7 T. A 3D-GRE sequence with TE/TR/flip angle of 5.6/49/20° was used. Total scan time 6 minutes and 45 seconds. A TEM TX/RX coil was used.

maximum intensity projection (MIP) technique, provided the B_1 variations across the VOI are small. Figure 21 shows a “mipped” TOF scan acquired at 7 T. Still the B_1 inhomogeneity is visible when using a TEM TX/RX coil. Better results are expected when using receive array coils: specifically, a more homogeneous background.

4.4. T_2 -Weighted Imaging

Turbo Spin Echo (TSE) imaging is the standard for T_2 -weighted clinical imaging. As successive 180° RF pulses are used in order to acquire the T_2 -weighted information quickly, SAR becomes an issue at 7 T. In general one can cope with this by minimizing the number of slices or prolonging RF pulse duration. Typically 8–16 slices can be scanned simultaneously in one scan. Further slices have to be concatenated as additional scans.

The existing B_1 profile can be compensated by using normalization techniques known for a long time in the MR world [86–89].

Figure 22 shows the native T_2 -weighted image on the left and the normalized image on the right. In the normalized image noise levels are slightly elevated in regions where the original image has low signal intensity. In general, normalization is a well-accepted procedure and results in good clinical image quality.

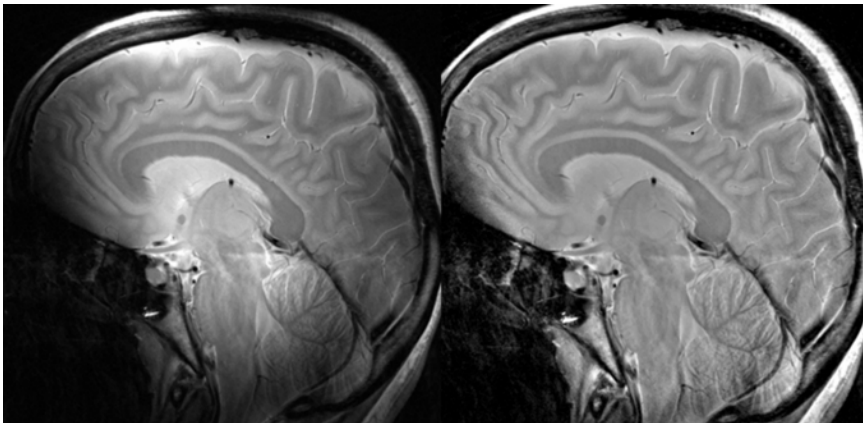


Figure 22. Image normalization: TSE, 11 echoes, 7-min exam, 20-cm FOV, 512 x 512 (0.4 x 0.4 mm) 9 slices, 3 mm thick. Left: un-normalized image. Right: Image intensity normalized.

Figure 23 shows a T_2 -weighted TSE full coverage of the brain acquired at high resolution of 512 x 760 pixels, resulting in $0.27 \times 0.27 \times 2 \text{ mm}^3$ pixel size. Overall scan time was 9 minutes. An 8-channel phased array RX coil was used. Even the stripe of Gennari [90] can be resolved, which is a fine layer in the cortex. Excellent

SNR is achieved. SNR is at least a factor of 2 above what can be reached at 3 T with a 32-channel head array coil

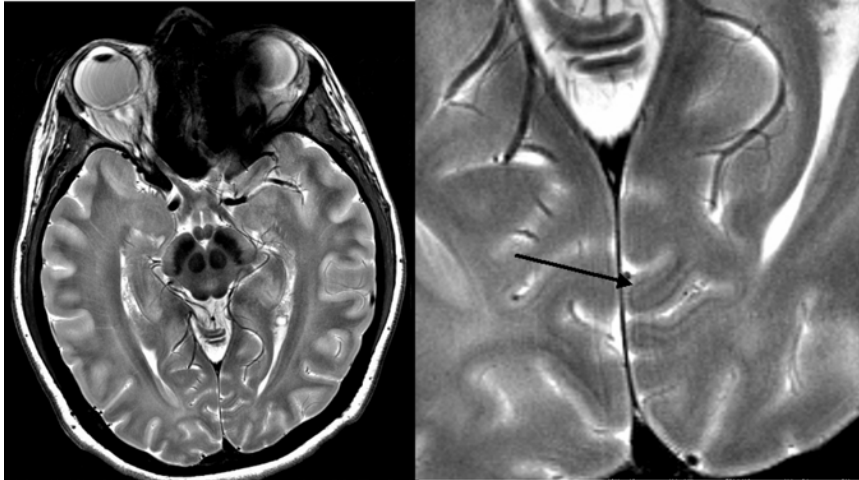


Figure 23. High-resolution T_2 -weighted TSE images. 512 x 760 matrix, resulting in $0.27 \times 0.27 \times 2 \text{ mm}^3$ pixels size. Overall scan time was 9 minutes. An 8-channel phased array RX coil was used. The line of Gennari can be resolved. Excellent SNR is achieved. SNR is at least a factor of 2 above what can be reached at 3 T with a 32-channel head array coil.

4.5. Low SAR T_2 -Weighted Imaging

One way to alleviate SAR problems at ultra high field is by employing the Hyper-Echo or Prescribed Signal Evolution (PSE) techniques described by Hennig et al. [63,91] and Mugler et al. [64], respectively. Both techniques are applied for 2D and in particular also for 3D imaging. The basic principle behind them is that a 2D or 3D TSE sequence is modified in a way that some or the majority of the refocusing pulses are no longer 180° pulses. Typically, full 180° pulse are only applied when the k -space center raw data are acquired, as the low k -space raw data lines define the contrast in the TSE imaging scheme. That reduces the SAR significantly. In some cases 30% of the original SAR can be achieved. These methods work best in human head imaging, as there are only three types of tissue to be considered (neglecting fat): gray and white matter and CSF.

Figure 24 shows a high-resolution T_2 -weighted Hyper-Echo scan acquired at 7 T. Pixel size was $0.4 \times 0.4 \times 3 \text{ mm}^3$. Good T_2 contrast was achieved. In this case SAR was reduced by about 40%.

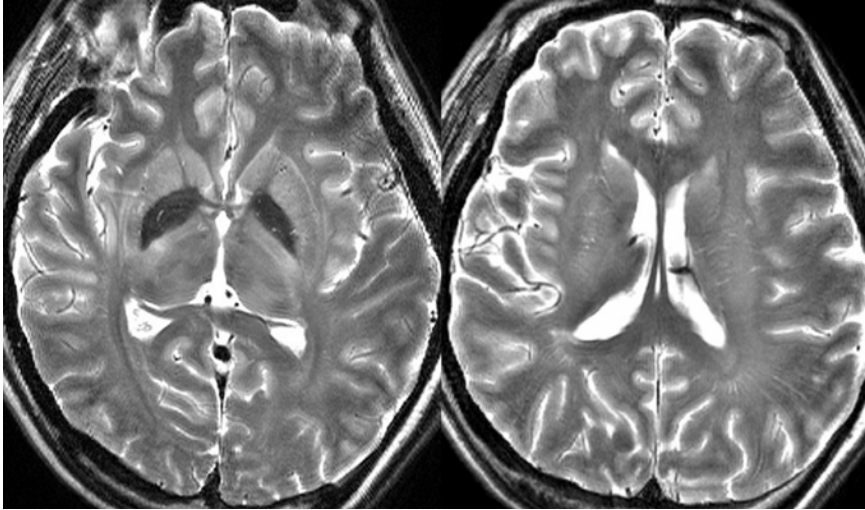


Figure 24. Axial T_2 hyperecho scan ($0.4 \times 0.4 \times 3$ mm); intensity normalized. FOV = 17.3 cm x 18.5 cm, matrix = 512 x 512, slthk = 2 mm, TE = 66 ms, TR = 4500 ms, ETL = 15. Image courtesy of J. Hennig, University of Freiburg, Germany.

4.6. T_2^* -Weighted Imaging — Echo Planar Imaging

Echo Planar Imaging, EPI [16,92], is the fastest T_2 - and T_2^* -weighted sequence in use for a clinical applications, such as gadolinium perfusion imaging [93–95], scanning stroke patients with diffusion-weighted imaging [96,97], and BOLD imaging for fMRI [98,99]. In all cases EPI is used to acquire the MR signal. The advantage of EPI at high fields is that it employs only a few RF pulses per image (1 RF pulse for GRE-type EPI, 2 RF pulses for SE-type EPI, and 3 RF pulses for typical eddy current balanced DTI; fat saturation pulses not included), and is therefore low in SAR. The disadvantage of EPI is its vulnerability to local B_0 inhomogeneities introduced by the human body's inherent susceptibility. As susceptibility scales linearly with B_0 , so too will signal void artifacts and distortions. Figure 15 shows a field map of the same subject acquired at 3 and 7 T. The air/bone/tissue interface is commonly known as a troublesome location in head imaging. The nasal sinus region clearly shows an increased field gradient. Nevertheless, whole-brain echo-planar imaging is feasible at 7 T, as can be seen from Figure 25, where whole-brain coverage is demonstrated. A matrix size of 128 x 128 was applied, resulting in a 1.5×1.5 mm² pixel size at an echo time TE of 20 ms. Slice thickness was set to 2 mm, minimizing the susceptibility-induced phase cancellations across the slice profile. However, it has to be mentioned that EPI image quality varies due to individual head shapes and corresponding susceptibility differences.

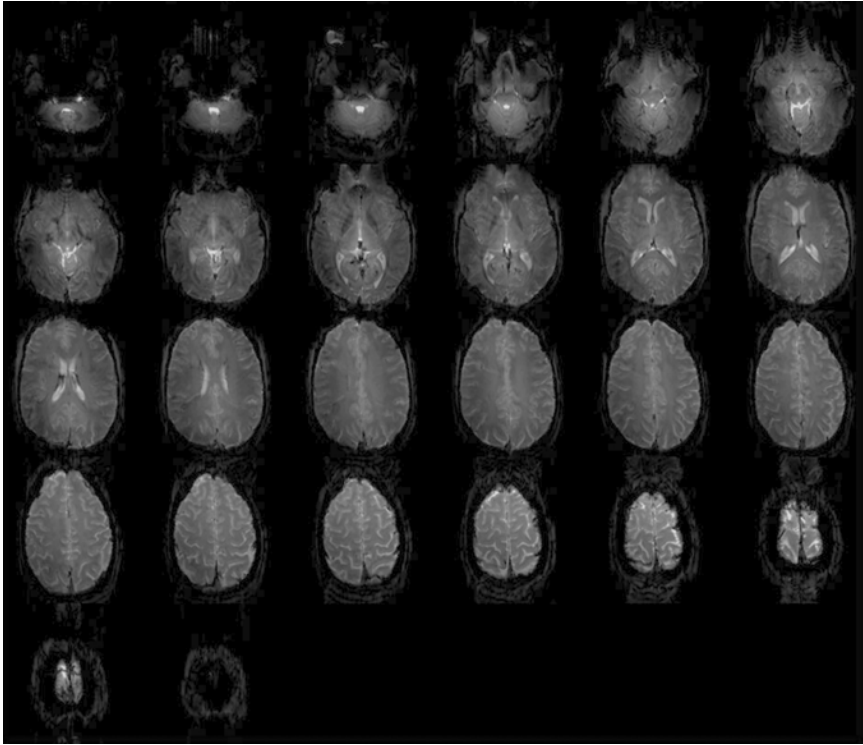


Figure 25. Gradient echo EPI scan acquired with the head insert gradient coil: 26 slices of a 128^2 matrix, TE of 20 ms; FOV = 20 cm, 1.5×1.5 mm pixel size; 2-mm slice thickness.

5. SUMMARY

MR imaging at field strengths up to 3 T is now in clinical practice. Already, however, image quality-related issues such as B_1 center brightening effects and limits on the use of particular sequences due to SAR have become noticeable, if not limiting factors as to how clinical imaging is to be performed at 3 T. Meanwhile, 7T human imaging is proving itself for research studies. Whether or not 7T systems will emerge as a mature market for clinical evaluations remains to be seen. Some of the advantages have been noted in research scans — the steady increase in SNR, favorable increases in T_1 , susceptibility contrast, and spectral dispersion crucial to selection. Important clinical applications have motivated many researchers to attempt to refine the technology toward more routine clinical application.

For example, the sensitivity increases alone justify specialized clinical applications and the need for increased image resolution in order to explore finer and finer details of the brain. Clinical spectroscopy benefits from a similar sensitivity for resolution tradeoff, and in addition can benefit from the increased spectral dispersion. Thus in addition to providing the clinician with the ability to examine a heterogeneous structure such as a recurring brain tumor in more spatial detail, the ability to spectrally resolve additional peaks may allow a wider range of metabolic changes to be mapped. Similarly, susceptibility-based contrast is seen to scale favorably with field. While the image artifacts associated with macroscopic susceptibility (e.g., image distortions from the frontal sinuses) also increase with field, preliminary research results show that fast gradients and application of SENSE reconstruction techniques can provide high-quality whole-brain EPI images even at 7 T.

SAR is already a limiting factor for many applications at 3 T and becomes more limiting at 7 T, especially for spin echo-based scanning. Here new concepts — for T_2 -weighted scanning, the hyperechoes introduced by Hennig et al. [63], and PSE introduced by Mugler et al. [64] — will help.

It is not clear yet what the introduction of B_1 shimming using individually programmed B_1 phase and amplitude to multiple transmit elements will achieve with respect to reducing SAR, but development of these techniques is definitely needed to mitigate the constructive and destructive behavior of the B_1 field inside the head at 300 MHz, where the RF wavelength is smaller than the head dimensions. Imaging under the influence of varying B_1 field strength across the head is especially limiting for sequences where image contrast is strongly B_1 dependent, such as many T_1 -weighted sequences. Some methods already exist to increase B_1 field homogeneity: for example, independent TX and RX coils whose spatial drop-off is roughly the inverse of the observed center brightening pattern can be used to mitigate the transmit side contrast spatial profile and the receive-side detection sensitivity profile. Like the B_1 shimming methods, multichannel RX array coils are needed to implement this strategy. For other types of imaging, such as 3D T_1 weighted MPRAGE imaging, it may be sufficient to take advantage of B_1 -insensitive RF inversion pulses or composite pulses [100], although it is not clear that this approach alone will satisfy clinicians' need for homogeneous imaging.

Additional promising conceptual ideas that have been presented over the last years in order to counteract dielectric B_1 inhomogeneity effects include excitation with 2D and 3D spatially shaped RF pulses. While quite complicated spatial profiles can be excited to exactly cancel the expected profile dielectric pattern in the head, these methods traditionally employ quite lengthy RF excitations schemes. For this reason, the emerging field of transmit SENSE might be useful to reduce the excitation down to clinically relevant lengths.

Thus, for mitigating the excitation and detection inhomogeneities imposed by the wavelength effects in the head at 300 MHz and above, we are currently in the position of having a variety of appealing options, which await application to clinical practice. While many of the solutions are likely to quickly satisfy specific re-

search applications, clinical demands for image and contrast homogeneity have always been quite rigorous and broad.

Future trends in the development of ultra high field technology are likely to include further noise insulation and dampening in the clinical setting and reduction in the bulky size and magnetic footprint of the ultra high field magnet. The siting considerations for unshielded magnets with their massive passive shielding are likely to impede introduction of ultra high field systems in the clinic. Thus, further development is mandatory to shrink the size and provide self-shielded magnets in order to minimize the 5-gauss line area. Head-only magnets for imaging the brain might be a good starting point, considering the prevalence of neuro MR examinations in the clinic together with the experience in the research community of using ultra high field systems for brain applications.

Overall there are many topics to be explored and diverse methodologies to be polished before 7T and higher field strengths become routinely useful in the clinical setting. But solid preliminary experience exists in each of the needed areas and is actively being addressed, one by one, in the research setting. Looking backward to the same sort of engineering effort undertaken to transform 3T human scanning from a research novelty (as was the case in 1995) to clinical reality (ca. 2002), we can expect a similar 5- to 10-year timeline for 7 Tesla imagers.

6. ACKNOWLEDGMENT

We want to thank Peter Starewicz, Resonance Research Inc., for helpful comments and discussions on the shimming part of this chapter.

7. REFERENCES

1. Barfuss H, Fischer H, Hentschel D, Ladebeck R, Oppelt A, Wittig R, Duerr W, Oppelt R. 1988. Whole-body MR imaging and spectroscopy with a 4-T system. *Radiology* **169**:811–816.
2. Barfuss H, Fischer H, Hentschel D, Ladebeck R, Oppelt A, Wittig R, Duerr W, Oppelt R. 1990. In vivo magnetic resonance of humans with a 4T whole body magnet. *NMR Biomed* **1**:31–45.
3. Akbudak E, Markham J, Kotys M, Foster G, Conturo T. 2002. Whole-brain bolus perfusion imaging in humans at 3T compared to 1.5T. *Proc Int Soc Magn Reson Med* 1004.
4. Hoult DI, Lauterbur PC. 1979. The sensitivity of the zeugmatographic experiment involving human samples. *J Magn Reson* **34**:425–433.
5. Triantafyllou C, Hoge RD, Krueger G, Wiggins CJ, Potthast A, Wiggins GC, Wald LL. 2005. Comparison of physiological noise at 1.5 T, 3 T and 7 T and optimization of fMRI acquisition parameters. *Neuroimage* **26**(1):243–250.
6. Basser PJ, Mattiello, LeBihan D. 1994. MR Diffusion tensor spectroscopy and imaging. *Biophys J* **66**:259–267.
7. Pruessmann KP, Weiger M, Scheidegger MB, Boesiger P. 1999. SENSE: sensitivity encoding for fast MRI. *Magn Reson Med* **42**:952–962.

8. Sodickson DK. 2000. Tailored SMASH image reconstructions for robust in vivo parallel MR imaging. *Magn Reson Med* **44**:284–289.
9. Griswold MA, Jakob PM, Heidemann RM, Nittka M, Jellus V, Wang J, Kiefer B, Haase A. 2002. Generalized autocalibrating partially parallel acquisitions (GRAPPA). *Magn Reson Med* **47**(6):1202–1210.
10. Budinger T. 1990. Private communication.
11. Robitaille PML, Warner R, Jagadeesh J, Abduljalil AM, Kangarlu A, Burgess RE, Yu Y, Yang L, Zhu H, Jiang Z, Bailey RE, Chung W, Somawiharja Y, Feynan P, Rayner D. 1999. Design and assembly of an 8 tesla whole body MRI scanner. *J Comput Assist Tomogr* **23**:808–820.
12. Vaughan JT, Garwood M, Collins CM, Liu W, Delabarre L, Adriany G, Anderson P, Merkle H, Goebel R, Smith MB, Ugurbil K. 2001. 7T vs. 4T: RF power, homogeneity, and signal-to-noise comparison in head images. *Magn Reson Med* **46**(1):24–30.
13. Vaughan JT, DelaBarre L, Snyder C, Adriany G, Collins C, Van de Moortele P-F, Moeller S, Ritter J, Strupp J, Andersen P, Tian J, Smith MB, Ugurbil K. 2005. RF Image Optimization at 7T & 9.4T. *Proc Int Soc Magn Reson Med* 953.
14. Neurospin. 2005. <http://www.meteoreservice.com/neurospin/>.
15. Bottomley PA, Foster TH, Argersinger RE, Pfeifer LM. 1984. A review of normal tissue hydrogen NMR relaxation times and relaxation mechanisms from 1–100 MHz: dependence on tissue type, NMR frequency, temperature, species, excision, and age. *Med Phys* **11**:425–448.
16. Mansfield P. 1977. Multi-planar image formation using NMR spin echoes. *J Phys C* **10**:L55–L58.
17. Bottomley P, Edelstein WA. 1981. Power deposition in whole body NMR imaging. *Med Phys* **8**:510–512.
18. Collins CM, Smith MB. 2001. Signal-to-noise ratio and absorbed power as functions of main magnetic field strength, and definition of "90 degrees" RF pulse for the head in the birdcage coil. *Magn Reson Med* **45**(4):684–91.
19. Roeschmann P. Radiofrequency penetration and absorption in the human body: limitations to high-field whole-body nuclear magnetic resonance imaging. *Med Phys* **1987****14**(6):922–931.
20. IEC, E., 60601-2-33.
21. Brown IJ, Bird JM, McDouglass IL, Black D. 1986. Magnet assembly for use in NMR apparatus. US Patent 4587504.
22. Bollenbeck J, Vester M, Oppüelt R, Kroeckel H, Schnell W. 2005. A high performance multi-channel RF receiver for magnetic resonance imaging systems. *Proc Int Soc Magn Reson* 860.
23. Ugurbil K. 2005. Personal communication.
24. Katscher U, Börner P, Leussler C, Van den Brink JS. 2003. Transmit SENSE. *Magn Reson Med* **49**:144–150.
25. Ibrahim TS. 2004. A numerical Analysis of radio-frequency power requirements in magnetic resonance imaging experiments. *IEEE Trans Microwave Theory Tech* **52**(8):1999–2003.
26. Boskamp EB, Lee RF. 2002. Whole body LPSA transceive array with optimized transmit homogeneity. *Proc Int Soc Magn Reson Med* 903.
27. Adriany G, Van de Moortele P-F, Wiesinger F, Moeller S, Strupp J, Andersen P, Snyder C, Zhang X, Chen W, Pruessmann KP, Boesiger P, Vaughan JT, Ugurbil K. 2005.

- Transmit and receive transmission line arrays for 7 Tesla parallel imaging. *Magn Reson Med* **53**(2):434–445.
28. Adriany G, Van de Moortele P-F, Wiesinger F, Moeller S, Strupp J, Andersen P, Snyder C, Zhang X, Chen W, Pruessmann KP, Boesiger P, Vaughan JT, Ugurbil K. 2005. Transmit and receive transmission line arrays for 7 Tesla parallel imaging. *Magn Reson Med* **53**(2):434–445
 29. Katscher U, Bornert P, Leussler C, van der Brink JS. 2003. Transmit SENSE. *Magn Reson Med* **49**:144–150.
 30. Zhu Y. 2004. Parallel excitation with an array of transmit coils. *Magn Reson Med* **51**:775–784.
 31. Wald LL, Wiggins GC, Potthast A, Wiggins JC, Triantafyllou C. 2005. Design considerations and coil comparisons for 7 Tesla brain imaging. *Proc Int Soc Magn Reson Med* 921.
 32. Collins CM, Yang QX, Wang JH, Zhang X, Liu H, Michaeli S, Zhu XH, Adriany G, Vaughan JT, Anderson P, Merkle H, Ugurbil K, Smith MB, Chen W. 2002. Different excitation and reception distributions with a single-loop transmit-receive surface coil near a head-sized spherical phantom at 300 MHz. *Magn Reson Med* **47**(5):1026–1028.
 33. Tropp J. 2004. Image brightening in samples of high dielectric constant. *J Magn Reson* **167**(1):12–24.
 34. Vaughan JT, Adriany G, Garwood M, Yocoub E, Duong T, Merkle H, Andersen P, DelaBarre L, Kim SG, Ugurbil K. 2002. A detunable volume coil for high field NMR. *Magn Reson Med* **47**:990–1000.
 35. Vaughan, JT. 1998. *Cavity Resonator for NMR systems*. Birmingham, AL: UAB Research Foundation.
 36. Wiggins GC, Triantafyllou C, Potthast A, Reykowsky A, Nittka M, Wald LL. 2005. A 32 channel receive-only phased array coil for 3T with novel geodesic tiling geometry. *Proc Int Soc Magn Reson Med* 679.
 37. Wintersberger BJ, Reeder SB, Dietrich O, Huber A, Lanz T, Greiser A, Reiser MF, Schoenberg SO. 2005. Multi-slice TSENSE cardiac CINE SSFP imaging with a 32 channel cardiac coil. *Proc Int Soc Magn Reson Med* 277.
 38. Hardy CJ, Cline HE, Giaquinto RO, Niendorf T, Grant AK, Sodickson DK. 2005. A 32-element cardiac receiver-coil array for highly accelerated parallel imaging. *Proc Int Soc Magn Reson Med* 951.
 39. Wiggins GC, Potthast A, Triantafyllou C, Lin F, Benner T, Wiggins CJ, Wald LL. 2005. A 96 channel MRI system with 23- and 90-channel phased array head coil at 1.5 Tesla. *Proc Int Soc Magn Reson Med* 671.
 40. Rausch M, Gebhardt M, Kaltenbacher M, Landes H. 2005. Computer-aided design of clinical magnetic resonance imaging scanners by coupled magnetomechanical-acoustical modelling. *IEEE Trans Magn* **41**(1):72–81.
 41. Wedeen VV, Song SKV, Wald LL, Reese TG, Benner T, Tseng WYI. 2000. Diffusion Spectrum MRI of cortical architectonics: visualization of cortical layers and segmentation of cortical areas by analysis of planar structure. *Proc Int Soc Magn Reson Med* 622.
 42. Imrich W. 1994. Electrostimulation by time-varying magnetic fields. *MAGMA* **2**:43–49.
 43. Reilly JP. 1989. Peripheral nerve stimulation by induced electric currents: exposure to time varying magnetic fields. *Med Biol Eng Comput* **27**:101–110.
 44. Schmitt F, Stehling MK, Turner R. 1998. *Physiological side effects of fast gradient switching*. Echo-Planar Imaging. ISBN 3-540-63194-1.
 45. Kimmlingen R, Eberlein E, Gebhardt M, Hartinger B, Ladebeck R, Lazar R, Reese T, Riegler J, Schmitt F, Sorensen GA, Wedeen V, Wald LL. 2004. An easy to exchange

- high performance head gradient insert for a 3T whole body MRI system: first results. *Proc Int Soc Magn Reson Med* 1630.
46. Kimmlingen R, Eberlein E, Gebhardt M, Hartinger B, Ladebeck R, Lazar R, Reese T, Riegler J, Schmitt F, Sorensen GA, Wedeen V, Wald LL. 2005. An easy to exchange high performance head gradient insert for a 3T whole body MRI system: first results. *Proc Int Soc Magn Reson Med* 1630.
 47. Hedeen RA, Edelstein WA. 1997. Characterization and prediction of gradient acoustic noise in MR images. *Magn Reson Med* 37:7–10.
 48. Edelstein WA. Acoustic noise considerations of a MRI system. 2001.
 49. Arm., r., 3rd Arm artifact.
 50. Stringer M, Dty GN, Shevgoor S, Xiao C, Laws N, Staab JP, Wald LL, Ackerman JL, Doty D. 2005. Progress in the development of a quiet, high performance head gradient coil. *Proc Int Soc Magn Reson Med* 406.
 51. Augustinack J, Kouwe AVD, Salat D, Wald LL, Blackwell M, Wiggins C, Fischl B. 2004. Detection of entorhinal islands using 7T MRI. Paper presented at Human Brain Mapping 2004. Poster MO288.
 52. Bowtell R, Schmitt F. 1998. Echo-planar imaging hardware. *Echo-planar imaging*. ISBN 3-540-63194-1.
 53. Rohan M. 1995. Electromechanical coupling at high fields: increased gradient resistance. *Proc Soc Magn Reson* 937.
 54. Ludeke KM, Röschmann P, Tischler R. 1985. Susceptibility artifacts in NMR imaging. *Magn Reson Med* 3:329.
 55. Abduljalil AM, Robitaille PML. 1999. Macroscopic susceptibility in ultra high field MRI. *J Comput Assist Tomogr* 23(6):832–841.
 56. Jesmanowicz A, Hyde JS, Puchard WFB, Starewicz PM. 2001. Ferroshimming. US Patent 6,294,972.
 57. Wilson JL, Jezzard P. 2003. Utilization of an intra-oral diamagnetic passive shim in functional MRI of the inferior frontal cortex. *Magn Reson Med* 50(5):1089–1094.
 58. Hsu JJ, Glover G. 2005. Mitigation of susceptibility-induced signal loss in neuro imaging using localized shim coils. *Magn Reson Med* 53(2):243.
 59. Gruetter R, Boesch C. 1992. Fast, non-iterative shimming on spatially localized signals: in vivo analysis of the magnetic field along axes. *J Magn Reson* 96:323–334.
 60. deGraaf RA, Brown PB, McIntyre S, Rothman DL, Nixon TW. 2003. Dynamic shim updating (DSU) for multislice signal acquisition. *Magn Reson Med* 49(3):409–416.
 61. Hsu JJ, Glover G. 2005. Towards dynamic shimming for fMRI. *Proc Int Soc Magn Reson Med* 1535.
 62. Hinton D, Wald LL, Pitts J, Schmitt F. 2003. Comparison of cardiac MRI on a 1.5T and 3T clinical whole body scanner. *Invest Radiol* 38(7):436–442.
 63. Hennig J, Scheffler K. 2001. Hyperechoes. *Magn Reson Med* 46(1):6–12.
 64. Mugler JP, Brookeman JR. 2001. T_2 -weighted 3D spin-echo train imaging of the brain at 3 Tesla: reduced power deposition using low flip-angle refocusing RF pulses. *Proc Int Soc Magn Reson Med* 438.
 65. Kangarlu A, Baertlein BA, Lee R, Ibrahim TS, Abduljalil AM, Yang L, Robitaille PML. 1999. Dielectric resonance phenomena in ultra high field MRI. *J Comput Assist Tomogr* 23(6):821–831.
 66. Roeschmann P. 1999. Comments on "Human magnetic resonance imaging at 8 T." *NMR Biomed* 12(5):315–319.

67. Schmitt M, Feiweier T, Voellmecke E, Lazar R, Krueger G, Reykowsky A. 2005. B₁ homogenization in abdominal imaging at 3T. *Proc Int Soc Magn Reson Med* 331.
68. Liu F, Zhao H, Crozier S. 2003. Calculation of electric fields induced by body and head motion in high magnetic fields. *J Magn Reson* **161**(1):99.
69. Schenk J. 1992. Health and physiological effects of human exposure to whole body four-tesla magnetic field during MRI. *Ann Acad Sci NY* **649**:285–301.
70. Geim AK, Simon MD, Boamfa MI, Heflinger LO. 1999. Magnetic levitation at your fingertips. *Nature* **400**:323–324.
71. Berry MV, Geim AK. 1997. Of flying frogs and levitrons. *Eur J Phys* **18**:307–313.
72. Kangarlu A, Abduljalil AM, Robitaille PML. 1999. T₁- and T₂-weighted imaging at 8 Tesla. *J Comput Assist Tomogr* **23**(6):875–878.
73. Burgess RE, Yu Y, Christoforidis GA, Bourekas EC, Chakeres DM, Spigos D, Kangarlu A, Abduljalil AM, Robitaille PML. 1999. Human leptomeningeal and cortical vascular anatomy of the cerebral cortex at 8 Tesla. *J Comput Assist Tomogr* **23**(6):850–856.
74. Burgess RE, Yu Y, Abduljalil AM, Kangarlu A, Robitaille PML. 1999. High signal-to-noise FLASH imaging at 8 Tesla. *Magn Reson Imag* **17**(8):1099–1103.
75. Christoforidis GA, Bourekas EC, Baujan M, Abduljalil AM, Kangarlu A, Spigos DG, Chakeres DW, Robitaille PML. 1999. High resolution MRI of the deep brain vascular anatomy at 8 Tesla: susceptibility-based enhancement of the venous structures. *J Comput Assist Tomogr* **23**(6):857–866.
76. van der Kouwe A, Gicquel S, Chen G. 2003. On-line automatic slice positioning and between-scan correction for brain MR protocols. *Proc Int Soc Magn Reson Med* 797.
77. van der Kouwe AJW, Benner T, Fischl B, Schmitt F, Salat HD, Harder M, Sorensen AG, Dale AM. 2005. On-line automatic slice positioning for brain MR imaging. *Neuroimage*.
78. Mugler IJP, Brookeman JR. 1990. Three-dimensional magnetization-prepared rapid gradient-echo imaging (3D MPRAGE). *Magn Reson Med* **15**:152–157.
79. Detre JA, Leigh JS, Williams DS, Koretsky AP. 1992. Perfusion imaging. *Magn Reson Med* **23**:37–45.
80. Detre JA, Alsop DC, Samuels OB, Gonzalez-Atavales J, Raps EC. 1998. Cerebrovascular reserve testing using perfusion MRI with arterial spin labeling in normal subjects and patients with cerebrovascular disease. *Proc Int Soc Magn Reson Med* 243.
81. Edelman RR, Siewert B, Darby DG, Thangaraj V, Nobre AC, Mesulam MM, et al. 1994. Qualitative mapping of cerebral blood-flow and functional localization with echo-planar MR-imaging and signal targeting with alternating radio-frequency. *Radiology* **192**:513–520.
82. Edelman RR, Chen Q. 1998. EPISTAR MRI: multi-slice mapping of cerebral blood flow. *Magn Reson Med* **40**:800–805.
83. Wong EC, Buxton RB, Frank LR. 1997. Implementation of quantitative perfusion imaging techniques for functional brain mapping using pulsed arterial spin labeling. *NMR Biomed* **10**:237–249.
84. Wong EC, Buxton RB, Frank LR. 1998. Quantitative imaging of perfusion using a single subtraction (QUIPSS and QUIPSS II). *Magn Reson Med* **39**:702–708.
85. Ruggieri PM, Laub GA, Masaryk TM, Modic MT. 1989. Intracranial circulation: pulse-sequence considerations in three-dimensional (volume) MR angiography. *Radiology* **171**:785–791.
86. Jellus V, Kiefer B. 2005. Optimization of the homomorphic filter for bias field correction. *Proc Int Soc Magn Reson Med* 2248.

87. Cho I, Song JOH, Kim T, Jeong D. 2004. The effect of optimal design of low-pass filter with image type in RF field inhomogeneity correction using homomorphic filtering-based method. *Proc Int Soc Magn Reson Med* **11**:2192.
88. Triantafyllou C, Dale A, Fischl B, Knake S, Wald LL. 2005. Optimized B₁ inhomogeneity correction for high field magnetic resonance imaging. *NeuroImage* **19**(2, Suppl 1):1347.
89. Wald LL, Carvajal L, Moyher SE, Nelson SJ, Grant PE, Barkovich AJ. 1995. Phased array detectors and an automated intensity-correction algorithm for high-resolution MR imaging of the human brain. *Magn Reson Med* **34**(3):433–439.
90. Barbier EL, Marret S, Danek A, Vortmeyer A, Gelderen PV, Duyn J, Bandettini P, Grafman J, Koretsky A. 2002. Imaging cortical anatomy by high resolution MR at 3.0T: detection of the stripe of Gennari in visual area 17. *Magn Reson Med* **48**:735–738.
91. Hennig J, Weigel M, Scheffler K. 2004. Multiecho sequences with variable refocusing flip angles: Optimization of signal behavior using smooth transitions between pseudo steady states (TRAPS). *Magn Reson Med* **49**(3):527–535.
92. Schmitt F, Stehling MK, Turner R. 1998. *Echo-Planar Imaging*. ISBN 3-540-63194-1.
93. Rosen BR, Belliveau JW, Aronen HJ, et al. 1991. Susceptibility contrast imaging of cerebral blood volume: human experience. *Magn Reson Med* **22**:221–226.
94. Kucharczyk J, Vexler ZS, Roberts TP, et al. 1993. Echo-planar perfusion-sensitive MR imaging of acute cerebral ischemia. *Radiology* **188**:711–717.
95. Ostergaard L, Sorensen AG, Kwong KK, et al. 1996. High resolution measurement of cerebral blood flow using intra vascular tracer bolus passages, II: experimental comparison and preliminary results. *Magn Reson Med* **36**:726–736.
96. Warach, S, Li W, Ronthal M, et al. 1992. Acute cerebral ischemia: evaluation with dynamic contrast-enhanced MR imaging and MR angiography. *Radiology* **182**:41–47.
97. Warach S, Gaa J, Siewert B, Wielopolski P, Edelman R. 1995. Acute human stroke studied by whole brain echo planar diffusion-weighted MRI. *Ann Neurol* **37**:231–241.
98. Belliveau JW, Kennedy DN, McKinstry RC, et al. 1991. Functional mapping of the human visual cortex by magnetic resonance imaging. *Science* **254**:716–719.
99. Ogawa S, Menon R, Tank D, Kim S, Merkle H, Ellermann J, Ugurbil K. 1993. Functional mapping by blood oxygenation level-dependent contrast magnetic resonance imaging: a comparison of signal characteristics with biophysical model. *Biophys J* **64**:803–812.
100. Thomas DL, De Vita E, Deichmann R, Turner R, Ordidge R. 2005. 3D MDEFT imaging of the human brain at 4.7T with reduced sensitivity to radiofrequency inhomogeneity. *Magn Reson Med* **53**:1452–1458.

THE CHALLENGES OF INTEGRATING A 9.4T MR SCANNER FOR HUMAN BRAIN IMAGING

Keith R. Thulborn

University of Illinois, Chicago

1. INTRODUCTION

The increasing appreciation of neuroradiologists, other healthcare professionals, neuroscientists, and cognitive scientists for the exquisite detail of anatomical, physiological, and functional magnetic resonance imaging (fMRI) of the human brain has encouraged increasing use of MRI in medical care and research. As MRI has no adverse biological effects when performed within FDA guidelines, longitudinal studies of development and aging and detailed studies through repetitive measurements on single subjects can be undertaken with insignificant risk. Scanner performance for clinical MR scanners has been enhanced as field strengths have migrated upward to 3.0 Tesla. It is appropriate to consider the technical challenges of further improving sensitivity by moving from 3.0 to 9.4T, the highest magnetic field scanner now available for human MRI that became operational in 2004.

The development of clinical MRI at 3.0 Tesla commenced in 1993, driven by the potential of obtaining robust fMRI in individual patients [1–7]. Research applications have matured over the last decade as this technology has been disseminated throughout the cognitive psychology and neuropsychology research communities. This technology has provided new insight into the biological basis of human cognitive function. Clinical applications of fMRI have evolved more slowly because of the increased complexities of individual patient studies, but presurgical planning for neurosurgical interventions has always been recognized as an immediate goal. The implementation of fMRI technologies on clinical scanners has promoted such developments by removing the need for large and expensive research teams [4]. The success of this new standard of neuroimaging at 3.0 Tesla has promoted the desire to proceed to even higher magnetic fields. The signal-to-noise performance and chemical shift range of MRI increases with magnetic field. Access to signals from non-proton nuclei such as sodium, phosphorus, carbon, oxygen, and nitrogen becomes feasible on acceptable timescales for human experimentation and possible

clinical application. The development of biochemical imaging in humans using MR signals from endogenous non-proton metabolites is dependent on the development of ultra high field magnet and gradient technology and the associated electronics and power amplifiers. Having been involved in the development of the clinical 3.0T product from GE Healthcare from its inception and now having brought the first 9.4T scanner for human imaging to operational status, it is appropriate to take this opportunity to highlight the challenges of such high field MRI scanners. This chapter is not written for engineers and physicists who are already well aware of the issues but rather for other investigators and visionaries who see the potential of this technology but for whom the risks and challenges remain an apparent insurmountable hurdle. Although commercial solutions can promise simplified fMRI, care must be taken to avoid becoming dissociated from the technology and its installation. Careful planning of performance specifications establishes appropriate expectations by both the purchaser and the vendors. To avoid disappointment and considerable lost time, strict quality assurance should be applied across each step of the purchase, installation, and maintenance of the scanner. This chapter discusses each of the issues, emphasizing its relevance with respect to both 3.0 and 9.4 Tesla scanners. These issues must be understood by the purchaser to obtain the optimal performance with minimum frustration.

2. CHOICE OF MAGNETIC FIELD STRENGTH

The choice of magnetic field strength for human imaging has been constrained by the development of large-bore magnet technology over the last decade, beginning with early 4T scanners [8] and migrating upward to an 8.0T human system described by Robitaille and colleagues in 1999 [9]. Although the clinical scanner manufacturers (GE Healthcare, Siemens, Phillips) have elected to step back to develop 7T whole-body scanners for their research and development efforts [8,10–12], magnet technology was ready for a further step to 9.4 Tesla, the limit of the electrical current density supported on current superconducting wire technology at 4.2°K. The development of the 9.4T scanner has been a partnership between the University of Illinois through financial support from the State of Illinois and a number of companies. The magnet and gradient systems have been products of GE Healthcare. Having chosen the field strength, the rest of the scanner was assembled from systems from other vendors. The spectrometer/scanner is based around electronics with a four-channel proton excitation/reception arrangement and single-channel non-proton excitation/reception channel and customized pulse sequences for biochemical imaging from Bruker Biospin.. This system provides RF power monitoring on all channels to ensure that imaging is performed within FDA guidelines. The power amplifiers (Copley Model 281) to drive the gradients come from Copley Controls Corp. newly developed to deliver currents of 550 amperes at 1000 volts and matched to the load of the gradient set and cables. The room temperature shims built into the gradient set are driven and controlled by power amplifiers from Resonance Research Inc. through the Bruker console. The temperature monitoring

of the gradients was done by Kisor Controls Company and integrated into the Bruker control system. Despite the potential for integration conflicts, the multiple-vendor subsystems were integrated into an operational scanner according to plan with surprisingly little difficulty.

3. SITE PLANNING

Irrespective of field strength, the first step in the purchase of an MRI scanner is consideration of the installation site. Each aspect will now be considered in detail:

3.1. Fringe Field Containment

The fringe field is the magnetic field that extends outside of the magnet. The safety regulations developed for clinical scanners state that the 5 gauss must be secured from accidental entry by an unknowing passerby. This concern is because of the potential impact of static magnetic fields on such medical devices as implanted cardiac pacemakers. Because of the use of active shielding in modern clinical scanners, the fringe field can be minimized in extent. Such active shielding for 3.0T scanners minimizes the footprint of the magnet to that of a 1.5T scanner, thereby conserving expensive real estate for siting. For optimal performance of active shielding, care must still be taken to avoid having large moving ferromagnetic masses such as elevators within reasonable proximity to the active shielding volume. For the latest 3.0T clinical magnets, the space requirements are essentially the same as for 1.5 Tesla. Although this is the simplest issue to resolve, it is often the primary focus of most decisions to move to state-of-the-art clinical imaging at 3.0 Tesla. Containment of the fringe field was a primary focus for the 9.4T whole-body magnet, but other issues should not be overshadowed.

For the 9.4T and other ultra high field scanners the siting issue is not trivial. Active shielding is not yet technically possible. Thus passive shielding with large masses of iron is required. Even with 520 tons of iron placed symmetrically as a six-sided box around the magnet, the 5-gauss line still extends more than 1 meter outside the walls. This has required that the surrounding areas remain secured by limiting access to the building. The areas outside the magnet room that are above 5 gauss are highlighted visually by a curvilinear red terrazzo floor while the 1-, 2-, and 3-gauss lines are displayed by red terrazzo lines set on a black background. The same floor concept is also used in areas of carpeting and computer flooring. The curvilinear dropped ceiling reflects the floor design. Although there is limited access to the building, support personnel, such as maintenance and service staff, who may not be constantly working in the building, are immediately warned by this environmental design that care must be taken within the 5-gauss line. Large ferromagnetic objects (e.g., elevators) and all electrical equipment (e.g., cooling systems, electronics, motors) are not permitted to move within or through the 5-gauss line.

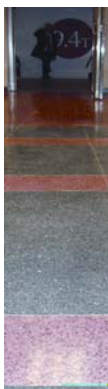


Figure 1. The fringe field extends beyond the iron room and is reflected in the coloring of the red lines on black terrazzo floor. This same color coding is used on the carpet and computer flooring to mark the 5-gauss fringe field to address safety concerns. See attached CD for color version.

The other safety aspect of the fringe field arises from emergency response personnel such as medical personnel, firemen, and police. Despite an ongoing magnet safety education program, the emergency services must balance rapid access with the potential dangers of untrained personnel walking into a high magnetic field with ferromagnetic articles (stethoscope, fire-axe, gun, etc.) or implanted medical devices (cardiac pacer, cochlear implant). At 3.0 Tesla, medical emergencies can be dealt with most effectively by moving the patient out of the magnet room. A detachable patient table facilitates this strategy. An identical approach of detachable table has been adopted for the 9.4T system. Because human studies are always done under the control of experienced personnel, risks of the “missile effect” from inadvertently carrying ferromagnetic objects into large magnetic fields are minimized. However, when an alarm triggers an emergency response team such as police or fire brigade outside of normal business hours, then locked doors may be ignored. Signs specifically designed for the emergency services have been used to halt their advance and to provide contact numbers to authorized personnel to prevent forced entry into a potentially hazardous situation for response personnel.

3.2. Climate Control

Because the electronics and gradients of the scanner produce heat, sufficient temperature control must be available to maintain thermal equilibrium in the equipment room that houses these heat-producing devices. The equipment room should be designed with appropriate air circulation. Some equipment racks are designed to have cool air circulating from below a computer floor upward through the equipment racks. These racks are designed for such circulation and should always be operated with the covers in place. Other racks release heat into the surrounding room. As most equipment rooms are designed with computer floors to allow convenient distribution of cables between cabinets and the magnet room without tripping hazards, consideration of the path of air circulation between above and below floor spaces should be given to ensure optimal control. The temperature and humidity of the equipment room should be monitored, which is usually uncomforta-

bly cool. Temperatures of 64 to 66°F are acceptable for optimal performance. Humidity should be low to avoid condensation of water vapor at these temperatures.

As there is considerable valuable electrical equipment in the equipment room that can be damaged by water, care should be taken to ensure that water pipes and air conditioning ducts are not run above the areas holding this equipment. If not defined in the architectural design, water pipes and pumps are placed at the convenience of the construction crew without concern for the potential disasters caused by leaking pipes and water dripping from condensation. Similarly, a floor drainage system should be installed to prevent accumulation of water on the floor if a flood from a broken pipe does occur.

The fire protection system should be a dry dual-action triggering system. This means that no pipes carry water above the electronics until the first activation signal (e.g., smoke) and a second signal (e.g., high temperature) is required for the release of water from the sprinkler system. Such planning offers the greatest protection for expensive equipment from inadvertent false alarms. Similarly, a simple canopy over the electronics can divert water off the electronics should sprinkler activation occur.

For the 9.4T magnet room, the sprinkler heads for the fire protection system were tested for functionality at a high magnetic field (3 Tesla). This compatibility ensured that function was maintained and that no ferromagnetic projectiles were produced when activated. Complete drainage of the sprinkler system is essential once the system is filled for testing or by alarm.

The iron room is intimately connected to the magnet through the magnetic field. Any expansion or contraction of the iron room due to temperature variations adversely affects the homogeneity of the magnetic field. This problem is eliminated by strict climate control ($\pm 1^\circ\text{C}$) of the enclosure around the iron box, which is effectively another room around the iron box. The air must be able to circulate adequately to avoid temperature gradients across the room.

3.3. Vibration Control

Vibrations of the magnet arise from a number of sources and can degrade image quality. The magnet should be sited to isolate any building mechanical vibrations that arise from air conditioning/heating systems and elevators. Typically this can be achieved on ground-floor installations by using a concrete slab that is independent from the building, used to support only the magnet room and not the surrounding building. Care must be taken not to defeat this strategy by making multiple other rigid connections to the magnet room through piping, air conditioning, and doorways. Such mechanical vibrations can be readily assessed by a vibration consultant and isolated by specific frequencies to the likely sources. This was achieved, albeit with great effort, even for an installation of a 3.0T scanner on the 8th floor of a building in which the mechanical floor was immediately below on the 7th floor.

For the 9.4T magnet weight considerations (40 tons for the filled magnet, 520 tons of iron shielding) required an independent reinforced concrete slab supported

by six caissons extending to a depth of 60 feet. The slab surface had to be below grade level as the iron room had to be symmetrically placed around the isocenter of the magnet. Because of the desire to maintain a single floor level throughout the building, and a standard patient table height for the magnet, the iron room had to be filled to a certain level to support the magnet in isocenter. To maintain magnetic symmetry, no reinforcement was used. Instead, a cement mix was custom designed and tested to a compressive strength sufficient to support the magnet but also with a composition that allowed no contraction upon solidification. It is expansion and contraction during setting that leads to cracking when reinforcement is not used. This cement composition succeeded in avoiding cracking but did require several days of hardening in order to bear any significant weight. Sealing the gap between the slab carrying the magnet and the surrounding slab carrying the building was achieved with non-rigid clay that dampened transmission of vibration while maintaining a waterproof seal. The connection at the doorsill of the magnet room to the surrounding building was also non-rigid, with the sill resting on but without fixation on an electrical insulated pad on the reinforced overhang from the outer building. The doorsill is flat at floor level with no bump to interfere with passage of the patient table through the door. This sill is electrically isolated from the surrounding building to avoid electrical grounding, as is discussed below under electrical aspects of MRI siting.

The piping for medical gases, vacuum, fire protection, ventilation, and electrical conduits are all mechanically and electrically isolated through electrically non-conducting flexible sections to avoid transmission of mechanical vibrations to the magnet room.

3.4. Electrical Supply

The electronics of the scanner should be powered by a stable electrical supply. For 3T scanners, as for lower field systems, conditioning of the electricity removes electrical fluctuations that are one cause of image instability, particularly for applications in which series of images are acquired. Power conditioning should be available not only for the equipment room but also for the control room where the control computer is located. A stable electrical power supply can be expected to prolong the usefulness of the electrical subsystems of the scanner. For the 9.4T scanner an electrical substation separate from the university grid was installed to support the electronics and computers through separate power conditioners. Other less important electrical outlets for the building were taken from the substation without conditioning. Even with this well-protected electrical supply, emergency electrical power from the generators of the University Medical Center was installed as a backup electrical system for the cryocoolers of the helium refrigeration system for the 9.4T magnet. In the event of power failure, helium boil-off cannot escalate in the absence of functional cryocoolers. This should avoid expensive emergency helium filling during power failures.

The electrical supply into the magnet room must be filtered to prevent radio-frequency interference with the MR signal. The filters should be appropriate across

the range of operating frequencies of the scanner. The filters for the gradient cables must be able to take the appropriate current and voltage for the gradient amplifiers. For the 9.4T system this is 550 A at 1000 V for each of the three axes of the gradient set.

The magnet room should have a single ground point at the penetration panel. This means that as the magnet room is built all types of electrical grounding must be avoided. This can and should be monitored using an alarm system that triggers a warning when the electrical resistance between the room and ground is less than 1000 Ω . Immediate feedback allows an inadvertent ground point to be removed immediately rather than going through the frustrating task of finding this problem once the room is completed. This alarm system requires conscientious monitoring by the owner as the time-conscious construction crews often ignore or turn off this alarm system.

The sources of electrical leakage can be readily listed. The iron shielding sits on a concrete slab and would be an electrical ground, especially if moisture were to be trapped between the slab and iron floor unless insulation is used. For the 9.4T room, the concrete was coated with a polymer layer and then covered with contiguous thick plastic sheets (10-mm thick PVC) that support the weight of the entire room and magnet (560 tons) (see Figure 2). These materials were dry when put in place as the site was protected from the weather during this stage of construction. Prior to making the piping connections, the electrical isolation of this room was 14 M Ω , well above the 1000- Ω resistance specification.



Figure 2. Electrical isolation of the iron room was ensured by isolating the iron floor from the concrete slab with a dielectric polymer paint and 10-mm thick PVC plastic sheets. The inside joints of the iron blocks were welded continuously to ensure RF integrity. The concrete slab was made independent of the surrounding building to prevent vibration transmission into the magnet room. Electrical grounding was achieved at a single point at the penetration panel and used for all electrical grounding of the scanner electronics. See attached CD for color version.

The electrical isolation of the piping should be straightforward, as commercially available fitting are available for this purpose. However, experience indicates that quality assurance on the final result is important as the dielectric components

of the fittings can be readily damaged by extreme tightening and/or overheating during soldering of adjacent piping joints.

The electrical circuits including the RF filters are much more of a concern, as the building code may produce conflicts in that grounding, for the electrical wiring may be required back to the electrical source rather than via the penetration panel ground point. This issue becomes a discussion with the electrical contractor to meet the desirable goal of a single ground plane for the penetration panel and all of the scanner electronics.

The dry dual-action fire protection sprinkler system has an additional issue beyond the MR compatible fittings. Although the system is normally dry, it must be tested for building code passage during construction by filling with water. Unless the system can be completely drained, residual water can provide an electrical bridge across the dielectric joint, thereby defeating its purpose. This problem can be resolved by providing an appropriate drainage circuit to ensure that water cannot pool across the dielectric connections.

The final result for the 9.4T room with all connections in place was an order of magnitude above the specification of 1000 Ω .

There are two cryocoolers used for recirculation of the helium boiled off from the magnet. These electrically operated units are an essential part of system maintenance. Cryocooler malfunction from electrical failure can result in increased helium boil-off and increased costs. An alternative power source through the emergency electrical supply of the hospital has been installed to prevent such events that can happen when personnel are not available for intervention (e.g., weekends, holidays).

3.5. Radiofrequency Isolation

Although higher magnetic fields increase the magnitude of the MR signal, the performance of a scanner is measured as a signal-to-noise ratio (SNR), where the signal and noise should be arising from the sample being measured. Unless good RF isolation is achieved in the magnet room, the noise level is not only determined by noise from the sample but also from many possible sources of environmental RF energy. The magnet room should be a Faraday cage and attenuate all stray RF noise. A standard of specifications is the government document MIL-STD-285: "Military Standard Attenuation Measurements for Enclosures, Electromagnetic Shielding, for Electronic Test Purposes, Method of," from the Office of the Assistant Secretary of Defense, dated June 25, 1956.

Several types of RF rooms can be purchased. The best experience for 1.5 and 3.0T rooms has been obtained from a solid copper room in which all joints are continuously soldered and all screw penetrations through the copper are soldered. Such rooms may be more expensive but performance has been maintained over many years.

For the 9.4T room, the iron room was welded continuously along all inside seams to produce a solid iron box (Lindgren RF Enclosures Inc., Glendale Heights, IL). The only potential sources of RF leaks are limited to the RF door and the pene-

tration panel. Experience dictates that every weld should be closely inspected to ensure that a continuous solid weld is completed before any part of the inside of the room is finished and cover sites of potential RF leaks. This inspection should be done by the customer or an outside consultant to ensure attention to detail if lost time and frustration are to be avoided.

The RF door is the most problematic source of leaks over time. Experience indicates that pneumatically sealed doors are the best approach. These doors do need to be serviced at least annually but seem to maintain performance considerably longer than other types of doors with mechanical seals. As a safety feature, the door of the 9.4T room opens outwards to avoid not being able to open the door against a high internal pressure.

Most clinical scanner rooms have an RF-sealed window for patient observation. The 9.4T scanner is monitored via fiberoptics and video camera rather than using a window. This is more expensive but avoids another source of leaking joints. The window for the 9.4T room would not be useful, as the control computer for the operator is well away from the room to avoid the high fringe field interference with the computer.

The penetration panel is without doubt the most troublesome source of RF leakage. It is important to minimize all unnecessary metal-metal joints and to ensure that all joints are very tight against flexible RF seals. Waveguides allow openings in the room without loss of RF isolation. The rule of thumb is that the length of the guide must be four times the diameter of the guide to achieve RF isolation (110 dB), and this was achieved for the four waveguides inserted into the penetration panel for the 9.4T room. The penetration panel was at the opposite end of the room to the door to maintain magnetic symmetry. The penetration panel was made of aluminum sheet bolted to the iron wall with an intervening compression RF gasket. It was only after insertion of the smaller penetration panel carrying the electronics that the RF isolation was decreased. This loss was expected based on the vendor's specifications.

The generic specification of 100 dB is the reduction of noise from a noise source operating at the specified highest operating frequency of the scanner in units of decibels (dB). The specification should include the measurement system, including the types of antennae and the distance of antennae from the walls, doors, and openings being tested. Testing should be done at three stages during construction of the magnet room. The first test should occur when the RF shield is complete before cutting the penetration panel and before any finishes are installed. The doorway can be covered with a copper sheet if the RF door is not already in place. This dB value is the best that can be expected and must exceed the specification before further work is commenced. The best way to ensure adequate performance is to have the testing performed by a consultant other than the contractor building the room. This avoids any appearance of conflict of interest.

3.6. Acoustical Dampening

High performance gradients produce considerable acoustical noise, especially when combined with demanding pulse sequences. Such noise must be reduced for the patient being scanned, usually with earplugs and other forms of ear protection. This noise also represents an occupational hazard for the personnel using the scanner on a daily basis. The best hearing protection can be built into the room. The walls can be lined with acoustical dampening materials. Added protection comes from covering reflecting interior surfaces, walls, and ceiling with acoustically contoured foam tiles.

The 9.4T iron room is contained inside a larger room that allows for climate control (to avoid temperature changes that affect iron room coupling to the magnet) and noise control. It has composite walls that are lined with three layers of acoustic dampening materials between the drywall. The drywall on the inside and outside of the wall are supported on separate studs that are offset to allow the sound control materials to weave continuously across the room. There are no direct connections between the inner and outer drywall surfaces. The interior room wall and ceiling surfaces are also covered with contoured foam to enhance destructive interference of gradient noise inside the room. The absence of a window also removed another source of noise leaks.

The door bridges the magnet room with the control room and can be the largest source of noise transmission. Doors for MR rooms have acoustical ratings and should be chosen appropriately to avoid environmental contamination. The 9.4T room has a pneumatically sealed door with an acoustical rating of 100 dB. The ventilation system is insulated for temperature control but also controls noise transmission. The 9.4T room is virtually silent from the outside even under gradient demanding pulse sequences.

The patient end of the room has been finished with wood paneling on walls, thick padded linoleum floor tiles, and high-performance acoustic ceiling tiles. The impression on entering the room is anticlimactic, as the magnet is not visible except for the entry as a hole in the wall.

3.7. Lighting

As the fringe field on the inside of the wall of the 9.4T magnet room is 1000 gauss, normal MR compatible lighting cannot be used. A fiberoptic lighting system has been used with six remote high-power xenon lamps mounted outside the 5-gauss magnetic field. The lamps are rated for fiber of a maximum length of 40 feet that is sufficient to fully illuminate comfortably the entire room with multiple light fixtures. The lights can be turned on in two stages to offer different lighting levels at each end of the magnet room.

The bore of the magnet is illuminated with the same fiberoptic system, with the lighting fixtures mounted on adjustable swivels at each opening of the magnet bore. This is necessary to have sufficient light for the fiberoptic visual monitoring system for human subjects within the bore of the magnet.



Figure 3. (top) Acoustically contoured lining of inside of magnet room reduces sound reflections from flat surfaces of walls and ceiling. Also seen are the fiberoptic lighting fixtures and the fire sprinkler heads suspended from the ceiling above the magnet (bottom left corner). (bottom) Acoustic noise dampening of the walls of the room surrounding the iron magnet room is shown as: (1) inner aluminum stud, (2) acoustical insulating fiber, (3) flexible separating material, second layer of acoustical insulating fiber not seen, and (4) outer aluminum stud with (5) outer dry-wall screwed to stud. See attached CD for color version.



Figure 4. Fiberoptic light fixture suspended from the ceiling with fiberoptic cable transmitting light from outside the magnet room from xenon light sources 40 feet away outside the 5-gauss line. Fiberoptic cables enter the room from the access ports in the ceiling of the iron room. The lighting in the magnet room operates at above 1000 gauss. See attached CD for color version.

3.8. Cabling

The cabling systems for control of and input to the imaging gradients, room temperature shims, and RF power carry electrical currents through the large fringe field. The large currents in the gradient cables are rapidly switched during imaging, and so experience considerable force that results in flexing which will ultimately lead to metal fatigue and failure. Mechanical fixation of these cables from the penetration panel to the gradient set minimizes flexing, thereby prolonging the longevity of the cabling (Figure 5). The problem is of less concern for the other cabling carrying direct currents or high-RF frequencies. Such precautions do not prolong the life of the gradient set itself, which experiences even greater forces. However, improved image quality is expected with better mechanical stability of the cabling. The cabling support is machined from horizontal Garolite rectangular bars that clamp around the cables and are held with phosphor bronze nuts and bolts. The clamps are mounted on a fiberglass and aluminum stand.



Figure 5. The gradient cables carry large direct currents through the large fringe field within the magnet room, thereby experiencing very large forces that are expected to produce eventual metal fatigue and breakage. Mechanical support severely restricts any significant movement to slow this failure onset. The gradient cables are clamped along their entire length within grooves machined into Garolite bars held in a horizontal orientation along the z -axis of the magnet from point of exit from the gradient set to the penetration panel. See attached CD for color version.

3.9. Gradient and Gradient Power Amplifier Cooling

The imaging gradient set is cooled efficiently with a glycol–water (1:2) mixture circulated to maintain a steady temperature during imaging to enable stable signal intensity. The cooling system (Neslab 750) maintains the flow conditions (4.25 gallons per minute with a pressure drop of 17 pounds per square inch at 20°C) specified by the gradient vendor (General Electric Medical Systems, Oxford Ltd., Abingdon, England) as registered by both an in-line analog flow meter as well as an electrical flow meter. If the electrical monitoring detects low flow below an acceptable specified level, the Bruker control supervisor interrupts the gradient power amplifiers (Model 281, Copley Controls Corp, Canton, MA).

When integrating subsystems from different vendors, connections should be simplified as much as possible. An important feature of the cooling system is to make the piping connections both MR-compatible and self-sealing after disconnection inside the magnet room (Swagelok Company, Solon, Ohio). This allows safe, easy, and dry disconnection when exchanging the gradients without having to drain the cooling system. It also limits the need for additional tools within the magnet room during this exchange process to improve safety. The flexible piping used for cooling the 9.4T system is double contained and separated from electrical wiring to avoid cascading electrical problems, should flooding occur.

The gradient power amplifiers are also cooled via the same type of cooling system as used for the gradients but as a separate system. The amplifiers operate at a higher temperature from the gradients, and cooling is based on a glycol-water (1:1) mixture. This cooling system also has both an in-line analog flow meter as well as an electrical flow meter to ensure that flow (8.5 gallons per minute with a 30 pounds per square inch pressure drop at 25°C) is maintained as specified by the amplifier vendor. This flow rate is also monitored by the Bruker supervisor system.

An important point to emphasize so that an unexpected and expensive problem can be avoided is the composition of the coolant. Initially in the setup stage, the gradients and amplifiers were run from the same cooling unit using only water as the coolant. This very quickly resulted in failure of the power amplifiers due to corrosion of the heat-exchanging surfaces and overheating. The glycol serves as both an anticorrosion agent and a bioinhibitory agent.

3.10. Human Delivery System

For human scanners, the patient bed and delivery system must be designed around safety and comfort and should also maximize image quality. This means appropriate positioning and stability of the patient within the RF coil and appropriate choice of cable lengths from the coil to the preamplifiers. Such systems are an integral part of commercial 3T scanners.

The configuration chosen for the 9.4T system has used the same approach. The patient bed is transferable from a freely mobile transporter that allows the human subject to be supinely positioned on a comfortable foam mattress (Tempurpedic Medica Inc., Lexington, KY) with their head correctly located within the RF coil with comfortable foam pads (Tempurpedic Medica Inc., Lexington, KY). This positioning can be done outside the magnet room at a low fringe field (<5 gauss). The mobile transporter carrying the patient on the bed is then moved into the magnet room (>1000 gauss) along the long axis of the magnet. It docks at the end of a fixed table, allowing the patient table to be moved from the transporter onto the fixed table and then into the magnet. The rate of movement from the fixed table into the magnet is slow (9 inches per 360° turn of the manual handle) through a geared pulley drive and handle system but can be controlled manually by the technologist. This steady slow insertion minimizes the sensation of vertigo that results from rapid movements of the head through the large magnetic field gradient. Such

controlled rate of movement removes this sensation for most people who are currently working with this magnet. Further adjustment may be required with subjects who are completely naïve to such large magnetic field gradients. Initial concerns of not being able to work and move around conveniently within the magnet room have proven to be unfounded. Human subjects can be placed on the moveable subject bed when it is at least a meter away from the end of the magnet without a sensation of vertigo from the subject. The detachable table remains useful for safety reasons if a subject needs to be quickly removed from the magnet room in the setting of a medical emergency.

The materials used for the subject bed, transporter, and fixed table are MR-compatible, with wood, plastic, and fiberglass being used in preference to aluminum and stainless steel.

3.11. RF Coils

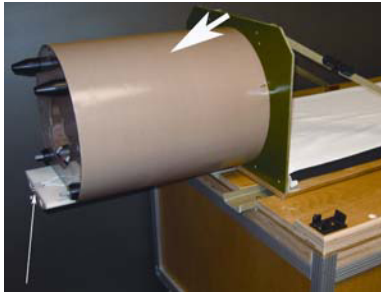
The RF coils are an area of development at 9.4 Tesla. For nuclei with a low gyromagnetic ratio like sodium, the same coil technology as used for proton imaging at clinical field strengths can be used. The first volume RF coil for sodium imaging of the human brain has been generously supplied by Dr. Ed Boscamp, Chief Scientist, Applied Science Laboratory, GE Healthcare Technologies (Waukesha, WI, USA). This coil is a dome birdcage resonator with a lumped element 90-degree hybrid splitter/combiner needed to set up circular polarization of the B1 field (Figure 6). The capacitors in the coil are 3 kV to accommodate the high B1 amplitudes needed for sodium imaging. The dome shape of the coil is optimized for uniformity of B1 over the brain. This coil produces well-defined 90 and 180° pulses and a duty cycle for twisted projection imaging of sodium that is well below the FDA guidelines for specific absorption rate as monitored by the RF supervisor (Bruker Biospin MRI Inc., Billerica, MA, USA).

The RF coils used for quality assurance of the instrumentation are 3-inch diameter single-tuned coils for protons, sodium and phosphorus, respectively, supplied by the spectrometer/scanner vendor (Bruker Biospin MRI Inc., Billerica, MA, USA). These coils are used to set acceptable performance of the scanner electronics (Bruker Biospin) on small spherical samples without concern for magnet performance (GE Healthcare).

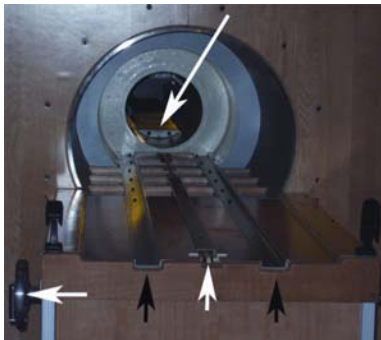
As seen in Figure 6, the RF coil is mounted to the patient table with a fiberglass adjustable mounting system that maintains the coil on axis with the gradient set for simple insertion. The coil makes electrical connection via blind mate connectors that insert into female connectors mounted semirigidly inside the gradient set. These connectors are mounted in Teflon blocks that have guides that ensure appropriate location for a firm low-loss electrical connection. The cabling remains mounted in the bore of the magnet exiting via a hybrid splitter/combiner to a pre-amplifier immediately outside the magnet. Cabling is in units of half-wavelength for the nucleus of interest.



(a)



(b)



(c)

Figure 6. (a) MR-compatible mobile patient transporter with transferable bed and mattress that has the (b) RF coil (short white arrow) attached at one end. The electrical connection for the RF coil uses blind mate connectors mounted at the base of the leading edge of the coil (long white arrows in b) that automatically connect when the table is moved into the magnet (long white arrows in c). The patient bed and RF coil moves on rails (short black arrows, c) onto the fixed table (c) at the end of the magnet for transfer into the magnet. This transfer is done at a controlled rate manually by twisting a wheel on a pulley (short white arrows, c). The system is geared to produce 10-cm linear motion for every 360° turn. This avoids any sensation of moving through the magnetic field. See attached CD for color version.

3.12. Supervision of Specific Absorption Rate

The 9.4T electronics is designed with four separate proton (3.5 kW, 380–405 MHz) channels for excitation and reception as well as a fifth broadband channel for non-proton frequencies (3.5 kW, 40–170 MHz). The RF supervisor supplied with the electronics (Bruker Biospin MRI Inc., Billerica, MA) monitors all five channels at the output of the RF power amplifiers and ensures that the total power is within the FDA guidelines of 3 watt/kg over different time averages. If the coil is for the

head only, the supervisor checks the body weight given in the setup of the study and then calculates an appropriate head weight. The supervisor recognizes the coil configuration as each coil is specified by a code that sets the power for that coil. Each new coil must be calibrated for power delivery. As the transmission lines from the RF power amplifiers are not included in the SAR levels, these losses can be calibrated but currently serve as an added conservative safety margin. Similarly, the system monitors only the forward power. Any reflected power adds further to a conservative threshold. This system encourages the development of well-tuned and matched RF coils. Initial experience is that sodium imaging using twisted projection imaging at high flip angles and severe duty cycles remains within FDA guidelines. This is unlikely to be the case for proton imaging without the use of the multichannel excitation/reception approach. This remains an area of development.

Table 1. Magnet Parameters and Measured Values

Feature	Measurement
Magnet length	3600 mm
Magnet width	2580 mm
Overall height	3908 mm
Field (frequency)	9.405 Tesla (400.13MHz)
Clear bore diameter	800 mm
Length of superconducting wire	542 km
Number of turns of wire	122,330
Weight of wire	27,600 kg
Inductance	6255 H
Stored energy	151.1 MJoules
Cryogen (volume)	helium (1500 l)
Cryogen boil off rate	<0.35 l/hr
Homogeneity	<±0.8 ppm hhlw over 30cm dsv 0.1 ppm hhlw over 25 cm dsv
Field stability	<0.02 ppm/hr
Current at persistence	220 A
Magnet weight (unfilled without gradients)	45,000 kg
Cold weight (filled without gradients)	48,300 kg

3.13. Magnet

The specifications and measured values of the magnet, manufactured by General Electric Medical Systems (Oxford Ltd., Abington, England) are given in Table 1. The original purchase order specified a guarantee of 9.0 Tesla with an expect-

tation of 9.4 Tesla. The manufacturing of ultra high field magnets has a number of critical steps that should be monitored, although the customer is not in a position to control this process. These steps ultimately determine the delivery schedule. During manufacture, testing of vacuum, cooling, and boil-off rates are useful results to compare with specifications. The ultimate factory test is successful ramping to field. Loss of persistence (quenching) during or after ramping should be inquired about. Quenching is done under controlled testing but can happen spontaneously. These critical events test the safety mechanisms for protecting the magnet during rapid release of energy and loss of cryogenes. The magnet should meet acceptance criteria before shipping from the factory. A remote monitoring capability for cryogen levels and magnet shield temperatures was part of the original purchase. A plan for access to the magnet for cryogen filling was established to ensure appropriate ceiling heights and filling tube lengths.

Although manufacture took much longer than expected (3 years), the delays were used to complete the building in which the magnet is now housed. This building project was also not without its delays. It was designed to allow easy delivery of the magnet into the magnet room along with completion of the steel room and building exterior. Delivery was straightforward by road, ship, and road with due consideration of the weight of the load and its security and stability. Magnets were shipped with a monitoring system for forces that may have been experienced during transport and handling. No significant abuse was reported for this 9.4T magnet. Installation of the magnet on site was readily achieved. The gradient set was loaded while at zero field. The loading was performed from the patient end through the magnet room door. This simplified the completion of the less-accessible service end of the magnet room. This front-loading approach also simplifies replacement of the gradients when that is required. Magnet and gradient installation, cooling, and ramping were uneventful.

Cooling of the magnet required a considerable number of dewars of nitrogen and helium. A safe storage space was required for these many containers. Initial cooling with nitrogen can be achieved more conveniently if magnet access can be provided conveniently to a nitrogen transportation truck from outside the building. As this was not made clear, no simple access was available for the 9.4T magnet. Access was provided by removing an outside door to allow an insulated pipe to run directly from the nitrogen transportation truck through an adjacent room to the magnet. This was not an optimal approach and could have been avoided with better planning.

The cooling was completed in two phases. Initial cooling was with liquid nitrogen followed by liquid helium. The system was left standing at liquid helium temperatures for several weeks prior to ramping. Ramping on site was different from in the factory, as the magnet on site was now closely coupled to the iron room. Any miscalculations on positioning could have resulted in unexpected forces producing movement of the superconducting solenoidal coil within the magnet with resultant quenching. Care needs to be taken to ensure that the isocenter is correctly calculated within the iron room. This calculation must be verified by independent

qualified personnel, as was the case for this system, and no disappointment was incurred. Ramping was also performed in two phases, with an initial ramp to 3.8 Tesla and then continued a few weeks later to field. The magnet came to field on site without any training quenches and has remained stable over the last 12 months (Figure 7).



Figure 7. The 9.4T magnet in position in the iron magnet room just prior to closing the wall to cover all but the opening of the bore of the magnet (covered with red 9.4T sign). See attached CD for color version.

The homogeneity of the final static magnetic field was specified as a peak-to-peak variation in B_0 of points plotted over 12 planes on a surface of a sphere of stated diameter (dsv) using a teslameter to record B_0 at each point based on a deuterium signal (limited in sensitivity to an equivalent of 60 Hz on protons). As the presence of the head gradient insert prevented using the specified 40-cm diameter, a sphere of 30 cm was used. Rather than using planar plotting, helispherical mapping was performed using a proton spectrometer to map the proton signal to 1 Hz in a more densely sampled helispherical trajectory along the z -axis (Figure 8).

Shimming the magnetic field with superconducting, passive, and room temperature shims required effort to ensure that the long time constants of changes in the magnetic field were satisfied before the next adjustment. The homogeneity was at 1 ppm peak-to-peak at 30-cm dsv, which is comparable to 7T systems and better than some 3 and 4T scanners. The superconducting shims were well below maximum current. The room temperature shims were below 10% of maximum current except for the Z^4 shim that was at 14% maximum current (Resonance Research Inc., Billerica, MA). A compensation system for correction of temperature changes in the bore of the magnet was implemented to correct for temperature effects (26 Hz/degree, B_0 shift per $^{\circ}\text{C}$ of temperature change in magnet bore, Resonance Research Inc., Billerica, MA).

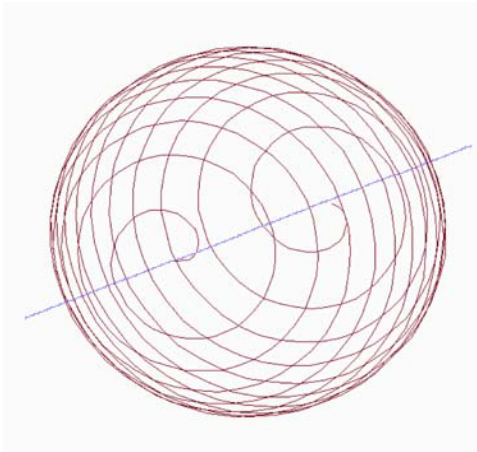


Figure 8. Helispherical trajectory used for magnetic field mapping at the proton frequency with a spectrometer. This approach maps to 1 Hz as compared to less sensitive standard approaches using 12 plane plots based on a deuterium signal measured with a teslameter. Reproduced with permission from Piotr Stareowicz, Resonance Research Inc. See attached CD for color version.

3.13. Gradient Set

The dimensions and specifications of the head gradient set are given in Table 2. The gradient assembly integrates imaging gradients, room temperature shims, and passive shimming system. The gradient set is heavy and long, so a delivery system must be specified. The system for delivery through the magnet room door from the patient end of the magnet was very streamlined and rapid. The first experience with this installation was simplified by working at zero field. Changing the gradient set in the future will entail lowering the magnetic field. The room temperature shimming system uses 12 shims with X, Y, and Z offsets on the imaging axes.

The gradients are monitored by multiple redundant temperature sensors (26 NTC thermistors). A separate contractor (Kisor Controls Co., Burr Ridge, IL) provided the interface to convert the output of these sensors into a signal that could be used by the Bruker supervisor to shut down the gradient power amplifiers if an excessive temperature rise occurred.

The magnet has been designed for whole-body imaging; however, at the time of this writing a whole-body gradient design with acceptable longevity under the conditions of 9.4 Tesla remains illusive. Even the head gradient set has a limited lifetime, and development efforts in materials and manufacturing are required. As has been the case in the past, human brain imaging is likely to lead the effort into ultra high magnetic fields for some time.

4. RESULTS

The 9.4T magnet and gradient have met top level testing requirements by producing high-quality images on small biological samples. The proton cross-sectional image of a kiwi fruit is shown in the accompanying Figure 9. The comparison of

images from 9.4 with 3.0T is probably not justified given the differences in T1 and T2 and the different RF coils used. However, the comparison (not shown) did imply that significant spatial resolution gains had been achieved at the high signal-to-noise performance over small fields of view at 9.4 Tesla.

Table 2. Gradient Assembly Parameters and Measured Values

Gradient property	Gradient specification
Outside diameter	792 ± 3 mm
Inside diameter	>360 mm
Overall length	2.46 m
Iso-center to shoulder at patient end	180 ± 1 mm
Iso-center to patient end	650 mm
Weight	1531 kg
Mounting	Adjustable vibration isolating mounts to magnet bore
Gradients	X, Y, Z
Room Temperature Shims	ZX, ZY, XY, X ² -Y ² , ZXY, Z(X ² -Y ²), Z ² X, Z ² Y, Z ⁰ , Z ² , Z ³ , Z ⁴
Water Cooling (flow, pressure, coolant)	15 liters/min, 3 bar, 33% glycol:water
Strength	>95mT/m at 550A
Slew Rate	400T/m/s

The use of sodium imaging with twisted projection imaging (TPI) has been demonstrated on phantoms and on non-human primates to be possible within FDA guidelines for specific absorption rate (SAR) for RF power (Figure 10). This sequence allows very short TE values (i.e., TE < 0.3 ms). The short T1 of sodium allows rapid repetition times and a very high duty cycle for SAR. Thus, sodium imaging is the prototypical biochemical application that serves to show the feasibility of biochemical imaging of humans at 9.4 Tesla.

The step toward human brain imaging has not been taken at the time of this writing, as approval for human imaging remains pending prior to further animal testing of RF power monitoring. Imaging with humans in the magnet room indicates that acoustical noise is controllable with standard ear protection (30-dB ear-plugs). The imaging gradients cannot be heard outside the magnet room. Vertigo (i.e., dizziness) and retinal stimulation (i.e., flashes of light in the peripheral vision) are common initial sensations for personnel working around the magnet but not when lying still within the magnet. Moving more slowly reduces these effects and justifies the use of the rate-controlled delivery system for human subjects. The nonhuman primate study, in which an animal was imaged at 3.0 Tesla before and after exposing the animal to 9.4 Tesla at a higher (x10) RF power level than required for human sodium imaging, demonstrated no changes in brain MR signal characteristics on any of the standard high-resolution imaging including T2-

weighted fast spin echo, FLAIR, gradient recalled echo, and T1-weighted gradient echo imaging. Although no adverse irreversible effects of imaging at 9.4 Tesla within the FDA guidelines are expected, this is particularly true for non-proton frequencies where local B1 fields are relatively homogeneous (comparable to proton imaging at 3.0 Tesla).

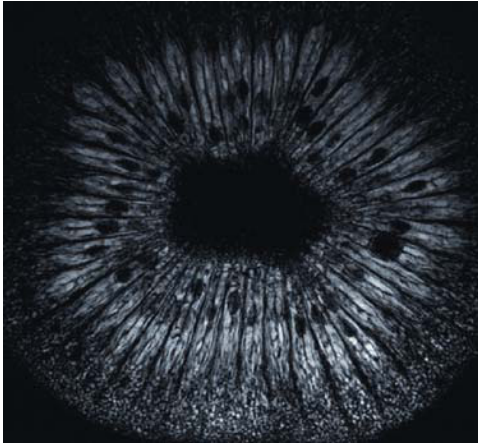


Figure 9. The first image from the 9.4T scanner was acquired with an axial T2-weighted spin-echo RARE sequence (TR = 4000 ms , TE = 35 ms, slice thickness = 1.5 mm, FOV = 6 cm², averages = 1) of a kiwi fruit using a 3-inch surface coil along the lower border of the image. There is some decrease in signal toward the top of the image consistent with limited penetration from the surface coil. The septa and seeds of the fruit are clearly evident. The straight septa suggest a high-fidelity image albeit over a small field of view. See attached CD for color version.

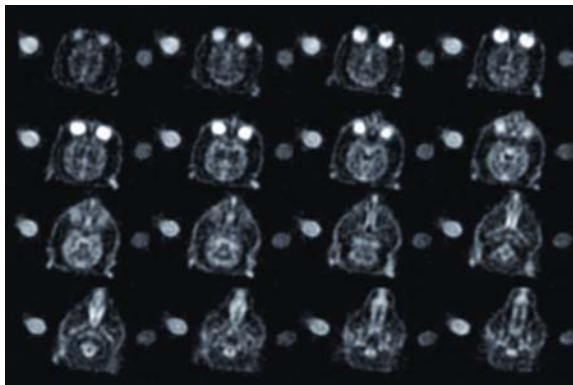


Figure 10. Sodium image of the head of a non-human primate acquired using a twisted projection acquisition (TR = 100 ms, TE < 0.2 ms, FOV = 16 cm³, total acquisition time ~6 minutes) from the birdcage head coil in the 9.4T scanner. The 3D data are presented in the axial plane. Concentration calibration phantoms (40, 80 mM) are on either side of the head. Eyes are toward the top of the figure (anterior orientation).

5. ACKNOWLEDGMENTS

The author wishes to acknowledge the help of many people who provided technical assistance and advice during this setup phase of this 9.4T scanner, including, in alphabetical order: Ed Boscamp, Theodore Claiborne, Dennis Cooke, Fred Damen, Scott Hinks, Douglas Kelley, Jim Lennon, Z.-P. Liang, Arno Nauerth, Hans Post, Jos Schouten, Matt Schuck, Piotr Stareowicz, Matt Ursino, Larry Wald, Rory Warner, Dan White, and X. Joe Zhou. As with all university projects of this magnitude, thanks go to the continuing patience and encouragement of the UIC Dean of the College of Medicine, Gerald Moss, and the UIC Vice-Chancellor for Research, Eric Gislason. The enthusiasm and ongoing guidance from the UIC Chancellor, Sylvia Manning, is greatly appreciated.

6. REFERENCES

1. Thulborn KR, Voyvodic J, Chang S, Strojwas M, Sweeney JA. 1998. New approaches to cognitive function by high field functional MRI. In *Current progress in functional brain mapping: science and applications*, pp. 15–23. Ed T Yuasa, JW Prichard, S Ogawa. Niigata/London: Nishimura/Smith-Gordon.
2. Thulborn KR. 1999. Why neuroradiologists should consider very high field magnets for clinical applications of fMRI. *Top Magn Reson Imag* **10**:1–2.
3. Thulborn KR. 1999. Clinical rationale for very high field (3.0 Tesla) functional MR imaging. *Top Magn Reson Imag* **10**:37–50.
4. Thulborn KR, Davis D. 2001. Clinical functional magnetic resonance imaging (fMRI). In *Current protocols in MRI*, Ed EM Haacke. New York: Wiley.
5. Thulborn KR, Gisbert A. 2001. Clinical applications of mapping neurocognitive processes in the human brain with functional MRI. In *Functional magnetic resonance imaging of the brain: methods for neuroscience*, pp. 329–350. Ed PM Matthews, P Jezard, SM Smith. Oxford: Oxford UP.
6. Thulborn KR. 2001. "Clinical fMRI". In *Magnetic resonance imaging of the brain and spine*, pp. 1973–1992. Ed SW Atlas. Philadelphia: Lippincott, Williams & Wilkens.
7. Thulborn KR, Shobat DM. 2003. Functional MRI moves into clinical service. *Advanced MR: Diagnostic Imaging Supplement*. October.
8. Ugurbil K, Garwood, Ellermann J, Hendrich K, Hinke R, Hu X, Kim S, Menon R, Merkle H, Ogawa S, Salmi R. 1993. Imaging at high magnetic fields: Initial experiences at 4 T. *Magn Reson Q* **9**(4):259–277.
9. Robitaille PML, Warner R, Jagadeesh J, Abduljalil AM, Kangarlu A, Burgess RE, Yu Y, Yang L, Zhu H, Jiang Z, Bailey RE, Chung W, Somawiharja Y, Feynan P, Rayner DL. 1999. Design and assembly of an 8 Tesla whole-body MR scanner. *J Comput Assist Tomogr* **23**:808–820.
10. Wiggins GC, Potthast A, Triantafyllou C, Wiggins CJ, Wald LL. 2005. Eight-channel phased array coil and detunable TEM volume coil for 7T brain imaging. *Magn Reson Med* **54**(1):235–240.
11. Wald LL, Wiggins CG, Potthast A, Wiggins CJ, Triantafyllou C. 2005. Design considerations and coil comparisons for 7 Tesla brain imaging. *Appl Magn Reson* In press.
12. Triantafyllou C, Hoge RD, Krueger G, Wiggins CJ, Potthast A, Wiggins GC, Wald LL. 2005. Comparison of physiological noise at 1.5T, 3T and 7T and optimization of fMRI acquisition parameters. *NeuroImage* **26**(1):243–250.

ULTRA HIGH FIELD MRI: HIGH-FREQUENCY COILS

J. Thomas Vaughan

University of Minnesota, Minneapolis

This chapter reviews RF volume, array, and surface coil modeling, design, construction, control, safety, and human in-vivo application examples for field strengths from 4 to 9.4 T. While a comprehensive variety of coils is included, focus is on the transmission line (TEM) technology head, body, surface, and array coils developed by the author over the past 16 years. References provide a supplement to this material for the many details that cannot be covered in a single book chapter.

1. INTRODUCTION

High-frequency coils are as important as high field magnets for high signal MRI. High-signal clinical MRI is presently performed with magnets of 3 Tesla field strength. Magnets of 7, 8, and 9.4T field strengths are currently operational for human research, and 11.74T magnets are being planned. Radio frequency (RF) coils must inductively couple to human anatomy at Larmor frequencies of up to 500 MHz to make these magnets useful. RF coil efficiency is inversely proportional to wavelength, both the wavelength of the coil circuit itself and the wavelength(s) of the media (air, plastic, anatomy, etc.) through which the RF field propagates. To maximize coil efficiency by minimizing its electrical wavelength dimension (λ), the physical dimension of the coil can be reduced, and/or the coil circuit elements can be more highly distributed. Practical considerations such as the image field of view (FOV), field homogeneity, count and control of transmit elements, count and control of receive elements, and RF safety features are applications dependent. Surface coils are typically designed for more localized and topical applications such as imaging a superficial organ or tissue. By contrast, volume coils are often designed to encompass a head or body for global imaging. Surface and volume coils can be tuned to two or more Larmor frequencies for multi-nuclear “metabolic imaging”. Volume coils are often used to “transmit” a uniform excitation field, in combination with surface coils being applied for receiving the excited

NMR signal from a local region of interest with high sensitivity. Global FOV coverage and local sensitivity can be acquired by receiving with arrays of surface coils. “Parallel” reception from surface coil arrays can achieve imaging speed benefit as well. Multichannel control over the coil transmit functions can be used to interactively or automatically control the nuclear excitation field in magnitude, phase, time, and/or frequency to effect a number of imaging optimization criteria. The design and application of high-frequency coils are considered in this chapter.

2. RF COIL LOSSES

Increased signal-to-noise (SNR) and its dependent spatial resolution, temporal resolution, and contrast are among the chief reasons for performing NMR studies at higher magnetic field strengths [1–7]. In theory the SNR increases to the power of 7/4 with field strength for “ideal” lossless samples [8]. However, for biomedical MRI of lossy tissue, RF-dependent losses, defined as energy dissipated or signal reduced, diminish the theoretical $\text{SNR} \sim B_1/\sqrt{R}$, where B_1 is the strength of the RF magnetic field generated by a unit current in the coil, and R is the effective resistance of the coil and load [9]. In human studies SNR is thus reduced by decreasing the numerator while increasing the denominator in real RF coils and in human tissues. Additionally, much of the coil generated RF energy is dissipated in the tissues as thermal energy [10–14]. The potential safety risk of excessive heating is increasingly present at higher fields. The chief objective in high field coil design therefore is to minimize these RF tissue and circuit losses critical to the quality and safety of high-field human studies. To achieve this objective, high-frequency RF loss mechanisms must first be better understood.

Increased SNR is sought by making NMR measurements at higher-magnitude B_0 magnetic fields. However, magnetic field strength is only one of several parameters affecting the NMR signal-to-noise ratio. RF coil and tissue losses can significantly limit the potential SNR gains to be realized at higher field strengths. SNR and transmit efficiency will suffer when any one of the parameters in the following proportionality is not optimized [9]:

$$\text{SNR} \propto (\omega^2 B_1) / \sqrt{(R_\Omega + R_r + R_{\text{tissue}})} \quad (1)$$

where R_Ω , R_r , and R_{tissue} are the coil’s ohmic resistance, radiation resistance, and coupled tissue losses, respectively.

RF losses in the NMR experiment can be categorized as coil losses, and as tissue losses R_{tissue} . Coil losses can be further divided into resistive losses to the coil circuit R_Ω , and radiative R_r losses to the coil’s field. Tissue losses result from B_1 field-induced eddy current losses to the tissue conductor, and radiated E field displacement current losses to the tissue dielectric. The physical nature of these RF losses is discussed in more detail in what follows.

At higher frequencies the phase change due to the finite propagation velocity of transmit and receive signals on coil conductors is no longer negligible. As coils

approach wavelength dimensions, the performance of the conventional lumped element designs succumb to (1) nonuniform current distributions resulting in decreased homogeneity, decreased fill factor, and increased radiated field losses, (2) increased ohmic losses in the coil circuit inductors due to decreased $1/e$ skin depths, (3) increased dielectric losses in the coil circuit capacitors due to decreased conductance efficiency compounded by an increased requirement for series capacitance to achieve high-frequency resonance, and (4) self-resonance below the desired frequency of operation. The ideal RF coil conserves energy in its circuit and its surrounding field. The real coil loses some of its energy at the average rate of P_{loss} , the power dissipated to the ohmic resistance, R_{Ω} , of the coil circuit, and to the radiation resistance, R_r , of the coil field. The peak RF current, I , in the coil loss (eq. (2) below) is measured at the coil's terminals. Equation (2) applies reciprocally to transmit and receive conditions for the resonant coil whose reactance is tuned to zero at the desired Larmor operating frequency. The “ Q ” factor, often used as a figure of merit for a resonant coil's efficiency, is defined by the ratio of the average energy conserved over the energy lost per cycle to $R_{\Omega} + R_r$. These two RF coil loss sources together with their impact on the NMR experiment will be further described:

$$P_{\text{loss}} = (I^2/2)(R_{\Omega} + R_r). \quad (2)$$

2.1. Coil Resistive Losses

The ohmic resistance, R_{Ω} , in the coil circuit is the sum of the real resistance of the coil conductor (inductor), R_L , and the real capacitor loss, R_C . R_{Ω} dissipates RF power $P_{\Omega \text{ loss}}$ as heat in the coil circuit. Because RF currents tend to flow near the surface of a conductor, R_{Ω} is dependent on the resistance, R_s , of a coil conductor's surface area. For an arbitrary coil loop with wire length (cross-sectional perimeter w_p , conductivity σ , and permeability μ , the ohmic resistance at the resonant frequency, ω , is given by [15,16]

$$P_{\Omega \text{ loss}} = (I^2/2)R_{\Omega}, \quad (3)$$

$$R_{\Omega} = R_L + R_C, \quad (4)$$

$$R_L = R_s(\ell/w_p), \quad (5)$$

for

$$R_s = \sqrt{(\omega\mu/2\sigma)} = 1/\sigma\delta, \quad (6)$$

$$R_C = 1/(\omega QC).$$

The skin depth δ is defined as the depth below the conductor surface at which the current density has decreased 1 neper below its surface value [17]. By the relationships (eqs. (3)–(6)), R_{Ω} losses increase with $\sqrt{\omega}$ and ω , for conductor and capacitor

losses, respectively. The consequences of this loss source for the NMR signal are a coil circuit wavelength (frequency and size) dependent erosion of both the RF transmit efficiency and received signal-to-noise. Ohmic losses of a head or body coil can be minimized by increasing the skin (surface) area and decreasing the inductance of the coil conductors. In a distributed circuit (vs. lumped-element circuit) this resistance will contribute a diminishing fraction of the total loss accumulating with increasing field strength.

2.2. Coil Radiation Losses

The RF energy loss to the radiated field of the coil is termed “radiation resistance.” This field loss is to the coil environment, including loss to the human subject, the magnet bore conductors, and to free space. The radiated power can be broadly defined as the difference between the input power, P_{in} , to the coil and the ohmic losses in the coil:

$$P_{r\text{ loss}} = P_{in} - (I^2/2)R_{\Omega}. \quad (7)$$

The general field equation describing the complex power lost (flowing out) through closed surfaces encompassing a coil is the following, where the quantity $\mathbf{S} = 0.5\mathbf{E} \times \mathbf{H}^*$ is the complex Poynting vector [18]:

$$P_{r\text{ loss}} = 0.5 \int_S (\mathbf{B} \times \mathbf{H}^*) \cdot d\mathbf{S}. \quad (8)$$

For an electrically small coil loop enclosing area S , radiation resistance R_r is found by calculating the power radiated using eq. (8), which can be shown to yield [16]

$$P_{r\text{ loss}} = 10 I^2 (\beta^2 S)^2 \text{ for phase constant } \beta = \omega\sqrt{(\mu\epsilon)}. \quad (9)$$

The radiation resistance, R_r , for an arbitrarily shaped wire loop such as an NMR surface coil is then

$$R_r = 2P_r / I^2 = 20(\beta^2 S)^2 \approx 31,200(S/\lambda^2)^2. \quad (10)$$

The radiation resistance for the cage-type volume coil can be approximated by substituting $I = \sum_n I_0 \cos \Theta$ into (10) and the length–width product for S .

In eq. (10) the radiation resistance and associated losses of an NMR coil are proportional to ω^4 and S^2 . For high-field clinically dimensioned NMR coils, ω^4 and S^2 respectively can significantly increase the coil’s $P_{r\text{ loss}}$. At higher NMR frequencies, clinical-sized RF circuits begin to behave less like energy-conserving coils and more like energy-radiating antennas. Decreased RF transmit power efficiency, increased RF power absorption in the human subject, and decreased signal-to-noise of highly radiative coils can potentially limit the efficacy of high-field human NMR experiments. Problematic RF radiation resistance can potentially be decreased by TEM coil design [19–22]. These designs apply Transverse ElectroMag-

netic (TEM) theory, also known as transmission line theory, to minimize high-frequency radiation losses.

2.3. Coil: Tissue Losses

RF losses in the tissue loading the coil become even more significant at higher frequencies. Loss to the tissue conductor increases with frequency due to a proportional increase in tissue conductivity and resulting eddy currents. Loss to the tissue dielectric increases with frequency due to a proportional increase in displacement currents. The Larmor wavelength becomes significantly shorter in the tissue dielectric as well. At 128 MHz (3 T) the wavelength in high-water-content anatomy is on the order of 27 cm. At 300 MHz (7 T) this wavelength decreases to 12 cm. Consequently a homogeneous RF coil can no longer generate a uniform B_1 field in the head or body at higher magnet field strengths. The high-frequency coil's field propagation and losses in its human tissue load are described by the time-dependent field equations. A time-harmonic magnetic field B_1/μ in a lossy, anisotropic, inhomogeneous coil–tissue system can be described by the differential form of the Maxwell-Ampere Law [23]:

$$\nabla \times \mathbf{B}_1/\mu = \mathbf{J}_c + \partial \mathbf{D}/\partial t. \quad (11)$$

By Ohm's Law, the current density $\mathbf{J}_c = \sigma \mathbf{E}$, and by Euler's Law the electric field displacement $\partial \mathbf{D}/\partial t = \partial \epsilon \mathbf{E}/\partial t = j\omega \epsilon \mathbf{E}$, so that eq. (9) can be rewritten as

$$\nabla \times \mathbf{B}_1/\mu = (\sigma + j\omega \epsilon) \mathbf{E}. \quad (12)$$

The complex value of \mathbf{E} can be written in terms of the magnetic vector potential \mathbf{A} and the electric scalar potential ϕ , such that

$$\nabla \times \mathbf{B}_1/\mu = (\mathbf{J}_c + \mathbf{J}_d) = (\sigma + j\omega \epsilon)(-j\omega \mathbf{A} - \nabla \phi). \quad (13)$$

Influencing the B_1 distribution and loss in human tissues loading the coil are the B_1 field-induced eddy current density \mathbf{J}_c :

$$\mathbf{J}_c = \sigma \mathbf{E} = -j\omega \sigma \mathbf{A}, \quad (14)$$

and the accompanying electric field displacement current density \mathbf{J}_d for tissue specific values of σ and ϵ :

$$\mathbf{J}_d = -j\omega \epsilon \mathbf{E} = \omega^2 \epsilon \mathbf{A}. \quad (15)$$

The sum and distribution of RF eddy current losses to the tissue conductor and RF displacement current losses to the tissue dielectric are determined by the total power loss density $P_{t \text{ loss}}$:

$$P_{t \text{ loss}} = 0.5 \int_v (\mathbf{J} \cdot \mathbf{J}^*/\sigma) dv \quad \text{for} \quad \mathbf{J} = \mathbf{J}_c + \mathbf{J}_d. \quad (16)$$

Note that the displacement current density, \mathbf{J}_d , increases with ω^2 compared to the eddy current density's \mathbf{J}_e linear proportionality with frequency. This is consistent with the observations of interfering wave phenomena (commonly though inaccurately referred to as dielectric resonance) for head images at high B_0 fields. In contrast to early concerns that \mathbf{J}_e would severely limit B_1 penetration and lead to excessive power absorption, \mathbf{J}_d -related inhomogeneities and losses may dominate at fields of 3 T and higher in the human head and body, leading to B_1 , SNR, loss, and heating patterns not predicted by Biot-Savart, quasi-static, or otherwise oversimplified models [20,22,24–26].

2.4. Coil: Tissue Heating

As noted, suboptimal SNR is not the only consequence of lossy coils. RF loss-induced temperature contours in the human anatomy can be calculated by equating the total losses, $P_{t\text{loss}}$, from the coil's RF field of eq. (16) to the bio-heat (perfusion) equation below [25,27]. Table values can be used to supply tissue specific thermal parameters for perfusion rate R , tissue and blood densities ρ and ρ_b , blood temperature T_b , blood-specific heat c_b , and tissue thermal conductivity K [28–30]:

$$P_{t\text{loss}} = R\rho\rho_b c_b [T_b - T] - \nabla \cdot K \nabla T. \quad (17)$$

With the increased RF losses, $P_{t\text{loss}}$, expected in higher-field studies, the potential for excessive RF heating increases.

3. EFFICIENT COIL DESIGN

RF signal losses to the coil circuit and its magnet bore environment can be minimized by coil design. Similarly, RF field propagation and losses in the tissue load of the coil can be controlled by coil design. The RF field can be optimized over a region of interest for homogeneity, SNR, or other criteria. The specific absorption rate (SAR) and consequential RF heating can be minimized by proper RF coil design and excitation. The remainder of this chapter will show examples of coil designs and approaches that have been used to control RF loss and penetration for human biomedical applications from 3 to 9.4 T and beyond.

3.1. Surface Coils

One approach toward limiting RF losses and controlling RF fields in high-frequency applications is to limit the electrical length of the coil, preferably to less than $\lambda/10$. The electrical length of a coil can be limited by reducing its physical dimensions. Doing so reduces the coil's ohmic and radiative losses (eqs. (3)–(10)). The low inductance of a small coil also extends the upper frequency limit at which the coil will resonate. The most common small coil is exemplified by a simple LC circuit loop (Figure 1a) whose current generates an RF magnetic dipole that induc-

tively couples to a nuclear spin system for NMR excitation and reception of the FID signal. This coil is generally known as a “surface coil.” While small loop coils ($\lambda < 2\pi\sqrt{LC}/10v$) are efficient at high frequencies, they couple to only superficial fields of view (FOV) of limited range. Series capacitance can be used to divide the loop into smaller resonant sections thereby reducing voltage node peaks and consequential E field radiative losses, and improving current and B_1 field uniformity around the loop (see Figure 1b). Series capacitance can also increase the size or operational frequency of the coil by reducing the total capacitance achievable with common capacitor values. Summed series capacitance however can be lossy, each capacitor being both an E field radiator and a source of ohmic (conductance) loss. These losses add algebraically for the number of lumped capacitors and inductors used and are shown in Figure 1b as “R”. Single-loop coils of this design must be reduced to only a few centimeters diameter for relatively efficient use at 7 T or above.

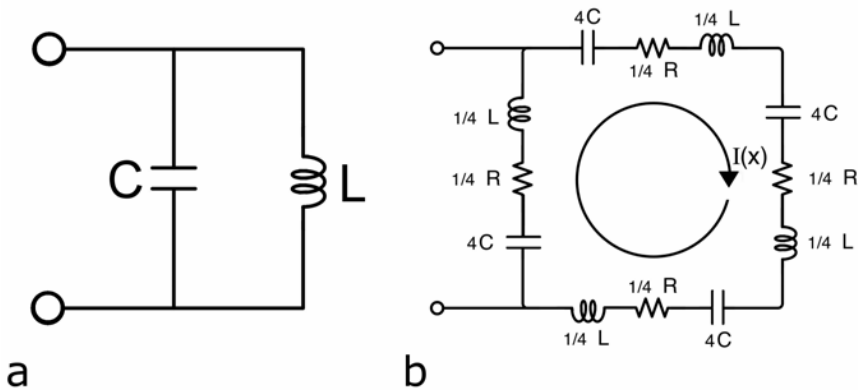


Figure 1. (a) Lumped-element “LC” loop, surface coil. (b) Divided lumped-element surface coil.

3.1.1. Surface Coil Tissue Losses

To better visualize RF tissue losses and resultant SNR, B_1 penetration, SAR, and heating from simple surface coils, eqs. (11)–(17) were graphically solved for a simple symmetrical model by the Finite-Element Method (FEM). In the example a small 7-cm-diameter surface coil as in Figure 1 was used to acquire the human calf image in Figure 2a at 4 T (170 MHz). The RF field propagation and loss phenomena for this simple experiment were calculated by the FEM and presented in Figures 2b–h. The model constructed for this demonstration consisted of a small circular LC current loop adjacent to the bottom of a larger two-layer tissue load. The thin layer nearest the coil was assigned the frequency-dependent low relative per-

mittivity (ϵ') and low conductivity (σ) typical of skin and subcutaneous fat. The skull might also be considered a part of this layer for head models. The more extensive upper layer was assigned the frequency-dependent electrical parameters for the high-water-content, high-conductivity properties of muscle or brain. Tissue-specific static and dynamic thermal properties were also assigned per eq. (17). Figure 2b shows the RF magnetic dipole “flux lines” generated by the iso-current coil model. This flux is presented as RF magnetic vector potentials in Webers. The

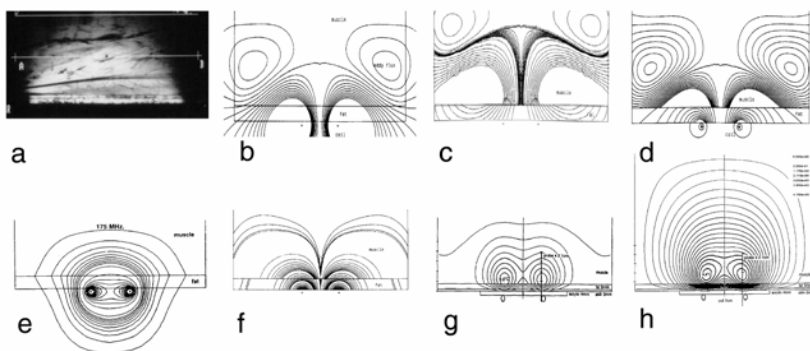


Figure 2. Gastrocnemius muscle imaged at 170 MHz (4 T): (a) showing modeled magnetic vector potential (Webers); (b) conduction current density (A/mm^2); (c) displacement current density (A/mm^2); (d) magnetic flux density (Webers/ mm^2); (e) power loss density (W/kg); (f) temperature ($^{\circ}C$) with perfusion (g) and temperature ($^{\circ}C$) without perfusion (h).

shielding flux induced by the counter-rotating eddy and displacement currents in the muscle tissue is clearly visible in this 170-MHz model. Increasing with frequency, this flux shielding tends to limit and distort the B_1 field penetration in tissue compared to the free space field profile. Figures 2c,d, illustrate the eddy current density and the displacement current density log equipotentials, (A/mm^2), respectively. It can be seen here that both current sources generate distinct current patterns, with each having an independent effect on the superposed B_1 field. In this model for an electrically small iso-current coil, both eddy currents and counter-rotating displacement currents are generated in approximately the same region in the muscle layer. For this case, both tissue current sources generate shielding fields opposing the coil dipole. Displacement current losses to the tissue dielectric increase quadratically with frequency compared to a linear loss increase from dissipated eddy currents (eqs. (14) and (15)). In this model displacement, current losses approximately equal eddy current ohmic losses in magnitude. In contrast to early literature attributing RF tissue heating to the ohmic losses of induced eddy currents only [14,31,32], at high frequency losses derive from displacement currents as well. The primary displacement current loss mechanism is thought to be due to the lossy cyclic charging of cell membranes and tissue planes [33,34]. Figure 2e shows two

log cycles of the B_1 field penetration (magnetic flux density, Wb/mm^2) in the two-layer tissue model. The practical tissue-dependent B_1 field penetration at high frequencies ranges between a radius and a diameter for a small coil ($<0.1\lambda$). The B_1 contours in Figure 2e are nearly the same within the tissue and without at this range. Beyond a diameter, however, the on-axis penetration tends to flatten due to shielding as the tissue RF skin depth is reached. Off-axis field broadening also occurs. Note also the abrupt B_1 interface between low- and high-water tissues, where the permittivity steps by an order of magnitude.

3.1.2. Surface Coil Safety

The total tissue losses from the combined eddy current losses and the displacement current losses in the tissue model are plotted in Figure 2f as power loss density contours (W/kg). This is the familiar power loss or specific absorption rate (SAR) used by the FDA to specify guidelines for RF safety assurance in the human MRI study. The MRI industry monitors this power loss to the patient (and coil) by means of negative feedback to automatically limit excessive RF power output from the power amplifier to the coil. Whereas the FDA guidelines specify both temperature and RF power loss (SAR) limits [35], commercial MRI consoles typically monitor average power loss only [36]. The model shows that power loss is not uniform over the tissue volume, but is a very localized event for the surface coil application. In the four-cycle log plot for the 170-MHz coil the power loss density can be four orders of magnitude higher at the coil elements than at the coil center one radius away. RF safety concerns might more appropriately consider predicting and monitoring RF heating rather than the SAR. As the models in Figures 2g,h illustrate, RF heating like the SAR is a localized event in tissue. However, thermal “hot spots” rarely occur in the same physical locations as do maximum SAR values. Because excessive temperature and not SAR is the cause most directly linked to tissue damage, the local RF heating potential of a coil and its excitation protocol need to be known prior to high field human application. By eq. (17) the power loss density (Figure 2f) for the model was equated to temperature in perfused (Fig. 2g) and unperfused (Fig. 2h) tissues. The temperature models include an additional layer for the thermally insulating acrylic coil package. All layers were assigned table values for the appropriate electrical properties, thermal properties including perfusion rates, and physical properties [28]. The top of the model was clamped to a constant 37°C core temperature “plate.” Physical dimension and mass were chosen to mimic a 160-lb human. The ambient boundary conditions were those of air at 22°C . Whereas the SAR contours (Fig. 2f) show highest magnitudes in tissue immediately adjacent to the small surface coil with a second intensity at the conductive muscle boundary, the highest temperature magnitudes are not spatially coincident with these maximum SAR values. The thermal hotspots were displaced into the tissue by a centimeter or two depending on the tissue parameters and frequency [37–39]. It is important to note that with a surface coil at high frequencies this model predicts and measurements validate that it is possible to exceed local SAR guidelines without exceeding the average guidelines as monitored on the MRI

system power meter. Further, it is possible to exceed local heating guidelines in tissue regions not easily monitored. RF safety for a surface coil study is best assured by knowing the thermal contours in neighboring tissue for a given experiment. These simple loop models and conclusions are easily extended to loop elements of phased and parallel arrays for high field applications.

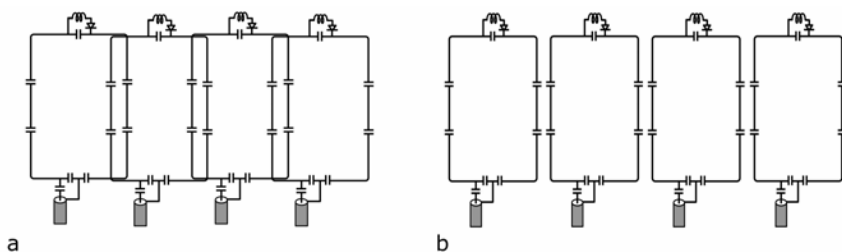


Figure 3. (a) Phased-array coil. (b) Parallel array.

3.1.3. Arrays

The small-surface coil maximizes SNR by minimizing RF losses. The electrically small coil circuit minimizes resistive and radiative losses. The small tissue volume to which the coil field is coupled limits tissue losses, but also limits the field of view. To extend the FOV while maintaining small-coil efficiency, an array of small coils can be composed. In phased arrays [40,41] (Figure 3a) and parallel arrays [42–44] (Figure 3b), array loops or elements are mutually decoupled and operated as independent coils in typically multiple channel receiver configurations. Signal from these arrays is received in “parallel,” digitally detected at the RF or IF level, and then added by a variety of algorithms to render the desired image or other data format. A popular approach to coil design at all field strengths, arrays can be configured for and fitted to any surface or volume on the human body.

3.1.4. Mutual Decoupling

The loop elements for the phased array extend directly from Figure 1. So that the tuned circuit elements may operate in close proximity without tight mutual inductance shifting the resonance frequencies of both coils off center, this inductance must be reduced to or below the critical coupling value. This may be accomplished reactively through cancellation of overcritical inductance by inductive overlap (Figure 3a) or capacitive bridging between loops in the array. Alternatively, the elements of an array may be geometrically decoupled by orienting the element dipoles for critical phase cancellation, or by simply increasing the distance between array elements until critical coupling or less is reached. This distance, measured in wavelengths, can be manipulated by the dielectric constant of the substrate on

which the array elements are assembled. Teflon, for example, with a dielectric constant of more than 2, will double the electrical spacing between elements packaged within a Teflon substrate, allowing for more compact array structures and continuous FOV coverage between decoupled array elements. Nonoverlapping arrays such as depicted in Figure 3b are more suitable for parallel imaging applications, benefiting from a minimum of FOV overlap between the array elements.

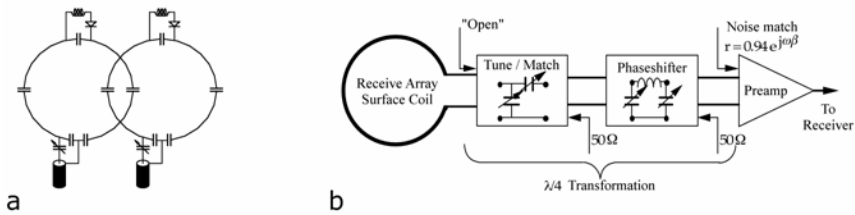


Figure 4. (a) Inductively decoupled loops in a two-element array. (b) Single-loop surface coil or array element with dedicated receiver circuit.

3.1.5. System Integration

Surface coils and arrays are commonly used as local receive-only coils together with more larger head or body transmit coils. In this arrangement, the small-loop surface coil or array maximizes reception sensitivity (SNR) from a local region of interest (ROI). The larger head or body coil maximizes excitation uniformity over the same ROI, and beyond. Additional to mutual flux decoupling through reactive, geometric, or material means, most array receivers must be temporarily decoupled from larger-volume coil transmitters. The local receiver array must be decoupled or detuned when a head or body coil is tuned for transmit. The receiver must then be tuned, and the body coil detuned during FID signal reception. This switching between tuned and detuned states for receive and transmit coils is accomplished quickly and efficiently with PIN diode circuits imbedded in the coil circuit (Figure 4a). PIN diodes are electronic gates that can be switched “on” or “off” by switching bias voltages and/or currents to the diodes. The diodes are typically used to connect or disconnect a small circuit within a coil, tuned to present a high impedance to effectively “open” the receiver coil circuit when the transmit coil is tuned. To maximize the SNR from the receiver and to facilitate imaging processing strategies, each receiver array element is interfaced to the MRI system through a tune-and-match network, possibly a phase shifter or phased line with diode protection, and a low-noise preamplifier (Figure 4). Coupling between coils is often further minimized by using a low-noise preamplifier and a transforming network between coil output circuitry and preamplifier [39–41,45]. These circuit components are usually nonmagnetic, miniaturized, and mounted in or very near to

the coil circuit. Baluns in the coaxial RF signal lines from the array elements attenuate sheath currents due to unbalanced receiver coils and load-dependent coupling between coil elements.

3.2. Transmission Line (TEM) Coil Circuits

Thus far, high-frequency coil circuit design has focused on improving coil efficiency by reducing coil size. The resonant lumped-element (LC) loop has been described as a simple surface coil and as an array element. This fundamental LC loop can be improved upon, however, especially when larger coil dimensions are required such as in head or body coils at 3 T and above. Lumped-element circuits can be replaced with distributed circuits in the form of transmission lines. Transmission line circuits are used to limit radiation loss and to preserve current uniformity in circuits exceeding one tenth the wavelength of its carrier signal. The rule of thumb for any resonant circuit in the electronics industry is: “When circuit length exceeds 0.1λ , use a transmission line.”

Two or more parallel conductors capable of supporting a transverse electromagnetic (TEM) mode of energy propagation define a transmission line. Common examples of TEM or transmission line circuits include coaxial lines, strip lines or microstrip lines, waveguides, and other conductive cavities for which two or more walls can support the TEM mode. Most RF coils for biomedical applications at 3 T and above can benefit from TEM design. It was no accident that the very first RF coil, designed by Robert Pound and employed by Ed Purcell, was a coaxial line cavity resonator of a type used for centimeter-band radar applications [46]. Many transmission line resonators have been applied to NMR since [20,46–55]. Because of the importance of TEM or transmission line design to high-frequency circuits, a primer on the topic follows.

The fundamental building blocks of all RF coils are the simple circuits shown in Figure 5. Series and parallel lumped-element (RLC) coil circuits have respective open- and short-circuit transmission line analogues. The lumped elements of a conventional RF circuit become integrally distributed coefficient quantities in a transmission line or TEM circuit. Lumped-element circuit theory is used to write the familiar equations for the time harmonic series and parallel lumped-element circuits (Figures 5a,b) in terms of R , L , C and input impedance Z_{in} , and admittance Y_{in} :

$$Z_{in} = R + j(\omega L - 1/\omega C), \quad (18)$$

$$Y_{in} = j\omega C + 1/(R + j\omega L). \quad (19)$$

The resonance frequency, f , for each circuit is

$$f = \omega/2\pi = 1/[2\pi\sqrt{LC}]. \quad (20)$$

Transmission line theory is used to write analogous equations for the TEM circuits [56].

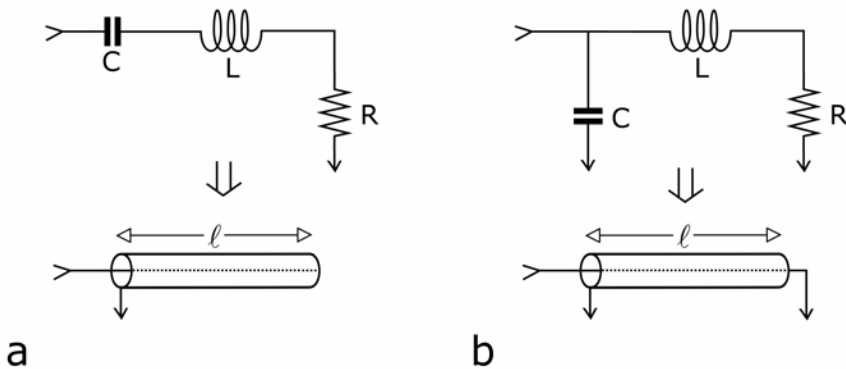


Figure 5. (a) Series RLC circuit & TEM analog. (b) Parallel RLC circuit & TEM analog.

For a voltage, V , and current, I , varying at angular frequency ω along a general transmission line, the input impedance is

$$Z_{in} = V/I = (V_1e^{-\gamma z} + V_2e^{+\gamma z}) / (I_1e^{-\gamma z} + I_2e^{+\gamma z}) \tag{21}$$

for

$$\gamma = \alpha + j\beta = \sqrt{[(R + j\omega L)(G + j\omega C)]}. \tag{22}$$

The parameter G is defined as the conductance, $1/\Omega$, of the transmission line's dielectric layer. The phasors V_1 and I_1 propagate in the forward $+z$ direction, while V_2 and I_2 are reflected in the $-z$ direction. The propagation constant γ is the complex sum of the attenuation constant α , nepers/m, and the phase constant $\beta = 2\pi/\lambda$, radians/m. In the absence of reflected waves, the characteristic impedance Z_0 of a line is defined as

$$Z_0 = V_1/I_1 = (R + j\omega L) / (\alpha + j\beta) = \sqrt{[(R + j\omega L) / (G + j\omega C)]} = R_0 \pm jX_0. \tag{23}$$

For high-frequency, low-loss, resonant lines where $\omega L \gg R$ and $\omega C \gg G$, and the reactance $X_0 = 0$,

$$Z_0 \approx \sqrt{L/C}, \quad \alpha \approx R/2Z_0 + GZ_0/2, \quad \text{and} \quad v \approx \omega/\beta = 1/\sqrt{LC}. \tag{24}$$

In the air dielectric transmission line the phase velocity is equal to $v = 3.0 \times 10^8$ m/s, the free space velocity of light. The lossless coaxial transmission line's characteristic impedance can be specified by its outer conductor i.d. = $2b$, its center conductor o.d. = $2a$, and its dielectric material ϵ separating the two conductors:

$$Z_0 = \sqrt{L/C} = (\eta/2\pi)(\ln(b/a)) \text{ for } \eta = \sqrt{(\mu/\epsilon)}. \tag{25}$$

For the intrinsic TEM mode wave impedance, η , of the coaxial line, the typical permeability, μ , closely approximates that of free space, $\mu_0 = 4\pi(10^{-7})$, H/m. The

permittivity, ϵ , of the free space (or air) dielectric is $\epsilon_0 = 8.854(10^{-12})$, F/m. The input impedance for the general transmission line of length ℓ terminated in Z_T can be written

$$Z_{in} = [Z_T + Z_0 \tanh((\alpha + j\beta)\ell)] / [1 + (Z_T/Z_0) \tanh((\alpha + j\beta)\ell)]. \quad (26)$$

When $Z_T = \infty$, the general open-circuited line input impedance becomes

$$Z_{in} = Z_0 \coth((\alpha + j\beta)\ell). \quad (27)$$

The open quarter wave line ($\ell = \lambda/4$) shown in Figure 5a is analogous to the series resonant circuit of Figure 5a (eq. (18)). When $\alpha = 0$ the lossless line approximation for the input impedance to the open line is

$$Z_{in} = -jZ_0 \cot \beta\ell. \quad (28)$$

For $Z_T = 0$ the short-circuited line input impedance is

$$Z_{in} = Z_0 \tanh((\alpha + j\beta)\ell). \quad (29)$$

The shorted quarter wave line shown in Figure 5b is analogous to the parallel resonant circuit of Figure 5b (eq. (19)). For $\alpha = 0$ the lossless approximation for the input impedance to the shorted line is

$$Z_{in} = jZ_0 \tan \beta\ell. \quad (30)$$

Expansion of eq. (29) by a standard identity gives

$$Z_{in} = Z_0(\sinh 2\alpha\ell + j\sin 2\beta\ell) / (\cosh 2\alpha\ell + \cos 2\beta\ell). \quad (31)$$

Assuming Z_0 is real, the input impedance of a line segment will be real at all frequencies for which $\beta\ell = n\pi/2$, where n is an integer. The frequencies for which the shorted (or open) lines will be resonant are

$$f_r = \omega_r/2\pi = \beta v/2\pi = n v/4\ell = n/[4l\sqrt{LC}], \quad n \equiv \text{integer}. \quad (32)$$

For the resonance frequency of a quarter wavelength ($n = 1$) shorted (or open) transmission line segment, eq. (32) reduces to the analog of eq. (20), where L and C are the distributed reactance coefficients for the resonant line segment. If line losses are attributed entirely to R ($G = 0$), the resonant Q_r value for a section of low-loss line terminated in an open or short can be shown to be

$$Q_r = \beta/2\alpha = \omega_r L/R. \quad (33)$$

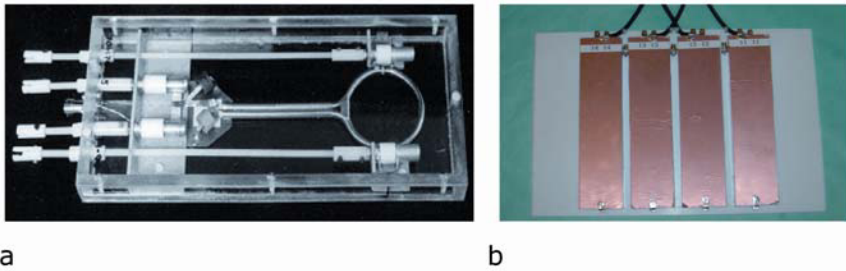


Figure 6. (a) Coaxial transmission line, loop surface coil. (b) Strip line or microstrip line surface coil. See attached CD for color version.

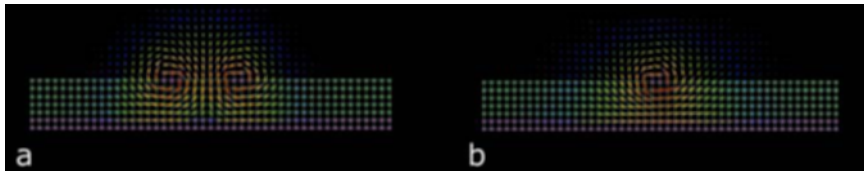


Figure 7. (a) B_1 field generated by a single-loop coil. (b) B_1 field generated by single line element. See attached CD for color version.

3.2.1. TEM Surface Coil Examples

Examples of high-frequency transmission line surface coils are seen in Figure 6. In Figure 6a, semi-rigid coaxial line is used to form a double-balanced, double-tuned, 8-cm diameter surface coil for 4T, ^1H and ^{31}P frequencies [19,57]. This coil was used in transmit and receive mode. A four-element array using linear strip lines is shown in Figure 6b. This 20 x 25-cm array is comprised of four line elements using parallel copper conductors separated by 2-cm Teflon dielectric, and capacitively tuned to 300 MHz with terminal chip capacitors. Two of these four-element strip line receive arrays were employed together with a body transmit coil for the first successful body imaging at 7 T.

These examples open the question of the relative merits of a loop-coil vs. a linear-element coil. An FDTD model in Figure 7 shows the RF magnetic field vectors of a single element of each type. In each model, the red-colored horizontal baseline represents the copper ground plane in the model. A Teflon dielectric is shown as the horizontal green layer in each model. Conductive strip lines, also red, are centered in the vector fields. There are two such strip line conductors in the cross-section model of a loop, and one for the linear transmission line element. Both elements were excited with equal magnitude: 300 MHz signals. Both loop and line “penetrate” as deeply into the black space above them. The loop-element vector field is broader, by two elements. The key difference between the two is the vector phase in the FOV above the coils. The loop’s dipole would be perpendicular

to a sample surface; the line's vector field would be horizontal. Use of the loop and the line element together produces geometrically decoupled coils generating a circularly polarized field. Considerations for using each of these element types in arrays will be further discussed in the "Volume Coil" section following.

4. VOLUME COILS

At the time of this writing, most surface coils and arrays commercially available for high field biomedical applications are receive-only coils. Large-head or body-sized volume coils are generally required for uniform excitation of the ROI to which the receiver is applied. A large number of head coils operate in transmit and receive modes without an independent receiver. Head and body coils are necessarily very large circuits and contain very lossy electrical loads. Building head or body coils that are efficient, or even operational at 3, 4, 7, 8, 9.4T, or higher presents significant challenges.

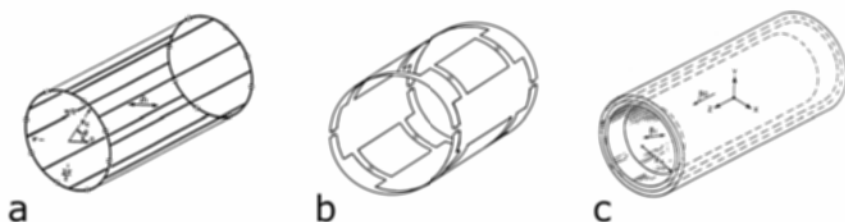


Figure 8. (a) High-pass birdcage; (b) bandpass birdcage; (c) birdcage shield.

4.1. Birdcages

Beginning with the lumped-element LC circuits, high-pass cage structures such as the Alderman Grant coil [58] and the birdcage resonator [59], as shown in Figure 8a, have been favored starting points for industry. The birdcage, built about twice the length of its diameter, is a highly homogeneous coil circuit. Locating capacitance in the end rings, where they are in series with end ring currents, allows for very small net capacitances to be summed from readily available lumped values to elevate the resonant frequency of this circuit. The bandpass birdcage circuit (Figure 8b) is a further extension of this design. In the Siemens example shown, lumped capacitance is distributed in the axial elements "rungs" and in the rings. The conductors are made wide to minimize inductance and ohmic resistance. Many capacitors are placed in parallel to minimize conductance losses, and placed in series to improve current uniformity, to divide peak voltages thereby minimizing

radiative losses and to achieve lower net capacitance making higher frequency resonance possible. The length of the coil is also shortened to achieve lower inductance, higher efficiency and frequency, and less load coupling at the expense of a reduced and less homogeneous FOV. The high-frequency performance of high-pass and bandpass birdcage circuits is further improved by the addition of a Faraday shield, thereby creating a multi-element coaxial transmission line of sorts with the combined structure [60]. The combination of coil and shield must be correctly executed to achieve desired results. For many years the necessity of a Faraday shield between the coil and the gradients in the magnet bore was considered to be “parasitic” to the coil’s performance. By designing the cage and shield together as a transmission line with characteristic impedance matched to load conditions, the shielded band pass birdcage has achieved body images at 3 T and head images to 7 T [61].

4.2. TEM Volume Coils

With the first NMR coil, a coaxial line cavity resonator built by Robert Pound and Ed Purcell 60 years ago at Harvard, the benefits of TEM design were realized [46]. Since then, Schneider and Dullenkopf [47], Krause [24,62], Bridges [49], and Röschmann [48], among others, have made use of transmission line principles. As mentioned, the optimized shielded birdcage design can be viewed as a transmission line coil where its foil strip rungs (strip lines or center conductors) define a load-matched characteristic impedance with its shield (ground plane or outer conductor) [59,60]. Building on this work, modern TEM coil designs have achieved new levels of performance at unprecedented frequencies for human head and body imaging at the highest field strengths available [20,22,54].

The modern TEM volume coil was designed to resonate efficiently for high frequencies and large volumes [22,54]. It is composed of multiple electrically short transmission line elements (Figure 9b). As with TEM surface coils, these line elements may be coaxial, strip line or microstrip, waveguides, or other transmission line executions. Being both electrically short and shielded, these elements lose little energy to ohmic or radiation resistance compared to larger, more inductive, lumped-element structures. Because this design can be built without lumped elements, capacitor losses can be very low and the current on the elements highly uniform. And because this design is not dependent on end ring currents, there are no losses to end ring paths or to the nonproductive E and B fields they generate. Independent of inductive end ring return paths, the resonance frequency of the TEM volume coil is established by the resonance achieved by its individual short transmission line elements. Accordingly, a TEM volume coil of given length can be built to arbitrarily large diameters without lowering its resonant frequency or circuit Q .

In addition to high-frequency performance advantages for this design, there are practical advantages as well. The independent line elements can be directly driven, inductively excited, or a combination of the two. The line elements and the

field-generating currents they carry may be independently controlled as well. Each line current may be used as a transmit element, a receive element, or both. Independent elements may be switched on or off, tuned or detuned. The currents on each element may be independently modulated in magnitude, phase angle, frequency, or time. Points of attachment for these independent drive or control lines and circuits are marked A, B, and C on the drawing in Figure 9a. This control at the coil provides for RF gradients and RF shimming for optimizing criteria, including SNR, SAR, homogeneity, etc., for a targeted ROI. This control may be preset, interactive, or automated through negative feedback. This structure provides many new degrees of freedom in the high field NMR experiment [54].

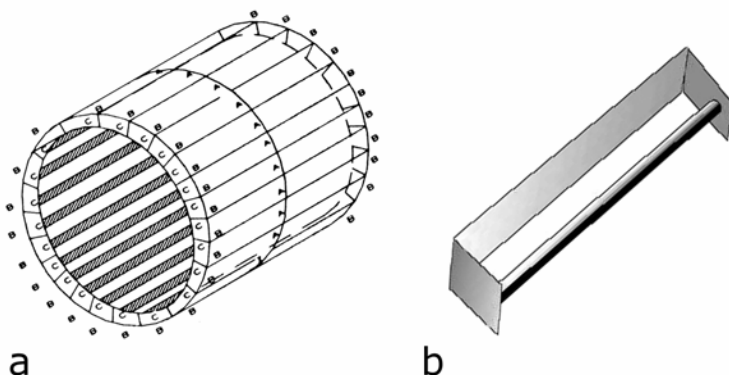


Figure 9. (a) TEM volume coil [19]. (b) TEM volume coil element.

By reactive decoupling of its elements the TEM coil effectively becomes a line-element array. In this form it has proven useful for parallel imaging applications [63]. Its SENSE performance improves with increasing element count. A one-dimensional reduction factor of approximately 5.2 has been achieved with a 16-element coil and a factor of 6.3 was reached with a 32-element coil TEM “array,” for example.

4.2.1. Multichannel Coil Interface

The multichannel TEM coil described above is the transducer of a more complex, multichannel transceiver as depicted in Figure 10. In this example, a low-level shaped transmit signal from the console is split into multiple equal-phase and -magnitude signals. Each of the split signal paths can then be independently modified via console control by programmable phase shifters and attenuators. Each of the independently modulated signals is then amplified by multiple-channel dedicated RF Power Amplifiers. Transmit-receive (TR) switches temporally isolate transmit from receive signals at each coil element. Each coil element interfaces a

decoupling digital receiver in this scheme. An alternative scheme would use separate transmit elements and receive elements. Perhaps the most advanced approach would forego the RF signal source splitter and generate 16 shaped RF signals at the console. While this level of control at the coil has arguably not been required at lower fields, examples given later in this chapter will demonstrate the necessity of dynamic control of multiple coil elements for ultra high field human head and body imaging. Conversely, the short wavelengths of high field MRI facilitate these new dimensions of control at the coil.

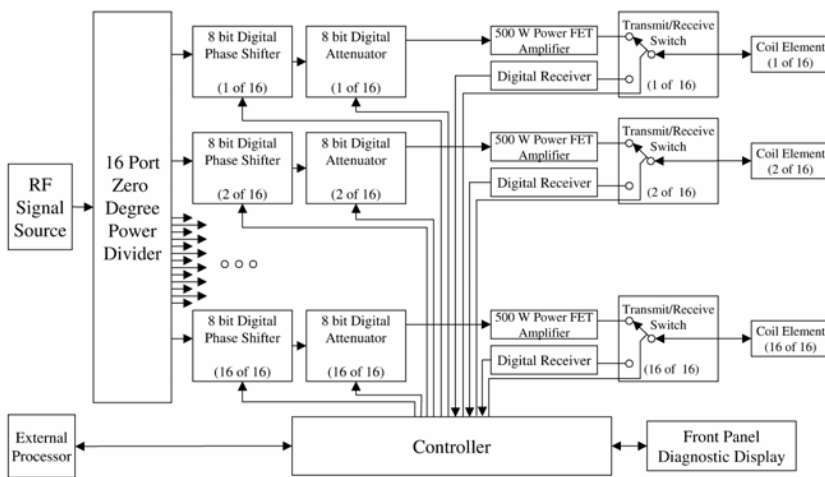


Figure 10. Parallel transceiver [64].

4.2.2. TEM arrays

As discussed for surface coils, transmission line approaches render both linear elements and loop elements. Both were addressed as independent elements, the main difference being that the linear element generates a flux vector typically parallel to the sample surface, and the loop generates a perpendicular vector. To describe the performance of line and loop elements as high-frequency arrays, an eight-element head coil is considered (Figure 11). The linear element is shorter for a given coil length, and therefore electrically more efficient at high frequencies. The coil comprised of linear elements also generates a more uniform to the periphery of its volume. The current phase angles on the linear array mimic those of other TEM or birdcage rungs, incrementally phased over 360° to generate a theoretically uniform transverse field through the coil volume. In the loop array, however, cur-

rents in adjacent element legs are in approximately phase opposition. This results in severe phase gradients in the RF field near the elements of the coil.

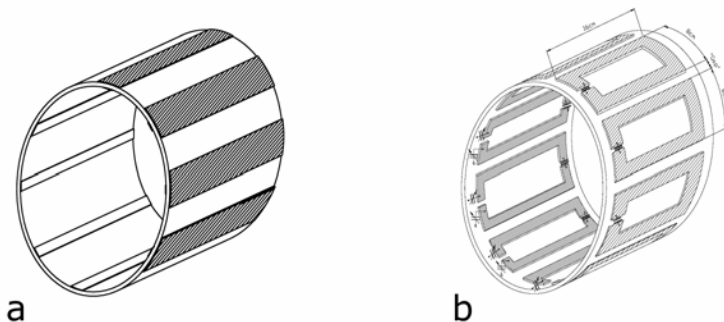


Figure 11. (a) Linear-element TEM volume coil; (b) loop-element TEM volume coil.

To demonstrate the assertions above, the two coils of Figure 11 were built on equal-sized Teflon cylinders (15 cm long x 23 cm i.d. x 25 cm o.d.). The transmit and receive gradient echo head images of Figure 12 were acquired at 7 T. All pulse protocol parameters were controlled, and the same head was imaged. Homogeneity is better in the image acquired with the linear-element coil compared to the image acquired with the loop-element coil. The homogeneity is especially degraded in the periphery of the head for the loop array, as predicted. The SNR (circled) of the loop array image appears to have suffered as well, possibly also due to phase cancellations (destructive interference) [63].

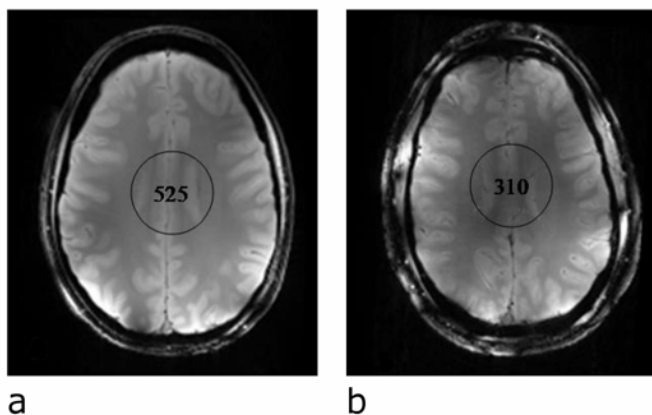


Figure 12. (a) Linear-element volume coil image; (b) Loop-element volume coil image.

4.2.3. TEM Coil Fields, Losses, and Safety

A simple Maxwell model of an eight-element TEM coil with a three-layer head model illustrates a discussion of RF fields and losses affecting the success and safety of human imaging with volume coils at high frequencies. The head model includes a layer for low-water-content/low-conductivity skin, scalp, and skull; a layer for high-water-content/high-conductivity brain, and a layer mimicking the aqueous humor in the eyes. All layers were adjusted to frequency-dependent electrical parameters and temperature-dependent thermal parameters consistent with the conditions and tissue layers modeled at 170 MHz (4 T). The homogeneous coil was linearly excited to generate the nonuniform B_1 field contour shown in Figure 13b. This field profile, due to constructive interference of independent element field contributions coinciding in the center of the head and destructively

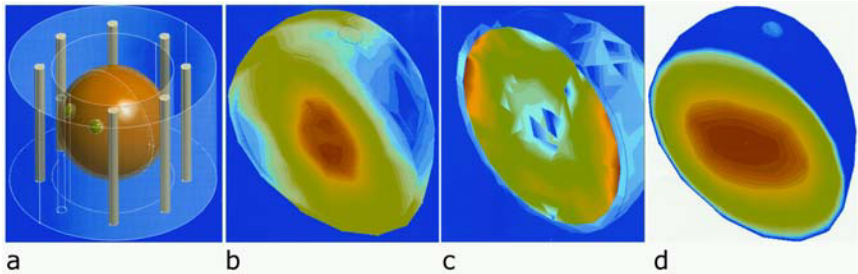


Figure 13. Simple FEM model of (a) a three-layer head inside a linear-element TEM volume coil, (b) an RF magnetic flux density “ B_1 field” (Webers/mm²) in a head model with linear coil excitation, (c) resultant power loss density (W/kg) in head model, and (d) consequential temperature contours (°C) in the perfused-head model. See attached CD for color version.

elsewhere, is typical of a high field head imaging. SAR contours are shown in Figure 13c. Maximum SAR is shown in the conductive brain layer at the periphery of the head nearest the coil elements. This result is also expected. Maximum temperature is reached in the center of the head, however, where SAR is minimum. This result is not to be confused with maximum ΔT , which occurs typically in or near regions of maximum SAR in the head periphery. Although maximum temperature change might occur in the scalp, the scalp is well perfused and adjacent to an infinite 22°C ambient heat sink. Within the FDA guideline power limits, superficial head tissues do not reach or exceed the core temperatures of the head center. Therefore, the normal profile of the head is similar to Figure 13d. Added energy raises the whole profile proportionately, as would a fever. This response assumes low power input to the head from a uniform incident field inducing a heat load distributed and dissipated by healthy, normal, thermoregulatory reflexes.

4.3. Image Optimization by Coil Design and Control

4.3.1. Design

While ultra high field head imaging has produced the signal-to-noise sought, image homogeneity has been problematic. As modeled in Figure 13 above, this inhomogeneity is caused by a B_1 field contour generated by field attenuation and interference in the head even though a homogeneous volume coil is used. These high field radiofrequency-related image nonuniformities have long been observed with various explanations [7,20,22,24,26,65–68]. Figure 14a shows an FDTD head-in-coil model predicting the inhomogeneity observed in the 7T head image of Figure 14b. Signal loss, contrast loss, flip angle errors, unwanted echoes, and quantification errors are but a few of the consequences of this nonuniform B_1 field. The following sequence of models, coil examples, and images demonstrates a coil design and control approach for improving image uniformity and other criteria at the highest fields available for human MRI.

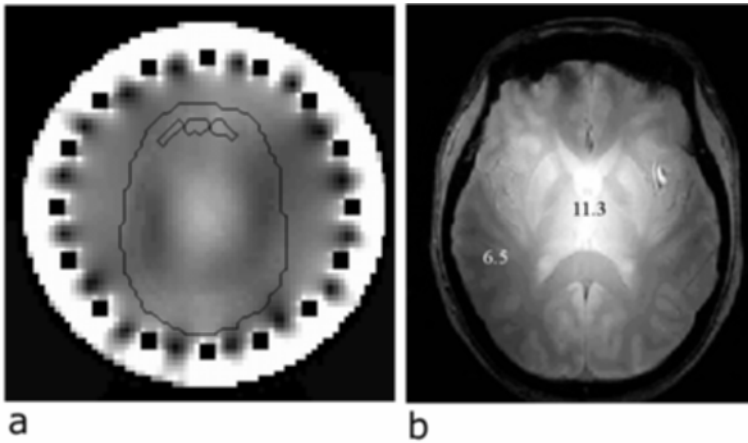


Figure 14. (a) An FDTD model of a head inside a uniform, circularly polarized TEM volume coil resonant at 300 MHz; (b) a 7T gradient echo head image.

To mitigate the RF nonuniformity issue in high field imaging, “RF field shimming” techniques have been considered [20,22,54,68,69]. The multichannel TEM coil of Figure 9 lends itself well to this approach. The impedance (magnitude and phase angle) of each element can be independently adjusted to establish sensitive control over the B_1 field with the coil. In the coil of Figure 15b, a B_1 field magnitude contour (B_1 gradient) was designed into the coil. This was accomplished by coil geometry, element-to-shield spacing, and specification of dielectric material between the inner elements (rungs) and the outer elements (shield). Both dielectric constant and physical spacing of the region ϵ in Figure 9b determine the electrical

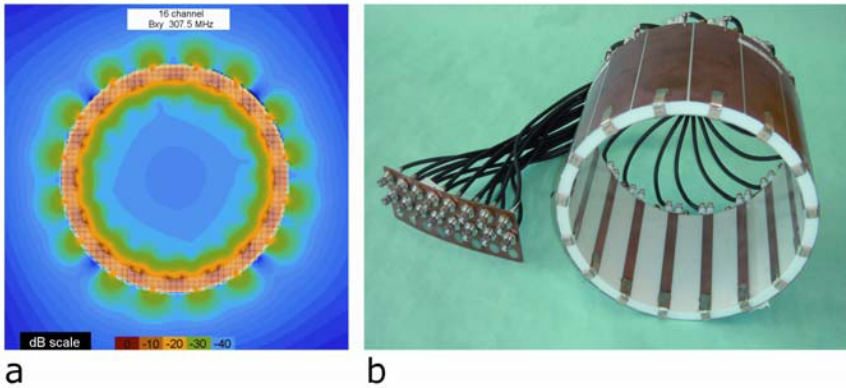


Figure 15. (a) Model of TEM head coil with B_1 gradient; (b) TEM head coil with B_1 gradient and multi-element phase and magnitude control. See attached CD for color version.

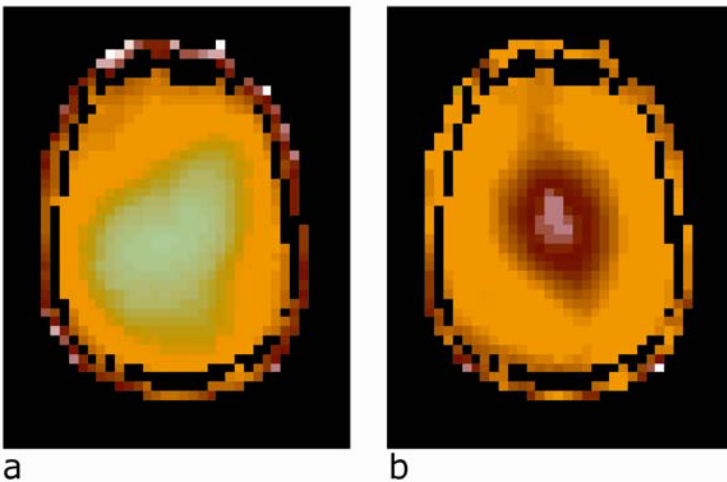


Figure 16. (a) Model of central sensitivity profile ΣB_1^- calculated to partially compensate for the B_1 field peak, ΣB_1^+ ; (b) in the center of the head coil of Fig. 15. See attached CD for color version.

distance between the rung and the shield of the TEM element. This electrical dimension controls both the transverse B_1 gradient in the coil volume and the mutual inductance (coupling) between the elements. Narrowing the dielectric space between the conductors and/or increasing the dielectric constant imparts a B_1 gradient to partially compensate the artifact of the image in Figure 14. The rung element to shield spacing modeled in Figure 15a shows the resultant B_1 gradient for a 16-element coil (Fig. 15b). The central receive sensitivity deficit ΣB_1^- (Figure 16a)

balances the transmit B_1 field peak ΣB_1^+ (Fig. 16b). The B_1 field magnitude of this gradient can be further adjusted by changing the symmetry of the coil (e.g., to elliptical) to better fit the long axis of the head, for example. The receive sensitivity is enhanced in the periphery of the head nearest the coil. The transmit profile is likely suppressed in the periphery of the head due to destructive interference. The two effects combine to compensate the apparent inhomogeneity of the image, as modeled in Figure 17a. In this image the central signal intensity is more uniform, though the periphery is still nonuniform due to head proximity to the coil elements, where B_1 magnitude and phase angle gradients are greatest. Phase angle adjustment of the independent element currents can further improve this image, as predicted in Figure 17b.

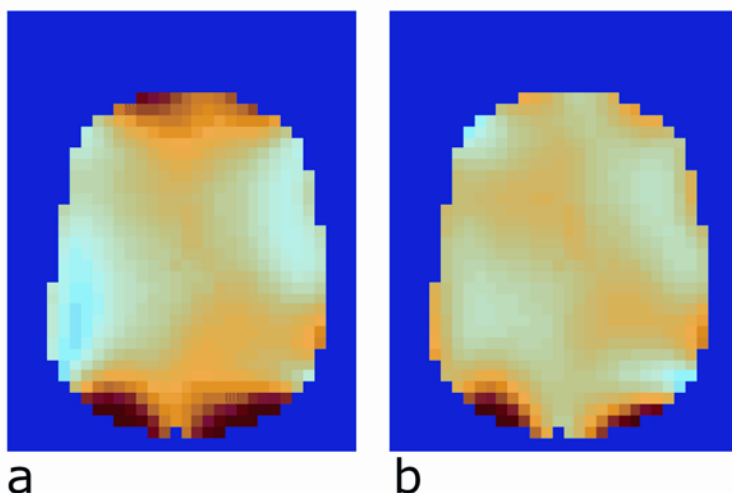


Figure 17. Model of head with B_1 transmit magnitude optimization: (a) combined with phase angle optimization; (b) to render a more uniform head image at 300 MHz. See attached CD for color version.

4.3.2. Control

The history of NMR is rich with fortuitous paradoxes where anticipated high field artifacts become BOLD new solutions. The artifacts due to extremely short tissue wavelengths of 7 T (12 cm) and 9.4 T (9 cm) MRI will be the increasingly powerful RF shims and gradients used to localize ROIs and optimize selected criteria therein by a new family of RF protocols and feedback-driven algorithms only now being imagined. The problem that every element of a TEM coil *must* be independently tuned (as opposed to monolithic birdcage resonators) becomes a solution for B_1 field control because every element *can* be tuned. Every element in the TEM

coil can be independently controlled, driven, and received, unlike the end ring-bound cage, although the homogeneity advantages of the cage structure are preserved. Implementation of phase and gain control is therefore best performed with a TEM coil (Figure 9) interfaced to the MR system by a parallel transceiver (Figure 10).

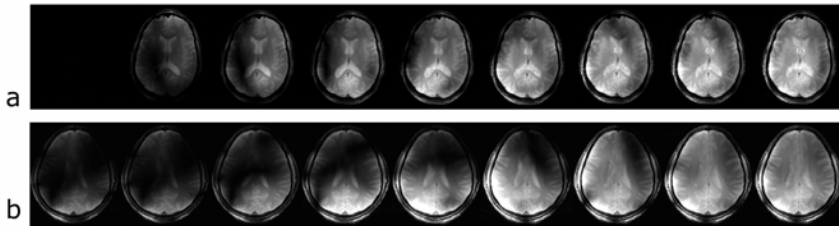


Figure 18. B_1 field control: (a) B_1 gain (magnitude) control is shown; (b) B_1 phase control is demonstrated.

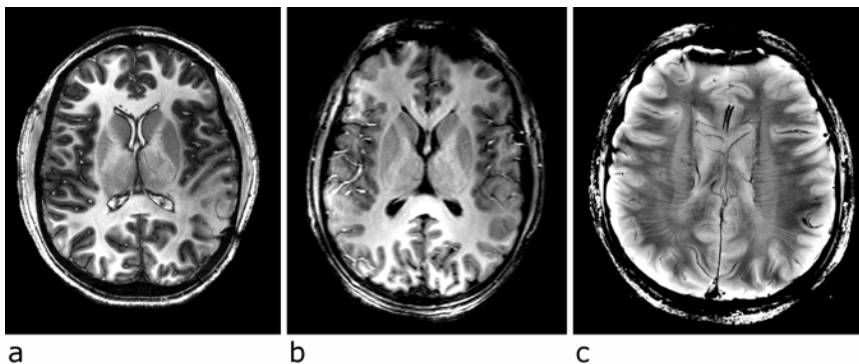


Figure 19. (a) RF-shimmed 7T IR-turbo FLASH; (b) RF-shimmed 9.4T IR-gradient echo image; (c) RF-shimmed 9.4T FLASH image.

Early results of programmable B_1 phase and gain control are shown in Figures 18 and 19 below. To acquire the images, an eight-element TEM coil (Figure 11) was driven by an eight-channel parallel transceiver (Figure 10) with 500 W per channel RF power amplification [70]. The solid-state RF power amplifiers are broadbanded to facilitate the addition of programmable frequency shifters to the Figure 10 system for multi-nuclear control (Figure 20). Behind TR switches, eight home-built digital receivers were used as in the Figure 10 configuration. Phase and gain values were entered on a web table for the coil-transceiver channel matrix. Demonstrating this programmable B_1 field magnitude (gain) control capability, Figure 18a shows a 9.4T FLASH image data set with TR/TE = 50/5 ms, 256 x 128

22 x 19 cm, thk = 5 mm. Each image shows a different gain setting, starting with the amplifiers disabled on the far left, and then adding equal gain to each element, one at a time in a clockwise pattern until all channels are driven on the far right. The element phase angles traverse 360° in equal increments to circularly polarize the coil. The images are constructed by simple sum-of-squares magnitude addition without intensity correction. Phase control is demonstrated in Figure 18b. Driving all elements with iso-magnitude RF signal, the phase angles of all eight coil elements were set to iso-phase “0°” at the far left. Progressing to the right in Figure 18b, incrementally increasing 45° phase angles were added to each element around the coil in the clockwise direction until the coil was circularly polarized at the far right. Gain and phase control per coil element can steer the B_1 field for shortwave NMR.

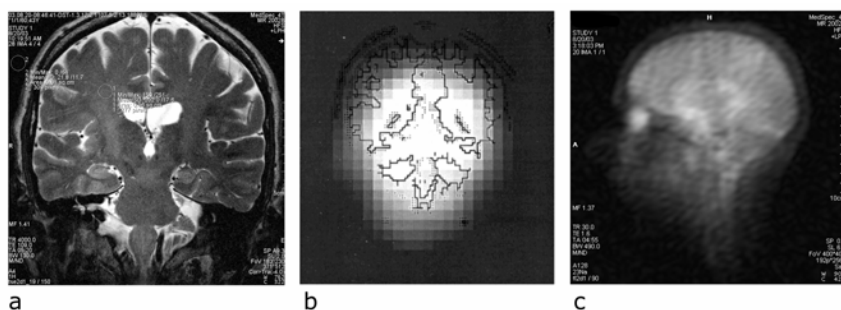


Figure 20. Double-tuned TEM head coil: (a) proton, (b) phosphorus, and (c) sodium at 4 T.

High-frequency coil optimization methods employing RF field gradients together with RF field magnitude and phase shimming have been practiced to produce fairly homogeneous head images at 7 T and more recently at 9.4 T (Figure 19). The inversion recovery turbo FLASH image in Figure 19a is an example from 7 T, where $TR/TE = 14/5$ ms, $TI = 1.45$ s, $thk = 5$ mm, and $matrix = 1024^2$, with intensity correction. Figure 19b shows a first 9.4T gradient echo image from an 8-element TEM coil acquired with the parameters $TR/TE = 40/5$ ms, $TI = 1.55$ sec, $thk = 3$ mm, $matrix = 256 \times 128$, $SAR = 0.4$ W/kg. A 9.4T FLASH image, $TR/TE = 50/9$ ms, nicely contrasts the medullary veins, Virchow-Robins spaces, possible tracts, and other features as shown in Figure 19c [71].

4.4. Multi-Nuclear Coils

In addition to magnitude and phase angle, the independent TEM coil elements can be tuned to multiple frequencies for multi-nuclear imaging at ultra high fields [20,54,72]. One method of tuning this coil for simultaneous operation at two or more frequencies is to tune independent elements to dedicated frequencies in a periodic pattern. For example, a dual-frequency coil of 24 total line elements

would have 12 even count elements tuned typically to the ^1H frequency, alternating with 12 odd count elements tuned to the “X” nucleus Larmor frequency. This design approach enjoys a number of advantages. The double-tuned TEM coil behaves essentially as two independent coils of the same form factor and field profile. Decoupling between circularly polarized ^{31}P , ^{13}C , or ^{29}Na and ^1H Larmor operational modes at 3 and 4 T, for example, typically exceeds 20 dB in a double-tuned head coil. The dual-tuned head coil couples to the same FOV at each frequency, facilitating ^1H shimming on the same volume from which the X nuclei signal is acquired. The double-tuned TEM head coil couples to the same FOV with approximately equal transmit efficiency and receive sensitivity at each frequency. The coil efficiency at each frequency approaches 90% that of a single-tuned TEM coil at either frequency. Results from double-tuned TEM head coils are shown in Figure 20. TEM coils have been simultaneously tuned to three or more frequencies. The TEM coil can be mechanically or electronically switched between two or more frequencies as well. The means of frequency switching provides multi-nuclear facility for interleaved studies and for two or more frequencies in close spectral proximity, such as ^{19}F and ^1H .

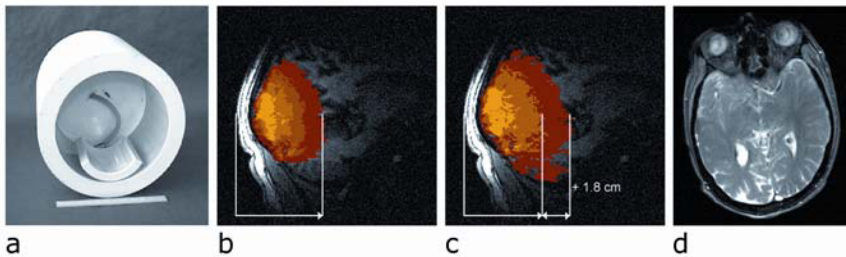


Figure 21. (a) Actively detunable TEM transmit head coil with local receiver coil. (b) Signal-to-noise contours acquired with transmit-receive surface coil only. (c) Signal-to-noise contour of transmit volume coil combined with surface coil receiver. (d) A local four-loop receiver array used with a homogeneous transmit coil improves both SNR and homogeneity at 4 T and above. See attached CD for color version.

4.5. Actively Detuned Coils

The TEM coil can also be actively detuned for use with local surface coils and receive arrays [22,54,73]. A preferred practice in clinical imaging makes use of a larger-volume coil, most typically a body coil, to uniformly excite a region of interest. A smaller "specialty" receiver coil, typically an array, is used to maximize sensitivity from a localized region of interest. Figure 21a shows a homogeneous head coil transmitter with a surface coil receiver. Use of a head coil rather than a body coil for a transmitter can conserve nearly an order of magnitude in RF transmit power required for some head imaging applications. Figure 21b profiles the

highest signal field of view to which the surface coil couples when used in transmit and receive mode. When the same surface coil is used in receive-only mode together with the homogeneous transmit coil of Figure 21a, the high SNR profile is extended. Alternatively, a smaller receive-only surface coil would increase the SNR over the transmit and receive surface coil field of view of Figure 21b. In addition to enhanced sensitivity, an array of surface coil receivers can be used to compensate the image intensity gradient observed in high field head images. As discussed earlier, destructive interference in the head periphery and constructive interference of the excitation field in the center of a head in a homogeneous volume coil results in a region of high image signal intensity in the head center (see Figure 14). The sensitivity profile of phased or parallel receivers, however, favors the head periphery. The combination of a transmit volume coil and an array receiver coil can be therefore be used to acquire an image of more uniform intensity, if not uniform transmit field-dependent contrast (see Figure 21d). Similar results have been found with a shielded bandpass birdcage at 4 T [74].

4.6. Body Coils

The TEM volume coil has also demonstrated its utility as an ultra high field body coil to 7 T and higher [22]. Because the TEM coil is essentially an array of independent transmission line elements, its achievable frequency and performance are dependent on the line elements and their geometric arrangement about a volume. The resonant frequencies achievable with TEM volume coils are independent of coil diameter because there are no inductive end rings limiting frequency and performance. Full-sized TEM body coils can therefore be built to resonate at the Larmor frequencies for 8 T and higher [22]. Many degrees of freedom in coil control are another advantage of independence from "hard-wired" end ring connections. The current elements of the TEM volume coil can be inductively driven, or capacitively driven by one or more signal lines. Because of increasing energy loss to large loads (e.g., body) at high frequencies, driving four or more elements is often required as demonstrated in Figure 22. As with the head coil in Figure 15b or the surface coil in Figure 6b, individual TEM elements can be independently and interactively controlled for magnitude, phase, frequency, and time. Dynamic spatial adjustment of individual coil elements adds another degree of control [75]. The TEM elements may be reactively coupled or decoupled, and arranged or manipulated in a variety of geometries [76]. These five degrees of freedom of control at the coil provide the capability to manipulate the B_1 field in these dimensions to compensate for high field problems such as B_1 inhomogeneity and excessive SAR, and to optimize performance criteria such as SNR for a targeted region of interest in the body.

Cardiac imaging at 4T offers one example of how a high field problem is presented, and how it is then corrected by RF shimming. Human body dimensions are measured in multiple wavelengths at ultra high fields. Accordingly, B_1 field penetration is highly nonuniform. RF-related image artifacts result, as exemplified by the sharp signal drop out in the right atrium shown in Figure 23a. By adjusting the

relative impedance (magnitude and phase) of the TEM elements, the RF field of the coil is manipulated to compensate for this artifact as shown in Figure 23b.

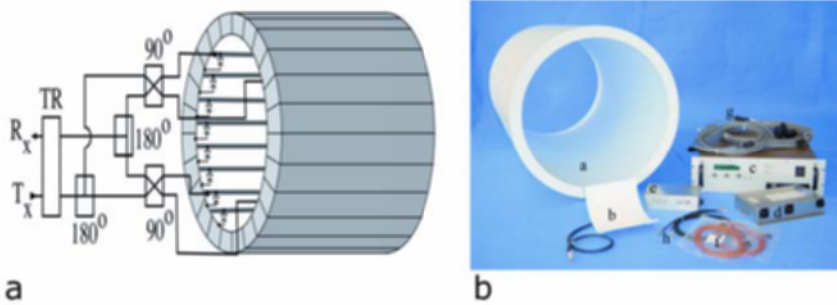


Figure 22. (a) Body coil with active detuning and multi-port drive. In this drawing a simple network of 180 and 90° splitters establishes circular polarization for the transmit field. Actively switched shunt-detuning diodes are shown for each transmission line element of the coil. The segmented cavity serves as both a transmission line component and an eddy current-free shield for the coil. (b) RF body imaging subsystem including body coil (a), surface array receiver (b), power supply and detuning control unit (c), detuning diode driver unit (d), multichannel receiver preamp and bias tees (e), fiberoptic diode control lines (f), data lines (g), and RF signal cables (h). See attached CD for color version.

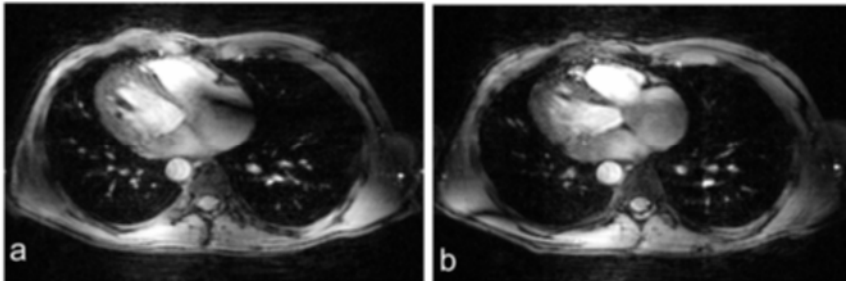


Figure 23. (a) 4T cardiac image acquired with a homogeneous TEM body coil transmitter and a four-loop phased-array receiver with two loops on the anterior and posterior thorax, respectively. EKG cardiac gating was employed in these breath-held acquisitions. (b) The right atrium artifact was corrected by interactive impedance adjustments coil elements (RF shimming). No intensity correction was applied to these images.

At 7T body imaging artifacts become more severe. As the FDTD model in Figure 24a and the images in Figure 24b indicate, sharp RF gradient artifacts are observed. At the time of this writing, these global artifacts have not been entirely removed. A number of approaches are being attempted, however, with promising

results. The artifacts due to destructive interference and eddy current shielding can be removed from or minimized in local regions of interest by RF shimming with the body coil and signal reception with local receiver coils. Local transmit and receive arrays have also been shown to couple well to local regions, and are significantly more efficient than the body coil [77]. Dielectric materials can be strategically placed to change the boundary conditions of the incident RF field [54]. Coil geometry and placement give more latitude in the possible solution set. Importantly, early results indicate that all anatomic regions can be safely and successfully imaged at 7 T with some combination of coils and approaches.



Figure 24. (a) B_1 field calculated for body-loaded, homogeneous, circularly polarized TEM volume coil at 300 MHz (7 T). (b) Sagittal images of human body at 7 T showing RF artifact predicted. Image acquisition parameters were: GE, TR/TE = 50/4 ms, matrix = 256^2 , thk = 3 mm, FOV = 35 cm^2 , NT = 2, 55-sec scan. See attached CD for color version.

5. CONCLUSION

RF coil solutions exist for all magnets and field strengths currently available for human imaging. This includes 9.4 T. Human head- and body-dimensioned coils resonant at the highest Larmor frequencies for these magnets have been successfully demonstrated using TEM (transmission line) design approaches and principles. Transmission line volume coils and arrays may be used separately in transmit and receive mode, and together where one coil excites a uniform field and the other receives from a localized area with high sensitivity. High-frequency anatomic loading conditions require current control at the coil element level to compensate RF artifacts, minimize RF power requirements, and to optimize NMR performance criteria per subject in localized regions of interest. This control is enabled by new programmable transceivers together with interactive feedback. Such technological innovations will in turn facilitate the development of a new family of pulse sequences and automated optimization algorithms. Much new and creative work lies ahead to fully exploit the many possibilities facilitated by short-wavelength NMR. New developments and applications using RF shims, gradients, and the general

ability to optimize desired image criteria for targeted regions by "steering" RF fields in magnitude, phase angle, frequency, space, and time will be the future for UHF coils.

6. ACKNOWLEDGMENTS

Staff and Collaborators: C. Snyder (Figs. 1, 3, 6b, 8); C. Akgun (Fig. 7); G. Adriany (Figs. 11, 12); J. Harrison (Fig. 13); C. Collins, M. Smith (Figs. 14a, 16, 17); M. Garwood (Fig. 14b); J. Tian (Figs. 15a, 24a); P-F. Van de Mortelle (Fig. 19a); L. DelaBarre (Fig. 18, 19b,c, 24b); T. Thiel (Fig. 20a,c); H. Hetherington (Fig. 20b); L. Bolinger (Fig. 23).

Laboratory Directors: R.L. Nunnally at UT Southwestern ('84-'89), G.M. Pohost at UAB ('89-'95), T.J. Brady/R.G. Gonzales at MGH ('95-'99), K. Ugurbil ('99-present).

Mentor: P. Röschmann at PFH ('89-'91)

Active Grant Support: NIH-S10 RR139850, NIH-R33 CA94318, NIH-R01 CA94200, NIH-R42 RR13230, NIH-R01 EB000895, NIH-PAR 02-010, NIH-P41 RR08079, Keck Foundation.

7. REFERENCES

1. Ugurbil K, Garwood M, Ellermann J, Hendrich K, Hinke R, Hu X, Kim S-G, Menon R, Merkle H, Ogawa S. 1993. Imaging at high magnetic fields: initial experiences at 4T. *Magn Reson Q* **9**:259-277.
2. Pan J, Vaughan J, Kuzniecky R, Pohost G, Hetherington H. 1995. High resolution neuroimaging at 4.1T. *Magn Reson Imag* **13**:915-921.
3. Hetherington H, Kuzniecky R, Pan J, Mason G, Morawetz R, Harris C, Faught E, Vaughan T, Pohost G. 1995. Proton nuclear magnetic resonance spectroscopic imaging of human temporal lobe epilepsy at 4.1T. *Ann Neurol* **38**:396-404.
4. Gruetter R. 1996. Observation of resolved glucose signals in ¹H NMR spectra of human brain at 4 tesla. *Magn Reson Med* **36**:1-6.
5. Robitaille PML, Abduljalil A, Kangarlu A, Zhang X, Yu Y, Burgess R, Bair S, Noa P, Yang L, Zhu H, Palmer B, Jiang Z, Chakeres D, Spigos D. 1998. Human magnetic resonance imaging at 8T. *NMR Biomed* **11**:263-265.
6. Yacoub E, Pfeuffer P, Van de Mortelle P-F, Adriany G, Andersen P, Vaughan T, Merkle H, Ugurbil K, Hu X. 2001. Imaging brain function in human at 7 tesla. *Magn Reson Med* **45**(4):588-594.
7. Vaughan J, Garwood M, Collins C, Liu W, DelaBarre L, Adriany G, Andersen P, Merkle H, Goebel R, Smith M, Ugurbil K. 2001. 7T vs. 4T: RF power, homogeneity, & signal-to-noise comparison in head images. *Magn Reson Med* **46**:24-30.
8. Abragam A. 1978. *The principles of nuclear magnetism*. Oxford: Clarendon Press.
9. Hoult D, Lauterbur P. 1979. The sensitivity of the zeugmatographic experiment involving human samples. *J Magn Reson* **34**:425.
10. Dickenson R. 1986. Measurement changes in tissue temperature using MR imaging. *J Comput Assist Tomogr* **10**:468.

11. Brown R, Martens H, Patrick J, Zypman F. 1988. A layer model for RF penetration, heating and screening in NMR. *J Magn Reson* **80**:225–247.
12. Shellock F, Crues J. 1988. Temperature changes caused by MR imaging of the brain. *Am J Neuroradiol* **9**:287–291.
13. Athey T. 1989. A model of the temperature rise in the head due to magnetic resonance imaging procedures. *Magn Reson Med* **9**:177–184.
14. Bottomley P, Andrew E. 1978. RF magnetic field penetration, phase shift and power dissipation in biological tissue: implications for NMR imaging. *Phys Med Biol* **23**:630–643.
15. Stutzman W, Thiele G. 1981. *Antenna theory and design*. New York: John Wiley & Sons.
16. Libby L. 1945. Special aspects of balanced shielded loops. *Proc IRE Waves Electrons* **34**:641–646.
17. Graf F. 1991. *Modern dictionary of electronics*. Indianapolis: Howard W. Sams.
18. Halliday D, Resnick R. 1974. *Fundamentals of physics*. New York: John Wiley & Sons.
19. Vaughan J, Hetherington H, Harrison J, Otu J, Pan J, Noa P, den Hollander J, Pohost G. 1993. High frequency coils for clinical nuclear magnetic resonance imaging and spectroscopy. *Physica Medica* **9**:147–153.
20. Vaughan J, Hetherington H, Otu J, Pan J, Pohost G. 1994. High frequency volume coils for clinical NMR imaging and spectroscopy. *Magn Reson Med* **32**:206–218.
21. Vaughan J, Adriany G, Garwood M, Yacoub E, Duong T, DelaBarre L, Andersen P, Ugurbil K. 2002. A detunable TEM volume coil for high field NMR. *Magn Reson Med* **47**(5):990–1000.
22. Vaughan J, Adriany G, Snyder C, Tian J, Thiel T, Bolinger L, Liu H, DelaBarre L, Ugurbil K. 2004. Efficient high-frequency body coil for high-field MRI. *Magn Reson Med* **52**:851–859.
23. Harrington R. 1961. *Time-harmonic electromagnetic fields*. New York: McGraw-Hill.
24. Barfuss H, Fischer H, Hentschel D, Ladebeck R, Vetter J. 1988. Whole body imaging and spectroscopy with a 4 tesla system. *Radiology* **169**:811–816.
25. Harrison J, Vaughan J. 1996. Finite element modeling of head coils for high frequency magnetic resonance application. *Ann Rev Prog Appl Comput Electromagn* **12**:1220–1226.
26. Yang Q, Wang J, Zhang X, Collins C, Smith M, Liu H, Zhu X-H, Vaughan J, Ugurbil K, Chen W. 2002. An analysis of wave behavior in lossy dielectric samples at high field. *Magn Reson Med* **47**:982–989.
27. Brezovich I, Young J, Wang M. 1983. Temperature distributions in hyperthermia by electromagnetic induction: a theoretical model for the thorax. *Med Phys* **10**:57.
28. Duck F. 1990. *Physical properties of tissue*. New York: Academic Press.
29. Durney C, Massoudi H, Iskander M. 1986. *Radiofrequency radiation dosimetry*. Brooks Airforce Base, TX: USAF School of Aerospace Medicine.
30. Pennes HH. 1948. Analysis of tissue and arterial blood temperature in the resting human forearm. *J Appl Physiol* **1**:93–122.
31. Carlson J. 1988. Radiofrequency field propagation in conductive NMR samples. *J Magn Reson* **78**:563–573.
32. Brown R, Haacke M, Martens M, Patrick J, Zypman F. 1988. A layer model for RF penetration, heating, and screening in NMR. *J Magn Reson* **80**:225–247.
33. Foster K, Schwan H. 1989. Dielectric properties of tissues and biological materials: a critical review. *Crit Rev Bioeng* **17**:25.

34. Stuchly M. 1990. Applications of time-varying fields in medicine. *Crit Rev Bioeng* **18**:89.
35. Kanal E, Shellock F, Lalith T. 1990. Safety considerations in MR imaging. *Radiology* **176**:593–606.
36. Röschmann P. 1987. Radiofrequency penetration and absorption in the human body: limitations to high-field whole-body nuclear magnetic resonance imaging. *Med Phys* **14**:922–931.
37. Vaughan J, Harrison J, Hetherington H, Evanochko W, Pohost G. 1992. Radiofrequency surface coil heating measurements in porcine muscle. *Proc Soc Magn Reson* 4026.
38. Vaughan J, Harrison J, Thorn B, Pohost G. 1993. Hot rings: high frequency heating patterns in tissues. *Proc Soc Magn Reson* 1369.
39. Vaughan J, Haupt N, Noa P, Vaughn J, Pohost G. 1995. RF front end for a 4.1 tesla clinical NMR spectrometer. *IEEE Trans Nucl Sci* **42**(4):1333–1337.
40. Reykowski A, Wright S, Porter J. 1995. Design of matching networks for low noise preamplifiers. *Magn Reson Med* **33**:848–852.
41. Roemer P, Edelstein W, Hayes C, Sousa S, Mueller O. 1990. The NMR phased array. *Magn Reson Med* **16**:192–225.
42. Sodickson D, Manning W. 1997. Simultaneous acquisition of spatial harmonics (SMASH): fast imaging with radiofrequency coil arrays. *Magn Reson Med* **38**:591–603.
43. Pruessmann K, Weiger M, Scheidegger M, Boesiger P. 1999. SENSE: sensitivity encoding for fast MRI. *Magn Reson Med* **42**:952–962.
44. Griswold M, Jakob P, Edelman R, Sodickson D. 2000. A multicoil array designed for cardiac SMASH imaging. *MAGMA* **10**:105–113.
45. Edelstein W, Hardy C, Mueller O. 1986. Electronic decoupling of surface coil receivers for NMR imaging and spectroscopy. *J Magn Reson* **67**:156–161.
46. Purcell E, Torrey H, Pound R. 1946. Resonance absorption by nuclear magnetic moments in a solid. *Phys Rev* **69**:37.
47. Schneider H, Dullenkopf P. 1977. Slotted tube resonator: a new NMR probe heat at high observing frequencies. *Rev Sci Instrum* **48**:68.
48. Röschmann P [Philips, assignee]. 1988. High-frequency coil system for a magnetic resonance imaging apparatus. US Patent 4746866.
49. Bridges J. 1988. Cavity resonator with improved magnetic field uniformity for high frequency operation and reduced dielectric heating in NMR imaging devices. US Patent 4751464.
50. Baertlein B, Ozbay O, Ibrahim T, Lee R, Yu Y, Kangarlu A, Robitaille P. 2000. Theoretical model for an MRI radio frequency resonator. *IEEE Trans Biomed Eng* **47**:535–545.
51. Beck B, Plant D, Grant S, Thelwall P, Silver X, Mareci T, Benveniste H, Smith M, Collins C, Crozier S. 2002. Progress in MRI at the University of Florida. *MAGMA* **13**:152–157.
52. Bogdanov G, Ludwig R. 2002. Coupled microstrip line transverse electromagnetic resonator model for high-field magnetic resonance imaging. *Magn Reson Med* **47**:579–593.
53. Peshkovsky AS, Kennan RP, Fabry ME, Avdievich NI. 2005. Open half-volume transverse electromagnetic coil for high field magnetic resonance imaging. *Magn Reson Med* **53**:937–943.

54. Vaughan J. [Massachusetts General Hospital, assignee]. 2003. RF coil for imaging system. US Patent 6633131.
55. Zhang X, Ugurbil K, Chen W. 2003. A microstrip transmission line volume coil for human head MR imaging at 4T. *J Magn Reson* **161**:242–251.
56. Chipman R. 1968. *Theory and problems of transmission lines*. New York: McGraw-Hill.
57. Vaughan J, Roschmann P, Pan J, Hetherington H, Chapman B, Noa P, Vermeulen J, Pohost G. 1991. A double resonant surface coil for 4.1 tesla whole body NMR. *Proc Soc Magn Reson* 722.
58. Alderman D, Grant D. 1979. An efficient decoupler coil design which reduces heating in conductive samples in superconducting spectrometers. *J Magn Reson* **36**:447–451.
59. Hayes C, Edelstein W, Schenck J, Mueller O, Eash M. 1985. An efficient highly homogeneous radiofrequency coil for whole-body NMR imaging at 1.5T. *J Magn Reson* **63**:622–628.
60. Roemer P, Edelstein W [General Electric, assignee]. 1989. Double-sided RF shield for RF coil contained within gradient coils of NMR imaging device. US Patent 4879515.
61. Watkins R, Rohling K, Piel J, Rosenfeld D, Kelley D, Lenkinski R, Kressel H, Montag A. 2001. Whole body RF coil for 3 tesla MRI system. *Proc Int Soc Magn Reson Med* 1123.
62. Krause N [Siemens Aktiengesellschaft, Munich, assignee]. 1985. High frequency field system for nuclear magnetic resonance apparatus. US Patent 4506224.
63. Adriany G, Van de Mortelee P-F, Wiesinger F, Moeller S, Strupp J, Andersen P, Snyder C, Zhang X, Chen W, Pruessmann K, Boesiger P, Vaughan J, Ugurbil K. 2005. Transmit and receive transmission line arrays for 7 tesla parallel imaging. *Magn Reson Med* **53**:434–445.
64. Vaughan J, Adriany G, Ugurbil K, Andersen P, Strupp J [University of Minnesota, assignee]. 2005. Parallel transceiver for nuclear magnetic resonance system. US Patent Application 0050116715.
65. Bomsdorf H, Helzel T, Kunz D, Roschmann P, Tschendel O, Wieland J. 1988. Spectroscopy and imaging with a 4 tesla whole-body MR system. *NMR Biomed* **1**:151.
66. Collins C, Li S, Smith M. 1998. SAR and B_1 field distributions in a heterogeneous human head model within a birdcage coil. *Magn Reson Med* **40**:1–10.
67. Ibrahim T, Lee R, Abduljalil A, Baertlein B, Robitaille PML. 2001. Dielectric resonances and B_1 field inhomogeneity in UHFMRI: computational analysis and experimental findings. *Magn Reson Imag* **19**:219–226.
68. Van de Mortelee P-F, Akgun C, Adriany G, Moeller S, Ritter J, Collins C, Smith M, Vaughan J, Ugurbil K. 2005. B_1 destructive interferences and spatial phase patterns at 7 tesla with a head transceiver array coil. *Magn Reson Med*. In press.
69. Ibrahim TS, Lee R, Robitaille PML. 2001. Effect of RF coil excitation on field inhomogeneity at ultra-high fields: a field optimized TEM resonator. *Magn Reson Imag* **19**:1339–1347.
70. Vaughan J, Myer D. 2005. *Parallel transceiver*. New York, Minneapolis: Collaboration CPC, Bioengineering Inc.
71. Vaughan J, DelaBarre L, Snyder C, Adriany G, Collins C, Van de Mortelee P-F, Ritter J, Strupp J, Andersen P, Tian J, Smith M, Ugurbil K. 2005. RF image optimization at 7T and 9.4T. *Proc Int Soc Magn Reson Med* 953.
72. Vaughan J [University of Alabama Birmingham, assignee]. 1996. High frequency volume coils for nuclear magnetic resonance applications. US Patent 5557247.

73. Vaughan J, Adriany G, Garwood M, Yacoub E, Duong T, DelaBarre L, Andersen P, Ugurbil K. 2002. A detunable transverse electromagnetic (TEM) volume coil for high field NMR. *Magn Reson Med* **47**:990–1000.
74. Barberi E, Gati J, Rutt B, Menon R. 2000. A transmit-only/receive-only (TORO) RF system for high field MRI/MRS applications. *Magn Reson Med* **43**:284–289.
75. Adriany G, Ritter J, Van de Mortelee P-F, Moeller S, Snyder C, Voje B, Vaughan J, Ugurbil K. 2005. A geometrically adjustable 16 channel transceive transmission line array for 7 tesla. *Proc Int Soc Magn Reson Med* 673.
76. Vaughan J, Garwood M, Ugurbil K. 2001. Volume coils for highest field MRI. *IEEE Trans Ant Prop Soc Int Symp* **1**:378–381.
77. Vaughan J. 2005. How to do RF at high fields. *Proc Int Soc Magn Reson Med* 10.

A PERSPECTIVE INTO ULTRA HIGH FIELD MRI RF COILS

Tamer S. Ibrahim

*School of Electrical and Computer Engineering,
and the Bioengineering Center, The
University of Oklahoma, Norman*

The advancement of MRI as a radiological instrument has been associated with a constant drive toward higher magnetic field strengths, resulting in higher operational frequencies. More powerful magnets bring the promise of enhanced signal to noise ratio resulting in exquisite resolution, and reduced scan times. At the same time, however, operating MRI at higher frequencies adds significant physical and engineering complexities to the MRI experiment, most notably in designing safe, versatile, and high-performance radiofrequency (RF) coils. This chapter provides RF coil studies that span frequencies ranging from 1.5 to approx. 12 T. The results and conclusions are based on experimental findings using 8 and 1.5T whole-body MRI systems, computational electromagnetics using the finite-difference time-domain method, and analytical derivations using electromagnetic theory. The outcome of these studies is then utilized to provide new avenues and techniques to improve the performance of RF head coils for human MRI at very high fields.

1. INTRODUCTION

Nuclear magnetic resonance (NMR) phenomena in electrically conducting samples such as human tissue involves weak interactions unless observed within high applied magnetic fields. Since the advent of human MRI in the early 1970s, the impetus for improved MRI has driven progressive increases in magnetic field strengths from fractions of a Tesla (1 T) to 1.5 T in the 1980s, to 3.0 T by the late 1990s. In addition to other advantages, higher field systems have the potential to obtain an increased signal-to-noise ratio (SNR) [1], greater chemical shift dispersion [2], and increased BOLD contrast [3]. During the maturing process of magnet technology, which pushed the limits of field strength, research magnets for small samples have made even greater strides to reach 20 T and beyond. Increases in

magnet field strength at small sample sizes have been followed rapidly by increases in magnet size to accommodate samples up to the size of humans and large animals. Magnet technology for humans has now reached 7 T at the University of Minnesota, Massachusetts General Hospital, New York University, and the NIH, 8 T at Ohio State University, and 9.4 T at the University of Minnesota and the University of Illinois at Chicago. That is in addition to about 25 T and higher large-bore animal magnets around the world. MRI at such field strengths has resulted in visualizing in-vivo human anatomical details [4] that had never been seen before with any other imaging technique.

The improved performance from operating at higher field strength, however, is associated with other technical as well as physical challenges, most notably in designing the associated radiofrequency (RF) coils/probes. Higher field strengths correspond to increased operational frequencies. A 7T coil, for example, operates at approximately 298 MHz for proton imaging. At this frequency and higher, the wavelengths of the electromagnetic waves produced by currents on RF coils become on the order of the size of the human head/body. Hence, from a technical perspective, circuit modeling techniques that are used to describe and design lower field RF coils are no longer appropriate to accurately describe the interactions of the electromagnetic waves with the human head/body. Rather, more complicated and computationally intense full-wave techniques must be used [5–8]. Furthermore, from a physical perspective, at such field strengths localized energy deposition and inhomogeneous B_1 field distribution in biological tissues tend to be prevalent. Since homogeneous fields are generally extremely desired over imaging areas, designing the required high field MRI RF coils is difficult.

Although the nonuniformity of the B_1 field partially defeats the traditional imaging technology used at lower field strength, such patterns offer the challenge and opportunity to find new ways to generate images. The goal of this chapter is to provide a perspective into the electromagnetics-associated RF coils at low and high fields, lay out current technological and physical problems, and provide potential solutions to these problems.

2. THE APPROACH TO RF COIL DESIGN: NOW AND THEN

2.1. Why Full-Wave Modeling?

The design of RF coils in MRI has been based on the use of circuit concepts [9] and transmission line theories [9,10]. These concepts invoke quasistatic field approximations [11]. At relatively low frequencies (< 3 T), quasistatic approximations are valid for head coils because the RF coil is small compared to the wavelength of the RF field. For instance, 1.5T (64 MHz) clinical systems use RF coils such as the birdcage resonator [9], which is usually driven in quadrature (two ports) [10]. At this frequency, circuit concepts [11,12] can be applied to predict the resonance frequency and to determine the magnetic field distribution, by assuming

that the currents on the coil structure are uniform and then using the Biot-Savart Law to determine the magnetic field produced by these currents.

Even though the circuit model is a zero-dimensional approximation for the three-dimensional electromagnetic resonance behavior in the coil, it can be very accurate for modeling relatively complex coil geometries. Under certain conditions, however, these models start to fail because of two major limitations. First, the circuit models approximation breaks down when the coil geometry is a significant fraction of the wavelength. This limitation is not critical at 64 MHz, since the wavelength is 4.7 m. Thus, even the diameter of a body coil (approximately 80 cm diameter) is less than 15% of a wavelength. Even at high frequencies (200–300 MHz), analytical models [13,14] based on transmission line concepts and circuit models can still adequately describe the electromagnetic operation of empty head coils. However, these models start to fail as we look into 7T empty body coils. Second, as these analytical models start to break down with increasing frequency, they fail at a much faster rate with the presence of tissue. Tissue distorts the ideal easily modeled (from an analytical point of view) transverse electromagnetic (TEM) field structure leading to hybrid modes (to be discussed later). These hybrid modes are extremely challenging to model analytically.

Since the inception of MRI, the goal of RF volume coil designs has been to produce a uniform circularly polarized component of the transverse magnetic (B_1^+) field and low values of the specific absorption rate (SAR) in the imaged subject. These qualities are easily attainable at 64 MHz. As the resonant frequency increases with field strength, however, not only does the quasistatic approximation begin to fail but the homogeneity of the B_1^+ field deteriorates and the tissues become more prone to localized heating (hot spots) due to electromagnetic absorption. In order to retain the desirable properties of a uniform magnetic field and low SARs, redesigning current RF coils is essential. With the failure of quasistatic approximations as the MRI operational frequency increases, a computational tool based on full-wave electromagnetics becomes essential in conducting feasibility studies and in designing and evaluating the performance of high field RF coils.

Until the last decade, full-wave numerical methods have seldom been used to model the fields in RF coils for MRI systems. Before that there was not much need for such an approach because most of the systems were at magnetic field strengths of 1.5 T and below. In the last decade, however, there have been numerous applications of full-wave numerical methods to analyze a variety of MRI RF coils. For instance, Han and Wright utilized a 2D finite-difference time-domain (FDTD) method to model surface MRI coils loaded with phantoms [15]. The FDTD method has also been used to analyze a head-sized TEM resonator [16–18] loaded either with a phantom [16,19,20] or with a human head model [6,21–25]. The finite-elements method (FEM) has also been used to approximate the specific absorption rate (SAR) inside the human head in a saddle-shaped MRI head coil at 64 MHz [26]. In 1996, Jin et al. employed the conjugate gradient method with the fast Fourier transform to study the birdcage coil. Later, the FDTD method was also used to analyze the same problem [5,23,24,27–31]. In addition, simulations have also made

advancements to predict temperature distributions by thermal modeling [32–35]. Many of these full-wave studies have shown excellent quantitative correlation with experimental data at 7 and 8 T for surface [36,37] and volume head [19,21,24,37–40] coils. With so many full-wave approaches available, an important question remains: which of these methods is mostly suited for modeling loaded MRI RF coils?

2.1.1. Finite-Difference Time-Domain Method

There are three major numerical methods used in electromagnetics: the finite-element method (FEM), the finite-difference time-domain (FDTD) method, and the integral equation method, the method of moments (MM). Although MM and FEM can be solved in the time domain, they are rarely used in this way; FEM and MM are usually associated with the frequency domain. MM is different from FEM and FDTD in that MM can be formulated in terms of unknown surface currents on perfect conductors and unknown volume currents in materials, whereas the unknowns in FEM and FDTD are the fields values everywhere within the volume of interest. Because of this, MM has great advantages over FDTD and FEM when applied to geometries consisting of only perfect conductors, since the number of unknowns in MM is much less than with the other two methods.

For problems where large portions of the geometry are non-perfectly conducting, the number of unknowns for all three methods is comparable; however, the computation times are very different. Both MM and FEM require solution of the matrix equation. Since the number of unknowns required to model the coil is very large, iterative methods offer the only viable way to solve the matrix equation. Assuming the number of unknowns in the problem is N , the computation time is proportional to N^θ , where θ is 2 for MM and 1.5 for FEM. It should be noted that when there are large permittivity and conductivity contrasts in the geometry, which occurs when human tissue is present, the values for θ may be significantly larger than the nominal given values. On the other hand, the FDTD method does not require a matrix solution, and its computation time is proportional to $N^{4/3}$.

There is also a wide disparity in terms of memory requirements between the three methods. The memory needed to solve an MM problem with 50,000 unknowns can be used to solve an FEM problem with 5,000,000 unknowns and an FDTD problem with 100,000,000 unknowns. The one disadvantage of FDTD relative to FEM is that it is less flexible for modeling arbitrary geometries, because FEM can be applied to an unstructured grid. However, for the electrically large geometries that are encountered in high field MRI, one can argue that it is better to use FDTD than FEM, because in many cases the number of unknowns needed to solve the problem is relatively very large. In addition, many other tailored algorithms can also be utilized to optimize the standard FDTD scheme. In fact, many such algorithms have been successfully applied for MRI simulations [7]. The next section will address: “How to build an in-house RF coil simulator using the FDTD method.”

3. RF COIL SIMULATOR USING THE FDTD METHOD

The FDTD technique introduced by Kane [41] is used to give a direct solution of Maxwell's time-dependent curl equations. The FDTD method is essentially based on replacing the spatial and time-domain derivatives of Maxwell's equations with finite-difference approximations. An excellent source for the FDTD formulation can be obtained from [42]. To create an FDTD model for MRI, we will need an anatomically detailed human model (for the coil load) as well as a coil grid. In the following two sections, we will briefly discuss these tasks (an MRI head coil simulation will be used as an example). Detailed descriptions of these modeling steps can be obtained from [43].

3.1. The Anatomically Detailed Human Head Model

An example of developing an anatomically detailed human head model is presented in [22]. The mesh data were obtained from $0.5 \times 0.5 \times 2$ mm 1.5T MR images. The model was constructed with the assistance of a physician who assigned tissue types in each image and then encoded these types on a digital image. Figure 1 describes the girding process [22,23].

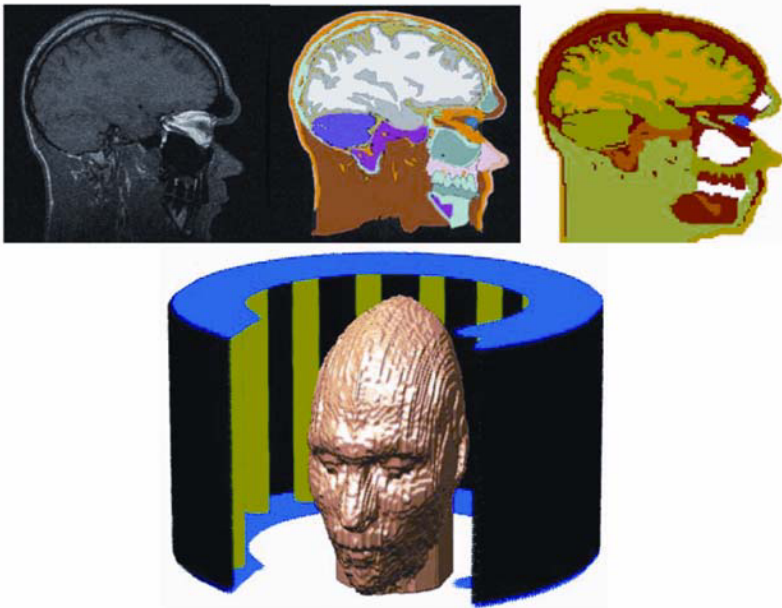


Figure 1. Top: Creation of the 17-tissue anatomically detailed human head model; left is the 1.5T image, center is the manually digitized grid, and right is the FDTD grid. Bottom left: 3D FDTD model of the human head and the TEM resonator. Adapted with permission from [23]. See attached CD for color version.

Several error-correction and validation procedures were performed. First, the digitally encoded tissue types were processed to remove voids in the data caused by human error in tissue delineation. Erroneous voids were distinguished from true voids (air spaces in the mouth and nasal passages) and were filled by assigning an adjacent tissue type. Automated image-processing software was developed to accomplish this task. Next, differences from layer to layer (image to image) in the data set were reconciled by re-slicing the data along a different axis and re-examining the imagery to identify discontinuities in tissue boundaries. Some interpolation of the data was also required because of the difference in sample spacing within an image and between images. Finally, the image data were output as a single volumetric data set that specifies tissue types at each sample position. The tissue-type information stored at each pixel is used with a look-up table that provides dielectric constant and conductivity values for any frequency of interest. To obtain an accurate detail of the internal human head structure, 18 different tissue types, in addition to air, were identified in the images. By having 18 different tissues types and small pixel size, one can obtain very accurate results in modeling the internal electromagnetic fields within the biological tissues which greatly affect the SAR calculations and the B_1 field distribution in the human [22].

3.2. The Coil Models: How to Grid?

As we have created the anatomically detailed human head model (the load), we will examine the needed steps for setting up the grid of the coil and the load followed by designing the FDTD source code. In particular, we will look at examples using the birdcage [9] and TEM [16] resonators.

3.2.1. The Birdcage Coil

3D FDTD models of highpass birdcage coils were developed where the width of the coil conductors was set to an infinitesimal value [5,30,31] or to 0.3 in [39,44]. In order to obtain accurate electromagnetic field calculations with the FDTD algorithm, an octagonal geometry was utilized in which the lumped capacitive elements could be properly modeled. Figure 2 shows the FDTD grid and the human head, where eightfold symmetry is maintained. The different color points on the grid correspond to different algorithms utilized to describe the desired geometry. For instance, a lumped element FDTD algorithm was used to model the tuning capacitors [45]. This algorithm requires that the capacitive-lumped elements be positioned along the Cartesian axes, namely x or y . Thus, in order to maintain symmetry, the orientation of the capacitors along the eight slanted edges of the rings may change. Another example is an FDTD algorithm that was utilized to account for the curvatures of the rings and strips, which results in removing stair-stepping errors from these critical coil components.

To simulate quadrature excitation, the same input was applied to two different excitation points, as is done in experiment. The only difference between the two ports is a 90° relative phase shift on the input excitations. The perfectly matched layer (PML) absorbing boundary condition was used to absorb RF radiation from the coil [46]. A total of 4,000,000 cells were utilized in the case of the thin conduc-

tor model and 25,000,000 cells in the case of the 0.3-in conductor model to generate the complete grid. Note that the magnet shield was modeled in the 25,000,000-cell system. A differentiated Gaussian pulse was used to excite the system [5,30,31,39,44].



Figure 2. FDTD grid of the top circular ring of the birdcage coil. The different shadings on the grid correspond to different nonstandard FDTD algorithms used to achieve an accurate representation of the physical performance of the coil. These include lumped capacitors and slanted non-cubical cells for the curvatures of the ring as well as the struts. See attached CD for color version.

The electrical performance of the coil was well maintained since the modeled geometry did not deviate too far from the circular shape. Figure 3 clearly demonstrates this issue where an FDTD calculated frequency spectrum [39,44] of a 3T highpass birdcage coil that is numerically loaded with the visible human project head/shoulder anatomical mesh ([ftp://starview.brooks.af.mil/EMF/dosimetry models](ftp://starview.brooks.af.mil/EMF/dosimetry/models)) is shown. Note that the dielectric properties of the mesh are assigned from [47]. The capacitor values used along the end rings were the values of the actual lumped capacitors used in the GE birdcage coil in clinical operation (15.5 pF for 3 T). First the spectrum shows 9 modes corresponding to the 16 struts in the coil. Second, the resonance frequency of mode 1, the homogenous mode of operation (will be exploited later), only differs by less than 7.5% from what is actually obtained in the real coil (128 MHz).

In terms of distributions of electromagnetic fields, Figure 4 displays the circularly polarized component of the B_1 (B_1^+) field as a function of anterior–posterior direction in the center of a highpass birdcage coil (top) and as a function of the median–lateral direction 10 cm down from the center plane of the coil (bottom) [5].

The numerical FDTD solution (dashed curve) is compared to experimental 1.5T extracted B_1^+ field measurements [48] (solid curve). The coil is operating at 64 MHz with quadrature excitation and is loaded with a cylindrical phantom that is numerically and experimentally [49] filled with material with muscle-like dielectric properties [49]. The sharp variations (spikes) in signal intensity in the MRI curve were due to the presence of air bubbles in the phantom. These bubbles, which were unavoidable in the construction of the phantom, in turn generated inhomogeneities in the phantom. The results show excellent agreement between the numerical FDTD solution and the experimental MRI measurements [5].

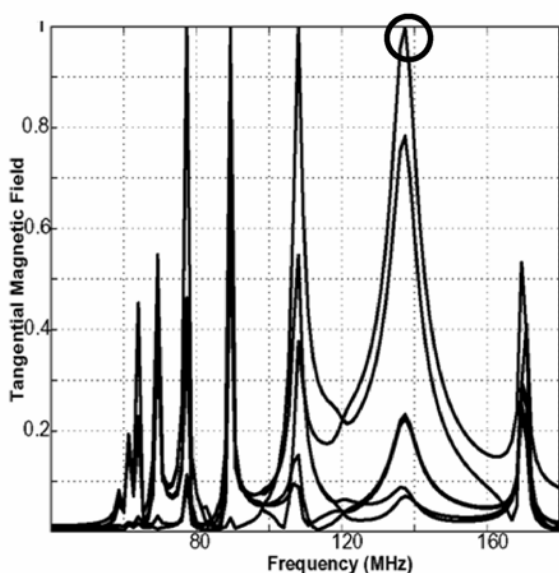


Figure 3. FDTD calculated frequency response of highpass birdcage coil loaded with the head model. The capacitance value used was 15.5 pF (currently utilized for 3T operation). The spectrum shows 9 modes representing the 16 struts of the coil. The circle represents the linear mode of operation; its frequency is within 7.5% of the experiment value.

3.2.2. The TEM Resonator

Experiences with high field human imaging have shown that distributed circuit RF coils, such as the TiO_2 -filled toroidal resonator [50] and the TEM resonator for head [16–18] and body [51] imaging, provide more applicability and versatility when compared to conventional lumped-circuit coils. Aside from the losses that the lumped elements, such as capacitors, possess at high frequencies, a major factor leading to the difference in performance between these coils is frequency tuning.

At ultra high field (≥ 7 T), the human head causes a significant frequency shift when loaded in the coil. With different head sizes, flexible and robust techniques should be used to tune the RF head coils. Compared to the lumped-circuit coils, these techniques are more easily realized when using distributed circuit coils.

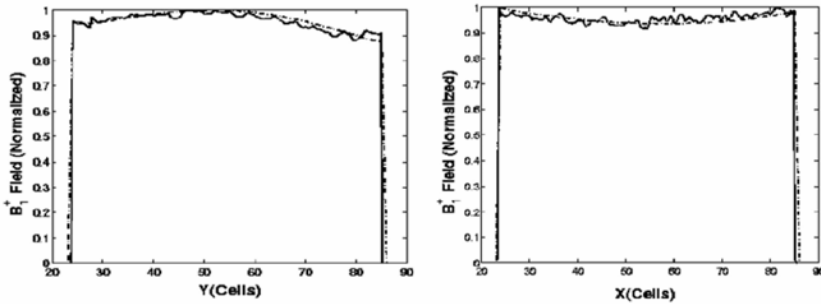


Figure 4. The B_1^+ field as a function of anterior–posterior direction in the center of a high-pass birdcage coil (left) and as a function of the median–lateral direction, 10 cm down from the center (right). The FDTD solution (dashed curve) is compared to experimental MRI measurements (solid curve) at 1.5 T inside a head-sized phantom filled with muscle-like (in terms of dielectric properties) material. Adapted with permission from [30].

A typical TEM head coil consists of 16 or 24 struts [6,16–18,21], which are contained in an open resonant cavity. Two circular rings are attached to the top and bottom of the open cavity. Each of the struts consists of a coaxial line with a circular cross-section. Teflon is typically used as dielectric filler between the inner and outer rods of each strut. The coil is tuned by adjusting the gap between the two inner rods of each strut. In the experimental setting, this operation is done while the sample is loaded in the coil structure. Analytical models based on multi-conductor transmission line theory [13,52] have accurately described the operation of empty TEM coils. They have shown that for an empty N -strut TEM coil, $N/2 + 1$ TEM modes exist. The second mode on the spectrum, mode 1, produces a linearly polarized field that can be utilized for imaging. The other modes produce nulls in the center of the coil, rendering them ineffective for conventional imaging.

Similar to the birdcage coil, the TEM resonator and the object to be imaged (phantoms or human head models) were modeled as a single system with the FDTD method [18,19,21–25,43]. Several resolutions were considered. The highest resolution (2 mm) constituted a grid that is composed of approximately 8 million cells. A stair-step approximation was used to model the shield and the top and bottom rings of the coil. The coaxial rods were modeled in a similar manner, while an FDTD algorithm was used to account for the curvatures of the rods to minimize the errors caused by stair-stepping.

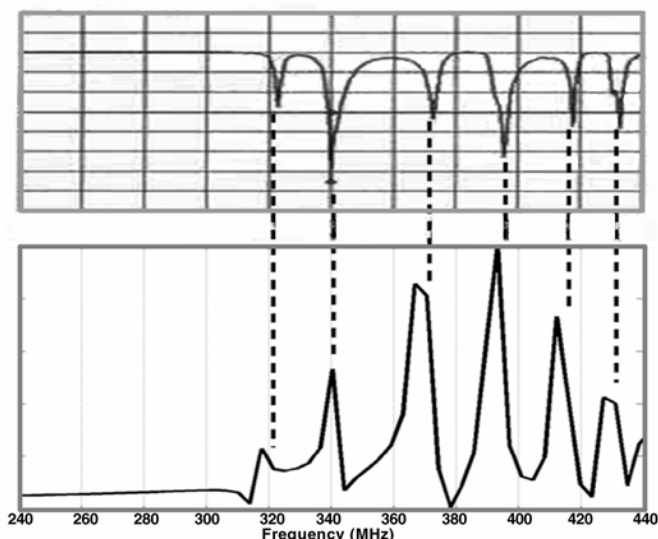


Figure 5. Measured and FDTD-calculated response of an empty 16-strut TEM resonator where the mode of operation, mode 1, is tuned to 340 MHz.

Figure 1 displays the FDTD grid of a 16-strut TEM resonator loaded with the 17-tissue human head model. To account for the RF coil radiation from the top and bottom of the coil, the PML was used as an absorbing boundary condition. The coil was numerically tuned by adjusting the gap between the TEM stubs until any mode of interest was resonant at the desired frequency of operation. For a loaded coil, this process was performed while the human head model was simultaneously present within the coil structure. Figure 5 presents the tuning process of the model by displaying an FDTD-calculated frequency response of a point inside a 16-strut TEM resonator (empty) and a corresponding experimentally measured S11 spectrum for the same coil dimensions. For verification purposes only, the coil in this situation was tuned to near the 8T Larmor frequency (340 MHz). Since the FDTD-calculated data is for a point inside the head mesh, the width and the peak of each mode are irrelevant (they vary across the head volume) and should not be compared to the actual shape and peak of the S11 measured by the network analyzer. In this figure the intended comparison criteria between FDTD calculations and the measured S11 is to show the frequency locations of the modes and to give a perspective on FDTD tuning.

In terms of the distributions of the fields, Figure 6 displays infrared images and the FDTD-calculated square of the transverse electric field distribution of an axial slice inside an empty 24-strut TEM resonator [53]. The resonator was experimentally and numerically excited at one port and tuned to 340 MHz. Excellent agreement is obtained between the FDTD and infrared results. It is also observed

that one cannot identify the location of the excitation source from the presented data. In §5.1.2 we will exploit the effect of the excitation source when the coil is loaded.

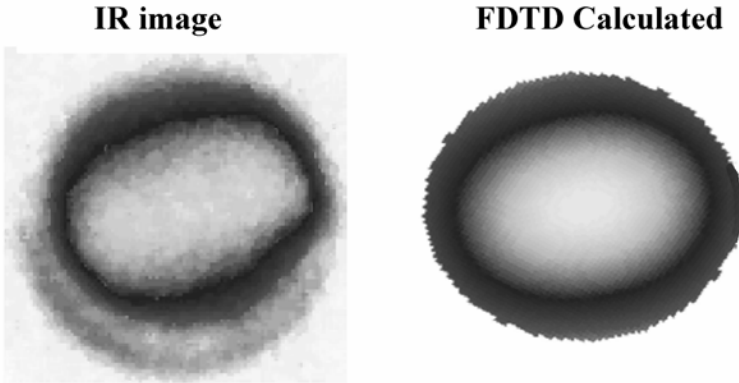


Figure 6. Infrared images and FDTD-calculated transverse E -Field² distribution of an axial slice inside an empty 24-strut TEM resonator. The resonator was excited at one port and tuned to 340 MHz. Comparisons between simulations and MRI experimental data for loaded TEM coils are presented throughout the chapter. Adapted with permission from [53].

3.3. The FDTD Code

The in-house FDTD code [5,18,19,21–24,30,31,43] starts by dynamically allocating the memory requirements for all the arrays including electric field vectors, magnetic field vectors, permittivity, conductivity, and capacitance. With different coil geometries, cell sizes, and coil loading (empty, phantoms, or human head models), dynamic allocations provide convenience and conservation of memory. The next step is assigning the electrical properties to the desired portions of the grid, including the phantom or the biological tissues of the human head model. The time loop then starts with no coil excitations, so the initial field values are set to be zero. The time is incremented by a time step. The excitation is turned on in the specified excitation location. The shape of the excitation is unimportant as long as its frequency spectrum contains the frequencies of interest. The electric field values are then updated everywhere in the grid. A lumped-element FDTD algorithm is used to model the tuning capacitors (if they are used) at their corresponding positions on the coil. The electric field components that are tangent to a perfectly conducting surface (coil structure) are forced to zero. To avoid stair-stepping errors, algorithms are used to create slanted perfect conductors. Using the calculated electric field values, the magnetic field values are then updated over the entire grid.

This is the end of the time step. The time step procedure is repeated until the simulation has run a prescribed number of time steps. Because the updated field values are only functions of the previous field values, memory is conserved. At any cell, memory conservation is accomplished by overwriting the updated field value into the same memory location that contains the previous value at the same cell.

In actuality, the goal is to obtain the field distribution within the coil at the resonance frequency where the lumped capacitors must be tuned or the gap between inner struts must be adjusted to set the resonance at the Larmor frequency. From the magnetic field distribution one can extract the B_1 field distribution. From the electric field distribution one can find the SAR as well as the total power absorbed by the phantom or the human head. Finding the field distribution is a two-step process. In the first step, an initial guess is made for the capacitor values (birdcage coil) [5,30,31,52] or for the gap between each of the two inner struts (TEM resonator) [18,19,21–25,54]. An FFT (Fast Fourier Transform) is then applied to the FDTD solution at a few points within the grid to obtain the frequency response of the coil. The location of the points where the data is collected is not important, since the frequency response of points within the coil should not differ significantly. The only difference should be due to variations in the field distribution of the coil. If the resonance frequency of the solution is not at the desired location, the capacitor values are changed, or the gap is adjusted and the FDTD program is rerun. This step is repeated until the desired resonance frequency is obtained. In the second step, the FDTD solution is run with the correct capacitor values or gap sizes, but instead of applying an FFT at a few points in the grid, a DFT (Discrete Fourier Transform) is applied on the fly at all points within the grid at the resonant frequency. Thus, the time data do not need to be stored and at the end of the code, and the field distribution is known at the resonant frequency.

4. RF POWER REQUIREMENTS IN MRI

The first physical issue that will be discussed in this chapter is the RF power requirement in MRI, namely: “how does RF power relate to field strength?”

In human MRI experiments, the dependence of radiofrequency (RF) power deposition on the frequency of operation (Larmor frequency) has been a topic of interest [55,56] since MRI was introduced as a clinical imaging technique. This interest has been more academic than practical, since the technology to build high field systems did not exist. Now, as MRI human imaging is performed at very high field strengths, the RF deposition/frequency dependence has drawn even more interest [25,57,58]. Some of the approaches that were used in studying the RF power-frequency dependence have included quasistatic [55] and full-wave models [25,57,58]. In this section, we will closely study the RF power/frequency dependence up to frequencies nearing 12 T on different electrical size loads, configurations, methods of calculations, and RF coils.

4.1. The Quasistatic Approach: Square Dependence & Conditions

The nature of the RF power/frequency dependence has been extensively studied, which has, interestingly, provided several different answers. Originally, quasistatic models predicted a square (power \propto square of the operating-frequency/field-strength) dependence [55]. Before we go further into other methods, let us briefly visit the origins of the square dependence. The power dissipated in a cylinder (assumed for all practical purposes to be the required RF power to obtain a specified flip angle) with radius r and length l is given by $P = \pi r^4 l \omega^2 \sigma B^2$, where B is the magnetic field intensity, σ is the conductivity, and ω is the frequency. Therefore, until recently, it was established that the power required for a specified flip angle varies with ω^2 , or, equivalently, it varies with the square of the static magnetic field strength, i.e., B_0^2 .

If we examine the quasistatic power equation, it can be easily shown that B was assumed to be the field that excites the spins. This can only be accomplished if in the transmitted magnetic field that exists in the load is only a circularly polarized magnetic field in a specified sense of rotation, typically referred to as the B_1^+ field. The B_1^+ field (which will be extensively studied in the next section) is the magnetic field component that excites the spins. This is only valid when the coil is excited in quadrature at low frequency where the dimensions of coil and object to be imaged are small compared to operating wavelength [18], which is clearly not the case with UHF MRI. In addition, for the ω^2 dependence to hold, it was also assumed that inhomogeneity and the strength of the B field do not vary with frequency. If we relate that to the B_1^+ field, that would require that the fraction of the total transmitted field that contributes/projects to the B_1^+ field direction be constant at all field strengths. When dealing with high field clinical (large loads) imaging, these assumptions utilized in calculating the power requirements are no longer valid, and therefore it is expected that the ω^2 /RF power dependence will not hold.

Before we go further into analyzing the nature of this RF power/frequency dependence, we will verify the validity of the square dependence on the conditions mentioned above. We can consider a single strut coil [59,60] with an electrically small load (9.4-cm long cylinder phantom with a circular cross-section of a diameter equal to 4.6 cm and filled with material with the following properties: dielectric constant = 78, conductivity = 1.154 s/m). (The dimensions and properties of this load resemble that of a rat.) A 3D FDTD model of this coil was developed (the grid is shown in Figure 17 (left)) [19]. Note that the coil strut was shifted 2 mm in the Y direction to resemble some expected inaccuracy in the coil structure. The results (displayed in Figure 18), in general, show excellent homogeneity in the distributions of both of the circularly polarized field components, B_1^+ (transmit) and B_1^- (receive) [19], indicating that linear excitation is effectively producing close to ideal linearly polarized field such that it can be evenly be split into B_1^+ and B_1^- fields [19].

Based on a description of the single-strut coil loaded with the electrically small-sized phantom and the homogenous distributions of the B_1 fields, the above assumptions (used for quasistatic power calculations) are valid, at least to much

higher frequencies when compared to loads like the human head. Figure 7 (top) displays the required power to obtain a constant value of the circularly polarized field (B_1^+ and B_1^-) (average value in the phantom volume) as a function of frequency. Two points can be deduced from this plot. First, the power requirements are almost identical, except near the high-frequency values, for both the field components, even with slight asymmetry in the coil model. Second, the expected square dependence is clearly apparent with slight deviation as frequency increases.

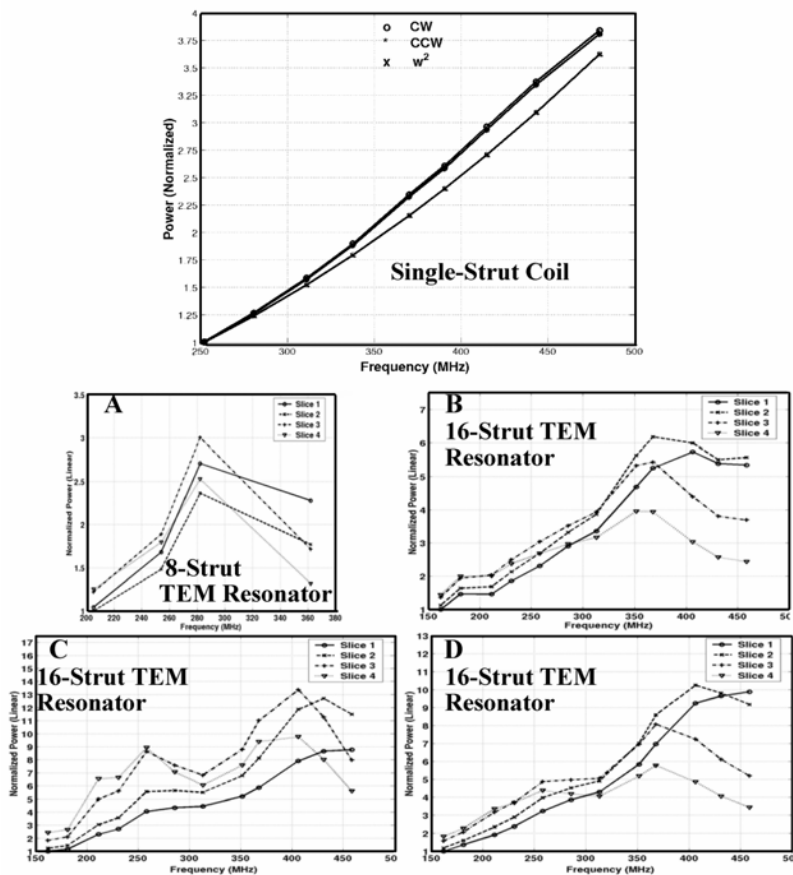


Figure 7. The power required to obtain a specified average value of the B_1^+ field as a function of frequency using the FDTD method. The results are presented in a single-strut coil for a 9.4-cm long cylinder phantom with a circular cross-section of a diameter equal to 4.6 cm and filled with 0.125 M NaCl, and for the visible human (A) and the 17-tissue (B,C,D) anatomically detailed head models loaded in a TEM resonator operating under linear (1-port) excitation (A,B,C), and quadrature (2-port) excitation (D). The locations of the slices are shown in Figure 8. Adapted with permission from [25] (TS Ibrahim, 2004. A numerical analysis of radiofrequency power requirements in magnetic resonance imaging experiments. *IEEE Trans Microwave Theory Tech* 52:1999–2003). Copyright © 2004 IEEE.

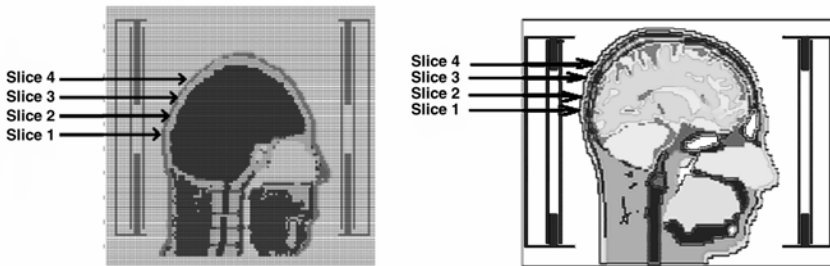


Figure 8. FDTD grids of the 6-tissue visible human (left) and the 17-tissue (right), anatomically detailed human head models loaded inside a 16-strut TEM resonator. The denoted 4 slices represent the locations at which the RF power/frequency dependence was evaluated in Figure 7. Adapted with permission from [25] (TS Ibrahim. 2004. A numerical analysis of radiofrequency power requirements in magnetic resonance imaging experiments. *IEEE Trans Microwave Theory Tech* 52:1999–2003). Copyright © 2004 IEEE.

4.2. The Full Wave Approach

Clearly, the aforementioned quasistatic assumptions are not valid for a load like the human head and for frequencies as low as 5 T. As a result, full-wave models have predicted otherwise. For example, ones that utilized idealized current sources [58] have shown that the power depends on the square of the frequency and then reduces to linear dependence [58]. For other models that utilized rigorous modeling of the coil source and treated the coil and the load as a single system, the results were different [25,57]. Using the FDTD model and the rigorous modeling of the coil mechanism, Figure 7 displays the power required to obtain a constant value of the B_1^+ field as a function of frequency for a 6-tissue (visible human project) model (A) loaded in an 7-strut TEM coil and for the 17-tissue model (C–D) loaded in a 16-strut TEM coil. The results are presented for 4 axial slices spatially positioned in the brain region [25,57]. The locations of these slices are shown in Figure 8 [57].

The results show that the power required in order to obtain a specified average B_1^+ field value increases with frequency, plateaus at a specified value, and then starts to drop as the frequency increases [25,57]. This was observed experimentally with initial studies with the 8T magnet [61]. When comparing the head models and coils, the peak power value has occurred in the 17-tissue head model at a frequency higher than that for the visible human project model. This model has a relatively larger (consequently electrical) size than the 17-tissue model. This is a factor that can contribute to the phenomena describing the difference between the results of the two head models. This result and other similar simulations have also shown

that the power required for a certain flip angle depends on the coil load and on its position in the coil. In addition, the electromagnetic interactions between the load and the coil, and between the load and the excitation source, contribute also to the power-frequency dependence. Therefore, many more experimental and numerical studies are needed in order to reach well-defined conclusions if applicable. In any event, these results seem to reaffirm earlier experimental findings at 8 T [61].

5. THE ROAD TO CLINICALLY USEFUL IMAGES

In this section we will examine the performance of current RF coils utilized in UHF MRI. We will closely study current technological and physical problems and provide potential solutions.

5.1. A Numerical and Experimental Look at Current Coils Operating at High Fields

Many of the modeling approaches utilized for RF coil simulations employed idealized current distributions that do not fully consider the coupling between the head resonator and the sample. These studies shared the common assumption that the RF coil functions as an azimuthal transmission line at all the frequencies of interest. For instance, this was done by determining the current distribution in the coil without the head being present using the method of moments [28] or by replacing the lumped capacitors with voltage sources whose magnitudes varied sinusoidally [27,58]. As a result, the currents on the coil elements were required to have a sinusoidal distribution, i.e., the coil was assumed solely operating in the transverse electromagnetic (TEM) mode of interest, the ideal mode of operation for the birdcage or the TEM resonator. Therefore, the currents on the coil elements were assumed to vary as

$$I_i = I_{\max} \cos(i2\pi/N) \quad (1)$$

where I_i is the current in the i th element, I_{\max} is the maximum current, and N is the number of coil elements. Although the resulting inaccuracies may not be too significant at 64 MHz, the field distribution calculations at higher frequencies are much more prone to be invalid, most especially for volume coils. The next two sections will provide detailed studies concerning this issue for an unshielded birdcage coil and a TEM resonator.

5.1.1. The Birdcage Coil: 1.5T vs. 4.7T

In this section we will evaluate the performance of an unshielded birdcage coil at 1.5 and 4.7 T, namely, current distribution, interactions between the drive port(s) and the load, and B_1^+ field distribution. In Figure 9 (left), the current on each wire (coil element) is calculated using the in-house FDTD package at 64 MHz for (1) an unloaded coil, (2) a coil loaded with a head-sized cylindrical phantom with a circu-

lar cross-section called a “small phantom,” and (3) a coil loaded with a coil-sized cylindrical phantom with octagonal cross-section called a “large phantom” [5]. Both phantoms were filled with muscle-like dielectric properties. The ideal sinusoidal coil current is also plotted for comparison. As expected, the unloaded coil current is close to the ideal case. When the coil is loaded by a phantom, the interaction between the coil and the phantom can induce additional currents on the wires. At 64 MHz, the induced currents are not too significant for the small phantom, but for the octagonal phantom the induced currents can be very large. The interaction is stronger for the octagonal phantom because it is electrically larger and thus closer to the coil elements and the excitation port. Also, the phantom does not have circular symmetry, which produces greater asymmetries in the induced currents.

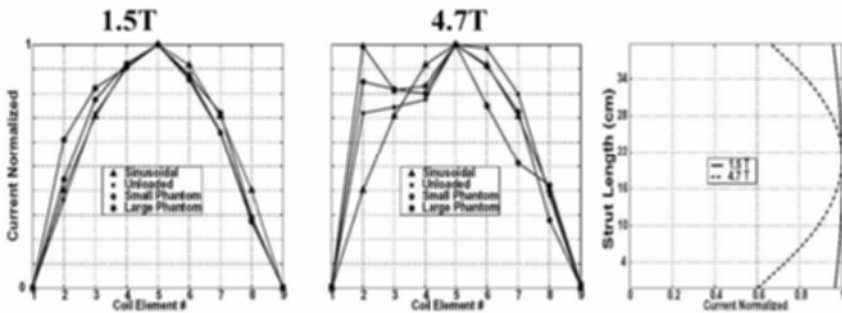


Figure 9. Current distribution on the birdcage coil elements for different loadings at 64 and 200 MHz. The sub-figure on the right corresponds to the absolute value of the current as a function of distance on one of the empty coil elements at 64 and 200 MHz. Adapted with permission from [30].

In Figure 9 (middle), the currents on the wires are once again plotted for the case where the unshielded birdcage coil has been retuned to resonate at 200 MHz [5]. In all three cases, whether the coil is loaded or unloaded, the currents do not follow the ideal sinusoidal curve. At 200 MHz, each strut of the coil is one quarter wavelength long, which means that the coil acts more like an antenna than a resonator [5]. To demonstrate this point, Figure 9 (right) displays the current on one of the coil elements along its length at both 64 and 200 MHz. It is observed that at 64 MHz the current is relatively constant. At 200 MHz a standing wave has formed on the wire.

By exciting the coil in one point (on the top ring) and allowing the coil currents to be properly calculated with Maxwell’s equations, one can properly account for the coupling between the drive port and the object to be imaged. At high frequency it is expected for this coupling to have a significant effect on the SAR values, especially near the source. To demonstrate this point, Figure 10 shows a volumetric three-dimensional view of the SAR inside the “small” and “large” mus-

cle phantoms for linear excitation at 64 and 200 MHz. While the drive port does not have much of an effect on the SAR values at 64 MHz (except minimally for the large phantom), the maximum SAR values are located near the source for both the cylindrical and octagonal phantoms at 200 MHz. Because the “large” phantom is present along the length of the coil and is larger than the cylindrical phantom, the source is much closer to the “large” phantom and consequently a high local hot spot is observed near the source (see Figure 10) [5,18,19,23,31,62].

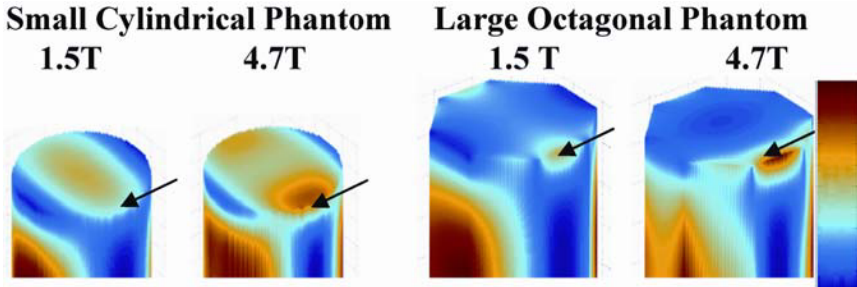


Figure 10. Specific absorption rate calculated using the FDTD method inside loaded high-pass birdcage coil. The phantoms contain material with muscle-like dielectric properties. The coil is operating under linear excitation where the drive port is positioned near the top of the phantom. See attached CD for color version.

For the large phantom, the SAR values near source are about 20% higher than those for the small phantom. This is despite the fact that these calculations are given for 1-watt CW absorption and the volume of the “large” phantom is about 2.5 times that of the “small” one, where on average, the SAR values should be 2.5 times lower than the “small” phantom case. Hence, the interaction between the excitation source(s) and the object to be imaged is critical at high frequency; it depends on the size and the shape of the object and its placement inside the coil. From a full-wave analysis point of view, this physical observation associated with high-frequency operation and/or electrically large loads cannot be accounted for by utilizing ideal current distributions on the coil elements nor by calculating the currents on the coil elements without the load and then forcing these currents on the elements when the load is present. Therefore, (1) rigorous modeling of the excitation source(s) and the lumped capacitors, (2) accurate consideration of their spatial positioning on the coil, and (3) numerical tuning as it is done in experiment must all be computationally carried out in order to accurately describe the electromagnetic interactions between the coil and the tissues during high field operation.

Let us now analyze the B_1^+ field distribution during low and high field operation. It is noted here that the coil tested at 200 MHz was not optimized geometrically for this frequency. It was simply tested by reducing the lumped capacitor values such that the mode of operation was tuned to 200 MHz. Figure 11 displays the

B_1^+ field inside the “small” phantom for axial slices at 64 MHz for linear and quadrature excitations [5]. For linear excitation, the B_1^+ field distribution is about 60% homogeneous (the difference between the maximum and the minimum values of the B_1^+ field in this slice is 40% the maximum value). A better overall homogeneity (90%) is obtained from linear to quadrature excitation. The results at 200 MHz, however, are quite different. Unlike the 64 MHz case, there is not much improvement in the homogeneity of the fields from linear to quadrature (29% homogeneity) drive. This is due to the fact that the ideal current distribution predicted from circuit analysis is no longer present, rendering the conventional quadrature drive ineffective [5].

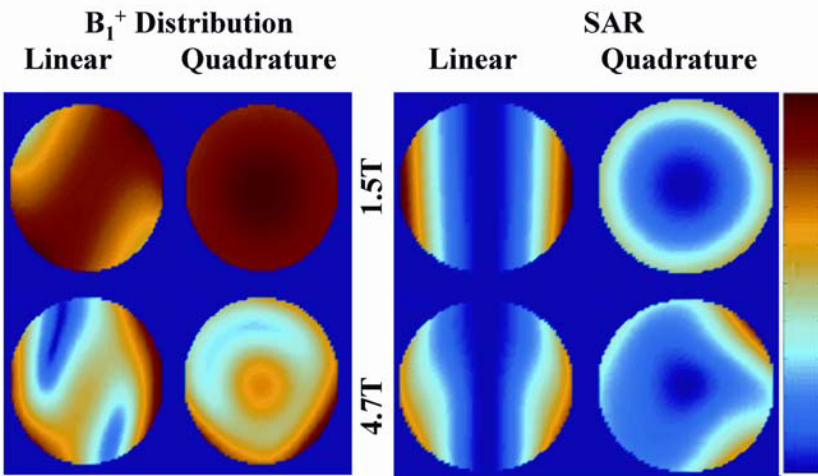


Figure 11. Axial slices displaying the calculated normalized B_1^+ field and SAR of a highpass birdcage coil loaded with the “small” phantom at 64 and 200 MHz using linear and quadrature excitations. Adapted with permission from [5]. See attached CD for color version.

The corresponding SAR values for 1-watt absorption are also shown in Figure 11. The two-port quadrature excitation for the unloaded coil (or for the birdcage coil loaded with the “small” phantom) produces fields that are approximately circularly polarized at low frequency. For the “small” phantom, simulations and experiments have shown that at 64 MHz the polarization of the tangential electric fields is almost circular when the excitation is applied in quadrature [5]. Because the SAR is an indication of the electric field for the homogeneous medium, Figure 11 shows that the SAR distribution is symmetric about the azimuthal direction [5]. It is also well documented that quadrature excitation reduces the transmitting power and consequently the absorbed power by approximately a factor of 2 at 64 MHz (the ratio of the absorbed and radiated power is independent of the source at the same frequency). As the absorbed RF power deposition in the phantom is an indication of the SAR, Figure 11 shows that at 64 MHz, by applying quadrature

excitation, the SAR peak values have decreased by approximately a factor of 2 compared to the case when the coil is linearly excited [5].

At 200 MHz the situation is quite different, however. Because linear excitation does not give a sinusoidal current distribution on the coil elements nor linear polarization for the loaded case at 200 MHz, it is impossible to obtain circularly polarized fields using the conventional (two-port) quadrature drive. This can be clearly seen from Figure 11, where the azimuthal symmetry is lost at the 4.7T case. In addition, the fields induced by each of the two drive ports can now add up either constructively or destructively, depending on the geometrical shape and material properties of the head or phantom. As a result, it is expected that the peak SAR values may increase when switching from linear to conventional quadrature excitation (unlike that at 64 MHz). This is also demonstrated in Figure 11 [5].

5.1.2. The TEM Resonator at 8 T

The TEM resonator [16] was designed to produce “TEM” modes, that is, transverse electromagnetic modes to the resonator’s axis. This notion, however, is only valid when the resonator is empty. It should be noted that theoretically these modes including normal mode of operation (mode 1) are not TEM due to two major factors [38]. First, the resonator is loaded with a dielectric/lossy phantom/head. Second, the feed and termination loads introduce perturbations to the fields. Therefore, these modes will be referred to as hybrid modes. In this section, we will address three main issues with these modes: (1) what kind of polarization they possess, (2) how far their distributions differ from those associated with the TEM ones, and (3) how their corresponding coil current distributions deviate from TEM ones. Using experimental and numerical calculations on what is so called the “homogeneous mode of operation” (mode 1), we will address these three questions.

Figure 12 displays axial slices of the FDTD calculated polarization vector (during linear excitation) of TEM mode 1 (second mode on spectrum in Figure 5) of an empty TEM resonator, and of hybrid mode 1 (second mode on spectrum) of a loaded (18.5-cm diameter spherical phantom filled with 0.125 M NaCl dielectric-like properties) TEM resonator. From examining these figures, it can be clearly shown that the linear polarization characteristics of the empty coil’s mode (TEM) have been severely altered, [62] resulting in distinct elliptical polarization (except for a small area in the center of the slice).

Figure 13 displays the numerically calculated B_1^+ field distribution of TEM mode 1 in the empty coil and the calculated and experimentally extracted B_1^+ field distribution of hybrid mode 1 of the loaded coil. The slices presented are central, sagittal, and coronal slices through the spherical 0.125 M NaCl phantom. The results show remarkable agreement between the FDTD-calculated and extracted B_1^+ field. When compared to the empty case, as expected, the loss of the linear polarization in mode 1 has caused severe inhomogeneity in the B_1^+ field.

At this juncture, there remains a very important question: Are the differences in the field distributions and polarizations (as seen in Figures 12 and 13) within the coil between the loaded and unloaded cases caused simply because the electrical

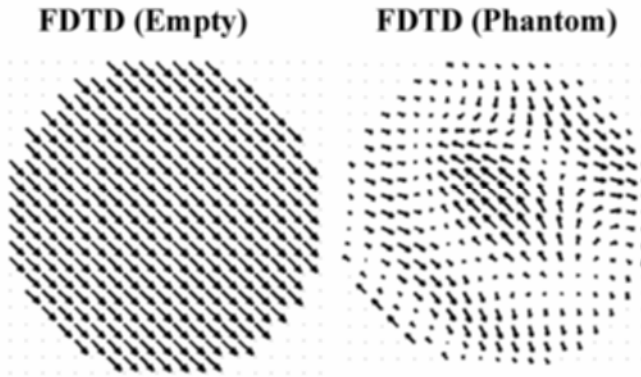


Figure 12. Axial slice of FDTD-calculated polarization vector plots of the coil’s mode of operation (mode 1) in a TEM resonator under two loading conditions: loaded with an 18.5-cm spherical phantom filled with 0.125 M NaCl (right) and empty (left). The coil was linearly (1-port) excited and numerically tuned to 340 MHz. The empty coil plot represents an imaginary axial area, spatially positioned in the same location as for the loaded case.

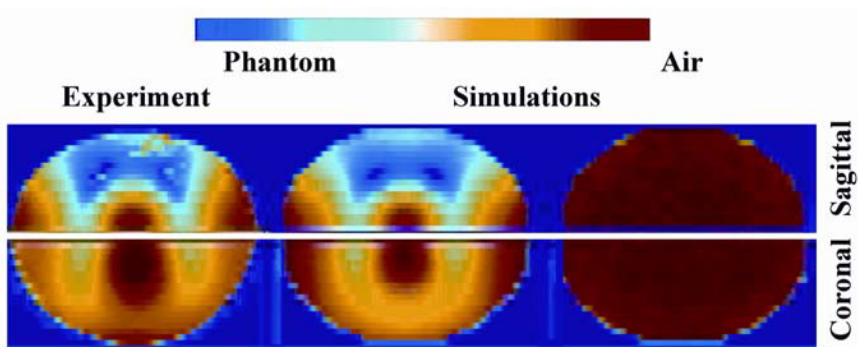


Figure 13. Mode 1 B_1^+ field distribution. The results are obtained experimentally (left) using an 8T whole-body magnet and a 16-strut TEM resonator operating under linear excitation and loaded with an 18.5 cm spherical phantom filled with 0.125 NaCl M and utilizing the FDTD model for the same conditions as experiment (middle) and for an empty coil (right), where imaginary sagittal and coronal slices shown are spatially positioned in the same location as the displayed slices for the loaded case. See attached CD for color version.

properties over the volumes in which the fields are being compared are different due to loading, or has the behavior of the resonator actually changed as well? The answer can easily be observed in Figure 14, where the currents on the coil struts have been calculated for the aforementioned empty and loaded coils. While the empty coil produces near the ideal sinusoidal current distribution, this is clearly not the case for the loaded coil. As such, it is concluded that the behavior of the reso-

nator has significantly changed. This finding leads to a more methodological conclusion in MRI RF volume coil modeling, namely, the performance of loaded volume coils at UHF MRI cannot be predicted utilizing “idealized current modeling or idealized conditions,” and the rigorous treatment of the excitation port is a must.

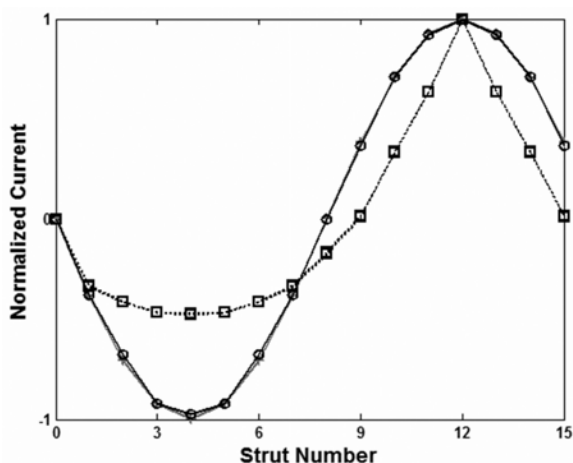


Figure 14. FDTD calculated current distributions of mode 1 in a 16-strut TEM resonator under two loading conditions: loaded with an 18.5-cm spherical phantom filled with 0.125 M NaCl (\square), empty (\circ), and for a reference sinusoidal function (*). The coil was linearly excited and numerically tuned to 340 MHz.

In terms of evaluating the TEM coil with a human head, Figure 15 displays gradient echo and corresponding simulated images at 8 T [18]. The results demonstrate a very good correlation between the experiment and the simulations. It can be seen that the coil’s most sensitive region is highly focused on the central portion of the cerebral hemispheres and the upper brainstem, while evaluation of the lateral portions of the cerebral cortex is poor.

The existing TEM head volume coils generate relatively widely variable image quality for different regions of the head, resulting in considerable challenges to acquire a quality brain survey series of the whole brain at high field strengths [18] (§5.5 provides possible solution for global and localized imaging). An approach to dealing with this problem is to utilize multiple coil designs (shapes, geometries, and/or dimensions) to evaluate different regions of the brain that may be in close proximity. For instance, if the deep midline or para-midline brain structures are of interest, the shown coil is an excellent choice. On the other hand, the high cerebral cortex near the vertex, the lateral cerebral cortex, and the cortical motor strip are all in regions where image quality has been marginal for subjects that have been studied at 8 T (for this particular coil design and dimensions) [18].

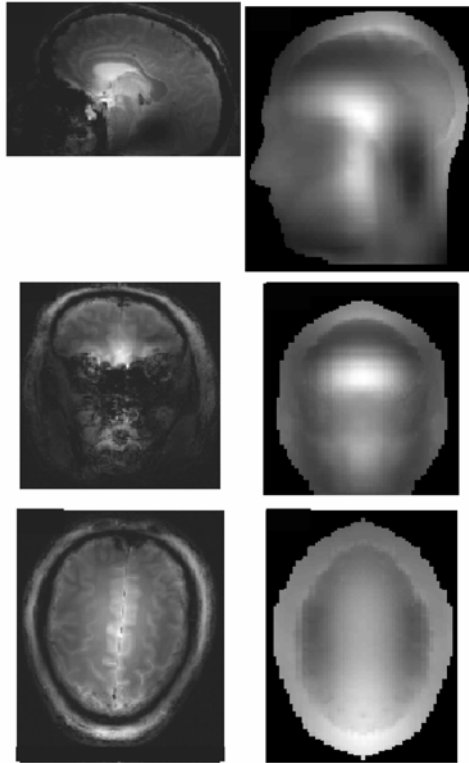


Figure 15. Axial, coronal, and sagittal slices displaying gradient echo images of a cadaver obtained experimentally at 8 T and the corresponding simulated low-flip-angle images obtained using the FDTD method. The results were obtained using a 16-strut TEM coil. The coil was tuned to the standard mode of operation, mode 1, and was driven using 2-port back-of-the-head quadrature excitation. Adapted with permission from [18] (TS Ibrahim, A Kangarlu, DW Chakeres, 2005, Design and performance issues of RF coils utilized in ultra high field MRI: experimental and numerical evaluations, *IEEE Trans Biomed Eng* **52**:1277–1284). Copyright © 2005 IEEE.

Until a single coil that is much more flexible in exciting the entire head can be experimentally implemented, the use of multiple coils may be the standard solution. This is similar to the concept of using dedicated coils for orbit or temporal bone imaging at lower fields. In contrast, at ultra high fields, specialty coils are needed for different segments of the brain itself [18].

5.2. The RF Component into MRI: A Look at the NMR Signal

Since the inception of ultra high field (UHF) MRI [61], the issue of the MR received signal [10,63,64] has been in debate within the MRI scientific community

[36,65]. In 2000 D. I. Hoult at the Canadian National Research Council published an article that elegantly described the strength of the MRI signal using the principle of reciprocity [65]. In [65] reciprocity was utilized based on an experiment that was conducted in Hoult's research lab utilizing two small current loops, where the magnetic flux density was assumed to be constant across its surface. One of the coils was immersed in a flask filled with saline and the other was held in the air some distance away from the first coil. One coil was fed by a coaxial line, and the voltage induced on the other coil was measured using a network analyzer. The reverse experiment was also conducted. The voltage induced in both cases was found to be the same. Based on these results, Hoult asserted that reciprocity held and it could be applied to the MRI experiment.

Hoult [65] indicated that if a small loop is used as a transmit coil, transverse magnetic dipoles are created in the sample. The fields induced by these dipoles could be approximated as if they were produced by a small current loop where the magnetic flux density is constant across its surface. From this assumption, the strength of the received signal in the small loop coil was found to be proportional to the rotating B_1 field produced by this coil where the frame of rotation is opposite to that used for the forward problem (transmission). In the above evaluation, it was experimentally shown that reciprocity holds for this particular problem, involving the two small loop coils. In this section we will briefly look at the NMR signal from an electromagnetic perspective. First, let assume a general \mathbf{B}_1 field was excited by a current in an RF coil; the component that is responsible for exciting the spins is then given as

$$B_1^+ = (\mathbf{x} - jy) \cdot \mathbf{B}_1 / \sqrt{2} = (B_{1x} - jB_{1y}) / \sqrt{2} \quad (2)$$

A component that has an opposite sense of rotation to that of B_1^+ is given as

$$B_1^- = (\mathbf{x} + jy) \cdot \mathbf{B}_1 / \sqrt{2} = (B_{1x} + jB_{1y}) / \sqrt{2} \quad (3)$$

The transverse magnetization is then given [66] as

$$\mathbf{M} = \mathbf{x} M_x + \mathbf{y} M_y \quad (4)$$

$$M_x \approx M_0 \gamma T_2 (-jB_{1x} - B_{1y})/2 = -j (M_0/\sqrt{2}) \gamma |B_1^+| T_2 \exp(j\angle B_1^+) \quad (5)$$

$$M_y \approx M_0 \gamma T_2 (B_{1x} - jB_{1y})/2 = (M_0/\sqrt{2}) \gamma |B_1^+| T_2 \exp(j\angle B_1^+) \quad (6)$$

where M_0 is the longitudinal magnetization equilibrium value. If we examine electromagnetic theory, we find that in order for the standard form of the reciprocity to hold in a medium, its constitutive parameters must be reciprocal. A reciprocal material is one in which

$$\bar{\bar{\epsilon}} = \bar{\bar{\epsilon}}^T \quad (7)$$

$$\bar{\bar{\mu}} = \bar{\bar{\mu}}^T \quad (8)$$

$$\bar{\bar{\sigma}} = \bar{\bar{\sigma}}^T \tag{9}$$

where $\bar{\bar{a}}$ represents a matrix tensor quantity, and superscript T denotes a transpose of a tensor. When examining the standard formulation of reciprocity, an assumption is made: the materials contained in the problem of interest are reciprocal, i.e., $\mathbf{A}_1 \times \bar{\bar{\phi}} \times \mathbf{A}_2 = \mathbf{A}_2 \times \bar{\bar{\phi}} \times \mathbf{A}_1$, where \mathbf{A} represents \mathbf{E} or \mathbf{H} and $\bar{\bar{\phi}}$ represents ϵ , μ , or σ . This clearly indicates that $\bar{\bar{\phi}} = \bar{\bar{\phi}}^T$ [67].

Let us now apply permeability tensors [68] and complex susceptibility [69] formulation to NMR. One assumption will be made, however — susceptibility effects are only introduced due to NMR (not electrons as is usually done in EM theory). The hypothesis of this approach is to investigate the validity of relating the excitation of spins in the transverse plane to the standard reciprocity equation [67]. If the MR transverse magnetization is given by \mathbf{M} , the total magnetic flux density is then given as

$$\mathbf{B}_{\text{tot}} = \mu_0 H_1 \mathbf{e}_z + \mathbf{M} \tag{10}$$

$$\mathbf{B}_{\text{tot}} = \bar{\bar{\mu}} \cdot \mathbf{H}_1 \tag{11}$$

where \mathbf{H}_1 is the applied magnetic field intensity = \mathbf{B}_1 / μ_0 . Therefore, the solution for the tensor $\bar{\bar{\mu}}$ can then be expressed as follows [67]:

$$\begin{bmatrix} \mathbf{B}_{\text{tot}x} \\ \mathbf{B}_{\text{tot}y} \\ \mathbf{B}_{\text{tot}z} \end{bmatrix} = \mu_0 \begin{bmatrix} 1 - \frac{j\gamma M_0 T_2}{2} & \frac{-\gamma M_0 T_2}{2} & 0 \\ \frac{\gamma M_0 T_2}{2} & 1 - \frac{j\gamma M_0 T_2}{2} & 0 \\ 0 & 0 & 1 \end{bmatrix} \begin{bmatrix} \mathbf{H}_{1x} \\ \mathbf{H}_{1y} \\ \mathbf{H}_{1z} \end{bmatrix} \tag{12}$$

Typically, in dealing with solutions to NMR magnetization, a rotation matrix formulation is utilized [66]. However, in the scope of electromagnetic theory the permeability tensor relates the applied time harmonic magnetic field intensity to the total time harmonic magnetic field density as it is defined with the constitutive relations. It is apparent that the matrix is *not reciprocal*, i.e., the tensor is asymmetrical around its diagonal elements and therefore the standard form or reciprocity cannot be applied if reciprocity is to be used in explaining the excitation of the spins. Rather, a more generalized reciprocity equation needs to be utilized in such a case. This equation is given in [67]. It is noted, however, that neither the standard reciprocity equation nor Maxwell’s formulations have been utilized in solving for NMR magnetization; the equation of motion is usually used for this purpose. On the other hand, the presence of static and RF fields within media (as is the situation with NMR) is within the context of Maxwell’s equations; therefore, the permeability tensor, given above, can be correctly used with Maxwell’s equations [67].

The signal that contributes to an MRI image is related to the induced transverse magnetization. The curl of \mathbf{H} equation (in Maxwell equations) [70] indicates

that the derivative of the electric flux density (\mathbf{D}) with respect to time is equivalent to a displacement electric current density (A/m^2) or mathematically an electric current density source. As such, the derivative of the magnetic flux density (\mathbf{B}) with respect to time is mathematically equivalent to a displacement magnetic current density (V/m^2), or mathematically a magnetic current density source given as

$$\mathbf{MC}_2 = j\omega \mathbf{M} \quad (13)$$

$$MC_{2x} = \omega (M_0/\sqrt{2}) (\gamma|B_1^+|T_2) \exp(\angle B_1^+) \quad (14)$$

$$MC_{2y} = j\omega (M_0/\sqrt{2}) (\gamma|B_1^+|T_2) \exp(\angle B_1^+) \quad (15)$$

$$MC_{2x} = -j MC_{2y} = F/\sqrt{2} \quad (16)$$

The sense of rotation of this current is still equal to that of the (B_1^+) field. The resultant magnetic current density source will then excite electromagnetic fields that will be received by RF coil(s) and induce a voltage (MRI signal). Figure 16 displays the reciprocity problem [67] for the MRI experiment, where a highpass birdcage resonator is used as the receive coil.

The signal measured with the resonator induces a voltage between the coil terminals. This open circuit voltage was found to be [65,67]

$$V_{oc} = -\frac{F \frac{(\mathcal{B}_1^+)}{|\mathcal{B}_1^+|} \cdot \mathbf{H}_1}{I_{tr}} \quad (17)$$

$$V_{oc} = -\frac{F \frac{(\mathcal{B}_1^-)^*}{|\mathcal{B}_1^+|} \cdot \mathbf{H}_1}{I_{tr}} \quad (18)$$

$$V_{oc} = -\frac{F\mathbf{H}_1^-}{I_{tr}}$$

where * denotes the complex conjugate, I_{tr} is a current, which can be set to unity, and F is given in Eq. (16). In this equation, the \mathcal{B}_1^+ field is a fictitious component of the fictitious \mathcal{B}_1 field, induced by the receive coil. This component would excite the magnetization of interest if the \mathcal{B}_1 field was used for excitation. The current source \mathbf{MC}_2 (Eq. (13)) could have been excited by that coil, by any other coil, or by any combination of coils. Note that $\mathbf{H}_1^- = \mathcal{B}_1^-/\mu_0$, where the \mathcal{B}_1^- field is a fictitious component of the \mathcal{B}_1 field (defined in Eq. (3)), which always has an opposite sense of rotation to that associated with the \mathcal{B}_1^+ field as described in Eq. (18). We go back to electromagnetic theory, there is an uncommon characteristic about \mathbf{MC}_2 (the resultant current source from the transverse magnetization). It responds to a specified sense of polarization that is defined according to the direction

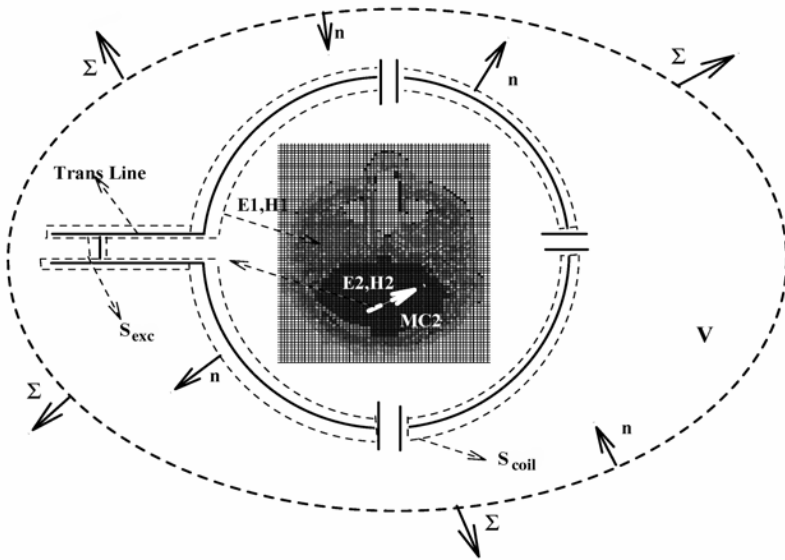


Figure 16. The reciprocity problem for the signal reception during the MR experiment. Reprinted with permission [67].

of \mathbf{B}_0 , since the rotation sense of \mathbf{MC}_2 is always fixed. In electromagnetic theory the polarization sense is defined according to the direction of wave propagation (the term “propagation” here is given for definition purposes and is not used to imply that the B_1 field is associated with a propagating wave). Therefore, \mathbf{MC}_2 responds differently to the same sense of polarization if it is defined with different directions of propagation (using the electromagnetic theory definition). This is similar to a non-reciprocal antenna except in the near field, of course. To relate the excite and receive fields to electromagnetic theory, the definition of the B_1^+ field is as follows. For $\mathbf{B}_0 = |B_0| \mathbf{z}$, the B_1^+ field produced by a coil is the circularly polarized component of the \mathbf{B}_1 field in the counterclockwise (CCW) sense if the direction of the EM energy is $+\mathbf{z}$, or the circularly polarized component of the \mathbf{B}_1 field in the clockwise (CW) direction if the direction of EM energy is $-\mathbf{z}$. If $\mathbf{B}_0 = -|B_0| \mathbf{z}$, the polarization sense of the B_1^+ field will be reversed. For any specified coil, the sense of rotation of H_1^- is always opposite to that associated with B_1^+ . The previous analysis is expected from antenna reaction theory. The voltage induced in antenna AA by another BB is identical to that induced on BB by AA. If we assume that AA is the coil and BB is the magnetic current source resultant from the transverse magnetization, the voltage induced on BB is proportional to a vector representing the polarization of the field that AA transmits and the conjugate of a polarization vector that represents a field perfectly received by BB. The field that is perfectly received by BB is the B_1^+ field and the conjugate of it is the $H_1^-(B_1^-/\mu_0)$ field. Al-

though the transmission is from AA (coil) to BB (magnetic current source), in this situation it is completely unrelated to the excitation of the spins.

The derived formula [10,65,67] shows that the NMR signal is dependent on two electromagnetic quantities:

- (1) the B_1^+ field, which is the circularly polarized component of the magnetic flux density that is responsible for exciting the spins. Note that the B_1^+ field is produced by the transmit coil, and
- (2) the H_1^- field, which is the circularly polarized component of the magnetic field intensity with a sense of rotation that is opposite to the B_1^+ field. Note that the H_1^- and B_1^+ fields in this case are fictitious components that are produced by the receive coil, if that coil were to be used for excitation.

In the next section, numerical and experimental analyses to validate the derived formula will be presented. Studies will be performed on the field polarization of volume RF coils for both head and extremity applications that demonstrate the transition between the case where the distributions of H_1^- and B_1^+ fields are similar to the case where they are completely different.

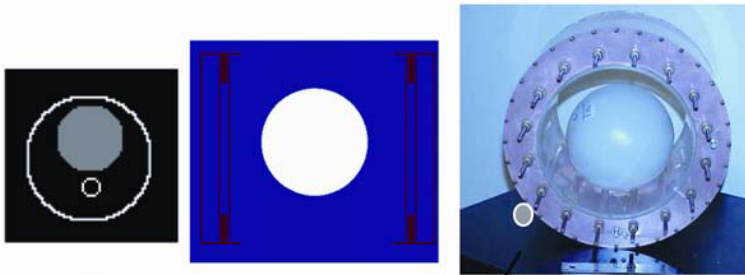
5.3. A Perspective into the Transmit and Receive Fields

In this section we evaluate the electromagnetic field behavior for low and high field imaging. We numerically and experimentally analyze the MR signal given in the last section. This analysis is carried out for a single-strut TEM-based extremity coil and the TEM resonator. The experimental studies were performed using an 8T whole-body magnet. The numerical calculations were performed at frequencies up to 485 MHz. Experimental and numerical studies of similarities or differences between the B_1^+ (excite) and H_1^- (receive) fields' distributions as a function of frequency (field strength) and coil loading were performed using the aforementioned two coils.

5.3.1. Theory

Figure 17 shows the FDTD grids of the single-strut (loaded with the phantom described in section 5.4) and the TEM coils, and a picture of the TEM resonator loaded with the saline phantom (described in §5.1.2). Figure 18 displays the 3D FDTD solutions of different magnetic field intensities inside the single-strut coil operating under linear excitation [19]. The results are presented for both an empty coil and a coil computationally loaded with the cylindrical phantom specified earlier at 254 MHz (6T for ^1H imaging) and 485 MHz (11.7 T for ^1H imaging). The results show that the B_y field clearly dominates the transverse magnetic field (B_x is negligible) for the empty coil at both frequencies and for the loaded coil at 254 MHz. This indicates that for these specific cases linear excitation is clearly effective in producing linearly polarized fields (only B_y is present while B_x is negligible). Equations (2,) and (3) also demonstrate that with negligible B_x in the coil (effec-

tively linear polarization in this situation) the CCW (B_1^+) and CW (H_1^-) fields are equal in magnitude; hence, for MRI purposes the distributions of B_1^+ and H_1^- are nearly identical. This can be easily observed for the empty coil at both frequencies and for the loaded coil at 254 MHz [19].



Excitation port at a 45° angle with respect to the X and Y axes

Figure 17. Left: Axial slice of the FDTD grid utilized in modeling the single-strut coil. The coil was mathematically loaded with a 9.4-cm long cylinder phantom with a circular cross-section of diameter 4.6 cm and the following properties: dielectric constant = 78 and conductivity = 1.154 s/m. Middle: Photograph of the TEM resonator. Photograph of the associated FDTD grid utilized in its modeling. The coil was computationally and experimentally loaded with an 18.5-cm-diameter sphere filled with 0.125 M NaCl and 0.5 mM Gd DTPA (same electromagnetic properties). The solid gray disc surrounded by a white ring represents the location of the excitation source with respect to the phantom. Reprinted with permission from [19]. See attached CD for color version.

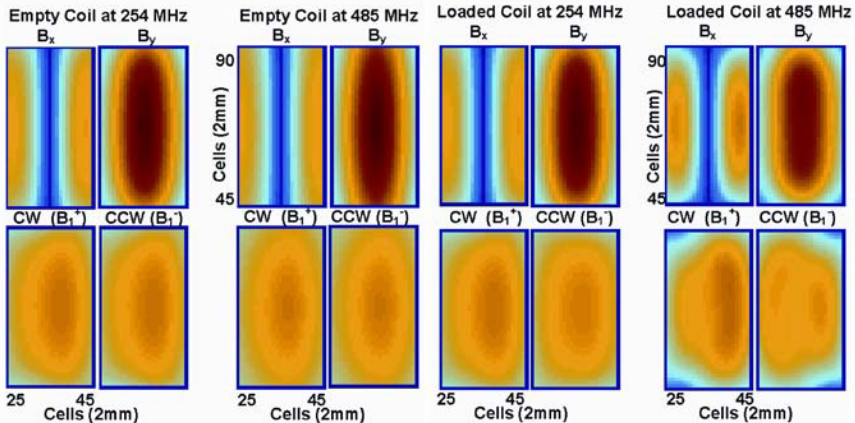


Figure 18. Calculated magnetic flux densities inside a single-strut TEM coil empty and loaded with the cylindrical phantom at 254 MHz (6 T) and at 485 MHz (11.4 T). B_x and B_y represent the magnetic flux density in the x and y directions respectively, while B_1^+ and B_1^- or $\mu_0 H_1^-$ correspond to the counterclockwise and clockwise circularly polarized components of the magnetic field, respectively. Reprinted with permission from [19]. See attached CD for color version.

When the dimensions of the coil and/or the load become a significant fraction of the operating wavelength, the electromagnetic interactions between the coil, excitation source, and the load dominate the fields within the coil. Thus, linearly polarized fields are no longer feasible, even though the coil is excited in the linear mode. This is demonstrated in Figure 18 when the coil is operating at 485 MHz and loaded with the cylindrical phantom. In this case, B_x is not negligible when compared to B_y . Thus, Eqs. (2) and (3) show that the distribution of the resulting CCW field is different from that of the CW field for the loaded coil at 485 MHz. In this case, it is clearly erroneous to consider the coil's distributions of the B_1^+ and H_1^- fields as similar. Compared to the electrical size of the human head at 7 T and the human body at 3 T, the electrical size of the utilized cylindrical phantom is smaller, even at 11.7 T. Since the distributions of the B_1^+ and H_1^- fields are different for the specified phantom, the same is expected to be true for head applications at 7 T and higher and whole-body applications at 3 T and higher.

5.3.2. Experimental Results

It is well documented that the distributions of the B_1^+ and H_1^- fields are very similar at 1.5 T for head applications. Consider the following simple experiment. Utilizing the quad-hybrid, the transverse electromagnetic field induced inside a loaded head coil at 1.5 T is approximately the B_1^+ field. If the quad hybrid ports that are connected to the coil are switched while maintaining the same input signal, the coil would excite a total field that is proportional to the H_1^- field. Such configuration is almost completely ineffective in exciting the spins. This in turn indicates that linear excitation on either of the quad hybrid ports connected to the coil is capable of producing linear polarization, and consequently comparable B_1^+ and H_1^- field distributions. This is similar to cases described for the empty single-strut coil at 254 and 485 MHz, and for the loaded coil at 254 MHz (Figure 18).

Let us look numerically and experimentally at a situation where the B_1^+ and H_1^- field distributions are different. Figure 19 displays low and high flip angle (approx. 6 and 154° in the voxel near the center of the phantom) gradient echo images and extracted B_1^+ and H_1^- fields obtained at 8 T; also displayed are their corresponding simulated results obtained at 340 MHz using the FDTD model and the MR signal equation presented in the previous section. Excellent agreement is obtained between the experimental data including images, and H_1^- and B_1^+ field distributions and the data obtained utilizing the simulations. Note that the physical location of the excitation source in the simulations differs from the experimental source location by a small shift azimuthally. Before we go further into excite and receive field studies, a note worth mentioning here is the strong coupling (high signal intensity near the source) observed between the excitation port and the phantom. This physical effect cannot be observed utilizing idealized current modeling. However, it is demonstrated here due the rigorous treatment of the excitation port (see §3) [19].

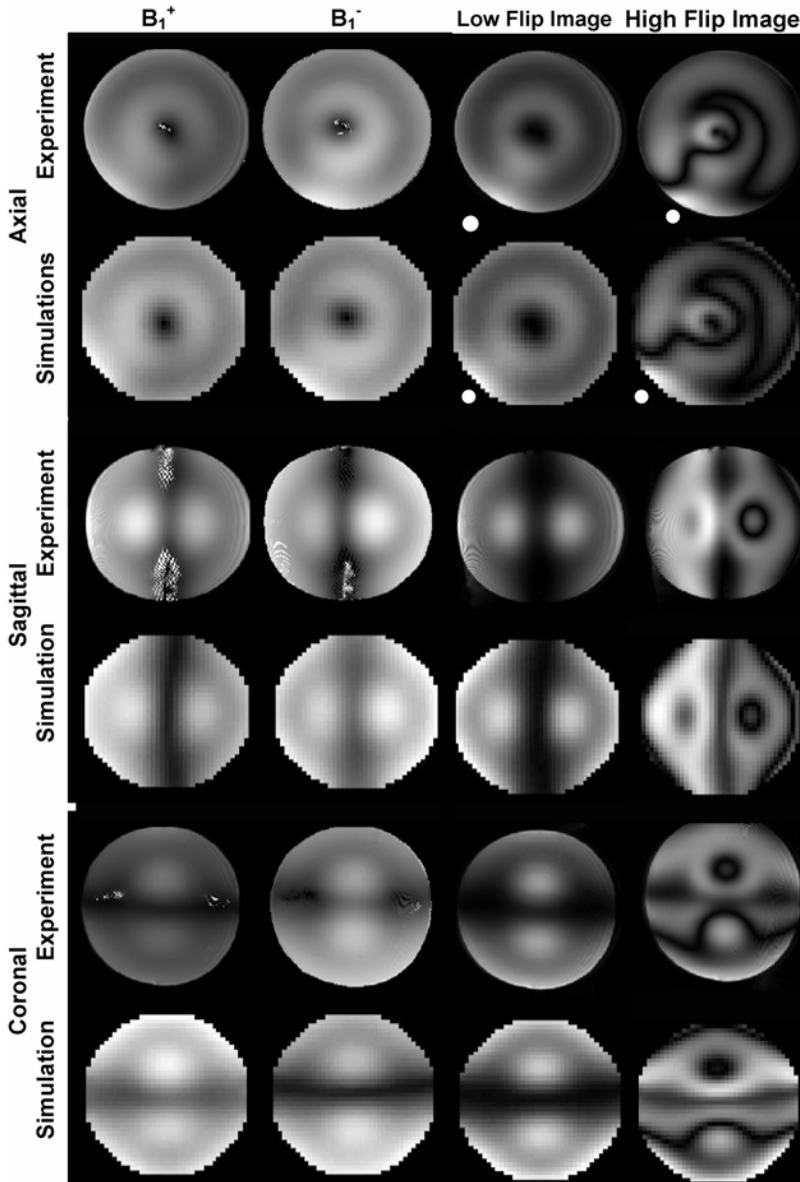


Figure 19. Axial, sagittal, and coronal, measured transmit (B_1^+) and receive (B_1^-) fields, low and high (154° near the center of the phantom) flip-angle images obtained at 8 T, and their corresponding simulated results obtained at 340 MHz using the FDTD model of mode 0 (first mode on the spectrum). The coil used was a 16-strut TEM resonator and the load utilized in the experiments and numerical modeling was an 18.5-cm-diameter sphere filled with 0.125 M NaCl. The solid white circle corresponds to the position of the excitation source. Adapted with permission from [19].

From the numerical analysis presented earlier with the single-strut coil, it is expected that with such a phantom size (sphere with a diameter of 18.5 cm), properties (dielectric constant = 78 and conductivity = 1.154 s/m), and operational frequency (340 MHz), the difference between the distributions of the H_1^- and B_1^+ fields will be significant for this experiment. This can clearly be observed in the axial slices. In addition, there is semi-symmetry in the distributions of the H_1^- and B_1^+ fields. The plane of symmetry is at a 45° angle with respect to any of the Cartesian axes, i.e., through the excitation source. Therefore, for low flip angle gradient echo images, where the signal is approximately linearly proportional to $(H_1^- \times B_1^+)$, it is expected that the axial images will be symmetric around the aforementioned plane, i.e., around the source location. As the flip angle increases, however, the fields can no longer be approximated by $(H_1^- \times B_1^+)$ and the semi-mirror symmetry of the H_1^- and B_1^+ fields will be overshadowed in the axial images since the gradient echo sine dependence can no longer be neglected. Consequently, the axial images will become asymmetric around the source location even for linear excitation, symmetric coil, symmetric load, and symmetric positioning of the excitation source. This can be verified from the 154° flip angle gradient echo axial image obtained numerically at 340 MHz and experimentally using the 8T magnet (Figure 19). Clearly, the symmetry around the excitation source is completely lost, and again, remarkable agreement is achieved between the experimental and the simulated results.

An interesting point arises upon analysis of the coronal and sagittal slices. With the given arrangement (45° from any of the Cartesian axes) and symmetric positioning of the excitation port as well as the azimuthally symmetric load, the corresponding mathematics suggest that at the center of the coil the B_1^+ field distribution for the coronal slice is linearly proportional to the H_1^- field distribution of the sagittal slice; similarly, the H_1^- field distribution for the coronal slice is linearly proportional to the B_1^+ field distribution of the sagittal slice. Therefore, both sagittal and coronal low flip angle gradient echo images are expected to be identical. This is clearly evident in Figure 19, where experimental and simulated coronal and sagittal 6° gradient echo images are shown. Note that there is a 90° rotation between the two slices to follow the conventional display of coronal and sagittal images. The small deviation in the experimental results is due to a small shift in source location. At high flip angles, the situation will be quite different — these gradient echo images (sagittal and coronal) will no longer have identical distributions since the sine dependence can no longer be neglected. This can clearly be verified in Figure 19, where 154° simulated and experimental coronal and sagittal slices are shown inside the spherical phantom. As can be shown, the distribution of the sagittal and coronal images are no longer similar.

Some key observations from this analysis are as follows. If the coil is excited in a linear fashion, the excitation port location is symmetric with respect to the load, and the load geometry is symmetric with respect to the excitation port, it is expected that:

- Low flip angle gradient echo images will be symmetric with respect to the excitation source
- High flip angle gradient echo images will be asymmetric with respect to the excitation source.

Under linear excitation and the conditions described above, if the load is azimuthally symmetric, it is expected that:

- The distribution of low flip angle gradient echo coronal and sagittal images will closely match.
- The distribution of high flip angle gradient echo coronal and sagittal images will differ considerably.

When imaging the head at ultra high field, the distributions of the H_1^- and B_1^+ fields are expected to be different. From this study [19] as well as other studies presented with surface coils [36], both the transmit and the receive fields must be optimized to achieve homogeneous and high signal-to-noise images. Therefore, it is imperative to design the transmitter and receiver coil(s) accordingly. In addition, it is also expected that the interactions between the excitation port and the coil load will dominate the distributions of these fields. This was apparent from both the simulations and the experiments, where the distributions of the H_1^- and B_1^+ fields were clearly distinct near the excitation port even for symmetrical loads such as a sphere.

5.4. Dielectric Resonances: Are they Dominant?

In early UHF MRI experiences at 8 T [61] it was demonstrated numerically and experimentally [24,54,71,72] that "... homogeneity at 8 Tesla is dominated by RF coil/head interactions and not by the presence of fundamental dielectric resonances" [24]. This is unlike what was originally perceived with early 4T experiments [73–78]. Since that time, the absence of fundamental dielectric resonances has been verified in numerical and experimental studies [79,80]. In this section, field inhomogeneity and the relative effects of "dielectric resonances" are analyzed within the context of UHF MRI. This is accomplished by calculating the electromagnetic fields inside spherical phantoms in the presence and absence of an RF coil. These calculations are then compared to gradient echo images. In the calculations, plane incident wave analysis is initially presented, followed by a full-wave FDTD study [24]. The section underscores the significance of electromagnetic interactions between the coil/drive-ports and the load compared to "dielectric resonances".

Analytical calculations for a plane wave excitation (the coil is not present) for an 18.5-cm diameter spherical water phantom are displayed in Figure 20a, where simulated low flip angle gradient echo image intensity ($B_1^+ \times B_1^-$) is presented. Note that when a plane wave excitation is utilized the coupling with the physical RF source is neglected. In Figure 20b a low flip angle gradient echo image of distilled water (dielectric constant 80, conductivity 0.029 S/m) in the same phantom is

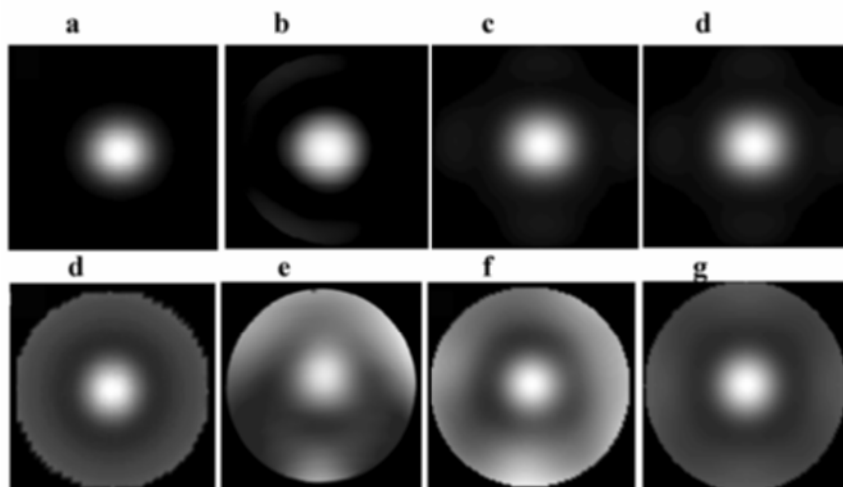


Figure 20. Computational (a,c,d,e,g,h) and experimental (b,f) studies of an 18.5-cm spherical phantom filled with either distilled water (a–d) or 0.125 M NaCl (e–h) at 340 MHz. GRE images (b,f) were obtained at low flip angles using an 8T scanner and a TEM resonator, which was operating under 2-port quadrature excitation. Images a (pure water) and e (0.125M NaCl) correspond to the electromagnetic simulated intensity images using a plane-wave excitation (the resonator is not present) for a low-flip-angle pulse exciting the 18.5-cm spherical phantoms. Images c (pure water) and g (0.125 M NaCl) correspond to low-flip-angle simulated images obtained using the FDTD model for the same resonator size, geometry, and excitation (2-port quadrature) as was used for the MRI images. Images d (pure water) and h (0.125 M NaCl) correspond to low-flip-angle simulated images obtained using the FDTD model for the same resonator size and geometry and using 4-port quadrature excitation. Adapted with permission from [24].

presented. The study was performed using a TEM resonator and two-port quadrature excitation. The distribution of image intensity shows clear dielectric focusing effects. A general agreement between the two images (Figure 20a,b) is apparent. Both images have a central bright region, but there are notable differences in the regions far from the center of the sphere. A concentric null is apparent surrounding the central brightness in both images, and a faint outer ring is present in both images. However, in Figure 20b, this faint outer ring is not perfectly uniform as in Figure 20a. This reflects the influence of the drive points in the MRI image. The general agreement between the two images (Figures 20a,b) is observed even though no RF coil was utilized in the analytical calculations, but detailed evaluation nonetheless reveals a minor influence of the RF coil/sample interaction. The FDTD-calculated low flip angle gradient image for the same spherical phantom is shown in Figure 20c. A TEM resonator with the same geometry and dimensions as used in Figure 20b was modeled for these calculations. The simulations were done using two-port quadrature excitation. The distribution in Figure 20c is near to that

obtained in Figure 20a,b, but the fields on the outer regions of the sphere more closely approximate the MRI image (Figure 20b) reflecting the minor RF coil/sample interaction. Therefore, it was concluded that the electromagnetic fields are dominated by the sample (distilled water phantom) and the presence of the coil has a minor effect on the MR image [24].

In Figure 20e an analytical result is presented for an 18.5-cm spherical filled with a 0.125 M NaCl (dielectric constant 78, conductivity 1.154 S/m) phantom. In this analytical treatment, the presence of the focusing effects is still evident, but it is reduced in intensity by more than an order of magnitude due to wave attenuation in the sample. This situation leads to somewhat more uniform images. Also, excellent circular symmetry still remains apparent in this result. In Figure 20f a low flip angle gradient echo image is presented for the same phantom loaded in the TEM resonator with two-port quadrature excitation at 8 T. It can be clearly seen that the azimuthal symmetry is not apparent in the experimental image. This is once again a result of RF coil/sample interactions. In the 0.125 M NaCl case and unlike the distilled water phantom, the experimental result clearly does not agree with the analytical treatment since, unlike the analytical treatment, the experimental results are dominated by the RF coil/sample interactions.

The FDTD-calculated low flip angle image in the 0.125 M NaCl spherical phantom is shown in Figure 20g, where circular symmetry is distorted. The experimental finding (Figure 20f) is nearly identical to the FDTD result (Figure 20g). Note that the locations of the excitation sources in Figure 20f,g differ by a small shift in azimuthal direction. The minor difference between these two images is likely due to experimental factors, which include difficulty in accurately tuning the loaded coil and in positioning the phantom exactly in the middle of the resonator. Conversely, the FDTD simulation involves perfectly symmetric sample/RF coil positioning and exact tuning situations, which could never be achieved experimentally. Nonetheless, it remains clear that the results in the 0.125 M NaCl phantom (Figure 20f,g) are dominated by the coupling between the RF coil/excitation source(s) and the sample. Unlike the distilled water phantom, this coupling dictates the distribution of the B_1^+ and B_1^- fields in the 0.125 M NaCl phantom as shown in the previous section [24].

Following this argument, increasing the number of excitation ports should have different effects on both of the phantoms, be negligible in the distilled water, and at this point unknown for the 0.125 M NaCl (since we do not know whether the drive ports and/or the RF coil is/are significantly affecting the field distribution). To examine the effect of 4-port excitation on the homogeneity of the image, the electromagnetic fields within the pure water and 0.125 M NaCl spherical phantoms were also calculated for this case. The mathematical resonator model used in these simulations was as before except operating under 4-port quadrature excitation. The 4-port excitation was implemented in the FDTD model by applying a progressive $\pi/2$ phase shift on each drive point. Figure 20d,h display the FDTD calculated low flip angle image distribution inside pure water (d) and inside 0.125 M NaCl (h) spherical phantoms using 4-port excitation. As expected, the simulated image dis-

tribution in the pure water case (Figure 20d) is almost identical to the distribution obtained using 2-port quadrature excitation (Figure 20c). Therefore, increasing the number of excitation ports would not significantly alter the B_1 field distribution. Unlike the case with the pure water phantom, the uniformity and symmetry of the image in the 0.125 M NaCl phantom significantly improves from 2-port (Figure 20g) to 4-port quadrature excitation (Figure 20h) [24].

This leads to several conclusions for head-sized loads at UHF MRI. First, for symmetric homogeneous loads, 4-port quadrature excitation reduces the load-resonator interactions, leading to more uniform circularly polarized components (transmit and receive) of B_1 fields when compared to conventional 2-port quadrature excitation [5,24]. Second, dielectric resonances are most strongly excited in objects similar in size to the human head when the conducting medium has a high dielectric constant and a low conductivity (unlike the head). It is concluded that in clinical UFH MRI the most important determinants of electromagnetic field behavior consist of (1) the RF coil design, (2) the interaction between the RF coil, the excitation source(s), and the sample, and finally (3) the geometry and electrical properties of the sample [24]. The fact that homogeneity at UHF MRI is dominated by RF coil/head interactions and not by the presence of fundamental dielectric resonances is very encouraging. The head simply has too high conductivity, too low geometrical symmetry, too low Q , and too great local inhomogeneity to significantly support such resonances. This is fortunate, for, had dielectric resonance fundamentally dominated this problem, UHF MRI for human [6,61,81] and for 11.1 T animal imaging [8] may have been unfeasible and not useful. However, since this is not the case, it is likely that as RF technology continues to improve with multiple transceiver and arrays [82–87], phased array excitation [5,22,86,88] (as will be seen in next section), matching materials [89] (as was used for animal imaging at 11.1T [89]), and different coil designs, high-quality head-size images are within reach at these field strengths.

5.5. Field Optimized Coils Using Phased Array Excitation Concepts: Whole-Slice and 2D/3D Localized Imaging

In the last section we have shown that “dielectric resonances” clearly do not dominate the fields at UHF MRI operation. We have also demonstrated numerically and experimentally the role of the drive port(s) (excitation source(s)/load interactions) on the field distributions for symmetrical phantoms. In this section we show how antenna-array excitation can be utilized to obtain homogeneous whole-slice images and further magnify the sensitivity of UHF MRI, through the use of 2D and 3D localization techniques that are solely based on electromagnetic theory.

Before UHF human MRI, many techniques for achieving field homogeneity or any specific type of field distribution within load (head/abdomen) have been studied [90–94]. Since all of these algorithms were proposed for low field imaging, incorporating the specific characteristics of the load into the design parameters of these methods was not needed and therefore was not implemented. The situation at UHF human MRI, however, is quite different, and the load has to be an integral

part of the coil design. To do that, let us first extend the study of the electromagnetic interactions to that between the excitation source(s) and biological (asymmetrical, irregular-shaped, and inhomogeneous) loads. Figure 21 displays sagittal slices of the SAR values at 340 MHz. The results are obtained using a 16-strut TEM resonator loaded with the 17-tissue human head mesh and under back (left), side (middle), and side (front) of the head 2-port quadrature excitation.

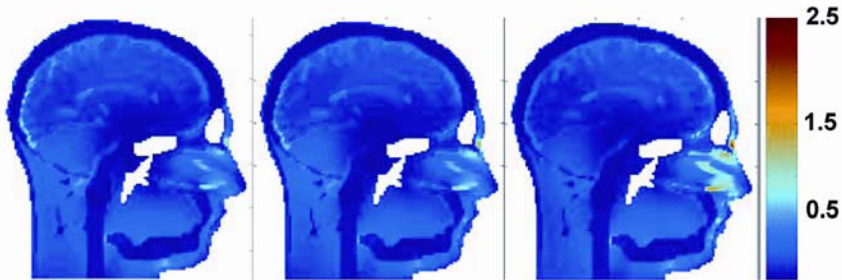


Figure 21. Sagittal slices of the SAR distribution inside the 17-tissue human head model at 340 MHz. The results are obtained using the FDTD model and utilizing a 16-strut TEM resonator operating under back (left), side (middle), and front (right) of the head 2-port quadrature excitation. The transmitted power is equal to 1 watt CW: a square pulse with a 100-Watt peak power, 5-ms width, and 500-ms time recovery. Adapted with permission from [23]. See attached CD for color version.

Due to localization and the irregular shape of the nose, complex electromagnetic interactions are expected between this structure and the coil in general and the excitation source(s) in particular. The 2-port head quadrature excitations reveal that the SAR peak values concentrated in the nose significantly increase from back excitation (exciting the 2 drive ports furthest from the nose) (left subfigure), to side excitation (exciting 2 drive ports, 1 of which is closest to the nose) (middle subfigure), to front excitation (exciting the 2 drive ports closest to the nose) (right subfigure). Thus, the SAR values are dominated by the interactions between the drive ports of the volume RF coil and the tissue [23]. These kinds of observations were new to MRI because of the new (higher) operating frequencies associated with UHF operation. On the other hand, these interactions have been intensely studied and utilized in designing hyperthermia systems [95–97]. Based on these interactions (biological load and excitation sources), multiport (or, in electromagnetic terms, “near-field antenna-array”) excitation can be viewed as a possible solution for achieving uniform/useful images.

Antenna-array excitation in MRI is based on the fact that for high-frequency operation and asymmetrical, inhomogeneous, and irregular shape loading, multiple fractions of phase shifts and fixed uniform amplitudes are not necessarily the required characteristics of the voltages driving the coil in order to obtain global ho-

mogeneous excitation. Combining this fact with the significant role of the drive ports demonstrated in this and in the previous two sections, volume and localized imaging with the same coil design could potentially be achieved through manipulation of these excitation sources. Achieving homogenous whole-slice excitation in UHF human imaging was proposed [5,22,98] and implemented numerically (on axial slices through the head) by varying the phases, or the phases and the amplitudes of the drive ports at 200 MHz (4.7 T) using 4-port excitation with a highpass birdcage coil [5] and at 340 MHz (8T) using 4- to 24-port excitation with a TEM resonator [22]. In recent years, several modifications have been introduced to MRI antenna-array excitation [99,100] as well as its experimental implementation [100].

To investigate the possibility of achieving homogeneous volume as well as localized imaging with the same coil, a 9.4T TEM head coil [101] and a 7T TEM body-coil [102] were numerically designed such that the coil was tuned to approx. 400 MHz for the human head case and 298 MHz for the human body case. As done before, the mathematical model of the coil was tuned while the coil was loaded with the human head/body mesh, in order to ensure that the calculations accurately account for the electromagnetic interactions between the coil, drive ports, and the sample. The coil struts (16 in the head-coil and 32 in the body-coil) were all driven using standard (uniform amplitude and progressive phase shifts) excitation, and RF-optimized (variable phase and variable amplitude) excitation to achieve whole-slice and 2D surface-localized (within whole-slice) coverage for 9.4T head imaging and whole-slice, and 3D volume-localized (to the human-heart) coverage for 7T abdominal imaging. The whole-slice and localized coverage were obtained using optimization algorithms that utilize phased array antennas and superposition theories. The whole-slice coverage criterion is to obtain the highest possible B_1^+ field homogeneity (lowest standard deviation) in a slice of interest. The main approach taken in the localized coverage is to use the nonuniform nature of the fields as an advantage rather than a disadvantage. In other words, relocate the high-intensity spots (which always exist with current RF coils in 9.4T head and 7T body imaging due to the nonuniformity of the B_1^+ field) to other regions of interest, or simply in electromagnetics terms, produce a strong and uniform B_1^+ field in a localized region. Interestingly enough, this approach requires significant inhomogeneity in the fields; as the load becomes electrically large and as the frequency of operation increases, the field inhomogeneities should increase. Two criteria were simultaneously implemented: (1) maximize the spin excitation in the region of interest, and (2) minimize the spin excitation everywhere else.

When compared to the standard uniform amplitude and progressive phase shifts excitation, Figure 22 demonstrates that for whole-slice homogenous coverage mechanism 2.25- and 3.5-fold improvement (in terms of the overall B_1^+ field homogeneity measured by the standard deviation) were obtained for axial and sagittal head slices at 9.4 T, and 4.5- and 11.75-fold improvement were obtained for the axial and sagittal body slices at 7 T. This technique has also shown that whole-slice homogenous coverage could be obtained over the entire volume of the head at 7 T [103]. As a result it is possible to obtain highly homogeneous UHF MRI images using this method. This has been recently verified through experimental implementation [80], and the preliminary results show excellent uniformity in axial

plementation [80], and the preliminary results show excellent uniformity in axial images at 7 and 9.4 T [88]. For the localized 2D coverage mechanism at 9.4 T, the results in these particular sagittal and axial slices demonstrate that the average flip angle in a surface area (16–24 cm²) could be on the order of 3 to 6 times higher than the average everywhere else in the respective slice. For the 3D heart localization mechanism, the average value of B_1^+ inside the heart over the average value of B_1^+ outside the heart and contained inside the rectangular volume shown in Figure 22 was 4 over 1. Ongoing work has shown that a focal excitation can be achieved in various localized regions that are enclosed within the resonator structure.

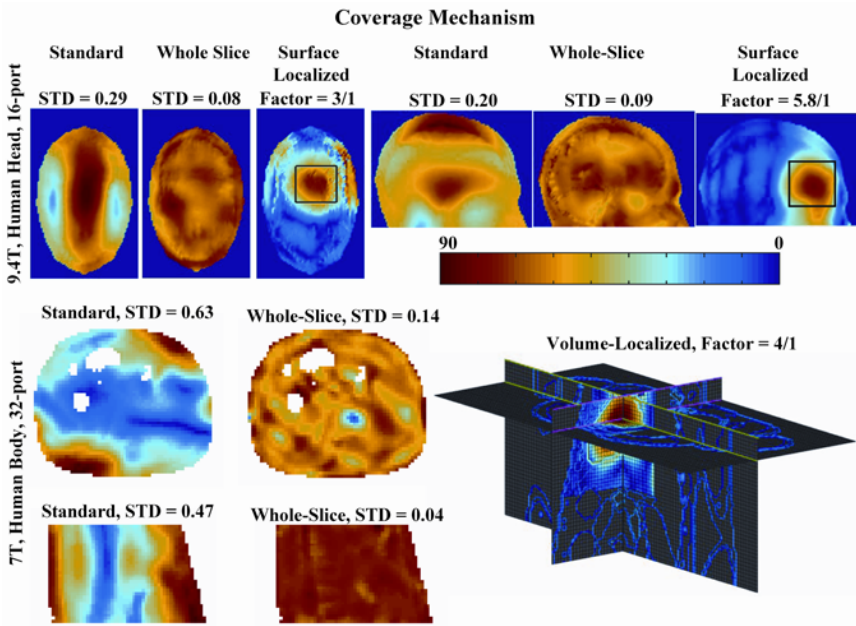


Figure 22. Top Set: Calculated B_1^+ field distribution for standard (uniform amplitude and progressive phase shifts) and RF optimized (whole-slice and 2D surface-localized within whole-slice) excitation for 9.4T head imaging. The electromagnetic simulations and optimizations were performed using a TEM-based head coil loaded with an anatomically detailed human head model and driven at all of its 16 possible ports. Bottom Set: Calculated B_1^+ field distribution for standard and RF optimized (whole-slice and 3D volume-localized to the human-heart) excitation for 7T abdominal imaging. Note that heart volume comprises 20% of the total volume through which the B_1^+ field is considered. The results were obtained utilizing a TEM-based body-coil model loaded with an anatomically detailed human body model. The coil was driven at all of its 32 possible ports. “STD” represents the standard deviation of the B_1^+ field distribution, and “Factor” in the “Surface Localized” case represents the average B_1^+ field intensity in the superficial region of interest over the average everywhere else in the slice. In the “Volume Localized” case, “Factor” represents the average B_1^+ field intensity in the heart over the average everywhere else in the chosen volume. See attached CD for color version.

The benefits of whole-slice homogenous MRI excitation are obvious: combined with slice-selective gradients, it is potentially possible to image the entire head if whole-slice homogenous excitation can be achieved across the whole-head volume. The localized approach is drastically different from using a surface coil since it achieves a predetermined accurate localization by redistributing the B_1^+ field to any deep structures in the head/body. Combined with RF tailored pulses by itself [104–107] and/or combined with multiple RF coils for transmit SENSE [108], this technique can reduce the number of spatial encoding steps to increase spatial resolution while maintaining a reasonable scanning time. With such a localized approach, a significant increase in the signal can be achieved for in-vivo studies for large animal and human head applications at UHF MRI and body applications at ≥ 3 Tesla. This in turn can have a significant impact on many applications such as fMRI, microscopy, and parallel imaging [85,86,109–113].

6. CONCLUDING REMARKS

The physical and technical issues associated with ultra high field MRI RF coils are complex and challenging, but as MRI history has proven, the milestones of this discipline are often, frequent, and usually a product of the integration of many fields. This chapter shows how the field of computational electromagnetics has become a vital foundation in not only understanding but also advancing ultra high field MRI.

7. REFERENCES

1. Hoult DI, Richard RE. 1976. The Signal to noise ratio of the nuclear magnetic resonance experiment. *J Magn Reson* **24**:71–85.
2. Gruetter R, Weisdorf SA, Rajanayagan V, Terpstra M, Merkle H, Truwit CL, Garwood M, Nyberg SL, Ugurbil K. 1998. Resolution improvements in vivo ^1H NMR spectra with increased magnetic field strength. *J Magn Reson* **135**:260–264.
3. Gati JS, Menon RS, Ugurbil K, Rutt BK. 1997. Experimental determination of the BOLD field strength dependence in vessels and tissue. *Magn Reson Med* **38**:296–302.
4. Robitaille PM, Abduljalil AM, Kangarlu A. 2000. Ultra high resolution imaging of the human head at 8 tesla: 2K x 2K for Y2K. *J Comput Assist Tomogr* **24**:2–8.
5. Ibrahim TS, Lee R, Baertlein BA, Kangarlu A, Robitaille PML. 2000. Application of finite difference time domain method for the design of birdcage RF head coils using multipoint excitations. *Magn Reson Imag* **18**:733–742.
6. Vaughan JT, Garwood M, Collins CM, Liu W, DelaBarre L, Adriany G, Andersen P, Merkle H, Goebel R, Smith MB, Ugurbil K. 2001. 7T vs. 4T: RF power, homogeneity, and signal-to-noise comparison in head images. *Magn Reson Med* **46**:24–30.
7. Wei Q, Liu F, Xia L, Crozier S. 2005. An object-oriented designed finite-difference time-domain simulator for electromagnetic analysis and design in MRI—applications to high field analyses. *J Magn Reson* **172**:222–230.

8. Beck BL, Jenkins K, Caserta J, Padgett K, Fitzsimmons J, Blackband SJ. 2004. Observation of significant signal voids in images of large biological samples at 11.1 T. *Magn Reson Med* **51**:1103–1107.
9. Hayes EC, Wdelstein WA, Schenck DF, Mueller OM, Eash M. 1985. An efficient highly homogeneous radiofrequency coil for whole-body NMR imaging at 1.5 T. *J Magn Reson* **63**:622–628.
10. Glover H, Hayes CE, Pelc NJ, Edelstein WA, Mueller OM, Hart HR, Hardy CJ, O'Donnell M, Barber WD. 1985. Comparison of linear and circular polarization for magnetic resonance imaging. *J Magn Reson* **64**:255–270.
11. Tropp J. 1989. The theory of the bird-cage resonator. *J Magn Reson* **82**:51–62.
12. Pascone RJ, Garcia BJ, Fitzgerald TM, Vullo T, Zipagan R, Cahill PT. 1991. Generalized electrical analysis of low-pass and high-pass birdcage resonators. *Magn Reson Imag* **9**:395–408.
13. Baertlein BA, Ozbay O, Ibrahim TS, Yu Y, Lee R, Kangarlu A, Robitaille PML. 2000. Theoretical model for an MRI radio frequency resonator. *IEEE Trans Biomed Eng* **47**:535–546.
14. Bogdanov G, Ludwig R. 2002. Coupled microstrip line transverse electromagnetic resonator model for high-field magnetic resonance imaging. *Magn Reson Med* **47**:579–593.
15. Han Y, Wright SM. 1993. Analysis of RF penetration effects in MRI using finite-difference time-domain method. *Proc Soc Magn Reson Med* 1327.
16. Vaughan JT, Hetherington HP, Otu JO, Pan JW, Pohost JM. 1994. High frequency volume coils for clinical NMR imaging and spectroscopy. *Magn Reson Med* **32**:206–218.
17. Robitaille PML. 1999. Black body and transverse electromagnetic resonators operating at 340 MHz: volume RF coils for ultra high field MRI. *J Comput Assist Tomogr* **23**:879–890.
18. Ibrahim TS, Kangarlu A, Chakeres DW. 2005. Design and performance issues of RF coils utilized in ultra high field MRI: experimental and numerical evaluations. *IEEE Bio Med Eng* **52**:1277–1284.
19. Ibrahim TS, Mitchell C, Lee R, Schmalbrock P, Chakeres DW. 2005. Perspective into the operation of RF coils from 1.5 to 11.7 Tesla. *Magn Reson Med* **54**:683–690.
20. Kangarlu A, Ibrahim TS, Shellock FG. 2005. Effects of coil dimensions and field polarization on RF heating inside a head phantom. *Magn Reson Imag* **23**:53–60.
21. Ibrahim TS, Abduljalil AM, Lee R, Baertlein BA, Robitaille PML. 2001. Analysis of B_1 field profiles and SAR values for multi-strut transverse electromagnetic RF coils in high field MRI application. *Phys Med Biol* **46**:2545–2555.
22. Ibrahim TS, Lee R, Baertlein BA, Robitaille PML. 2001. Effect of RF coil excitation on field inhomogeneity at ultra high fields: a field optimized TEM resonator. *Magn Reson Imag* **19**:1339–1347.
23. Ibrahim TS, Lee R, Abduljalil AM, Baertlein BA, Robitaille PML. 2001. Calculations of EM interactions with biological tissue: magnetic resonance imaging at ultra high field. *Appl Comput Electromagn* **16**:137–144.
24. Ibrahim TS, Lee R, Abduljalil AM, Baertlein BA, Robitaille PML. 2001. Dielectric resonances and B_1 field inhomogeneity in UHFMRI: computational analysis and experimental findings. *Magn Reson Imag* **19**:219–226.

25. Ibrahim TS. 2004. A numerical analysis of radiofrequency power requirements in magnetic resonance imaging experiments. *IEEE Trans Microwave Theory Tech* **52**:1999–2003.
26. Simunic D, Watch P, Renhart W, Stollberger R. 1996. Spatial distribution of high-frequency electromagnetic energy in human head during MRI: numerical results and measurements. *IEEE Trans Biomed Eng* **43**:87–94.
27. Collins CM, Li S, Smith MB. 1998. SAR and B_1 field distributions in a heterogeneous human head model within a birdcage coil: specific energy absorption rate. *Magn Reson Med* **40**:847–856.
28. Chen J, Feng Z, Jin JM. 1998. Numerical simulation of SAR and B_1 -field inhomogeneity of shielded RF coils loaded with the human head. *IEEE Trans Biomed Eng* **45**:650–659.
29. Gandhi OP, Chen XB. 1999. Specific absorption rates and induced current densities for an anatomy-based model of the human for exposure to time-varying magnetic fields of MRI. *Magn Reson Med* **41**:816–823.
30. Ibrahim TS, Lee R, Baertlein BA, Yu Y, Robitaille PML. 2000. Computational analysis of the high pass birdcage resonator: finite difference time domain simulations for high-field MRI. *Magn Reson Imag* **18**:835–843.
31. Ibrahim TS, Lee R, Baertlein BA, Robitaille PML. 2001. B_1 field homogeneity and SAR calculations in the high pass birdcage coil. *Phys Med Biol* **46**:609–619.
32. Collins CM, Smith MB, Turner R. 2004. Model of local temperature changes in brain upon functional activation. *J Appl Physiol* **97**:2051–2055.
33. Trakic A, Crozier S, Liu F. 2004. Numerical modelling of thermal effects in rats due to high-field magnetic resonance imaging (0.5–1 GHz). *Phys Med Biol* **49**:5547–5558.
34. Hand JW, Lau RW, Lagendijk JJ, Ling J, Burl M, Young IR. 1999. Electromagnetic and thermal modeling of SAR and temperature fields in tissue due to an RF decoupling coil. *Magn Reson Med* **42**: 183–192.
35. Cline H, Mallozzi R, Li Z, McKinnon G, Barber W. 2004. Radiofrequency power deposition utilizing thermal imaging. *Magn Reson Med* **51**:1129–1137.
36. Collins CM, Yang QX, Wang JH, Zhang X, Liu H, Michaeli S, Zhu X H, Adriany G, Vaughan JT, Anderson P, Merkle H, Ugurbil K, Smith MB, Chen W. 2002. Different excitation and reception distributions with a single-loop transmit-receive surface coil near a head-sized spherical phantom at 300 MHz. *Magn Reson Med* **47**:1026–1028.
37. Wang J, Yang QX, Zhang X, Collins CM, Smith MB, Zhu XH, Adriany G, Ugurbil K, Chen W. 2002. Polarization of the RF field in a human head at high field: a study with a quadrature surface coil at 7.0 T. *Magn Reson Med* **48**:362–369.
38. Ibrahim, TS, Mitchell C, Schmalbrock P, Chakeres DW. 2003. The TEM resonator modes: A study at high field MRI. *Proc Int Soc Magn Reson Med* 2553.
39. Ibrahim TS, Lee R. 2003. Specific absorption rate at 1.5T and 3T: a numerical study of the birdcage coil. *Proc Int Soc Magn Reson Med* 2602.
40. Ibrahim TS, Mitchell C, Schmalbrock P, Chakeres DW. 2004. Computational and experimental analysis of electromagnetic fields induced by RF coils for high field imaging. *Proc Int Soc Magn Reson Med* 488.
41. Yee KS. 1966. Numerical solutions of the initial boundary value problems involving Maxwell's equations in isotropic media. *IEEE Trans Ant Prop* **14**:302–317.
42. Taflove A, Hagness SC. 2000. Computational electrodynamics: the finite difference time domain method. Boston: Artech House.

43. Ibrahim TS. 2003. Design of radiofrequency coils for magnetic resonance imaging applications: a computational electromagnetic approach. PhD Dissertation. The Ohio State University, Columbus.
44. Ibrahim TS, Lee R. 2003. Effects of geometry, excitation and spatial positioning on the birdcage coil performance. *Proc Int Soc Magn Reson Med* 2518.
45. Tsuei, Y, Cangellaris AC, Prince JL. 1993. Rigorous electromagnetic modeling of chip-to-package (first-level) interconnections. *IEEE Trans Comp Hybrids Manuf* **16**:876–882.
46. Berenger JP. 1994. A perfectly matched layer for the absorption of electromagnetic waves. *J Comput Phys* **114**:185–200.
47. Gabriel C, Gabriel S. Compilation of dielectric properties of body tissues at RF and microwave frequencies. www.brooks.af.mil/AFRL/HED/hedr/reports/dielectric/Report/Report.html.
48. Insko EK, Bolinger L. 1993. Mapping of radiofrequency field. *J Magn Reson A* **103**:82–85.
49. Field S, Francon C. 1987. *Physics and technology of hyperthermia*. Boston: Martinus Nijhoff Publishers.
50. Butterworth EJ, Walsh EG, Hugg JW. 2001. A TiO₂ dielectric filled toroidal radio frequency cavity resonator for high-field NMR. *NMR Biomed* **14**:184–191.
51. Vaughan JT, Adriany G, Snyder CJ, Tian J, Thiel T, Bolinger L, Liu, H, DelaBarre L, Ugurbil K. 2004. Efficient high-frequency body coil for high-field MRI. *Magn Reson Med* **52**:851–859.
52. Baertlein BA, Ozbay O, Ibrahim TS, Yu Y, Lee R, Kangarlu A, Robitaille PML. 2002. Theoretical model for an MRI radio frequency resonator. *IEEE Trans Biomed Eng* **49**:495–496.
53. Ibrahim TS, Lee R. 2005. Evaluation of MRI RF probes utilizing infrared sensors. *IEEE Trans Biomed Eng*. In press.
54. Kangarlu A, Baertlein BA, Lee R, Ibrahim TS, Abduljalil AM, Yang L, Robitaille PML. 1999. Analysis of the dielectric resonance phenomenon in ultra high field magnetic resonance imaging. *J Comput Assist Tomogr* **26**:821–831.
55. Hoult DI, Lauterbur PC. 1979. The sensitivity of the zeumatographic experiment involving human samples. *J Magn Reson* **34**:425–433.
56. Bottomley PA, Redington RW, Edelstein WA, Schenck JF. 1985. Estimating radiofrequency power deposition in body NMR imaging. *Magn Reson Med* **2**:336–349.
57. Ibrahim TS, Lee R, Baertlein BA, Robitaille PML. 2001. Classical analysis of RF power requirements in MRI. *Proc Int Soc Magn Reson Med Eur Soc Magn Reson Med Biol* 1578.
58. Collins CM, Smith MB. 2001. Signal-to-noise ratio and absorbed power as functions of main magnetic field strength, and definition of "90 degrees" RF pulse for the head in the birdcage coil. *Magn Reson Med* **45**:684–691.
59. Robitaille PML, Abduljalil AM, Ibrahim TS, Baertlein BA, Lee R, Ashman C. 2001. A shielded single element TEM Resonator: a simple extremity RF coil for UHFMRI. *Proc Int Soc Magn Reson Med Eur Soc Magn Reson Med Biol* 1095.
60. Roschmann PK. 1988. High-frequency coil system for magnetic resonance imaging apparatus. US Patent 4,746,866.
61. Robitaille PML, Abduljalil AM, Kangarlu A, Zhang X, Yu Y, Burgess R, Bair S, Noa P, Yang L, Zhu H, Palmer B, Jiang Z, Chakeres DM, Spigos D. 1998. Human magnetic resonance imaging at 8 T. *NMR Biomed* **11**:263–265.

62. Ibrahim TS, Lee R, Baertlein BA, Yu Y, Robitaille PML. 1999. On the physical feasibility of achieving linear polarization at high-field: a study of the birdcage coil. *Proc Int Soc Magn Reson Med* 2058.
63. Edelstein WA, Glover GH, Hardy CJ, Redington RW. 1986. The intrinsic signal-to-noise ratio in NMR imaging. *Magn Reson Med* 3: 604–618.
64. Chen CN, Sank VJ, Cohen SM, Hoult DI. 1986. The field dependence of NMR imaging, I: laboratory assessment of signal-to-noise ratio and power deposition. *Magn Reson Med* 3:722–729.
65. Hoult DI. 2000. The principle of reciprocity in signal strength calculations: a mathematical guide. *Conc Magn Reson* 12:173–187.
66. Haacke EM, Brown RW, Thompson MR, Venkatesan R. 1999. *Magnetic resonance imaging: physical principles and sequence design*. New York: Wiley-Liss.
67. Ibrahim TS. 2005. Analytical approach to the MR signal. *Magn Reson Med* 54:677–682.
68. Abragam A. 1961. *The principles of nuclear magnetism*. London: Oxford UP.
69. Decker AJ. 1965. *Solid state physics*. London: MacMillan.
70. Balanis CA. 1989. *Advanced engineering electromagnetics*. New York: John Wiley and Sons.
71. Ibrahim TS, Lee R, Baertlein BA, Kangarlu A, Robitaille PML. 2000. Dielectric resonance in ultra high field MRI. *Proc Int Soc Magn Reson Med* 1681.
72. Ibrahim TS, Lee R, Baertlein BA, Kangarlu A, Robitaille PML. 2000. The effect of tissue–coil electromagnetic interactions on field inhomogeneity: study at high field MRI. *Proc Eur Soc Magn Reson Med Biol* 237.
73. Bomsdorf H, Helzel T, Kunz D, Roschmann P, Tschendel O, Wieland J. 1998. Spectroscopy and imaging with a 4 tesla whole-body MR system. *NMR Biomed* 1:151–158.
74. Roschmann P. 1987. Radiofrequency penetration and absorption in the human body: limitations to high-field whole-body nuclear magnetic resonance imaging. *Med Phys* 14:922–931.
75. Barfuss H, Fischer H, Hentschel D, Ladebeck R, Oppelt A, Wittig R, Duerr W, Oppelt R. 1990. In vivo magnetic resonance imaging and spectroscopy of humans with a 4 T whole-body magnet. *NMR Biomed* 3:31–45.
76. Ugurbil K, Garwood M, Ellermann J, Hendrich K, Hinke R, Hu X, Kim SG, Menon R, Merkle H, Ogawa S. 1993. Imaging at high magnetic fields: initial experiences at 4 T. *Magn Reson Q* 9:259–277.
77. Jin JM, Chen J, Chew WC, Gan H, Magin RL, Dimbylow PJ. 1996. Computation of electromagnetic fields for high-frequency magnetic resonance imaging applications. *Phys Med Biol* 41:2719–2738.
78. Singerman RW, Denison TJ, Wen H, Balaban RS. 1997. Simulation of B_1 field distribution and intrinsic signal-to-noise in cardiac MRI as a function of static magnetic field. *J Magn Reson* 125:72–83.
79. Collins CM, Liu W, Schreiber W, Yang QX, Smith MB. 2005. Central brightening due to constructive interference with, without, and despite dielectric resonance. *J Magn Reson Imag* 21:192–196.
80. Van deMoortele PF, Adriany G, Akgun C, Moeller S, Ritter J, Vaughan JT, Ugurbil K. 2005. B_1 phase spatial pattern at 7 Tesla: impact on b_1 inhomogeneities with a head transceiver. *Proc Int Soc Magn Reson Med* 2748.
81. Hoge R, Wiggins W, Wiggins G, Triantafyllou CD, Potthast A, Wald L. 2004. High spatial resolution functional imaging of perfusion and BOLD contrast in humans at 7 Tesla. *Proc Int Soc Magn Reson Med* 1015.

82. Porter JR, Wright SM. 2001. A sixteen-channel multiplexing upgrade for single channel receivers. *Magn Reson Imag* **19**:1009–1016.
83. Bankson JA, Wright SM. 2001. Multi-channel magnetic resonance spectroscopy through time domain multiplexing. *Magn Reson Imag* **19**:1001–1008.
84. Bankson JA, Griswold MA, Wright SM, Sodickson DK. 2000. SMASH imaging with an eight element multiplexed RF coil array. *MAGMA* **10**:93–104.
85. Lee RF, Hardy CJ, Sodickson DK, Bottomley PA. 2004. Lumped-element planar strip array (LPSA) for parallel MRI. *Magn Reson Med* **51**:172–183.
86. Hoult DI, Kolansky G, Kripiakevich D, King SB. 2004. The NMR multi-transmit phased array: a Cartesian feedback approach. *J Magn Reson* **171**:64–70.
87. Lee RF, Westgate CR, Weiss RG, Newman DC, Bottomley PA. 2001. Planar strip array (PSA) for MRI. *Magn Reson Med* **45**:673–683.
88. Vaughan JT. 2005. How to do RF at high fields: human MRI and MRS at high static magnetic fields. *Proc Int Soc Magn Reson Med*. In press.
89. Caserta J, Beck BL, Fitzsimmons JR. 2004. Reduction of wave phenomena in high-field MRI experiments using absorbing layers. *J Magn Reson* **169**:187–195.
90. Tincher M, Meger CR, Gupta R, Williams DM. 1993. Polynomial modeling and reduction of RF body coil spatial inhomogeneity in MRI. *IEEE Trans Med Imag* **12**: 361–365.
91. Li S, Collins CM, Dardzinski BJ, Chin CL, Smith MB. 1997. A method to create an optimum current distribution and homogeneous B_1 field for elliptical birdcage coils. *Magn Reson Med* **37**:600–608.
92. Forbes LK, Crozier S, Doddrell DM. 1987. An analysis and optimization of RF probes used in magnetic resonance imaging. *Meas Sci Techn* **7**:1281–1290.
93. Ocali O, Atalar E. 1998. Ultimate intrinsic signal-to-noise ratio in MRI. *Magn Reson Med* **39**:462–473.
94. Riauka TA, Zanche NF, Thompson R, Vermeulen FE, Capjack CE, Allen PS. 1999. A numerical approach to non-circular birdcage RF coil optimization: verification with a fourth-order coil. *Magn Reson Med* **41**:1180–1188.
95. Chen JY, Gandhi OP. 1992. Numerical Simulation of annular-phased arrays of dipoles for hyperthermia of deep-seated tumors. *IEEE Trans Biomed Eng* **39**:209–216.
96. Dimbylow PJ, Gandhi OP. 1991. Finite-difference time-domain calculations of SAR in a realistic heterogeneous model of the head for plane-wave exposure from 600 MHz to 3 GHz. *Phys Med Biol* **36**:1075–1089.
97. Zhu XL, Gandhi OP. 1988. Design of RF needle applicators for optimum SAR distributions in irregularly shaped tumors. *IEEE Trans Biomed Eng* **35**:382–388.
98. Hoult DI. 2000. Sensitivity and power deposition in a high-field imaging experiment. *J Magn Reson Imag* **12**:46–67.
99. Lee RF, Foresto CM. 2004. A Focused MRI with Coupled Phased Array at 7T. *Proc Int Soc Magn Reson Med* 34.
100. Adriany G, VandeMoortele PF, Wiesinger F, Moeller S, Strupp JP, Andersen P, Snyder C, Zhang X, Chen W, Pruessmann KP, Boesiger P, Vaughan T, Ugurbil K. 2005. Transmit and receive transmission line arrays for 7 Tesla parallel imaging. *Magn Reson Med* **53**:434–445.
101. Ibrahim TS. 2005. RF selective excitation for localized imaging at 9.4 Tesla. *Proc Int Soc Magn Reson Med* 890.
102. Ibrahim TS, Abraham R, Abraham D. 2005. Optimized whole-body RF coil for imaging applications at 7 Tesla. *Proc Int Soc Magn Reson Med* 820.

103. Ibrahim TS. 2005. Homogenous distributions of RF fields over the human head volume at 7 Tesla. *Proc Int Soc Magn Reson Med* 2752.
104. Pauly JM, Hu BS, Wang SJ, Nishimura DG, Macovski A. 1993. A three-dimensional spin-echo or inversion pulse. *Magn Reson Med* **29**:2–6.
105. Conolly S, Pauly J, Nishimura D, Macovski A. 1992. Two-dimensional selective adiabatic pulses. *Magn Reson Med* **24**:302–313.
106. Carlson JW, Kramer DM. 1990. Rapid radiofrequency calibration in mri. *Magn Reson Med* **15**:437–445.
107. Davies NP, Jezzard P. 2005. Calibration of gradient propagation delays for accurate two-dimensional radiofrequency pulses. *Magn Reson Med* **53**:231–236.
108. Katscher U, Bornert P, Leussler C, van denBrink JS. 2003. Transmit SENSE. *Magn Reson Med* **49**:144–150.
109. Sodickson DK, McKenzie CA, Ohliger MA, Yeh EN, Price MD. 2002. Recent advances in image reconstruction, coil sensitivity calibration, and coil array design for SMASH and generalized parallel MRI. *MAGMA* **13**:157–163.
110. Sodickson DK, McKenzie CA. 2001. A generalized approach to parallel magnetic resonance imaging. *Med Phys* **28**:1629–1643.
111. Wiesinger F, Van deMoortele PF, Adriany G, De Zanche N, Ugurbil K, Pruessmann KP. 2004. Parallel imaging performance as a function of field strength: an experimental investigation using electrodynamic scaling. *Magn Reson Med* **52**:953–964.
112. Wiesinger F, Boesiger P, Pruessmann KP. 2004. Electrodynamics and ultimate SNR in parallel MR imaging. *Magn Reson Med* **52**:376–390.
113. Pruessmann KP, Weiger M, Scheidegger MB, Boesiger P. 1999. SENSE: sensitivity encoding for fast MRI. *Magn Reson Med* **42**:952–962.

RADIOFREQUENCY FIELD CALCULATIONS FOR HIGH FIELD MRI

Christopher M. Collins

*The Pennsylvania State University
College of Medicine, Hershey*

In MRI, increasing radiofrequency magnetic (B_1) field frequency is a consequence of employing higher static magnetic (B_0) field strengths in the drive to improve signal-to-noise ratio (SNR). Due to the direct proportionality between B_0 field strength and B_1 field frequency in MRI, B_1 field distributions become more complex at higher B_0 fields due in part to shorter wavelengths and penetration depths. Consequently, it becomes both more difficult to calculate RF field behavior and more important to do so accurately for high-field MRI. In this chapter the basics of electromagnetic properties of tissue, the method of radiofrequency field calculation currently most prevalent in high-field MRI (the FDTD method), and methods for relating calculation results to MRI are covered briefly before results from calculations are used to discuss current challenges in high-field MRI including central brightening, SNR, power absorption by tissue, and image homogeneity.

1. INTRODUCTION

Calculations of radiofrequency (RF) fields have been valuable throughout the history of MRI for purposes including RF coil design, evaluation of safety, and prediction and interpretation of experimental results.

In MRI, increasing RF magnetic (B_1) field frequency is a consequence of employing higher static magnetic (B_0) field strengths in the drive to improve signal-to-noise ratio (SNR). Due to the direct proportionality between B_0 field strength and B_1 field frequency in MRI, B_1 field distributions become more complex at higher B_0 fields due in part to shorter wavelengths and penetration depths. Consequently, it becomes both more difficult to calculate RF field behavior and more important to do so accurately for high-field MRI.

2. ELECTROMAGNETIC PROPERTIES OF TISSUE AS FUNCTIONS OF B_1 FREQUENCY

Although relative magnetic susceptibility, μ_r , is a major cause of B_0 field perturbations in MRI leading to both artifacts and detection of important physiological information [1], its effect on the B_1 fields is negligible compared to those of relative electrical permittivity (ϵ_r) and electrical conductivity (σ). While the perturbations of the magnetic field caused by μ_r of normal tissues is on the order of 10^{-6} times the applied field, at the radiofrequencies used in MRI today the perturbations of the B_1 fields caused by ϵ_r and σ of normal tissues in the human body can easily be on the order of 10^{-1} times the applied field.

An oscillating magnetic field B_1 will induce an oscillating electrical field E_1 with a necessarily different spatial distribution and orientation. In tissue this field will both (1) cause conduction currents (roughly in proportion to tissue σ times local E_1 at the frequency of interest) resulting in electromagnetic energy lost to the tissue in the form of heat and in concomitant field attenuation, and (2) induce further oscillating magnetic fields that may propagate further into the tissue (roughly in proportion to ϵ_r at the frequency of interest). These effects of attenuation and propagation are coupled in a complex manner to each other, and their net effect also depends largely on the source of the fields and the morphology of the tissue to which the fields are applied.

The properties ϵ_r and σ in tissue are both functions of frequency and are related to each other. An electrical field will induce translational motion of charged particles and rotational motion of dipolar molecules, resulting in an electrical current. This current is related to the applied field by the value of σ . If the electrical field is applied for a long enough time, or varies at a low enough frequency, many of the charges will accumulate at boundaries such as cell membranes and many of the dipolar molecules will become fully aligned with the applied field. As this occurs the electrical current decreases and the polarization field in the sample increases. The polarization field is related to the electrical field by the value of ϵ_r . As the frequency of oscillation of the electrical field increases, fewer of the charged particles and dipoles will be able to reach their fully “relaxed” — or aligned — state in a single cycle, and more of them will be in motion throughout the cycle. Thus, in general tissue σ increases and tissue ϵ_r decreases with increasing B_1 frequency.

In the past two decades the high end of frequencies used in MRI of the human head has increased from 64 to 340 MHz. In this frequency range human tissues are generally neither good conductors nor good dielectric materials, and both ϵ_r and σ must be considered in the calculation of either electromagnetic wavelength (λ) or penetration depth [2]. Here penetration depth (δ) is defined as the distance along the direction of propagation at which fields in a plane wave traveling within a material are attenuated to e^{-1} times (or roughly 37% of) their value at the reference location. While simple plane waves are not found in MRI, the concepts of both wavelength and penetration depth can be used to explain behavior of B_1 fields and their corresponding electrical (E_1) fields. Although tissue relative electrical permit-

tivities generally decrease while tissue electrical conductivities increase with B_1 frequency, the effect of frequency itself on wavelength is seen to override that of decreasing permittivity. Thus, both electrical wavelength and penetration depth decrease with an increase in B_1 frequency.

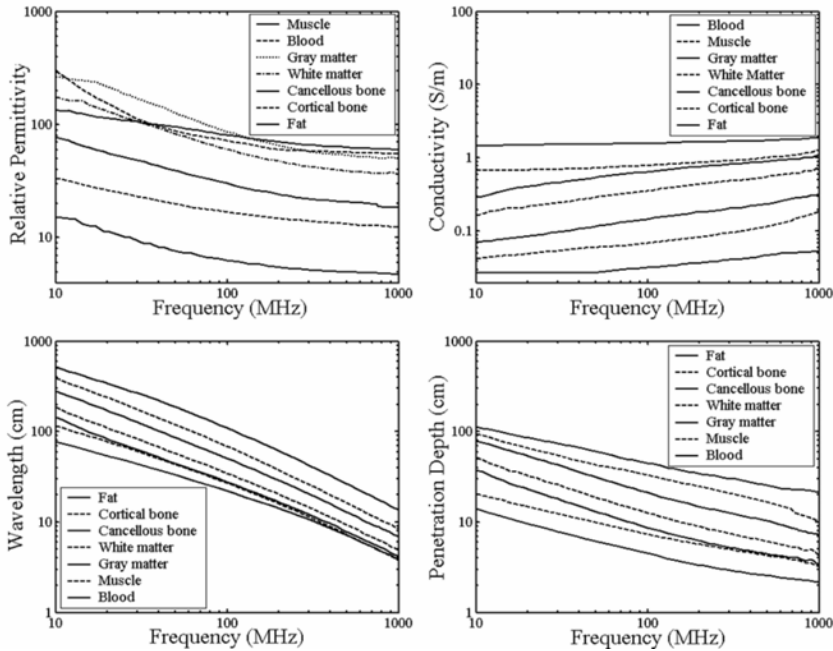


Figure 1. Relative electrical permittivity (top left), electrical conductivity (top right), wavelength (bottom left), and penetration depth (bottom right) plotted as functions of frequency for several different tissues. Tissues are listed in each legend in order from highest to lowest of the respective value plotted at 1000 MHz. Experimentally measured data from Gabriel [3].

In Figure 1 the values of ϵ_r , σ , λ , and δ are plotted as functions of B_1 frequency for several tissue types. Generally, tissues with high water content have a shorter wavelength and a shorter penetration depth than do tissues with a lower water content, with as much as an order of magnitude difference between them at a given frequency. This is because much of the permittivity and conductivity in tissues comes from processes such as the rotational motion of water dipoles until they are aligned with the E_1 field and the translational motion of ions as discussed previously [4].

3. NUMERICAL RF FIELD CALCULATIONS: THE FDTD METHOD

Because the wavelengths and penetration depths are significantly shorter in human tissue than in air and are as short as dimensions of the human body at high field, it is necessary to consider the effects of the body in predicting RF field behavior. Because there is great disparity in electrical properties among different tissues and these tissues are arranged in a very complex manner in the human body, it is not possible to make highly accurate predictions of field behavior in human subjects using simple shapes and analytical methods. Nonetheless, analytical methods of calculation are still found to be very valuable for simulations of RF fields for high-field MRI in many cases today [5,6], and will doubtlessly continue to be of value in the future.

Although many different types of numerical methods have been used in calculations of RF fields in simple shapes for MRI, one method has become the favorite for models of the human body in recent years. The attribute of the Finite Difference Time Domain (FDTD) method that makes it attractive is its capacity for calculations considering very complex, heterogeneous objects using relatively little memory and requiring a relatively short time. This section is devoted to describing briefly in very basic terms how this is accomplished with the FDTD method. More thorough descriptions are available [7,8], including different formulations for frequency-dependent materials [9].

Maxwell's curl equations can be written as

$$\begin{aligned}\frac{\partial \mathbf{B}}{\partial t} &= -\nabla \times \mathbf{E}, \\ \frac{\partial \epsilon \mathbf{E}}{\partial t} &= -\sigma \mathbf{E} + \frac{\nabla \times \mathbf{B}}{\mu},\end{aligned}\tag{1}$$

where \mathbf{B} is magnetic induction, \mathbf{E} is electrical field, t is time, σ is electrical conductivity, ϵ is electrical permittivity ($\epsilon = \epsilon_r \epsilon_0$), and μ is magnetic permeability (for the purposes of this chapter, μ in all materials is equal to that of air). In the FDTD method these equations are discretized and written in a form suitable for solution with a computer. An initial condition of no fields anywhere in space is assumed [7], and then the fields induced by known excitations are calculated at consecutive future points in time.

3.1. Maxwell's Divergence Relations Satisfied

It can be shown that Maxwell's divergence relations are satisfied by these curl equations when the initial condition of no fields existing anywhere in space is used. Consider the divergence of the first of Maxwell's curl equations in Eq. (1):

$$\begin{aligned} \nabla \bullet \frac{\partial \mathbf{B}}{\partial t} &= -\nabla \bullet \nabla \times \mathbf{E}, \\ \frac{\partial}{\partial t}(\nabla \bullet \mathbf{B}) &= 0, \\ \nabla \bullet \mathbf{B} &= \text{constant}. \end{aligned} \tag{2}$$

So if the divergence of \mathbf{B} is equal to zero initially (all fields everywhere are set to zero initially in the FDTD method), then it is equal to zero at all times, and Maxwell’s second divergence relation ($\nabla \bullet \mathbf{B}=0$) is satisfied. Likewise, consider the divergence of the second curl equation:

$$\begin{aligned} \nabla \bullet \frac{\partial \epsilon \mathbf{E}}{\partial t} &= -\nabla \bullet \sigma \mathbf{E} + \nabla \bullet \frac{\nabla \times \mathbf{B}}{\mu}, \\ \frac{\partial}{\partial t}(\nabla \bullet \mathbf{D}) &= -\nabla \bullet \mathbf{J} + 0, \end{aligned} \tag{3}$$

where $\mathbf{D} = \epsilon \mathbf{E}$ and $\mathbf{J} = \sigma \mathbf{E}$ is the current density. For continuity to exist,

$$\nabla \bullet \mathbf{J} = -\frac{\partial \rho}{\partial t}, \tag{4}$$

where ρ is the charge density. Now

$$\begin{aligned} \frac{\partial}{\partial t}(\nabla \bullet \mathbf{D} - \rho) &= 0, \\ \nabla \bullet \mathbf{D} - \rho &= \text{constant}. \end{aligned} \tag{5}$$

Again, because initially all fields are set equal to zero with most implementations of the FDTD method [7], this constant is equal to zero. This will satisfy Maxwell’s first divergence relation ($\nabla \bullet \mathbf{D}=\rho$).

3.2. Discretizing Maxwell’s Curl Equations for Solution by Computer

Rewriting them with their component vectors in Cartesian coordinates and replacing the cross product with its definition, Maxwell’s curl equations become

$$\begin{aligned} \frac{\partial}{\partial t}(B_x \mathbf{i} + B_y \mathbf{j} + B_z \mathbf{k}) = \\ - \left[\left(\frac{\partial E_z}{\partial y} - \frac{\partial E_y}{\partial z} \right) \mathbf{i} + \left(\frac{\partial E_x}{\partial z} - \frac{\partial E_z}{\partial x} \right) \mathbf{j} + \left(\frac{\partial E_y}{\partial x} - \frac{\partial E_x}{\partial y} \right) \mathbf{k} \right], \end{aligned} \quad (6)$$

$$\begin{aligned} \frac{\partial}{\partial t} \epsilon(E_x \mathbf{i} + E_y \mathbf{j} + E_z \mathbf{k}) = -\sigma(E_x \mathbf{i} + E_y \mathbf{j} + E_z \mathbf{k}) \\ + \frac{1}{\mu} \left[\left(\frac{\partial B_z}{\partial y} - \frac{\partial B_y}{\partial z} \right) \mathbf{i} + \left(\frac{\partial B_x}{\partial z} - \frac{\partial B_z}{\partial x} \right) \mathbf{j} + \left(\frac{\partial B_y}{\partial x} - \frac{\partial B_x}{\partial y} \right) \mathbf{k} \right]. \end{aligned}$$

where subscripts x , y , and z denote components in their respective directions, and \mathbf{i} , \mathbf{j} , and \mathbf{k} are unit vectors in those three orthogonal directions. These two vector equations can now each be broken into three equations with no vectors: one for each orthogonal direction. The result is six simpler equations.

$$\begin{aligned} \frac{\partial}{\partial t} B_x &= - \left(\frac{\partial E_z}{\partial y} - \frac{\partial E_y}{\partial z} \right), \\ \frac{\partial}{\partial t} B_y &= - \left(\frac{\partial E_x}{\partial z} - \frac{\partial E_z}{\partial x} \right), \\ \frac{\partial}{\partial t} B_z &= - \left(\frac{\partial E_y}{\partial x} - \frac{\partial E_x}{\partial y} \right), \\ \frac{\partial}{\partial t} \epsilon E_x &= -\sigma E_x + \frac{1}{\mu} \left(\frac{\partial B_z}{\partial y} - \frac{\partial B_y}{\partial z} \right), \\ \frac{\partial}{\partial t} \epsilon E_y &= -\sigma E_y + \frac{1}{\mu} \left(\frac{\partial B_x}{\partial z} - \frac{\partial B_z}{\partial x} \right), \\ \frac{\partial}{\partial t} \epsilon E_z &= -\sigma E_z + \frac{1}{\mu} \left(\frac{\partial B_y}{\partial x} - \frac{\partial B_x}{\partial y} \right). \end{aligned} \quad (7)$$

The finite-difference time-domain method utilizes a 3D grid in space and takes finite steps forward in time. For a grid with constant spacing in the x , y , and z directions, an example of a finite-difference approximation for the first partial derivative of E_z with respect to y at time step n and position (i, j, k) could be written

$$\frac{\partial E_z}{\partial y} = \frac{E_z(i, j+1, k, n) - E_z(i, j-1, k, n)}{2\Delta_y}, \quad (8)$$

where i , j , and k are indices for position on the 3D grid in the x , y , and z directions, n indicates the time step, and Δ_y is the grid spacing in the y -direction. Similarly, an

example of a finite-difference approximation for the first derivative of B_x with respect to t at time step n and position (i, j, k) could be written

$$\frac{\partial B_x}{\partial t} = \frac{B_x(i, j, k, n+1) - B_x(i, j, k, n-1)}{2\Delta_t} \tag{9}$$

Substituting such finite-difference approximations into the first and fourth of Eqs. (7) would yield

$$\frac{B_x(i, j, k, n+1) - B_x(i, j, k, n-1)}{2\Delta_t} = \frac{E_z(i, j+1, k, n) - E_z(i, j-1, k, n)}{2\Delta_y} - \frac{E_y(i, j, k+1, n) - E_y(i, j, k-1, n)}{2\Delta_z}, \tag{10}$$

and

$$\frac{\varepsilon E_x(i, j, k, n+1) - \varepsilon E_x(i, j, k, n-1)}{2\Delta_t} = -\sigma E_x(i, j, k, n) + \frac{1}{\mu} \left(\frac{B_z(i, j+1, k, n) - B_z(i, j-1, k, n)}{2\Delta_y} - \frac{B_y(i, j, k+1, n) - B_y(i, j, k-1, n)}{2\Delta_z} \right). \tag{11}$$

The values for ε and σ used in the equations above are those at location (i, j, k) in the 3D mesh. The value of μ throughout space is assumed to be that of free space. If the fields are known in all space at time steps n and $n - 1$, these equations are easily solved for B_x and E_x at all (i, j, k) at time step $n + 1$. The other four of Eqs. (7) yield $B_y, B_z, E_y,$ and E_z at all (i, j, k) at time step $n + 1$ just as easily. If initially all fields are set equal to zero in all space (and are assumed to have been zero at all times previous to $t = 0$), and then at each subsequent time step the electric fields at the voltage sources are set appropriately and the resulting fields in the entire problem region are calculated with finite-difference approximations, in theory the fields in the entire problem region can be calculated for any future point in time, provided that the grid spacings and steps forward in time are small enough to ensure stability and accuracy, and the computer resources necessary to complete the calculation in a reasonable amount of time are available.

In essence, the equations developed above are sufficient to explain how finite-difference approximations can be used to solve Maxwell’s equations in the time domain. The equations actually solved in FDTD calculations require a little more explanation because the reference points for the various field components are strategically staggered in space and time in order to increase the accuracy of the finite difference approximations. Figure 2 depicts a three-dimensional representation of the relative placement of the reference points in a “Yee cell” mesh arrangement [10].

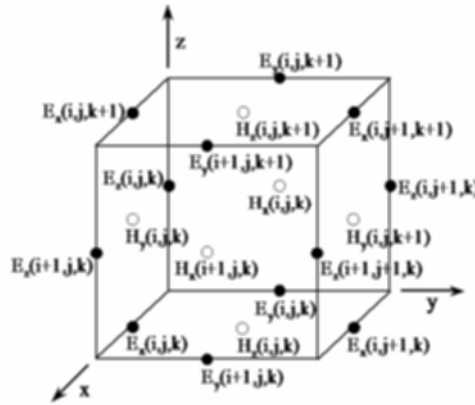


Figure 2. Diagram of a Yee cell cube showing how reference points for **E** and **H** fields are staggered relative to each other to improve accuracy in central difference approximations.

Reference points for electric and magnetic field components are strategically offset from each other by one half of a grid spacing in all three directions. Reference points for electric and magnetic fields are also offset from each other by half a step in time. This allows for smaller distances, and thus greater accuracy, in finite-difference approximations of spatial and temporal derivatives. Now Eqs. (10)–(11) become

$$\frac{B_x(i, j, k, n + \frac{1}{2}) - B_x(i, j, k, n - \frac{1}{2})}{\Delta_t} = \frac{E_z(i, j + 1, k, n) - E_z(i, j, k, n)}{\Delta_y} - \frac{E_y(i, j, k + 1, n) - E_y(i, j, k, n)}{\Delta_z}, \tag{12}$$

and

$$\frac{\varepsilon E_x(i, j, k, n + 1) - \varepsilon E_x(i, j, k, n)}{\Delta_t} = -\sigma E_x(i, j, k, n) + \frac{1}{\mu} \left(\frac{B_z(i, j, k, n + \frac{1}{2}) - B_z(i, j - 1, k, n + \frac{1}{2})}{\Delta_y} - \frac{B_y(i, j, k, n + \frac{1}{2}) - B_y(i, j, k - 1, n + \frac{1}{2})}{\Delta_z} \right). \tag{13}$$

In essence these equations and four others (identical except for component orientations) are used at each time step n and $n - 1/2$, where all quantities are known, to

find all magnetic field components (B_x , B_y , and B_z) at time step $n + 1/2$, which are then used to find all electric field components (E_x , E_y , E_z) at time step $n + 1$. There is only one unknown in each equation at each point in space, and thus no matrix operations or simultaneous solution of equations are necessary. Again, assuming all field component magnitudes are zero at time steps $n = 0$ and $n = -1/2$, it is possible to step forward in time with an arbitrary excitation (pre-defined voltages at specific locations as a function of time) and solve for the fields in the problem region at all future points in time.

3.3. Stability and Accuracy

The general conditions for stability of a 1D, 2D, and 3D FDTD problem, respectively, are

$$\begin{aligned} \Delta_t &\leq \Delta_x / c, \\ \Delta_t &\leq \left(c \sqrt{\frac{1}{(\Delta_x)^2} + \frac{1}{(\Delta_y)^2}} \right)^{-1}, \\ \Delta_t &\leq \left(c \sqrt{\frac{1}{(\Delta_x)^2} + \frac{1}{(\Delta_y)^2} + \frac{1}{(\Delta_z)^2}} \right)^{-1}. \end{aligned} \tag{14}$$

While rigorous mathematical proofs of these relationships are available, it is intuitive to expect that the size of the time step can not be so large that electromagnetic energy (traveling at the speed of light, c) will travel across more than one lattice plane in a time step. What is meant by a lattice plane is easily seen in a 2D grid (see Figure 3).

The length, d , of segment BD is easily found after realizing that triangles ABC and CDB are both right triangles that share angle BCD. Therefore, the sine of this angle is equal for both triangles and

$$\begin{aligned} \frac{d}{\Delta_y} &= \frac{\Delta_x}{\sqrt{\Delta_y^2 + \Delta_x^2}}, \\ d^2 &= \frac{\Delta_y^2 \Delta_x^2}{\Delta_y^2 + \Delta_x^2} = \left(\frac{1}{(\Delta_x)^2} + \frac{1}{(\Delta_y)^2} \right)^{-1}, \\ d &= \left(\sqrt{\frac{1}{(\Delta_x)^2} + \frac{1}{(\Delta_y)^2}} \right)^{-1}. \end{aligned} \tag{15}$$

This shows, in principle, the fundamental limit for stability in the FDTD method. A rigorous mathematical proof for the general 3D case is described by Taflove and Hagness [8].

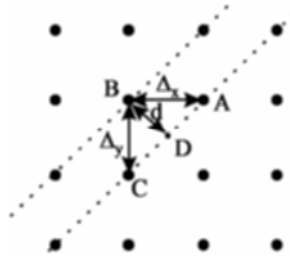


Figure 3. Diagram showing relationship between Δ_x , Δ_y , and the distance, d , between FDTD lattice planes in a 2D grid.

The central difference approximations in space and time used in the FDTD method are called “second-order accurate.” What this means for practical purposes is that the error of one approximation is proportional to the square of Δ_x or Δ_t . Given the condition for stability described above, if Δ_x , Δ_y , and Δ_z in a 3D problem are all decreased proportionally, Δ_t should be decreased by the same factor. Thus the accuracy of an FDTD calculation is controlled primarily by decreasing the grid spacing. The proportionality of the error to the square of Δ_x is seen by considering a plane waveform u with wave number k and amplitude A described by

$$u = Ae^{ikx}. \tag{16}$$

The exact first derivative with respect to x of this will be

$$\begin{aligned} \frac{du}{dx} &= ikAe^{ikx}, \\ \frac{du}{dx} &= iku. \end{aligned} \tag{17}$$

The central difference approximation as used in the FDTD method, with the staggered reference points for **B** and **E** fields, would be

$$\begin{aligned} \frac{\Delta_u}{\Delta_x} &= \frac{Ae^{ik(x+\Delta_x/2)} - Ae^{ik(x-\Delta_x/2)}}{\Delta_x}, \\ \frac{\Delta_u}{\Delta_x} &= Ae^{ikx} \frac{e^{ik(\Delta_x/2)} - e^{ik(-\Delta_x/2)}}{\Delta_x}, \\ \frac{\Delta_u}{\Delta_x} &= u \frac{i2 \sin(k\Delta_x/2)}{\Delta_x}. \end{aligned} \tag{18}$$

For small Δ_x we can approximate $\sin(k\Delta_x/2) = k\Delta_x/2$, and this result becomes iku , as in the exact differential. To determine the error of this estimation we can expand $\sin(k\Delta_x/2)$ in a Taylor series to get

$$\frac{\Delta_u}{\Delta_x} = \frac{i2u}{\Delta_x} \left[\frac{k\Delta_x/2}{1!} - \frac{(k\Delta_x/2)^3}{3!} + \frac{(k\Delta_x/2)^5}{5!} - \dots \right]$$

$$\frac{\Delta_u}{\Delta_x} = iku \left[1 - \frac{(k\Delta_x)^2}{24} + \frac{(k\Delta_x)^4}{1920} - \dots \right]$$
(19)

So the first term in the error of the approximation is proportional to the square of Δ_x . For an entire FDTD calculation, where several million to a few billion such approximations are carried out, some accumulated error would be expected.

A rule of thumb often used to ensure accurate calculations is to have the grid spacing be less than or equal to about 0.1 times the smallest wavelength. Then, in Eq. (19), $k = 0.1/\Delta_x$ or smaller. In calculations with accurate representations of the human body at MRI frequencies used today, Δ_x (typically 5 mm or less) is almost always much less than 0.1λ (Figure 1).

3.4. Outer Boundary Conditions for the FDTD Method

In the formulation for FDTD given thus far it is assumed that each point in the problem region will be surrounded by points also in the problem region. In most cases, the speed of light times the duration of the problem being solved will be many times the dimensions of the problem region, and thus there will be fields to be calculated at the ends of the problem region where the reference points are not surrounded by others. Thus special formulations have been developed for use in these areas.

Although the objects typically simulated for MRI — namely coils, shields, and samples — are in practice surrounded by many highly conductive objects including gradient coils, the static magnet casing, and the magnet room RF screen, most simulations for MRI today include the use of an absorbing boundary condition. This type of boundary condition is designed to have the effect of allowing electromagnetic fields at the boundary to behave as they would if the problem region were infinitely large and RF fields could be radiated into free space. In some methods, such as the Mur [11] and Liao [12] boundary conditions, this is accomplished by examination of the fields at interior points in the 3D grid and predicting from them how the fields at the boundaries would behave if the fields at the interior points were allowed to propagate through the boundary. In the popular perfectly matched layer (PML) boundary condition [13], the appearance of the problem region being surrounded by free space is accomplished by the addition of extra layers of cells outside the boundary that have special rules allowing, ideally, all fields that enter the layers to be absorbed in entirety, with no energy reflected back into the problem region. Although this is easily stated in words, in order for boundary conditions to function effectively they must attempt to allow for the possibility that the fields at the interior points may come from any combination of waves traveling in any combination of many possible directions and potentially having many different frequencies. The theoretical development and implementation of boundary condi-

tions typically used today is many times more complicated than the development of the algorithm for finding field values at interior points and description of these boundary conditions is not possible within this chapter, but many excellent references are available [7,8].

Although some researchers prefer some boundary conditions over others for various reasons regarding accuracy or speed, the differences in accuracy are less relevant for MRI applications compared to some others considering, again, that the RF coil, shield, and sample are not surrounded by an infinite amount of free space but are in close proximity to large amounts of highly conductive materials. In some recent calculations for a human being in a body coil at 128 MHz, it was found that simulations including the metallic inner bore of the magnet casing and a perfect electrically conducting (PEC) boundary shortly beyond that yielded results similar to those considering the entire magnet room and outer RF screen [14], although this result may differ for different situations including, for example, less lossy loads and higher frequencies. A PEC boundary can be implemented by merely keeping the electrical fields at the boundary of the problem region and tangential to the boundary plane equal to zero at all times [8].

3.5. Modeling Three-Dimensional Objects with Yee Cells

The tissue electrical properties (σ and ϵ) used in Eq. (13) are those associated with $E_x(i,j,k)$. Thus, the equation could be rewritten as follows:

$$\frac{\epsilon_x(i,j,k)E_x(i,j,k,n+1) - \epsilon_x(i,j,k)E_x(i,j,k,n)}{\Delta_t} = -\sigma_x(i,j,k)E_x(i,j,k,n) + \frac{1}{\mu} \left(\frac{B_z(i,j+1,k,n+\frac{1}{2}) - B_z(i,j,k,n+\frac{1}{2})}{\Delta_y} - \frac{B_y(i,j,k+1,n+\frac{1}{2}) - B_y(i,j,k,n+\frac{1}{2})}{\Delta_z} \right) \quad (20)$$

Different electrical properties can be associated with each mesh location (i,j,k) and orientation ($x, y, \text{ or } z$). While this can allow for modeling of anisotropic materials, that topic is not of importance in this work except for methods of modeling coils to be discussed shortly. In general, anisotropy of tissue electrical properties is limited to frequencies below those typically used in MRI.

Examination of Figure 2 shows that there are twelve “edges” or “mesh elements” of a “Yee cell cube” [7], each being associated with a different electrical field value and thus a different material property assignment. For the Yee cell cube shown in the figure, the associated material parameters are

$$\begin{aligned}
&\sigma_x(i,j,k), \varepsilon_x(i,j,k), \\
&\sigma_x(i,j,k+1), \varepsilon_x(i,j,k+1), \\
&\sigma_x(i,j+1,k+1), \varepsilon_x(i,j+1,k+1), \\
&\sigma_x(i,j+1,k), \varepsilon_x(i,j+1,k), \\
\\
&\sigma_y(i,j,k), \varepsilon_y(i,j,k), \\
&\sigma_y(i,j,k+1), \varepsilon_y(i,j,k+1), \\
&\sigma_y(i+1,j,k+1), \varepsilon_y(i+1,j,k+1), \\
&\sigma_y(i+1,j,k), \varepsilon_y(i+1,j,k), \\
\\
&\sigma_z(i,j,k), \varepsilon_z(i,j,k), \\
&\sigma_z(i,j+1,k), \varepsilon_z(i,j+1,k), \\
&\sigma_z(i+1,j+1,k), \varepsilon_z(i+1,j+1,k), \\
&\sigma_z(i+1,j,k), \varepsilon_z(i+1,j,k).
\end{aligned}$$

Generally, in creating models of large-volume three-dimensional objects, such as the human body, for use with the finite-difference time-domain method, it is useful to use the Yee cell cube as the fundamental unit. When property assignments are made to whole cubes at a time there will be no single mesh elements like short, thin wires extending into free space that might confound the location of the object boundary. For Yee cell cubes not at a boundary, each element is shared by four Yee cell cubes. With this approach, what properties a given mesh element will have in the final model is determined by the order in which the Yee cell cubes it is shared by were assigned electrical properties.

3.6. Modeling RF Coils with the FDTD Method

The most common exceptions to the rule of modeling objects by assigning properties to entire Yee cell cubes at a time is when thin wires (approximately one-dimensional objects) are modeled by assigning properties only to elements connected end to end in the orientation of the wire, or when thin conductive plates (approximately two-dimensional objects) are modeled by assigning properties only to elements in the plane of conduction. It is also possible to model capacitors as single elements of a dielectric material, or model the dielectric material in a coaxial conductor by using only elements oriented in the radial direction: the principal orientation of the electrical fields [15].

Coils are generally modeled by using these techniques to place conductive materials in all the appropriate places, with gaps filled with a dielectric material at the locations of capacitors or dielectric objects. Coil models can then be driven in either of two broad categories.

If it can be assumed that the voltages or currents in the coil are fairly predictable, the resulting voltages across or currents through each capacitor can be calculated beforehand and the appropriate result (including both magnitude and phase) can be implemented across each capacitive gap in the coil by placement of a voltage or current source. Here this method will be referred to as modeling coils in an

“idealized” fashion. This method has proven to be in good agreement with experiment in a head-sized birdcage coil up to at least 128 MHz [16], and in a head-sized surface coil up to at least 300 MHz [17]. Because it is not necessary to “tune” the coil model, the first excitation can be with sources varying sinusoidally at the frequency of interest, and the first simulation is often the final one. Coil models assuming a particular current pattern over a range of frequencies have proven valuable in examining trends with frequency and field behavior in the sample for general types of coils using many different numerical and analytical techniques [5,6,18–20].

Alternatively, if it is desired to model a particular coil and driving configuration, or to examine the resonance characteristics of various modes, it is also possible to simulate the coil by modeling the desired capacitors across each gap and placing voltage sources only in the locations as in experiment. When this is done, the coil must be properly tuned, as in experiment, before calculations at the desired frequency can be performed. If desired, it is also possible to match the coil model to a 50-Ohm source, but this is generally unnecessary for examinations of field patterns. Tuning of the coil model is typically accomplished by first exciting with an impulse-type (such as a Gaussian pulse) excitation, then performing a Fourier transform of the resulting time-domain fields at some location in the coil to identify the frequency of the desired resonant mode, then making adjustments to capacitor values or rod lengths, etc., as would be done to tune the coil in experiment, before repeating the process. Note that the Gaussian pulse typically used in FDTD simulations is not RF modulated, as a Gaussian pulse in an MRI sequence typically is. It is also possible to use an idealized excitation to determine the capacitors necessary to tune the coil in a noniterative manner [21]. Once the coil is tuned, either a sinusoidal excitation at the desired frequency can be applied and resulting field entities at specific points in time can be recorded, or, in some cases [22], another impulse-type excitation is applied and a Fourier transform is performed on the time-domain response of all fields in the problem region and magnitude and phase information at the desired frequency or frequencies is extracted. A model of a surface coil complete with capacitors with the FDTD method and compared to experiment was presented by Han and Wright [23]. Models of birdcage coils complete with capacitors have been demonstrated by several authors using various numerical methods [24–29]. Models of TEM coils with coaxial elements as in experiment have also been demonstrated using the FDTD method [15,30].

4. RELATING FIELD CALCULATION RESULTS TO MRI

With the FDTD method it is possible to generate vast quantities of data, only some of which is relevant for a given MR experiment. To extract the pertinent results and relate them to the MR experiment requires some forethought and manipulation.

4.1. Signal, Noise, and SNR

In recent years MRI in humans has been performed with B_0 field strength ranging from less than 0.1 Tesla to upwards of 8 Tesla, requiring B_1 field frequencies (ν) from less than 5 MHz to upwards of 340 MHz. Even at 128 MHz, λ within tissues is on the order of the dimensions of the human body and quasistatic approximations used to describe the relationships between Signal-to-Noise Ratio (SNR) or dissipated power and B_0 at lower frequencies begin to lose relevance. Here we will examine the relationship between B_0 and SNR, which requires consideration of power deposition as a function of B_0 . We will also briefly address related topics such as safety considerations of power deposition and relation of “radiated” RF power to SNR.

Although this chapter is designated primarily for discussion of high-field MRI, appreciation of why trends in SNR at high field may differ from those at lower field strengths requires understanding of the mechanisms for trends in lower field regimes. Thus, in this section, a systematic review of expected trends in SNR in low-field, mid-field, and high-field regimes is presented.

In examining the relationship between B_0 and SNR, we will assume for simplicity that many factors are held constant as we increase B_0 , including the RF coil and sample size and geometry. Of course, in practice these factors can vary with B_0 , the imaging system being used, and the experiment being performed. While T_1 and T_2^* dependence on B_0 and related SNR and contrast-to-noise ratio changes for various imaging parameters are also very important topics, they are beyond the scope of this chapter.

4.1.1. Signal as a Function of B_0 Strength

In considering signal strength, we will include four B_0 -dependent terms, each of which is directly proportional to SNR.

Bulk magnetization proportional to B_0

While each nuclear spin is aligned either with or against \mathbf{B}_0 (emboldened to indicate a vector quantity), the number of spins aligned with \mathbf{B}_0 (N^\uparrow) versus the number of spins aligned against \mathbf{B}_0 (N^\downarrow) follows a Boltzmann distribution so that

$$\frac{N^\downarrow}{N^\uparrow} = e^{\left(\frac{-\Delta E}{kT}\right)}, \quad (21)$$

where ΔE is the difference between energy levels of the two spin states, k is Boltzmann’s constant (1.38×10^{-23} J/K), and T is the absolute temperature of the spin system. Since ΔE in our case is equal to $\gamma\hbar B_0$, $\Delta E \ll kT$ for in vivo MRI and after some work [31] we can write

$$N^{\uparrow} - N^{\downarrow} \approx N_s \left(\frac{\gamma \hbar B_0}{2kT} \right), \quad (22)$$

where N_s is the total number of spins. Because the bulk magnetization is proportional to $N^{\uparrow} - N^{\downarrow}$, the available signal strength is proportional to B_0 . Here γ is the gyromagnetic ratio (2.675×10^8 radians/s/Tesla for ^1H MRI) and \hbar is Planck's constant divided by 2π (1.055×10^{-34} Js).

Detectable signal strength proportional to $\sin(\gamma V B_1^+ \tau)$

Using pulse-based MR imaging techniques, the signal detected is proportional to the magnitude of the transverse component of the bulk magnetization after application of an RF excitation pulse, or proportional to the sine of the flip angle α , where for a rectangular pulse $\alpha = \gamma V B_1^+ \tau$. Here B_1^+ is used to indicate the magnitude of the transverse circularly polarized component of the B_1 field that rotates in the direction of nuclear precession when the coil has a driven current of 1 Amp, V is a dimensionless normalization factor proportional to the coil current during the excitation pulse, and τ is the duration of the rectangular pulse. At high B_0 field strengths and corresponding high B_1 field frequencies, RF wavelengths affect the B_1^+ distribution in the human body and local B_1^+ is dependent on B_0 . At low B_0 , where λ is much greater than the dimensions of the human body this dependence can typically be ignored.

Signal induced in coil proportional to v_L

According to Faraday's Law,

$$\oint \mathbf{E} \cdot d\vec{l} = - \frac{d}{dt} \int \mathbf{B} \cdot d\vec{s}, \quad (23)$$

the magnitude of electrical field \mathbf{E} induced on a closed loop is proportional to the time rate of change of the net magnetic flux passing through the loop. In the case where the magnetic flux is caused by the transverse component of the nuclear spins in the sample, the time rate of change is proportional to the frequency of nuclear precession, $v_L = \gamma B_0 / 2\pi$. When the closed loop is any loop of wire in the coil, \mathbf{E} can result in an electrical current and detected signal.

Signal induced in coil is proportional to coil receptivity, B_1^- , at location of spins

By argument of reciprocity, the magnitude of the current induced in the coil by the precessing nuclei is proportional to the magnitude of the pertinent magnetic field component produced by the coil when the coil is driven with 1 Amp. It turns out that this pertinent field component is the one that precesses in the direction *opposite* that of precession, or B_1^- [17,32–34]. This relationship is most easily demonstrated by application of the principle of reciprocity to a quadrature coil through a quadrature splitter-combiner. Figure 4 illustrates the workings of a quadrature

ature splitter-combiner in normal use during transmission and reception during MRI. Simple mathematical formulae and diagrams are provided to illustrate the necessity for the $\lambda/4$ delay to be on the opposite channel during reception than it is during transmission. To apply the principle of reciprocity, we consider the field created when we apply a current at the receive (Rx) channel of the splitter-combiner. Figure 5 illustrates that this will produce a field rotating in the direction opposite precession. A full mathematical demonstration of the relationship between coil receptivity and B_1^- from basic physical principles and applicable to linear and quadrature coils has been published recently [34]. Just as the B_1^+ distribution at high ν and short λ is a function of B_0 strength, so is the B_1^- distribution.

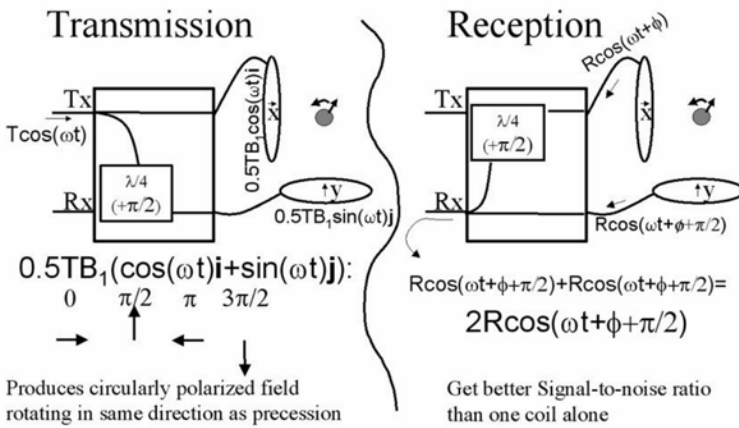


Figure 4. Quadrature splitter-combiner under normal usage during transmission (left) and reception (right).

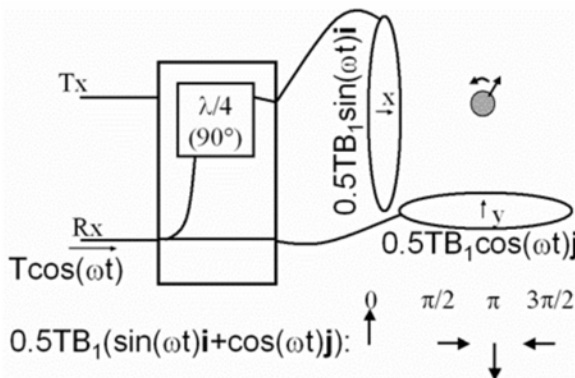


Figure 5. Application of reciprocity — transmission through receive channel of splitter-combiner results in field rotating in direction opposite precession.

Bringing it all together

Signal strength at one location can now be expressed as

$$V_{\text{signal}} \propto B_0 v_L \sin(\gamma V B_1^+ \tau) B_1^- \quad (24)$$

It can also be valuable to add a tissue signal weighting factor, W , so that

$$V_{\text{signal}} \propto W B_0 v_L \sin(\gamma V B_1^+ \tau) B_1^- \quad (25)$$

To be accurate, W could potentially contain information about tissue T_1 , T_2 and proton density, sequence TE and TR, B_0 inhomogeneities, blood flow, and a host of other factors. Later in this chapter some examples where W is proportional to water content will be presented.

Calculating B_1^+ and B_1^-

In the case of a single-channel coil, B_1^+ and B_1^- can be calculated as

$$B_1^+ = \left| \left(\hat{B}_x + i \hat{B}_y \right) \div 2 \right|, \quad (26)$$

and

$$B_1^- = \left| \left(\hat{B}_x - i \hat{B}_y \right)^* \div 2 \right|, \quad (27)$$

where \hat{B}_x and \hat{B}_y are complex values as denoted with a circumflex, i is the imaginary unit, the asterisk indicates the complex conjugate, and imaginary components are 90° out of phase with real components at the frequency of interest. In practice with the FDTD method and a sinusoidal excitation, \hat{B}_x and \hat{B}_y can be constructed with magnetic field values recorded at two different times 90° out of phase with each other at the frequency of interest. With this method the value recorded at the earlier time point becomes the imaginary component and the value recorded at the later time point becomes the real component. Whether it is B_1^+ or B_1^- that is the component that rotates in the direction of nuclear precession and thus induces the flip angle depends on whether the B_0 field is oriented with or against the z -axis. In this chapter it is assumed that B_1^+ rotates in the direction of nuclear precession and is thus the flip-inducing component. For a coil driven in quadrature it is necessary to calculate B_1^+ and B_1^- from two separate field calculations: the first with the driving voltages as if to create counterclockwise rotating field and the second as to create a clockwise rotating field.

4.1.2. Noise as a Function of B_0 Strength

The thermal motion of charges and dipoles in the coil and sample can create or induce currents in the RF coil. To utilize Nyquist's equation for thermal noise [35] measured at the coil terminals, $V_{\text{noise}} = \sqrt{4kT\Delta\nu R}$ (where $\Delta\nu$ equates to receiver

bandwidth in MRI), it is necessary to find effective resistance values for both the coil and sample, R_{coil} and R_{sample} . Knowing that the dissipated power P is equal to the square of the coil current I times the resistance R ($P = I^2R$), we can say that $R \propto P$, defining P as the dissipated power when $I = 1$ Amp. Note that we are again using an argument based on reciprocity — calculating power lost when the coil is driven to indicate noise voltage induced in the coil by thermal motion at the location of power loss. Treating the coil and sample as two resistors in series we can say

$$V_{\text{noise}} \propto \sqrt{4kT_{\text{coil}}\Delta vP_{\text{coil}} + 4kT_{\text{sample}}\Delta vP_{\text{sample}}} \tag{28}$$

To proceed further requires analysis of P_{coil} and P_{sample} as functions of B_0 . This analysis requires different degrees of rigor depending again on ν and the presence or absence of appreciable wavelength effects in the sample.

4.1.3. SNR at Low-Field

At low B_0 , B_1^+ , and B_1^- distributions are relatively independent of B_0 because electromagnetic wavelengths at the RF frequency ν are very long compared to sample dimensions. Thus, in expressing SNR dependence on B_0 we can eliminate the B_1^+ and B_1^- related terms in the expression for V_{signal} above and express SNR as

$$\begin{aligned} \frac{V_{\text{signal}}}{V_{\text{noise}}} &\propto \frac{B_0 \nu_L}{\sqrt{4kT_{\text{coil}}\Delta vP_{\text{coil}} + 4kT_{\text{sample}}\Delta vP_{\text{sample}}}} \\ &\propto \frac{B_0^2}{\sqrt{4kT_{\text{coil}}\Delta vP_{\text{coil}} + 4kT_{\text{sample}}\Delta vP_{\text{sample}}}} \end{aligned} \tag{29}$$

Dependence of P_{coil} on B_0 at low field

Alternating electrical current in a good conductor tends to flow along the outer surface of the conductor. The exact current distribution depends on the shape of the conductor, as well as the electromagnetic fields around it [36–38], but for a round wire we can approximate the cross-sectional area across which the current flows as $2\pi\rho\delta$, where ρ is the wire radius and δ is the penetration depth. For a good conductor,

$$\delta = \sqrt{\frac{2}{2\pi\nu\mu_c\sigma_c}}m, \tag{30}$$

where μ_c and σ_c are the magnetic permeability and electrical conductivity of the conductor. Since wire resistance $R \approx \text{Length}/(\sigma_c 2\pi\rho\delta) \propto \nu^{1/2}$ and $P = (1 \text{ Amp})^2R$, we find $P_{\text{coil}} \propto \nu^{1/2} \propto B_0^{1/2}$.

Dependence of P_{sample} on B_0 at low field

Referring to Faraday's Law in time-harmonic form,

$$\oint_1 \mathbf{E} \cdot d\vec{l} = -i2\pi\nu \int_s \mathbf{B} \cdot d\vec{s} \quad (31)$$

(where i is the imaginary unit) we see that for a B field independent of ν (approximately the case at low field), $E \propto \nu$. Since at each location $P = \sigma E^2$, the integrated power dissipated throughout the sample is $P_{\text{sample}} \propto \nu^2 \propto B_0^2$.

Coil noise dominance as $B_0 \rightarrow 0$

Allowing all of the B_0 -independent experiment-specific factors (e.g., coil and sample geometries and temperatures) that determine the exact relationship between P and B_0 to be absorbed into factors a and b , we can now write [39]

$$\frac{V_{\text{signal}}}{V_{\text{noise}}} \propto \frac{B_0^2}{\sqrt{aB_0^{1/2} + bB_0^2}} \quad (32)$$

As B_0 approaches zero, $aB_0^{1/2}$ (the contribution from coil noise) will become much greater than bB_0^2 (the contribution from sample noise), indicating that the noise will be dominated by the contribution of the coil. Thus, in the low-field limit we can expect [40]

$$\frac{V_{\text{signal}}}{V_{\text{noise}}} \propto \frac{B_0^2}{\sqrt{aB_0^{1/2}}} \propto B_0^{7/4} \quad (33)$$

4.1.4. SNR in the Mid-Field Regime

Assuming use of well-designed coils, the contribution of sample noise becomes dominant as B_0 is increased above only a fraction of 1 Tesla, depending on the coil being used and the anatomy being imaged in MRI of humans. If we say that wavelength effects don't really become important until B_0 is at least 1.5 Tesla in imaging of humans, then in the region in between we can say [41]

$$\frac{V_{\text{signal}}}{V_{\text{noise}}} \propto \frac{B_0^2}{\sqrt{bB_0^2}} \propto B_0 \quad (34)$$

4.1.5. SNR in High-Field MRI

In high-field MRI, sample noise is still dominant, but the B_1 field distribution varies with ν , precluding use of quasistatic assumptions and approximations for B_1^+ ,

B_1^- , and P_{sample} appropriate in low- and mid-field MRI and forcing expression of SNR at a single location as [42]

$$\frac{V_{\text{signal}}}{V_{\text{noise}}} \propto \frac{B_0 \omega_L \sin(\gamma V B_1^+ \tau) B_1^-}{\sqrt{4kT_{\text{sample}} \Delta v P_{\text{sample}}}} \propto \frac{B_0^2 \sin(\gamma V B_1^+ \tau) B_1^-}{\sqrt{P_{\text{sample}}}}. \tag{35}$$

Since in MRI we are typically interested not in a single location, but in a three-dimensional volume, it is often more appropriate to use an expression such as [5,20]

$$\frac{V_{\text{signal}}}{V_{\text{noise}}} \propto \frac{B_0^2 \int_{\text{VOI}} W \sin c(\gamma V B_1^+ \tau) B_1^- dv}{\sqrt{P_{\text{sample}}}}, \tag{36}$$

where the integration is performed over the volume of interest VOI and W is a weighting factor accounting for tissue-specific and sequence-specific factors affecting signal intensity such as T_1 , T_2 , proton density, TE, and TR. Further complicating the matter, signal before Fourier reconstruction, such as in an FID, will also have phase-related terms so that [5, 20]

$$\frac{V_{\text{signal}}}{V_{\text{noise}}} \propto \frac{B_0^2 \int_{\text{VOI}} W \sin(\gamma V B_1^+ \tau) e^{i\beta_1^+} (\hat{B}_1^-)^* dv}{\sqrt{P_{\text{sample}}}}, \tag{37}$$

where the circumflex indicates that \hat{B}_1^- is complex, having both magnitude and phase, and where β_1^+ is the phase of \hat{B}_1^+ .

Occasionally, for simplification and discussion purposes, it may be desirable to consider maximum SNR at one location, assuming flip angle $\alpha = \pi/2$ there. In this case SNR can be expressed as

$$\frac{V_{\text{signal}}}{V_{\text{noise}}} \propto B_0^2 \frac{B_1^-}{\sqrt{P_{\text{sample}}}}. \tag{38}$$

4.2. B_1 Homogeneity

In volume coils it is usually considered desirable to have a homogeneous B_1 field. If the B_1^+ distribution is perfectly homogeneous then the ^1H nuclei in the plane will have the same flip angle. If the B_1^- distribution is perfectly homogeneous then the coil will be equally sensitive to signal from ^1H nuclei in the region of interest. A number of methods for evaluating the B_1 field homogeneity have been used previously. Probably the most often used in comparing homogeneity of a few different coils, or of the same coil at a few different frequencies, is to present experimental or theoretical field magnitude maps or images [32, 43–46]. Yang et al.

[47] presented a method for calculating the field histogram of a coil and compared histograms of the B_1 fields for several coils. In optimization routines it is necessary to have an objective, quantitative measure of homogeneity that is sensitive enough to distinguish between coils with very similar current patterns. Often the measure of homogeneity used in optimization routines is the sum of the square of the deviation from the desired field pattern at several points in the region of interest [37,48,49]. This measure has proved very useful in optimization routines, but lacks a definition that is intuitively meaningful. That is to say, while in a list of such numbers it would be possible to pick out the smallest number, whether or not the coil had good or poor homogeneity would require reference to another means of assessing homogeneity, such as a field magnitude plot. Other methods for quantifying homogeneity is to give the percentage of the region of interest that has a B_1 field magnitude within a certain range of the mean in that area [50,51] or the standard deviation of the B_1 field magnitude [52].

4.3. Determination of Necessary Driving Voltage

In an MR experiment, what is called a “90° pulse” is usually a pulse resulting in a maximum signal detected from a region of interest. Whether this signal is evaluated before (as is usually the case) or after Fourier transforms are used to translate magnitude and phase information into amplitude and location information can have serious implications in high field imaging [5,20]. After the field calculation, all fields and SAR values can be normalized as if to produce, for example, a rectangular excitation pulse with a duration (τ) of 3 ms on the axial plane at the center of the coil (later referred to as the “imaging plane”). The field magnitude during this pulse can be defined in several different ways at each frequency, but here we will discuss three possibilities.

In the first method (center $\alpha = \pi/2$) a flip angle α of 90° is induced at a single location of interest. Thus a normalization factor, V , is determined so that $V|\hat{B}_1^+| = \alpha/\gamma\tau = 1.957 \mu\text{T}$ at the coil center, where $|\hat{B}_1^+|$ is the absolute value of \hat{B}_1^+ and γ is the gyromagnetic ratio of ^1H .

In the second method (Max. A_{FID}) the amplitude of the FID (with no phase- or frequency-encoding) is maximized. In order to calculate the FID amplitude, it is necessary to sum the contribution of all voxels considering both the magnitude and phase of the induced signal. With increasing B_1 frequency the electromagnetic wavelength in tissue decreases. Consequently, the spatial variation in the phase of \hat{B}_1^+ and \hat{B}_1^- in Eqs. 26–27 increases and so does the spatial variation in phase of \hat{B}_1^+ and \hat{B}_1^- . The signal induced in the coil by nuclei at different locations may interfere destructively in a given FID. The FID amplitude can be calculated as (see (17))

$$A_{\text{FID}} \propto \left| \sum_N W_n \sin(V|\hat{B}_{1n}^+|\gamma\tau) e^{i\beta_{1n}^+} (\hat{B}_{1n}^-)^* \right|, \quad (39)$$

where β_{1n}^+ is the phase of \hat{B}_{1n}^+ ($\beta_{1n}^+ = \text{atan}[\text{Imag}(\hat{B}_{1n}^+)/\text{Real}(\hat{B}_{1n}^+)]$) in the n th voxel, \hat{B}_{1n}^+ is \hat{B}_1^+ of the n th voxel, W_n is the water content (by percent mass) of the n th voxel, and V is a normalization factor. The summation is performed over all voxels on the imaging plane, where one voxel is represented by each Yee cell. The summation is maximized by varying V . Only the first local maximum (closest to $V = 0$) is considered.

In the third method (Max. A_{image}) the amplitude of the total signal contributing to a reconstructed gradient echo image is maximized. While in a single FID with no frequency- or phase-encoding (as in Eq. (2)), the phase of signal from different locations may result in signal cancellation, in the reconstructed image where the signal from each voxel has been separated according to position, only the magnitude of the signal in each voxel and the sensitivity of the coil to the location of each voxel is important. A_{image} can be calculated as

$$A_{\text{image}} \propto \sum_N \left| W_n \sin(V |\hat{B}_{1n}^+| \gamma \tau) \left| (\hat{B}_{1n}^-)^* \right| \right| \tag{40}$$

The summation is performed over all voxels on the imaging region, where one voxel is represented by each Yee cell. The summation is maximized by varying V . Only the first local maximum (closest to $V = 0$) is considered.

If the voltage sources provided 1 volt in the initial calculation, the normalization factor, V , necessary to achieve these three criteria will be equal to the voltage value (in volts) in the coil voltage sources associated with the final field patterns.

4.4. Specific Energy Absorption Rate (SAR)

As mentioned earlier, a time-varying magnetic field B_1 induces a time-varying electrical field E_1 .

Dissipation of RF energy in the human body results in heating [53,54]. In order to reduce the risk of resulting thermoregulatory distress or local tissue damage in the patient, the International Electrotechnical Commission has issued guidelines for safe operation of MRI equipment, suggesting limits for the Specific energy Absorption Rate (SAR; units of Watts of RF power per kilogram of tissue) allowable over the whole body, averaged over the head, and in any one gram of tissue.

If enough information is given, it is possible to relate one set of published calculation results to several possible experiments. In this section, equations are given that allow for calculation of SAR levels assuming SAR values are while a rectangular, 3 ms, $90^\circ B_1$ pulse (1.957 μT B_1^+ field magnitude) is being applied [20,42] as functions of major imaging parameters: pulse type, pulse duration, flip angle, and pulse sequence. Similar equations could be developed if SAR values for differing conditions are published.

SAR at every location in the problem region can be calculated as

$$\text{SAR} = \frac{\sigma_x}{2\rho_x} |E_x|^2 + \frac{\sigma_y}{2\rho_y} |E_y|^2 + \frac{\sigma_z}{2\rho_z} |E_z|^2 = \text{SAR}_x + \text{SAR}_y + \text{SAR}_z, \tag{41}$$

where E , σ , and ρ are the electric field magnitude, material conductivity, and material density, respectively, for Yee cell elements in the x , y , and z directions (as indicated by the subscripts) at the specific location.

SAR increases with the square of driving voltage in any given solution. The B_1 field magnitude is inversely proportional to pulse duration for a given flip angle, and is directly proportional to the flip angle for a given pulse duration. Therefore, SAR is inversely proportional to the square of pulse duration for a given flip angle, and is directly proportional to the square of the flip angle for a given pulse duration. The SAR levels induced during a pulse with flip angle α and duration τ would be

$$\text{SAR}_{\tau/\alpha} = f \left(\frac{3 \text{ ms}}{\tau} \right)^2 \left(\frac{\alpha}{90^\circ} \right)^2 \text{SAR}_{3 \text{ ms}/90^\circ}, \quad (42)$$

where f is a factor determined by the type of pulse used, calculated as a power ratio of the given pulse to a rectangular pulse with the same α and τ . If a rectangular pulse is used, $f=1.0$. If a Gaussian pulse is used, τ is defined as the full-width half-maximum of the Gaussian, and $f=0.67$ [55]. If a sine pulse is used, τ is defined as the width of the central lobe at the zero crossings, and $f=2.0$ [55]. The SAR levels of a given pulse sequence will be equal to the sum of the energy absorbed from the pulses during one repetition time (TR) divided by TR. This can be written in general as

$$\text{SAR} = \frac{\sum_{n=1}^N (\text{SAR}_{\tau n/\alpha n} \times \tau n)}{\text{TR}}, \quad (43)$$

where αn and τn are the flip angle and pulse duration of the n th pulse in a sequence of N RF pulses in a given TR.

The Center for Devices and Radiologic Health (CDRH) of the Food and Drug Administration (FDA) has suggested limits on maximum SAR levels to be administered to patients during MRI examinations. The current suggested limits are 4 W/kg averaged over any 15-minute period for whole-body SAR, 8 W/kg (12 in extremities) over any 5 minutes in any one gram of tissue, and 3 W/kg averaged over any 10 minutes for head SAR [56]. The International Electrotechnical Commission (IEC) has published detailed criteria more recently [57]. The current IEC normal operating limits are 2 W/kg averaged over any 6-minute period for whole-body SAR, 3.2 W/kg averaged over any 6 minute period for head SAR, and 10.0 W/kg in any 10-gram region of tissue in the head or torso (20.0 W/kg in any 10-gram region of tissue in the extremities) averaged over any 6-minute period. Theoretically based [58] and experimentally based [59] rationale for a conservative limit on whole-body SAR below which no thermoregulatory effects should occur is cited by the IEC. Similarly, theoretical reasoning assuming a homogeneous head [60] is given for a conservative limit on head-average SAR that should not result in a rise in brain temperature of more than 1°C, or in a rise in eye temperature of more than 1.6°C [57]. Specific rationale for the limit on SAR in one gram of tissue is not

given. A calculation of the rise in temperature of unperfused muscle tissue (specific heat of about $3.5 \text{ Jg}^{-1}\text{C}^{-1}$ [61]) that absorbs 10.0 W/kg of energy for 6 minutes, and assuming no thermal energy leaves the tissue by any mechanism in that time, shows that a rise of about 1.0°C is expected. Given that loss of thermal energy due to perfusion, conduction, and radiation are significant [62] and not considered in this calculation, and that a transient rise in temperature of 1.0°C is not expected to damage tissue, this limit can be viewed as conservative. But further discussion of the limits themselves is beyond the scope of this chapter.

5. RESULTS OF RF FIELD CALCULATIONS FOR HIGH FIELD MRI

5.1. RF Magnetic Field Patterns

5.1.1. Central Brightening

In some early publications describing images at 4 Tesla and above the term “dielectric resonance” was used to describe a high-intensity region toward the center of the head [63,64]. Since that time, RF field and signal intensity patterns having a high central intensity have occasionally been loosely attributed to “dielectric resonance” in the literature of MRI, although many authors have avoided use of the term [33,49,65–67]. There have recently been a number of publications discussing the appropriateness of this term in MRI [16, 68–73]. In a strict sense, any scientific definition of “resonance” has more to do with a peak in field amplitude or energy absorption near a particular frequency than it has to do with a particular field pattern. Although true dielectric resonances certainly have particular associated field patterns, the existence of a field pattern (such as a central brightening) is not by itself demonstration of a resonance. It is possible to demonstrate true resonances in some particular dielectric objects with methods more similar to those used to find resonances in an RF coil. Such approaches of looking for amplitude of some quantity as a function of frequency has been used in experiment [73–75] and to some degree with simulation [76,77] in the MR literature. True dielectric resonators have been tuned to the imaging frequency by adjusting the effective size [74] or electrical properties [75] of the sample. It is also possible to analytically calculate the resonance frequencies and corresponding field patterns for dielectric resonators of simple geometry [68,69,78].

Although a true resonance is also typically associated with a particular field pattern, and while strong true dielectric resonances unquestionably exist in low-conductivity high-dielectric samples (such as consisting of pure water) with dimensions near those of the human body, the conductive properties of the human body effectively dampen any strong resonances [68,69,71,73,75] or patterns of central brightening [64]. Importantly, a central brightening can be created by mechanisms other than a dielectric resonance. Although arguments in favor of using the term “dielectric resonance” to describe central brightening in the head at high field are

still presented [68,72], and this term for this purpose is currently engrained in the language of the MRI community, following is an explanation for central brightening based on the placement of source currents and wavelengths within the coil volume with no reliance on a sample resonance.

At any frequency, midway between two parallel current sources aligned in the longitudinal direction, having equal lengths and current magnitudes, but opposite phases (i.e., opposite current directions at any one time), will be a location where the magnetic fields from the two sources interfere in a constructive manner, causing a local field maximum. One quarter wavelength away from this location in either direction along the axis of propagation will be a location where the field will interfere in a destructive manner, causing a local field minimum. This is assuming that the waves from the two sources travel through the same media for the same distance. As noted previously, there are no plane waves in MRI, but this basic principle can be used to describe central brightening in many situations. In general, volume coils at high field consist largely of elements arranged in a cylindrical manner and conducting currents such that each element is opposite another with approximately equal magnitude and approximately opposite phase. In the center of the coil is a location where magnetic fields from the sources will interfere constructively creating a local field maximum.

As shown in Figure 6, this can occur even in an empty coil with no dielectric material present. Here an empty hybrid body-sized birdcage coil is driven with ideal currents at both 64 and at 300 MHz. At 64 MHz the field within the coil is fairly homogeneous, as expected from low-frequency predictions. At 300 MHz the wavelength in air is much longer than the coil dimensions and therefore wavelength effects are not evident within the coil. At 300 MHz, however, the coil diameter (63 cm) is a little larger than one-half of one wavelength ($\lambda/2 = 50$ cm), so while there is constructive interference of the magnetic fields in the coil center, at approximately one-quarter wavelength from there, near the coil elements, a dark ring is seen where destructive interference occurs.

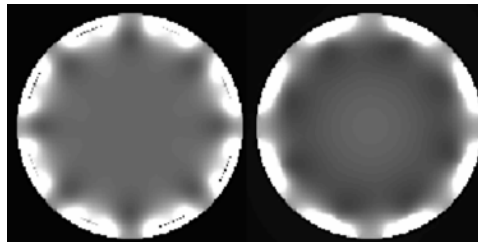


Figure 6. B_1 field magnitude on a mid-axial plane through an empty body-sized birdcage coil at 64 (left) and 300 (right) MHz. Even with no sample present a “central brightening” effect is seen at 300 MHz due to interference of fields from different conductive elements.

In the human body, where wavelengths are much shorter than in air, this type of effect is evident at lower frequencies and in smaller coils. Figure 7 shows RF magnetic field patterns in the human head at several frequencies.

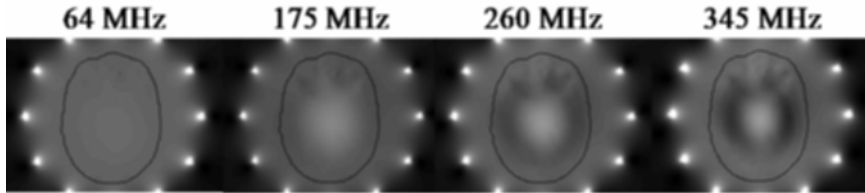


Figure 7. B_1^+ distribution for a head in an ideal birdcage coil at several frequencies.

This interference pattern can be described as either setting up a system of standing waves, standing wave envelopes, wavelength effects, or resulting from RF coil/sample interactions [16,33,65,66,70,71,73] and can result in central brightening without the existence of a true dielectric resonance.

5.1.2. Penetration Effects

Although central brightening may be the dominant effect seen in high-field MRI of the head with a volume coil, effects resulting from a decreasing depth of penetration are evident with use of surface coils at high field [45], and perhaps also in imaging of the torso with volume coils [79].

In Figure 8 is shown the calculated field from a surface coil on a model of the human chest at several frequencies. Clearly, at higher frequencies the fields are more severely attenuated as they penetrate the chest. This is evident by the faster spatial rate of decrease (more closely spaced contours) at 345 MHz than at 64 MHz. It is also apparent that the penetration depth at 345 MHz is shorter in the heart and blood (tissues having relatively high conductivities) than in the surrounding lung, where the rate of decrease is more gradual.

In Figure 9 is shown the RF magnetic fields for a large muscular human body within a hybrid body-sized birdcage coil driven with ideal currents at 64 and 300 MHz. Although the field pattern is complex, overall there appears to be more central darkening than central brightening. In contrast to results for the human head or an empty coil, here a central field dampening occurs at the higher frequency.

5.2. Induced Electrical Currents and SAR

In experiment it is possible to estimate the SAR over the whole body or portion exposed to RF fields by monitoring the RF power delivered to the coil and dividing by the mass of the body or the portion exposed to the RF fields. With numerical methods it is possible not only to estimate these average SAR values, but

also to predict where in the body the SAR will be the highest. Due to the large differences in electrical properties between tissues and the complex arrangement of tissues in space, SAR distributions are neither simple nor homogeneous in the body.

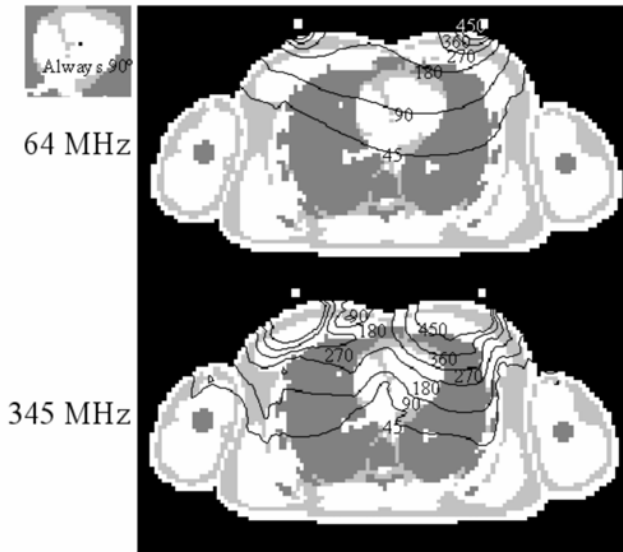


Figure 8. Flip angle distribution in a human chest model while maintaining a 90° flip at center of heart and imaging with a surface coil at 64 and 345 MHz.

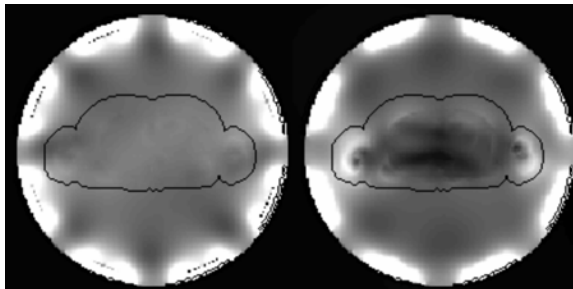


Figure 9. B1 field magnitude on a mid-axial plane through a body-sized birdcage coil loaded with a human body at 64 and 300 MHz.

In MRI of humans at increasing B_0 there is a general expectation that power requirements will increase, although some interesting possible exceptions are discussed later in the section dealing with SNR. This indicates that a given pulse sequence will generally result in higher power deposition and SAR levels at increasing B_0 , and may require longer TR, longer RF pulse durations, or lower flip angles to avoid exceeding IEC limits on SAR [20,42,55].

Several other investigators have performed calculations of SAR for MRI of human samples. Jin et al. [80] presented results as a function of frequency and current magnitude in the coil. Simunic et al. [81] and Grandolfo et al. [82] present results for during a 180° pulse of specific duration. Ibrahim et al. [22] present SAR levels for a given input power to the coil. Some researchers have also used the FDTD method to investigate the effects on SAR of lead wires and catheters connected to or inserted into subjects [83, 84].

Because it is not SAR by itself that is a concern, but a possible increase in temperature resulting from this absorption of power, a few researchers have also recently begun to investigate the use of numerical methods for predicting RF-related temperature increases in MRI [62,85].

5.3. Signal Intensity Patterns

The signal intensity patterns on different axial planes for spin echo and gradient echo signals is shown in Figure 10 in comparison to experimental images at 300 MHz for spin echo (SE) and gradient echo (GE) sequences. Although the calculated signal intensity distributions are weighted with a factor W proportional only to water content so that the tissue contrast is different than in the experiment where many more factors are in play, and though the calculation is for an idealized birdcage coil while a quadrature-driven TEM coil was used in experiment, the overall field pattern is very similar in each case. (Note that the dark region above the nasal sinus in the GE experimental image is an artifact of B_0 distortion.)

Plots of signal intensity distribution on an axial plane through the human head in an idealized birdcage coil at 345 MHz for several different flip angles at the center are presented in Figure 11 for SE (top) and GE (bottom) images. By merely changing the flip angle of the excitation pulse it is possible to dramatically change the homogeneity of the signal intensity distribution at this frequency.

Plots of signal intensity distribution on an axial plane through the human head in an idealized birdcage coil at several different frequencies are likewise presented in Figure 12. As B_0 field strength and B_1 frequency increase, the concomitant effect of decreasing λ is clearly apparent in the distributions with the radius of the dark ring surrounding the central bright region becoming smaller as λ decreases.

5.4. Signal-to-Noise Ratio

Calculations using a number of different methods for various samples and coils indicate that there are many possible trends for SNR in high field MRI. De-

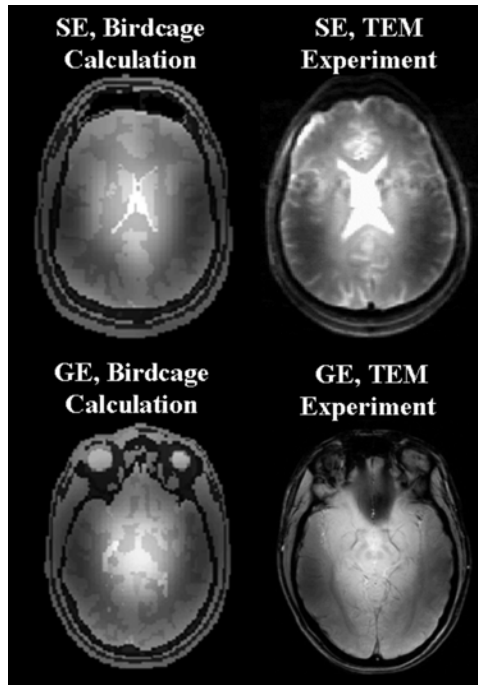


Figure 10. Calculated (left) and experimental (right) signal intensity distributions for gradient echo (bottom) and spin echo (top) images in the human head.

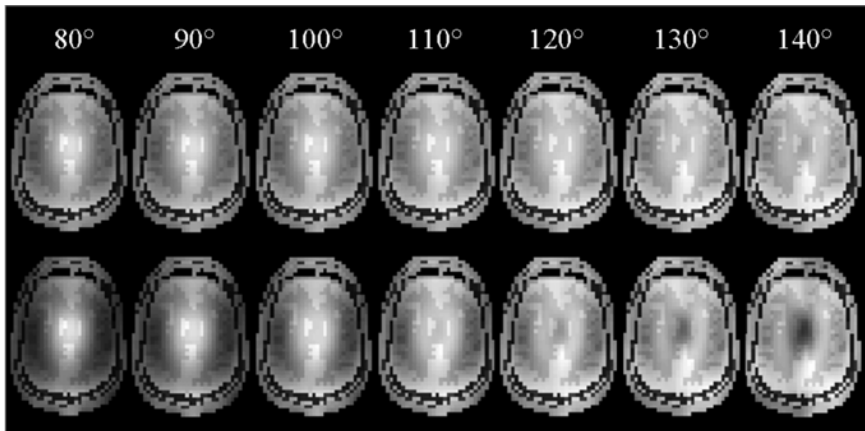


Figure 11. Calculated signal intensity distributions for several different average flip angles in gradient echo (top) and spin echo (bottom) sequences at 345 MHz.

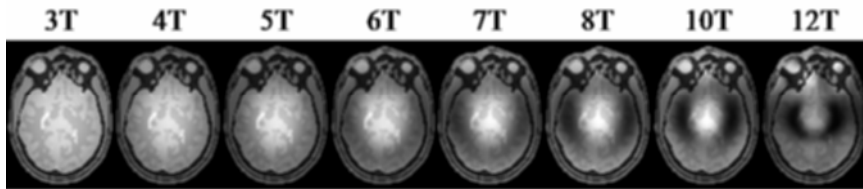


Figure 12. Calculated gradient echo images at several different field strengths.

pending on coil and sample geometries and sample electrical properties, SNR at high field can have a wide array of trends with increasing B_0 [5,18,20,42,44,66]. Generally, as ν increases the B_1 field distribution becomes less homogeneous, making the flip angle equal to $\pi/2$ in a smaller portion of the VOI, and causing a decrease in the integrand in the numerator of Eq. 36.

If $P_{\text{sample}} \propto B_0^2$ (as in imaging at lower B_0) this would result in a less-than-linear increase in SNR with B_0 . However, experiments and calculations in many cases [5,15,18,20,44,66,77,86], including those for the head in volume coils, indicate that $P_{\text{sample}}/(B_1^-)^2$ (a quantity relevant to SNR via Eq. (38) and expected to increase with the square of B_0 at low field via Eq. (31)) increases at a less-than-quadratic rate with B_0 , maintaining a nearly linear increase in SNR with B_0 . In fact, some of these studies indicate that at very high frequencies (above 400 MHz in the head) $P_{\text{sample}}/(B_1^-)^2$ could actually decrease with increasing B_0 [66,77,86]. This less-than-quadratic increase can be understood by once again considering Faraday’s Law, Eq. (31) [20]. At very high frequencies used today in MR of the head with volume coils, the B_1 field will have various — even opposing — phases at different locations on a given plane through the head. This results in a decrease in net flux through the plane and lower induced electric field magnitudes around the perimeter of the head than would be predicted with estimates assuming a field with homogeneous phase. This results in lower conduction current densities and lower absorbed power than predicted assuming homogeneous fields, or a less-than-quadratic increase in P_{sample} .

In other experiments and calculations [42,44,45,66,87], including those for a surface coil on the chest, a greater-than-quadratic increase in $P_{\text{sample}}/(B_1^-)^2$ with B_0 and corresponding less-than-linear increase in SNR have been predicted or observed. Although in many ways an unsatisfactory analogy, consideration of the penetration of a plane wave into a lossy dielectric material can yield insight into this type of phenomenon. In general, as ν increases the penetration depth of a plane wave into a semi-infinite slab of material decreases, causing $P_{\text{sample}}/(B_1^-)^2$ at any depth to increase at a greater rate than if the penetration depth remained independent of ν , or at a greater-than-quadratic rate. So even if the flip angle is maintained at $\pi/2$ at the depth of interest, SNR will have a less-than-linear relationship with B_0 in this case (Eq. (38)).

The differences between Eqs. (36) and (38) can have important implications regarding the common practice of determining of flip angles based on maximizing the FID amplitude. This approach at high field can result in interesting possibilities, such as in specific values of ν where SNR as measured on an FID is at a minimum, or even at a null while SNR on an image might still be increasing at a linear rate or better with B_0 [5,20]. Related to this, the RF power to maximize the FID amplitude may be much different than the RF power required to maximize the image SNR at high B_0 [20].

As the B_1 field frequency increases it is generally expected that the percent of power applied to the coil that will be radiated from the coil will increase [18,19,88]. While studies of the effect of coil radiation on SNR are scant, growing interest in this topic makes it worthy of mention here. Although greater radiation during transmission usually indicates greater sensitivity to background RF energy from numerous sources, in MRI we should be able to assume that this background RF energy is effectively shielded from the coil energy by the closed RF screen present at the boundary of most magnet rooms. The RF screen will also cause the radiated power to be dissipated somewhere in the magnet room, and, by reciprocity, limit the sensitivity of the coil to noise due to thermal motion of charges and dipoles in objects within the magnet room. Knowledge of where the radiated power is dissipated should allow us to determine the effect of radiated power on SNR. Although this is still an area of current research, recent calculations [14] indicate that for a body-sized birdcage coil loaded with the human body at 128 MHz, practically all of the coil input power is dissipated in the human body when the entire magnet room is modeled (including RF coil shielding, stainless steel magnet casing, and external copper magnet room RF screen, and assuming no lossy dielectric materials but the body of the subject are present in the magnet room), as opposed to about 88% dissipated in the body and 12% radiated when no conductive surfaces are modeled outside of the RF coil shielding. This indicates that radiated power will generally be coupled to body noise, but further study is needed.

5.5. RF Coil Design

To produce homogeneous images it is generally desirable to have a homogeneous RF magnetic field that covers a large portion of the sample to both excite a uniform distribution of flip angles in a large portion of the sample and to detect available signal equally well throughout the sample. To reduce the amount of sample noise detected and thus improve SNR it is desirable to reduce the extent to which the coil is affected by random motion of charges and rotation of dipoles in the sample, or, by reciprocity, reduce the volume of the sample in which the coil can produce electrical fields. At any field strength these are conflicting goals requiring, in general, larger coils for more homogeneous images and smaller coils for better SNR.

In high-field MRI additional challenges are introduced as the RF wavelength in tissue decreases and coils that produce very homogeneous fields at lower frequencies do so less effectively. The FDTD method has been used to compare the

homogeneity of different coils [51,89]. Some approaches which seem counter-intuitive at lower frequencies seem to be effective at high field. For example, although at low frequencies it is expected that a longer birdcage or TEM-type coil will produce a more homogeneous field at the center, at high field it appears that in some cases a shorter coil may actually be better for both homogeneity and SNR [90]. Also, in a comparison of coils, the coil that produces the most homogeneous field when empty can sometimes produce the least homogeneous field by some measures when loaded with a human head [51].

An important development in MRI that may have particularly promising potential at high field is the use of multiple coils. The use of multiple decoupled receive coils, each with a separate preamplifier and digitizer, has proven very valuable in allowing for some flexibility in acquiring images with greater speed and/or improved SNR near the coils using a variety of tailored acquisition and post-processing methods which fall broadly under the description “parallel imaging” [91,92]. Recent studies have indicated that parallel imaging may be even more effective at high fields than at lower fields because of how the decreasing wavelengths reduce the overlap in receptivity distribution from the separate coils [93,94]. One clear, immediate advantage in high-field imaging of the head is that the use of surface coils in parallel results in increased signal receptivity towards the periphery, offsetting the tendency for central brightening. Designing coils for improved parallel imaging performance requires optimization of the geometry and placement of each coil in the array while considering the fields in the sample. A number of researchers have used the FDTD method to evaluate different coil array designs [95–97].

The presence of these multiple coils for receive purposes also raises the possibility of using them with customized amplitude and phase combinations during excitation. Using different approaches with the FDTD method, a number of researchers have investigated the potential for improving image homogeneity by driving separate coils with specially selected magnitudes and phases [98–102].

In Figure 13 is shown preliminary results for adjusting the driving phase of individual elements in an eight-coil array. The desired phases were first determined using numerical field calculations (top) and a simple optimization routine. These phases were then implemented in an experimental coil (bottom). The improvement in homogeneity in experiment is notable in the experiment, but it is not as great as in the simulation partly because the head geometry in simulation did not match that in the experiment [99]. In the future it may be beneficial to develop methods to adjust the distribution of driving magnitudes and phases in a coil array for each individual subject, much as the B_0 field is shimmed for each subject. In Figure 14 the potential improvement for adjusting individual phases in a sixteen-element elliptical array is shown.

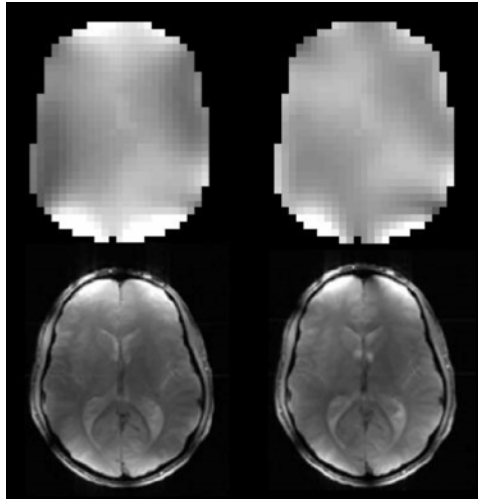


Figure 13. Computed (top) signal intensity pattern without weighting for different tissues in a gradient echo image before (left) and after (right) numerical optimization of driving phases for an 8-element cylindrical coil array and experimental images (bottom) acquired with corresponding driving phases in a similar coil. Experimental images courtesy of J. Thomas Vaughan and Kamil Ugurbil at the University of Minnesota.

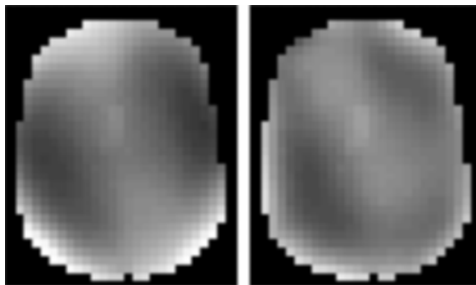


Figure 14. Signal intensity pattern in a gradient echo image before (left) and after (right) optimization of driving phases for a 16-element elliptical coil array.

6. REFERENCES

1. Ugurbil K, Hu X, Chen W, Zhu XH, Kim SG, Georgopoulos A. 1999. Functional mapping in the human brain using high magnetic fields. *Phil Trans R Soc Lond B* **35**:1195–1213.

2. Johnk CTA. 1988. *Engineering electromagnetic fields and waves*, pp. 154–156. New York: John Wiley & Sons.
3. Gabriel C. 1996. *Compilation of the dielectric properties of body tissues at RF and microwave frequencies*, AL/OE-TR-1996-0037. Brooks Air Force Base, TX: Air Force Materiel Command.
4. Foster KP, Schwan HP. 1989. Dielectric properties of tissues and biological materials: a critical review. *Crit Rev Biomed Eng* **17**(1):25–104.
5. Hoult DI. 2000. The sensitivity and power deposition of the high field imaging experiment. *J Magn Reson Imag* **12**(1):46–67.
6. Wiesinger F, Van deMoortele PF, Adriany G, DeZanche N, Ugurbil K, Pruessmann KP. 2004. Parallel imaging performance as a function of field strength: an experimental investigation using electrodynamic scaling. *Magn Reson Med* **52**:953–964.
7. Kunz KS, Luebbers RJ. 1993. *The finite difference time domain method for electromagnetics*. Boca Raton, FL: CRC Press.
8. Taflov A, Hagness SC. 2000. *Computational electrodynamics: the finite difference time domain method*. Boston: Artech House.
9. Young JL. 1995. Propagation in linear dispersive media: finite difference methodologies. *IEEE Trans Ant Propag* **43**:422–426.
10. Yee KS. 1966. Numerical solution of initial boundary value problems involving Maxwell's equations in isotropic media. *IEEE Trans Ant Propag* **14**:302–307.
11. Mur G. 1981. Absorbing boundary conditions for the finite-difference approximation of the time-domain electromagnetic-field equations. *IEEE Trans Electromagn Compat* **23**:1073–1077.
12. Liao Z, Wong HL, Baipo Y, Yifan Y. 1984. A transmitting boundary for transient wave analyses. *Scientia Sinica* **27**:1063–1076.
13. Berenger JP. 1994. A perfectly matched layer for the absorption of electromagnetic waves. *J Comput Phys* **114**:185–200.
14. Collins CM, Liu W, Smith MB, Yang QX. 2003. Dissipation of radiated rf power in magnet room: implications for snr considerations. *Proc Int Soc Magn Reson Med* 714.
15. Vaughan JT, Garwood M, Collins CM, Liu W, DelaBarre L, Adriany G, Andersen P, Merkle H, Goebel R, Smith MB, Ugurbil K. 2001. 7t vs. 4t: rf power, homogeneity, and signal-to-noise comparison in head images. *Magn Reson Med* **46**:24–30.
16. Alecci M, Collins CM, Smith MB, Jezzard P. 2001. Radio frequency magnetic field mapping of a 3 tesla birdcage coil: experimental and theoretical dependence on sample properties. *Magn Reson Med* **46**:379–385.
17. Collins CM, Yang QX, Wang JH, Zhu XH, Adriany G, Michaeli S, Vaughan JT, Zhang X, Liu H, Anderson P, Ugurbil K, Smith MB, Chen W. 2002. Different excitation and reception distributions with a single-loop transmit-receive surface coil near a head-sized spherical phantom at 300 MHz. *Magn Reson Med* **47**:1026–1028.
18. Keltner JR, Carlson JW, Roos MS, Wong STS, Wong TL, Buddinger TF. 1991. Electromagnetic fields of surface coil in vivo NMR at high frequencies. *Magn Reson Med* **22**:467–480.
19. Harpen MD. 1993. Radiative losses of a birdcage resonator. *Magn Reson Med* **29**:713–716.
20. Collins CM, Smith MB. 2001. Signal-to-noise ratio and absorbed power as functions of main magnetic field strength and definition of 90 degree rf pulse for the head in the birdcage coil. *Magn Reson Med* **45**:684–691.

21. McKinnon G, Wang Z. 2003. Direct capacitor determination in FDTD modelling of RF coils. *Proc Int Soc Magn Reson Med* 2381.
22. Ibrahim TS, Lee R, Baertlein BA, Robitaille PML. 2001. B_1 field homogeneity and SAR calculations in the high-pass birdcage coil. *Phys Med Biol* **46**:609–619.
23. Han Y, Wright SM. 1994. Wide-band RF coil behavior analysis using FDTD method. *Proc Soc Magn Reson* 1133.
24. Ochi H, Yamamoto E, Sawaya K, Adachi S. 1992. Calculation of electromagnetic field of an MRI antenna loaded by a body. *Proc Soc Magn Reson Med* 4021.
25. Ochi H, Yamamoto E, Sawaya K, Adachi S. 1993. Analysis of MRI antenna inside an RF shield using moment method. *Proc Soc Magn Reson Med* 1356.
26. Yang QX, Maramis H, Li S, Smith MB. 1994. Three-dimensional full wave solution of MRI radio frequency resonator. *Proc Soc Magn Reson* 1110.
27. Junge S, Haerberlen U. 1998. 3D simulations of B and E fields in RF-resonators by CONCEPT and MAFIA. *Proc Int Soc Magn Reson Med* 2042.
28. Junge S, Haerberlen U. 1999. Optimization of a quadrature whole-body resonator for 2T. *Proc Int Soc Magn Reson Med* 2053.
29. Ibrahim TS, Lee R, Baertlein BA, Yu Y, Robitaille PML. 2000. Computational analysis of the high pass birdcage resonator: finite difference time domain simulations for high-field MRI. *Magn Reson Imag* **18**:835–843.
30. Ibrahim TS, Abduljalil AM, Lee R, Baertlein BA, Robitaille PML. 2001. Analysis of B_1 field profiles and SAR values for multi-strut transverse electromagnetic RF coils in high field MRI applications. *Phys Med Biol* **46**:2545–2555.
31. Liang ZP, Lauterbur PC. 2000. Principles of magnetic resonance imaging, a signal processing perspective. New York: IEEE Press.
32. Glover GH, Hayes CE, Pelc NJ, Edelstein WA, Mueller OM, Hart HR, Hardy CJ, O'Donnell M, Barber WD. 1985. Comparison of linear and circular polarization for magnetic resonance imaging. *J Magn Reson* **64**:255–270.
33. Sled JG, Pike GB. 1998. Standing-wave and rf penetration artifacts caused by elliptic geometry: an electrodynamic analysis. *IEEE Trans Med Imag* **17**(4):653–662.
34. Hoult DI. 2000. The principle of reciprocity in signal strength calculations: a mathematical guide. *Conc Magn Reson* **12**(4):173–187.
35. Nyquist H. 1928. Thermal agitation of electric charge in conductors. *Phys Rev* **32**:110.
36. Li S, Yang QX, Smith MB. 1994. RF coil optimization of B_1 field homogeneity using field histograms and finite element calculations. *Magn Reson Imag* **12**(7):1079–1087.
37. Forbes LK, Crozier S, Doddrell DM. 1996. An analysis and optimization of elliptical RF probes used in magnetic resonance imaging. *Meas Sci Technol* **7**:1281–1290.
38. Crozier S, Forbes LK, Roffman WU, Luescher K, Doddrell DM. 1997. A methodology for current density calculations in high frequency RF resonators. *Conc Magn Reson* **9**:195–210.
39. Hoult DI, Lauterbur PC. 1979. The sensitivity of the zeugmatographic experiment involving human samples. *J Magn Reson* **34**:425–433.
40. Hoult DI, Richards RE. 1976. The signal-to-noise ratio of the nuclear magnetic resonance experiment. *J Magn Reson* **24**:71–83.
41. Edelstein WA, Glover GH, Hardy CJ, Redington RW. 1986. The intrinsic signal-to-noise ratio in NMR imaging. *Magn Reson Med* **3**:604–618.
42. Collins CM, Smith MB. 2001. Calculations of B_1 distribution, SNR, and SAR for a surface coil against an anatomically-accurate human body model. *Magn Reson Med* **45**:692–699.

43. Hayes CE, Edelstein WA, Schenck JF, Mueller OM, Eash M. 1985. An efficient, highly homogeneous radiofrequency coil for whole-body NMR imaging at 1.5T. *J Magn Reson* **63**:622–628.
44. Singerman RW, Denison TJ, Wen H, Balaban RS. 1997. Simulation of B_1 field distribution and intrinsic signal-to-noise in cardiac MRI as a function of static magnetic field. *J Magn Reson* **125**:72–83.
45. Wen H, Denison TJ, Singerman RW, Balaban RS. 1997. The intrinsic signal-to-noise ratio in human cardiac imaging at 1.5, 3, and 4 T. *J Magn Reson* **125**:65–71.
46. Li S, Collins CM, Dardzinski BJ, Chin CL. 1997. A method to create an optimum current distribution and homogeneous B_1 field for elliptical birdcage coils. *Magn Reson Med* **37**:600–608.
47. Yang QX, Li S, Smith MB. 1994. A method for evaluating the magnetic field homogeneity of a radiofrequency coil by its field histogram. *J Magn Reson A* **108**:1–8.
48. Lu N, Jin J, Michielssen E, Magin RL. 1995. Optimization of RF coil design using genetic algorithm and simulated annealing method. *Proc Soc Magn Reson* 1002.
49. Collins CM, Yang QX, Smith MB. 1998. A simple, accurate, and effective method for birdcage-type coil design. *Proc Int Soc Magn Reson Med* 643.
51. Liu W, Collins CM, Delp PJ, Smith MB. 2004. Effects of end-ring/shield configuration on homogeneity and signal-to-noise ratio in a birdcage-type coil loaded with a human head. *Magn Reson Med* **51**:217–221.
50. Collins CM, Li S, Smith MB. 1998. SAR and B_1 field distributions in a heterogeneous human head model within a birdcage coil. *Magn Reson Med* **40**:847–856.
52. Ibrahim TS, Lee R, Robitaille PML. 2001. Effect of RF coil excitation on field inhomogeneity at ultra high fields: a field optimized TEM resonator. *Magn Reson Imag* **19**:1339–1347.
53. Budinger TF. 1981. Nuclear magnetic resonance (NMR) in vivo studies: known thresholds for health effects. *J Comput Assist Tomogr* **5**:800–811.
54. Schwan HP, Foster KR. 1980. RF-field interactions with biological systems: electrical properties and biophysical mechanisms. *Proc IEEE* **68**(1):104–113.
55. Bottomley PA, Redington RW, Edelstein WA, Schenck JF. 1985. Estimating radiofrequency power deposition in body nmr imaging. *Magn Reson Med* **2**:336–349.
56. Center for Devices and Radiologic Health. 2003. *Criteria for significant risk investigations of magnetic resonance diagnostic devices*. Rockville, MD: Food and Drug Administration.
57. IEC. 2002. International standard, medical equipment, part 2: particular requirements for the safety of magnetic resonance equipment for medical diagnosis, 2nd revision, 601-2-33. Geneva: International Electrotechnical Commission.
58. Adair ER, Berglund LG. 1986. On the thermoregulatory consequences of NMR imaging. *Magn Reson Imag* **4**:321–333.
59. Shellock FG, Schaefer DJ, Crues JV. 1989. Alterations in body and skin temperatures caused by magnetic resonance imaging: is the recommended exposure for radiofrequency radiation too conservative? *Br J Radiol* **62**:904–909.
60. Athey TW. 1989. A model of temperature rise in the head due to magnetic resonance imaging procedures. *Magn Reson Med* **9**:177–184.
61. Duck FA. 1990. *Physical properties of tissue*. New York: Academic Press.
62. Collins CM, Liu W, Wang JH, Gruetter R, Vaughan JT, Ugurbil K, Smith MB. 2004. Temperature and SAR calculations for a human head within volume and surface coils at 64 and 300 MHz. *J Magn Reson Imag* **19**:650–656.

63. Bomsdorf H, Helzel T, Hunz D, Roschmann P, Tschendel O, Weiland J. 1988. Spectroscopy and imaging with a 4 tesla whole-body system. *NMR Biomed* **1**:151–158.
64. Barfuss H, Fischer H, Hentschel D, Ladebeck R, Oppelt A, Wittig R, Duerr W, Oppelt R. 1990. In vivo magnetic resonance imaging and spectroscopy of humans with a 4T whole-body magnet. *NMR Biomed* **3**:31–45.
65. Tofts PS. 1994. Standing waves in uniform water phantoms. *J Magn Reson B* **104**:143–147.
66. Ocali O, Atalar E. 1998. Ultimate intrinsic signal-to-noise ratio in MRI. *Magn Reson Med* **39**:462–473.
67. Robitaille PML, Abduljalil AM, Kangarlu A, Zhang X, Yu Y, Burgess R, Bair S, Noa P, Yang L, Zhu H, Palmer B, Jiang Z, Chakeres DM, Spigos D. 1998. Human magnetic resonance imaging at 8T. *NMR Biomed* **11**:263–265.
68. Roschmann P. 2000. Role of B_1 eigenfields of dielectric objects in high-field MRI. *Proc Int Soc Magn Reson Med* 151.
69. Kangarlu A, Baertlein BA, Lee R, Ibrahim TS, Abduljalil AM, Yang L, Robitaille PML. 1999. Dielectric resonance phenomena in ultra high field MRI. *J Comput Assist Tomogr* **23**:821–831.
70. Ibrahim T, Lee R, Abduljalil AM, Baertlein BA, Robitaille PML. 2001. Dielectric resonances and B_1 field inhomogeneity in UHFMRI: computational analysis and experimental findings. *Magn Reson Imag* **19**:219–226.
71. Yang QX, Wang JH, Collins CM, Smith MB, Zhang X, Liu H, Michaeli S, Zhu XH, Adriany G, Vaughan JT, Anderson P, Ugurbil K, Chen W. 2002. Analysis of wave behavior in dielectric samples at high field. *Magn Reson Med* **47**:982–989.
72. Tropp J. 2004. Image brightening in samples of high dielectric constant. *J Magn Reson* **167**:12–24.
73. Collins CM, Liu W, Schreiber W, Yang QX, Smith MB. 2005. Central brightening due to constructive interference with, without, and despite dielectric resonance. *J Magn Reson Imag* **21**:192–196.
74. Wen H, Jaffer FA, Denison TJ, Duewell S, Chesnick AS, Balaban RS. 1996. The evaluation of dielectric resonators containing H_2O or D_2O as RF coils for high-field imaging and spectroscopy. *J Magn Reson B* **110**:117–123.
75. Wiesinger F, Van de Moortele PF, Adriany G, De Zanche N, Snyder C, Vaughan T, Ugurbil K, Pruessmann KP. 2004. An investigation into the role of dielectric resonance in parallel imaging. *Proc Int Soc Magn Reson Med* 2393.
76. Han Y, Wright SM. 1995. Wide-band RF field inhomogeneity analysis for a birdcage coil using FDTD method. *Proc Soc Magn Reson* 1005.
77. Schenck JF. 1999. Spherical Model with analytical solutions for estimating the high frequency performance of loaded birdcage and similar coils. *Proc Int Soc Magn Reson Med* 2056.
78. Gastine M, Courtois L, Dormann JL. 1997. Electromagnetic resonances of free dielectric spheres. *IEEE Trans Microwave Theory Tech* **15**:694–700.
79. Vaughan JT, Snyder C, Adriany G, Bolinger L, Liu H, Stolphen A, Ugurbil K. 2003. The technology and techniques of 4T body imaging. *Proc Int Soc Magn Reson Med* 425.
80. Jin JM, Chen J, Chew WC, Gan H, Magin RL, Dimbylow PJ. 1996. Computation of electromagnetic fields for high-frequency magnetic resonance imaging applications. *Phys Med Biol* **41**:2719–2738.

81. Simunic D, Wach P, Renhart W, Stollberger R. 1996. Spatial distribution of high-frequency electromagnetic energy in human head during MRI: numerical results and measurements. *IEEE Trans Biomed Eng* **43**:88–94.
82. Grandolfo M, Vecchia P, Gandhi OP. 1990. Magnetic resonance imaging: calculation of rates of energy absorption by a human-torso model. *Bioelectromagnetics* **11**:117–128.
83. Angelone LM, Bonmassar G. 2004. Use of resistances and resistive leads: implications on computed electric field and SAR values. *Proc Int Soc Magn Reson Med* 1652.
84. Bonmassar G. 2004. Resistive tapered striplines (RTS) lower SAR in electrophysiology recordings during MRI. *Proc Int Soc Magn Reson Med* 1669.
85. Hand JW, Lau RW, Lagendijk JJW, Ling J, Burl M, Young IR. 1999. Electromagnetic and thermal modeling of SAR and temperature fields in tissue due to an RF decoupling coil. *J Magn Reson Imag* **42**:183–192.
86. Ibrahim TS. 2004. A numerical analysis of radio-frequency power requirements in magnetic resonance imaging experiment. *IEEE Trans Microwave Theory Tech* **52**(8):1999–2003.
87. Roschmann P. 1987. Radiofrequency penetration and absorption in the human body: limitations to high-field whole-body nuclear magnetic resonance imaging. *Med Phys* **14**(6):922–931.
88. Liu W, Yang QX, Collins CM, Smith MB. 2002. Numerical evaluation of power radiated and dissipated by a loaded surface coil at high field. *Proc Int Soc Magn Reson Med* 915.
89. DeMeester GD, Zhail Z, Morich MA, Leussler C, Findekle C. 2004. Numerical comparison between TEM head coil and birdcage head coil at 7T. *Proc Int Soc Magn Reson Med* 35.
90. Ibrahim TS, Kangarlu A, Abduljalil A, Schmalbrock P, Gilbert R, Chakeres DW. 2002. Optimization of RF coils at ultra high field MRI: correlation with patient comfort. *Proc Int Soc Magn Reson Med* 917.
91. Sodickson DK, Manning WJ. 1997. Simultaneous acquisition of spatial harmonics (SMASH): fast imaging with radiofrequency coil arrays. *Magn Reson Med* **38**:591–603.
92. Pruessmann KP, Weiger M, Scheidegger MB, Boesiger P. 1999. SENSE: sensitivity encoding for fast MRI. *Magn Reson Med* **42**:952–962.
93. Ohliger MA, Grant AK, Sodickson DK. 2003. Ultimate intrinsic signal-to-noise ratio for parallel mri: electromagnetic field considerations. *Magn Reson Med* **50**:1018–1030.
94. Weisinger F, Boesiger P, Pruessmann KP. Electrodynamics and ultimate SNR in parallel imaging. *Magn Reson Med* **2004****52**:376–390.
95. Kim HW, Caserta J, Peterson DM, Fitzsimmons JR. 2004. Evaluation of SAR and B_1 for a transceive pelvic phased-array coil at 3T using FDTD simulations. *Proc Int Soc Magn Reson Med* 1567.
96. Li BK, Liu F, Gregg I, Shuley N, Crozier S, Galloway G. 2004. Investigating tissue-coil interactions of an 8-elements transmit/receive torso phased array coil. *Proc Int Soc Magn Reson Med* 1599.
97. Wei J, Qu P, Shen GX. 2004. Comparison of RF penetration and G-factor of different coil arrays for parallel imaging. *Proc Int Soc Magn Reson Med* 1603.
98. Ibrahim TS, Lee R, Robitaille PML. 2001. Effect of RF coil excitation on field inhomogeneity at ultra high fields: a field optimized TEM resonator. *Magn Reson Imag* **19**:1339–1347.

99. Collins CM, Swift BJ, Liu W, Vaughan JT, Ugurbil K, Smith MB. 2004. Optimal multiple-element driving configuration depends on head geometry, placement, and volume of interest. *Proc Int Soc Magn Reson Med* 1566
100. Lee RF, Foresto CM. 2004. A focused MRI with coupled phased array at 7T. *Proc Int Soc Magn Reson Med* 34.
101. Ledden PJ, Cheng Y. 2004. Improved excitation homogeneity at high frequencies with RF pulses of time varying spatial characteristics. *Proc Int Soc Magn Reson Med* 38.
102. Wuebbeler G, Seifert F, Junge S, Rinneberg H. 2004. Assessment of SAR values and coil performance for an adaptive 4-channel 3T proton head coil array. *Proc Int Soc Magn Reson Med*. 665.

MAGNETIC SUSCEPTIBILITY EFFECTS IN HIGH FIELD MRI

Qing X. Yang, Michael B. Smith, and Jianli Wang

*The Pennsylvania State University
College of Medicine, Hershey*

In high-magnetic-field MRI, both valuable image contrast and undesirable artifacts associated with the magnetic susceptibility effects are significantly increased. The magnetic field distortion in and by the human body is described with computer modeling methods in the human head. The manifestations of the resultant image artifacts include signal loss, blurring, and geometric distortion and are dependent on imaging methods. The treatments of the artifacts in the specific imaging sequences are described and demonstrated with human studies at 3 and 7 Tesla and animal studies at field strengths as high as 14 Tesla. With these in vivo studies, the enhanced image contrast produced by the increased field strength and the improved image quality by the artifact reduction methods provide strong and stimulating evidence for exciting potential scientific applications of high field MRI.

1. INTRODUCTION

Analogous to the endeavor of the Hubble Space Telescope, which allows us to peer deep into the universe, the development of ultra high field MRI allows us to look into the living bodies of our own with greater sensitivity and resolution that has never been previously achieved [1]. Our bodies are certainly a great mystery to us, and having the ability to explore inside them is more than just scientifically interesting — it is fascinating!

The development of ultra high field MRI is synergistically coupled with major biological research forefronts such as molecular imaging and cell research. They all demand in-vivo imaging capabilities with high resolution and versatile contrasts. The resolving power of MRI greatly enhanced by ultra high field strength meets such a demand precisely and timely. However, the increased magnetic susceptibility effects of biological tissues in high static magnetic fields result in severe image artifacts that seriously limit the applications of high field MRI technology. One of

the critical research frontiers is to develop bioengineering solutions to the limitations of high field MRI. This chapter is to provide a concise description of the magnetic susceptibility effects in high field MRI and reviews some of the techniques that can be used to best demonstrate important issues for understanding the physical underpinnings of the associated artifacts.

2. MAGNETIC SUSCEPTIBILITY

Magnetic susceptibility, χ_m , is a dimensionless quantity and is used to describe how a bulk material is magnetized when exposed to an external field, B_0 , and subsequently perturbs B_0 . If χ_m is positive, the material is called *paramagnetic*, and the magnetic field is strengthened by the presence of the material. If χ_m is negative, then the material is *diamagnetic* and the magnetic field is weakened in the presence of the material. In modern physics, however, the magnetic permeability, μ_m , is normally used to describe the magnetic property of a material. The use of χ_m is due to historic reasons. μ_m and χ_m follow a simple relationship:

$$\mu_m = \mu_0 (1 + \chi_m) = \mu_0 \mu_r, \quad (1)$$

where $\mu_r = 1 + \chi_m$ is a dimensionless quantity, called relative permeability, and μ_0 is the permeability in free space and is given in the SI unit system as

$$\mu_0 = 4\pi \times 10^{-7} \text{ Wb A}^{-1} \text{ m}^{-1} = 1.2566 \times 10^{-6} \text{ Wb A}^{-1} \text{ m}^{-1}, \quad (2)$$

where Wb is an abbreviation for Webers, and A stands for amps. Equivalent units are N A^{-2} and H m^{-1} (where N stands for Newtons and H for Henries).

Magnetic permeability and susceptibility are both used to describe the bulk magnetic property of a material and are referenced interchangeably in the literature. However, precise definitions of these two quantities must be kept in mind when quantitative analysis is involved. The magnetic susceptibilities of biological samples are generally small. Table 1 lists the relative permeability of some biologically relevant media.

The magnetic susceptibility effect on MRI describes the distortion of a magnetic field caused by the spatial variations of magnetic susceptibility of biological media. This effect is most intense near the interfaces of media with distinctively different magnetic susceptibilities. The abrupt change of magnetic susceptibility results in a *bound surface current* distribution that induces an additional magnetic field, ΔB , perturbing B_0 . For in vivo MRI, this can be the interface between gray and white matters, or brain tissues and air-containing bone structures such as paranasal sinuses, auditory canals, and mastoid cells. The ΔB in tissue has a simple linear relationship with B_0 :

$$\Delta B = \chi_m B_0. \quad (3)$$

The magnetic susceptibility effect is increased with the magnetic field strength, leading to a greater impact on image spatial encoding and contrast formation.

Table 1. Relative Magnetic Permeability (μ_r) Values Assigned to Different Tissues

Material	μ_r	Reference
Free Space	1.00000000	–
Air	1.00000040	9
Water	0.99999096	10
Fat	0.99999221	10
Bone	0.99999156	10
Blood	0.99999153	11
Gray Matter	0.99999103	–
White Matter	0.99999120	–

The μ_r values of air, water, bone, fat, and deoxygenated blood are obtained from published sources [2-4], while the μ_r values of gray matter and white matter are estimated using weighted averages of fat and water content.

3. T_2^* CONTRAST AT HIGH MAGNETIC FIELD

The magnetic susceptibility effect on MRI is directly related to T_2^* relaxation, in contrast to gradient echo (GE) imaging. Initially introduced by Frahm et al. [5] as a technique for increasing the speed of MRI data acquisition, GE techniques have become increasingly useful for their sensitivity to tissue contrast. Unlike spin-echo (SE) techniques, GE methods are sensitive to variation in tissue bulk magnetic susceptibility. Because GE sequences lack the 180° refocusing pulse used in SE methods, regional differences in the static magnetic field produce an additional mechanism for the transverse magnetization relaxation. The MR signal relaxation for GE and SE techniques are characterized by the time constants T_2^* and T_2 , respectively. T_2^* and T_2 follow a simple relationship: $1/T_2^* = 1/T_2 + \gamma\Delta B/2$. This additional relaxation term is scaled with the field strength because of the increased magnetic susceptibility effect and, thus, becomes dominant in T_2^* relaxation and contrast [6].

The T_2^* contrast provides unique information on tissue magnetic susceptibility, which can be altered biologically from normal to pathologic state. Sensitivity in detection of brain activity with BOLD contrast is directly proportional to the degree of T_2^* contrast. Because T_2^* contrast increases with increasing magnetic field strength, there is significant advantage in using high field for functional MRI (fMRI) applications [6].

From a physical point of view, the vascular structures in the brain are very unique and provide an ideal environment for using T_2^* contrast to study brain function and physiology. As shown in Figure 1, the sponge-like structures of gray matter contain abundant and densely packed vasculatures. Blood, especially the deoxygenated blood in the vasculatures, as endogenous contrast agent, gives rise to

the magnetic susceptibilities of the gray matter different from the adjacent white matter and cerebrospinal fluid. The drastic susceptibility changes on the boundaries of gray matter with white matter and with cerebrospinal fluid result in a magnetic field gradient distribution on their interfaces. In turn, these gradient distributions on the brain surface directly affect the T_2^* contrast of the gray matter. Any functional and physiological brain processes, as well as pathological alterations that change the brain blood oxygenation distribution, can be directly observed by T_2^* contrast imaging. Thus, the potential applications of T_2^* contrast in ultra high field for brain research are tremendous once the susceptibility artifact problems are resolved.

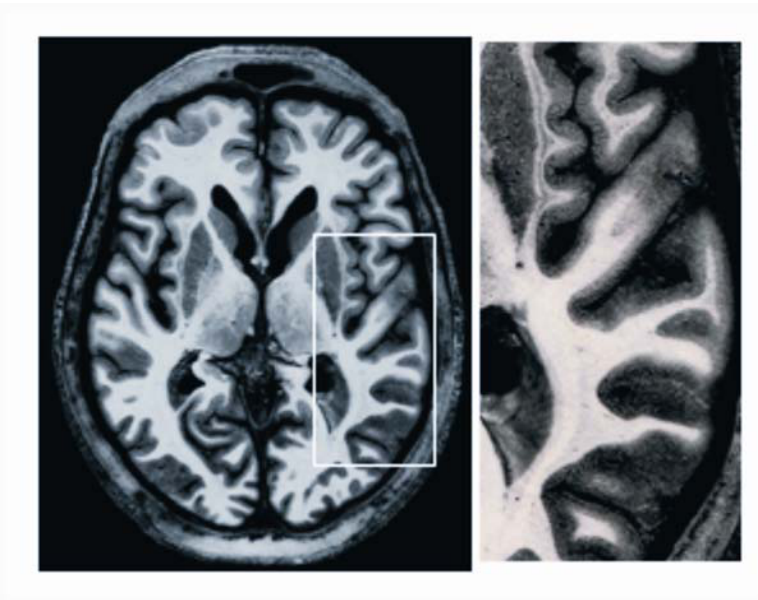


Figure 1. In the brain, the gray matter has substantially more blood vessels and capillaries than white matter. The magnified image on the right displays the rich vasculature in gray matter forming porous, sponge-like structures. The high concentration of blood in the gray matter vasculature makes the gray matter highly sensitive to the blood oxygen level-dependent (BOLD) effect. See attached CD for color version.

The importance of enhancing T_2^* contrast in brain research can be clearly signified by the rapid increase in the number of high field human MRI systems (3 to 8 Tesla) around the world despite their extremely high costs. One of the motivations of such a high concentration of investments to high field systems is to enhance T_2^* contrast for brain research. Undoubtedly, T_2^* contrast is becoming an important research frontier in high field MRI technology.

The magnetic susceptibility differences in tissues and their temporal changes that occur with functional, physiological, and pathological processes produce a unique contrast mechanism in T_2^* -weighted images. Utilizing this relationship, many functional and pathological changes can be studied with MRI. The advances in fMRI exemplify the importance of T_2^* contrast in brain imaging. In addition to fMRI, other neuroimaging methods dependent on T_2^* contrast includes:

1. Assessment of the relative brain iron concentration [7–11]. Brain iron dysregulation and resultant deposition have been implicated in several neuropathologies such as Alzheimer's disease (AD), Parkinson's disease (PD), multiple sclerosis, Pick's disease, Huntington's disease, Hallervorden-Spatz disease, and aceruloplasminemia [12–20]. Qualitative and quantitative assessment of brain iron distribution with T_2^* contrast provides a useful tool for studying these diseases.
2. Characterization of intracranial hemorrhage and calcification [21,22].
3. Qualitative assessment of regional cerebral blood flow (rCBV) during the dynamic injection of susceptibility-based contrast agents [23–26]. The rCBV measurements have been clinically used for the detection and evaluation of brain lesions in strokes, vascular stenoses or occlusions, and brain tumors.

Enhanced T_2^* contrast with ultra high field increases the sensitivity for qualitative and quantitative evaluations of these diseases with T_2^* imaging.

4. MAGNETIC SUSCEPTIBILITY EFFECT: A BLESSING AND A CURSE FOR HIGH FIELD MRI

Despite its broad application, the quality of heavily T_2^* -weighted images using the conventional GE method is far inferior to SE images. The utilization of T_2^* contrast for scientific and clinical investigations has been severely limited by magnetic field inhomogeneity artifacts and low contrast to noise ratio (CNR).

Magnetic field inhomogeneity artifacts in T_2^* -weighted images arise from two major forms:

1. Large macroscopic field gradients are produced by the susceptibility differences between tissue and air-containing structures in the head. As shown later in Figure 9 at §6.2.4, these field gradients produce large signal voids in the inferior frontal and inferolateral temporal lobes. The size of this artifact increases with magnetic field strength, or by increasing echo time (TE). These artifacts will be even more significant with high field cardiac applications, where extensive air/tissue interfaces between lung and mediastinum generate large regional field gradients. Movement of the heart itself will create temporal B_0 field distortion.
2. Smaller field gradients arise from heterogeneous magnetic susceptibility of tissue. Because these gradients are not reproducible and vary

over the entire image volume, it is difficult, and often impossible, to eliminate them with field adjustment (shimming). Artifacts from these gradients degrade image contrast resolution, obscure anatomic detail, and decrease reproducibility and accuracy of experimental results derived from T_2^* contrast. As shown later in Figure 10 at §6.2.4, these artifacts are most severe with MR microscopy, and limit the potential benefits of using ultra high static magnetic field strengths.

A second limitation of T_2^* -weighted images is low CNR [27]. For example, motor cortex activation produces approximately a 1% and 3% change in signal intensity at 1.0 and 3.0 Tesla, respectively. Enhancing such subtle signal changes related to brain function and pathology is difficult because of two inverse relationships:

1. Signal-to-noise ratio (SNR) vs. image acquisition speed: Rapid image acquisition decreases image SNR [28,29]. Conventional methods for increasing SNR, such as signal averaging and increasing acquisition time, are not generally applicable for dynamic studies. In clinical applications, minimizing scan time also requires rapid data acquisition.
2. SNR vs. image contrast: Conventionally, heavily T_2^* -weighted images are generated by a long TE to allow signals to decay, which decreases image SNR. Image CNR is the determining factor in the sensitivity for detecting small T_2^* -weighted signal changes. Since CNR is directly proportional to image SNR, the advantage in enhancing image contrast is frequently compromised by the decreased SNR with longer TE.

Because magnetic field inhomogeneity artifacts and T_2^* contrast are derived from the same physical origin, removing artifacts while maximizing T_2^* contrast is a formidable task. Simply enhancing T_2^* contrast by increasing magnetic field strength or increasing the TE of a GE pulse sequence leads to greater artifacts. Thus, developing methodology to analyze, quantify, and ultimately eliminate static magnetic field distortion artifacts in high field MR images is pivotal for ultra high field MRI development.

5. CHARACTERIZATION OF MAGNETIC SUSCEPTIBILITY-INDUCED FIELD DISTORTION

Detailed knowledge of the B_0 field distribution in the human body is necessary for a better understanding of associated image artifacts so that more effective correction techniques can be devised. The ability to accurately evaluate the B_0 field in the human body will also provide insight into many important physiological and pathological alterations associated with susceptibility changes. However, derivation of an analytical solution of B_0 in a realistic mathematic model of the human body is extremely difficult because of the irregular geometry and complicated μ distribution of the human body. Thus, a computer numerical approach is generally used for studies of both RF and static magnetic fields.

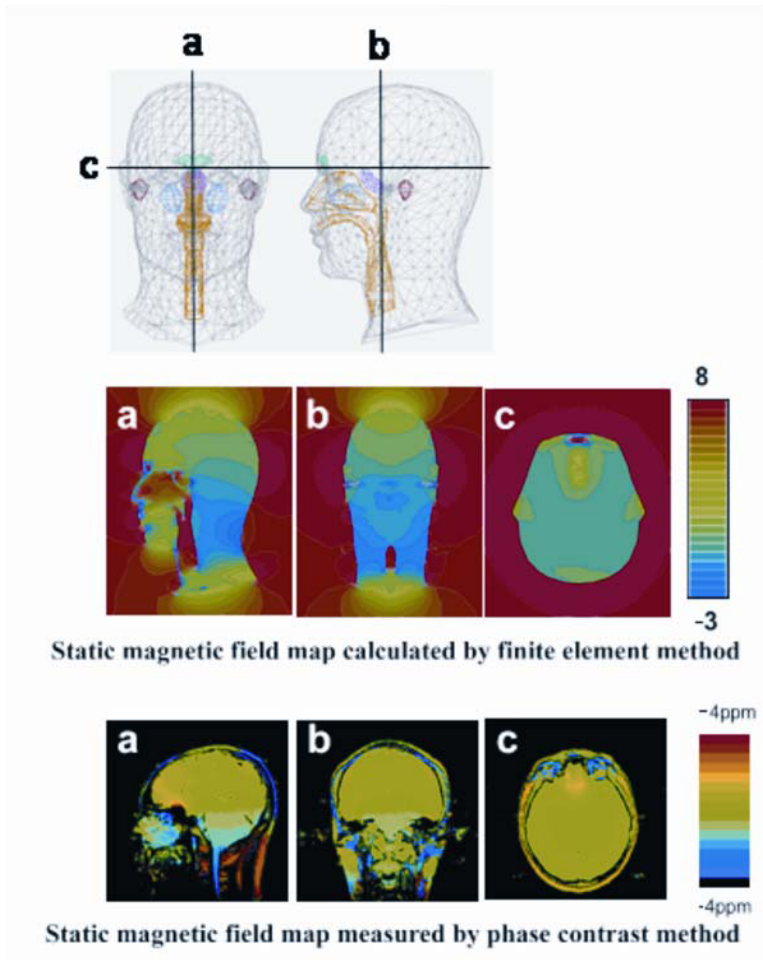


Figure 2. The major air-containing structures included in the model are the frontal sinus (turquoise), the sphenoid sinus (pink), the maxillary sinuses (blue), mastoid air cells (red), nasal and oral cavities, and trachea (yellow). Calculated (top) and measured (bottom) B_0 distributions demonstrate local gradients in the sagittal (a), coronal (b), and axial (c) planes. Magnetic field deviations are color coded in parts per million (ppm). Reprinted with permission from S Li, BJ Dardzinski, CM Collins, QX Yang, MB Smith. 1996. Three-dimensional mapping of the static magnetic field inside the human head. *Magn Reson Med* 36:705–714. Copyright © 1996, John Wiley & Sons Inc. See attached CD for color version.

5.1. Numerical Calculation of B_0 with Finite Element Analysis Method

As a first-order approximation, the B_0 field has been calculated numerically in a simplified head model [30]. In this study, the magnetic field distribution inside the human brain subjected to a uniform B_0 is calculated with a realistic three-

dimensional head geometry using the finite-element analysis method [31,32]. In addition, this model includes several air-containing structures in the human head, as shown in Figure 2. Localized field distributions were evaluated using the magnetic field histogram technique. Figure 3 shows two cross-sectional views of B_0 inside the human head model. The severe distortion of the magnetic field by the air-containing structures in the human head is clearly demonstrated. The calculated results are validated experimentally by in vivo measurements with phase contrast method [33] on a slice-by-slice basis. Figure 2 also shows the quantitative agreement between the calculated and experimental B_0 maps in a human head in three representative orthogonal planes. Field deviations and gradients inside the human head cause MR signal frequency shifts and line broadening, respectively. As we shall see later, these two effects lead to different kinds of image artifacts, which require different corrective approaches. In the human head, a $2 \times 2 \times 0.5 \text{ cm}^3$ voxel may have frequency differences of more than 2.0 ppm. The linewidth of a single voxel may be broadened by more than 0.5 ppm. The field inhomogeneity due to the air/tissue interface extends far beyond the interface area into major brain regions. As the field strength increases, the absolute value of the associated magnetic field gradient is amplified proportionally, producing more severe image artifacts in larger brain areas.

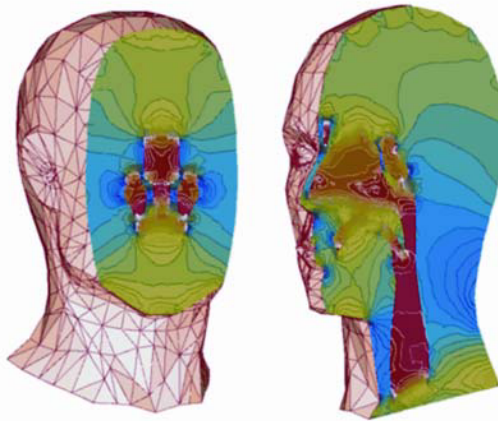


Figure 3. Calculated B_0 distributions inside the human head model demonstrate the remarkable distortion by the air-containing structures inside the human head. Illustration courtesy of Drs. Shizhe Li, C.M. Collins, Q.X. Yang, and M.B. Smith. See attached CD for color version.

5.2. Numerical Calculation of B_0 in Three-Dimensional Multi-Tissue Models with the Finite-Difference Method

The above approach is well suited for general information of the gross field distortion in the human head due to the susceptibility difference between air and tissues and their corresponding geometrical shapes. With this approach, however, it

is not possible to evaluate the subtle B_0 distortions caused by intra-tissue permeability differences that are important for ultra high field MRI applications, because all tissues were treated as water. Susceptibility-induced perturbation of B_0 by the human body during MRI leads to undesirable artifacts as well as valuable physiological information. The ability to quantify these perturbations is extremely useful for understanding the physiological origins of observed image contrast. To address this issue, a more detailed multi-tissue human model was later developed and used for the numerical calculation [34]. The models developed in this work take into account many more tissues, including the permeability values of air, water, bone, gray matter, white matter, fat, and blood listed in Table 1. The model is obtained by segmenting a set of 3D MRI brain images with $2 \times 2 \times 2.5$ mm resolution. With a 3D model of such resolution, the *finite-element analysis* method is no longer suitable for B_0 calculation because of an enormous number of tetrahedron needed for numerical calculation. A more efficient and deliberate static magnetic field solver was developed by Collins et al. with the *finite-difference* (FD) numerical method [35]. The accuracy of the FD method was rigorously validated using regular geometries with known analytical solutions and with experimental results acquired from the head of the same human subject used for computer modeling. In addition to the gross field distortions caused by the air-tissue interfaces in the head described in the previous section, the perturbation by the subtle differences in μ_r between different tissue types was revealed. As demonstrated in Figure 4, the subtle variation in local magnetic field between gray and white matter can be seen on an axial slice of the brain. This result closely reproduced the experimental result with

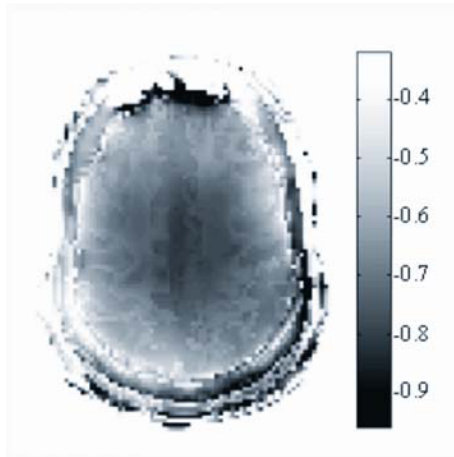


Figure 4. Axial plane view of numerically calculated B_0 field magnitudes in ppm deviation from applied field. The gray scale is set to reveal the B_0 deviation due to the susceptibility difference between gray and white matter in the brain. Reprinted with permission from CM Collins, B Yang, QX Yang MB Smith. 2002. Numerical calculations of the static magnetic field in three-dimensional multi-tissue models of the human head. *Magn Reson Imag* 20:413–424. Copyright © 2002, Elsevier. See attached CD for color version.

susceptibility contrast demonstrated by Reichenbach et al. [36]. The pure susceptibility contrast shown here can be used for studying the susceptibility-related pathological and physiological changes such as iron deposition in Parkinson's disease and the BOLD effect in fMRI. This example demonstrates the utilization of FD numerical method with a multi-tissue model for ultra high field application.

The two major developments in B_0 mapping described in this section provide fundamental understanding of B_0 field distortion in the human head and quantitative analytical tools for many future studies. This information and these research tools are essential for ultra high field MRI development.

6. MAGNETIC FIELD INHOMOGENEITY ARTIFACTS AND REDUCTION

The effects of magnetic field inhomogeneity on the MR signal include frequency shifts and T_2^* relaxation distortion. The manifestation of the resultant artifacts in MR images depends on imaging sequences used and, for the most part, can be categorized as signal loss, image blurring, and geometric distortion. The signal-loss and image blurring artifacts are caused by the distortion of T_2^* relaxation predominantly due to the through-plane local gradient, while the geometric distortions primarily present in EPI are caused by the frequency shift of the MR signal due to the in-plane local gradient.

6.1. Signal-Loss Artifact and Correction

Signal-loss artifact has been a subject of extensive studies [26, 37–44]. Frahm et al. [39] showed that the signal-loss artifact was caused by intravoxel phase dispersion, $\delta\phi$, mainly by the local field gradients in the slice dimension. This is illustrated in the timing diagram in Figure 5. The local gradient in the slice selection dimension, denoted by G_z^1 , causes the phase of the magnetization in a voxel to disperse during TE (intravoxel phase dispersion), which subsequently results in signal loss in a GE image. In this case, the *gradient-echo condition* is no longer valid:

$$A \cdot T_c - 2B \cdot \tau_c + G_z^1 \cdot TE \neq 0. \quad (4)$$

This condition can be reestablished by refocusing this phase dispersion with an additional gradient, G_c , called the compensation gradient, applied in the opposite direction of G_z^1 such that

$$A \cdot T_c - 2B \cdot \tau_c + G_z^1 \cdot TE - G_c \cdot \tau_c = 0, \quad (5)$$

or simply

$$G_c \cdot \tau_c = G_z^1 \cdot TE. \quad (6)$$

Evidently, for the same reason, G_c reduces the signal of other areas where the above relationship does not hold in the image slices. Since G_z^1 generally varies

from voxel to voxel over an image slice, this approach requires acquisition of multiple images with the application of multiple different values of G_c . Each image has appropriate signal intensity only in a certain area where the above criterion is met. The 2D-FT image set in Figure 6 shows a brain axial image set obtained with variable values of G_c . In this set of images, each image only has certain areas with appreciable signal intensity. To produce a signal-loss artifact reduced image of the slice, these images can then be “pieced together” by addition of the magnitude images or with maximum intensity projection. A number of investigations have been carried out to increase the efficiency and effectiveness of Frahm’s compensation gradient method which is later referred as the “z-shim” method [45].

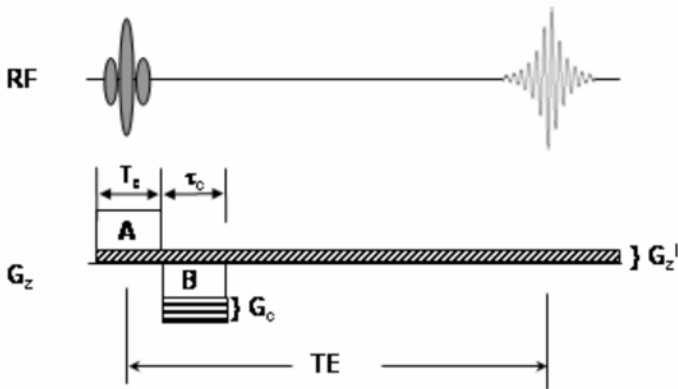


Figure 5. Timing diagram of 2D gradient echo sequence for a voxel. A, slice selection gradient; B, slice rewinding gradient. During TE the local gradient in the slice selection dimension, G_z^1 , causes intravoxel phase dispersion, which results in signal loss in GE images. A compensation gradient, G_c , or a tailored RF pulse, $\alpha[\phi_0(z)]$ can be applied to cancel the phase dispersion by G_z^1 .

A simple and efficient way to integrate these image components is to use the Fourier transform as demonstrated in Figure 6. In the resultant 3D-FT image set, two apparent features are evident: (1) there are only 6 images (images 4–9) that show strong signal intensity; and (2) the signal-loss artifact is removed in these six images. Later we will show that the signal intensity distribution of the 3D-FT image set follows the profile of the excited slice. Thus, this method is referred as *Gradient Echo Slice Excitation Profile Imaging* (GESEPI) [46]. This technique has been shown to be the most effective signal-loss artifact reduction method at ultra high field.

Another alternative approach for signal-loss artifact reduction is to use the so-called tailored RF pulse (TRFP). With this approach, in addition to exciting a slice

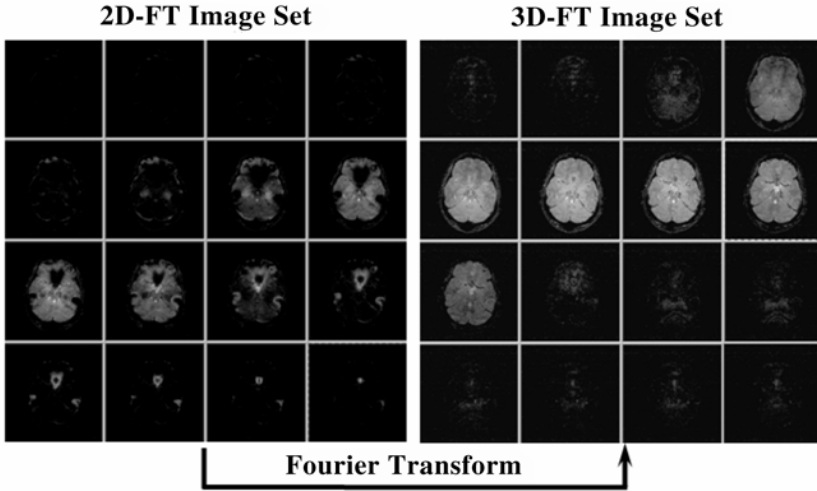


Figure 6. The GESEPI image sets of the human brain obtained at 3.0 Tesla before (2D-FT data set) and after (3D-FT) a Fourier transform along the slice direction with respect to k_z by the compensation gradient. The 2D-FT image set was obtained by sequentially incrementing G_c to obtain $N = 16$ frames. Note the removal of the dark artifacts in the images from 4–6 sub-slices (ca. 1 mm). Reprinted with permission from QX Yang, GD Williams, RJ Demeure, TJ Mosher, MB Smith. 1998. Removal of local field gradient artifacts in T_2^* -weighted images at high fields by gradient-echo slice excitation profile imaging. *Magn Reson Med* 39:402–409. Copyright © 1998, John Wiley & Sons Inc.

with a desired slice profile, the RF pulse is “tailored” to create a given phase distribution across the slice during excitation, $\phi_{(z)}$. This “pre-implanted” phase distribution is later canceled by G_z^1 at TE, yielding full gradient echo signal intensity. Thus, the compensation gradient method and TRFP method, in fact, produce the same effect, i.e., a phase dispersion along slice direction that can be refocused later by G_z^1 when the center of a gradient echo is sampled. Since a TRFP must be tailored to specific G_c and TE prior to data acquisition, a disadvantage for TRFP is the difficulty in implementation for general applications. However, the TRFP method is more versatile because it can produce quadratic or higher order phase variation while the compensation gradient method only produces a linear phase distribution. In addition, Stenger et al. demonstrated that TRFP could be implemented three dimensionally using spiral trajectory during excitation [47,48]. This approach can be advantageous for rapid imaging, because it produces a desirable phase distribution in a 3D volume with a single excitation pulse. This will eliminate the multiple acquisitions required by the compensation gradient techniques. Lastly, Haacke et al. showed that signal-loss artifact could be significantly reduced in a three-dimensional gradient-echo (3D-GE) image [41]. On the surface, these three approaches for signal-loss artifact reduction appear quite different even though they

deal with the same physical problem. In order to evaluate the effectiveness of these methods, it is necessary to establish a comprehensive understanding of these different approaches.

6.2. A Mathematic Analysis of Signal-Loss Artifact and Correction with GESEPI

Among the artifact reduction techniques discussed above, the GESEPI method, in most cases, achieves a complete removal of the signal-loss artifact in the heavily T_2^* weighted images at high and ultra high field. The development of GESEPI also provides a mathematical framework for a clear understanding of the signal-loss artifact and its reduction.

6.2.1. Theory

The understanding of artifact reduction of GESEPI or any other methods can be gained by examining the basic 3D MR imaging process with a focus on the slice (slab) dimension. To simplify the mathematical formalism, phase dispersion and frequency shift effects of the local field gradients in the phase-encoding and read-out directions are first ignored in the present discussions and addressed later. Experimentally, this can be achieved by considering a *quasi point source*, of which the image in-plane dimension is insignificant. The excitation profile of the magnetization along the slice selection direction, $M(z)$, and the radiofrequency (RF) excitation pulse are a Fourier conjugate pair. This relation can be expressed in k -space as [49]

$$M(z) = M_0 F[B_0(k_z)] = M_0 \int B_1(k_z) e^{-ik_z z} dk_z, \quad (7)$$

where M_0 is initial net magnetization density, which includes all other factors that affect the voxel signal, $B_1(k_z)$ is the RF excitation weighting function in the k -space, and F represents a Fourier transform operator. The Fourier operation occurs physically during the slice excitation process.

At time TE after slice excitation, local field gradient G_z^1 generates phase dispersion within the excited slice along the z direction:

$$M_{TE}(z) = M(z) e^{-i\gamma G_z^1 TE z}. \quad (8)$$

The image pixel intensity of conventional two-dimensional (2D) imaging, $I_{\text{vox}}^{2D}(k_z)$, can be viewed as the center of the k -space data point with respect to slice selection direction in 3D imaging. To examine the influence of the phase dispersion factor in Eq. (8) on the k -space signal, an inverse Fourier transform is applied to Eq. (8):

$$I_{\text{vox}}^{2D}(k_z) = F^{-1}\{M_{TE}(z)\} = F^{-1}\left\{M(z) e^{-i\gamma G_z^1 TE z}\right\}. \quad (9a)$$

In the case of a linear intravoxel field gradient (first-order approximation), G_z^1 is constant across the voxel. Then the shift theorem can be applied to the above equation to yield

$$I_{\text{vox}}^{2\text{D}}(k_z) = M_0 B_1(k_z - k_z^0) = M_0 B_1(\alpha), \quad (9\text{b})$$

where $k_z^0 = \gamma G_z^1 \text{TE}$, $k_z = \gamma G_c \tau_c$, and $\alpha = k_z - k_z^0$. This equation describes two important relations. First, the time-domain signal has the same waveform as the excitation pulse (normally a sinc or Gaussian shape), which can be regarded as an echo signal in the k_z dimension. Secondly, the signal intensity reaches maximum (echo peak) when the argument, α , in Eq. (9b) is 0. Thus, the phase factor produced by G_z^1 causes an echo shift to k_z^0 .

The above Fourier operation can be experimentally carried out with the pulse sequence in Figure 5. A series of N images are acquired with sequential increments (ΔG_z) of G_c within a range of $\pm G_c^{\text{max}}$. Application of a two-dimensional FT to the acquired k -space data generates N images (2D-FT data set), in which the intensity of each pixel varies with k_z as described by Eq. (9a). The conventional 2D-GE imaging can be viewed in the 3D imaging setting as a single point in Eq. (9b) at $k_z = 0$. For the regions where the magnetic field is uniform, $G_z^1 = 0$, the signal intensity is maximum at the center of the k -space. For voxels where $G_z^1 \neq 0$, the signal maximum shifts from the center to k_z^0 , and thus, a GE image acquired conventionally with k_z centered in the k -space results in a loss of signal. The signal loss can be recovered by moving the acquisition point to $k_z = k_z^0$, corresponding to the case where the maximum number of voxel spins are in phase. This is the property utilized by the compensation gradient methods for the signal-loss artifact reduction [39,45]. With Frahm's method, the final artifact-reduced image is composed by summation of the 2D-FT image set. However, combining these images by simple addition decreases the SNR in the resultant image. The reason is that the images acquired with varying G_c contain complementary fractional areas of the image plane. Combining these areas by adding 2D-FT images increases noise to the resultant image. In the GESEPI method, this problem can be solved by integrating the 2D-FT data set with a third complex FT with respect to k_z to generate a 3D-FT data set with voxel signal intensity, $I_{\text{vox}}^{3\text{D}}(z)$, given by:

$$I_{\text{vox}}^{3\text{D}}(z) = F \left\{ I_{\text{vox}}^{2\text{D}}(k_z) \right\} = M(z) e^{-i\gamma G_z^1 \text{TE} z}. \quad (10)$$

Equation (10) shows that the signal intensity for the 3D-FT data set in the image-space is modulated by the excitation profile of the slice. $I_{\text{vox}}^{3\text{D}}(z)$, thus, represents the image of the slice (or slab) excitation profile in Eq. (8). The k -space signals that are shifted by different values of G_z^1 and refocused in separate images with corresponding different values of G_c are now all located in the same set of images within the excited slice. The intravoxel gradients at various locations in the image plane only cause a phase variation, which has no effect on the final magnitude image. The signal intensity of the images within the excited slice in the 3D-FT image set is proportional to the echo magnitude regardless of how the echo shifts in the k -space.

The SNR of the final GESEPI artifact-free image is maintained. The above discussion can be easily extended into the nonlinear intravoxel gradient case [46]. Therefore, the GESEPI method also, in principle, removes the intravoxel phase dispersion due to nonlinear terms of the local field gradients.

6.2.2. Relationship between GESEPI and Conventional 3D Imaging

In the GESEPI method, the role of G_c is to compensate the phase dispersion due to G_z^1 . G_c also effectively acts as a phase-encoding gradient in 3D imaging in the slice selection direction, and thus the signal intensity along the slice selection direction represents slice excitation profile. Consequently, each image slice thickness (Δz) in the 3D-FT data set is different from the slice thickness in the 2D-FT data set, and depends on the maximum strength and duration of the compensation gradient offset:

$$\Delta z = 1/k_z^{\max} = 1 / (\gamma G_c^{\max} \tau_c). \quad (11)$$

The images within the excited-slice profile of the 3D-FT data set can be summed to produce a resultant image with similar slice thickness as the 2D-FT image set.

There are two essential differences between 3D and GESEPI data acquisition. First, since the role of G_c is to compensate the intravoxel phase dispersion due to G_z^1 , the maximum compensation gradient offset, G_c^{\max} , is determined by the maximum value of G_z^1 in the image slice and by TE. That is, $G_c^{\max} \tau_c > G_z^1 \text{TE}$ in order to include the shifted echo peak from all the voxels within the acquisition window. The maximum phase encoding gradient for the excitation-selected slab 3D-GE image is determined by the user-defined slice (slab) thickness. The phase encoding gradients for the 3D-GE method are independent of TE. As observed by Haacke et al., the 3D-GE method is beneficial but not adequate or optimized for compensation of intravoxel phase dispersion at a given TE. Second, the acquisition bandwidth for the phase encoding produced by G_c is $N/\gamma G_c^{\max} \tau_c$ (N is number of G_c incremental steps), which is much larger than the bandwidth of the slice-selective excitation RF pulse. GESEPI over-samples the image space in the second phase encoding direction by G_c . Over-sampling in GESEPI plays an essential role in removing the image ghost artifacts due to high-order field gradients.

6.2.3. Experimental Validation

The above mathematic analysis can be illustrated with the phantom shown in Figure 7. An axial slice image was taken such that the two spheres are located at equal distances on opposite sides of the image plane. With this setup, the values of G_z^1 at voxels P and Q are equivalent in magnitude but in opposite direction. The voxel at point R is in the region of uniform magnetic field.

Figure 7 shows the conventional GE and GESEPI images from the same slice of the phantom. The dark areas at points P and Q are the typical signal-loss artifacts produced by the adjacent air-filled spheres. These artifacts are removed in the GESEPI image. In Figure 8, voxel intensity at P , Q , and R from the phantom image

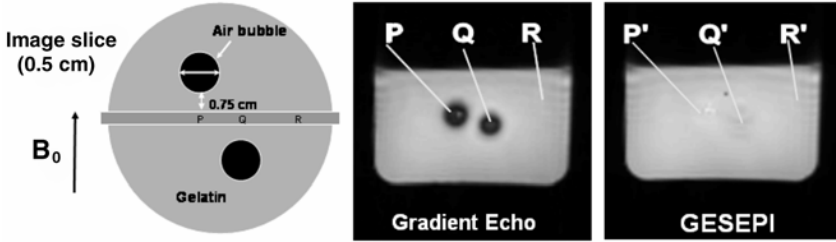
A Susceptibility Phantom and T_2^* -Weighted Images

Figure 7. A coronal view of the phantom and images of the axial slice along the midline between the two spheres with the GE and GESEPI methods. The phantom consists of two air-filled spheres positioned inside a gelatin-filled cylindrical container with its longitudinal axis perpendicular to B_0 . The voxels P , Q , and R indicated in the GE image are labeled P' , Q' , and R' in the corresponding GESEPI images. The phantom images were obtained with a flip angle of 25° , $TR/TE = 80 \text{ ms}/25 \text{ ms}$, $FOV = 25 \times 25 \text{ cm}^2$, image matrix = 128×128 , slice thickness = 5 mm . Adapted with permission from QX Yang, GD Williams, RJ Demeure, TJ Mosher, MB Smith. 1998. Removal of local field gradient artifacts in T_2^* -weighted images at high fields by gradient-echo slice excitation profile imaging. *Magn Reson Med* **39**:402–409. Copyright © 1998, John Wiley & Sons Inc.

is plotted following the initial two-dimensional Fourier transform as a function of k_z , and following the third Fourier transform, as a function of position z along the slice direction. As shown by Eq. (9) for voxel R in the homogeneous region, the intensity as a function of k_z has a sinc-shaped profile corresponding to the waveform of the excitation pulse. Signal intensity is maximum where $k_z = 0 \text{ rad/cm}$ (the 32nd image). As predicted, the signal intensities from voxels P and Q are greatly reduced in this central image, since the signal maxima are shifted in opposite directions by the opposing local field gradients, G_z^1 , to the 47th and 19th images, respectively. From the prospective of the GESEPI data, it clearly demonstrates that the signal loss due to intravoxel dephasing can be equivalently regarded as a result of echo shift in k_z and can be recovered by shifting the acquisition point to k_z^0 . Following the initial 2D-FT, this signal spreads amongst all images of the data set according to the strength and direction of G_z^1 . Each image in the 2D-FT data set contains only a portion of the imaged object. After performing the third Fourier transform with respect to k_z , the voxel intensity of magnitude images is modulated by the excitation profile. Unlike the signal intensity plots for P , Q , and R in the 2D-FT data set, the voxel intensities in the homogeneous region R' and inhomogeneous regions, P' and Q' , are all maximum in the center of the slice profile (see Figure 8). Note that there are five images in the excited slice position. Summation of these five images generates an image, free of artifacts, with the same slice thickness as the conventional gradient echo image shown in Figure 7. The SNR for the GESEPI image is 35% higher than that for the conventional GE image. In general, the SNR

for GESEPI should be the same or better than that for the conventional gradient-echo image, depending on the extent of over-sampling.

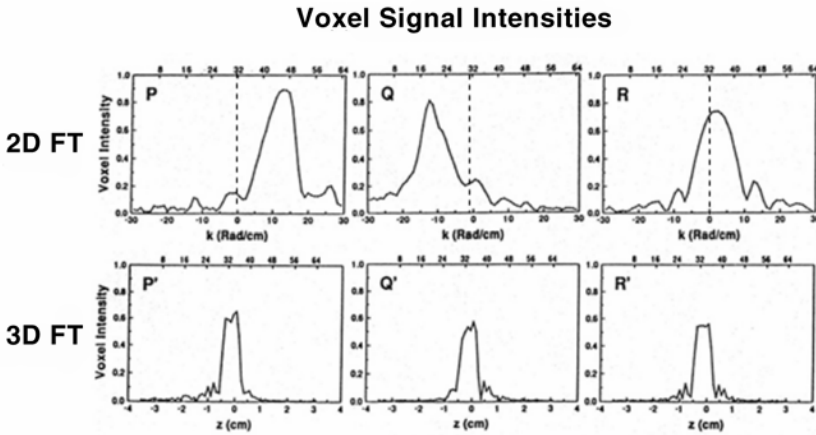


Figure 8. Serial signal intensity plots from the representative voxels P , Q , and R (see Figure 7) in the 2D-FT data set, and from the corresponding voxels P' , Q' , and R' in the 3D-FT data set. The image number axis is shown above each plot, corresponding to either k_z (2D-FT, top row) or position z along the slice direction (3D-FT, bottom row). The dashed lines in the top row plots indicate $k = 0$, where 2D images were acquired. Reprinted with permission from QX Yang, GD Williams, RJ Demeure, TJ Mosher, MB Smith. 1998. Removal of local field gradient artifacts in T_2^* -weighted images at high fields by gradient-echo slice excitation profile imaging. *Magn Reson Med* 39:402–409. Copyright © 1998, John Wiley & Sons Inc.

The theoretical underpinning of the difference in signal characteristics between the k -space and the image-space is that for the magnetization in a voxel with various phases the signal intensity at any point in the k -space is the vector sum while for the magnitude image-space the signal is proportional to the scalar sum (echo peak). The phase dispersion of the magnetization reduces the vector sum and has no effect on the scalar sum. As long as the time-domain acquisition window includes all of the shifted echo peaks from the voxels of the excited slice, the signal attenuation due to intravoxel phase dispersion can be recovered. The role of the third Fourier transform is to effectively bring the voxel signals that are spread into different images in the 2D-FT data set to the images within the excited-slice profile.

As discussed previously, the image-space bandwidth defined by $N/\gamma G_c^{\max} \tau_c$ is wider than the excitation pulse bandwidth such that regions outside the excited slice are also imaged. This appears to be wasteful since presumably there is no signal coming from these regions to image. There are two reasons why over-sampling is necessary to remove the phase dispersion artifacts. First, the sampling in k_z must be fine enough to capture and define the echo peak that is shifted due to the heterogeneous distribution of G_z^1 in the excited slice. The intensity of the echo

peak determines the pixel intensity in the 3D-FT images. Accurate sampling of the echo peak improves the final image quality. Second, the local field gradients (especially the nonlinear components) in the voxels produce frequency shifts that may exceed the slice bandwidth. Thus, it can be seen explicitly from Figure 6 that the images outside the excited slice exhibit an increasing proportion of signal intensity from the inhomogeneous areas. Without over-sampling, these signals would alias into the central images, creating ghost artifacts. This is why significant magnetic susceptibility artifacts are still present, although reduced, with conventional 3D-GE images at 3.0 Tesla. The extent of over-sampling needed depends on the distribution of local field gradients within a specific imaging slice. For the slice of the human brain at 3.0 Tesla shown in Figure 6, 16 G_c steps are adequate to completely remove the signal-loss artifact with TE as long as 50 ms. For the phantom image in Figure 7, 64 G_c incremental steps were used to obtain an excellent representation of the echo shape, although only 16 incremental steps are necessary to remove the signal-loss artifact in the areas around the voxels P and Q . This excessive over-sampling produces an increase in SNR in the GESEPI image due to multiple sampling on the echo peak. Thus, excessive over-sampling is preferable to signal averaging for generating T_2^* -weighted images in high field microimaging where the voxel volume is small and the magnetic susceptibility effect is strong.

6.2.4. Application of GESEPI at High Magnetic Field

The applications of GESEPI to high field brain imaging at 3.0 and 7.0 Tesla for human and at 14.0 Tesla for mouse demonstrate the significant improvement in quality of T_2^* contrast images. Figure 9 shows conventional GE transverse human brain images and the corresponding GESEPI images at 3.0 and 7.0 Tesla. The two types of artifacts due to the field inhomogeneity are shown clearly in the GE images. The signal losses in the GE images, which produce large signal voids in both the frontal and temporal areas and at the brain-skull interface, are completely recovered in the GESEPI images. Image blurring and uneven signal intensity artifacts are also reduced. The overall signal intensity is more uniform in the GESEPI images than in the GE images, reflecting the signal recovered from losses attributed to inherent field inhomogeneities, yielding a spin-echo image quality. The overall SNR of the GESEPI images is better than the corresponding GE images because the signal intensity in the latter is attenuated by the intravoxel field gradients, while in the GESEPI images it is amplified by the summation of the component sub-slice images. The T_2^* -weighted image obtained from the inferior human brain area with TE as long as 15 ms at 7.0 Tesla demonstrates the enhancement of the magnetic susceptibility effect at ultra high field with unprecedented high contrast between iron-rich brain structures. The superior T_2^* contrast clearly delineates iron-rich brain regions such as the globus pallidus, substantia nigra, and red nucleus. Evidently, information brought about by the enhanced magnetic susceptibility effect at high field will have wide clinical applications.

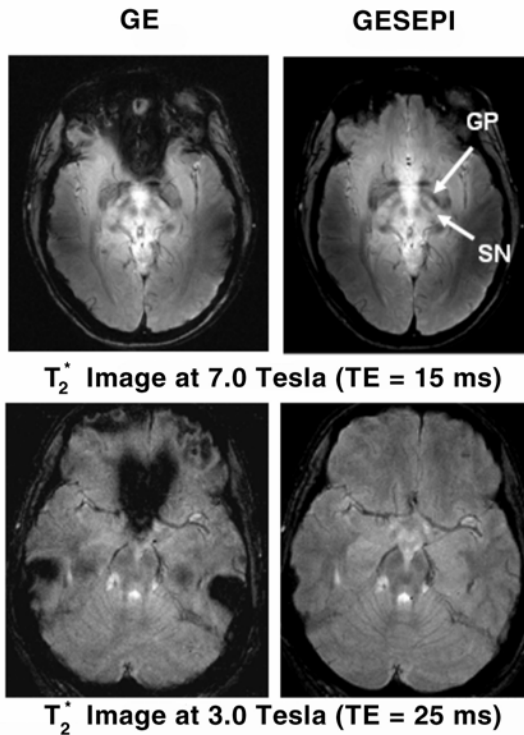


Figure 9. GESEPI effectively removed signal-loss artifacts in heavily T_2^* -weighted images at 3.0 and 7.0 Tesla. All the images have the same slice thickness — 5 mm. The GESEPI images were obtained with 8 G_c steps. The intensities of the globus pallidus (GP) and substantia nigra (SN) are obscured in the GE images and enhanced in the GESEPI images. Note that the signal nonuniformity in the GESEPI image at 7.0 Tesla is caused by the B_1 field distortion due to the wave effect.

Figure 10 displays a GE and a GESEPI mouse brain image taken at 14.0 Tesla. Even at TE = 4.5 ms, severe signal loss near the skull and auditory canals obscures most of the GE image. A key observation in this image is that in a presumably homogeneous region of the brain the GE image has poor contrast resolution, while the GESEPI image exhibits greater contrast resolution and more anatomic detail. This striking difference has not been observed at lower field strengths. At such a high field strength, one would expect greater T_2^* contrast resolution because of T_2^* enhancement with stronger field. However, contrary to our expectation, the contrast in the GE image appears to be diminished. The loss of contrast resolution in the GE image and its restoration by GESEPI may be related to properties of susceptibility-induced higher-order gradients with respect to field strength.

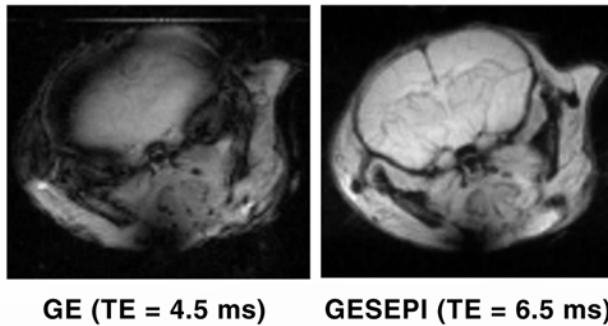


Figure 10. T_2^* -weighted images of a mouse brain at 14.0 Tesla. By removing the artifacts in the GE image, the GESEPI image improves contrast resolution and displays anatomic details not observable in spin-echo images. Reprinted with permission from QX Yang, MB Smith, RW Briggs, RE Rycyna. 1999. Microimaging at 14 tesla using GESEPI for removal of magnetic susceptibility artifacts in T_2^* -weighted image contrast. *J Magn Reson* **141**:1–6. Copyright © 1999, Elsevier.

The theoretical basis for separating static magnetic field inhomogeneities that produce artifacts from those that yield contrast is based on the difference in size of the field gradient relative to the image voxel. As proposed by Yablonskiy et al., the B_0 field gradients occurring in the tissue can be approximately classified into the following three categories according to the spatial properties [51]. **Macroscopic:** These linear or lower-order gradients in the spatial domain are larger than, or similar in size to, the image voxel. These gradients produce undesirable image artifacts, and can be removed by GESEPI. **Atomic/Molecular:** These gradients in the atomic and molecular scale are many orders of magnitude smaller than the voxel size. Their fluctuations contribute to T_2 and T_1 contrast, and cannot be removed with either an 180° RF refocusing pulse or GESEPI. **Mesoscopic:** These gradients are smaller than the voxel size and greater than atomic/molecular level. This category is defined more by image resolution than by any actual physical constraint. They are nonlinear higher-order gradients. These gradients, which produce useful tissue-specific T_2^* contrast, are retained by GESEPI, but removed with the 180° RF refocusing pulse used in SE sequences. As demonstrated by the images in Figure 10, GESEPI effectively removes macroscopic field inhomogeneity artifacts while maintaining T_2^* contrast.

With GESEPI, quantitative T_2^* mapping can be performed reliably at ultra high field strengths. Figure 11 shows the conventional GE and GESEPI image series as a function of TE for the immature rat brain at 9.4 Tesla. The conventional GE images at short TEs appear blurry with uneven signal intensity over the images. These artifacts become progressively worse as TE increases. The GESEPI images, however, provide superior image quality at all TE values. At TE = 22.4 ms, the GESEPI image displays significant anatomical details, which are absent in the conventional GE images. The GE image at TE = 33.5 ms is completely distorted by

the artifacts, while details from the GESEPI image at TE = 50 ms are still discernible with enhanced T_2^* weighting. Thus, the GESEPI technique extends the TE observation window for magnetic T_2^* contrast, rendering a more sensitive and reliable T_2^* mapping for clinical applications. Figure 12 shows the average R_2^* ($= 1/T_2^*$) maps from seven 25–28-year-old normal human subjects. The R_2^* distribution exhibits high heterogeneity in the brain. The known iron-rich brain regions (i.e., putamen, globus pallidus, substantia nigra and red nucleus) are clearly delineated by the sharp contrast in the R_2^* maps. The unprecedented superior quality of the R_2^* maps in the figure is attributed to effective artifact removal using the GESEPI method.

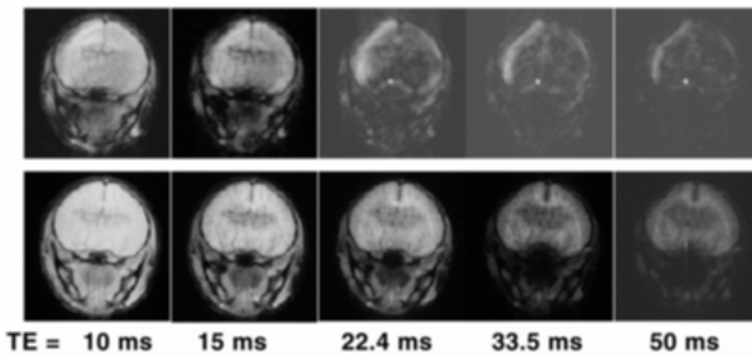


Figure 11. GE (top row) and GESEPI (bottom row) images of an immature rat brain as a function of TE taken on a 9.4T system. TR = 80 ms, matrix = 128×128 , FOV = 20×20 mm², slice thickness = 1 mm. Reprinted with permission from QX Yang, GD Williams, RJ Demeure, T Mosher, MB Smith. 1998. Removal of local field gradient artifacts in T_2^* -weighted images at high fields by gradient-echo slice excitation profile imaging. *Magn Reson Med* 39:402–409. Copyright © 1998, John Wiley & Sons Inc.

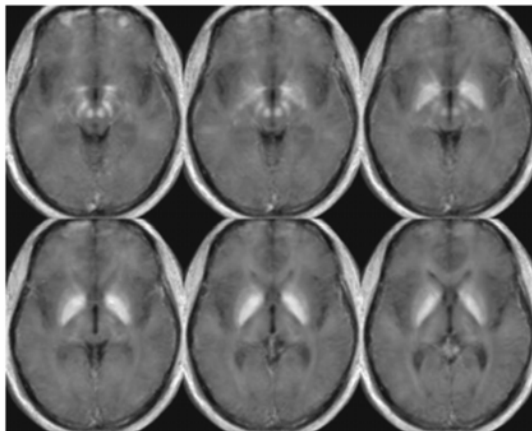


Figure 12. Average R_2^* map of the human brain with GESEPI.

The total image time is significantly increased in GESEPI and the other methods utilizing compensation gradient technique. Although the GESEPI method is not suitable for dynamic studies, the high SNR achieved with minimal artifacts allows for true T_2^* imaging for comparison with spin-echo methods. As we show later in the §7, the development of parallel imaging techniques allow GESEPI for dynamic applications.

7. IMAGE BLURRING AND GEOMETRIC DISTORTION ARTIFACTS IN RAPID IMAGING AND CORRECTION

The amplified magnetic susceptibility effect at high field strength increases the difficulty in performing rapid imaging (EPI and spiral imaging) considerably [52,53]. EPI and spiral images are typically acquired with a long acquisition trajectory during which the MR signal is modulated by T_2^* relaxation. This makes rapid imaging inherently vulnerable to magnetic field inhomogeneity artifacts. Given the important role of these techniques in dynamic imaging, significant efforts have been made in developing techniques to reduce or eliminate these artifacts [11, 37–41,44,46,47,51,54–70]. The presentations of magnetic field inhomogeneity artifacts in rapid imaging include signal loss, image blurring, and geometric distortion. For 2D-EPI, image blurring and signal loss are caused by the distortion of T_2^* relaxation predominantly due to the through-plane local gradient, while the geometric distortion artifact is caused by the frequency shift of the MR signal due to the in-plane local gradient. For 2D spiral imaging, both in- and through-plane gradients result in image blurring. Since we have examined the signal-loss artifact and its correction in the previous section, in the following we focus on methods for correcting blurring and geometric distortion artifacts specific to rapid imaging sequences.

7.1. Image Blurring Artifact in Rapid Imaging

To simplify the discussion, let us again consider the quasi-point source or a voxel and examine how the local gradient impacts its signal during data acquisition. The effect of local magnetic field gradients can be decomposed into through-plane and in-plane components and treated separately. The through-plane local gradient plays a dominant role in distortion of tissue-specific T_2^* relaxation characteristics [11,38,39,46]. The signal intensity during a 2D rapid acquisition can be described as:

$$S = M_0 \exp(-t/T_2^*) \operatorname{sinc}[\gamma G_z^1 z_0 t / 2], \quad (12)$$

where M_0 is the magnetization density and z_0 the slice thickness (46). In the above expression, an ideal excitation profile is assumed. With given G_z^1 , the T_2^* decay during the data acquisition time, t , is distorted with a sinc-function modulation. With this equation, the signal-loss artifact can be easily understood as a result of

signal dropout at effective TE as the signal of the center of the k -space is sampled. On the other hand, the distortion of T_2^* relaxation characteristics results in a strong attenuating modulation of the MR signal along the k -space trajectory of rapid imaging sequences. This modulation acts as a low-pass filter on the k -space signal, resulting in image blurring for conventional rapid acquisition methods. The local gradient modulation on the voxel signal can be removed with the GESEPI technique. In this case, the signal intensity of a voxel in the excited slice is expressed in the k -space along z as

$$S = M_0 \exp(-t/T_2^*) \text{sinc}[\pi(k_c - k_l(t))z], \tag{13}$$

where $k_c = \gamma G_c \tau_c / 2\pi$ and $k_l = \gamma G_z^1 t / 2\pi$. Applying Fourier transform to Eq. (13) with respect to k_c yields a set of images of N sub-slices with intensity I , given by

$$I = M_0 \exp(-t/T_2^*) \exp[i\gamma G_z^1 z_0 \tau_c] \text{rect}, \tag{14}$$

where $i = \sqrt{-1}$, and rect is a rectangular function representing the signal intensity profile of the N sub-slice images in the excited slice. The sinc-function modulation on the T_2^* relaxation in Eq. (12) is replaced with a phase modulation that does not affect the magnitude image. By removing the sinc-function modulation due to G_z^1 during data acquisition, the GESEPI technique recovers signal loss and reduces image blurring for rapid data acquisition.

To help understand the above mathematical analysis, let us plot Eq. (13) and its Fourier transform in Figure 13. Figure 13a shows the voxel intensity as a function of k_c and t . For conventional 2D imaging, the signal intensity change with time along the trajectory is obtained by intersecting the plot with plane $k_z = 0$, which is shown as Plot II in Figure 13c. It shows the sinc-modulation on T_2^* relaxation due

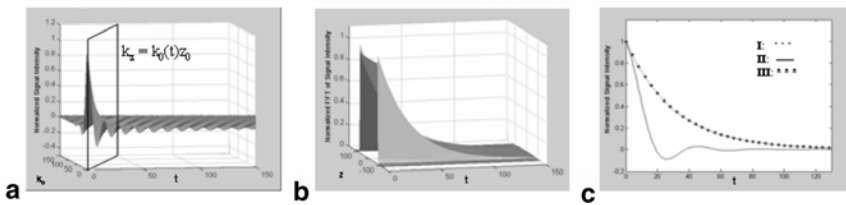


Figure 13. The voxel signal intensity from the excited slice of the GESEPI data is plotted as a function of k_c and acquisition time t along the trajectory (a) and its Fourier transform (b). The plots were calculated using Eqs. (13) and (14) with $T_2^* = 30$ ms, $G_z^1 = 0.5$ ppm/cm, $z_0 = 5$ mm, and $B_0 = 3.0$ Tesla. The plots in (c) are standard 2D voxel signal intensity along the trajectory with $k_l = 0$ (Plot I), $k_l \neq 0$ (Plot II), and GESEPI intensity with $k_l \neq 0$ (Plot III), respectively. The Plot II in (c), obtained by intersecting the two-dimensional plot in (a) with $k_z = 0$, shows a sinc-function modulation of T_2^* decay. Plot III, obtained by intersecting the plot in (b) with $z = 0$, coincides with Plot I of normal T_2^* relaxation.

to G_z^1 . In the normal case where $G_z^1 = 0$, the plot in Figure 13a would vary independently as an exponential decay with t and a sinc-function with k_c . As indicated in Figure 13a, the effect of G_z^1 on the signal is to rotate the plot from the t -axis to $k_c = k_1(t)$. Only along this line, the effect of G_c is compensated by G_z^1 , yielding a normal exponential T_2^* decay shown as Plot I in Figure 13c. As depicted in Figure 13b, the signal intensity after Fourier transform of the plot in Figure 13a with respect to k_z varies as a normal T_2^* relaxation with respect to t , and a rect-function with respect to z . In other words, the sinc-modulation on the signal along the trajectory in Figure 13a is removed. Restoration of normal T_2^* modulation results in complete removal of the signal-loss and image-blurring artifacts.

The plots in Figure 13c demonstrate three typical cases. In the homogeneous region where $k_1 = 0$, the voxel signal intensity follows a normal T_2^* relaxation shown as Plot I. For voxels in the inhomogeneous region where $k_1 \neq 0$, the standard EPI signal intensity is modulated with a sinc-function shown as Plot II. In this case, the normal relaxation curve would be found only along the intersection with plane $k_c = k_1$ because of the rotation of the plot by k_1 . Plot III was obtained by intersecting Figure 13b with plane $z = 0$, which represents the voxel signal along the k -space trajectory with GESEPI. The overlap of Plot I and III indicates a complete restoration of the T_2^* relaxation characteristic.

7.2. Reduction of Blurring Artifact in EPI

The above analysis can be illustrated experimentally with a quasi-point source phantom. Figure 14 shows a comparison of EPI images acquired with and without application of the GESEPI technique from a homogenous and inhomogeneous B_0 region of the quasi-point source phantom. The three images in the top row were obtained without phase-encoding gradient in the left–right direction. These images are projection images from the point-source phantom. The plot in the center row under each image represents the signal intensity profile from the same horizontal line passing through one of the point sources in the image. Since no gradient was applied, the image intensity distributions along this direction are determined by T_2^* relaxation characteristics only. Therefore, each plot represents the profile of the point spread function (PSF) along the horizontal direction using the corresponding acquisition method. The EPI image signal intensity profile in the homogeneous region yields a sharp peak as expected, rendering a well-defined PSF. Assuming the plot is a single Lorentzian, the linewidth (FWHM) is 0.71 pixels wide. In the inhomogeneous region, however, the signal intensity spreads out into the entire FOV in the horizontal direction, representing a broad PSF. The corresponding linewidth is 3.5 pixels wide. The image resolution under such a condition is significantly compromised. The PSF profile of the corresponding image when the GESEPI method is applied is significantly improved, with its linewidth reduced to 1.2 pixels. The images in the bottom row in Figure 14 are the actual EPI and GESEPI-EPI images of the point-source phantom in the homogeneous and inhomogeneous regions. The blurring artifact due to the local field gradient and its re-

duction with the GESEPI is clearly demonstrated. As we shall see in the following section, similar results can be shown for spiral acquisition.

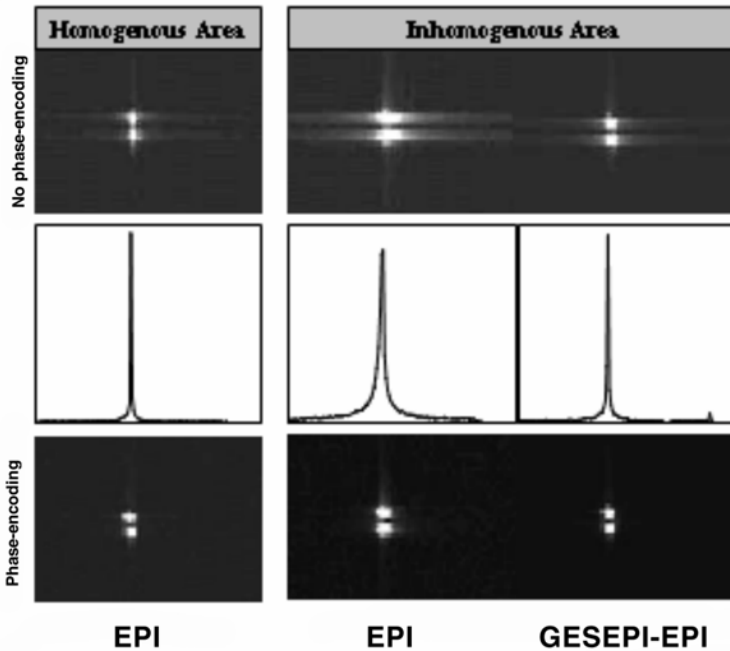


Figure 14. Top row: the signal intensities acquired without phase-encoding in the left-right direction. Center row: image intensity plot, representing point-spread function (PSF) profile in phase-encoding direction. Bottom row: images acquired with phase-encoding, demonstrating the reduction of blurring artifacts in EPI using the GESEPI method. The quasi-point source phantom for axial images consists of two 5-mm diameter tubes filled with gelatin, with a 1.8-mm distance between the tubes. The tubes are aligned with the B_0 field. The image intensities are adjusted to facilitate visualization of PSF. Adapted with permission from QX Yang, J Wang, MB Smith, M Meadowcroft, X Sun, PJ Eslinger, X Golay. 2004. Reduction of magnetic field inhomogeneity artifacts in echo planar imaging with SENSE and GESEPI at high field. *Magn Reson Med* **52**:1418–1423. Copyright © 2004, John Wiley & Sons Inc.

The signal-loss and image-blurring artifacts occur concomitantly in T_2^* -weighted EPI images, because both artifacts are caused by T_2^* relaxation distortion due to the through-plane local gradient. It is important to recognize, however, that a method removing the signal-loss artifact does not necessarily remove the image-blurring artifact in EPI. For example, methods of adding multiple magnitude images acquired with different strengths of the slice-refocusing gradient result in a stronger image-blurring artifact. The reason for this is that the refocusing gradient

utilized in these techniques only compensates the MR signal phase dispersion occurring at the center of the k -space while modulation by the distorted T_2^* remains along the rest of the EPI k -space trajectory. The composite image obtained by adding the magnitude images acquired with different refocusing gradients would evidently inherit the blurring artifacts of all its component images. As shown theoretically and demonstrated experimentally with phantom and human studies, the GESEPI technique is capable of correcting both artifacts. Since the EPI k -space signal of spin-echo is also modulated with T_2^* relaxation, the associated blurring artifact exists in spin-echo EPI images and becomes aggravated at higher field strengths. Therefore, the GESEPI method is also useful for reduction of blurring artifact in spin-echo EPI at ultra high field.

7.3. Reduction of Geometric Distortion in EPI with SENSE

The geometric distortion artifact is prevalent and most prominent for EPI. The frequency shift of the MR signal by the in-plane local gradient results in pixel shift and thus distorts the echo planar images. This artifact poses a problem for fMRI in the inferior brain regions, since the severe distortion of the anatomy in the images from each subject make intersubject comparison and statistical data analysis difficult. The reason for the increased severity of the artifacts is the accumulative effect of the in-plane susceptibility gradient during the elongated k -space trajectory in the EPI sequence. This kind of artifact is mainly in the phase-encoding direction because the encoding gradient and the effective spectral bandwidth in this direction are relatively small and more susceptible to the local gradients and the resultant frequency-shift perturbations. The parallel imaging techniques such as SENSitivity Encoding (SENSE) imaging technique provide a means to ameliorate this problem [72–74]. For example, with the SENSE technique, multiple images are acquired simultaneously from multiple reception coils with a reduced number of phase-encoding steps, while maintaining the k -space sampling area the same as the conventional method. The ratio of k -space sampling between the conventional and SENSE methods is called the reduction factor, r . Skipping the phase-encoding steps in the k -space in SENSE acquisition leads to a reduction of FOV in the image space, which results in aliasing. Thus, the images from each coil will be aliased. Since the signal distributions in the images from different coils are distinctively different, the aliased images can then be used to construct an “unwrapped” image using the prior spatial sensitivity information from each coil. Thus, SENSE technique only needs a fraction of the conventional EPI acquisition time. With current hardware, to acquire an EPI image with 128×128 pixels will require about 100 msec. By using the SENSE technique the k -space trajectory and the corresponding acquisition time will be reduced two to threefold, which, in turn, significantly mitigates the artifacts due to the in-plane gradient. In order to exclusively demonstrate the geometric artifacts and their correction by SENSE, Figure 15 shows a pair of spin-echo EPI images without and with SENSE. It is evident that SENSE significantly reduced the geometric distortions in the EPI image in Figure 15a. The SENSE-EPI image in Figure 15b was acquired with a reduction factor of 3. Further

improvement is expected with a higher reduction factor at higher field strength [75]. Decreasing acquisition time will also improve the image point-spread function, which will facilitate through-plane artifact reduction with GESEPI.

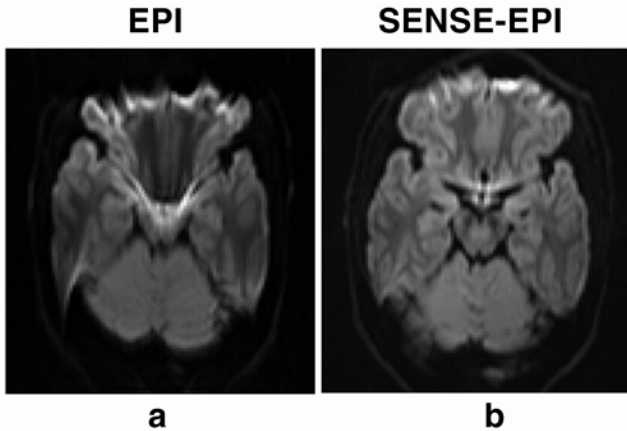


Figure 15. Spin-echo EPI images acquired without (a) and with SENSE with a reduction factor $r = 3$ (b) from an inferior brain slice. In spin-echo images, the signal-loss artifact is minimal so that the geometric distortion due to the in-plane gradient can be demonstrated clearly. In order to highlight the brain geometry, a diffusion gradient was applied to reduce the CSF signals. Both images were acquired from a Philips Intera 3.0T MRI system with the same acquisition parameters. Reprinted with permission from T Jaermann, G Crelier, KP Pruessmann, Golay X, T Netsch, AM Van Muiswinkel, S Mori, PC Van Zijl, A Valavanis, S Kollias, P Boesiger. 2004. SENSE-DTI at 3 T. *Magn Reson Med* **51**:230–236. Copyright © 2004, John Wiley & Sons Inc.

Figure 16 shows three sets of EPI images from a human brain acquired using the GE, GESEPI, and SE methods with SENSE ($r = 3$). As indicated by the arrows, severe signal-loss artifacts in the inferior-frontal and temporal brain regions can be seen in all the slices acquired with the GE method. Thus, the interference of the signal-loss artifact remains a serious problem for T_2^* brain imaging with SENSE method at 3.0 Tesla. As seen in Figure 16b, complementary to the SENSE method, the signal-loss artifact was significantly reduced with the GESEPI technique. The effectiveness in signal-loss artifact reduction can be seen when comparing to the corresponding SE images. Incorporation of GESEPI with SENSE allows effective reduction of all three types of artifacts in EPI. Thus, the SENSE and GESEPI methods are complementary and mutually facilitating in artifact reduction, and combining these two techniques allows for effective correction of all three kinds of artifacts in EPI images. In addition, the limitation of increased image acquisition time for GESEPI is addressed efficiently with SENSE.

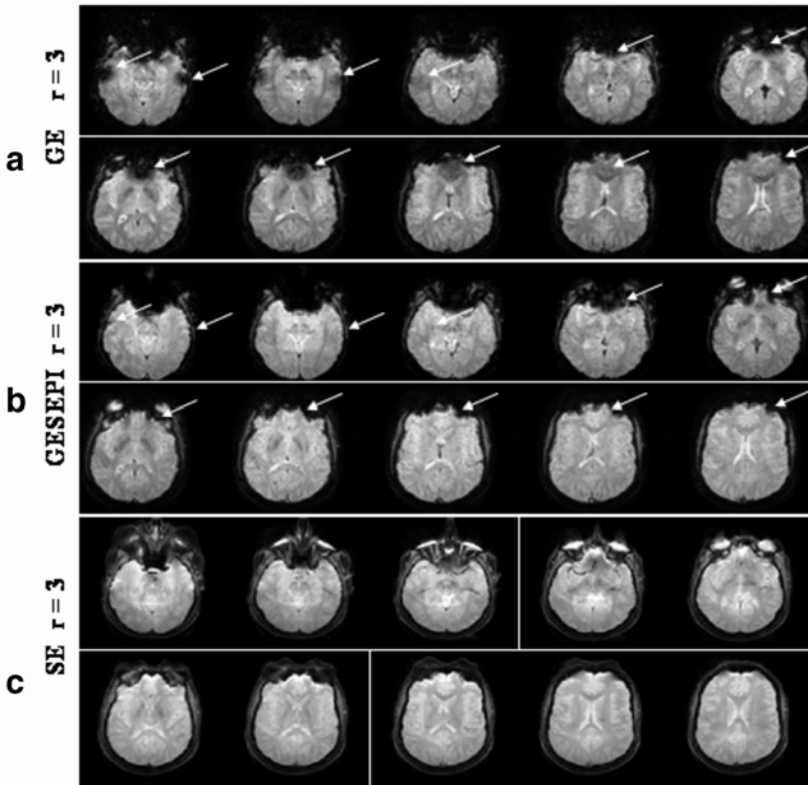


Figure 16. The EPI images were acquired from the same human brain volume with SENSE ($r = 3$) using the GE (a), GESEPI (b), and SE (c) methods. The typical signal-loss artifact in the GE images (a) in the inferior frontal and temporal brain regions indicated by the arrows is reduced significantly with GESEPI (b). Reprinted with permission from QX Yang, J Wang, MB Smith, M Meadowcroft, X Sun, PJ Eslinger, X Golay. 2004. Reduction of magnetic field inhomogeneity artifacts in echo planar imaging with SENSE and GESEPI at high field. *Magn Reson Med* 52:1418–1423. Copyright © 2004, John Wiley & Sons Inc.

7.4. Reduction of Field Inhomogeneity Artifacts with Reversed Spiral Imaging

Spiral imaging conventionally acquires data from the center to the edge of the k -space using the simplified gradient diagram shown in Figure 17. To improve TR efficiency, Bornert et al. introduced the reversed spiral that sample the k -space in reverse order [76]. Glover et al. later demonstrated that the reversed spiral trajectory reduces the signal-loss artifact and increases the BOLD contrast [64]. This

effect can be illustrated with the simulated signal from the point source along the trajectory in Figure 18. With the reversed spiral, the modulation of T_2^* on the signal is also reversed, leading to a filtering effect that emphasize higher spatial frequency. This, in effect, makes the images sharper, instead of blurred. With conventional forward spiral, the k -space data are acquired starting at TE, where MR signal

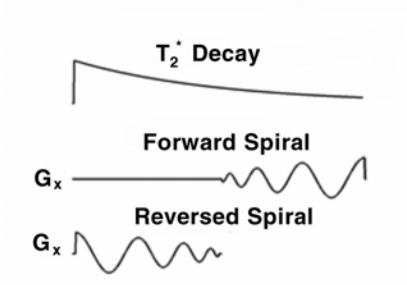


Figure 17. Relationship of T_2^* decay with Forward and Reversed spiral acquisition. Illustration provided courtesy of Dr. V. Andrew Stenger.

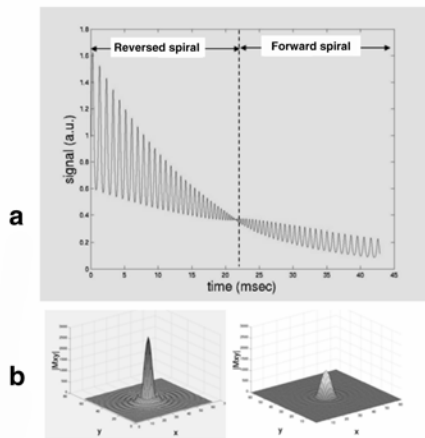


Figure 18. Simulated k -space signals of a point source with reversed and forward spiral acquisitions (a) and the corresponding image profiles (b). Illustration provided courtesy of Dr. V. Andrew Stenger.

is significantly attenuated and continually modulated with T_2^* decay, leading to a filtering effect that deemphasizes higher spatial frequency. The corresponding signal intensity profiles of the point source on the bottom demonstrate the difference in the filtering effect with reversed and forward spiral. In this regard, the filtering effect of reversed spiral is generally beneficial. However, in the case where a strong local gradient is present, the effect produces some high “focused” pixel in-

tensities. The signal-loss artifact is also reduced by the reversed spiral because the entire k -space is acquired with reversed spiral during TE such that the effect of signal attenuation by G_z^1 is cut in half.

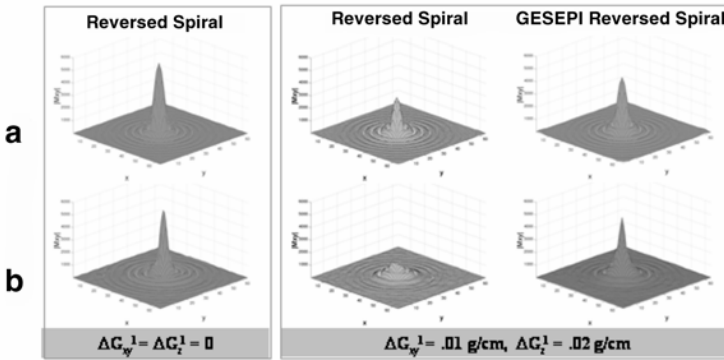


Figure 19. Simulated (a) and experimental (b) image profiles with different data acquisition methods in the absence and presence of local gradients. Illustration provided courtesy of Dr. V. Andrew Stenger.

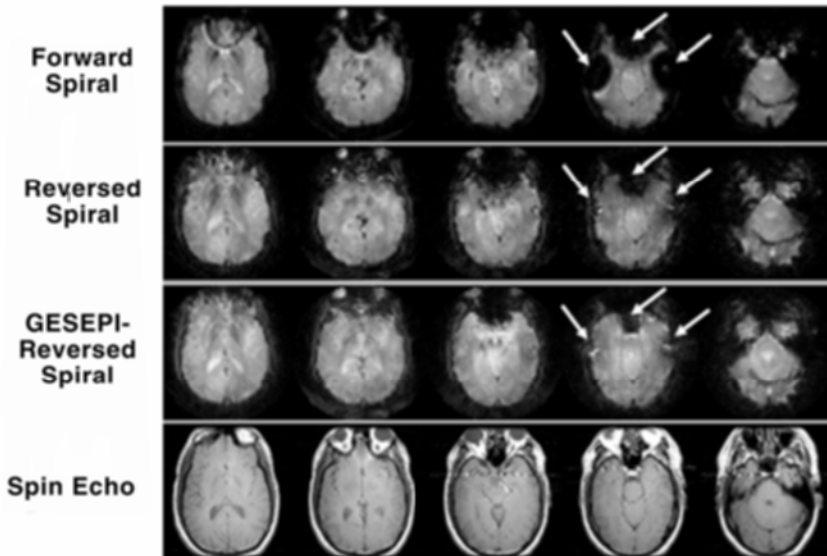


Figure 20. Spiral images taken from the inferior brain region show remarkable signal-loss artifact. As indicated by the arrows, the artifact is mitigated by reversed spiral and removed when GESEPI is incorporated into the reversed spiral technique.

Incorporating reversed spiral with GESEPI leads to a highly effective method for reducing both signal-loss and blurring artifacts. Figure 19 shows a comparison of simulated and experimental results using reversed spiral with and without GESEPI from a point source phantom. In the presence of a local gradient, G_z^1 , the reversed spiral only has a limited success in regaining the loss of the signal. By incorporating GESEPI, the signals from the inhomogeneous region (right column) are nearly the same as those from the homogeneous region (left column). Further in vivo data validate the phantom results.

Figure 20 shows axial human brain images acquired with the forward, reversed spiral, and GESEPI-reversed-spiral methods, along with a spin-echo image for reference. Comparing with forward spiral, the reversed spiral significantly reduced signal-loss artifact in the orbital-frontal and temporal brain areas (arrows). Combining with GESEPI, the signal-loss artifact is nearly completely removed, rendering superior image quality similar to the corresponding spin-echo images. To rigorously test the effectiveness of the technique for fMRI studies, Figure 21 shows an olfactory activation map in the inferior frontal cortex obtained with GESEPI-reversed-spiral method. Brain activation in the olfactory track right above the paranasal sinus was impossible to detect previously due to severe field inhomogeneity artifacts.

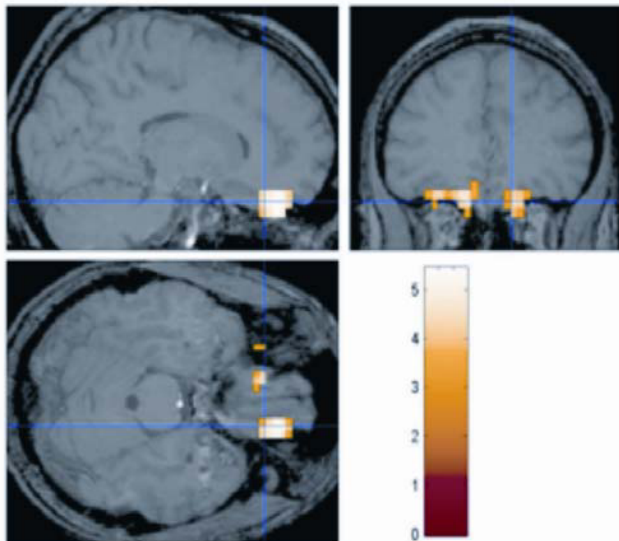


Figure 21. Olfactory fMRI activation at orbitofrontal and olfactory tract with GESEPI-reversed-spiral imaging. See attached CD for color version.

8. FINAL REMARKS

The magnetic susceptibility effects impact MRI broadly and high field MRI most significantly. This chapter is dedicated to magnetic susceptibility-induced artifacts and various correctional techniques. Given the limited scope and pedagogic considerations, it is not possible to provide a comprehensive account of all the published results pertaining to the topic during recent years. The methods that are not referenced are by no means ineffective or unimportant. For example, the recently developed local shimming techniques with either a local coil [77] or diamagnetic pyrolytic graphite [78] and the single-shot TRFP method [47–48] are all extremely important work in overcoming magnetic field inhomogeneity artifacts. Our goal is to present a clear understanding of magnetic susceptibility-induced contrast and artifacts through our experience at high field MRI. With this, we hope that we could stimulate greater interest and more new approaches in this area of research. We are convinced that the combined approach with the automated local shimming scheme, parallel imaging technology, and sequence design will find optimal solutions for the artifact problem in various applications of high field MRI. Thus, a concerted and synergetic effort in these areas of research will unleash the full potential power of high field MRI for scientifically applications.

9. REFERENCES

1. Robitaille PM, Abduljalil AM, Kangarlu A. 2000. Ultra high resolution imaging of the human head at 8 tesla: 2K x 2K for Y2K. *J Comput Assist Tomogr* **24**:2–8.
2. Krauss JD. 1984. In *Electromagnetics*, p. 216. New York: McGraw-Hill.
3. Hopkins JA, Wehrli FW. 1997. Magnetic susceptibility measurement of insoluble solids by NMR: magnetic susceptibility of bone. *Magn Reson Med* **37**:494–500.
4. Weisskoff RM, Kiihne S. 1992. MRI susceptometry: image-based measurement of absolute susceptibility of MR contrast agents, and human blood. *Magn Reson Med* **24**:375–383.
5. Frahm J, Haase A, Matthaei D. 1986. Rapid NMR imaging of dynamic processes using the FLASH technique. *Magn Reson Med* **3**:321–327.
6. Yacoub E, Shmuel A, Pfeuffer J, Van De Moortele PF, Adriany G, Andersen P, Vaughan JT, Merkle H, Ugurbil K, Hu X. 2001. Imaging brain function in humans at 7 Tesla. *Magn Reson Med* **45**:588–594.
7. Gorell JM, Ordidge RJ, Brown GG, Deniau JC, Buderer NM, Helpert JA. 1995. Increased iron-related MRI contrast in the substantia nigra in Parkinson's disease. *Neurology* **45**:1138–1143.
8. Miszkiel KA, Paley MNJ, Wilkinson ID, Hall-Craggs MA, Ordidge R, Kendall BE, Miller RF, Harrison MJG. 1997. The measurement of R_2 , R_2^* , and R_2^{pr} in HIV-infected patients using the prime sequence as a measure of brain iron deposition. *Magn Reson Imag* **15**:1113–1119.
9. Drayer B, Burger P, Darwin R, Riederer S, Herfkens R, Johnson GA. 1986. MRI of brain iron. *Am J Roentgenol* **147**:103–110.

10. Steffens DC, McDonald WM, Tupler LA, Boyko OB, Krishnan KR. 1996. Magnetic resonance imaging changes in putamen nuclei iron content and distribution in normal subjects. *Psychiatry Res* **68**:55–61.
11. Ordidge RJ, Gorell JM, Deniau JC, Knight RA, Helpert JA. 1994. Assessment of relative brain iron concentrations using T_2 -weighted and T_2^* -weighted MRI at 3.0 Tesla. *Magn Reson Med* **32**:335–341.
12. LeVine SM. 1997. Iron deposition in multiple sclerosis and Alzheimer's disease brains. *Brain Res* **760**:298–303.
13. Deibel MA, Ehmann WD, Markesbery WR. 1996. Copper, iron, and zinc imbalance in severely degenerated brain regions in Alzheimer's disease: possible relation to oxidative stress. *J Neurol Sci* **143**:137–142.
14. Connor JR, Snyder BS, Arosio P, Loeffler DA, LeWitt P. 1995. A quantitative analysis of isoferitins in select regions of aged, Parkinsonian, and Alzheimer's diseased brains. *J Neurochem* **65**:717–724.
15. Connor JR, Menzies SL, St Martin SM, Mufson EJ. 1992. A histochemical study of iron, transferrin, and ferritin in Alzheimer's in the evaluation diseased brains. *J Neurosci Res* **31**:75–83.
16. Loeffler DA, Connor JR, Juneau PL, Snyder BS, Kanaley L, DeMaggio AJ, Nguyen H, Brickman CM, LeWitt PA. 1995. Transferrin and iron in normal, Alzheimer's disease, and Parkinson's disease brain regions. *J Neurochem* **65**:710–716.
17. Good PF, Perl DP, Bierer LM, Schmeidler J. 1992. Selective accumulation of aluminum and iron in the neurofibrillary tangles of Alzheimer's disease: a laser microprobe (LAMMA) study. *Ann Neurol* **31**:286–292.
18. Halliday W. 1995. The nosology of Hallervorden-Spatz disease. *J Neurol Sci* **134**(suppl):84–91.
19. Miyajima H, Takahashi Y, Kamata T, Shimzu H, Sakai N, Bitlin JD. 1997. Use of desferrioxamine in the treatment of Aceruloplasminemia. *Ann Neurol* **41**:404–407.
20. Steinberg PM, Ross JS, Modic MT, Tkach J, Masaryk TJ, Haacke EM. 1990. The value of fast gradient-echo MR sequences of brain disease. *Am J Neuroradiol* **11**:59–67.
21. Henkelman M, Kucharczyk W. 1994. Optimization of gradient-echo MR for calcium detection. *Am J Neuroradiol* **15**:465–472.
22. Atlas SW, Grossman RI, Hackney DB, Gomori JM, Campagna N, Goldberg HI, Bilaniuk LT, Zimmerman RA. 1988. Calcified intracranial lesions: detection with gradient-echo-acquisition rapid MR imaging. *Am J Roentgenol* **150**:1383–1389.
23. Guckel F, Brix G, Rempp K, Deimling M, Rother J, Georgi M. 1994. Assessment of cerebral blood volume with dynamic T_2^* contrast enhanced gradient-echo imaging. *J Comput Assist Tomogr* **18**:344–351.
24. Rosen BR, Belliveau JW, Vevea JMT, Brady J. 1990. Perfusion imaging with NMR contrast agents. *Magn Reson Med* **14**:249–265.
25. Yamaguchi H, Igarashi H, Katayama Y, Terashi A. 1998. An evaluation of ischemic stroke using dynamic contrast enhanced perfusion MRI. *Nippon Ika Daigaku Zasshi* **65**:148–156.
26. Ida M, Yamashita M, Shimizu S, Kurisu Y. 1997. T_2^* -contrast perfusion study: principles, theory and clinical utility in evaluating cerebral hemodynamics. *Nippon Rinsho* **55**:1719–1725.
27. Menon RS, Ogawa S, Tank DW, Ugurbil K. 1993. Tesla gradient recalled echo characteristics of Photic stimulation-induced signal changes in the human primary visual cortex. *Magn Reson Med* **30**:380–386.

28. Ernst RR. 1966. Sensitivity enhancement in magnetic resonance. *Adv Magn Reson* **2**:1–135.
29. Brunner P, Ernst RR. 1979. Sensitivity and performance time in NMR imaging. *J Magn Reson* **33**:83–106.
30. Li S, Dardzinski BJ, Collins CM, Yang QX, Smith MB. 1996. Three-dimensional mapping of the static magnetic field inside the human head. *Magn Reson Med* **36**:705–714.
31. Ferziger JH. 1981. *Numerical methods for engineering application*. New York: John Wiley & Sons.
32. Krauss JD. 1984. *Electromagnetics*. New York: McGraw-Hill.
33. Hopkins JA, Wehrli FW. 1997. Magnetic susceptibility measurement of insoluble solids by NMR: magnetic susceptibility of bone. *Magn Reson Med* **37**:494–500.
34. Collins CM, Li S, Smith MB. 1998. SAR and B_1 field distributions in a heterogeneous human head model within a birdcage coil. *Magn Reson Med* **40**:847–856.
35. Collins CM, Yang B, Yang QX, Smith MB. 2002. Numerical calculations of the static magnetic field in three-dimensional multi-tissue models of the human head. *Magn Reson Imag* **20**:413–424.
36. Reichenbach JR, Venkatesan R, Yablonsky DA, Thompson MR, Lai S, Haacke EM. 1997. Theory and application of static field inhomogeneity effects in gradient-echo imaging. *J Magn Reson Imag* **7**:266–279.
37. Yang QX, Dardzinski BJ, Li S, Smith MB. 1997. Multi-gradient echo with susceptibility inhomogeneity compensation (MGESIC): demonstration of fMRI in the olfactory cortex at 3.0 T. *Magn Reson Med* **37**:331–335.
38. Ro YM, Cho ZH. 1995. Susceptibility magnetic resonance imaging using spectral decomposition. *Magn Reson Med* **33**:521–528.
39. Frahm J, Merboldt KD, Hancicke W. 1988. Direct FLASH MR imaging of magnetic field inhomogeneities by gradient compensation. *Magn Reson Med* **6**:474–480.
40. Cho ZH, Ro YM. 1992. Reduction of susceptibility artifact in gradient-echo imaging. *Magn Reson Med* **23**:193–200.
41. Haacke EM, Tkach JA, Parrish TB. 1989. Reduction of T_2^* dephasing in gradient field-echo imaging. *Radiology* **170**:457–462.
42. Posse S, Aue WP. 1990. Susceptibility artifacts in spin-echo and gradient-echo imaging. *J Magn Reson* **88**:473–492.
43. Yang QX, Dardzinski BJ, Williams GD, Smith MB. 1996. Magnetic susceptibility contrast using an imbalanced slice refocusing gradient: a gradient-echo method for high field MRI. *Proc Int Soc Magn Reson Med* 1676.
44. Frahm J, Merboldt KD, Hancicke W. 1995. The effects of intravoxel dephasing and incomplete slice refocusing on susceptibility contrast in gradient-echo MRI. *J Magn Reson B* **109**:234–237.
45. Constable RT, Spencer DD. 1999. Composite image formation in z-shimmed functional MR imaging. *Magn Reson Med* **42**:110–117.
46. Yang QX, Williams GD, Demeure RJ, Mosher TJ, Smith MB. 1998. Removal of local field gradient artifacts in T_2^* -weighted images at high fields by gradient-echo slice excitation profile imaging. *Magn Reson Med* **39**:402–409.
47. Stenger VA, Boada FE, Noll DC. 2000. Three-dimensional tailored RF pulses for the reduction of susceptibility artifacts in T_2^* -weighted functional MRI. *Magn Reson Med* **44**:525–531.
48. Stenger VA, Boada FE, Noll DC. 2003. Variable-density spiral 3D tailored RF pulses. *Magn Reson Med* **50**:1100–1106.

49. Pauly J, Nishimura D, Macovski A. 1989. A k-space analysis of small-tip angle excitation. *J Magn Reson* **81**:43–56.
50. Yang QX, Smith MB, Briggs RW, Rycyna RE. 1999. Microimaging at 14 tesla using GESEPI for removal of magnetic susceptibility artifacts in T_2^* -weighted image contrast. *J Magn Reson* **141**:1–6.
51. Yablonskiy DA, Haacke EM. 1994. Theory of NMR signal behavior in magnetically inhomogeneous tissues: the static dephasing regime. *Magn Reson Med* **32**:749–763.
52. Abduljalil AM, Robitaille PML. 1999. Macroscopic susceptibility in ultra high field MRI. *J Comput Assist Tomogr* **23**:832–841.
53. Yang QX, Smith MB, Zhu X, Liu H, Michaeli S, Zhang X. 2000. T_2^* -Weighted human brain imaging with the GESEPI at 7.0 Tesla. *Proc Int Soc Magn Reson Med* 1684.
54. Constable RT. 1995. Functional MR imaging using gradient-echo echo-planar imaging in the presence of large static field inhomogeneities. *J Magn Reson Imag* **5**:746–752.
55. Chen NK, Wyrwicz AM. 1999. Removal of introvoxel dephasing artifact in gradient-echo images using a field-map based RF refocusing technique. *Magn Reson Med* **42**:807–812.
56. Posse S, Shen Z, Kiselev V, Kemna LJ. 2003. Single-shot T_2^* mapping with 3D compensation of local susceptibility gradients in multiple regions. *Neuroimage* **18**:390–400.
57. Zwart JA, van Gelderen P, Kellman P, Duyn JH. 2002. Application of sensitivity-encoded echo-planar imaging for blood oxygen level-dependent functional brain imaging. *Magn Reson Med* **48**:1011–1020.
58. Glover GH. 1999. 3D z-shim method for reduction of susceptibility effects in BOLD fMRI. *Magn Reson Med* **42**:290–299.
59. Weiger M, Pruessmann KP, Osterbauer R, Bornert P, Boesiger P, Jezzard P. 2002. Sensitivity-encoded single-shot spiral imaging for reduced susceptibility artifacts in BOLD fMRI. *Magn Reson Med* **48**:860–866.
60. Fernandez-Seara MA, Wehrli FW. 2000. Postprocessing technique to correct for background gradients in image-based R_2^* measurements. *Magn Reson Med* **44**:358–366.
61. Merbold KD, Finsterbusch J, Frahm J. 2000. Reducing inhomogeneity artifacts in functional MRI of human brain activation-thin sections vs gradient compensation. *J Magn Reson* **145**:184–191.
62. Yang Y, Gu H, Zhan W, Xu S, Silbersweig DA, Stern E. 2002. Simultaneous perfusion and BOLD imaging using reverse spiral scanning at 3T: characterization of functional contrast and susceptibility artifacts. *Magn Reson Med* **48**:278–289.
63. Yang QX, Stenger VA, Smith MB, Boada F, Noll D. 2001. Reduction of the blurring artifacts due to the local field inhomogeneity in spiral imaging. *Proc Int Soc Magn Reson Med* 741.
64. Glover GH, Law CS. 2001. Spiral in/out BOLD fMRI for increased SNR and reduced susceptibility artifacts. *Magn Reson Med* **46**:515–522.
65. Schmithorst VJ, Dardzinski BJ, Holland SK. 2001. Simultaneous correction of ghost and geometric distortion artifacts in EPI using a multiecho reference scan. *IEEE Trans Med Imag* **20**:535–539.
66. Wild JM, Martin WR, Allen PS. 2002. Multiple gradient echo sequence optimized for rapid, single-scan mapping of R_2^* at high B_0 . *Magn Reson Med* **48**:867–876.
67. Gu H, Feng H, Zhan W, Xu S, Silbersweig DA, Stern E, Yang Y. 2002. Single-shot interleaved z-shim EPI with optimized compensation for signal losses due to susceptibility-induced field inhomogeneity at 3 T. *Neuroimage* **17**:1358–1364.

68. Li Z, Wu G, Zhao X, Luo F, Li SJ. 2002. Multiecho segmented EPI with z-shimmed background gradient compensation (MESBAC) pulse sequence for fMRI. *Magn Reson Med* **48**:312–321.
69. Wilson JL, Jenkinson M, Jezzard P. 2003. Protocol to determine the optimal intraoral passive shim for minimisation of susceptibility artifact in human inferior frontal cortex. *Neuroimage* **19**:1802–1811.
70. Deichmann R, Gottfried JA, Hutton C, Turner R. 2003. Optimized EPI for fMRI studies of the orbitofrontal cortex. *Neuroimage* **19**:430–441.
71. Yang QX, Wang J, Smith MB, Meadowcroft M, Sun X, Eslinger PJ, Golay X. 2004. Reduction of magnetic field inhomogeneity artifacts in echo planar imaging with SENSE and GESEPI at high field. *Magn Reson Med* **52**:1418–1423.
72. Pruessmann KP, Weiger M, Scheidegger MB, Boesiger P. 1999. SENSE: sensitivity encoding for fast MRI. *Magn Reson Med* **42**:952–962.
73. Bammer R, Keeling SL, Augustin M, Pruessmann KP, Wolf R, Stollberger R, Hartung HP, Fazekas F. 2001. Improved diffusion-weighted single-shot echo-planar imaging (EPI) in stroke using sensitivity encoding (SENSE). *Magn Reson Med* **46**:548–554.
74. Golay X, Pruessmann KP, Weiger M, Crelier GR, Folkers PJM, Kollias SS, Boesiger P. 2000. PRESTO-SENSE: an ultra-fast whole brain fMRI technique. *Magn Reson Med* **43**:779–786.
75. Jaermann T, Crelier G, Pruessmann KP, Golay X, Netsch T, Van Muiswinkel AM, Mori S, Van Zijl PC, Valavanis A, Kollias S, Boesiger P. 2004. SENSE-DTI at 3 T. *Magn Reson Med* **51**:230–236.
76. Bornert P, Aldefeld B, Eggers H. 2000. Reversed spiral MR imaging. *Magn Reson Med* **44**:479–484.
77. Kim DH, Adalsteinsson E, Glover GH, Spielman DM. 2002. Regularized higher-order in vivo shimming. *Magn Reson Med* **48**:715–722.
78. Wilson JL, Jenkinson M, Jezzard P. 2002. Optimization of static field homogeneity in human brain using diamagnetic passive shims. *Magn Reson Med* **48**:906–914.

HIGH MAGNETIC FIELDS FOR IMAGING CEREBRAL MORPHOLOGY, FUNCTION, AND BIOCHEMISTRY

Kâmil Uğurbil, Gregor Adriany, Can Akgün, Peter Andersen, Wei Chen, Michael Garwood, Rolf Gruetter, Pierre-Gilles Henry, Malgorzata Marjanska, Steen Moeller, Pierre-François Van de Moortele, Klaas Prüssmann,* Ivan Tkac, J. Thomas Vaughan, Florian Wiesinger,* Essa Yacoub, and Xiao-Hong Zhu**

University of Minnesota Medical School, Department of Radiology, Center for Magnetic Resonance Research, Minneapolis

** Institute for Biomedical Engineering, University and ETH Zurich, Switzerland*

***after the first, authors listed in alphabetical order*

1. INTRODUCTION

In the last two decades, magnetic resonance imaging (MRI) instruments operating at a magnetic field strength of 1.5 Tesla have emerged as the most commonly employed high-end platform for clinical diagnosis. Despite the dominant position enjoyed by this field strength, even its promotion as the “optimum” field to work for human applications, the late 1980s witnessed the beginnings of an interest in substantially higher magnetic fields. After brief and cursory explorations, however, high field strengths were virtually abandoned by industry leaders while their efforts were focused on further refinements of the 1.5T or even lower field platforms. Nevertheless, a handful of 3 and 4-Tesla instruments were established in academic research laboratories by about 1990. Since these early beginnings, work conducted in these academic sites has demonstrated that magnetic fields substantially beyond 1.5 Tesla provide numerous advantages in aspects of magnetic resonance imaging and spectroscopy (MRS) applications in humans, even though such high fields also pose serious challenges. In considering these accomplishments, however, it is imperative to recognize that, to date, virtually all of the research at high magnetic fields, especially at field strengths greater than 3 Tesla, has been carried out only in a few laboratories and using instruments that are definitely far less than optimized; as such, the amount of man-hours and talent dedicated to this effort has been minuscule compared to the clinical uses of MR and, even then, this effort has been hampered by suboptimal instrumentation. Therefore, any positive conclusions ob-

tained thus far, and there are many, can only be interpreted as harbingers of potential gains and definitely not as what can be ultimately achieved.

All the same, the work that has been conducted to date at high magnetic fields has provided the motivation and justification for the dramatic changes we are currently witnessing in the state of high field MR. Instruments operating at 3 Tesla are rapidly becoming the advanced clinical platform. Significantly better 4 and 7T systems are being installed in user sites, and further improvements of these instruments are being planned. Combined with these advances in instrumentation, the number of such high field systems is also rapidly multiplying, resulting in considerably more effort and talent focused on technological developments and biomedical applications. Consequently, we can expect to experience in the near future significant improvements in the quality and type of biological information content extracted from high field MR studies.

In our laboratory the effort to pursue high magnetic fields has been intricately tied to our interest in developing methods for the acquisition of physiological and biochemical information noninvasively using magnetic resonance imaging and spectroscopy. In this effort, a relatively recent and unique accomplishment has been the introduction of the ability to map human brain function noninvasively (fMRI). The concurrent and independent work performed at the University of Minnesota, Center for Magnetic Resonance Research [1], and at MGH [2] introducing fMRI, was, in our case, conducted at 4 Tesla. It was the first study performed at 4 Tesla in our laboratory after the system became marginally operational. At the time, we had expected a better chance of success for detecting alterations in brain activity at high fields based on mathematical modeling considerations [3]. These and other subsequent (e.g., [4–6]) modeling efforts are currently understood to be largely accurate, albeit incomplete with respect to mechanisms underlying functional imaging signals. Some of the mechanisms that were unaccounted for in the early modeling efforts form the basis for the successful use of lower field magnets, such as 1.5 T, for the acquisition of functional images with subcentimeter resolution of the entire human brain. Nevertheless, increased understanding of the origin of fMRI signals has also reconfirmed our initial expectations that there are major advantages for fMRI for high resolution and high accuracy functional mapping, and these have been largely demonstrated by a plethora of studies conducted with higher magnetic fields such as 4 Tesla, and recently 7 Tesla in humans, and up to 11.7 Tesla in animal models.

The rationale for pursuing high magnetic fields for human studies in our laboratory in the late 1980s was also based on the experimentally demonstrated richness of biochemical information contained in multinuclear MR spectroscopy studies of intact cell cultures, isolated perfused organs, and whole animals. These experiments, however, were carried out at very high magnetic fields, ranging from 4.7 to 9.4 Tesla, using small-bore magnets that were available at the time. In contrast, human spectroscopy applications that are contemporary with these high field animal models or isolated organ experiments were pursued at the highest magnetic field available for human investigation then, which was only 1.5 Tesla; these human studies were, in general, unable to produce data of quality comparable to the

high field experiments performed on perfused organs or intact animals. This has changed with the introduction of high magnetic fields for human applications. While the use of ultra high magnetic fields such as 7 to 9.4 Tesla in human investigations is still in its infancy, the data gathered to date suggest that there are significant gains for spectroscopy studies with all nuclei in general, and low-gyromagnetic ratio nuclei in particular.

Some of these accomplishments relevant to high magnetic fields are reviewed in this chapter.

2. SIGNAL-TO-NOISE RATIO

In all MR applications, image quality, measurement time, and/or spatial resolution depend on the signal-to-noise ratio (SNR). The SNR, however, becomes rather complex when high magnetic fields (hence high frequencies) are considered with conductive biological samples such as the human head. The relationship between SNR and field strength has been examined for biological samples in numerous theoretical studies [7–13], predicting increases with field magnitude and resonance frequency. Field dependence of SNR for ^1H was experimentally examined in the human head, initially comparing 0.5, 1.5, and 4 Tesla (~ 21 , 64, and 170 MHz, respectively) and documenting at least linear increases at the higher frequencies [14]. More recently, the B_1 field profile and SNR were examined in the human head for 4 and 7 Tesla carefully, using the same coil structure (a TEM “volume” head coil) and taking into account measured instrumental and coil performance differences [15]. It was expected that a volume coil with a uniform B_1 field profile when empty will nonetheless lead to a highly nonuniform B_1 , SNR, and power deposition over the human head and brain at these frequencies. The B_1 magnitude was directly mapped using magnetization preparation followed by ultrafast imaging (“TurboFlash”) so that the resultant longitudinal magnetization, and consequently the detected signal intensity, was directly proportional to $(\cos(\tau\gamma B_1))$, where γ is the gyromagnetic ratio and τ is the variable pulse duration in the magnetization preparation pulse. Thus, as a function of τ , the signal intensity should oscillate with the angular frequency of γB_1 . The results demonstrated that the signal intensity oscillates with higher frequency in the brain center than in the periphery at both field strengths but much more so at 7 Tesla (Figure 1). At 4 T, the B_1 strength in the brain periphery was down 23% from the center value. At 7 T, the peripheral B_1 was 42% lower than the central B_1 . The nonuniform B_1 profiles obtained experimentally were also reproduced by the Maxwell models of the TEM coil loaded with the human head [15]. Using virtually fully relaxed images, the SNR was shown to scale ~ 2 -fold, going from 4 to 7 T, more than linearly with field magnitude, in the center of the brain and less than linearly in the periphery [15]. The ratio of SNR at 7 vs. 4 Tesla is illustrated for five regions of interest (ROIs) in Figure 2A. For the same data as in Figure 2A, Figure 2B shows the ratio of SNR in the periphery of the brain relative to the center of the brain at 7 T [15]. Essentially

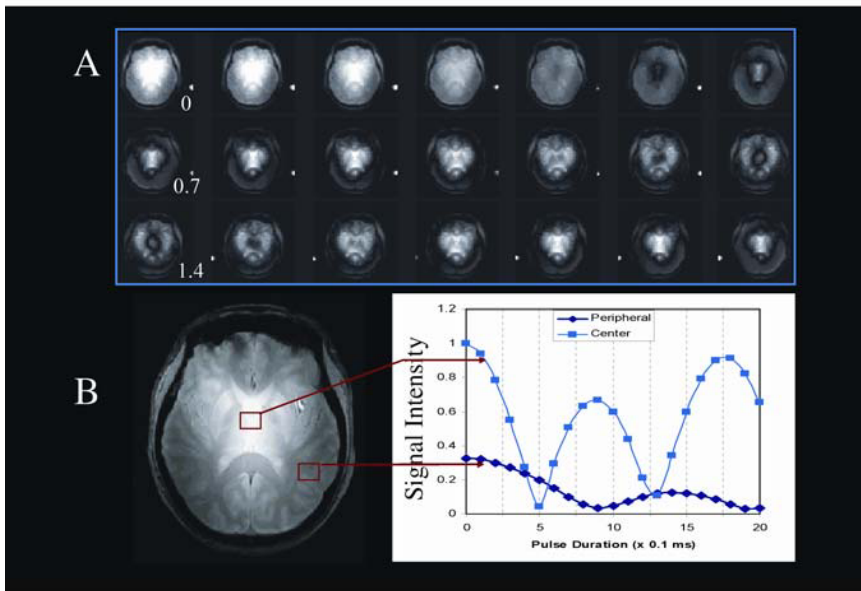


Figure 1. (A) Images of a transverse slice through the human head at 7 Tesla, obtained with magnetization preparation to encode B_1 magnitude as $[\cos(\tau\gamma B_1)]$ “Turboflash” (center-out k -space sampling, TR/TE = 4.2 ms/2.5 ms, slice thickness = 5 mm, flip angle = 10° at slice center, matrix size = 128 x 64). The different images correspond to different τ going from 0 to 2 ms in 0.1-ms steps (left to right). The starting image on the right corresponds to τ of 0, 0.7, and 1.4 ms for the first, second, and third rows, respectively, as shown in the figure. B_1 magnitude was kept constant. (B) The signal (magnitude) oscillation frequency plotted for two regions of interest in the middle and periphery of the brain. Oscillation frequency is equal to γB_1 , indicating that B_1 is substantially higher in the center of the brain. Reprinted with permission from [15]. See attached CD for color version.

a 50% decrease is seen in the periphery compared to the center of the brain. (The excitation pulse was adjusted to 90° at the center of the brain for these measurements, and SNR values were not corrected for the lower flip angle at the periphery compared to the center.)

Clearly, the afore-described results demonstrated that at high fields, transmit B_1 and SNR must be considered as a function of location within the head. Later work (discussed below) emphasized the importance of coil design for the spatial distribution of SNR. This is because the human head/RF interactions approach “far-field” conditions at magnetic fields like 7 T, where the wavelengths are comparable to or smaller than object dimensions, and B_1 exhibits a traveling wave behavior [16–20].

The diminished SNR in the periphery, however, can be recovered using multi-channel array coils [21]. The ratio of SNR in four peripheral voxels relative to the

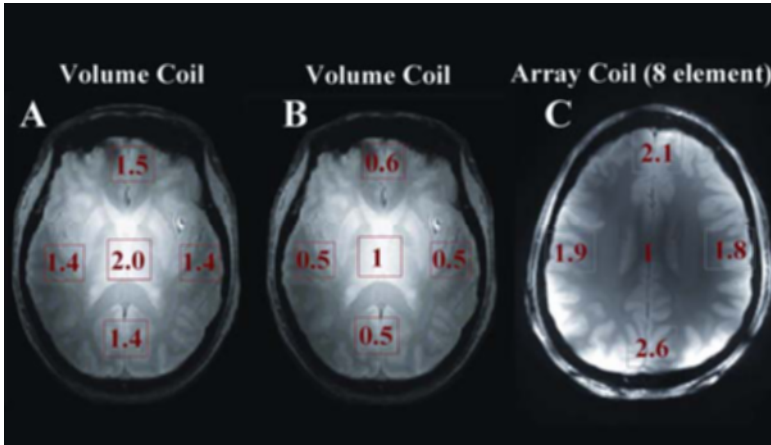


Figure 2. (A) SNR gains at 7 Tesla relative to 4 Tesla for 4-port driven TEM volume coil. The SNR gains are given as a ratio of 7 T SNR vs 4 T SNR as numbers in red at one central and four peripheral locations. Reprinted with permission from [15]. (B) SNR ratio of periphery vs. the center of the brain at 7 T with a four-port driven TEM volume coil (same data as in A). (C) SNR ratio of periphery vs. the center of the brain at 7 Tesla with an 8-element array coil. Reprinted with permission from [21]. See attached CD for color version.

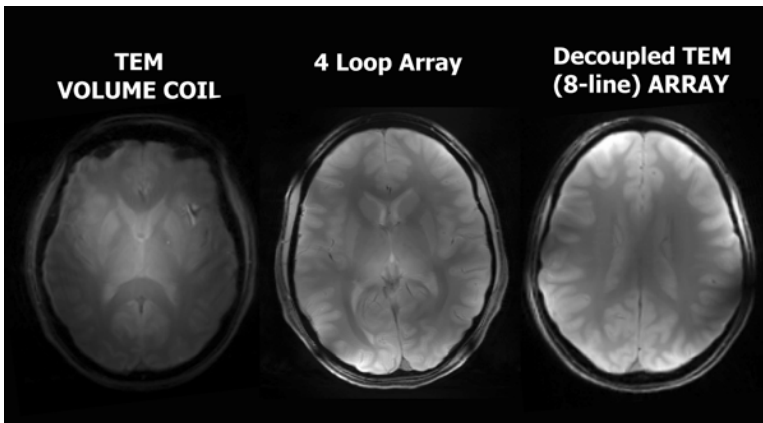


Figure 3. SNR at 7 Tesla of a TEM volume coil (4-port driven) vs. two different coil arrays. Images are scaled so that gray scale corresponds to SNR.

center of the brain as measured at 7 Tesla using an array coil is given in Figure 2C. Figure 3 shows human head images approximately scaled for SNR from two array coils and a volume TEM coil. (The same parameters were used for acquisition of the data. However, the subjects were not the same and slices were also somewhat different. Therefore, this should not be regarded as a precise SNR comparison be-

tween two coils. Nevertheless, the data illustrate that the central SNR is approximately the same for the volume coil and the array coils but the peripheral SNR increases in the array coils, leading to a flatter looking image.) The array coil used in this measurement was a transceive TEM array coil constructed using a stripline design [21] that is virtually identical to a TEM volume coil, except that the individual current carrying elements are now decoupled from each other. The TEM/stripline array coil in this case operated like a volume transmit coil in the transmit mode, generating a B_1 pattern that is strong in the center and weak in the periphery [21], identical to the results obtained from a volume TEM coil (Figure 1). This is expected since the geometry and construction of the current-carrying elements are similar in the two coils and in both cases, the spin excitation (flip angle) in the transmit mode is achieved by an RF field given by

$$\left| \sum_i B_{1i}^+(\vec{x}) \right|,$$

where i denotes individual current-carrying coil elements, \vec{x} describes spatial location, and B_{1i}^+ is a complex number that describes the magnitude and phase of the component of B_1 that precesses in the same direction as nuclear magnetization and is responsible for spin excitation (see [19,22,23] for discussion of B_1^+ and B_1^- components of the B_1 field). The B_{1i}^+ patterns of each element add constructively in some places (e.g., the center of the head) or lead to partial cancellation in others (e.g., between the elements in close proximity to them). In the volume TEM coil, or the array coil operating as a *single-volume* coil (e.g., hardware summation of signals are performed from the multiple elements as in the TEM volume coil), the *reception* sensitivity is proportional to

$$\left(\left| \sum_i B_{1i}^-(\vec{x}) \right| \right),$$

leading to analogous interferences expected in the transmit mode operation. On the other hand, in an array where signals from each array element are collected on *separate* channels, such a complex addition of signals is *not* performed in the *receive* mode. Instead, images from each individual coil are recorded separately and can be combined subsequently in different ways. For example, the SNR measurements presented in Figure 2C are based on images generated as the square root of sum-of-squares of all channels [21], where the final reception sensitivity is proportional to

$$\left(\sum_i |B_{1i}^-(\vec{x})|^2 \right)^{1/2}.$$

In this case, SNR is better by a factor of 2 or more in the periphery compared to the center (Figures 2C and 3; [21]).

Thus, it can be inferred that the lower SNR in the periphery of the human brain compared to the center is a result of the partial cancellation of the signals in the periphery in the complex addition:

$$\left(\left| \sum_i B_{i-}(\bar{x}) \right| \right)$$

[24,25], and, as it turns out, this cancellation is stronger at 7 T than at 4 T (see Figures 5 and 6 and relevant discussion further on). This implies that if one is to perform field dependence of SNR measurements with such an array coil, better than linear SNR gains observed in the center of the head are likely to be observed in the entire head; this, however, remains to be demonstrated experimentally.

The SNR increases measured in going from 4 to 7 T [15] were for conditions of same acquisition bandwidth and full relaxation. Such acquisition conditions may be quite appropriate for some imaging applications. If signal averaging is necessary with repetitions that do not permit full relaxation, then SNR will be inversely proportional to $\sqrt{T_1}$. Thus, for nuclear spins such as protons, where spin-lattice relaxation times get longer with increasing magnetic fields, the SNR gains will be diminished at higher fields, while other nuclei such as ^{17}O and ^{31}P [26,27] will be unaffected or even gain due to this effect. Similarly, under many conditions the bandwidth needs to be higher at the higher field strength. For example, in order to overcome the deleterious effects of increasing B_0 inhomogeneities (and consequently shorter T_2^*), the k -space coverage must be faster in echo planar imaging (EPI). This may be accomplished by scaling the bandwidth with the field magnitude as well, in which case the noise will increase as the square root of the bandwidth ratio. However, acquisition speed in EPI or analogous fast imaging techniques can also be cut by using restricted field-of-view (FOV) when possible [28,30] or using parallel imaging.

SNR gains with increasing magnetic field can be larger for low gyromagnetic nuclei that resonate at much lower frequencies. Such nuclei of biological interest include ^{17}O , ^{23}Na , ^{13}C , and ^{31}P . Among these nuclei, particularly ^{17}O and ^{23}Na resonate at low frequencies. For example, at 9.4 T while the ^1H frequency is 400 MHz, the ^{17}O frequency is 54 MHz. At such low frequencies SNR can vary with magnetic field according to $B_0^{7/4}$ [7,9] even in conductive biological samples. This approximate quadratic dependence on field strength was experimentally observed between 9.4 and 4.7 Tesla in the rat brain and in a saline solution [26] for direct detection of the ^{17}O nucleus. This sensitivity gain was critical in performing the biologically important measurement of oxygen consumption rate in the brain [31].

3. IMAGE INTENSITY AND B_1 NONUNIFORMITIES AT HIGH MAGNETIC FIELDS

When 4T magnets large enough to accommodate humans were first built, initial measurements in the manufacturer's laboratories suggested that high-quality

human brain imaging would not be feasible at such high field strengths. This conclusion was largely based on the nonuniform signal intensity that was quite striking not only in a non-conductive phantom where dielectric resonances are observed, but also in the human head, as shown in the figure reproduced from an early paper (Figure 4). However, while significant nonuniformities in B_1 patterns and signal intensities exist in the human head and body at these high magnetic fields, the cause is far from a *true* dielectric resonance.

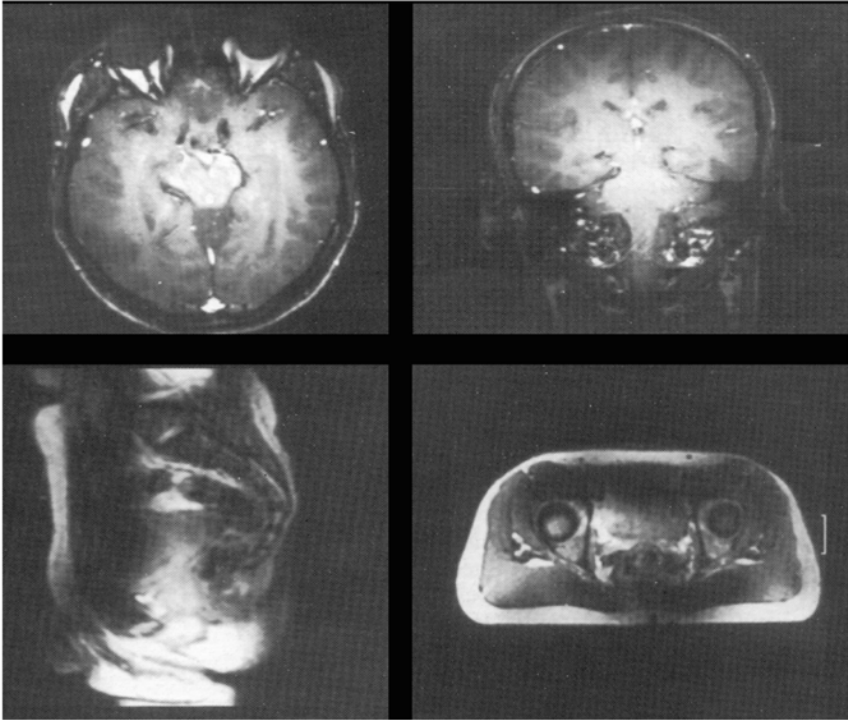


Figure 4. Early human head and body images at 4 Tesla. Reprinted with permission from [198].

The suggestion that dielectric resonances may not account for the image non-uniformities seen with volume coils at ultra high magnetic fields first emerged from 8 Tesla studies [32–35]. Subsequent 7 Tesla experimental data and corresponding simulations demonstrated that the conductivities applicable for the human head do not support dielectric resonances [16–19]. Recent studies performed at 7 Tesla further confirmed this point experimentally [21,24,25]. Figure 5 illustrates 7 Tesla experimental data from a spherical phantom containing an ionic solution mimicking the electrical properties of the human head [24,25]. The coil is an 8-element TEM/stripline coil [21] that can operate as a transmit

r e c e i v e a r r a y a n d

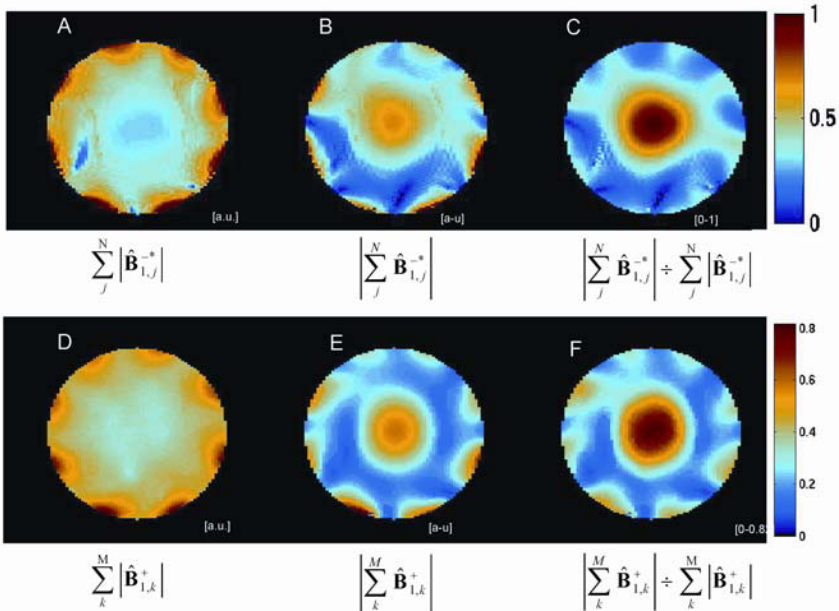


Figure 5. Receive and transmit patterns generated with an array coil either as the sum of magnitudes (SOM) or a magnitude of complex sum (MOS) to emulate a single-channel “volume coil” mode: (A) Sum of the eight individual B_1 receive magnitude maps. (B) B_1 receive magnitude map calculated from complex summation in order to simulate a single-channel “volume coil” mode. (C) Ratio of magnitude of the complex sum over the sum of the 8 magnitude receive B_1 fields, showing the loss of receive B_1 field in the periphery when merging complex data from multiple coil elements. Color scales are independently adjusted, in arbitrary units, for A and B maps in order to emphasize spatial profiles. In C, the color scale ranges from 0 to 1. *The performed calculations yield equal values in the center of the phantom for the maps shown in A and B.* (D) Sum of the eight individual B_1 transmit magnitude maps obtained when transmitting one channel at a time. (E) B_1 transmit magnitude map obtained when transmitting through 8 channels simultaneously (“volume coil” case). Note that, unlike for receive B_1 comparison, maps in A and B could not be obtained from a unique data set. (F) Ratio of the magnitude of “volume coil” transmit B_1 over the sum of the eight magnitude transmit B_1 . Color tables were independently adjusted, in arbitrary units, for A and B maps. In C the color scale ranges from 0 to 0.82. Reprinted with permission from [24,25]. See attached CD for color version.

duplicate in all other aspects a “volume” TEM coil with 8 current carrying rungs. With this coil, the signal can be received separately with the individual elements after excitation using all or some of the elements. Determining separately the B_1 field used for excitation then allows the calculation of both the phase and amplitude of $B_{1i}^-(\vec{x})$ for each channel. When these complex $B_{1i}^-(\vec{x})$ functions are summed as

$$\left(\sum_i |B_{1i}^-(\vec{x})| \right)$$

(Figure 5A) *versus*

$$\left(\left| \sum_i B_{i1}^-(\vec{x}) \right| \right),$$

which mimics a “volume coil” mode (Figure 5B), two different patterns are observed. The volume coil mode yields the center-bright pattern, whereas the

$$\left(\sum_i |B_{i1}^-(\vec{x})| \right)$$

mode yields low intensity in the center. In order to emphasize spatial profiles, color scales are independently adjusted for Figure 5A,B, and are in arbitrary units. However, the *magnitudes are actually the same in the center of the phantom for both maps*. Thus, we are looking at increasing values as we go away from the center in Figure 5A and decreasing values as we go away from the center in Figure 5B. (When we come very close to the conductors, the magnitudes again increase in Figure 5B. This is expected since very close to the conductor the B_1 field is dominated by that single conductor. Thus it is not relevant to this discussion which is really concerned with the consequences of the superimposition of B_1 from the different conductors.) This fundamental difference is clearly illustrated in the ratio

$$\frac{\left(\left| \sum_i B_{i1}^-(\vec{x}) \right| \right)}{\left(\sum_i |B_{i1}^-(\vec{x})| \right)}$$

(Figure 5C), where now the color scale denotes numbers going from 0 to 1.

So far we have discussed the receive profiles. However, with a multichannel transmit capability in such a transceive array coil, one can also make the same experimental measurements directly for $B_{i1}^+(\vec{x})$, pulsing one channel at a time while receiving with all channels. The results, determined totally independently from the receive profiles, are identical (compare Figure 5, lower row versus upper row) [24,25]. This would, of course, be expected based on the reciprocity principle,.

Thus, whether we measure directly $B_{i1}^+(\vec{x})$ or look at reception sensitivities, the “volume coil” mode leads to high intensity in the center (Figure 5) [24,25]. Human data yield identical results [24,25]. This center-bright appearance is often referred to as a “dielectric resonance,” but it is not. It is a consequence of destructive cancellation in the periphery when the complex summation,

$$\left(\sum_i B_{i1}^+(\vec{x}) \right) \text{ or } \left(\sum_i B_{i1}^-(\vec{x}) \right),$$

determines the end result as in a “volume coil.” Dielectric resonances do exist at these field strengths, but *not* under the conductive conditions mimicking the human brain.

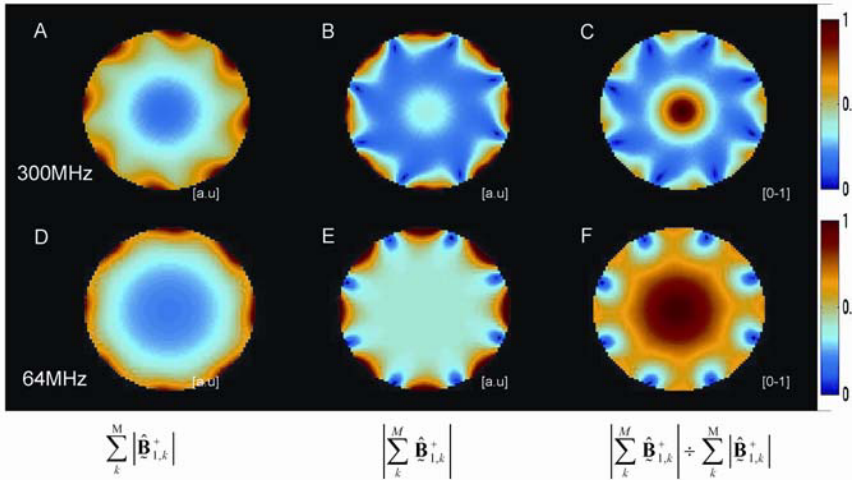


Figure 6. Transmit B_1 field summations for 300 MHz (A,B,C) and 64 MHz (D,E,F) obtained through simulations. (A,D) Sum of the eight transmit magnitude maps $|\hat{\mathbf{B}}_{1,j}^+|$ obtained when simulating transmission with one channel at a time; (B,E) B_1 transmit magnitude map obtained when simulating transmission through 8 channels simultaneously (“volume coil” case). (C,D) Ratio of, respectively, the map shown in B over the map shown in A, and the map shown in E over the map shown in D. Color tables were independently adjusted, in arbitrary units, for the A, B, D, and E maps. In C and F the color scales range from 0 to 1. Reprinted with permission from [24,25]. See attached CD for color version.

Figure 6, top row, shows calculations from our laboratory demonstrating excellent agreement with experimental data at 7 Tesla. Figure 6, lower row, illustrates that the same calculations yield less of this destructive addition in the periphery and a much larger and more uniform field in the center of the sample. This occurs because of the traveling wave behavior and the resulting complex phases that become more pronounced at 7 Tesla

4. MORPHOLOGICAL IMAGING OF BRAIN TISSUE

Clearly, we now understand that the signal-intensity inhomogeneities at high fields (Figure 4) that were considered so daunting initially are not an expression of a fundamental and unalterable RF behavior. Consequently, they can be dealt with using appropriate coil designs [21,36] (also see Figures 2 and 3), RF shimming [21,37], or pulse sequences that exhibit some tolerance to B_1 inhomogeneities [38].

Shortly after 4T magnets were placed in academic laboratories, excellent-quality brain images were demonstrated [38,39], followed by similar successes in the human body [37] (Figure 7). Today, excellent anatomical images of the human brain have also been demonstrated at 8 [40–47], 7 [15,21], and recently at 9.4 Tesla [48].

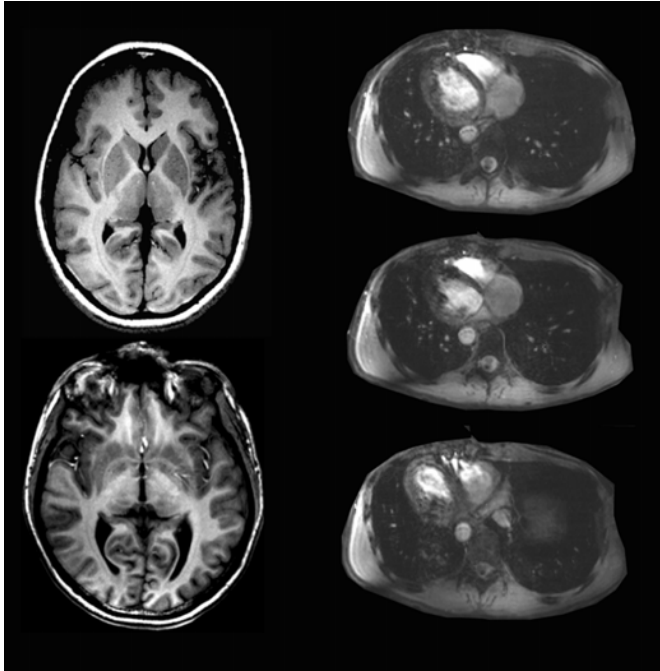


Figure 7. 4 Tesla head and body images from the University of Minnesota. Head images are obtained with 2D (top) and 3D MDEFT (bottom) [68]. Body images are obtained with a TEM body coil used for transmit and signal reception and EKG gated true FISP. Reprinted with permission from [37].

Image-intensity nonuniformities can be removed by a variety of strategies, including post-processing. As such, they do not pose a real impediment to anatomical imaging at high magnetic fields. However, it would be difficult, if not impossible, to overcome a lack of intrinsic contrast in the image to differentiate various anatomical structures. This was also a prediction for high magnetic fields based on expectations on the field dependence of T_1 , and T_2 . Anatomical images of brain tissue rely largely on proton density, T_1 and T_2 differences between tissue type and different regions (e.g., white matter vs. gray matter, cortex vs. subcortical nuclei). The region-specific values for these parameters have been reported in numerous papers for 1.5T field strength [49–61]. Proton density is clearly a magnetic field-independent parameter. However, relaxation times T_1 and T_2 are field dependent, generally increasing [62,63] and decreasing [30,64,65], respectively, with higher magnetic fields (also see review [66]). The conventional wisdom has been that T_1

not only increases with higher magnetic fields but T_1 values of different tissue types converge toward a single value. This, of course, would predict a lower contrast in the brain at higher magnetic fields. However, early human brain images obtained at 4 [38] and later at 7 Tesla [15] demonstrated this not to be the case. In fact, contrary to expectations, the distribution of T_1 values among different tissue types in the brain, including the difference between cortical gray matter and adjacent superficial white matter, increase with increasing magnetic field (Figure 8) [67]. The mechanisms underlying this unexpected behavior remain to be elucidated. However, excellent high-resolution T_1 -weighted images can be obtained at high fields, and this has been demonstrated at 4 [38,68], 7 [15], and 8 T [45] already. An example from 7 Tesla obtained with a 16-channel array coil is shown in Figure 9.

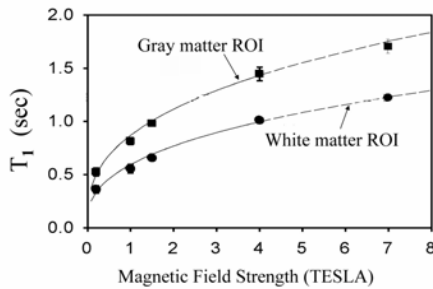


Figure 8. Dependence of GM and WM $^1\text{H}_2\text{O}$ T_1 values on B_0 . The solid squares represent T_1 data obtained from a ~ 0.05 mL ROI selected from the putamen, an internal gray matter structure. The solid circles represent T_1 data obtained from a 0.2-mL ROI selected from frontal white matter. Reprinted with permission from [67].

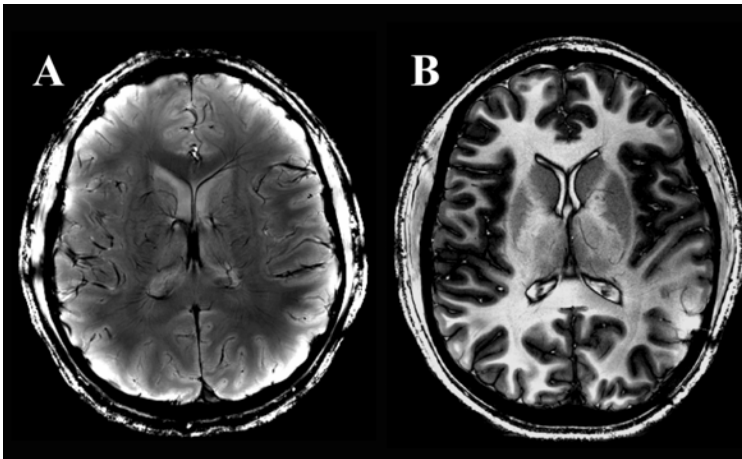


Figure 9. High-resolution imaging at 7 Tesla using a 16-channel array coil. (A) Gradient recalled echo (FLASH) image with some inherent T_2^* (512 x 512); (B) T_1 -weighted IR-Turboflash (4-segment acquisition) image $0.25 \times 0.25 \times 4 \text{ mm}^3$ ($\sim 1\text{K} \times 1\text{K}$), 3.2 min Acq. Time, $\text{TI} = 1.45 \text{ s}$.

Lengthening of T_1 with increasing magnetic field also holds true for blood. Blood T_1 is insensitive to its oxygenation state. Ex vivo measurements have shown that blood T_1 varies linearly with field strength going from 1.5 to 9.4 T according to $T_1 = 1.226 + 0.134B_0$ [69]. This imparts a clear benefit in time-of-flight type angiographic imaging, as well as perfusion imaging using spin-labeling techniques (discussed later on).

While the T_2 value in brain tissue decreases with increasing magnetic fields, the decrease is far from linear. Table 1 gives existing data on T_2 values at 4 and 7 Tesla together with values reported at 1.5 T in one publication. For example, going from 1.5 to 7 T, cortical gray matter T_2 is reduced by a factor of ~ 1.6 while the magnetic field increases 4.7-fold. Interestingly, the apparent T_2 values that are measured in a Carr-Purcell type sequence with multiple 180° pulses are longer and similar to those observed at the lower fields, suggesting that exchange and/or diffusion in the presence of gradients may be a dominant mechanism responsible for the shortening of T_2 with increasing magnetic field magnitude [64,65]. For blood, however, the T_2 decrease is dramatic and goes as the square of the magnetic field ([70] and references therein). While blood T_2 is longer than tissue T_2 at 1.5 Tesla, it is significantly shorter than tissue T_2 at 4 and in particular 7 Tesla.

Table 1. T_2 Values (ms) as a Function of Field Strength

	White matter	Gray matter	Source
1.5 Tesla	74 ± 5	87 ± 2	Wehrli et al. 1984 [55]
4 Tesla	49.8 ± 2.2	63 ± 6.2	Jezzard et al. 1996 [63]
	57.9 ± 3.8	67.1 ± 6.0	Yacoub et al. 2003 [30]
7 Tesla	45.9 ± 1.9	55.0 ± 4.1	Yacoub et al. 2003 [30]

At high magnetic fields, another contrast mechanism that gets utilized more frequently is T_2^* , which reports on susceptibility variations among different brain components (e.g., [71,72]). While this mechanism is clearly expected to be useful in visualizing deoxyhemoglobin containing vasculature, i.e., the venous system [72], it actually can provide contrast among brain tissues such as gray and white matter as well [71]. T_2^* contrast obviously gets better at high magnetic fields and has been already utilized at field strengths as high as 8 Tesla to depict vascular anatomy [42,44,47] and iron containing subcortical structures [46]. An example showing venous anatomy from 7 Tesla is illustrated in Figure 9A.

A recent and exciting example where the advantages of high magnetic fields were indispensable in morphological imaging is the in-vivo detection of amyloid plaques [73], a cardinal pathologic feature of Alzheimer's disease (AD). This application relied on high fields both for improved detectability (i.e., contrast-to-noise ratio (CNR)) and for improved SNR in order to reduce voxel size to the di-

mensions of the targeted pathology. Doubly transgenic mice develop “human-like” plaques, providing a mechanism to study amyloid plaque biology in a controlled manner. Imaging of labeled plaques has been accomplished with other non-MR modalities (see references in [73]). Unlike other modalities, however, MRI holds the potential for visualizing individual plaques non-invasively. Typical plaques in human AD subjects range from 2 to 200 μm in diameter, which is beyond the spatial resolution of PET.

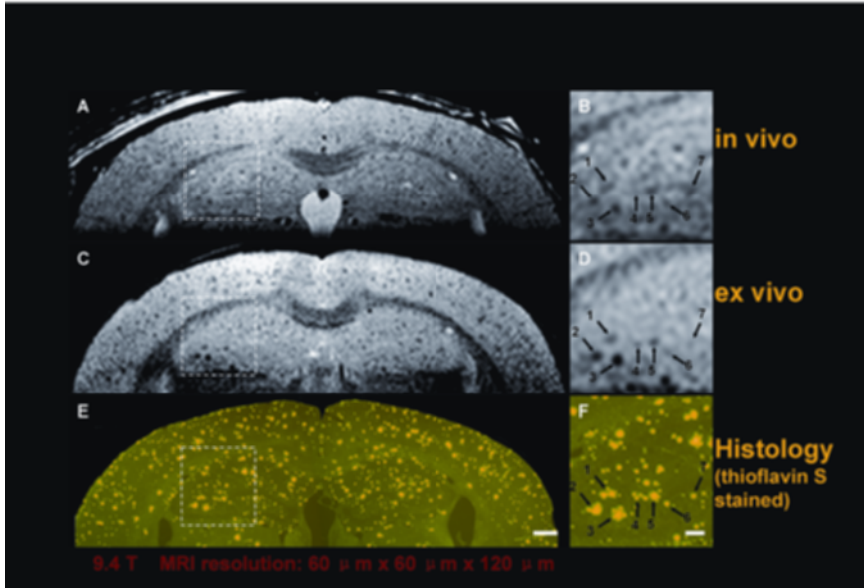


Figure 10. Imaging Alzheimer’s plaques in genetically modified mice using MR at 9.4 Tesla. Image resolution is $60 \times 60 \times 120 \mu\text{m}^3$. TE = 53 ms, and imaging time was 1 hour 7 minutes. The figure shows a three-way correlation in a 26-month AD mouse. Panels A, C, and E are full FOV and panels B, D, and F illustrate a magnified sub-sampled area centered on the hippocampus of the parent image to its left. The numbered arrows point to identical spatial coordinate positions in the common space of the three spatially registered volumes (in vivo, ex vivo, histological) using a linked cursor system. Spatially matched in-vivo (A,B), ex-vivo (C,D), and histological sections (E,F) conclusively demonstrate that the dark areas seen in vivo do indeed represent plaques. (E) Scale bar = 500 μm . (F) Scale bar = 200 μm . Plaque sharpness in vivo approaches but is clearly inferior to that obtained on ex-vivo MRI. See attached CD for color version.

Plaques were previously observed in T_2^* -weighted images of ex-vivo tissue specimens taken from the brain of AD mice. This was attributed to the known presence of metals, particularly iron, in plaques (e.g., [74–77]). Recently, however, the plaques were detected for the first time in vivo in anesthetized AD mice in reasonable imaging times (~ 1 hour) [73]. The study was carried out at 9.4 Tesla using T_2 weighting and strategies to minimize perturbations originating from breathing and brain pulsation. The in-vivo data were correlated with ex-vivo MRI and ex-vivo histology (Figure 10). Histologically verified plaques as small as 50 μm in

diameter were observed in the living animal. Figure 10 displays in-vivo and ex-vivo AD mouse MR images and histological sections from this study [73]. This work represents the first demonstration of noninvasive in-vivo visualization of individual AD plaques without the use of a contrast agent. It holds the potential that such plaques may be also detectable in the human brain at ultra high magnetic fields such as 9.4 T, which is now available for human measurement.

The observation that the plaques were better visualized in T_2 (TE = 52 ms) rather than T_2^* -weighted (gradient echo, TE = 16 ms) images suggests that the mechanism responsible for the contrast is diffusion in the presence of magnetic field gradients generated around the plaques. If this postulate is correct (which remains to be confirmed experimentally), the contrast will increase approximately quadratically with the magnetic field, as in Hahn Spin Echo fMRI (discussed further on). Combined with the SNR increase to attain high resolution, high fields, therefore, would provide a significant advantage here.

5. FUNCTIONAL AND PHYSIOLOGICAL IMAGING IN THE BRAIN

5.1. Mapping of Neuronal Activity Alterations (Functional Imaging or fMRI)

In the armamentarium of techniques used for investigating brain function, functional magnetic resonance imaging (fMRI) has come to play a dominant role in both human and animal model studies. Today, functional images in the brain can be obtained using the BOLD mechanism [1,2,78], cerebral blood flow (CBF) changes using arterial spin labeling (ASL) (e.g., [29,79–83] and references therein), intravoxel incoherent motion [84,85], and cerebral blood volume (CBV) alterations (e.g., [86–88]).

The most commonly used fMRI approach, introduced in 1992 [1,2,78], is based on imaging regional deoxyhemoglobin alterations that accompany changes in neuronal activity. This contrast mechanism is referred to as blood oxygen level dependent (BOLD) contrast [89–92]. It originates from the intravoxel magnetic field inhomogeneity induced by paramagnetic deoxyhemoglobin sequestered in red blood cells, which in turn are compartmentalized within the blood vessels. Magnetic susceptibility differences between the deoxyhemoglobin-containing compartments versus the surrounding space devoid of this strongly paramagnetic molecule generate magnetic field gradients across and near the boundaries of these compartments. Therefore, in images sensitized to BOLD contrast, signal intensities are altered if the regional deoxyhemoglobin content is perturbed. This occurs in the brain because of spatially specific metabolic and hemodynamic responses to enhanced neuronal activity. It has been suggested that regional blood flow (CBF) increases while oxygen consumption rate (CMRO₂) in the same area is not elevated commensurately [93,94], resulting in decreased extraction fraction and lower deoxyhemoglobin content per unit volume of brain tissue. Consequently, signal intensity in a BOLD sensitive image increases in regions of the brain engaged by a

"task" relative to a resting, basal state. In this approach, the vast majority of images are acquired using T_2^* weighting using gradient echoes (GE). Only a few studies have been conducted using Hahn-spin echoes (HSEs).

High magnetic fields provide the capability for obtaining robust, BOLD-based functional maps with increased contrast, resolution, and specificity (i.e., accuracy). It has already been demonstrated that T_2^* -weighted GE BOLD maps can be obtained in the human brain at 7 Tesla (e.g., see [28,70,83,95–99]), and in rodent brain up to 11.7 Tesla [100]. Examples of human brain functional imaging at 7 Tesla are illustrated in Figure 11 for two slices obtained with $1 \times 1 \times 3 \text{ mm}^3$ resolution in the visual cortex. Both negative and positive BOLD changes are clearly observed in these 7T functional maps (Figure 11A). This figure also demonstrates the reproducibility of these images in consecutively acquired but separate maps. With the exception of a few pixels at the edges, the functional maps (Figure 11B) as well as the correlation coefficient that determines the significance of activation (Figure 11C) are highly reproducible at this field strength.

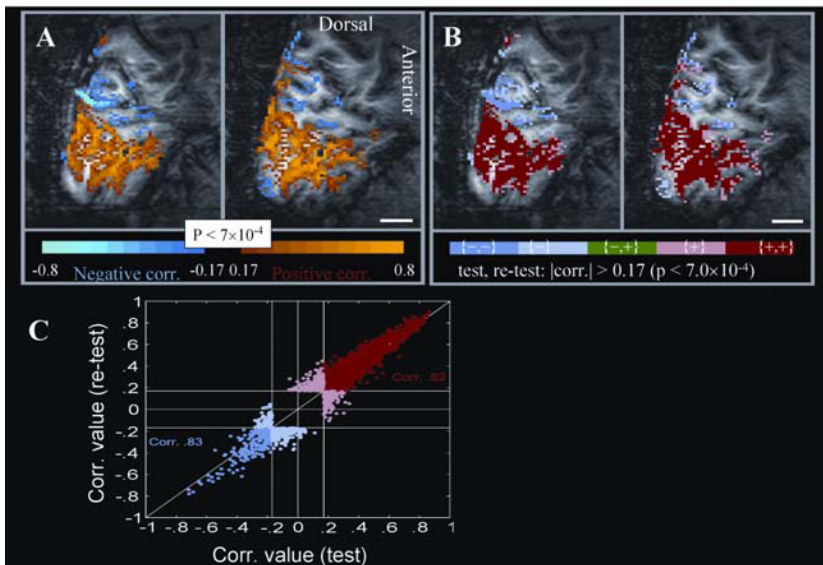


Figure 11. 7 Tesla, $1 \times 1 \times 3 \text{ mm}^3$ fMRI functional images in two sagittal planes in the human visual cortex obtained with T_2^* BOLD contrast, showing positive and negative signal intensity changes (A). Acquisition parameters were 4-segment gradient recalled echo EPI, TR = 150 ms per segment, TE = 20 ms. Reproducibility of images is illustrated in (B) for two consecutive runs in the same subject; the pixels that are deemed to have shown a statistically significant increase are color-coded as darker red for positive BOLD signals and darker blue for the negative BOLD signals. (C) The cross-correlation of all pixels with the activation template for the two runs against each other. Adapted with permission from A Shmuel, E Yacoub, J Pfeuffer, PF Van de Moortele, G Adriany, X Hu, K Ugurbil. 2002. Sustained negative BOLD, blood flow and oxygen consumption response and its coupling to the positive response in the human brain. *Neuron* 36(6):1195–1210. Copyright © 2002, Cell Press. See attached CD for color version.

In functional brain imaging, as in many other MR applications, a critical parameter aside from image SNR is the contrast-to-noise ratio (CNR). In fMRI, CNR is defined as the stimulus- or task-induced signal intensity change compared to temporal signal fluctuations in the fMRI time series. CNR in functional brain imaging, however, is intricately tied to the problem of spatial specificity. For example, increased neuronal activity can induce very large changes in MR signal intensity due to effects associated with large blood vessels; however, the origin of these large signal changes will not precisely colocalize with the actual site of neuronal activation [101,102]. Such signal increases, although very large in magnitude and possibly in CNR, are undesirable since they are not useful due to their lack of spatial specificity for most except the crudest of functional imaging studies. In functional imaging, ideally only signals associated with microvasculature are desired. Consequently, the important problem is to increase the CNR for contributions coming from these vessels while suppressing the CNR associated with large blood vessels. This is exactly what high fields provide in BOLD-based functional imaging. CNR specific to microvasculature is small, but increases supralinearly (almost quadratically) with the magnetic field ([30] and references therein). Even at 7 Tesla, however, they do not reach the very large magnitudes that are generated by a *large* vessel even at lower fields such as 1.5 T.

Thus, the most important attribute of high magnetic fields in BOLD functional imaging studies is improvements in spatial accuracy. This is an important, in fact an imperative, step if fMRI is to make contributions to brain sciences beyond its current achievements. Present fMRI capabilities are and may remain useful for a long time in cognitive psychology studies. Unfortunately, they are ultimately inadequate given what is known about brain function from single-unit studies. For example, it is well recognized from animal experiments that neurons in the visual system with similar functional behavior are clustered together in patches that can be as small as 300 to 500 microns in diameter on the cortical surface (e.g., ocular dominance columns, orientation columns, and whisker barrels). Electrophysiology studies indicate that analogous clusters may exist in higher-order visual areas (e.g., the inferio-temporal (IT) cortex in the monkey with respect to face and object recognition) [103,104]. Such clustering may and likely does exist for many other higher-order functions of the brain. The ability to examine this type of fine functional parcellation in cortical space requires accurate and noninvasive functional imaging methods that can provide high-resolution information over a large volume if not the whole brain. Electrode recordings, while precise, vastly under-sample the brain and cannot be practically performed over large areas of the cortex. Optical imaging methods do not provide information deeper than ~1 mm on the cortical surface and cannot access large areas of cortex within the multiple folds and sulci in the highly convoluted primate brains.

Degradation of specificity in functional images can arise from two mechanisms. First, blood flow increases that accompany neuronal activity alterations can exceed the boundaries of active neurons; second, coupling between the functional changes and MR detectable signals contain nonspecific contributions, such as those coming from large draining veins in BOLD signals. The first is a physiological

problem related to the point spread function of the blood flow response to increased neuronal activity; it concerns the question of how well the boundaries of the blood flow increase are confined to the region of elevated neuronal activity. This is a fundamental question for all current fMRI strategies because they do not directly detect neurotransmission or the electrical activity of neurons; instead, they rely on the secondary and tertiary signals that evolve as a result of an alteration in neuronal activity. Therefore, the spatial accuracy of these metabolic and hemodynamic responses that accompany elevated neuronal activity imposes a fundamental lower limit on the accuracy of the fMRI maps. This fundamental lower limit is, of course, unaffected by the magnetic field magnitude of the MRI measurement.

The second cause of degradation of accuracy in fMRI, however, is field dependent. This degradation in specificity is imposed by the nature of the coupling between MR detectable signals and metabolic and hemodynamic changes that track neuronal activity. For the BOLD mechanism, this coupling is mediated by the vasculature, the compartment that contains deoxyhemoglobin. The changes in deoxyhemoglobin concentration in blood are initiated at the point of altered neuronal activity and, consequently, altered oxygen consumption rate. They occur first in the capillary bed where oxygen exchange with tissue takes place. However, these deoxyhemoglobin alterations do not remain stationary. They propagate into large “draining” vessels because of blood flow where they can cause large activation-induced signal changes detected in fMRI. Thus, they appear incorrectly as “activation” distant from the actual site of neuronal activity. The presence of such large “draining” vessel contribution to the T_2^* -based BOLD signals was well documented experimentally [101] in the very early days of BOLD-based fMRI.

Clearly, the first question to tackle concerning the accuracy of functional maps in the brain is really the question of fundamental physiologic limitations on the blood flow response invoked by increasing neuronal activity. The accuracy of spatial coupling between neuronal activity and increased blood flow can be evaluated using perfusion imaging. This, of course, requires that perfusion-based functional maps do not contain contributions from large vessels. When blood flow to a volume of tissue increases, flow in the large arterial and venous blood vessels that supply or drain blood from that particular volume of tissue must also increase due to conservation of mass; thus, blood vessel dilation produced by neuronal activation propagates to distant blood vessels [105]. However, long tagging times (~ 2 s) in perfusion imaging with pulsed arterial spin tagging suppress arterial components in perfusion images [106]. Long tagging times are easily feasible at high magnetic fields because of the long blood T_1 . The long tagging times, on the other hand, may lead to tagged spins appearing in the venous side, thus leading to false activation in the draining veins. At high magnetic fields, the T_2 of venous blood is very short [70,96,107,108] so that this effect can be selectively eliminated by a brief delay after excitation of spins but before image acquisition (also see discussion in [109]).

In the absence of large-vessel contributions, perfusion-based fMRI can be used to examine the critical physiological question related to specificity of blood flow increases. Namely, are perfusion changes confined accurately to the region of in-

creased neuronal activity in the spatial scale of columnar organizations? Such a study was performed using iso-orientation columns in the cat visual system [81]. It demonstrated that while perfusion increases that follow neuronal activation were not “perfectly” localized at the iso-orientation column level, the difference between active and neighboring inactive columns was large and permitted single-condition mapping. Recent experiments in our laboratory put the full width at the half-maximum of the point spread function of this perfusion response at ~ 0.5 mm [110]. These studies also indicated that regulation of perfusion must also occur at the level of capillaries in the brain. The spacing between feeding arterioles is approximately 1.5 mm, and regulation of blood flow at this level alone obviously cannot produce columnar maps or a PSF of ~ 0.5 mm. These conclusions were initially seen as contradictory to optical imaging data on CBV changes during activation. However, a large body of recent optical imaging studies based on mapping CBV changes using intrinsic signals (e.g., [111–113]) are in total agreement with the conclusions of the perfusion imaging results.

Thus, the fundamental lower limit imposed by physiology is very good, in the scale that would permit mapping of the columnar organizations in the cortex. Any inaccuracies in the specificity of fMRI signals beyond this fundamental limit must originate from mechanisms between coupling of physiological responses to activation and the MR detectable signals. For BOLD-based fMRI, the paramount issue resolves around the contribution of different size blood vessels, as already mentioned. In discussing this issue, however, as a cautionary note we must first distinguish *single-condition vs. differential mapping*. Differential mapping refers to functional images obtained by using two analogous but orthogonal activation states designed specifically to eliminate or suppress common signals; the functional image generated in this fashion corresponds to a subtraction of the two similar conditions. In contrast, single-condition mapping does not rely on subtraction from a second orthogonal activated state. Mapping ocular dominance columns by stimulating one eye vs. the other in an alternating fashion is differential mapping. Stimulating one eye and using a dark state as the control would correspond to *single-condition mapping*. Even if the imaging signals are *not* specific enough to be confined to the territory of one column, a functional map of the columns can be obtained in the differential image if a given group of columns respond slightly differently to the stimulation of each eye and false (i.e., nonspecific) activation is induced equally by stimulating the two different eyes. Phase-encoded mapping of multiple areas using an activation paradigm that cycles through all possible stimulations (as employed in the visual system (e.g., [114–116]) is also a kind of differential mapping because it tends to suppress common, non-modulating components.

Magnetic field dependence of BOLD-based functional imaging signals

The BOLD effect has two components: extravascular and intravascular (i.e., blood related). First, let us ignore the intravascular space and focus on the *extravascular space* only. When deoxyhemoglobin is present in a blood vessel, magnetic susceptibility of the space within the blood vessel is different than outside the

blood vessel. This results in a homogeneous field within the blood vessel but an inhomogeneous field outside the blood vessel. In a BOLD-based fMRI experiment, images are acquired after a delay TE in order to sensitize the image to magnetic field inhomogeneities. If the typical diffusion distances during the delay TE are comparable to the distances spanned by the magnetic field gradients, then during this delay the tissue spins will experience a time-averaged magnetic field in the extravascular space where the magnetic field gradients exist.

Typical TE values used in fMRI experiments depend on the field strength and the specifics of the pulse sequence, but in general range from ~30 to ~100 ms. Thus, blood vessel size compared to diffusion distances in this ~30–100 ms time domain becomes a critical parameter in the BOLD effect. In this timescale, small blood vessels — e.g., capillaries — that contain deoxyhemoglobin will contribute to the dynamic averaging and result in a signal decay that will be characterized by a change in apparent T_2 [3,5,6]. In a spin-echo experiment with a single refocusing pulse in the middle of the delay period (i.e., a Hahn spin echo), the dynamic averaging that has taken place during the first half of the echo will not be recovered. Of course, applying many refocusing pulses as in a Carr-Purcell pulse train or applying a large B_1 field (relative to the magnitude of the magnetic field inhomogeneity) for spin-locking during this delay will reduce or even eliminate this signal loss due to dynamic averaging. In a gradient echo measurement, dynamic averaging will also occur during the entire delay TE. If the imaging voxel contains only such small blood vessels at a density such that the average distance between them is comparable to diffusion distances (as is the case in the brain where capillaries are separated on the average by 25 μm [117]), then the entire signal from the voxel will be affected by dynamic averaging.

In considering the movement of water molecules around blood vessels, we need not be concerned with the exchange that ultimately takes place between intra- and extravascular water across capillary walls. The typical lifetime of the water in capillaries exceeds 500 ms [118–120], significantly longer than the T_2 and T_2^* values in the brain tissue and longer than the period TE typically employed in fMRI studies.

For larger blood vessels, complete dynamic averaging for the entire voxel will not be possible. Instead, there will be “local” or “partial” dynamic averaging over a subsection of the volume spanned by the magnetic field gradients generated by the blood vessel. However, there will be signal loss from the voxel due to *static averaging* if refocusing pulses are not used or asymmetric spin echoes are employed. Following the excitation and rotation onto the plane transverse to the external magnetic field, the bulk magnetization vector of the nuclear spins will precess about the external magnetic field with the angular frequency ω_B^{out} . A water molecule at a given point in space relative to the blood vessel will see a “locally” time-averaged ω_B^{out} , ω_B^{out} , which will vary with proximity to the large blood vessel. Thus, signal in the voxel will then be described according to the equation

$$S(t) = \sum_k s_{0k} e^{-TE/T_{2k}} (e^{-i\bar{\omega}_k TE}), \quad (1)$$

where the summation is performed over parameter k , which designates small-volume elements within the voxel; the time-averaged magnetic field experienced within these small volume elements is ω_k in angular frequency units. Because $\omega_k TE$ varies across the voxel, the signal will be “dephased” and lost with increasing echo time TE . This signal loss occurs from “static averaging.” In this domain, if variation ω_k over the voxel is relatively large, signal decay can be approximated with a single exponential time constant, T_2^* . In a spin-echo, the static dephasing will be refocused and thus eliminated.

Consistent with the discussion above, modeling studies (again so far restricted to the extravascular volume) yield the following terms for contributions to R_2^* (i.e., $1/T_2^*$)

$$R_2^* = \alpha[\Delta\chi_0 B_0(1 - Y)] b_{vt} \quad (\text{large vessels, static averaging regime}), \quad (2)$$

$$R_2^* = R_2 = \eta[\Delta\chi_0 B_0(1 - Y)]^2 b_{vs} p \quad (\text{small vessels, dynamic averaging regime}), \quad (3)$$

where α and η are constants, Y is the fraction of hemoglobin that is oxygenated, B_0 is the external magnetic field, $\{\Delta\chi_0 B_0(1 - Y)\}$ is the frequency shift due to the susceptibility difference between the cylinder simulating the deoxyhemoglobin containing blood vessel and the space outside the cylinder, b_{vt} is the blood volume for large blood vessels (veins and venules with a radius greater than $\sim 5 \mu\text{m}$ for 4 T), and b_{vs} is the small vessel blood volume (capillaries and small venules, less than $\sim 5 \mu\text{m}$ in radius that permit dynamic averaging), and p is the fraction of active small vessels (i.e., filled with deoxyhemoglobin containing red blood cells).

An important prediction of the modeling studies is that the large and small vessel extravascular BOLD effects differ and the microvascular contribution varies as the square of the external magnetic field. In contrast, the dependence on the external magnetic field is linear for large blood vessels in the static averaging domain.

However, in considering the effect of magnetic fields on the BOLD mechanism, we must also consider purely blood effects (intravascular contribution) as opposed to extravascular contributions specified in Eq. (2) and (3). In the blood, hemoglobin is also compartmentalized within red blood cells. Thus, when the deoxy form is present, there are field gradients around the red cells. However, because the dimensions are very small compared to diffusion distances, the effect is dynamically averaged and becomes a T_2 effect only. The dynamic averaging in this case also involves exchange across the red blood cell membrane that is highly permeable to water. The exchange is between two compartments — plasma and the interior of the red blood cell — where the magnetic field is significantly different because of the presence of paramagnetic deoxyhemoglobin. Thus, in the presence of deoxyhemoglobin containing red blood cells, the apparent T_2 of blood decreases and can be expressed as $1/T_2 = A_0 + kB_0^2(1 - Y)^2$, where A_0 is a field-independent term, and k is a constant. Therefore, the T_2 of blood will change when the content of deoxyhemoglobin is altered by elevated neuronal activity, and this will lead to a signal change in the apparent T_2 or T_2^* -weighted image. This effect will be present

wherever the content of deoxyhemoglobin has changed, thus potentially both in large and small blood vessels.

Hahn spin echo-based BOLD images

BOLD-based functional maps with suppressed large vessel contribution can be obtained with the Hahn Spin Echo approach at high but *not* low magnetic fields. From the previous discussion, one can conclude that HSE fMRI responds to apparent T_2 (as opposed to T_2^*) changes both in the extravascular space around microvasculature [3,121], and in blood itself [122–124]. The former provides spatial specificity in the hundred micron spatial scale because capillaries are separated on the average by 25 μm [117]. The blood effect, however, can be associated with large and small blood vessels and hence degrades spatial specificity of fMRI. However, the apparent T_2 of venous blood decreases quadratically with magnetic field magnitude [107] and is diminished from ~ 180 ms at 1.5 Tesla [125] to ~ 6 ms at 9.4 Tesla [108], significantly smaller than brain tissue T_2 and the TE values that would be used at such field strengths.

The *extravascular* HSE BOLD effect which is microvascular in origin is a small effect, and so it is reasonable to question whether it is at all detectable at any field strength or whether HSE BOLD signals originate predominantly from blood contribution. Both of these questions were specifically examined using separate experiments.

Whether the extravascular BOLD effect exists was examined using weak but detectable ^1H resonances of metabolites, such as N-acetyl aspartate, that are sequestered intracellularly [126]. Any BOLD effect observed on such signals can only be *entirely* extravascular in origin. A BOLD effect on intracellular metabolites was clearly detectable at 4 and 7 Tesla, leading to the clear demonstration that *extravascular spin-echo* BOLD effects exist in the human brain.

The blood contribution to HSE BOLD fMRI was evaluated using a Stejskal and Tanner gradient pair, first introduced for diffusion measurements [127]. This gradient pair, often referred to as “diffusion weighting” gradients, also suppresses blood significantly more than tissue spins in the brain. This is because the diffusion of blood water is much faster than in tissue, and the gradient pair dephases blood spins. The latter effect arises because flowing spins acquire a velocity-dependent phase in the presence of these gradients. Flow rates are nonuniform within a blood vessel. Furthermore, the blood vessels change directions within a voxel, and/or there may be several different blood vessels with different flow rates and/or different orientations relative to the gradient directions. Since the blood signal detected from the voxel will be a sum of all of these, the net result can be signal cancellation due to dephasing of flowing spins (IVIM effect) [128].

The Stejskal-Tanner pulsed gradients can be used to distinguish between intra- and extravascular BOLD effects in functional images. Such experiments conducted at 1.5 Tesla have concluded that most of the BOLD-based signal increase during elevated neuronal activity is eliminated by bipolar gradients, leading to the conclusion that most of the fMRI signal at 1.5 T arises from *intravascular* or blood-related effects [129,130]. At 3 Tesla, $\sim 50\%$ of the HSE functional signal changes has been attributed to blood using the same type of experiments [131].

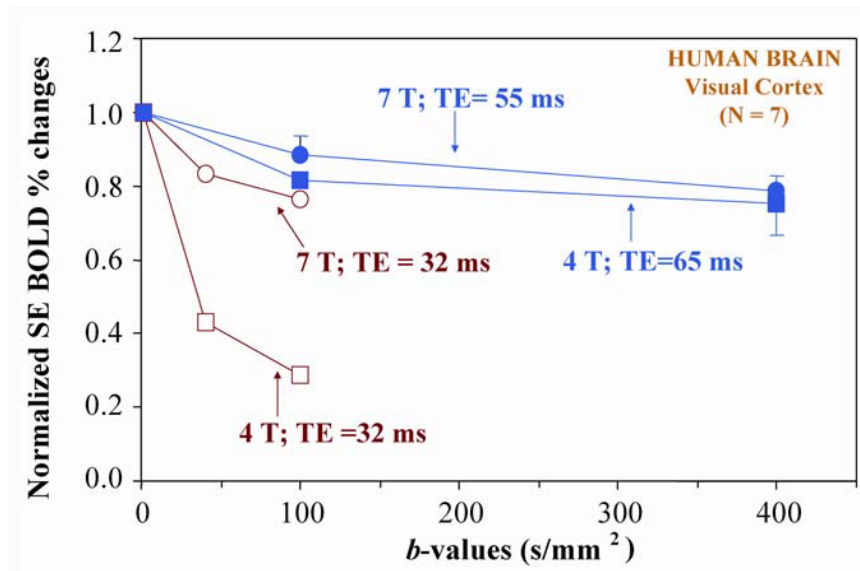


Figure 12. Experimental evaluation of blood contribution to 7 T Hahn spin echo functional images. Figure shows normalized HSE BOLD percent changes as a function of b value for short and long echo times at 4 and 7 T in a region of interest (ROI) defined in the $b = 1$ map. Percent changes were normalized to the BOLD change at $b = 1$ s/mm² for each subject and averaged for each field. Closed rectangles and circles indicate HSE data with TE of 65 ms at 4 T ($n = 7$) and with TE of 55 ms at 7 T ($n = 4$), respectively. Open rectangles and circles indicate HSE data with TE of 32 ms at 4 and 7 T, respectively, for two subjects at each field (six repeated measurements were made for each subject). Error bars are standard errors of the means. For long TE, the attenuation was not statistically different between 4 and 7 T ($p > 0.05$). Reprinted with permission from [70]. See attached CD for color version.

The effect of the Stejskal-Tanner gradients on brain tissue signal intensity at 4 and 7 Tesla was examined (Figure 12) and found to agree well with the modeling predictions (Figure 13) [70]. The dependence on the b -value for diffusion-weighted spin-echo BOLD data, averaged for all subjects, are illustrated in Figure 12 for an echo time of 32 ms for both 4 and 7 T, and for echo times of 65 and 55 ms for 4 and 7 T, respectively. The 32-ms echo time is shorter than tissue T_2 at both fields. Blood contributions are expected to be echo time dependent and diminish with increasing echo time for TE values exceeding the blood T_2 (Figure 13). At about 32 ms TE, blood contribution to 7 Tesla is expected to be minimal (Figure 13) since the T_2 of blood is short [96]. However, for 4 T, where the T_2 of blood is ~ 20 ms, the blood is still expected to contribute (Figure 13). The 32-ms TE data in Figure 12 emphasize that at this echo time signal changes associated with activation attributable to blood (and thus can be suppressed with diffusion gradients) are a small fraction of the total signal change at 7 T; in contrast, signal changes associated with activation at this echo time arise predominantly from blood at 4 Tesla. This would still be the case in gradient echo fMRI experiments where typical echo

times employed would be approximately 30 ms. At the longer echo times, however, as expected, percent changes at both fields were only slightly reduced by the diffusion-weighting gradients. There is a relatively small but persistent reduction in stimulation-induced signal intensity change that is field independent; this is ascribed to the elimination of so called “in-flow” effects that arise because full relaxation is not allowed between consecutive images.

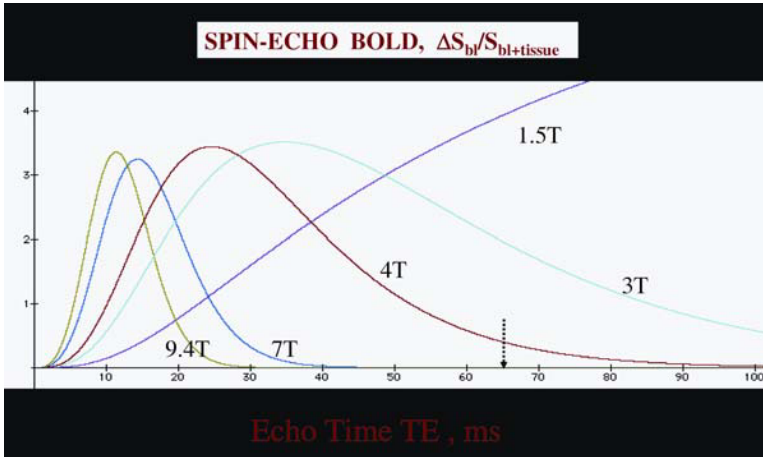


Figure 13. Simulation of the intravascular BOLD signal change, $\Delta S_{\text{blood}}/(S_{\text{blood}}+S_{\text{tissue}})$, as a function of echo time for a Hahn spin echo at 1.5, 3, 4, 7, and 9.4 T. We assumed a venous blood volume of 0.05, no stimulus-evoked blood volume change, and an increase in venous oxygenation level from 0.6 to 0.65 during stimulation. The T_2 values of blood water at different field strengths and as a function of echo time were calculated from experimental data (see [70] for details). Reprinted with permission from [70]. See attached CD for color version.

Similarly, at 9.4 Tesla the effect of the Stejskal-Tanner gradients are similar to the 7 T results reported for the human brain above [108]. In a Hahn spin-echo weighted fMRI study conducted in the rat brain (forepaw stimulation, symmetric spin-echo with one 180° pulse), we observed that the activation is not altered at all going from very small to very high b values.

Therefore, one can conclude that at these very high magnetic fields, unwanted blood contributions to the BOLD effect are virtually eliminated at typical TE values that correspond to gray matter T_2 . This TE value would represent the optimum TE for spin-echo fMRI assuming that the “noise” in the spin-echo fMRI data (i.e., image to image fluctuations in signal intensity) is TE independent; this certainly would be the case at very high resolution where intrinsic image SNR dominates the “noise” in the fMRI series and may be the case even when there is significant physiologic noise in the HSE experiment (see discussion later on and reference

[98]). Thus, at these “optimal” echo times, both 7 and 4T human fMRI data as well as 9.4T rat data are equally devoid of blood related degradations in specificity.

Even though both at 4 and 7 T undesirable blood contributions are suppressed at optimum TE, there is still an advantage of 7 over 4 Tesla. This advantage is the substantially improved CNR of the HSE functional images, which increases approximately quadratically with field magnitude. This was expected based on modeling studies and was also experimentally verified [30]. This CNR enhancement is extremely important in view of the fact that this CNR is low even at 4 Tesla. Note, however, that similarly long echo times are not useful for 1.5 T in suppressing the blood effect because blood T_2 exceeds tissue T_2 . At that field magnitude, the blood contribution is substantial at TE values in the vicinity of tissue T_2 (~90 ms), and are increasing with TE (Figure 13) until about 150 ms (not shown in Figure 13).

The experiments with the “diffusion”-weighted gradients confirm the expectation that blood effects are negligible at high fields. However, experimentally we are unable to judge at what level of the vascular tree we were able to eliminate the blood signals from the image using the diffusion gradients. Since the apparent T_2 of venous blood is so short, we expect that at all levels of the venous tree (venules to large veins), blood signals must be suppressed provided we use echo times that are about three fold larger than the apparent venous blood T_2 . The intracapillary blood, however, is unlikely to be fully suppressed. In the capillary, red blood cell density is nonuniform and oxygenation level varies from the arterial value to the venous value from one end of the capillary to the other end. However, this is *immaterial* as to whether capillary blood still contributes or not at high fields to functional maps; in either case, spatial resolution is dictated by capillary distribution.

Thus, as in perfusion imaging, HSE BOLD techniques are expected to yield columnar level mapping. That they are capable of distinguishing among different layers has already been shown [30].

Gradient echo (T_2^) BOLD functional imaging*

Virtually all current fMRI studies are carried out using GE (T_2^* weighted) BOLD technique. All other fMRI methods are primarily employed by investigators interested in mechanisms and methodology development. GE BOLD fMRI, however, suffers from inaccuracies in functional mapping because of large vessel contributions as already discussed. This is true at all magnetic fields because the extravascular BOLD effect associated with large vessels is always present and increase linearly with magnetic field, as previously mentioned (see Eq. (2)). However, the situation gets better even for this BOLD approach with higher magnetic fields.

The GE BOLD effect also comes from intravascular and extravascular sources. The intravascular effect originates from the same mechanism as in HSE BOLD, namely the T_2 changes induced by deoxyhemoglobin concentration perturbation when neuronal activity is altered. However, there is a second mechanism by which blood comes into the GE BOLD effect [132,133]. This mechanism is operative

when blood occupies a large fraction of the volume of the voxel. When deoxyhemoglobin is present in the blood, the blood water will dynamically average the gradients surrounding the red blood cells and will behave as if it encounters a uniform magnetic field. This will differ from the magnetic field experienced by the rest of the voxel. In the immediate vicinity of the blood vessel, the magnetic field will vary and approach a constant value in tissue distant from the blood vessel. For simplicity, we can neglect the gradients near the blood vessel and consider the voxel to be composed of two large bulk magnetic moments, one associated with blood and the rest with the extravascular volume. These magnetic moments will precess at slightly different frequencies; therefore, the signal from the voxel will decrease with time as the two moments lose phase coherence. In this scenario, the signal can even oscillate as the phase between the two magnetic moments increase and then decrease. This mechanism cannot be operative when a voxel only contains capillaries since the blood volume is $\sim 2\%$ [117]. This blood-related effect appears to be the main source of fMRI signals at 1.5 Tesla and explains the reason why there exists very large stimulation induced fractional changes at low magnetic fields [132,133]. It is diminished and even eliminated at high fields as the blood signal contributions becomes smaller due to the short T_2 . Note that, unlike the extravascular BOLD effect, these blood-related mechanisms do not require that ΔS be dependent on S (or equivalently, $\Delta S/S$ is independent of S), where S represents the voxel signal intensity and ΔS is the activity-induced signal change in the fMRI data.

As in HSE, all blood related effects diminish dramatically with increasing magnetic field as blood T_2 decreases and blood signals vanish in a typical fMRI acquisition. However, the extravascular BOLD effect persists and continues to be a source of inaccurate functional mapping signals. Nevertheless, at higher fields such as 7 Tesla, the microvascular contributions also become large enough so that its contributions is comparable to the large vessel effects [98]. Figure 14A displays a histogram of the number of activated voxels, defined by a statistical threshold of $p < 0.05$, vs. percentage signal change for one subject, for three different runs performed on different days at 7 Tesla [98]; the figure contains both HSE and GE fMRI data. An example of a GE image that was used to extract these data is illustrated in Figure 14B. In each case, anatomical landmarks were used to aim for selection of the same slice. Activation in the HSE data has a narrow distribution in percent signal change induced by visual stimulation, with only a few voxels showing increases larger than 10%. This is consistent with the concept that a single blood vessel type contributes to these signal changes. In contrast, the GE BOLD measurements are characterized by a broad distribution of stimulus-induced percent changes. In the GE data, there exists a large concentration of voxels at small percent changes just as in the HSE series; however, there are also a significant number of voxels displaying large signal changes ranging up to $\sim 25\%$. This would be expected if different blood vessels, from capillaries to draining veins, are all contributing.

The presence of large vessel contribution even at 7 Tesla in T_2^* BOLD fMRI images in the human brain was also demonstrated by comparing perfusion-based

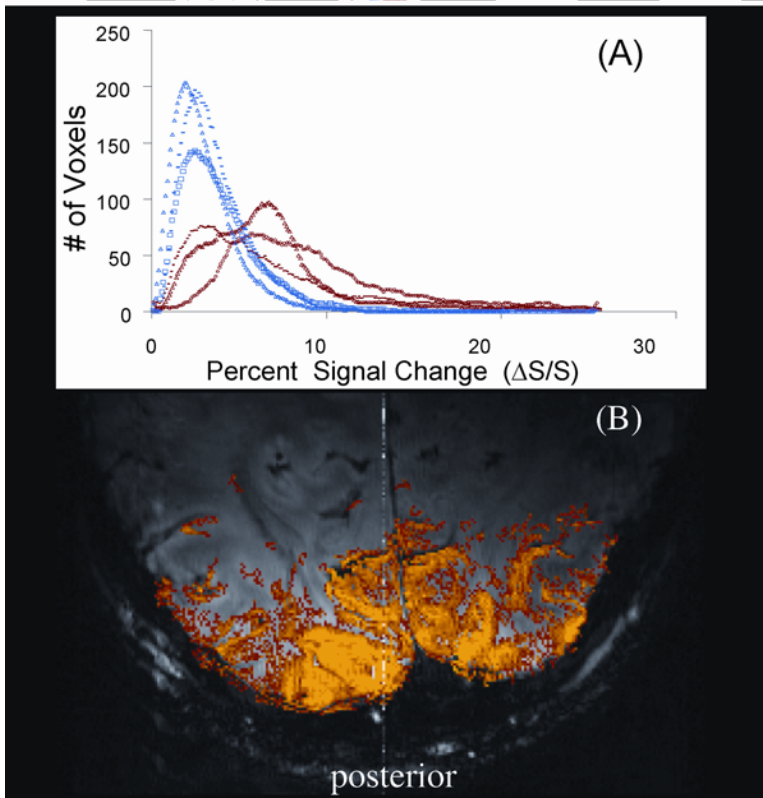


Figure 14. Stimulus-invoked percent signal change at 7 Tesla in the human visual cortex. (A) Histograms of percent changes of repeated (different days) HSE (in blue) and GE (in red) BOLD studies from the same subject, in the same anatomical location in. (B) Percent signal change vs. basal image signal intensity (normalized). Data were extracted from functional images obtained with $0.5 \times 0.5 \times 3 \text{ mm}^3$ spatial resolution at 7 Tesla, an example of which is shown in (B). Reprinted with permission from E Yacoub, PF Van De Moortele, A Shmuel, K Ugurbil. 2005. Signal and noise characteristics of Hahn SE and GE BOLD fMRI at 7 T in humans. *Neuroimage* **24**(3):738–750. Copyright © 2005, Elsevier. See attached CD for color version.

images in the human brain with T_2^* BOLD fMRI. Both because of the enhanced SNR and the long T_1 , high fields provide advantages for perfusion-based functional imaging. In high-resolution perfusion images that were obtained at 7 Tesla for the first time [29], the activity was found to be confined to the gray matter ribbon; in contrast, the T_2^* BOLD fMRI images showed highest intensity changes not in the cortex but in the cerebral spinal fluid (CSF) space in the sulci. Within the cortical gray matter, there are 50- to 100-micron veins separated by 1 to 1.5 millimeters that drain the capillaries. These are the blood vessels that can be seen in high-resolution T_2^* -weighted images as dark lines traversing the gray matter perpen-

dicular to the cortical surface (e.g., [91]). These small veins drain immediately into similarly sized or somewhat larger veins on the cortical surface. The draining “pial” veins located on the cortical surface are the likely source of intense but false activation seen within sulci in human GRE BOLD images at 7 Tesla [29].

Despite the presence of large-vessel contributions, high-resolution GE functional images at 7 Tesla look very different than very high-resolution GE functional images at lower fields because of the comparable microvascular contributions at the higher field strength. At lower fields, high-resolution functional images look like angiograms [102]; only if the spatial resolution is reduced does the functional image become diffuse and activated areas *appear* to cover gray matter areas rather than depicting vessels. At 7 Tesla the activity is diffuse and covers gray matter even at very high resolution (Figure 14B) [98], albeit together with contaminating signal from large vessels.

We should add that even with these inaccuracies a large number of questions about human cognition can be answered using GE fMRI even at 1.5 T. However, high-resolution images at the columnar level become impossible to attain by GE (T_2^*) BOLD fMRI at any field strength unless differential methods can be successfully applied. It was rigorously demonstrated that T_2^* BOLD fMRI method fails to generate *single-condition* functional images of iso-orientation domains in the cat cortex [134,135] at 4.7 Tesla. Although the image resolution was sufficiently good to detect columnar organizations associated with orientation preference in these studies, they were *not* observed. Furthermore, the images were not complementary when orthogonal orientations were used, and the highest “activity” was associated with a large draining vein, the sagittal sinus. Thus, spatial specificity in the submillimeter domain of iso-orientation columns does not exist in T_2^* BOLD fMRI. Additional limitations on the accuracy of T_2^* BOLD fMRI was provided by multiple-site single-unit recordings and fMRI studies on the same animal. These studies suggested that the limit of spatial specificity of T_2^* BOLD may be in the 2 to 3 mm range for *single-condition maps* [136,137]. In this study, high-resolution T_2^* BOLD fMRI was performed together with single-unit recording at multiple sites. The BOLD response was found to be proportional to the spiking rate when data from all recording sites were averaged and compared with the BOLD response from the entire area where it was deemed statistically significant. However, this correlation started breaking down when smaller and smaller areas were considered for averaging of the two distinct measurements, in particular when the area started decreasing below approximately $4 \times 4 \text{ mm}^2$. This result is also in excellent agreement with the numbers provided for the accuracy of fMRI maps at 1.5 T of the human brain using a phase-encoding method [116] where the full width at half-maximum of the point spread function was estimated to be 3.5 mm.

Functional mapping with initial “dip”

In principle, it is possible to obtain functional images with better spatial specificity than perfusion if one can map the changes in cerebral oxygen consumption (CMRO_2). CMRO_2 increases must occur through increased activity of the mito-

chondria in the “activated” neurons, and the mitochondrial density is high in the synapse-rich regions, predominantly in the dendrites [138]. It might be possible to image CMRO₂ increases directly using the magnetic isotope of oxygen (¹⁷O) (e.g., [26,31,139] and references therein). CMRO₂ increases can also be mapped indirectly through its perturbations on the deoxyhemoglobin content. It has been shown that optical imaging of intrinsic signals in the cat and monkey visual cortex display a transient and small signal change ascribed to the deoxyhemoglobin increase before the onset a larger increase in blood flow [140–144]. In this explanation, it is the lag in blood flow response that provides the *temporal opportunity* to detect the deoxyhemoglobin increase. Optical imaging data also showed that this deoxyhemoglobin increase yielded better maps of iso-orientation or ocular dominance columns than the signals associated with the hyperoxygenated state. Deoxyhemoglobin increase, however, can only be colocalized with elevated CMRO₂ at early time points after the onset of CMRO₂ elevation. Even if subsequent blood flow enhancement did not occur and the only response detected was a deoxyhemoglobin increase, this deoxyhemoglobin increase will colocalize with enhanced neuronal activity initially, but later will propagate down the vasculature and appear in the venous system as discussed previously.

The transient deoxyhemoglobin increase would yield a negative signal change in a BOLD-weighted MR image. Such a “dip” has been observed in human fMRI experiments [97,145–150] and in animal models [134,135,151]. However, both in optical imaging and fMRI literature, observation of this “dip” has been controversial. The source of this controversy in the early human fMRI studies has been the failure of several laboratories to detect this effect in 1.5T studies. However, this is a small effect at low magnetic fields but was shown to increase substantially with magnetic field magnitude [97] to yield easily detectable signals at 7 Tesla. Recently, in intraoperative studies in the human brain, the functional maps obtained from this early “dip” were also detected and shown to colocalize with electrical recordings, whereas T_2^* BOLD maps did not [150].

In anesthetized animal models, this small dip has not been highly reproducible presumably because of the perturbations of anesthesia on the animal physiology. When observed, it was found to yield accurate maps at the iso-orientation columnar level [134,135]. However, this early negative response corresponding to deoxyhemoglobin increase is a very small effect. Furthermore, in order to obtain accurate maps from it one must restrict the observation window to early time points where the signals are even smaller. Thus, as a general high-resolution MR imaging approach, it suffers from low contrast-to-noise.

“Noise” in fMRI data and field dependence of fMRI contrast-to-noise ratio

It is well recognized that the standard deviation of image-to-image fluctuations in an fMRI series (σ_{fMRI}) is usually not dominated by the thermal noise (σ_{Therm}) [152–157] that determines the intrinsic SNR of individual MR images. Instead, physiological processes contribute to σ_{fMRI} so that σ_{fMRI} can be expressed as $(\sigma_{\text{Phys}}^2 + \sigma_{\text{Therm}}^2)^{1/2}$, ignoring the potential contributions from instrument instabilities.

These physiological processes include brain motion due to cardiac pulsation, magnetic field perturbations induced by alterations in lung volume, and temporal instabilities in blood flow, blood volume, erythrocyte density, and oxygen consumption caused by vascular events and/or spontaneous activities of neurons. These may be mediated through BOLD mechanisms, but other mechanisms unrelated to BOLD are possible. Usually, respiration-dependent contributions, and sometimes cardiac pulsation-induced instabilities, are suppressed by post-processing (e.g., [158,159] and references therein).

Recently, it has been postulated that the physiological component of the noise, σ_{Phys} , is linearly proportional to signal magnitude S [155–157], and this postulate was supported by experimental data obtained at 1.5 and 3 Tesla for GE-based BOLD fMRI. A linear dependence of σ_{Phys} on S is, of course, expected for physiological noise that is mediated through the BOLD mechanism; for example, as blood volume, blood flow, and/or deoxyhemoglobin concentration in blood fluctuates, so will the basal BOLD effect. In fact, shortly after the introduction of fMRI it was demonstrated that the largest signal fluctuations in a GE fMRI time series occurs in and around large blood vessels, and that this can even be used as a mask for selectively eliminating large vessel regions in functional images [152]. However, recent studies demonstrate that the physiological noise characteristics are somewhat different at 7 Tesla compared to 1.5 or 3 T for GE fMRI [98]. More interestingly, the noise in an HSE and GE fMRI time series at 7 Tesla also differ dramatically from each other [98]; this is highly significant since one of the major benefits of the high fields is high specificity functional mapping using HSE BOLD effect. The results, however, demonstrate that HSE fMRI not only provides gains in accuracy of the functional imaging signals but also substantial gains in contrast-to-noise ratio as well.

A linear dependence of σ_{Phys} on signal intensity S has important implications on the field dependence of CNR in functional imaging. CNR is equal to the activation-induced signal change in the fMRI time series (ΔS) divided by σ_{fMRI} . Given that the activation-induced changes in $1/T_2$ and $1/T_2^*$ are very small, ΔS can be approximated as ($S_0 e^{-TE \cdot R} (\Delta R \cdot TE)$) and CNR can thus be expressed as:

$$\text{CNR} = \Delta S / \sigma_{\text{fMRI}} = (S_0 e^{-TE \cdot R} (\Delta R \cdot TE)) / \sigma_{\text{fMRI}}, \quad (4)$$

where R is either R_2 or R_2^* (i.e., $1/T_2$ or $1/T_2^*$) for HSE or GE FMRI, respectively. The signal difference between the activated and the basal state is

$$S_{\text{activated}} - S_{\text{basal}} = S_0 (e^{-TE \cdot R_{\text{activated}}} - e^{-TE \cdot R_{\text{basal}}}) = S_0 e^{-TE \cdot R_{\text{activated}}} (1 - e^{-TE \cdot \Delta R}),$$

and for $TE \cdot \Delta R \ll 1$, one has the approximation $e^{-TE \cdot \Delta R} \approx 1 - TE \cdot \Delta R$. We drop subscript 2 on R , but it is implicit that we are talking about either R_2 or R_2^* depending on whether we are considering an HSE or a GE experiment. TE is the echo time, S_0 is the signal intensity at $TE = 0$, and Δ represents the stimulus induced changes. Note that $S_0 e^{-TE \cdot R}$ is simply signal intensity S after echo delay TE . For

the *extravascular* BOLD effect, ΔR is calculated from Eqs. (2) and (3), based on changes in fractional deoxyhemoglobin content in blood ($1 - Y$), blood volume, etc.

At the limit of very-high-resolution functional imaging, for example, for mapping columnar organizations, image SNR decreases and we operate in a domain where σ_{Therm} dominates over σ_{Phys} ; in this limit,

$$\text{CNR} = \Delta S / \sigma_{\text{Therm}} \propto \text{SNR}_{io} \cdot e^{-\text{TE} \cdot R} (\Delta R \cdot \text{TE}). \quad (5)$$

In (5) SNR_{io} is the signal-to-noise ratio in the image corresponding to $\text{TE} = 0$. As was discussed at the beginning of the chapter, based on theoretical considerations and experimental results, SNR_{io} increases linearly or even somewhat better than linearly with field magnitude. Based on this information and using Eqs. (2) and (3) for ΔR , the implications of (5) for large vessels and microvasculature can be easily deduced as a function of TE for the *extravascular* BOLD effect. When (5) is applicable, the *optimum* CNR is obtained for TE equal to T_2^* or T_2 for GE or HSE experiments, respectively, in which case, $e^{-\text{TE} \cdot R} = e^{-1}$. (Optimum TE is calculated simply by solving $\partial(\text{CNR})/\partial(\text{TE}) = 0$, where CNR is given by Eq. (5)). Brain tissue T_2 changes slowly with magnetic field (Table 1). Thus, provided we are not comparing extremely different field strengths such as 1.5 vs. 9.4 T, one can consider keeping TE the same. Certainly the T_2 difference between 4 and 7 T is small enough so the same TE can be used. For HSE fMRI at high fields, the large blood vessels do not contribute significantly and the functional signals originate predominately from the *extravascular* BOLD effect associated with microvasculature (Eq. (3)). Then CNR for HSE fMRI will increase as the cubed power of the magnetic field magnitude, providing an enormous advantage in going to higher fields.

The situation is different for GE fMRI since T_2^* decreases approximately linearly with magnetic field and both large and small vessels contribute. Operating under conditions of $\text{TE} = T_2^*$ means, then, that $\Delta R \cdot \text{TE}$ will be field independent for large blood vessels, and will increase as B_0 for microvasculature. Thus, under conditions where thermal noise dominates σ_{fMRI} , CNR will increase with magnetic field as SNR_{io} for large blood vessels and as $(B_0 \cdot \text{SNR}_{io})$ for microvasculature in the GE fMRI approach executed with optimal TE. Therefore, for high-resolution imaging, higher magnetic fields provide major advantages for CNR even when GE fMRI is the method of choice. Not only does CNR increase in a GE experiment, but the CNR for microvasculature increases much more rapidly compared to the undesirable large vessels.

If we are in the limit where σ_{Phys} is much greater than σ_{Therm} (i.e., $\sigma_{\text{fMRI}} \sim \sigma_{\text{Phys}}$) then predictions of field dependence require that we define σ_{Phys} better. For BOLD-based noise one can write

$$\sigma_{\text{Phys(BOLD)}} = c \cdot S \cdot \Delta R \cdot \text{TE}, \quad (6)$$

where c is a constant and S is the signal intensity [155]. For other non-BOLD sources, such as respiration and cardiac pulsation,

$$\sigma_{\text{Phys(non-BOLD)}} = c' \cdot S . \quad (7)$$

The resultant physiological noise is given by $\sigma_{\text{Phys}} = (\sigma_{\text{Phys(BOLD)}}^2 + \sigma_{\text{Phys(non-BOLD)}}^2)^{1/2}$ [155]. The CNR is calculated from Eq. (4) with the substitution of σ_{fMRI} with σ_{Phys} and remembering that $S = S_0 e^{-TE \cdot \Delta R}$. For simplicity, the predictions for cases where physiological noise is only BOLD mediated or only non-BOLD mediated can be considered.

If the fMRI noise is exclusively BOLD mediated, in the limit $\sigma_{\text{fMRI}} \sim \sigma_{\text{Phys}}$, CNR is just a constant, *independent* of field magnitude, ΔR , and TE for either the HSE or GE experiment. No need to buy high field magnets for functional images just to gain CNR in this case, although one can still argue a utility for high fields based on the accuracy of functional imaging signals. On the other hand, if the noise is purely of non-BOLD variety given by Eq. (7), then CNR will be proportional to $\Delta R \cdot TE$, predicting an increasing CNR at longer TE values. (One cannot conclude that TE can be increased indefinitely since at some TE the condition $\sigma_{\text{fMRI}} \sim \sigma_{\text{Phys}}$ that leads to this prediction will fail, and thermal noise will dominate. But as long as $\sigma_{\text{fMRI}} \sim \sigma_{\text{Phys}}$ remains valid, longer TEs will yield higher CNR if the source of σ_{Phys} is non-BOLD type given by Eq. (7).). For the same TE, CNR will increase linearly for large blood vessels and quadratically for the microvasculature in a GE study. For an HSE experiment, quadratic increase in CNR with magnetic field magnitude will be applicable, since the contribution is predominantly microvascular. If we again use $TE = T_2^*$ in the GE measurement so that we change the TE linearly with $1/B_0$, then CNR in a GE experiment will be field *independent* for *large* vessels, and increase linearly with field for voxels dominated by the microvasculature only.

Thus, when σ_{Phys} dominates, it is possible to be in a scenario where higher magnetic fields provide no gains in CNR in the context of the noise models considered so far. However, studies conducted at 7 Tesla demonstrated that fMRI “noise” in GE and HSE data are fundamentally different at this field strength, and that, unlike GE data, σ_{Phys} in 7 Tesla HSE fMRI was virtually independent of voxel volume and hence S (Figure 15) [98]. Note that independence from S rules out the explicit formulation of BOLD and non-BOLD mechanisms given by Eqs. (6) and (7). The data that has led to these conclusions on HSE are discussed in greater detail in the next few paragraphs.

At 1.5 and 3 T, the dependence of physiological noise on signal level S was examined by altering either the echo time and the flip angle [155,156] or voxel volume [157]. However, it is important to distinguish between the dependence of σ_{Phys} on S at a *constant* voxel volume versus changing S only through voxel volume while keeping other parameters constant. In the postulate that σ_{Phys} is proportional to voxel volume, the inherent claim is that there is spatial coherence in the temporal behavior of physiological fluctuations. If such a spatial coherence does not exist in the scale of the voxel volumes used, then S but not σ_{Phys} will depend on voxel size linearly, even though σ_{Phys} may display a linear dependence on S at a constant voxel size. Therefore, we examined voxel size dependence as well as dependence

on S at a constant voxel size at 7 Tesla [98]; the same data were evaluated at different voxel dimensions in the plane of the slice (while keeping the slice thickness constant) simply by discarding appropriate outer k -space points [98]. This meant that thermal noise contribution was not constant as in Hyde et al. [157] but was averaged with additional k -space data collected for higher resolution so that image SNR, S/σ_{Therm} , increased as the square root of voxel volume.

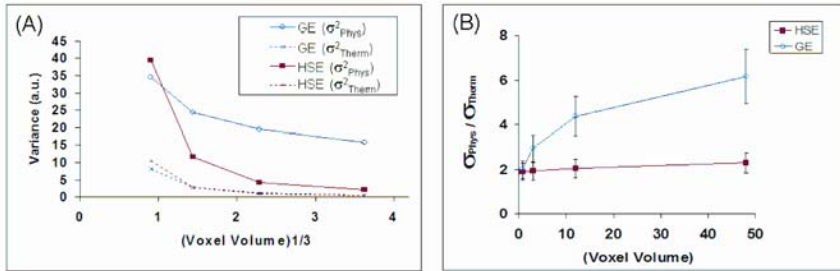


Figure 15. Noise characteristics of functional imaging data at 7 Tesla: (A) Plots depicting the variance of thermal noise (σ_{Therm}^2) and image-to-image fluctuations in the brain signals due to physiological processes (σ_{Phys}^2). Parameter σ_{Phys}^2 was calculated as the difference of the variance of temporal fluctuations of brain signals in the fMRI time series minus the variance of thermal noise. The data are for a single subject. In (B) the ratio of standard deviations ($\sigma_{\text{Phys}} / \sigma_{\text{Therm}}$) for all subjects for both GE (blue) and HSE (red). In (A), the data represent the average of all pixels in the brain of a single subject. In (B) the data represent the average over all subjects and all pixels. The error bars in (B) reflect the SD of the differences among the different subjects. In these plots, image signal intensities were normalized for the different resolutions so that effectively noise is decreasing as opposed to both signal and noise increasing as voxel size is increased. Reprinted with permission from E Yacoub, PF Van De Moortele, A Shmuel, K Ugurbil. 2005. Signal and noise characteristics of Hahn SE and GE BOLD fMRI at 7 T in humans. *Neuroimage* **24**(3):738–750. Copyright © 2005, Elsevier. See attached CD for color version.

In the 7T HSE data, proportionality between σ_{Phys} and S would have predicted that σ_{Phys}^2 plotted in Figure 11A remained constant with voxel size since S was normalized in that plot. This was not observed. Instead, when voxel size was altered, σ_{Phys}^2 decreased just like thermal noise, and the ratio of the standard deviation of the physiological noise to thermal noise ($\sigma_{\text{Phys}} / \sigma_{\text{Therm}}$) in the HSE fMRI time series remained relatively independent of voxel size (Figure 11B) for the voxel sizes covered in this study. Furthermore, at fixed voxel size there was a distribution of signal amplitude as expected, due to the surface coil sensitivity profile as well as the inhomogeneities of brain tissue. This provided the means by which temporal fluctuations of signal magnitude could be examined at a fixed voxel volume; when examined in this way, σ_{Phys} was also found to be independent of S [98].

Of course, one possible explanation for these observations is that thermal noise dominated the HSE fMRI data at all voxel volumes used in this study. However,

this was clearly not the case. Even at the highest resolution (i.e., smallest voxel size) used, $\sigma_{\text{Phys}} / \sigma_{\text{Therm}}$ was ~ 2 (Figure 11B), which is, in reality, a *lower limit* due to the possible presence of image artifacts outside the head contributing to the experimentally measured σ_{Therm} term because of the method of measurement used [98].

In the 7T HSE data, the source of the stimulus-induced signal changes are thought to be mainly microvasculature, and specifically the capillaries [30]. These blood vessels can also be the source of σ_{Phys} , for example, through fluctuations in the red blood cell content of capillaries that occur naturally or fluctuations in capillary volume. Temporal signal instabilities associated with capillaries, however, will not maintain any coherence over large distances; capillary effects will start averaging out due to the lack of coherence over distances larger than several-fold the intercapillary separation (~ 25 micrometers in the brain [117]), and will be significantly averaged in a typical voxel size attained even in a ultra high-resolution MR image.

When temporal signal fluctuations do not maintain coherence over space, then one must consider a voxel as a sum of many small volume elements with signal intensity s_i , where i is an index describing the individual subvoxel volume elements. Let us define $\underline{\sigma}_{\text{Phys}}(i)$ as describing the physiological noise of volume element i . The choice of size for the subvoxel volume element will affect the magnitude of $\underline{\sigma}_{\text{Phys}}(i)$ but ultimately, σ_{Phys} for the image voxel will be independent of this choice. If the fluctuations of the individual small volume element are not correlated with each other, and $\underline{\sigma}_{\text{Phys}}(i)$ is the same for all i , then for that imaging voxel,

$$\sigma_{\text{Phys}} = \left[\sum_{i=1}^N (\underline{\sigma}_{\text{Phys}}(i))^2 \right]^{1/2} = \sqrt{N} \cdot \underline{\sigma}_{\text{Phys}}(i)$$

(N is the number of small subvoxel volume elements in the voxel). Equations (6) and (7) can be applicable for $\underline{\sigma}_{\text{Phys}}(i)$ for the subvoxel volume element i . However, for the entire voxel, we can then surmise that $\sigma_{\text{Phys}} = \kappa \cdot S^{1/2} = \eta \cdot V^{1/2}$ where κ and η are constants. The constants η and κ will be TE independent for non-BOLD noise and will depend linearly on TE for BOLD physiological noise. Considering for simplicity either the BOLD or the non-BOLD noise by themselves (and *not* the sum of both), this leads to

$$\sigma_{\text{fMRI}}^2 / \sigma_{\text{Therm}}^2 = 1 + \sigma_{\text{Phys}}^2 / \sigma_{\text{Therm}}^2 = 1 + (\eta^2 \cdot V) / \sigma_{\text{Therm}}^2. \quad (8)$$

This equation would predict that parameters $\sigma_{\text{fMRI}}^2 / \sigma_{\text{Therm}}^2$, $\sigma_{\text{Phys}}^2 / \sigma_{\text{Therm}}^2$ or $\sigma_{\text{Phys}} / \sigma_{\text{Therm}}$ will all be constants as a function of voxel volume or signal intensity when σ_{Therm}^2 is proportional to V , as it was in our data because of the way we changed voxel volume. The HSE data (Figure 15B) are consistent with this model.

Thus, we concluded that HSE refocuses BOLD effects from *large* veins associated with physiological fluctuations, just as it refocuses task-induced signal changes associated with large vessels, and suppresses these effects [98]. The remaining physiological “noise” does not have spatial coherence over the voxel

scales used [98]. A corollary to this conclusion is that the *dominant* source of physiological noise in the commonly used GE BOLD fMRI are the large veins [98].

According to Eq. (8), σ_{fMRI} and CNR will be TE dependent if the noise is of BOLD type even though there is no dependence on S or voxel volume; this remains to be explored. However, since T_2 does not change rapidly with magnetic field magnitude, and somewhat similar TEs can be used, the TE dependence of physiological noise in this model will have little real significance for the field dependence of the CNR in the HSE fMRI experiment.

With respect to temporal signal fluctuations, the 7T GE data also do not *fully* fit into the postulate that image-to-image fluctuations are proportional to signal magnitude but it comes closer to it than the HSE data. The difference between the 7T and previously published 3T GE fMRI “noise” data is likely due to the heterogeneity of contributions to GE fMRI at 7 T, with detectable contributions to functional signals coming from both large vessels and the microvasculature. At lower field strengths, microvascular contributions are too small to be detectable, but they become significant contributors at 7 T as evidenced by the robust HSE-based functional images. Consequently, both the signal and image-to-image fluctuations can be expected to behave differently at 7 T versus much lower field strengths.

Perfusion imaging

Images of perfusion or perfusion changes associated with increased neuronal activity can be obtained using ASL techniques that utilize the water protons in the blood as an endogenous “transient” tag. These methods rely on either continuous (e.g., [160–162]) (or dynamic (i.e., modulated) versions of continuous [163,164]) or pulsed (e.g., [80,165,166]) tagging approaches. All of these techniques benefit from increased T_1 encountered in higher magnetic fields. This is expected to ameliorate errors introduced by transit delays, extend coverage over the brain and yield higher CNR, and specificity to tissue. Excellent perfusion images based on continuous arterial spin tagging have already been accomplished at 3 T [167], and this approach has also been used for functional mapping at 3 T [168].

The tissue specificity of ASL can improve at high magnetic fields because of the fact that tagged spins require a finite amount of time to reach the capillaries and exchange with tissue water. At shorter periods, larger blood vessels in the arterial side can dominate the measurement, confounding quantitation (e.g., [106]), and appearing as “activated” in perfusion-based functional images. In ASL measurements, generally the tag that can be detected in the veins subsequent to the tag’s passage through the capillaries is thought to be negligible and ignored, even though there has not been an experimental confirmation of this. At high fields this potential contribution should vanish due to the short T_2 of venous blood.

Diffusion-weighted imaging

This type of imaging is used either for tractography or clinically for determining the alterations with the overall diffusion properties of water subsequent to a pathological change such as stroke. This approach benefits from SNR gains of high

field. This gain is counteracted by the shortened T_2 with increasing magnetic fields (Table 1). However, since the decrease in T_2 is not strongly field dependent and SNR is elevated at least linearly, there are gains with higher magnetic fields, provided such gains are not lost in less than perfect hardware performance in the challenging environment of higher magnetic fields.

When diffusion is used for tractography to follow fiber bundles for obtaining information on connectivity, spatial resolution is of paramount importance. The main problem in tractography is the ambiguity generated when fibers cross each other. When crossing occurs within a voxel, it is no longer possible to identify uniquely which fiber coming into that voxel is associated with the fibers exiting the voxel. However, as spatial resolution is improved, the possibility of differentiating these fibers also improves.

Despite the potential of confounding problems that exist in tractography due to fiber crossing, remarkable fiber tracking has been possible in the human brain, reproducing connectivity maps that are expected based on invasive measurements on non-human primates. Most of these studies have so far been performed at 3 T as the highest magnetic field for humans and 9.4 T in animals. However, it is easy to predict that it will not be long before higher fields are used for this purpose in the human brain also.

6. PARALLEL IMAGING

High magnetic fields provide several advantages in human brain imaging as already discussed in detail. However, they also pose significant challenges in image acquisition, most notably with rapid imaging techniques, such as EPI or SPIRAL. Magnetic field inhomogeneities caused by the susceptibility differences between air filled cavities and tissue increase with higher magnetic fields. Consequently, images obtained with EPI or SPIRAL suffer from increased distortions or blurring, respectively, as well as signal loss due to the shorter T_2^* .

In many ultra high field studies to date, such as imaging of human brain function at 7 Tesla, the difficulties encountered in rapid imaging have been alleviated by restricting the image field of view (FOV) to a small local region along the phase encode direction [28,30], or by extensively segmenting the data acquisition. Both of these approaches have significant drawbacks; the first is unable to provide coverage over the entire or large portions of the sample, and the latter leads to long acquisition times and image artifacts. Another solution to the problems encountered with fast acquisitions at high magnetic fields is the use of recently introduced parallel imaging strategies based on multi-coil arrays [169,170]. This approach is potentially an attractive alternative because high fields are expected to improve parallel imaging performance due to the more complex sensitivity profiles of each coil element and the increased signal-to-noise ratio (SNR). This has been experimentally demonstrated recently in phantom studies using a phantom approximating the size of the human head. The electrical properties of solvent used in the phantom

was adjusted to mimic conditions corresponding to different magnetic fields even though the data were acquired at 7 Tesla ([20] and references therein).

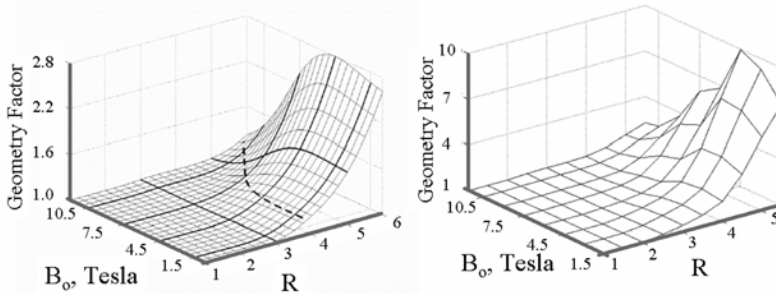


Figure 16. (A) Ultimate parallel imaging performance in terms of the geometry factor, calculated for a spherical object with a diameter of 20 cm, assuming average in-vivo brain permittivity and conductivity. The dashed line indicates the transition from favorable to prohibitive geometry factors, with the threshold set arbitrarily at $g = 1.2$. According to this analysis, high field is expected to facilitate enhanced parallel imaging performance. (B) Geometry factor as obtained experimentally for the center of the sphere, plotted vs. the reduction factor R and B_0 . Note the close correspondence between this plot and the theoretical prediction of the ultimate geometry factor (A). These results show that high field facilitates higher reduction factors, leading to higher parallel imaging performance. Reprinted with permission from [20].

Figure 16 illustrates both calculations and experimental data from this study [20]. The parallel imaging method employed was SENSE [170]; the geometry factor (g), which represents the degradation of the SNR as a result of the parallel imaging methodology is shown as a function of R , the reduction in the data collected, and magnetic field magnitude. The final SNR of an image acquired and reconstructed with the SENSE method is given as $SNR = (SNR_0 / g\sqrt{R})$ [170], where SNR_0 describes the SNR when all of the k -space data are acquired in the normal way; low g values are desirable, and a value of 1.2 would be typical of the acceptable range. The $g = 1.2$ contour is shown on the theoretical plot (Figure 16A). Both the experimental and simulation data show that as the field strength increases larger R values can be used while maintaining the same g value.

7. IMAGING USING LOW-GYROMAGNETIC NUCLEI

Low-gyromagnetic nuclei can in principle be used to obtain unique biological information. Molecules containing phosphorus, oxygen, and carbon (with magnetic isotopes — ^{31}P , ^{17}O , and ^{13}C) all appear in abundance within cells. Ions such as sodium and potassium (with magnetic isotopes ^{23}Na and ^{39}K) are critical in cellular

function. However, these low gyromagnetic nuclei suffer from limitation in sensitivity. The inherent MR sensitivity for detection of these nuclei is low because of their small magnetic moments. In addition, their abundance in the cells as a single chemical species (i.e., with one chemical shift) is also low. Therefore, sensitivity gains that can be realized with increasing magnetic fields become critically important for these nuclei.

At high frequencies attained by protons at magnetic fields like 7 or 9.4 Tesla, signal-to-noise ratio dependence on magnetic field becomes complex and approximately linearly dependent on magnetic field magnitude. However, for low frequencies or for non-conductive samples, the magnetic field dependence of SNR can be close to quadratic [7,9]. Motivated by the SNR gains expected from the availability of high field magnets, in recent years, we have examined the possibility of using ^{17}O for monitoring oxidative metabolism in intact animals and ultimately humans at 7 and 9.4 T at resonance frequencies of 40 and 54 MHz, respectively.

Oxygen 17 imaging

^{17}O spin is the only stable oxygen isotope having a magnetic moment that can be detected by the NMR approach. It has a spin quantum number ($I = 5/2$) greater than $1/2$ and possesses an electric quadrupole moment. This is the dominant source of T_1 and T_2 relaxation [171] for this nuclei. With respect to relaxation, the extreme narrowing limit (i.e., $\tau_c\omega \ll 1$, where τ_c is the rotational correlation time and ω is Larmor frequency in radians/sec) is applicable for the “free” water molecule. In this limit, T_1 and T_2 can be estimated by using the equation

$$\frac{1}{T_2} \cong \frac{1}{T_1} = \frac{3}{40} \left(\frac{2I+3}{I^2(2I-1)} \right) \left(1 + \frac{\eta^2}{3} \right) \left(\frac{\pi e^2 Qq}{h} \right)^2 \tau_c,$$

where the term of $(\pi e^2 Qq/h)$ is the quadrupolar coupling constant and equals to 6.7 MHz (or 4.21×10^7 radian/s) for the ^{17}O nucleus, and η is an asymmetry parameter ($0 \leq \eta \leq 1$) [171].

Because both η and τ_c are independent of the magnetic field strength, T_1 and T_2 (or T_2^*) for the ^{17}O spins should be field independent. If the τ_c value of 8.5×10^{-12} s is used for bulk water at 298 K [172], then estimated T_2 and T_1 should be between 2.8 ms (for $\eta = 0$) and 2.1 ms (for $\eta = 1$). The actual ^{17}O T_2 value should be smaller than the ^{17}O T_1 value due to the significant contributions of the ^{17}O - ^1H scalar coupling and the proton chemical exchange to the ^{17}O T_2 relaxation processes [173]. Consistent with these expectations, in experiments conducted at 4.7 and 9.4 Tesla, the ^{17}O relaxation times in water were found to be short, similar, and field independent for the rat brain ($T_2 = 3.03 \pm 0.08$ ms, and $T_1 = 4.47 \pm 0.14$ ms at 4.7 Tesla; $T_2 = 3.03 \pm 0.09$ ms, and $T_1 = 4.84 \pm 0.18$ ms at 9.4 Tesla), as well as for the saline solution at room temperature ($T_2 = 4.28 \pm 0.08$ ms, and $T_1 = 6.59 \pm 0.10$ ms at 4.7 Tesla; and $T_2 = 4.09 \pm 0.06$ ms, and $T_1 = 6.52 \pm 0.12$ ms at 9.4 Tesla) [26].

The ^{17}O NMR sensitivity was evaluated at 9.4 and 4.7 Tesla in the rat brain and a saline solution [26]. A consistent SNR gain of ~fourfold was observed at 9.4 Tesla as compared to 4.7 Tesla, indicating an approximate theoretical maximum power dependence of SNR on B_0 . These experimental results demonstrate the significant advantage provided by high field strength for direct detection of ^{17}O NMR signal. This trend for increasing ^{17}O NMR sensitivity is expected to hold beyond 9.4 Tesla.

With the dramatic sensitivity gains realized at 9.4 Tesla, it is possible to obtain 3D ^{17}O imaging and utilize it for calculation of oxygen consumption rates. This was shown to be feasible in the anesthetized rat at 9.4 Tesla [31]. The averaged CMRO_2 and CBF values in the rat brain from seven ^{17}O measurements (five rats) were measured to be $2.19 \pm 0.14 \mu\text{mol/g/min}$ and $0.53 \pm 0.07 \text{ ml/g/min}$, respectively, under conditions of α -chloralose anesthesia [31]. This is in excellent agreement with what can be calculated from an autoradiographic measurement [174] of cerebral metabolic rate of glucose (CMR_{glc}) ($\sim 0.37 \mu\text{mole/g/min}$) using the $\text{CMRO}_2/\text{CMR}_{\text{glc}}$ ratio of 5.5–6.0 [175]. In this autoradiographic study, both the anesthesia conditions and the CBF attained were similar to that in our own ^{17}O studies.

The CMRO_2 measurements described in this chapter involve two invasive procedures, one for determining $C_a(t)$ by means of an implanted ^{17}O RF coil, and the second for measuring CBF by an intraarterial catheter and bolus injection of H_2^{17}O . The CBF measurement can be performed noninvasively using the arterial spin tagging MR approaches. The use of the implanted RF coil, however, is not suitable for routine measurements of CMRO_2 or for human applications. Therefore, it is important to further explore the feasibility of the ^{17}O NMR approach for reliably imaging CMRO_2 without resorting to invasive $C_a(t)$ and/or CBF measurements. Recently, we have demonstrated the feasibility for imaging CMRO_2 in the rat brain using simplified models that only require noninvasive measurements of the cerebral H_2^{17}O concentration (i.e., $C_0(t)$) [176]. This work opens up the possibility of establishing a completely noninvasive ^{17}O NMR approach for CMRO_2 imaging. However, this possibility needs further validation under different physiological conditions and in different species.

The success of high-field ^{17}O NMR for imaging CMRO_2 in the human brain again relies on the ^{17}O NMR sensitivity gains with high magnetic fields. Recently, we have studied in-vivo NMR sensitivity for acquiring 3D ^{17}O images of natural abundance H_2^{17}O in the human visual cortex at 7 Tesla with a temporal resolution of 8.5 seconds and a voxel size of 6.6 ml. Figure 17 demonstrates the results obtained from a representative subject showing one coronal ^{17}O CSI of natural abundance H_2^{17}O (extracted from 3D ^{17}O CSI dataset). The CSI plane was located in the human visual cortex. Figure 17B displays a representative ^{17}O spectrum from one central voxel showing excellent SNR ($\approx 60:1$). This SNR is better than that obtained from rat brains at 9.4 Tesla ($\sim 40:1$) albeit with a smaller absolute voxel size but not relative to the size of brain [26,31]. Furthermore, the dynamic concentration change of metabolic H_2^{17}O during an $^{17}\text{O}_2$ inhalation is expected to be similar between the awake human brain and the rat brain anesthetized with α -chloralose be-

cause of the similar values for both CMRO_2 ($2.2 \mu\text{mol/g/min}$ in the anesthetized rat brain versus $1.7 \mu\text{mol/g/min}$ in the awake human visual cortex) and CBF (0.53 ml/g/min in the anesthetized rat brain versus 0.54 ml/g/min in the awake human visual cortex) [31,93]. This comparison indicates that the conditions in the rat brain in our studies and the awake human brain are similar relative to the parameters that impact determination of CMRO_2 from the ^{17}O data. Thus, it can be concluded that it will be possible to achieve 3D imaging of CMRO_2 in the human brain at 7 Tesla or greater magnetic fields. Realization and utilization of this potential could have an important impact on studying bioenergetics in the human brain.

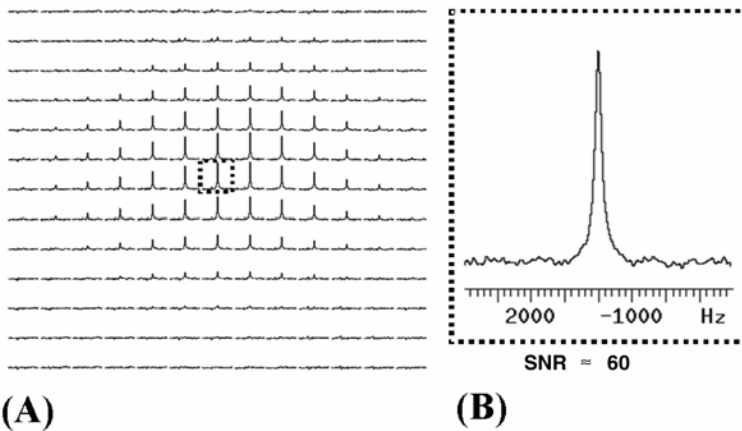


Figure 17. Direct detection of natural abundance ^{17}O in the human visual cortex at 7 Tesla. (A) ^{17}O chemical shift imaging of natural abundance H_2^{17}O in the coronal orientation acquired from the human visual cortex. (B) A representative ^{17}O spectrum from one central voxel as shown in (A). 8.5 sec of image acquisition time and 6.6 ml voxel size.

8. SPECTROSCOPY AT HIGH MAGNETIC FIELDS

Spectroscopy studies with biologically significant nuclei such as ^{31}P , ^{13}C , and ^1H benefit significantly from improved SNR and chemical resolution due to chemical shift and spectral simplifications of coupled spin systems.

In ^1H spectra obtained from the human brain, glutamate is resolved from glutamine partially at 4 T [177] but not at 1.5 T; these resonances are fully resolved at 9.4 Tesla [178]. For coupled spins, this resolution enhancement is attained even when the linewidths increase linearly with the magnetic field. This is because often the individual resonances of a multiplet are not resolved fully from each other in vivo. Consequently, what is critical is the resolution of the entire multiplet from

other multiplets. Even when the linewidths increase linearly with magnetic field, the effective width of the multiplet does *not* increase linearly since the splitting in the multiplet is due to field-independent J -coupling. The resolution gained in this fashion is illustrated in Figure 18 using simulation of glutamate and glutamine. The resonances of these metabolites are unresolvable at 1.5 T. However, even when the linewidth is scaled linearly with the magnetic field, the two metabolites can be distinguished at higher magnetic fields, especially at 7 and 9.4 Tesla, using the 2.4 ppm multiplets. The results for sensitivity and resolution gain are shown for human brain at 7 Tesla in Figure 19.

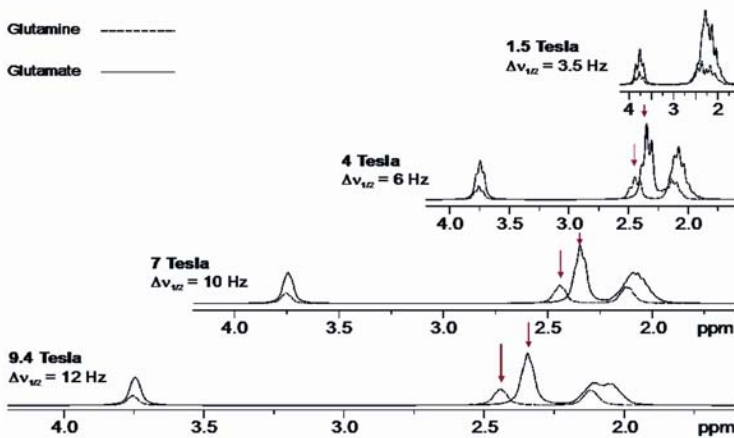


Figure 18. Simulated ^1H spectrum of glutamate and glutamine at four different field strengths assuming that the linewidths increase linearly with the magnetic field magnitude. Adapted with permission from [179]. See attached CD for color version.

An excellent example of the resolution afforded by high fields in ^1H spectroscopy is the detection of 5.23-ppm resonance of α -glucose at 4 T (and higher fields) despite its proximity to H_2O [178,179]. This resonance provided for the first time the ability to measure cerebral glucose quantitatively by ^1H MRS without complications from overlapping resonances. All previous ^1H MRS studies focused on detection of glucose (e.g., [180,182]) have relied on quantifying the 3.4-ppm peak of glucose. However, this region of the in-vivo proton spectrum suffers from an abundance of overlapping contributions. As such, the 3.4-ppm resonance cannot and should not be quantitatively used for measuring absolute glucose content in the human brain. The 5.23-ppm peak of glucose, on the other hand, is isolated and does not suffer from overlap. However, this resonance is too close to the very large H_2O peak to be detectable at the lower field strength because selective suppression of the latter without affecting the former is difficult at the lower magnetic fields. The increased chemical shift resolution at 4 T or higher fields, however, permits

selective suppression of the H₂O resonance and detection of the 5.23-ppm ¹H α-glucose peak.

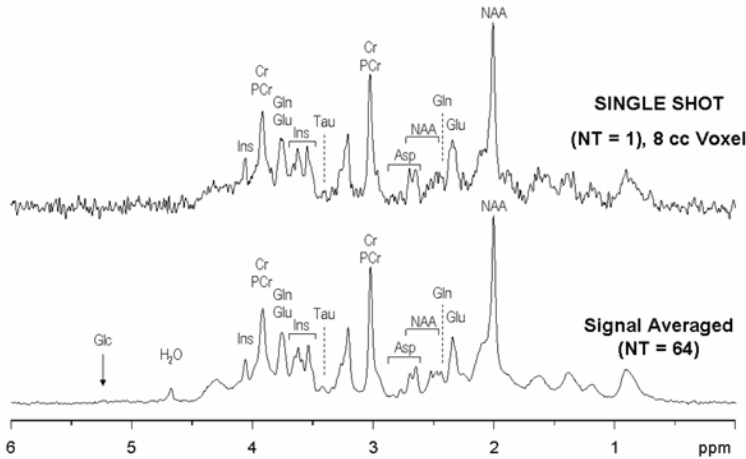


Figure 19. ¹H NMR spectrum of the human brain at 7 T acquired over the occipital lobe, largely over gray matter, using STEAM (TE = 6 ms, TR = 5 s, VOI = 8 ml) for single shot ($N=1$) and for 64 averages. Adapted with permission from [179].

³¹P NMR studies have been used both in animal models and in human studies to examine tissue bioenergetics, including the bioenergetics of increased neuronal activity. These studies have so far relied on detection of adenosine triphosphate (ATP), inorganic phosphate (Pi), and phosphocreatine (PCr). Figure 20 demonstrates ³¹P spectra from the human brain at 7 Tesla and the direct measurement of ATP and phosphocreatine (PCr) synthesis rate from the human brain using saturation transfer [27,183]. Especially, the ATP synthesis rate is a noteworthy accomplishment since it requires detection of Pi which is low in concentration. Furthermore, the Pi region of the spectrum contains very large and broad resonances at low magnetic fields, likely originating from large molecular assemblies such as membranes. These resonances largely obscure the detection of Pi. However, at the higher magnetic field, these resonances are undetected because their linewidths become too large. The SNR and chemical shift resolution available in these human brain 7 T spectra have not been attainable at lower fields, and the saturation transfer experiments shown here were only feasible in animal or isolated perfused organ models. The ATP synthesis rate measured here was assigned to oxidative ATP synthesis in neurons [183].

Spatially localized ¹³C MRS has been employed to measure aspects of brain function and neurotransmission directly. Recent efforts have focused on understanding the coupling between cellular bioenergetics and neuronal activity (e.g., [184-191]). If ¹³C-enriched glucose is given to a living organism, the ¹³C label is

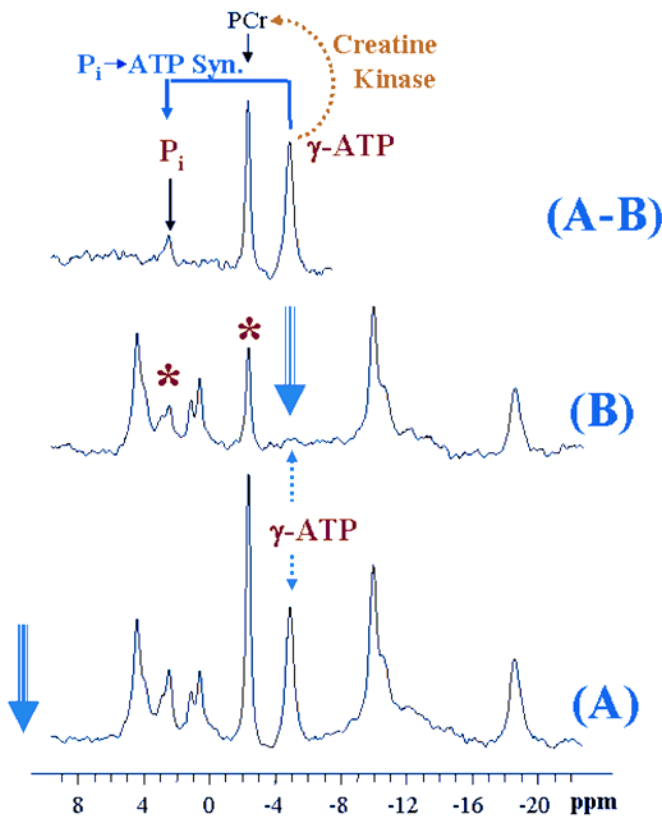


Figure 20. Direct measurement of neuronal ATP synthesis rate in the normal human brain at 7 Tesla. ^{31}P spectra were acquired with (A) and without (B) complete saturation of the γ -ATP resonance ($t_{\text{sat}} = 6.62$ s); the arrows indicate the position of saturation in the two spectra. The difference of the two spectra (A–B) illustrates that there is transfer of saturation to phosphocreatine (PCr) as a result of the creatine kinase reaction and to inorganic phosphate (Pi) due to ATP synthesis. The latter is thought to represent neuronal oxidative ATP synthesis rate. Reprinted with permission from [183]. See attached CD for color version.

incorporated through metabolism into several positions in many different metabolites. Of interest is the incorporation of label into the intermediates of the tricarboxylic acid (TCA) cycle, which generates reducing equivalents utilized in oxygen consumption. The label is then transferred into the amino acids glutamate, aspartate and glutamine. The ability to monitor the labeling of intracellular compounds in intact cells was first demonstrated using *E. coli* [192]. Today, such highly specific data can be obtained in human and animal brains from relatively small volume

elements. Figure 21 illustrates 9.4 Tesla spectra from the rat brain, before and after infusion of ^{13}C -labeled glucose.

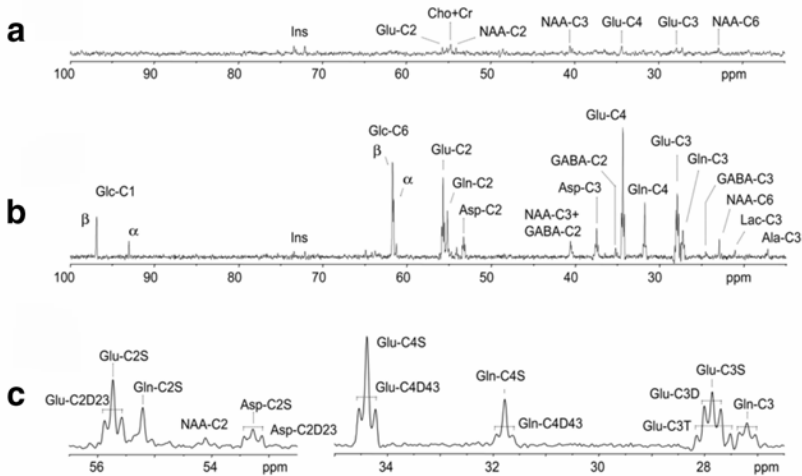


Figure 21. In-vivo ^{13}C spectra from a 400- μl volume in the rat brain, acquired using the modified DEPT sequence. (a) Natural abundance spectrum acquired for 3.5 hours (5120 scans, TR 2.5 s); (b) spectrum recorded for 1.8 hour (2560 scans, TR 2.5 s) during an infusion of 70%-enriched $[1,6\text{-}^{13}\text{C}_2]\text{glucose}$. Acquisition was started 1.8 hour after the beginning of glucose infusion; (c) expansion of (b) showing the detection of doubly labeled isotopomers of glutamate, glutamine and aspartate. Note the triplet of glutamate (Glu-C3T) at 27.9 ppm, corresponding to glutamate labeled simultaneously at the C2, C3 and C4 positions. Processing consisted of zero-filling, filtering (5-Hz Lorentzian line broadening for (a) and 2-Hz Lorentzian-to-Gaussian resolution enhancement for (b) and (c)), and fast Fourier transform. No baseline correction was applied. Reprinted with permission from [199].

In the human brain, ^{13}C spectra acquired at 4 Tesla in our laboratory illustrated detection of many labeled compounds from a relatively small, localized region in the visual cortex. These early studies led to the first measurement of the glutamatergic neurotransmission rate [189], which was performed in the human visual cortex. A subsequent effort on humans at 2.1 Tesla [190] was able to report basically the same results, but used at least threefold larger volumes (144 vs. 45 ml) and longer data acquisition times for signal detection due to the lower field employed.

In these studies, it is possible to extract information from the compartmentalized metabolic pathways. Most important is the glutamate–glutamine cycling between the glia and neurons, the two major cell types that are present in the brain: glutamate is the major excitatory neurotransmitter. Once it is released into the synaptic cleft and binds the postsynaptic receptors during neurotransmission, it is scavenged rapidly by nearby glial processes [193,194]. Glutamate is then con-

verted to glutamine by glutamine synthase, which is present only in the glia [195]; glutamine is subsequently transported to the neurons, and converted to glutamate to replenish vesicular glutamate. Thus, glutamine labeling in ^{13}C experiments can in principle occur predominantly through glutamate release through neurotransmission and hence reflect the kinetics of neurotransmission. Therefore, from such ^{13}C studies it is possible to calculate rates of glutamatergic neurotransmission, TCA cycle turnover, cerebral oxidative glucose utilization (CMR_{glc}), and even break down the latter into glial and neuronal contributions.

The most important finding from our studies on metabolism rates using ^{13}C MR was the conclusion that the neurotransmission rate equals $\sim 60\%$ of the total oxidative glucose consumption rate in the awake human brain and that there is significant oxidative ATP production rate in the glia, apparently in contradiction with earlier conclusions reached from experiments on the anesthetized rat brain data [196].

Such detailed studies have not yet been applied to investigate neuronal *activation* in the human or animal brains due to limitations in signal-to-noise ratio of the measurements. However, a subset of the information available in the direct ^{13}C measurements can be acquired with indirect detection with higher sensitivity using the protons attached to the ^{13}C nuclei. From this limited set it is possible to calculate changes in TCA cycle turnover and oxidative CMR_{glc} during neuronal activation. Such an experiment was performed at 4 T using hemifield visual stimulation. Spectroscopic data during ^{13}C infusion was used to obtain metabolic data in one hemisphere while the other hemisphere served as a control [184]. Hemifield visual stimulation selectively activates the primary visual cortex of the contralateral hemisphere, and thus approximately half the primary visual cortex volume that normally would be engaged during full-field stimulation. Spectra were acquired from two volumes positioned so that only one of the two covered the “activated” region within one hemisphere while the other covered the analogous but non-activated region within the other hemisphere. These data put an upper limit on the increase in CMRO_2 of 30% as opposed to larger increases in CBF, supporting the concept that CMRO_2 is not stoichiometrically coupled to increases in CBF and CMR_{glc} .

This measurement of stimulus-invoked CMRO_2 change is significant because of the controversy surrounding the coupling of oxidative metabolism and neuronal activity. It is well known that under resting conditions the cerebral metabolic rate of glucose consumption is coupled to CMRO_2 as well as to cerebral blood flow in the human brain ([175] and references therein), and glucose metabolism is almost completely through oxidation. However, this appears not to be the case during increased neuronal activity. Based on PET studies, stimulus-induced increases in CMRO_2 (0–5%) were found to be much less than the elevation in CBF and CMR_{glc} (40–51%) during visual and somatosensory stimulations [93,197]. This early PET result remains to this day highly debated, with the intensity of debate having increased recently in view of its significance in understanding the BOLD response that has come to play such a prominent role in neuroscience research. The difficulties and complexities associated with PET measurement of CMRO_2 have also led

to skepticism about the validity of the data that generated this controversial idea. The spectroscopic data support the concept that during increased neuronal activity the fractional increase in CBF significantly exceeds the fractional increase in CMRO_2 and by implication CMR_{glc} , which appears to track the changes in CBF.

9. CONCLUSION

Very high magnetic fields (4 Tesla and above) have been used in human biomedical research only recently and in only a few groups. The results so far suggest that while indeed technical challenges increase substantially, they can be overcome, and significant gains can consequently be realized in many applications, ranging from proton imaging to spectroscopy.

10. ACKNOWLEDGMENTS

The work reported here from the Center for Magnetic Resonance Research, University of Minnesota, was supported by the National Research Resources (NCR) division of NIH, grant P41 RR08079, the MIND Institute, and the Keck Foundation.

11. REFERENCES

1. Ogawa S, Tank DW, Menon R, Ellermann JM, Kim SG, Merkle H, Ugurbil K. 1992. Intrinsic signal changes accompanying sensory stimulation: functional brain mapping with magnetic resonance imaging. *Proc Natl Acad Sci USA* **89**(13):5951–5955.
2. Kwong KK, Belliveau JW, Chesler DA, Goldberg IE, Weisskoff RM, Poncelet BP, Kennedy DN, Hoppel BE, Cohen MS, Turner R, et al. 1992. Dynamic magnetic resonance imaging of human brain activity during primary sensory stimulation. *Proc Natl Acad Sci USA* **89**(12):5675–5679.
3. Ogawa S, Menon RS, Tank DW, Kim S-G, Merkle H, Ellermann JM, Ugurbil K. 1993. Functional brain mapping by blood oxygenation level-dependent contrast magnetic resonance imaging. *Biophys J* **64**:800–812.
4. Fujita N. 2001. Extravascular contribution of blood oxygenation level-dependent signal changes: a numerical analysis based on a vascular network model. *Magn Reson Med* **46**(4):723–734.
5. Boxerman JL, Hamberg LM, Rosen BR, Weisskoff RM. 1995. MR contrast due to intravascular magnetic susceptibility perturbations. *Magn Reson Med* **34**:555–556.
6. Kennan RP, Zhong J, Gore JC. 1994. Intravascular susceptibility contrast mechanisms in tissue. *Magn Reson Med* **31**:9–31.
7. Hoult DI, Richards RE. 1976. The signal-to-noise ratio of the nuclear magnetic resonance phenomenon. *J Magn Reson* **24**(71):71–85.
8. Hoult DI, Lauterbur PC. 1979. The sensitivity of the zeugmatographic experiment involving human samples. *J Magn Reson* **34**:425–433.

9. Wen H, Chesnick AS, Balaban RS. 1994. The design and test of a new volume coil for high field imaging. *Magn Reson Med* **32**:492–498.
10. Hoult DI. 2000. Sensitivity and power deposition in a high-field imaging experiment. *J Magn Reson Imag* **12**(1):46–67.
11. Keltner JR, Carlson JW, Roos MS, Wong STS, Wong TL, Budinger TF. 1991. Electromagnetic fields of surface coil in vivo NMR at high frequencies. *Magn Reson Med* **22**:46–480.
12. Vesselle H, Collin RE. 1995. The signal-to-noise ratio of nuclear magnetic resonance surface coils and application to lossy dielectric cylinder model, part II: the case of cylindrical window studies. *IEEE Trans Biomed Eng* **42**(5):507–520.
13. Vesselle H, Collin RE. 1995. The signal-to-noise ratio of nuclear magnetic resonance surface coils and application to lossy dielectric cylinder model, part I: theory. *IEEE Trans Biomed Eng* **42**(5):497–505.
14. Gati JS, Menon RS, Ugurbil K, Rutt BK. 1997. Experimental determination of the BOLD field strength dependence in vessels and tissue. *Magn Reson Med* **38**(2):296–302.
15. Vaughan JT, Garwood M, Collins CM, Liu W, DelaBarre L, Adriany G, Andersen P, Merkle H, Goebel R, Smith MB, Ugurbil K. 2001. 7T vs. 4T: RF power, homogeneity, and signal-to-noise comparison in head images. *Magn Reson Med* **46**(1):24–30.
16. Yang QX, Wang J, Collins CM, Smith MB, Zhang X, Ugurbil K, Chen W. 2004. Phantom design method for high-field MRI human systems. *Magn Reson Med* **52**(5):1016–1020.
17. Wang J, Yang QX, Zhang X, Collins CM, Smith MB, Zhu XH, Adriany G, Ugurbil K, Chen W. 2002. Polarization of the RF field in a human head at high field: a study with a quadrature surface coil at 7.0 T. *Magn Reson Med* **48**(2):362–369.
18. Yang QX, Wang J, Zhang X, Collins CM, Smith MB, Liu H, Zhu XH, Vaughan JT, Ugurbil K, Chen W. 2002. Analysis of wave behavior in lossy dielectric samples at high field. *Magn Reson Med* **47**(5):982–989.
19. Collins CM, Yang QX, Wang JH, Zhang X, Liu H, Michaeli S, Zhu XH, Adriany G, Vaughan JT, Anderson P, Merkle H, Ugurbil K, Smith MB, Chen W. 2002. Different excitation and reception distributions with a single-loop transmit-receive surface coil near a head-sized spherical phantom at 300 MHz. *Magn Reson Med* **47**(5):1026–1028.
20. Wiesinger F, Van de Moortele PF, Adriany G, De Zanche N, Ugurbil K, Pruessmann KP. 2004. Parallel imaging performance as a function of field strength: an experimental investigation using electrodynamic scaling. *Magn Reson Med* **52**(5):953–964.
21. Adriany G, Van de Moortele PF, Wiesinger F, Moeller S, Strupp JP, Andersen P, Snyder C, Zhang X, Chen W, Pruessmann KP, Boesiger P, Vaughan T, Ugurbil K. 2005. Transmit and receive transmission line arrays for 7 Tesla parallel imaging. *Magn Reson Med* **53**(2):434–445.
22. Glover GH, Hayes CE, Pelc NJ, Edelstein WA, Mueller OM, Hart HR, Hardy CJ, O'Donnell M, Barber WD. 1985. Comparison of linear and circular polarization for magnetic resonance imaging. *J Magn Reson* **64**:255.
23. Hoult DI. 2000. The principle of reciprocity in signal strength calculations: a mathematical guide. *Conc Magn Reson* **12**(4):173–187.
24. Van de Moortele P-F, Akgun C, Adriany G, Moeller S, Ritter J, Collin C, Smith MB, Vaughan JT, Ugurbil K. 2005. B₁ destructive to interferences and spatial phase patterns at 7 T with head transceiver array coil. *Magn Reson Med* **54**(6):1503–1518.

25. Van de Moortele P-F, Adriany G, Akgun C, Moeller S, Ritter J, Vaughan JT, Ugurbil K. 2005. B_1 phase spatial patterns at 7 Tesla: impact on B_1 inhomogeneities with a head transceive transmission line array coil. *Proc Int Soc Magn Reson Med* **13**:2748.
26. Zhu XH, Merkle H, Kwag JH, Ugurbil K, Chen W. 2001. ^{17}O relaxation time and NMR sensitivity of cerebral water and their field dependence. *Magn Reson Med* **45**(4):543–549.
27. Lei H, Zhu XH, Zhang XL, Ugurbil K, Chen W. 2003. In vivo ^{31}P magnetic resonance spectroscopy of human brain at 7 T: an initial experience. *Magn Reson Med* **49**(2):199–205.
28. Pfeuffer J, van de Moortele PF, Yacoub E, Shmuel A, Adriany G, Andersen P, Merkle H, Garwood M, Ugurbil K, Hu X. 2002. Zoomed functional imaging in the human brain at 7 Tesla with simultaneous high spatial and high temporal resolution. *Neuroimage* **17**(1):272–286.
29. Pfeuffer J, Adriany G, Shmuel A, Yacoub E, Van De Moortele PF, Hu X, Ugurbil K. 2002. Perfusion-based high-resolution functional imaging in the human brain at 7 Tesla. *Magn Reson Med* **47**(5):903–911.
30. Yacoub E, Duong TQ, Van De Moortele PF, Lindquist M, Adriany G, Kim SG, Ugurbil K, Hu X. 2003. Spin-echo fMRI in humans using high spatial resolutions and high magnetic fields. *Magn Reson Med* **49**(4):655–664.
31. Zhu XH, Zhang Y, Tian RX, Lei H, Zhang N, Zhang X, Merkle H, Ugurbil K, Chen W. 2002. Development of (^{17}O) NMR approach for fast imaging of cerebral metabolic rate of oxygen in rat brain at high field. *Proc Natl Acad Sci USA* **99**(20):13194–13199.
32. Robitaille PML, Abduljalil AM, Kangarlu A, Zhang X, Yu Y, Burgess R, Bair S, Noa P, Yang L, Zhu H, Palmer B, Jiang Z, Chakeres DM, Spigos D. 1998. Human magnetic resonance imaging at 8 T [see comments]. *NMR Biomed* **11**(6):263–265.
33. Robitaille PML. 1999. Black body and transverse electromagnetic resonators operating at 340 MHz: volume RF coils for ultra high field MRI. *J Comput Assist Tomogr* **23**(6):879–890.
34. Ibrahim TS, Lee R, Robitaille PML. 2001. Effect of RF excitation on field inhomogeneity at ultra high fields: a field optimized TEM resonator. *Magn Reson Imag* **19**:1339–1347.
35. Kangarlu A, Baertlein BA, Lee R, Ibrahim T, Yang L, Abduljalil AM, Robitaille PML. 1999. Dielectric resonance phenomena in ultra high field MRI. *J Comput Assist Tomogr* **23**(6):821–831.
36. Zhang X, Ugurbil K, Chen W. 2003. A microstrip transmission line volume coil for human head MR imaging at 4T. *J Magn Reson* **161**(2):242–251.
37. Vaughan JT, Adriany G, Snyder CJ, Tian J, Thiel T, Bolinger L, Liu H, DelaBarre L, Ugurbil K. 2004. Efficient high-frequency body coil for high-field MRI. *Magn Reson Med* **52**(4):851–859.
38. Ugurbil K, Garwood M, Ellermann J, Hendrich K, Hinke R, Hu X, Kim SG, Menon R, Merkle H, Ogawa S, et al. 1993. Imaging at high magnetic fields: initial experiences at 4 T. *Magn Reson Q* **9**(4):259–277.
39. Pan JW, Vaughan JT, Kuzniecky RI, Pohost GM, Hetherington HP. 1995. High resolution neuroimaging at 4.1T. *Magn Reson Imag* **13**(7):915–921.
40. Abduljalil AM, Kangarlu A, Zhang X, Burgess RE, Robitaille PML. 1999. Acquisition of human multislice MR images at 8 Tesla. *J Comput Assist Tomogr* **23**(3):335–340.
41. Burgess RE, Yu Y, Abduljalil AM, Kangarlu A, Robitaille PML. 1999. High signal-to-noise FLASH imaging at 8 Tesla. *Magn Reson Imag* **17**(8):1099–1103.

42. Burgess RE, Yu Y, Christoforidis GA, Bourekas EC, Chakeres DW, Spigos D, Kangarlu A, Abduljalil AM, Robitaille PML. 1999. Human leptomeningeal and cortical vascular anatomy of the cerebral cortex at 8 Tesla. *J Comput Assist Tomogr* **23**(6):850–856.
43. Christoforidis GA, Bourekas EC, Baujan M, Abduljalil AM, Kangarlu A, Spigos DG, Chakeres DW, Robitaille PML. 1999. High resolution MRI of the deep brain vascular anatomy at 8 Tesla: susceptibility-based enhancement of the venous structures. *J Comput Assist Tomogr* **23**(6):857–866.
44. Robitaille PML, Abduljalil AM, Kangarlu A. 2000. Ultra high resolution imaging of the human head at 8 tesla: 2K x 2K for Y2K. *J Comput Assist Tomogr* **24**(1):2–8.
45. Kangarlu A, Abduljalil AM, Robitaille PML. 1999. T_1 - and T_2 -weighted imaging at 8 Tesla. *J Comput Assist Tomogr* **23**(6):875–878.
46. Bourekas EC, Christoforidis GA, Abduljalil AM, Kangarlu A, Chakeres DW, Spigos DG, Robitaille PML. 1999. High resolution MRI of the deep gray nuclei at 8 Tesla. *J Comput Assist Tomogr* **23**(6):867–874.
47. Christoforidis GA, Bourekas EC, Baujan M, Abduljalil AM, Kangarlu A, Spigos DG, Chakeres DW, Robitaille PML. 1999. High resolution MRI of the deep brain vascular anatomy at 8 Tesla: susceptibility-based enhancement of the venous structures. *J Comput Assist Tomogr* **23**(6):857–866.
48. Vaughan JT, DelaBarre L, Snyder C, Adriany G, Collins CM, Van de Moortele P-F, Moeller S, Ritter J, Strupp J, Andersen P, Tian J, Smith MB, Ugurbil K. 2005. RF Image Optimization at 7T and 9.4T. *Proc Int Soc Magn Reson Med* **13**:953.
49. Darwin RH, Drayer BP, Riederer SJ, Wang HZ, MacFall JR. 1986. T_2 estimates in healthy and diseased brain tissue: a comparison using various MR pulse sequences. *Radiology* **160**(2):375–381.
50. Drayer B, Burger P, Darwin R, Riederer S, Herfkens R, Johnson GA. 1986. MRI of brain iron. *Am J Roentgenol* **147**(1):103–110.
51. Englund E, Brun A, Larsson EM, Gyroffly-Wagner Z, Persson B. 1986. Tumours of the central nervous system. Proton magnetic resonance relaxation times T_1 and T_2 and histopathologic correlates. *Acta Radiol Diagn (Stockh)* **27**(6):653–659.
52. Larsson EM, Englund E, Gyroffly-Wagner Z, Brun A, Cronqvist S, Persson B. 1986. Regional differences in the proton magnetic resonance relaxation times T_1 and T_2 within the normal human brain. *Acta Radiol Diagn (Stockh)* **27**(2):231–234.
53. MacKay A, Whittall K, Adler J, Li D, Paty D, Graeb D. 1994. In vivo visualization of myelin water in brain by magnetic resonance. *Magn Reson Med* **31**(6):673–677.
54. Vymazal J, Righini A, Brooks RA, Canesi M, Mariani C, Leonardi M, Pezzoli G. 1999. T_1 and T_2 in the brain of healthy subjects, patients with Parkinson's disease, and patients with multiple system atrophy: relation to iron content. *Radiology* **211**(2):489–495.
55. Wehrli FW, MacFall JR, Schutts D, Breger R, Herfkens RJ. 1984. Mechanism of contrast in NMR. *J Comput Assist Tomogr* **8**(3):369–380.
56. Whittall KP, MacKay AL, Graeb DA, Nugent RA, Li DK, Paty DW. 1997. In vivo measurement of T_2 distributions and water contents in normal human brain. *Magn Reson Med* **37**(1):34–43.
57. Antonini A, Leenders KL, Meier D, Oertel WH, Boesiger P, Anliker M. 1993. T_2 relaxation time in patients with Parkinson's disease. *Neurology* **43**(4):697–700.
58. Schenker C, Meier D, Wichmann W, Boesiger P, Valavanis A. 1993. Age distribution and iron dependency of the T_2 relaxation time in the globus pallidus and putamen. *Neuroradiology* **35**(2):119–124.

59. Vymazal J, Brooks RA, Baumgarner C, Tran V, Katz D, Bulte JW, Bauminger R, Di Chiro G. 1996. The relation between brain iron and NMR relaxation times: an in vitro study. *Magn Reson Med* **35**(1):56–61.
60. Vymazal J, Hajek M, Patronas N, Giedd JN, Bulte JW, Baumgarner C, Tran V, Brooks RA. 1995. The quantitative relation between T_1 -weighted and T_2 -weighted MRI of normal gray matter and iron concentration. *J Magn Reson Imag* **5**(5):554–560.
61. Zhou J, Golay X, van Zijl PC, Silvennoinen MJ, Kauppinen R, Pekar J, Kraut M. 2001. Inverse T_2 contrast at 1.5 Tesla between gray matter and white matter in the occipital lobe of normal adult human brain. *Magn Reson Med* **46**(2):401–406.
62. Kim SG, Hu X, Ugurbil K. 1994. Accurate T_1 determination from inversion recovery images: application to human brain at 4 Tesla. *Magn Reson Med* **31**(4):445–449.
63. Jezzard P, Duewell S, Balaban RS. 1996. MR relaxation times in human brain: measurement at 4 T. *Radiology* **199**(3):773–779.
64. Bartha R, Michaeli S, Merkle H, Adriany G, Andersen P, Chen W, Ugurbil K, Garwood M. 2002. In vivo $^1\text{H}_2\text{O}$ T_2^* measurement in the human occipital lobe at 4T and 7T by Carr-Purcell MRI: detection of microscopic susceptibility contrast. *Magn Reson Med* **47**(4):742–750.
65. Michaeli S, Garwood M, Zhu XH, DelaBarre L, Andersen P, Adriany G, Merkle H, Ugurbil K, Chen W. 2002. Proton T_2 relaxation study of water, N-acetylaspartate, and creatine in human brain using Hahn and Carr-Purcell spin echoes at 4T and 7T. *Magn Reson Med* **47**(4):629–633.
66. Norris DG. 2003. High field human imaging. *J Magn Reson Imag* **18**(5):519–529.
67. Rooney WD, Johnson G, Li X, Cohen R, Kim S-G, Ugurbil K, Springer CS. 2006. The magnetic field and tissue dependences of human brain longitudinal $^1\text{H}_2\text{O}$ relaxation in vivo. *Magn Reson Med*. In press.
68. Lee JH, Garwood M, Menon R, Adriany G, Andersen P, Truwit CL, Ugurbil K. 1995. High contrast and fast three-dimensional magnetic resonance imaging at high fields. *Magn Reson Med* **34**(3):308–312.
69. Dobre MC, Marjanska M, Ugurbil K. 2005. Blood T_1 measurement at high magnetic field strength. *Proc Int Soc Magn Reson Med* **13**:1162.
70. Duong TQ, Yacoub E, Adriany G, Hu X, Ugurbil K, Kim SG. 2003. Microvascular BOLD contribution at 4 and 7 T in the human brain: gradient-echo and spin-echo fMRI with suppression of blood effects. *Magn Reson Med* **49**(6):1019–1027.
71. Haacke EM, Xu Y, Cheng YC, Reichenbach JR. 2004. Susceptibility weighted imaging (SWI). *Magn Reson Med* **52**(3):612–618.
72. Reichenbach JR, Essig M, Haacke EM, Lee BC, Przetak C, Kaiser WA, Schad LR. 1998. High-resolution venography of the brain using magnetic resonance imaging. *MAGMA* **6**(1):62–69.
73. Jack Jr CR, Garwood M, Wengenack TM, Borowski B, Curran GL, Lin J, Adriany G, Grohn OH, Grimm R, Poduslo JF. 2004. In vivo visualization of Alzheimer's amyloid plaques by magnetic resonance imaging in transgenic mice without a contrast agent. *Magn Reson Med* **52**(6):1263–1271.
74. Zhang J, Yarowsky P, Gordon MN, Di Carlo G, Munireddy S, van Zijl PC, Mori S. 2004. Detection of amyloid plaques in mouse models of Alzheimer's disease by magnetic resonance imaging. *Magn Reson Med* **51**(3):452–457.
75. Helpert JA, Lee SP, Falangola MF, Dyakin VV, Bogart A, Ardekani B, Duff K, Branch C, Wisniewski T, de Leon MJ, Wolf O, O'Shea J, Nixon RA. 2004. MRI as-

- assessment of neuropathology in a transgenic mouse model of Alzheimer's disease. *Magn Reson Med* **51**(4):794–798.
76. Poduslo JF, Wengenack TM, Curran GL, Wisniewski T, Sigurdsson EM, Macura SI, Borowski BJ, Jack Jr CR. 2002. Molecular targeting of Alzheimer's amyloid plaques for contrast-enhanced magnetic resonance imaging. *Neurobiol Dis* **11**(2):315–329.
77. Benveniste H, Einstein G, Kim KR, Hulette C, Johnson GA. 1999. Detection of neuritic plaques in Alzheimer's disease by magnetic resonance microscopy. *Proc Natl Acad Sci USA* **96**(24):14079–14084.
78. Bandettini PA, Wong EC, Hinks RS, Tikofsky RS, Hyde JS. 1992. Time course EPI of human brain function during task activation. *Magn Reson Med* **25**(2):390–397.
79. Detre JA, Wang J. 2002. Technical aspects and utility of fMRI using BOLD and ASL. *Clin Neurophysiol* **113**(5):621–634.
80. Kim SG. 1995. Quantification of relative cerebral blood flow change by flow-sensitive alternating inversion recovery (FAIR) technique: application to functional mapping. *Magn Reson Med* **34**:293–301.
81. Duong TQ, Kim DS, Ugurbil K, Kim SG. 2001. Localized cerebral blood flow response at submillimeter columnar resolution. *Proc Natl Acad Sci USA* **98**(19):10904–10909.
82. Hoge RD, Atkinson J, Gill B, Crelier GR, Marrett S, Pike GB. 1999. Linear coupling between cerebral blood flow and oxygen consumption in activated human cortex. *Proc Natl Acad Sci USA* **96**(16):9403–9408.
83. Shmuel A, Yacoub E, Pfeuffer J, Van de Moortele PF, Adriany G, Hu X, Ugurbil K. 2002. Sustained negative BOLD, blood flow and oxygen consumption response and its coupling to the positive response in the human brain. *Neuron* **36**(6):1195–1210.
84. Song AW, Li T. 2003. Improved spatial localization based on flow-moment-nulled and intra-voxel incoherent motion-weighted fMRI. *NMR Biomed* **16**(3):137–143.
85. Song AW, Harshbarger T, Li T, Kim KH, Ugurbil K, Mori S, Kim DS. 2003. Functional activation using apparent diffusion coefficient-dependent contrast allows better spatial localization to the neuronal activity: evidence using diffusion tensor imaging and fiber tracking. *Neuroimage* **20**(2):955–961.
86. Mandeville J, Marota J, Keltner J, Kosovsky B, Burke J. 1996. CBV functional imaging in rat brain using iron oxide agent at steady state concentration. *Proc Int Soc Magn Reson Med* 292.
87. Kim SG, Ugurbil K. 2003. High-resolution functional magnetic resonance imaging of the animal brain. *Methods* **30**(1):28–41.
88. Lu H, Golay X, Pekar JJ, Van Zijl PC. 2003. Functional magnetic resonance imaging based on changes in vascular space occupancy. *Magn Reson Med* **50**(2):263–274.
89. Ogawa S, Lee T-M, Nayak AS, Glynn P. 1990. Oxygenation-sensitive contrast in magnetic resonance image of rodent brain at high magnetic fields. *Magn Reson Med* **14**:68–78.
90. Ogawa S, Lee T-M, Kay AR, Tank DW. 1990. Brain magnetic resonance imaging with contrast dependent on blood oxygenation. *Proc Natl Acad Sci USA* **87**:9868–9872.
91. Ogawa S, Lee TM. 1990. Magnetic resonance imaging of blood vessels at high fields: in vivo and in vitro measurements and image simulation. *Magn Reson Med* **16**:9–18.
92. Ogawa S, Lee TM, Barrere B. 1993. Sensitivity of magnetic resonance image signals of a rat brain to changes in the cerebral venous blood oxygenation. *Magn Reson Med* **29**:205–210.
93. Fox PT, Raichle ME, Mintun MA, Dence C. 1988. Nonoxidative glucose consumption during focal physiologic neural activity. *Science* **241**(4864):462–464.

94. Raichle ME. 1987. Circulatory and metabolic correlates of brain function in normal humans. In *Handbook of physiology — the nervous system*, Vol. 5, pp. 643–674. Ed F Plum. Bethesda: American Physics Society.
95. Pfeuffer J, McCullough JC, Van de Moortele PF, Ugurbil K, Hu X. 2003. Spatial dependence of the nonlinear BOLD response at short stimulus duration. *Neuroimage* **18**(4):990–1000.
96. Yacoub E, Shmuel A, Pfeuffer J, Van De Moortele PF, Adriany G, Andersen P, Vaughan JT, Merkle H, Ugurbil K, Hu X. 2001. Imaging brain function in humans at 7 Tesla. *Magn Reson Med* **45**(4):588–594.
97. Yacoub E, Shmuel A, Pfeuffer J, Van De Moortele PF, Adriany G, Ugurbil K, Hu X. 2001. Investigation of the initial dip in fMRI at 7 Tesla. *NMR Biomed* **14**(7–8):408–412.
98. Yacoub E, Van De Moortele PF, Shmuel A, Ugurbil K. 2005. Signal and noise characteristics of Hahn SE and GE BOLD fMRI at 7 T in humans. *Neuroimage* **24**(3):738–750.
99. Duong TQ, Yacoub E, Adriany G, Hu X, Ugurbil K, Vaughan JT, Merkle H, Kim SG. 2002. High-resolution, spin-echo BOLD, and CBF fMRI at 4 and 7 T. *Magn Reson Med* **48**(4):589–593.
100. Silva AC, Koretsky AP. 2002. Laminar specificity of functional MRI onset times during somatosensory stimulation in rat. *Proc Natl Acad Sci USA* **99**(23):15182–15187.
101. Menon RS, Ogawa S, Tank DW, Ugurbil K. 1993. 4 Tesla gradient recalled echo characteristics of photic stimulation-induced signal changes in the human primary visual cortex. *Magn Reson Med* **30**(3):380–386.
102. Segebarth C, Belle V, Delon C, Massarelli R, Decety J, Le Bas J-F, Decropts M, Benabid AL. 1994. Functional MRI of the human brain: predominance of signals from extracerebral veins. *NeuroReport* **5**:813–816.
103. Fujita I, Tanaka K, Ito M, Cheng K. 1992. Columns for visual features of objects in monkey inferotemporal cortex. *Nature* **360**:343–346.
104. Wang G, Tanaka K, Tanifuji M. 1996. Optical imaging of functional organization in the monkey inferotemporal cortex. *Science* **272**:1665–1668.
105. Iadecola C, Yang G, Ebner TJ, Chen G. 1997. Local and propagated vascular responses evoked by focal synaptic activity in cerebellar cortex. *J Neurophysiol* **78**(2):651–659.
106. Tsekos NV, Zhang F, Merkle H, Nagayama M, Iadecola C, Kim SG. 1998. Quantitative measurements of cerebral blood flow in rats using the FAIR technique: correlation with previous iodoantipyrine autoradiographic studies. *Magn Reson Med* **39**(4):564–573.
107. Thulborn KR, Waterton JC, Matthews PM, Radda GK. 1982. Oxygenation dependence of the transverse relaxation time of water protons in whole blood at high field. *Biochim Biophys Acta* **714**(2):265–270.
108. Lee S-P, Silva AC, Ugurbil K, Kim S-G. 1999. Diffusion weighted spin echo fMRI at 9.4 T: microvascular/tissue contribution to BOLD signal changes. *Magn Reson Med* **42**(5):919–928.
109. Duong TQ, Yacoub E, Adriany G, Hu X, Andersen P, Vaughan JT, Ugurbil K, Kim SG. 2004. Spatial specificity of high-resolution, spin-echo BOLD, and CBF fMRI at 7 T. *Magn Reson Med* **51**(3):646–647.
110. Park JC, Ronen I, Kim D-S, Ugurbil K. 2004. Spatial specificity of high resolution GE BOLD and CBF fMRI in the cat visual cortex. *Proc Int Soc Magn Reson Med* 1014.
111. Grinvald A, Vanzetta I. 2003. Personal communications.

112. Sheth S, Nemoto M, Guiou M, Walker M, Pouratian N, Toga AW. 2003. Evaluation of coupling between optical intrinsic signals and neuronal activity in rat somatosensory cortex. *Neuroimage* **19**(3):884–894.
113. Harrison RV, Harel N, Panesar J, Mount RJ. 2002. Blood capillary distribution correlates with hemodynamic-based functional imaging in cerebral cortex. *Cereb Cortex* **12**(3):225–233.
114. Sereno MI, Dale AM, Reppas JB, Kwong KK, Belliveau JW, Brady TJ, Rosen BR, Tootell RBH. 1995. Borders of multiple visual areas in humans revealed by functional magnetic resonance imaging. *Science* **268**:889–893.
115. DeYoe EA, Carman GJ, Bandettini P, Glickman S, Wieser J, Cox R, Miller D, Neitz J. 1996. Mapping striate and extrastriate visual areas in human cerebral cortex. *Proc Natl Acad Sci USA* **93**(6):2382–2386.
116. Engel SA, Glover GH, Wandell BA. 1997. Retinotopic organization in human visual cortex and the spatial precision of functional MRI. *Cereb Cortex* **7**(2):181–192.
117. Pawlik G, Rackl A, Bing RJ. 1981. Quantitative capillary topography and blood flow in the cerebral cortex of cats: an in vivo microscopic study. *Brain Res* **208**(1):35–58.
118. Eichling JO, Raichle ME, Grubb RL, Ter-Pogossian MM. 1974. Evidence of the limitations of water as a freely diffusible tracer in brain of the Rhesus monkey. *Circ Res* **35**(3):358–364.
119. Paulson OB, Hertz MM, Bolwig TG, Lassen NA. 1977. Filtration and diffusion of water across the blood–brain barrier in man. *Microvasc Res* **13**(1):113–124.
120. Paulson OB, Hertz MM, Bolwig TG, Lassen NA. 1977. Water filtration and diffusion across the blood brain barrier in man. *Acta Neurol Scand Suppl* **64**:492–493.
121. Boxerman JL, Weisskoff RM, Hoppel BE, Rosen BR. 1993. MR contrast due to microscopically heterogeneous magnetic susceptibility: cylindrical geometry. *Proc Int Soc Magn Reson Med* 389.
122. Ugurbil K, Hu X, Chen W, Zhu X-H, Kim S-G, Georgopoulos A. 1999. Functional mapping in the human brain using high magnetic fields. *Philos Trans R Soc Lond B Biol Sci* **354**(1387):1195–1213.
123. van Zijl PC, Eleff SM, Ulatowski JA, Oja JM, Ulug AM, Traystman RJ, Kauppinen RA. 1998. Quantitative assessment of blood flow, blood volume and blood oxygenation effects in functional magnetic resonance imaging [see comments]. *Nat Med* **4**(2):159–167.
124. Ugurbil K, Adriany G, Andersen P, Chen W, Gruetter R, Hu X, Merkle H, Kim DS, Kim SG, Strupp J, Zhu XH, Ogawa S. 2000. Magnetic resonance studies of brain function and neurochemistry. *Ann Rev Biomed Eng* **2**:633–660.
125. Barth M, Moser E. 1997. Proton NMR relaxation times of human blood samples at 1.5 T and implications for functional MRI. *Cell Mol Biol (Noisy-le-grand)* **43**(5):783–791.
126. Zhu XH, Chen W. 2001. Observed BOLD effects on cerebral metabolite resonances in human visual cortex during visual stimulation: a functional ^1H MRS study at 4 T. *Magn Reson Med* **46**(5):841–847.
127. Stejskal EO, Tanner JE. 1965. Spin diffusion measurements: spin-echoes in the presence of a time dependent field gradient. *J Chem Phys* **42**:288–292.
128. Le Bihan D, Breton E, Lallemand D, Grenier P, Cabanis E, Laval-Jeantet M. 1986. MR imaging of intravoxel incoherent motions: application to diffusion and perfusion in neurologic disorders. *Radiology* **161**(2):401–407.
129. Song AW, Wong EC, Tan SG, Hyde JS. 1996. Diffusion weighted fMRI at 1.5 T. *Magn Reson Med* **35**(2):155–158.

130. Boxerman JL, Bandettini PA, Kwong KK, Baker JR, Davis TL, Rosen BR, Weisskoff RM. 1995. The intravascular contribution to fMRI signal change: Monte Carlo modeling and diffusion-weighted studies in vivo. *Magn Reson Med* **34**(1):4–10.
131. Mildner T, Norris DG, Schwarzbauer C, Wiggins CJ. 2001. A qualitative test of the balloon model for BOLD-based MR signal changes at 3T. *Magn Reson Med* **46**(5):891–899.
132. Lai S, Hopkins AL, Haacke EM, Li D, Wasserman BA, Buckley P, Friedman L, Meltzer H, Hedera P, Friedland R. 1993. Identification of vascular structures as a major source of signal contrast in high resolution 2D and 3D functional activation imaging of the motor cortex at 1.5T: preliminary results. *Magn Reson Med* **30**(3):387–392.
133. Haacke EM, Hopkins A, Lai S, Buckley P, Friedman L, Meltzer H, Hedera P, Friedland R, Klein S, Thompson L, et al. 1994. 2D and 3D high resolution gradient echo functional imaging of the brain: venous contributions to signal in motor cortex studies [published erratum appears in *NMR Biomed* Dec 1994, **7**(8):374]. *NMR Biomed* **7**(1–2):54–62.
134. Duong QD, Kim D-S, Ugurbil K, Kim S-G. 2000. Spatio-temporal dynamics of BOLD fMRI signals: towards mapping submillimeter cortical columns using the early negative response. *Magn Reson Med* **44**(2):231–242.
135. Kim DS, Duong TQ, Kim SG. 2000. High-resolution mapping of iso-orientation columns by fMRI. *Nat Neurosci* **3**(2):164–169.
136. Toth LJ, Ronen I, Olman C, Ugurbil K, Kim D-S. 2001. Spatial correlation of BOLD activity with neuronal responses. *Proc Int Soc Magn Reson Med* **6**.
137. Ugurbil K, Toth L, Kim DS. 2003. How accurate is magnetic resonance imaging of brain function? *Trends Neurosci* **26**(2):108–114.
138. Wong-Riley M, Anderson B, Liebl W, Huang Z. 1998. Neurochemical organization of the macaque striate cortex: correlation of cytochrome oxidase with Na⁺K⁺ATPase, NADPH-diaphorase, nitric oxide synthase, and N-methyl-D-aspartate receptor subunit 1. *Neuroscience* **83**(4):1025–1045.
139. Ronen I, Lee JH, Merkle H, Ugurbil K, Navon G. 1997. Imaging H₂¹⁷O distribution in a phantom and measurement of metabolically produced H₂¹⁷O in live mice by proton NMR. *NMR Biomed* **10**(7):333–340.
140. Grinvald A, Frostig RD, Siegel RM, Bartfeld E. 1991. High-resolution optical imaging of functional brain architecture in the awake monkey. *Proc Natl Acad Sci USA* **88**(24):11559–11563.
141. Vanzetta I, Grinvald A. 1998. Phosphorescence decay measurements in cat visual cortex show early blood oxygenation level decrease in response to visual stimulation. *Neurosci Lett Supp* **51**:S42.
142. Vanzetta I, Grinvald A. 1999. Increased cortical oxidative metabolism due to sensory stimulation: implications for functional brain imaging. *Science* **286**(5444):1555–1558.
143. Malonek D, Dirnagl U, Lindauer U, Yamada K, Kanno I, Grinvald A. 1997. Vascular imprints of neuronal activity: relationships between the dynamics of cortical blood flow, oxygenation, and volume changes following sensory stimulation. *Proc Natl Acad Sci USA* **94**(26):14826–14831.
144. Grinvald A, Slovlin H, Vanzetta I. 2000. Non-invasive visualization of cortical columns by fMRI. *Nat Neurosci* **3**(2):105–107.
145. Hu X, Le TH, Ugurbil K. 1997. Evaluation of the early response in fMRI using short stimulus duration. *Magn Reson Med* **37**:877–884.

146. Menon RS, Ogawa S, Hu X, Strupp JP, Anderson P, Ugurbil K. 1995. BOLD based functional MRI at 4 Tesla includes a capillary bed contribution: echo-planar imaging correlates with previous optical imaging using intrinsic signals. *Magn Reson Med* **33**(3):453–459.
147. Twieg DB, Moore GG, Zhang YT. 1997. Estimating fast response onset time. *Proc Int Soc Magn Reson Med* 1645.
148. Yacoub E, Le TH, Ugurbil K, Hu X. 1999. Further evaluation of the initial negative response in functional magnetic resonance imaging. *Magn Reson Med* **41**(3):436–441.
149. Yacoub E, Vaughn T, Adriany G, Andersen P, Merkle H, Ugurbil K, Hu X. 2000. Observation of the initial "dip" in fMRI signal in human visual cortex at 7 Tesla. *Proc Int Soc Magn Reson Med* **8**:991.
150. Cannestra AF, Pouratian N, Bookheimer SY, Martin NA, Beckerand DP, Toga AW. 2001. Temporal spatial differences observed by functional MRI and human intraoperative optical imaging. *Cereb Cortex* **11**(8):773–782.
151. Logothetis NK, Gugenberger H, Peled S, Pauls J. 1999. Functional imaging of the monkey brain. *Nat Neurosci* **2**(6):555–560.
152. Kim S-G, Hendrich K, Hu X, Merkle H, Ugurbil K. 1994. Potential pitfalls of functional MRI using conventional gradient-recalled echo techniques. *NMR Biomed* **7**(1/2):69–74.
153. Hu X, Kim S-G. 1994. Reduction of physiological noise in functional MRI using navigator echo. *Magn Reson Med* **31**:495–503.
154. Hyde JS, Biswal B, Song AW, Tan SG. 1994. Physiological and instrumental fluctuations in fMRI data. Paper presented at Annual Midwest Functional MRI Workshop, pp. 73–76, Madison, WI.
155. Kruger G, Glover GH. 2001. Physiological noise in oxygenation-sensitive magnetic resonance imaging. *Magn Reson Med* **46**(4):631–637.
156. Kruger G, Kastrup A, Glover GH. 2001. Neuroimaging at 1.5 T and 3.0 T: comparison of oxygenation-sensitive magnetic resonance imaging. *Magn Reson Med* **45**(4):595–604.
157. Hyde JS, Biswal BB, Jesmanowicz A. 2001. High-resolution fMRI using multislice partial k-space GR-EPI with cubic voxels. *Magn Reson Med* **46**(1):114–125.
158. Pfeuffer J, Van De Moortele PF, Ugurbil K, Hu X, Glover GH. 2002. Correction of physiologically induced global off-resonance effects in dynamic echo-planar and spiral functional imaging. *Magn Reson Med* **47**(2):344–353.
159. Van De Moortele PF, Pfeuffer J, Glover GH, Ugurbil K, Hu X. 2002. Respiration-induced B0 fluctuations and their spatial distribution in the human brain at 7 Tesla. *Magn Reson Med* **47**(5):888–895.
160. Detre JA, Leigh JS, Williams DS, Koretsky AP. 1992. Perfusion imaging. *Magn Reson Med* **23**(1):37–45.
161. Zhang W, Williams DS, Koretsky AP. 1993. Measurement of rat brain perfusion by NMR using spin labeling of arterial water: in vivo determination of the degree of spin labeling. *Magn Reson Med* **29**(3):416–421.
162. Detre JA, Zhang W, Roberts DA, Silva AC, Williams DS, Grandis DJ, Koretsky AP, Leigh JS. 1994. Tissue specific perfusion imaging using arterial spin labeling. *NMR Biomed* **7**(1–2):75–82.
163. Barbier EL, Silva AC, Kim HJ, Williams DS, Koretsky AP. 1999. Perfusion analysis using dynamic arterial spin labeling (DASL). *Magn Reson Med* **41**(2):299–308.
164. Barbier EL, Silva AC, Kim SG, Koretsky AP. 2001. Perfusion imaging using dynamic arterial spin labeling (DASL). *Magn Reson Med* **45**(6):1021–1029.

165. Edelman RE, Siewer B, Darby DG, Thangaraj V, Nobre AC, Mesulam MM, Warach S. 1994. Quantitative mapping of cerebral blood flow and functional localization with echo-planar MR imaging and signal targeting with alternating radio frequency. *Radiology* **192**:513–520.
166. Wong EC, Buxton RB, Frank LR. 1998. Quantitative imaging of perfusion using a single subtraction (QUIPSS and QUIPSS II). *Magn Reson Med* **39**(5):702–708.
167. Talagala SL, Ye FQ, Ledden PJ, Chesnick S. 2004. Whole-brain 3D perfusion MRI at 3.0 T using CASL with a separate labeling coil. *Magn Reson Med* **52**(1):131–140.
168. Mildner T, Trampel R, Moller HE, Schafer A, Wiggins CJ, Norris DG. 2003. Functional perfusion imaging using continuous arterial spin labeling with separate labeling and imaging coils at 3 T. *Magn Reson Med* **49**(5):791–795.
169. Sodickson DK, Manning WJ. 1997. Simultaneous acquisition of spatial harmonics (SMASH): fast imaging with radiofrequency coil arrays. *Magn Reson Med* **38**(4):591–603.
170. Pruessmann KP, Weiger M, Scheidegger MB, Boesiger P. 1999. SENSE: sensitivity encoding for fast MRI. *Magn Reson Med* **42**(5):952–962.
171. Abragam A. 1961. *The principles of nuclear magnetism*. Ed NF Mott, EC Bullard, DH Wilkinson. London: Oxford UP.
172. Steinhoff HJ, Kramm B, Hess G, Owerdieck C, Redhardt A. 1993. Rotational and translational water diffusion in the hemoglobin hydration shell: dielectric and proton nuclear relaxation measurements. *Biophys J* **65**(4):1486–1495.
173. Meiboom S. 1961. NMR study of proton transfer in water. *J Chem Phys* **34**:375–388.
174. Nakao Y, Itoh Y, Kuang TY, Cook M, Jehle J, Sokoloff L. 2001. Effects of anesthesia on functional activation of cerebral blood flow and metabolism. *Proc Natl Acad Sci USA* **98**(13):7593–7598.
175. Siesjo B. 1978. *Brain energy metabolism*. New York: Wiley.
176. Zhang NY, Zhu XH, Lei H, Ugurbil K, Chen W. 2002. Calculation of cerebral metabolic rate of oxygen based on ^{17}O MRS imaging with 2 minutes $^{17}\text{O}_2$ Inhalation: a simplified approach. *Proc Int Soc Magn Reson Med* 344.
177. Hetherington HP, Mason GF, Pan JW, Ponder SL, Vaughan JT, Twieg DB, Pohost GM. 1994. Evaluation of cerebral gray and white matter metabolite differences by spectroscopic imaging at 4.1T. *Magn Reson Med* **32**:565–571.
178. Gruetter R, Garwood M, Ugurbil K, Seaquist ER. 1996. Observation of resolved glucose signals in ^1H NMR spectra of the human brain at 4 Tesla. *Magn Reson Med* **36**(1):1–6.
179. Tkac I, Andersen P, Adriany G, Merkle H, Ugurbil K, Gruetter R. 2001. In vivo ^1H NMR spectroscopy of the human brain at 7 T. *Magn Reson Med* **46**(3):451–456.
180. Chen W, Novotny E, Zhu X-H, Rothman D, Shulman RG. 1993. Localized ^1H NMR measurement of glucose consumption in human brain during visual stimulation. *Proc Natl Acad Sci USA* **90**:9896–9900.
181. Frahm J, Kruger KD, Merboldt KD, Kleinschmidt A. 1996. Dynamic uncoupling and recoupling of perfusion and oxidative metabolism during focal brain activation in man. *Magn Reson Med* **35**:143–148.
182. Merboldt KD, Bruhn H, Hanicke W, Michaelis T, Frahm J. 1992. Decrease of glucose in the human visual cortex during photic stimulation. *Magn Reson Med* **25**:187–194.
183. Lei H, Ugurbil K, Chen W. 2003. Measurement of unidirectional Pi to ATP flux in human visual cortex at 7 T by using in vivo ^{31}P magnetic resonance spectroscopy. *Proc Natl Acad Sci USA* **100**(24):14409–14414.

184. Chen W, Zhu XH, Gruetter R, Seaquist ER, Adriany G, Ugurbil K. 2001. Study of tricarboxylic acid cycle flux changes in human visual cortex during hemifield visual stimulation using ^1H - ^{13}C MRS and fMRI. *Magn Reson Med* **45**(3):349–355.
185. Hyder F, Chase JR, Behar KL, Mason GF, Siddeek M, Rothman DL, Shulman RG. 1996. Increased tricarboxylic acid cycle flux in rat brain during forepaw stimulation detected with ^1H - ^{13}C -NMR. *Proc Natl Acad Sci USA* **93**(15):7612–7617.
186. Hyder F, Rothman DL, Mason GF, Rangarajan A, Behar KL, Shulman RG. 1997. Oxidative glucose metabolism in rat brain during single forepaw stimulation: a spatially localized ^1H - ^{13}C nuclear magnetic resonance study. *J Cereb Blood Flow Metab* **17**(10):1040–1047.
187. Gruetter R, Novotny EJ, Boulware SD, Mason GF, Rothman DL, Prichard JW, Shulman RG. 1994. Localized ^{13}C NMR spectroscopy of amino acid labeling from [$1\text{-}^{13}\text{C}$] D-glucose in the human brain. *J Neurochem* **63**:1377–1385.
188. Sibson NR, Dhankhar A, Mason GF, Behar KL, Rothman DL, Shulman RG. 1997. In vivo ^{13}C NMR measurements of cerebral glutamine synthesis as evidence for glutamate–glutamine cycling. *Proc Natl Acad Sci USA* **94**(6):2699–2704.
189. Gruetter R, Seaquist ER, Kim SW, Ugurbil K. 1998. Localized in vivo ^{13}C NMR of glutamate metabolism in the human brain: initial results at 4 Tesla. *Dev Neurosci* **20**(4–5):380–388.
190. Shen J, Petersen KF, Behar KL, Brown P, Nixon TW, Mason GF, Petroff OA, Shulman GI, Shulman RG, Rothman DL. 1999. Determination of the rate of the glutamate/glutamine cycle in the human brain by in vivo ^{13}C NMR. *Proc Natl Acad Sci USA* **96**(14):8235–8240.
191. Gruetter R, Seaquist B, Ugurbil K. 2001. A mathematical model of compartmentalized neurotransmitter metabolism in the human brain. *Am J Physiol Endocrinol Metab* **281**(1):E100–E112.
192. Ugurbil K, Brown TR, den Hollander JA, Glynn P, Shulman RG. 1978. High-resolution ^{13}C nuclear magnetic resonance studies of glucose metabolism in *Escherichia coli*. *Proc Natl Acad Sci USA* **75**(8):3742–3746.
193. Bergles DE, Dzubay JA, Jahr CE. 1997. Glutamate transporter currents in bergmann glial cells follow the time course of extrasynaptic glutamate. *Proc Natl Acad Sci USA* **94**(26):14821–14825.
194. Bergles DE, Diamond JS, Jahr CE. 1999. Clearance of glutamate inside the synapse and beyond. *Curr Opin Neurobiol* **9**(3):293–298.
195. Martinez-Hernandez A, Bell KP, Norenberg MD. 1976. Glutamine synthetase: glial localization in brain. *Science* **195**:1356–1358.
196. Sibson NR, Dhankhar A, Mason GF, Rothman DL, Behar KL, Shulman RG. 1998. Stoichiometric coupling of brain glucose metabolism and glutamatergic neuronal activity. *Proc Natl Acad Sci USA* **95**(1):316–321.
197. Fox PT, Raichle ME. 1986. Focal physiological uncoupling of cerebral blood flow and oxidative metabolism during somatosensory stimulation in human subjects. *Proc Natl Acad Sci USA* **83**(4):1140–1144.
198. Barfuss H, Fischer H, Hentschel D, Ladebeck R, Oppelt A, Wittig R, Duerr W, Oppelt R. 1990. In vivo magnetic resonance imaging and spectroscopy of humans with a 4 T whole-body magnet. *NMR Biomed* **3**(1):31–45.
199. Henry PG, Tkac I, Gruetter R. 2003. ^1H -localized broadband ^{13}C NMR spectroscopy of the rat brain in vivo at 9.4 T. *Magn Reson Med* **50**(4):684–692.

HIGH-RESOLUTION AND MICROSCOPIC IMAGING AT HIGH FIELD

Lawrence L. Wald, Bruce Fischl, Bruce R. Rosen

*A.A. Martinos Center for Biomedical Imaging, Department of Radiology,
Massachusetts General Hospital and Harvard Medical School,
Harvard–MIT Division of Health Sciences and Technology*

1. INTRODUCTION

The goal of improved spatial resolution in magnetic resonance imaging for better visualization of finer and finer structural details in the body is driven by a long tradition of microscopy in conventional anatomy. Centuries of anatomical studies have underscored the success with which the study of function and dysfunction can be complemented by the study of normal and pathological structure. Since relevant structures in the body span spatial scales from meters to the subcellular level, imaging technology has been pushed toward increasing resolution. Although there are solid motivations for imaging biological samples and small animal models with MR, a principal attraction of MR technology is the potential that advances in methodology can ultimately be adapted for use in living humans.

The basic MRI technique is capable of studying structural organization from whole-body levels down to micrometers, but the tradeoffs in the design of the imaging technology highly favor adapting the scale of the instrument to the scale of the structures under study. These technical scaling considerations have led to three rough classes of biological MR imaging equipment and studies — microimaging of small biological samples, small animal microimaging, and human imaging. While sharing the basic principles of MR imaging, the scaling of sensitivity and performance as well as cost tradeoffs motivate that the magnet, gradient, and RF receiver coil scale with the length scale of the sample under study. In many cases the use of different instrumentation as well as specialized sample preparation methods has meant that these three subfields of MR are practiced by distinct subsets of researchers.

While this specialization will perhaps always be desirable, recent developments in high field human imaging technology hold the promise of being able to significantly close the gap between the level of structural detail that can be visualized in small-sample and animal preparations and that which can be seen in living humans. Specifically, the last 8 years have seen the development of high field

magnets for imaging systems capable of whole-body human studies that significantly equalize the field strength advantage enjoyed previously by small-sample and animal microimagers. Additionally, sensitivity advantages afforded by the small receive coils employed in traditional microimaging has been partially extended to human imagers by the proliferation of multiple receiver channels on clinical systems. Simultaneously recording from multiple small receive coils allows the receive coil to be reduced in size to near that utilized in small-animal imaging while maintaining human-sized coverage of the body. Thus, the technology is in the process of shifting the boundaries of MR microimaging, allowing human imaging to more directly incorporate methodology from animal and tissue preparation studies and to maximize the benefit of the intrinsic noninvasive nature of MRI. In this review, we will consider the microimaging field from this perspective. In addition to reviewing the current state of the art of high-resolution imaging with high field human systems, we will look toward microimaging in animal and pathological preparations with an eye toward the methodology and structures that are likely to ultimately find themselves in the territory of high field human clinical imaging. Most of the ultra high field human imaging technology has been focused on the brain. The brain has been a primary target for instrumental development due to its relatively small size, convenient location on the end of the human body, and its importance to human function and health. Thus particular emphasis will be placed on high field microimaging of the human brain and important brain diseases such as Alzheimer's disease (AD).

2. MR INSTRUMENTATION FOR MICROIMAGING

The steep cost in image Signal-to-Noise Ratio (SNR) imposed by improved spatial resolution is at the root of the difficulties in pushing in-vivo human imaging toward finer anatomical detail. The SNR of an MR image is proportional to the image voxel volume, V , and the square root of the total time, τ , in which the MR receivers collect the data. If the ability of MR to acquire true 3D images of the body is to be exploited in a general way, it is desirable for the image to be acquired with isotropic spatial resolution, $d = V^{1/3}$. If all other parameters are kept constant, trading increased imaging time for improved image resolution (at a fixed image SNR) quickly leads to impractical imaging times since τ scales with d^6 . For example, improving upon 1-mm³ image voxel volumes obtained in a 10-minute brain image (currently the highest resolution commonly used for clinical studies) to the 100 μm level required for resolving cortical laminar detail would require a highly impractical million fold increase in imaging time.

The tyranny of the $\tau \propto d^6$ scaling law at first seems formidable, but it can be at least partially addressed by taking advantage of higher field strength magnets and the favorable detection sensitivity of small receiver coils. SNR scales linearly with the static magnetic field strength, B_0 , for biological samples where the image noise is dominated by RF losses in the partially conductive sample. Thus the use of higher field strength magnets is an attractive option. In small-sample and animal imaging the small magnet bore diameters vastly lower the cost and construction difficulties of maintaining a uniform field over the sample. In addition, for small

samples the size of the detection (receiver) coil can be shrunk to the minimum to take advantage of an increase in receiver sensitivity per spin. This sensitivity scales roughly as $V^{-1/3}$ where, V is the volume of tissue contained in the tightly fitting receive coil [1]. For microimaging cell preparations, one can take advantage of a 10-mm³ volume coil, compared to a typical volume of $\pi(12\text{ cm})^2 \times 20\text{ cm} \approx 10^4\text{ cm}^3$ for a human head coil. Thus the factor of 10^7 in coil volume contributes an additional factor of approximately 200 in sensitivity for small-sample microimaging. Coupled with the tenfold gain obtained from imaging at 14 T compared to 1.5 T, the specialized instrumentation can make up more than 3 orders of magnitude in imaging sensitivity (and 6 orders of magnitude in imaging time). For the human head, true micro coils are not practical, but array coils derived from 5-cm diameter surface coils can cover the head if a sufficient number of receive channels is available (e.g., 96). The equivalent volume of such a coil is roughly the half sphere of tissue of the same volume under the coil. For our examples, this volume $\frac{2}{3}\pi(3\text{ cm})^3 = 57\text{ cm}^3$ translates to approximately a potential factor of 6 in sensitivity in the human cortex compared to whole-head volume coils. Together with an increase in the static magnetic field from 1.5 to 9.4 T, the current generation of human imagers has the potential to gain nearly 2 orders of magnitude in sensitivity compared to conventional clinical MRI.

A third factor favoring imaging technology tightly coupled to the sample or anatomy of interest is the strength and slew rate of the gradient coils used to encode the image. High gradient strengths are desirable since the resolution of the encoded image is determined by the time-amplitude product of the gradient pulses used to encode the image. The temporal length of the gradient pulses is generally limited by signal dephasing from T_2^* processes. The slew rate with which the gradient can switch is also an important part of the time efficiency of the imaging sequence. Both gradient strength and slew rates scale with the volume of the gradient coil, again favoring the idea of matching the hardware to the size of the sample by making the gradient coil no larger than is needed to accommodate the sample or animal of interest. For human imaging, optimization is achieved by forgoing large-field-of-view (e.g., whole-body) imaging in favor of shorter, less linear gradients. If brain imaging is the goal, small diameter head-only gradients provide substantial improvements due to their smaller inductance and more efficient gradient field generation capabilities. Additionally, current state-of-the-art gradients are nerve stimulation limited, so reducing their active volume to the head allows improved performance by reducing the maximum dB/dt invoked electromotive forces in the tissue. Head-only gradients can provide up to twice the gradient strength and 4 fold increases in slew rate compared to whole-body gradients when both are operating at the nerve stimulation threshold.

2.1. Technology for Microimaging of Biological Samples and Small Animals

With the above considerations in mind, MR microscopists have utilized the large magnetic fields available with small-bore-diameter magnets (most commonly,

5.6 and 8.9 cm) and magnetic field strengths up to 14 Tesla coupled with efficient small-diameter gradient and RF coils. The elegant images obtained with these microimaging systems probe down to the cellular level ($<10\ \mu\text{m}$ resolution). This literature has been recently reviewed in a number of sources [1–3]. The next natural size scale break in MR imaging applications is at an intermediate level between small biological samples and in-vivo human. Microscopic imaging of small animals has been motivated by the success of developing animal models of human disease. The recent proliferation of knockout rodent models of important human disease has made microimaging studies of mice particularly attractive. State-of-the-art rodent microimagers utilize horizontal bore magnets with field strengths up to 11.7 T and diameters ≥ 20 cm allowing, a clear bore of 8–12 cm for the animal, anesthesia, and monitoring equipment. Small-animal imaging has been recently reviewed by Ahrens and colleagues [2]. As an example of the type of image that can be obtained even under the difficult conditions, Figure 1 shows a high-resolution image from a CINE of the beating mouse heart. Although less than 1 cm in diameter and beating in excess of 500 beats per minute, a high-resolution Steady State Free Precession type CINE of the mouse cardiac cycle is obtainable in a state-of-the-art 9.4T rodent imager. This effort is motivated by the potential for utilizing MR to image phenotypes and dysfunctions associated with knockout genetic mouse models of important human diseases.

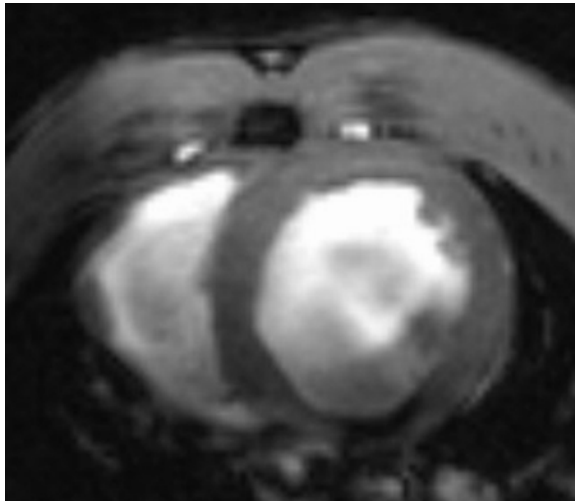


Figure 1. Single frame from an in-vivo mouse cardiac CINE study. Short axis frames from a fully refocused FLASH scan, FOV = 3 cm, 200 x 200 image matrix, TE/flip angle = 2.7 ms/30°, 4 averages, 16 frames per RR interval. The anesthetized mouse heart was beating at a rate of 450–600 bpm. Image courtesy of David Sosnovik, MD and George Dai, PhD of the Program in Cardiovascular Magnetic Resonance, MGH, A.A. Martinos Center for Biomedical Imaging.

2.2. Technology for Microimaging in Humans

Technology advances employed in the recently introduced ultra high field human systems have brought MR to the cusp of obtaining the sensitivity and specificity needed for studying the next level of detail in brain anatomy, including laminar and columnar structures in the human brain cortex. First and foremost, the sensitivity of the human experiment has been improved through the use of higher magnetic field strengths (7–9.4 T). The signal-to-noise advantages of high (3 and 4 T) and ultra high field (7 T and greater) MR have been established in a number of functional and structural studies [4–8]. Figure 2 shows the sensitivity of 7T human MRI compared directly to that obtained at 3 T using a nearly identical system (console, software, pulse sequence, and gradients). Over 3-fold increases are seen in regions of the brain that benefit from the dielectric lensing effect of the B_1 field (e.g., thalamus). Figure 3 shows the potential for utilizing favorable changes in MR contrast in addition to the sensitivity boost of high field signal detection illustrated in a high-resolution image obtained on an 8T human imager [6]. In addition to providing high-resolution depictions of venous architecture, improved deoxyhemoglobin contrast at high field provided favorable increases in functional MRI at high field. This has provided a major impetus for higher field strength systems. Studies of human neuronal activation and the interrelationship between cerebral activity, metabolism, and regional hemodynamics has thus pushed the capabilities of MR instrumentation to the limit of its sensitivity, and have fueled the development of 3 T, 4 T, and now higher field (7, 8, and 9.4 T) human MR systems.

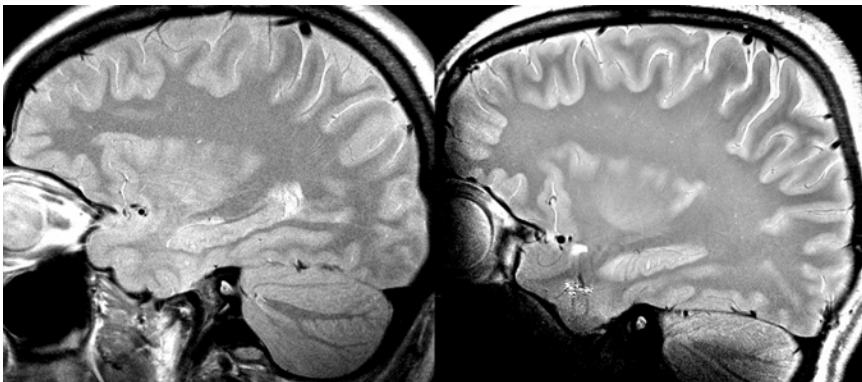


Figure 2. 7T human image (right) and 3T image (left) obtained with identical pulse sequence parameters, console, and gradient coil. Both obtained with volume head coil. The intensity of the 7T image has been intensity normalized to flatten the low spatial frequency dielectric lensing effect. The SNR of the 7T image exceeds the 3T acquisition by as much as a factor of 3 in the deep tissue, where dielectric effects aid the sensitivity to somewhat below a factor of 2 in the cortical areas.

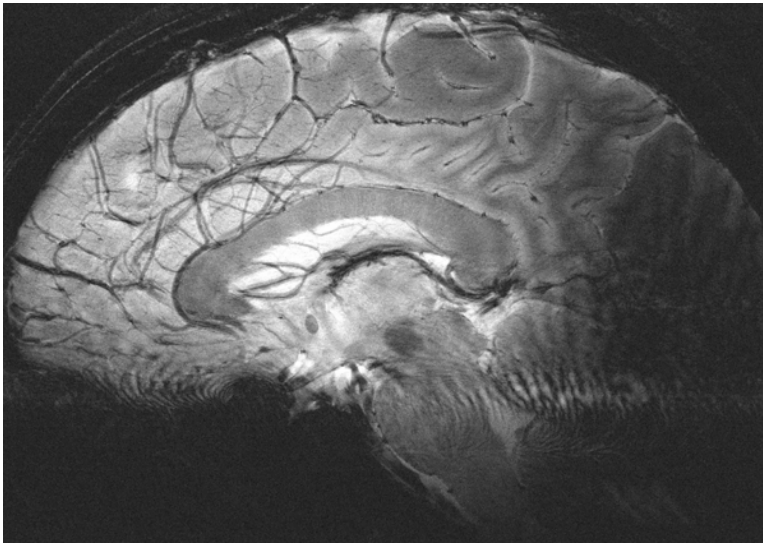


Figure 3. 8T gradient echo human image courtesy of P. Robitaille and colleagues of the Ohio State University (20 cm FOV, 2000 x 2000 gradient echo encoding).

2.2.1. Array Coils for Human Microimaging

While the advantages of performing MR experiments at higher magnetic fields are substantial, improved RF and gradient coil technology are equally necessary for improving the resolution of human imaging. Since the signal detection efficiency and noise characteristics of the RF receive coil improve as the coil becomes smaller and more tightly geometrically coupled to the anatomy of interest, reducing the size of the receive coil has always been a tool of the microimager [1,3]. At higher field strength, the use of small receive-only surface coils and a volume coil transmitter is even more advantageous for human microimaging, since power lost to tissue loading increases in proportion to the square of the frequency, and radiation losses rise as the fourth power of frequency and square of the coil's area [9,10]. Thus, both the loading and radiation effects increase dramatically with frequency and favor the use of smaller receive coils. The ability to cover the desired anatomy of interest (e.g., the human cerebrum) and the poor depth penetration of a single small surface coils has limited the ability to scale down the conventional surface coil receiver for human studies. Combining multiple receive surface coils into phased arrays of small coils extend the high-sensitivity detection of small-surface coils to substantially larger regions, including bilateral coverage of the brain. The phased array augments the coverage and sensitivity of surface coils by simultaneously receiving the MR signals from multiple small independent coils, each de-

signed to optimize the SNR in a small region adjacent to the coil. By combining the multiple receiver data digitally in a way that independently optimizes the SNR for each pixel in the combined image, a high SNR image is formed from a larger spatial region [11]. Figure 4 shows a photo of an 8-channel 3T coil of tightly fitting 8-cm diameter coil elements and a high-resolution 3T brain T_2 -weighted image acquired with the array. This coil performs up to 4-fold better than a conventional volume coil in areas under the coil elements, but 8 coils of this size are insufficient to cover the brain. While the phased array is already a proven choice for high SNR performance for 1.5 and 3T human imaging [11–13], its advantages are even more compelling at 7 T. Figure 5 shows a 7T human image obtained in clinical scan times (7 minutes) with an 8-channel coil similar to the 3T coil of Figure 4. At 330 μm in-plane resolution and 2-mm thick slices, the layer 4b myelination in the primary visual cortex is resolved as a stripe reduced in intensity (consistent with increased myelination in this layer) compared to the surrounding cortical layers.

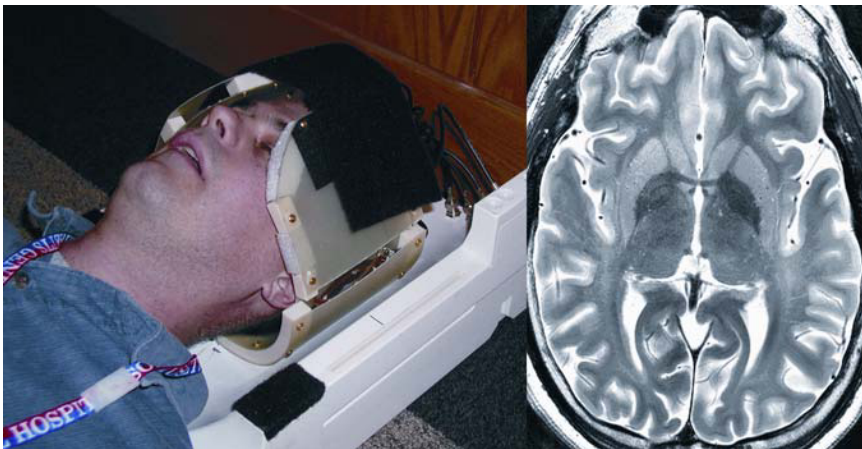


Figure 4. Photo of a 3T 8-channel receive-only array coil with its developer, Graham Wiggins, PhD of the A.A. Martinos Center at MGH. The coil, comprised of 8-cm diameter elements, provides wraparound coverage of a large area of cortex. High-resolution T_2 -weighted TSE image, 15 echoes, TR/TE = 1680/97 ms, FOV = 170 x 200 mm, 336 x 512 matrix (400 μm resolution), 3-mm slice, acq. time = 7:25 min. Image intensity normalized for surface coil drop-off. The SNR gain of this coil (compared to commercial birdcage headcoil) was fourfold in the near cortex and a factor of 1.3-fold in the center of the head. See attached CD for color version.

Most of the array development to date has used 4, 6, or 8 coils due to the limited number of receivers available on commercial MR systems. The desire for whole cerebrum coverage places a lower limit on the size of the receive element. Recently, however, the advantages of expanding beyond 8 channels have compelled several groups to construct and test “stand-alone” receiver systems with 16

and even 64 channels. Duyn and colleagues have demonstrated the benefit of a 16-channel system for 3T functional brain imaging with minimum integration with the imager [14]. With the 16-channel array, this group has produced what are probably the highest quality high-resolution functional EPI images to date. Zhu of General Electric explored two-directional SENSE acceleration in the torso with a prototype 32-channel system [15]. Finally, Wright et al. constructed a 64-channel system and linear surface array (penetrating ~ 1 cm) for a small-bore system to demonstrate 64-fold acceleration (encoding with a single readout gradient) [16]. The overall picture of these efforts has been to support the case that simultaneous acquisition strategies receive expanding benefits as the number of array elements is increased. The compelling data from these prototype efforts has quickly accelerated the availability of 32-channel receiver systems on clinical instruments with 1.5 and 3T 32-channel scanners currently being offered by the clinical manufacturers.

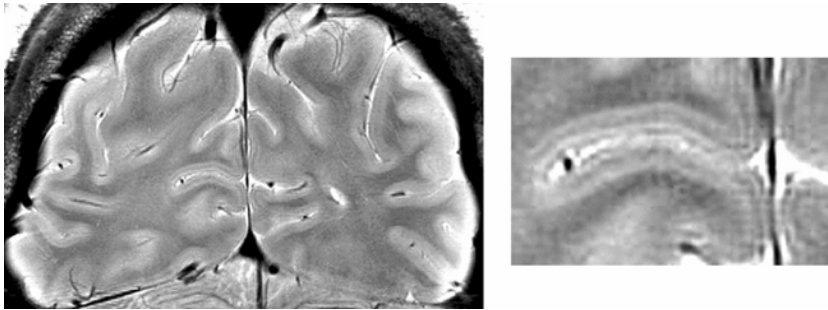


Figure 5. Coronal Turbo Spin Echo image of the human occipital pole obtained at 7 T using an 8-channel wraparound coil similar to that in Figure 4. The increased myelination band in layer IV (line of Gennari) can be visualized with a conventional clinical scan time (7 minutes). In plane resolution of $330 \mu\text{m}$ and 2-mm thick slices (220 nl voxel volumes).

2.2.2. Depth Penetration of Small-Array Coils

It is commonly considered that the size chosen for the individual array elements is governed by the drop-off in sensitivity with depth below the coil. In fact, other factors dominate this decision. The relatively large element diameters (10 cm and larger) used in current 1.5 and 3T arrays are driven by the need to cover the brain with the 8 receive channels typically available on most MRI scanners. The desire to produce images with uniform intensity distributions also biases the decision toward larger elements.

If a large number of receive channels are available, these two constraints are relaxed and a significantly different array configuration emerges that more resembles the push to micro-coils in MR microscopy. A large number of extremely small receive coils is favored to provide micro-coil-like sensitivity near the coil and full

coverage of the cerebrum. This arrangement of small coils is expected to provide less sensitivity in the center of the head, but still provide superior sensitivity in deep tissue compared with larger coils. Using the measurements of Hayes for a circular coil 0.6 cm above a loading half plane [17,18], an 8-cm diameter coil outperforms a 14-cm diameter coil by more than a factor of 2 at the location of the near cortex. For deeper cortex, such as the anterior cingulate and bottom of the calcarine fissure (~5 cm depth), the smaller coil still outperforms the larger one by 20%. The use of the phased array configuration tips the advantage even further toward smaller coils due to favorable benefits in combining the data if the noise between the individual array elements is uncorrelated. The combination of n channels with uncorrelated noise gives an SNR benefit that scales with the number of coils as $\text{SQRT}(n)$. This array advantage is diminished from this maximum due to the partially correlated nature of the noise in adjacent elements and the fact that not all coils detect a given voxel with equal sensitivity. Measurements of noise correlation in 23-, 32-, and 90-channel coils suggest that neighboring and next nearest neighbor coils have the highest noise correlation, but correlation coefficients rarely exceed 40%.

Two effects suggest that the array can do better at all depths than might be imagined at first glance. Because distant coils (e.g., on opposite sides of the head) are essentially uncoupled and have uncorrelated noise and because deep voxels are seen roughly equally well by all coils, the array gives a disproportional sensitivity boost from the “array $\text{SQRT}(n)$ advantage” exactly where it is most needed — the center of the head. Therefore the voxel at the center of the head has both the largest “effective n ” and the minimum reduction of the $\text{SQRT}(n)$ factor from noise correlation. Note that for a 90-channel array, even if half of the $\text{SQRT}(90)$ effect is achieved, this is an enormous boost in sensitivity. For voxels near the surface only the few nearby coils contribute significant signal, and these coils have the highest noise correlation due to their proximity to each other. But these locations enjoy high detection sensitivity due to their proximity to the small receive coils.

Simulation studies of large arrays as well as experience with 4-, 8-, and now 23-, 32-, and 90-brain-channel arrays has supported the picture that arrays of large number of small-diameter receive elements can be advantageous at all depths. Wright simulated sensitivity versus depth for a square array covering a given surface area utilizing either an 8 x 8 array (64 elements) or a 4 x 4, 2 x 2, or single coil (1 x 1), all covering the same area above a lossy half plane [19]. Thus the number of receivers were unconstrained and allowed to increase as needed to tile the region. The simulation showed two important findings. First, the sensitivity gain near the surface for the 8 x 8 array of small coils was substantial (nearly fourfold) compared to single or smaller n arrays. Second, with no limitation on number of elements, coil size was relatively unimportant at the deepest locations; arrays of larger coil sizes did not perform significantly better at deep locations. In fact, all of the arrays slightly outperformed the single element. Although the greatest sensitivity gain was near the surface as expected, the model showed that the maximum number of elements and minimum coil size was advantageous at all depths. Although the de-

coupling was assumed to be ideal due to perfectly implemented preamplifier decoupling, the model was planar and therefore could not take advantage of the minimal noise correlation from bilateral coverage of the head.

Figure 6 shows the first attempt to expand the brain array concept to 32 channels utilizing a 32-channel 3T scanner. Even with 32 receive channels, the coil elements had to be enlarged beyond to the size for optimum single-coil cortical imaging (~6 cm diameter) to provide whole-brain coverage. The 32-channel helmet array was found to have up to twofold higher SNR in the cortex and 1.3-fold higher sensitivity in the medial corpus callosum than a commercial 8-channel head array coil. A preliminary attempt to tile the head with smaller coils is shown in Figure 7. Here an additional 64 receive channels were added to a clinical 32-channel 1.5T scanner allowing a helmet to be constructed with 90 elements ranging in diameter from 4.5 to 5.5 cm.

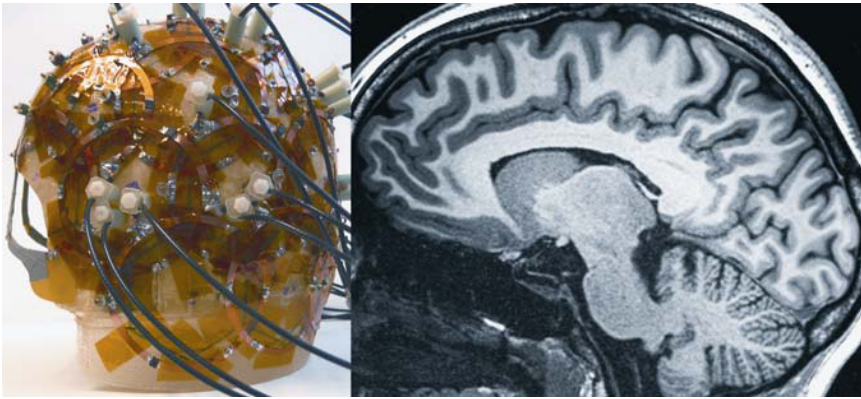


Figure 6. 32-channel array coil developed in collaboration with Graham Wiggins, PhD of the MGH, A.A. Martinos Center. Image resolution is 0.5 x 0.5 x 1 mm (250nl voxel volumes). See attached CD for color version.

3. MYELIN-BASED MICROIMAGING CORTICAL LAMINA

Some of the earliest successful attempts to divide the brain into anatomical and functional subunits were based on the cyto- and myelo-based architecture of the cortex [10,21]. Since the location of myelo and cyto architectonic boundaries can vary between individuals, noninvasive imaging of the laminar structure could augment functional studies by allowing direct comparison of anatomically and functionally defined regions. The use of myelination to delineate brain regions is particularly transferable to MR microimaging since the principal source of T_1 and T_2 contrast between gray and white matter in the living brain is the presence of myeli-

nated fibers. Thus either T_1 - or T_2 -weighted imaging is poised to provide information similar to that of myelin-stained material but potentially from a living individual.

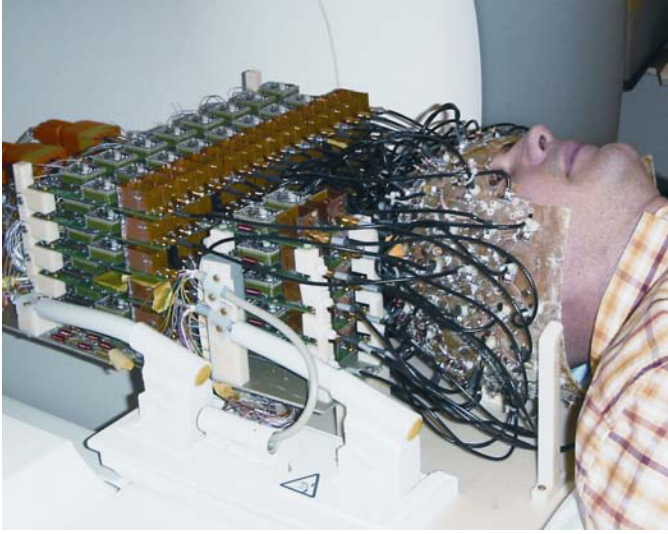


Figure 7. 90-channel array coil shown with its developer, Graham Wiggins, PhD of the MGH, A.A. Martinos Center. The extremely small elements can provide greatly increased sensitivity near the coil if they can maintain body-load dominance. The large number of non-interacting detectors can boost signal in the center of the head to exceed that of conventional detectors. See attached CD for color version.

The density and distribution of myelinated fibers vary as a function of depth from the cortical surface, giving rise to a distinct laminar appearance in the myelin-stained cortex. These structures are classified in 3–6 layers numbered starting from the cortex adjacent to the pial surface. The principal myelin features of these layers include [22]: Layer 1, characterized by the presence of tangential fibers of cortico-cortical connections and no cell bodies. Layer 2, the dysfibrous layer with few tangential fibers. Layer 3, weakly fibrous connections of the pyramidal neurons of layer 3. Layer 4, the heavily myelinated tangential fibers of the external band of Baillarger corresponding to the granular layer in Nissl-stained cortex. Layer 5, a weakly myelinated layer associated with the pyramidal cells. In some areas the deepest cortex in layer 5 contains the internal band of Baillarger consisting of horizontal fibers, and layer 6, which can contain both radial and horizontal populations of fibers. For example, in the primary visual cortex (V1 or area 17 of Brodmann), the myelin stained cortex shows a very prominently myelinated external band of Baillarger in layer 4 (stripe of Gennari) and a thinner section of relatively heavy myelination in layer 1 [22]. Figure 8 shows a proton density and T_2^* -weighted im-

age of a human ex-vivo brain hemisphere in the occipital pole region of an intact hemisphere obtained at 120- μm isotropic resolution in a human 7T scanner. This type of contrast clearly resolves the line of Gennari as an intermediate gray scale between that of gray matter and white matter and thus provides a high resolution 3D depiction of the borders of Brodmann area 17. Figure 9 shows the finer myelin structures of internal and external lines of Baillarger in human parietal lobe imaged at 150- μm isotropic resolution in a human 7T scanner.

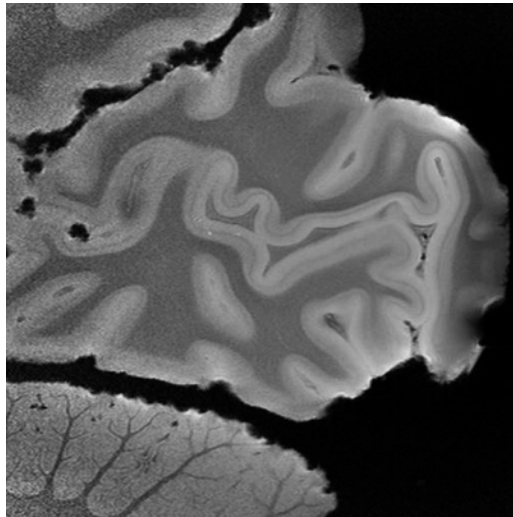


Figure 8. Sagittal section of the ex-vivo human occipital lobe from a 3D isotropic proton density-weighted FLASH scan acquired at 7 T with 120 μm isotropic resolution (1.7-nl voxel volume); acquisition time = 4 hours. Surface coil acquisition has been intensity normalized. The line of Gennari defining the Brodmann area 17 can be seen as an increase in myelin content (and thus a darker signal area) in the proton density-weighted scan.

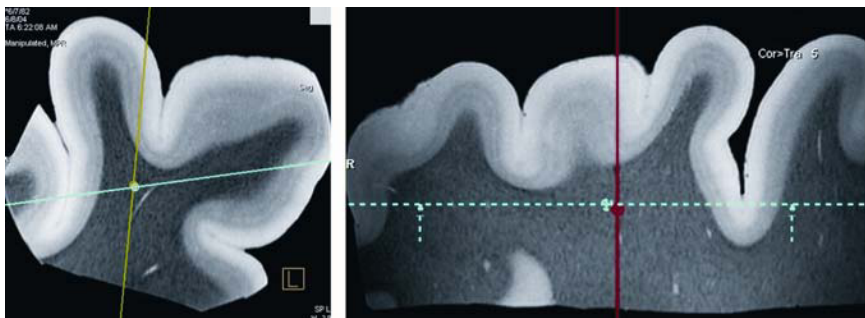


Figure 9. Reformatted section of the ex-vivo human parietal lobe from a 3D isotropic proton density and T_2 -weighted FLASH scan acquired at 7 T with 150- μm isotropic resolution (nominal voxel volume = 3.4 nl). TR/TE/flip angle = 55 ms/20 ms/10°, acquisition time = 1 hour. Myelin structures suggestive of the internal and external lines of Baillarger can be seen, especially in the thickened crowns of the gyrus. See attached CD for color version.

A goal of ultra high field microimaging technology is to supply sufficient spatial resolution and contrast-to-noise ratio to resolve the laminar and radial structures present. A rough estimate of the resolution needed for laminar imaging can be obtained by assuming the 6 lamina seen in myelin stained cortex are roughly evenly spaced and that the human cortex is roughly 2.5 mm thick. The Nyquist criterion requires at least 2 pixels in each lamina to minimally resolve its presence. Thus a 200- μm resolution image (orientated perpendicular to the cortical surface) with sufficient contrast-to-noise ratio is the minimum resolution expected to uncover the features of the myelin lamina given the simplistic assumption of equal thickness for the layers.

3.1. Primate Laminar Imaging

Several practical considerations make non-human primate imaging a natural proving ground for the ability of ultra high-field MR to ultimately resolve laminar features in humans. First, the cortical ribbon of non-human primates (such as the rhesus macaque) is only slightly thinner than that of the human brain. Thus, a resolution similar to that needed for human laminar imaging can resolve the macaque cortical lamina. But the considerably smaller brain volume of the macaque means that smaller, more sensitive RF detection coils can be used to cover the brain. This is especially beneficial for young animals lacking highly developed temporalis muscles. The smaller head size reduces the coil-brain distance, allowing the use of smaller-diameter and thus more sensitive array elements (e.g., 3–6-cm diameter coils). A more extreme extension of this approach is to remove the muscle and place an even smaller coil on the skull. For example, Logothetis and colleagues used an implanted surface coil to image primary visual cortex with voxel volumes as small as 11 nl [23] — a resolution approaching that obtainable in ex vivo human brain hemispheres. In addition to the coil benefits, the anesthetized animal can also be imaged for long periods of time with few motion artifacts. Finally, the simpler cortical folding pattern of the macaque brain facilitates analysis.

Figure 10 shows a T_1 map of the macaque visual cortex obtained from a human 7T horizontal bore imager and a single 5-cm diameter receive-only surface coil. T_1 values were constructed from a series of 8 inversion recovery Turbo Spin Echo (TSE) images with TI values ranging from 30 ms to 3 s (FOV = 100 mm, 512 x 512, resolution = 200 μm x 200 μm x 1 mm, 11-minute imaging time). The inversion time data were fit to the expected T_1 inversion recovery curve to generate a pixel-by-pixel T_1 map. The T_1 map shows clear differences, not only between gray and white matter, with their extreme myelination differences, but also a T_1 difference between layer 4 of the primary visual cortex and other layers. ROI analysis shows that the T_1 at 7 T for macaque striate cortex is 1360 ms for layers 2, 3, 5, and 6, and 1170 ms for layer 4 compared with 920 ms for white matter.

Somewhat higher spatial resolution can be obtained using a 3D T_1 -weighted imaging sequence in a 7T human imager. Figure 11 shows sagittal cuts from a 3D volume of 250 x 250 x 750 μm (46 nl) resolution MPRAGE images (FOV = 156 x

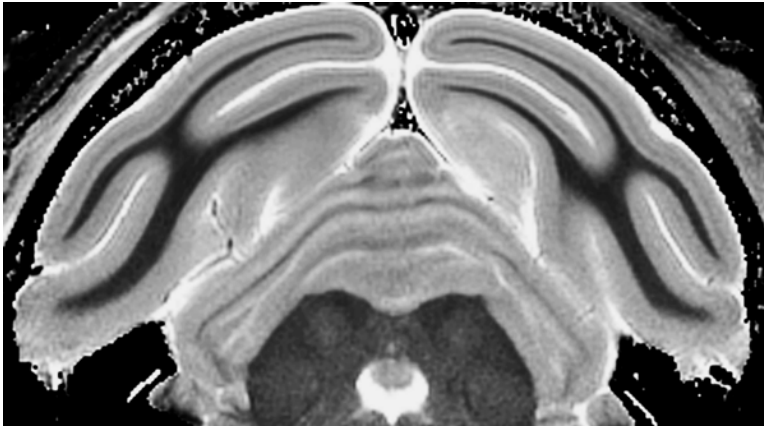


Figure 10. 7T macaque brain images. T_1 map at $200 \times 200 \times 1000 \mu\text{m}$ resolution (nominal voxel volume = 40 nl) computed from 8 inversion times in a 2D Turbo Spin Echo image. Grey, white, and V1 layer 4b T_1 values were found to be 1360, 920, and 1180 ms, respectively.

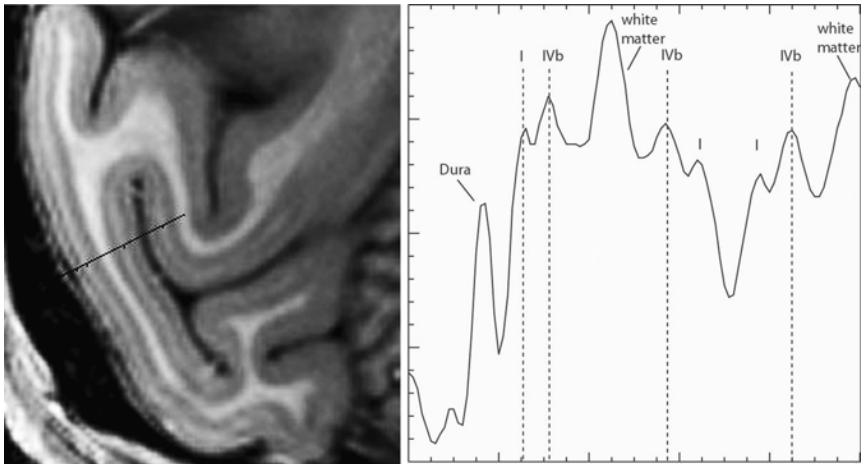


Figure 11. Sagittal detail from 7 Tesla 3D T_1 -weighted MPRAGE scan of in-vivo macaque brain. Resolution = $250 \times 250 \times 750 \mu\text{m}$ (voxel volume = 47 nl). Intensity profile from the line shown on the image showing increased signal intensity at the location expected for layers I and IVb. All images were acquired with 5-cm diameter receive-only and 10-cm diameter transmit-only surface coils.

156 x 72 mm, 512 x 512 x 96), TI/TR/TE = 1200/3300/3.3 ms). Imaging time was 21 minutes per run; 6 runs were averaged and the images were 2x zero-filled and normalized for surface coil drop-off. The volume T_1 images showed white matter SNR = 175 and gray-white CNR = 50. A similar study at 3 T with four averages produced SNR = 80 and gray-white CNR = 24. Features consistent with laminar structure was observed in area V_1 corresponding to the expected locations of myelinated layers in lamina 1 and 4. Figure 11 also shows an intensity profile through the primary visual cortex with the putative laminar features identified. The layer identified as lamina 1 appears to be ~3-fold thinner than layer 4 (line of Gennari) and also exhibits a smaller contrast differential from adjacent gray matter layers. Consistent with the T_1 measurements of Figure 10, layer 4 appears less myelinated than white matter. The V_1/V_2 border in this animal is putatively seen as the abrupt termination of the layer 4 myelination. Figure 12 shows the reproducibility of the layer 1 and 4 features across slices and across hemispheres.

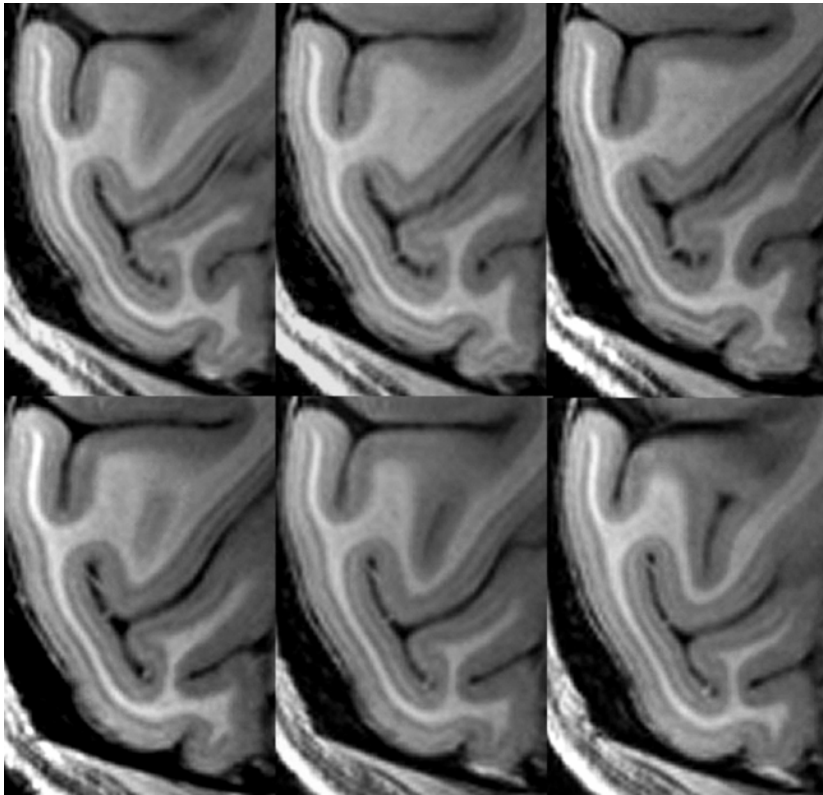


Figure 12. Sagittal detail from 7 Tesla 3D T_1 -weighted MPRAGE scan of in-vivo macaque brain showing reproducibility of the laminar features across slices and hemispheres. Resolution = 250 x 250 x 750 μm (voxel volume = 47 nl). All images were acquired with 5-cm diameter receive-only and 10-cm diameter transmit-only surface coils.

3.1.1. Gibbs Artifact

The Gibbs ringing phenomenon is a formable confounding factor of laminar imaging using Fourier encoding techniques. This phenomena occurs whenever the Fourier representation of a sharp edge feature in the image is truncated in the Fourier domain. Since MR sequences sample only a finite spatial frequency distribution (out to $1/\text{resolution}$), any edge in the object that is sharp compared to the nominal pixel size will be truncated, i.e., have significant Fourier components beyond the highest k -space values sampled. Thus, we expect Gibbs ringing for any object with structural features that are sharp compared to the image resolution unless some sort of spatial filter is applied to attenuate high spatial frequencies. The spatial filtering is undesirable since it reduces image resolution. Fortunately, Gibbs ringing has a characteristic appearance in the image. The primary effect is an 8% overshoot in signal intensity in the pixel adjacent to the edge and a quickly dying oscillatory behavior in subsequent pixels with a period of oscillation of 2 pixels. A common misconception of the Gibbs phenomena is that it is mitigated by large matrix sizes or that it is present only in the phase encode direction. In fact, it is present in non-spatial filtered Fourier imaging whenever a high-contrast feature is sharp compared to the pixel size, and it is a feature of Fourier encoding using either phase or frequency encoding methods. While motion artifacts typically produce a ringing artifact in the phase encode direction, unlike Gibbs ringing, artifactual edge ringing is preferentially in the phase encode direction and usually extends many oscillations.

Consider the sharp dark-to-bright step in the T_1 -weighted image seen at the boundary of the dark CSF space and brighter gray matter surface. The first pixel in the gray matter would be expected to be approximately 8% brighter followed by the next pixel, which will be somewhat darker than it would be in infinite resolution data. For the case where there are 2 pixels in each myelin layer of the cortex, this effect leads to a brightened first half of layer 1. The opposite effect is expected at the gray-white border. If the cortex is only a few pixels across, the oscillations from both boundaries (CSF-gray and gray-white) will interfere with each other. The worst case is constructive interference, which for the T_1 -weighted cortical image occurs when the cortex is exactly an even number of pixels across.

Since the Gibbs ringing phenomena can produce intensity artifacts that follow the CSF-gray and gray-white boundaries mimicking laminar structure within the cortex, it is useful to simulate the effect and compare the simulated Gibbs ringing with the observed intensity pattern. Figure 12 shows the results of this modeling. A high-resolution model of the monkey head was formed from the image itself by segmenting the image into gray, white, and CSF spaces. The segmentation model can be created at arbitrarily high resolution with exactly sharp boundaries. In Figure 13, the segmented region was created with sharp boundaries at 16x the image resolution. Each of regions was assigned the uniform pixel value of the in-vivo image. The high-resolution model was then taken into the Fourier space and truncated down to the resolution of the acquired image. Since the model contained no laminar features, the structure in the cortex is entirely due to Gibbs ringing. As

seen in Figure 13, the Gibbs ringing model showed false lamina, but with a considerably different pattern, width, and intensity than the observed structures.

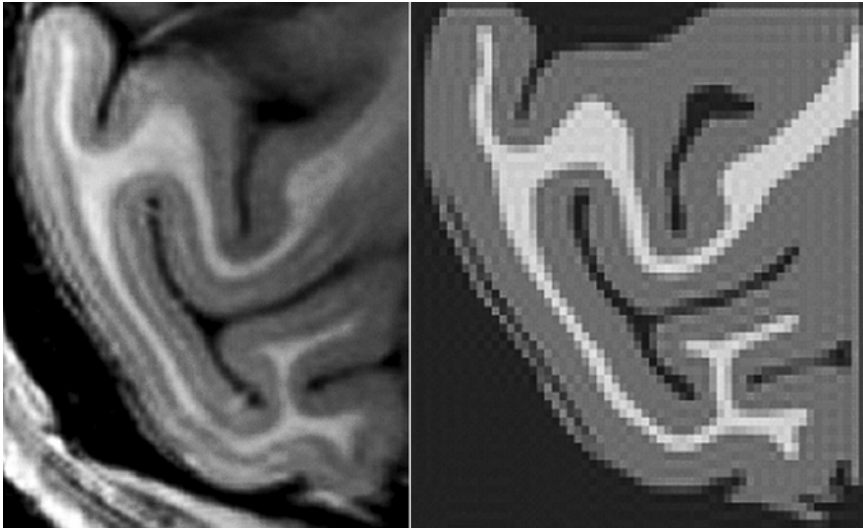


Figure 13. Original in-vivo data (left) and Gibbs simulation of macaque visual cortex. The Gibbs simulation consists of a high-resolution three-component model based on the original image, which was then truncated in the k -space domain to the resolution of the original image.

3.2. Human Laminar Imaging

Considerable progress has been made toward in-vivo resolution of prominent myelin features of the human cortex. The most conspicuous target is the line of Gennari in human the primary visual cortex. Several groups have shown a clear depiction of this myelinated lamina [24,25] including a correlation with functionally defined boundaries [26]. Other groups have noted hints of the myelin changes in primary auditory cortex (Heschel's gyrus) [27]. These initial studies clearly show that robustly imaging this function-specific laminar marker is within reach of human MRI. Improvements in field strength and array technology now allow definition of large laminar features such as the line of Gennari with conventional clinical length sequences. Figure 5 shows a 7T high-resolution ($330\ \mu\text{m} \times 330\ \mu\text{m} \times 2\ \text{mm} = 218\ \text{nl}$) Turbo Spin Echo image of the human occipital pole acquired in 7 minutes with an 8-channel phased array. The myelin-darkened layer 4 is seen in V_1 where the 2D slice is orthogonal to the cortical surface.

In addition to studying functional divisions in the brain, ultra high field MR offers the potential to resolve developmental disruption of the cortical lamina, and

in patients with focal epilepsies, to noninvasively identify epileptogenic lesions such as cortical dysplasias. High-resolution diagnostic evaluation of the cortex of patients poorly controlled by anticonvulsant therapies can have a significant impact in the selection of surgical candidates [28,29]. Figure 14 shows an example of a transmantle cortical dysplasia imaged with an array of small surface coils at 3 T. The cyto-architecture of this small region of cortex was likely disrupted during migration of the neuronal bodies, resulting in an abnormal number or distribution of myelinated cortical fibers. A cone-shaped region of increased T_1 and T_2 signal begins at the ventricular margin and extends to the depth of a sulcus.



Figure 14. Transmantle dysplasia — axial T_2 FSE (left) and axial MPRAGE, a thin section volumetric T_1 -weighted sequence (right) obtained with a 3T PA MRI. A cone-shaped region of increased T_2 signal begins at the ventricular margin and extends to the depth of a sulcus (arrow), seen as a more subtle region of decreased T_1 signal (arrow, right). Image courtesy of S. Knake and P.E. Grant, MGH Martinos Center. See attached CD for color version.

4. MICROIMAGING IN THE EX-VIVO HUMAN BRAIN

The ex-vivo brain provides a natural proving ground for technology designed to look for the next level of structure in human cortex. More importantly, it is directly comparable to a high-resolution gold standard — histology. Histologic staining of ex-vivo brain slices forms the historic basis for studying cortical structure culminating with the development of the detailed cyto- and myelo- architectonic maps that form the backbone of our current link between structure and function. While many of the features used to define cytoarchitecture appear to be too subtle to image unless cellular resolution could be achieved, laminar structures involving

substantial myelination differences and potentially even cell packing densities (which might lead to changes in relaxation rates or proton density) could be well suited to examination with MR. Exploitation of laminar differences in myelination are particularly attractive since the water relaxation properties of myelin form the basis for the contrast between gray and white matter in clinical brain imaging. Although the ultimate goal is in-vivo human imaging, microimaging the ex-vivo human brain provides an important test-bed for the abilities of the human ultra high field microimager. In addition to this "stepping stone" role, ex-vivo microimaging has the potential to complement conventional pathology in that it can readily acquire true 3D whole hemisphere images with isotropic resolution. The analysis of 3D volumes is a laborious task in traditional pathology, fraught with confounds from potential distortions and tears in multiple pathological sections required to form a volume study.

A handful of laboratories have examined the utility of MR microscopy for the study of ex-vivo human material and are obtaining promising findings [30–38]. A common approach is to image small samples of ex-vivo material at high resolution using small-bore microscopy or animal imagers, and then to correlate the imaging findings with true histologic and/or pathologic data. For example, early studies suggested that MR microscopy would be useful in identification of deep gray and brainstem nuclei [31] at resolutions approaching 50 μm . More recent studies have continued to push the resolution of MR microscopy while obtaining better SNR and larger image volumes. MR microscopy has been used to examine cortical cytoarchitecture, and research has found that MR signal intensity can vary inversely with cell density [36], suggesting that MRI will be useful in the construction of cytoarchitectonic atlases [33].

The relaxation properties of the fixed brain are altered compared to in vivo (shorter T_1) [39] and the potential for long, motion-free averaging makes higher resolutions easier to achieve than in vivo. For 3D FLASH imaging in the ex-vivo brain, the contrast between gray and white matter derives primarily from proton density (PD) and T_2^* differences, which provide the gray matter a higher signal intensity than white matter. Since T_1 weighting in the FLASH scan has the opposite gray and white contrast, it is desirable to minimize its effect. Shortening the T_1 of the tissue even further by soaking it in 1 mM gadopentate dimeglumine (Magnevist, Berlex Laboratories Inc) has been shown to be effective in improving the PD and T_2^* contrast since it allows more fully T_1 relaxed images to be taken with relatively short TRs, improving the contrast to noise ratio per unit time [40]. In addition, one can optimize over concentration, as shown in Figure 15. In this study, samples were imaged after being soaked in various concentrations of Gd. After imaging, the gray/white CNR was measured, and the optimal concentration was computed to be 1 mM. Interestingly, the optimum occurs because small concentrations apparently reduce or eliminate T_1 contrast while leaving PD and T_2^* contrast essentially unaffected. Given that the intrinsic T_1 differences in the tissue reduce the gray–white contrast in a PD or T_2^* -weighted image, the removal of T_1 contrast increases gray/white CNR. In a 1-mM solution, the optimum gray–white contrast at 7 T was

in FLASH imaging with $TR = 79$ ms, $TE = 18$ ms, and a flip angle of 24 degrees [40].

Although ultra high-resolution microscopy studies of small ex-vivo brain samples can be important, pathological imaging based on conventional light microscopy is very effective in this regime. If the ability of MR for volumetric analysis of large regions of the brain is to be exploited, human scale MR technology is needed. The ability of MR microscopic imaging to resolve features of functional regions such as the primary visual cortex based on myelination differences in the lamina was examined in Figure 9. This section from a proton density-weighted examination in a 7T human scanner was acquired with $120\text{-}\mu\text{m}$ isotropic resolution. The proton density weighting clearly resolves the line of Gennari in V_1 as an intermediate gray scale between that of gray matter and white matter and thus provides a high-resolution 3D depiction of the borders of Brodmann area 17. Figure 10 shows the finer myelin structures of internal and external lines of Baillarger in human parietal lobe imaged at $150\text{-}\mu\text{m}$ isotropic resolution in a human 7T scanner.

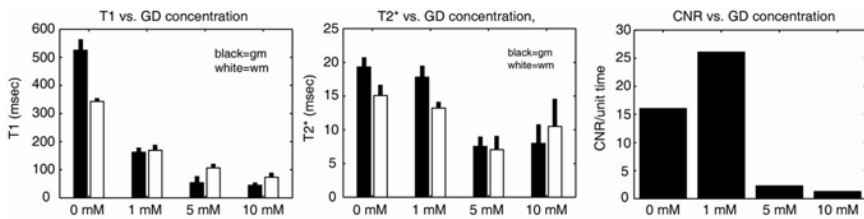


Figure 15. Effects of GD on (left to right) T_1 , PD, T_2^* , and optimal CNR for 0, 1, 5, and 10-mM concentrations.

4.1. Ex-Vivo Imaging in Alzheimer's Disease

The postmortem diagnosis of AD is based on the regional distribution of characteristic lesions including neuritic amyloid plaques and neurofibrillary tangles in limbic and association cortex [41–47]. Histological changes in the entorhinal cortex (EC) also occur early in the disease process [47–49]. In fact, even nondemented older adults occasionally show the required pathology for an AD diagnosis at autopsy [50]. Although still open to debate, a consensus is growing that such “incidental” changes represent the earliest (preclinical) stages of AD pathology, even in cognitively healthy adults [45,51]. Regional plaque and tangle deposition follows a characteristic spatiotemporal distribution in the brain [48,52]. These lesions appear earliest in entorhinal regions and progress to the hippocampal formation. The degeneration then progresses to temporo-parietal cortex and to prefrontal regions in later stages. Significant neuronal and synaptic loss accompanies the plaque and tangle deposition in limbic and association cortex [53–55].

4.1.1. *Imaging Plaques and Tangles in AD*

Attempting to resolve and characterize the burden and distribution of plaques and tangles is an obvious goal of high-resolution MR microimaging. Because plaques are expected to accumulate iron deposits [56] and magnetic disturbances like ferritin dephase MR signal forming a hypo-intense region larger than its actual size, T_2^* -weighted imaging has been suggested as a potential contrast mechanism for detecting plaques [57]. Others have successfully decorated the plaques with MR visible contrast agents to allow detection of plaques in high resolution ex-vivo [58,59] and in-vivo [59] microimages of transgenic mouse models. Recent work has also used ^{19}F MRI and a ^{19}F containing amyloidophilic Congo red type compound to visualize plaque in living mouse models of AD without the need to open the animal's blood brain barrier [60]. Recent high-resolution imaging of transgenic AD mouse models without contrast agent has shown that the plaques can be visualized with MR microimaging without contrast in this model [61,62]. A T_2 contrast better depicted the plaques both ex vivo [62] and in vivo [61]. Advanced work in MR microscopy in human ex-vivo samples has been performed by Benveniste et al. [63], who were able to differentiate the fimbria, granule, and molecular layers of the dentate gyrus, CA1, and other medial temporal structures using T_2^* contrast in ex-vivo human tissue. Most importantly, they were able to use T_2^* contrast to image neuritic plaques in vitro as hypo-intense spots using a voxel volume of 60 pL (39- μm isotropic voxels) with comparison to MK silver stained images of the same slices. Other studies, however, were not successful in seeing plaques on high-resolution T_2^* -weighted scans [64]. Jacobs and coworkers used an 11.7T microimager and 23.4- μm isotropic resolution and compared the 54 plaques seen in histological sections to the 6 hypo-intense spots on the MR slice. Only the largest (100- μm diameter) plaques corresponded to an MR visible hypo-intense area. Many MR hypo-intense spots seemed to correspond to blood vessels, but were not elongated like vessels. Presumably these features were due to blood clots. In all of the mouse and human work, MR detected signal abnormalities similar to plaques were seen that were not seen on histology. Additionally, many plaques identified on histology were not apparent on MR even though these histologically detected plaques appeared to be comparable in size to the other plaques that were resolved by MR.

4.1.2. *Medial Temporal Lobe Imaging*

In addition to resolving plaques and tangles directly, alterations of the substructure of the regions effected early in the disease could be a valuable tool for assessing disease progression and treatment. In the case of AD, this translates to improved resolution of the structures of the hippocampus and MTL — complex regions with a great deal of cytoarchitectonic substructure. The pathology of the EC is of particular interest since AD pathology might originate in specific layers of this multimodal cortex. The EC receives direct projections from the frontal, occipital, parietal, and other regions of temporal cortex, and provides the majority of input from these regions to the hippocampus, serving as a gateway for neocortical

information, presumably in part for memory processing. Profound degeneration of EC layer II, the entorhinal output layer to the hippocampus through the perforant pathway, is found early in the disease and results in isolation of the hippocampus from the neocortex [47]. Thus, in addition to hippocampal formation, identification of alterations in the perforant pathway and differentiation of layers within the EC would be very useful in detecting AD pathology in the earliest stages.

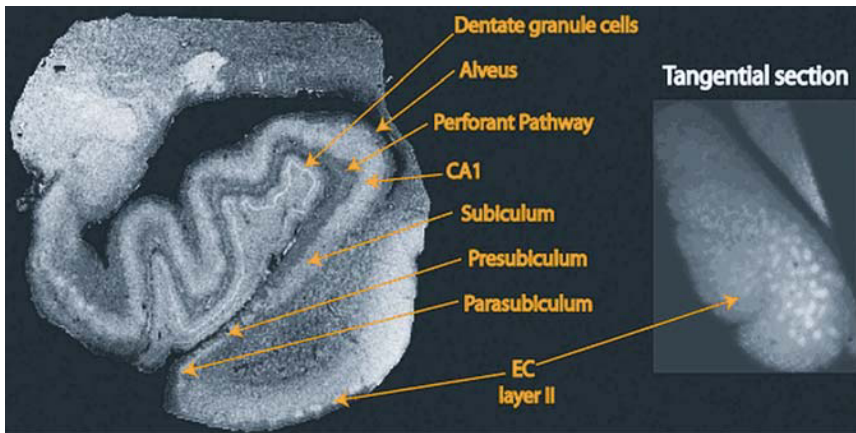


Figure 16. Image of the ex-vivo MTL (left) acquired at 7 T with 100 μm isotropic voxels (TR = 20, TE = 5, flip = variable). Nominal voxel volume = 1 nl. Right: oblique slice through layer II of EC showing the layer II islands as brighter regions. Layers in the CA fields of the hippocampus and the dentate gyrus are clearly visible. Image in collaboration with Jean Augustinack, PhD and Megan Blackwell. See attached CD for color version.

High-resolution studies of the ex-vivo temporal lobe (Figure 16) suggest that the subregions of the hippocampal formation could potentially be differentiated using in-vivo neuroimaging techniques due to their differing histological profiles. For example, the dentate gyrus is a region of densely packed granule cells while the bordering CA3 is a region of less dense pyramidal cells. The perforant pathway is a large projection arising from much of the EC. Additionally, it is possible that pathologic features could alter selected regional MR parameters in tissue that are vulnerable to degeneration, thereby highlighting regional features. For example, the CA1 subfield of the hippocampus is particularly vulnerable to degeneration in AD as well as other conditions such as ischemia, compared to other subfields, and such damage is clearly visible on histological sections.

Early ex vivo imaging of the hippocampus demonstrated an age-related decrease of an area of signal intensity corresponding to the perforant path [37]. Contrary to expectations, T_2 relaxation time was not a useful indicator of subfield anatomy or the presence of AD. Still, more recent studies suggest that these techniques are, in fact, useful for measuring AD-related pathology. Gilissen et al. [65] found that there was an age-related enhancement of iron-dependent contrast in regions of the brain mirroring regions of AD pathology in the mouse lemur (the only known

animal that shows an age-related increase in senile plaques and neurofibrillary degeneration).

Recent work bringing whole-body 7T MRI to bear on advancing MR microscopy of excised human temporal lobes has demonstrated the ability to delineating the granular cell layers of the dentate, the perforant pathway and other features of the MTL (Figure 16). Additionally, layer II cell "islands" dense with large stellate nuclei could be directly visualized in layer II of EC [66]. The axons of these cells give rise to the perforant pathway, which forms the major source of neocortical input to the hippocampus. Clinically, this is a critical region in the study of AD, as 60% of the cells in layer II have atrophied in the mildest stage of AD [67]. Image volumes were acquired using 3D 100- μm nominal resolution isotropic FLASH imaging with varying flip angles (10, 20, and 30°, two acquisitions each). These were used to estimate T_1 and PD of the underlying tissue, and an image with $\alpha = 23^\circ$ was synthesized and determined to be optimal for gray/white contrast [68]. A number of MTL structures are immediately apparent in Figure 16, including various lamina in the hippocampus and the dentate gyrus as well as the layer II islands in the EC. Further investigation reveals that these putative islands match what is known histologically in terms of their width, depth, and spacing [66]. The volumetric MR was also sliced tangential to the entorhinal cortex at the location of the islands is also shown in Figure 16, indicating how robust the islands are in these images, and opening up the possibility of performing neuropathological analysis with MRI. For example, with proper manipulation of the 3D postmortem MR, a count of the number of islands that occurs in EC could be obtained — a measure that is currently exceedingly labor intensive with conventional pathological evaluation.

From a qualitative standpoint, an example of the similarity in terms of information content between the histological images and the MR ones is given in Figure 17 that shows a block face image (left), a Nissl stain (center), and a high-resolution MRI of the medial temporal lobe as described before. The similarity of the Nissl and MR images raises the possibility of measuring bulk histological properties directly using MRI, which would allow such measures to be automated and carried out over the entire brain.



Figure 17. Example of a block face image (left), a Nissl stain (center), and a high-resolution MRI (right, 7 T), same as Figure 16. See attached CD for color version.

5. CONCLUSIONS

The development of MR microscopy methods to noninvasively image small-scale structure in living humans has achieved a number of important benchmarks. Advances in ultra high field human imagers and dedicated surface coil receivers has started to bridge the gap between what is possible in small-sample and animal microimagers and what is possible in human-sized instruments. The current generation of instrumentation allows in-vivo imaging of the cortex at a resolution sufficient to robustly visualize the most prominent cortical laminar features in the primate brain such as the line of Gennari in the primary visual cortex as well as subtle pathology of the cortex such as small dysplasias in humans and amyloid plaques in transgenic mice. While for many in-vivo human imaging will remain the ultimate goal, ex-vivo imaging of the human brain hemisphere illustrates the road ahead for human-scale MR microimaging technology. While the development of contrast "stains" for ex-vivo MR is in its infancy, a wealth of laminar and nuclear structure can be readily visualized at a 100- μm resolution, including cyto-architectural features such as the islands of large stellate and pyramidal neurons in layer 2 of the entorhinal cortex.

6. REFERENCES

1. Ciobanu L, Webb AG, Pennington CH. 2003. Magnetic resonance imaging of biological cells. *J Prog NMR Spectrosc* **42**:69–93.
2. Ahrens ET, Narasimhan PT, Nakada T, Jacobs RE. 2002. Small animal neuroimaging using magnetic resonance microscopy. *Prog NMR Spectrosc* **40**:275–306.
3. Webb AG. 1997. Radiofrequency microcoils in magnetic resonance. *Prog NMR Spectrosc* **31**:1–42.
4. Gati JS, Menon RS, Ugurbil K, Rutt BK. 1997. Experimental determination of the BOLD field strength dependence in vessels and tissue. *Magn Reson Med* **38**(2):296–302.
5. Ugurbil K, Garwood M, Ellermann J, Hendrich K, Hinke R, Hu X, Kim SG, Menon R, Merkle H, Ogawa S. 1993. Imaging at high magnetic fields: initial experiences at 4 T. *Magn Reson Q* **9**(4):259–277.
6. Robitaille PML, Abduljalil AM, Kangarlu A. 2000. Ultra high resolution imaging of the human head at 8 tesla: 2K x 2K for Y2K. *J Comput Assist Tomogr* **24**(1):2–8.
7. Robitaille PML, Abduljalil AM, Kangarlu A, Zhang X, Yu Y, Burgess R, Bair S, Noa P, Yang L, Zhu H, Palmer B, Jiang Z, Chakeres DM, Spigos D. 1998. Human magnetic resonance imaging at 8 T. *NMR Biomed* **11**(6):263–265.
8. Vaughan JT, Garwood M, Collins CM, Liu W, DelaBarre L, Adriany G, Andersen P, Merkle H, Goebel R, Smith MB, Ugurbil K. 2001. 7T vs. 4T: RF power, homo-

- geneity, and signal-to-noise comparison in head images. *Magn Reson Med* **46**(1):24–30.
9. Hoult DI, Lauterbur PC. 1979. The sensitivity of the zeugmatographic experiment involving human samples. *J Magn Reson* **34**:425.
 10. Carlson JW. 1989. Power deposition and noise correlation in NMR samples. *Magn Reson Med* **10**(3):399–403.
 11. Roemer PB, Edelstein WA, Hayes CE, Souza SP, Mueller OM. 1990. The NMR phased array. *Magn Reson Med* **16**(2):192–225.
 12. Hayes CE, Hattes N, Roemer PB. 1991. Volume imaging with MR phased arrays. *Magn Reson Med* **18**(2):309–19.
 13. Wald LL, Carvajal L, Moyher SE, Nelson SJ, Grant PE, Barkovich AJ, Vigneron DB. 1995. Phased array detectors and an automated intensity-correction algorithm for high-resolution MR imaging of the human brain. *Magn Reson Med* **34**(3):433–439.
 14. Ledden PJ, Zwart J, Gelderen P, Bodurka J, Duyn J. 2003. Sixteen channel gapped SENSE array for brain imaging at 3T. *Proc Int Soc Magn Reson Med* 466.
 15. Zhu Y, Hardy C, Giaquinto R, Rohling K, Dumoulin C, Sodickson DK, Ohliger M, Darrow R, Kenwood G. 2003. Highly parallel volumetric imaging with accelerated spatial encoding along two dimensions. *Proc Int Soc Magn Reson Med* 22.
 16. Wright SM, McDougall M, Brown D. 2003. Single echo acquisition (SEA) MR imaging. *Proc Int Soc Magn Reson Med* 23.
 17. Hayes CE, Axel L. 1985. Noise performance of surface coils for magnetic resonance imaging at 1.5 T. *Med Phys*. **12**(5):604–607.
 18. Lawry TJ, Weiner MW, Matson GB. 1990. Computer modeling of surface coil sensitivity. *Magn Reson Med* **16**(2):294–302.
 19. Wright SM, Wald LL. 1997. Theory and application of array coils in MR spectroscopy. *NMR Biomed* **10**(8):394–410.
 20. Brodemann K. 1909. Vergleichende Localisationslehre der Grosshirnrinde in ihren Prinzipien dargestellt auf Grund des Zellebaus. Leipzig: Barth.
 21. Vogt C, Vogt O. 1919. Allgemeiner Ergebnisse unserer Hirnforschung. *J Psychol Neurol* **25**:399–462.
 22. Annese J, Pitiot A, Dinov ID, Toga AW. 2004. A myelo-architectonic method for the structural classification of cortical areas. *Neuroimage* **21**(1):15–26.
 23. Logothetis N, Merkle H, Augath M, Trinath T, Ugurbil K. 2002. Ultra high-resolution fMRI in monkeys with implanted RF coils. *Neuron* **35**(2):227–242.
 24. Barbier EL, Marrett S, Danek A, Vortmeyer A, van Gelderen P, Duyn J, Bandettini P, Grafman J, Koretsky AP. 2002. Imaging cortical anatomy by high-resolution MR at 3.0T: detection of the stripe of Gennari in visual area 17. *Magn Reson Med* **48**(4):735–738.

25. Clark VP, Courchesne E, Grafe M. 1992. In vivo myeloarchitectonic analysis of human striate and extrastriate cortex using magnetic resonance imaging. *Cereb Cortex* **2**(5):417–424.
26. Bridge H, Clare S, Jenkinson M, Jezzard P, Parker AJ, Mathews PM. 2005. Independent anatomical and functional measures of the V1/V2 boundary in human visual cortex. *J Vision* **5**:93–102.
27. Yoshiura T, Higano A, Rubio A, Shrier DA, Kwok WE, Iwanaga S, Numaguchi Y. 2000. Heschl and superior temporal gyri: low signal intensity of the cortex on T_2 -weighted MR images of the normal brain. *Radiology* **214**(1):217–221.
28. Grant PE, Barkovich AJ, Wald LL, Dillon WP, Laxer KD, Vigneron DB. 1997. High-resolution surface-coil MR of cortical lesions in medically refractory epilepsy: a prospective study. *Am J Neuroradiol* **18**(2):291–301.
29. Grant PE, Vigneron DB, Barkovich AJ. 1998. High-resolution imaging of the brain. *Magn Reson Imag Clin N Am* **6**:139–154.
30. Johnson GA, Cofer GP, Gewalt SL, Hedlund LW. 2002. Morphologic phenotyping with MR microscopy: the visible mouse. *Radiology* **222**:789–793.
31. Johnson GA, Thompson MB, Drayer BP, Bone SN. 1986. Magnetic resonance microscopy in neurologic models. *Acta Radiol Suppl* **369**:267–268.
32. Eccles CD, Callaghan PT. 1986. High resolution imaging: the NMR microscope. *J Magn Reson Imag* **68**:393–398.
33. Zilles K, Schlaug G, Matelli M, Luppino G, Schleicher A, Qu M, Dabringhaus A, Seitz R, Roland PE. 1995. Mapping of human and macaque sensorimotor areas by integrating architectonic, transmitter receptor: MRI and PET data. *J Anat* **187**:515–537.
34. Zhou X, Magin RL, Alameda JC, Reynolds HA, Lauterbur PC. 1993. Three-dimensional NMR microscopy of rat spleen and liver. *Magn Reson Med* **30**(1):92–97.
35. Van der Linden A, Verhoye M, Van Audekerke J, Peeters R, Eens M, Newman SW, Smulders T, Balthazart J, DeVoogd TJ. 1998. Non invasive in vivo anatomical studies of the oscine brain by high resolution MRI microscopy. *J Neurosci Methods* **81**(1–2):45–52.
36. Fatterpekar GM, Naidich TP, Delman BN, Aguinaldo JG, Gultekin SH, Sherwood CC, Hof PR, Drayer BP, Fayad ZA. 2002. Cytoarchitecture of the human cerebral cortex: MR microscopy of excised specimens at 9.4 Tesla. *Am J Neuroradiol* **23**(8):1313–1321.
37. Huesgen CT, Burger PC, Crain BJ, Johnson GA. 1993. In vitro MR microscopy of the hippocampus in Alzheimer's disease. *Neurology* **43**(1):145–152.
38. Augustinack JC, van der Kouwe AJW, Blackwell ML, Salat DH, Wiggins CJ, Frosch MP, Wiggins GC, Potthast A, Wald LL, Fischl BR. 2005. Detection of entorhinal layer, II: using 7 Tesla magnetic resonance imaging. *Ann Neurol* **57**(4):489–494.

39. Tovi M, Ericsson A. 1992. Measurements of T_1 and T_2 over time in formalin-fixed human whole-brain specimens. *Acta Radiol* **33**(5):400–404.
40. Blackwell ML, Rosen BR, Farrar CT, Augustinack JC, van der Kouwe AJW, Salat DH, Wald LL, Fischl B. 2005. Optimization of extrinsic proton staining methods for ex vivo cytological magnetic resonance imaging. *Proc Int Soc Magn Reson Med*. In press.
41. Terry RD, Katzman R. 1983. Senile dementia of the Alzheimer type. *Ann Neurol* **14**(5):497–506.
42. Perry G, Selkoe DJ, Block BR, Stewart D, Autilio-Gambetti L, Gambetti P. 1986. Electron microscopic localization of Alzheimer neurofibrillary tangle components recognized by an antiserum to paired helical filaments. *J Neuropathol Exp Neurol* **45**(2):161–168.
43. Rogers J, Morrison JH. 1985. Quantitative morphology and regional and laminar distributions of senile plaques in Alzheimer's disease. *J Neurosci* **5**(10):2801–2808.
44. Arnold SE, Hyman BT, Flory J, Damasio AR, Van Hoesen GW. 1991. The topographical and neuroanatomical distribution of neurofibrillary tangles and neuritic plaques in the cerebral cortex of patients with Alzheimer's disease. *Cereb Cortex* **1**(1):103–116.
45. Hyman BT. 1997. The neuropathological diagnosis of Alzheimer's disease: clinical-pathological studies. *Neurobiol Aging* **18**(4 Suppl):S27–32.
46. Arriagada PV, Growdon JH, Hedley-Whyte ET, Hyman BT. 1992. Neurofibrillary tangles but not senile plaques parallel duration and severity of Alzheimer's disease. *Neurology* **42**(3 Pt 1):631–639.
47. Gomez-Isla T, Price JL, McKeel DW, Morris JC, Growdon JH, Hyman BT. 1996. Profound loss of layer II entorhinal cortex neurons occurs in very mild Alzheimer's disease. *J Neurosci* **16**(14):4491–4500.
48. Braak H, Braak E. 1991. Neuropathological staging of Alzheimer-related changes. *Acta Neuropathol* **82**(4):239–259.
49. Giannakopoulos P, Hof PR, Michel JP, Guimon J, Bouras C. 1997. Cerebral cortex pathology in aging and Alzheimer's disease: a quantitative survey of large hospital-based geriatric and psychiatric cohorts. *Brain Res Brain Res Rev* **25**(2):217–245.
50. Katzman R, Terry R., DeTeresa R, Brown T, Davies P, Fuld P, Renbing X, Peck A. 1988. Clinical, pathological, and neurochemical changes in dementia: a subgroup with preserved mental status and numerous neocortical plaques. *Ann Neurol* **23**(2):138–144.
51. Berg L, McKeel DW, Miller JP, Storandt M, Rubin EH, Morris JC, Baty J, Coats M, Norton J, Goate AM, Price JL, Gearing M, Mirra SS, Saunders AM. 1998. Clinicopathologic studies in cognitively healthy aging and Alzheimer's disease: relation of histologic markers to dementia severity, age, sex, and apolipoprotein E genotype. *Arch Neurol* **55**(3):326–335.

52. Braak H, Braak E. 1997. Staging of Alzheimer-related cortical destruction. *Int Psychogeriatr* **9**(Suppl 1):257–261 and 269–272.
53. Ball MJ. 1977. Neuronal loss, neurofibrillary tangles and granulovacuolar degeneration in the hippocampus with ageing and dementia: a quantitative study. *Acta Neuropathol (Berlin)* **37**(2):111–118.
54. Terry RD, Peck A, DeTeresa R, Schechter R, Horoupian DS. 1981. Some morphometric aspects of the brain in senile dementia of the Alzheimer type. *Ann Neurol* **10**(2):184–192.
55. Mountjoy CQ, Roth M, Evans NJ, Evans HM. 1983. Cortical neuronal counts in normal elderly controls and demented patients. *Neurobiol Aging* **4**(1):1–11.
56. Grundke-Iqbal I, Fleming J, Tung YC, Lassmann H, Iqbal K, Joshi JG. 1990. Ferritin is a component of the neuritic (senile) plaque in Alzheimer dementia. *Acta Neuropathol (Berlin)* **81**(2):105–110.
57. Budinger TF. 1994. Future research in Alzheimer's disease using imaging techniques. *Neurobiol Aging* **15**(Suppl 2):S41–48.
58. Poduslo JF, Wengenack TM, Curran GL, Wisniewski T, Sigurdsson EM, Macura SI, Borowski BJ, Jack CR. 2002. Molecular targeting of Alzheimer's amyloid plaques for contrast-enhanced magnetic resonance imaging. *Neurobiol Dis* **11**(2):315–329.
59. Wadghiri YZ, Sigurdsson EM, Sadowski M, Elliott JI, Li Y, Scholtzova H, Tang CY, Aguinaldo G, Pappolla M, Duff K, Wisniewski T, Turnbull DH. 2003. Detection of Alzheimer's amyloid in transgenic mice using magnetic resonance microimaging. *Magn Reson Med* **50**(2):293–302.
60. Higuchi M, Iwata N, Matsuba Y, Sato K, Sasamoto K, Saido T. 2005. ^{19}F and ^1H MRI detection of amyloid B plaques in vivo. *Nat Neurosci* **8**(4):527–533.
61. Jack CR, Garwood M, Wengenack TM, Borowski B, Curran GL, Lin J, Adriany G, Grohn OH, Grimm R, Poduslo JF. 2004. In vivo visualization of Alzheimer's amyloid plaques by magnetic resonance imaging in transgenic mice without a contrast agent. *Magn Reson Med* **52**(6):1263–1271.
62. Lee SP, Falangola MF, Nixon RA, Duff K, Helpem JA. 2004. Visualization of beta-amyloid plaques in a transgenic mouse model of Alzheimer's disease using MR microscopy without contrast reagents. *Magn Reson Med* **52**(3):538–544.
63. Benveniste H, Einstein G, Kim KR, Hulette C, Johnson GA. 1999. Detection of neuritic plaques in Alzheimer's disease by magnetic resonance microscopy. *Proc Natl Acad Sci USA* **96**(24):14079–14084.
64. Dhenain M, Privat N, Duyckaerts C, Jacobs RE. 2002. Senile plaques do not induce susceptibility effects in T_2^* -weighted MR microscopic images. *NMR Biomed* **15**(3):197–203.
65. Gilissen EP, Jacobs RE, Allman JM. 1999. Magnetic resonance microscopy of iron in the basal forebrain cholinergic structures of the aged mouse lemur. *J Neurol Sci* **168**(1):21–27.

66. Augustinack JC, van der Kouwe AJW, Salat D, Wald LL, Blackwell M, Wiggins C, Fischl B. 2004. Detection of entorhinal islands using 7T MRI. Paper presented at Human Brain Mapping 2004. Poster MO288.
67. Hyman BT, Van Hoesen GW, Damasio AR, Barnes CL. 1984. Alzheimer's disease: cell-specific pathology isolates the hippocampal formation. *Science* **225** (4667):1168–1170.
68. Fischl B, et al. 2005. *NeuroImage*. In press.

IN-VIVO NMR SPECTROSCOPY OF THE BRAIN AT HIGH FIELDS

Rolf Gruetter^{1,2}, Pierre-Gilles Henry¹, Hongxia Lei¹,
Silvia Mangia¹, Gülin Öz¹, Melissa Terpstra¹, and Ivan Tkac¹

*Departments of Radiology¹ and Neuroscience²,
University of Minnesota, Minneapolis*

1. INTRODUCTION

Increased magnetic fields in principle provide increased sensitivity and specificity. In vivo, however, the increase in magnetic field alone does not automatically result in obvious improvements. Among the factors that are set to impede the improvements in sensitivity for in-vivo NMR spectroscopy are the increased challenges in eliminating the macroscopic inhomogeneities caused by mainly the air-tissue interface and increased RF power requirements. Changes in relaxation times may in addition adversely affect the increases in sensitivity, as T_1 tends to increase and T_2 tends to decrease with higher magnetic field. In the past 10 years at field strengths of 4 Tesla and higher, we have delineated technical advances that have permitted garnering the advantages of higher field, resulting in substantial gains for ^1H and ^{13}C NMR spectroscopy. The improvements can be broadly classified into increased sensitivity, leading to smaller volumes and shorter acquisition times and increased specificity, leading to the detection of many novel compounds. In dynamic ^{13}C NMR it was shown that, in addition to measuring the label incorporation into several positions of many compounds, the time-resolved measurement of isotopomers was possible in the brain in vivo, leading to dynamic isotopomer analysis, a fusion of previously existing techniques. Improvements in sensitivity further advanced the use of localization in ^{13}C NMR spectroscopy, which was critical in detection of brain glycogen metabolism in humans and rodents. Advances in ^1H NMR spectroscopy permitted the precise measurement of an array of neurochemicals, ranging from Vitamin C, to glutathione, to glutamine, resulting in an extensive neurochemical profile of different extent that can be measured, e.g., in the unilateral mouse hippocampus, and human substantia nigra. In addition, at high field the simultaneous but separate measurement of PCr and Cr was shown to be possible. Sensitivity gains allowed minimization of the detrimental effects of motion by single-scan phase and frequency correction, as well as measurement of the

neurochemical profile in individuals. In summary, high field ultimately provides NMR spectroscopy with the power to measure highly specific changes in unilateral regions in individual subjects, making it a powerful investigative tool, ideally suited to study pathogenesis and therapy monitoring of disease in humans and animal models, as well as normal brain function. The high specificity of NMR spectroscopy at high fields is likely to result in new insights and improved treatment of human disease.

This chapter first reviews the solutions to some technological challenges at high B_0 , then reviews the methodologies of ^{13}C and ^1H NMR spectroscopy at high field, and then briefly reviews some of the biomedical problems uniquely addressed at high field. Current applications that will be reviewed include neurodegenerative diseases, diabetes, and mice.

2. GENERAL SENSITIVITY CONSIDERATIONS

It is well known that increasing the static field B_0 increases the sensitivity of NMR detection [1]. The increase in sensitivity for non-loading samples has been reported as being an exponential function of B_0 , which can be written as

$$S/N \propto B_0^\beta.$$

From theoretical considerations, it is clear that the signal S increases with B_0^2 , hence β must be 2 or lower, amounting to an upper limit for the gains in sensitivity achievable due to increases in B_0 alone. Even when the noise present in the RF coil is the dominant source of noise, its root-mean-square amplitude may increase with frequency (B_0), and it is generally accepted that in this case $\beta = 1.75$. For in-vivo spectroscopy, however, the sample is the most dominant source of noise, and thus the noise detection efficiency increases with frequency, and thus the sensitivity increase with B_0 is closer to linearity with $\beta \sim 1$. Because the sample may not be a completely dominant source of noise, it is plausible that in vivo β may lie somewhere between 1 and 1.75. In practice β is probably closer to the former. In this discussion it was assumed that resonance linewidths and relaxation times are very similar between the different field strengths. An increase in resonance linewidth can offset some of the sensitivity gains, as can an increase in longitudinal relaxation time, although both effects influence sensitivity only with the square root of T_1 or T_2^* . Given that the sensitivity decreases only with $T_1^{-1/2}$ and that T_1 appears to increase at most modestly with B_0 , T_1 relaxation is unlikely to substantially affect the sensitivity. In contrast, proton T_2 decreases with B_0 quite markedly, which will diminish the sensitivity advantage at long echo times [2].

Lastly, increased spectral resolution can result in increased sensitivity due to decreased signal overlap. Although spectral overlap may in general not be a problem for direct-detected ^{13}C NMR spectroscopy, the spectral region of the C2 of amino acids and the overlap between GABA C2 and glutamate C4 stand to gain from increased spectral resolution.

For ^1H NMR spectroscopy, spectral overlap is a much more prevalent problem, and increases in spectral resolution, expressed in ppm, may very well offset de-facto increases in intrinsic linewidth, expressed in Hz. For example, in the adult human brain (gray matter) the singlet linewidths are at 1.5 Tesla, typically ~ 3 Hz (0.05 ppm), and at 4 Tesla 7 Hz (0.04 ppm), whereas at 7 T singlet linewidths are approximately 10 Hz (0.03 ppm). The novel ability of ^1H NMR to resolve PCr from Cr at 9.4 T [3–6] illustrates the ability of increased spectral resolution to help detect new resonances. Furthermore, substantial gains in sensitivity are expected for quantification of signals from more weakly represented metabolites, of which almost all are J -coupled. For most resonances, J -coupling increasingly approaches the weak coupling limit, in which case the linewidth of a peak in vivo is typically dominated by the homonuclear coupling, as can be illustrated with the example of the apparent Glu H4 triplet at 2.35 ppm. Due to the homonuclear J -coupling the resonance spreads over an apparent linewidth of about 20 Hz at almost any field measured from 1.5 Tesla on upwards, and the linewidth is thus dominated by hyperfine splitting of the resonance. Even if the intrinsic linewidth (as measured, e.g., from the singlet resonances) increases by a few Hz with B_0 , this will have minimal impact on the apparent linewidth of the multiplet. This is illustrated in Figure 1, where the Glu H4 resonance is almost twofold narrower at 7 than at 4 Tesla, which enables separation of the H4 resonance of glutamate from the H4 of glutamine at 7 Tesla.

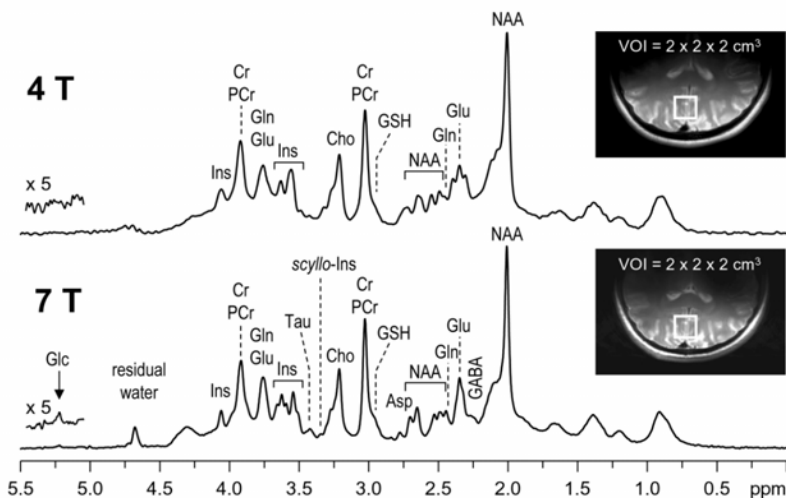


Figure 1. Increased spectral resolution in ^1H NMR spectra from the human brain at 7 Tesla (bottom) compared to 4 Tesla (top). Note the apparent and profound reduction in linewidth for the Glu H4 resonance at 2.35 ppm and the improved resolution even for singlets, as judged from the region separating the Cho and Cr resonances. The localization is shown in the inset (MRI, RARE, ETL = 8, TE = 60 ms). Spectra were obtained from 8-mL volumes of interest indicated in the same subject and identically processed.

In practice, it is very difficult to determine the precise value of β , but it is possible to state the sensitivity gains achieved over previously published results.

3. RF CONSIDERATIONS

In principle it may be desirable to have a homogenous RF field covering the entire brain, as it is being widely used for head imaging on conventional MR scanners. When compared to surface coils, the volume coils require increased RF power since the RF power is distributed into a larger volume [1]. Increased RF power implies decreased sensitivity from the reciprocity principle. It is not surprising that volume coils typically are 2–3 times less sensitive than surface coils with optimized dimensions, even when considering the most efficient coil design. With increasing B_0 , effects due to the substantial phase difference of the RF field in the human brain (dielectric resonances) can limit the usefulness of the classic volume coil as a transceiver. In rodents, given the unfavorable small portion of the head occupied by the brain, volume coils may not be the best method to detect the signal. When using surface coils it is advantageous to use adiabatic RF pulses to overcome the problems arising from inhomogenous RF fields, which have been used in a number of studies for NMR spectroscopy [7–15].

With these considerations, and given the unavoidable consequence of inhomogenous RF field at high B_0 , it is expected that multi-array RF coils are likely to be increasingly valuable at high B_0 .

One potential risk to an MR examination is the RF power being absorbed by the tissue converted to heat, which can potentially lead to excessive heating of the body and local tissue, resulting in damage. It is therefore important to limit the RF power administered to the brain, especially for human studies. A simple method to estimate the average specific absorption rate (SAR) is to divide the power dissipated into the organ by the organ volume. However, this calculation is probably an increasingly inaccurate approximation, with the increased spatial inhomogeneity of the RF field at higher frequencies, and other calculations may serve to estimate RF power deposition, such as the following: The current induced in a conducting tissue like the human body is typically dependent on the area of tissue (Faraday's law of induction), which implies that the power deposited increases with the area squared, whereas the volume into which this power is deposited is proportional to the area. These considerations imply that RF power deposition increases with the area of the tissue excited by a given coil. Recent simulations of SAR show that the areas of highest power absorption are at the periphery of the brain, rather than the center [16], probably due to the aforementioned effect. While the perils of so-called hot spots are well established for surface coils, it may also be worth considering the potential increases in local SAR when using whole-body RF coils due to the large organ size.

In general, most of the energy transferred by RF into tissue is converted to heat. While heat bears no specific characteristic related to the frequency of the applied RF, the power absorbed does increase with frequency. These considerations

make it clear that SAR considerations and application guidelines are largely independent of B_0 . The increased power absorption with frequency thus may simply imply reduced ability to apply the same pulse sequence as at lower field. To minimize the SAR requires that the pulse sequences and decoupling power are adjusted to operate at the minimum power threshold at which sequence performance is still acceptable. For ^{13}C NMR spectroscopy, optimization of RF power is most reliably achieved with an external reference sphere filled with a suitable ^{13}C -labeled compound, such as formic acid, placed at the coil center. Highly efficient and accurate methods for adjusting the decoupling power have been described [17,18]. In general, the brunt of the SAR is generated by decoupling. For ^1H NMR spectroscopy, the RF field (and RF power) can be calibrated on the VOI using the tissue water or fat signal. Typically for ^1H NMR spectroscopy, SAR is not of concern unless long RF pulse trains are applied, such as ^{13}C decoupling or broadband RF pulses for OVS.

3.1. Shimming

The ability to harvest the potential sensitivity gains at high field and the quality of any NMR spectrum stands or falls with the quality of the shimming achieved. This is especially crucial in vivo with increasing B_0 , where the difference between a diamagnetic subject and paramagnetic oxygen in air leads to susceptibility-induced spatial variations in B_0 that can be detrimental to the quality of the data obtained. When considering reaping the benefits of high field NMR spectroscopy, issues need to be addressed — namely the choice of shim coils to include in the set of coils provided, and the shim strength that needs to be attained. In this discussion it is important to recognize that the diameter of the shim coils is an important parameter, yet it is not the sole determining factor in defining shim strength. A second point to consider is the scope of the applications one wishes to pursue, as the shim correction currents increase with decreasing head size and they depend strongly on the area within an organ being investigated. First-order shimming is equivalent to adjusting an offset current in the gradient coils, which in general will be sufficient to eliminate first-order B_0 field variations. For higher-order corrections specialized shim coils will be necessary and the following pertains to their use. In our laboratory we have installed a set of custom-designed shim coils at 9.4 Tesla, capable of generating second-order shim fields up to 0.05 mT/cm^2 at a 4 Amp shim current. There are many design issues that need to be considered, but it is likely that the best solution is achieved when additional space outside the gradient coil is available to either accommodate more current within the voltage rail of the shim amplifier or to accommodate extra cooling.

Shim demands increase with decreasing object size, as illustrated by the increased demands on the shim strength when going from rat to mouse brain [19], as shown in Figure 2B. Typically, the quality of a shim current adjustment is based on the measurement of a rather arbitrary parameter — namely the full-width at half-height. However, this in itself may not be a very good indicator for local adjust-

ment of the shim coils, and the residual shim fields need to be measured to decide whether the shim process was successful. An algorithm was developed based on FASTMAP [20–23], and its echo-planar-based derivative FASTESTMAP [24], that can adjust with a predefined protocol the first- and second-order shim coils within 30 s at 4 Tesla and similarly at 7 Tesla in human brain. This method is widely used for high field ^1H NMR spectroscopy and can provide rms precision on the order of 0.1 Hz in the field residual. FASTMAP and closely related variants have been implemented on the platforms of Bruker, Varian, Siemens, SMIS, and Philips.

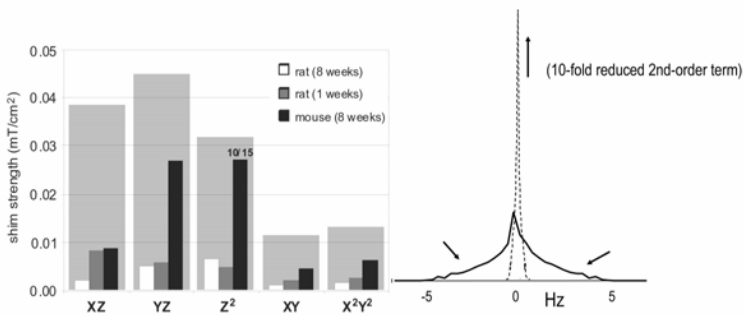


Figure 2. (A) Shim requirements increase with decreasing head size. Average shim strength requirements for mouse, and neonatal and adult rat brain in the unilateral hippocampus at 9.4 Tesla. 10 out of 15 Z_2 shim settings exceeded the maximum available in the mouse brain. Reprinted with permission from PB Barker, DO Hearshen, MD Boska. 2001. Single-voxel proton MRS of the human brain at 1.5T and 3.0T. *Magn Reson Med* 45:765–769. Copyright © 2001, John Wiley & Sons Inc. (B) Effect of second-order shims on lineshape, obtained using a simulation of the frequency distribution in a cubic volume. Shown is the effect of a second-order shim coil (YZ) on the field distribution in a cubic volume. Upon elimination of this term (by shimming), the intensity in the wings is moved underneath the central peak, indicated by the arrows, thereby increasing sensitivity and reducing potential quantification errors.

Even though the effect of B_0 inhomogeneity on the linewidth of a ^{13}C resonance is reduced by fourfold compared to that of ^1H , shimming remains an important issue: The low sensitivity of ^{13}C NMR typically precludes measurement of signals from small volumes, leading to comparatively large volumes. The measurement of substantially larger volumes likely results in the need for adjusting the currents in the second-order shim coils (which can be achieved using quantitative shim methods) [20,22,24]. The need to adjust second-order shim coils can be appreciated from the fact that the spatial distribution of the B_0 field of second-order shim coils results in significant signal intensity being distributed in the wings of the resonance (Figure 2B). Such signal distribution can be easily lost in peak integration or even peak fitting at low signal-to-noise ratios, or when using even modest resolution enhancement. The distribution of signal in the wings of a resonance is also likely to affect the quantitative result in ^1H NMR spectroscopy, as the precise recovery of such signal intensity even with advanced deconvolution methods is

difficult in the crowded ^1H NMR spectrum. Shimming with second-order shim coils typically has only a modest effect on the full-width at half-maximum of the resonance (Figure 2B). Nonetheless, a significant fraction of the total signal in the wings is shifted under the main resonance, thereby reducing the potential for quantification errors and increasing the sensitivity of the experiment further. These effects are expected to be of increased importance with increased B_0 . In summary, it is likely that adjusting second-order shim coils is necessary to harness the full sensitivity gains at higher field.

With the appropriate design in shim coil hardware and field mapping methods, it was shown that even in the extremely difficult-to-shim mouse brain, highly resolved ^1H NMR spectra can be achieved at 9.4 Tesla from distinct regions in the mouse brain (Figure 3), with a spectral quality comparable to that achieved in rat and dog brain [3–5,25,26].

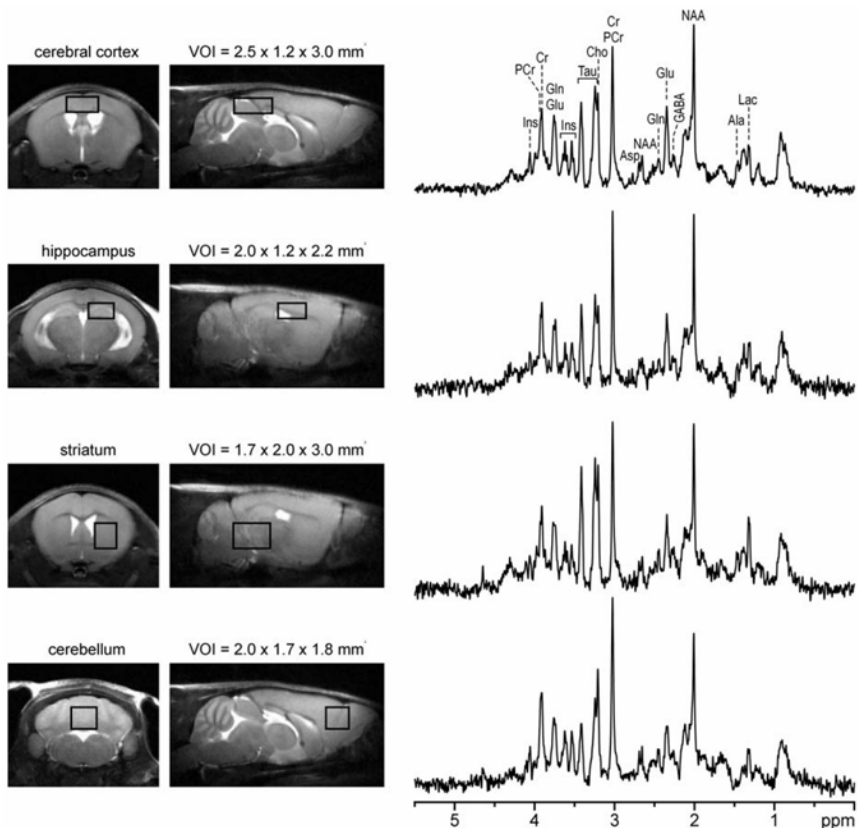


Figure 3. High-resolution in-vivo ^1H NMR spectra from distinct anatomic and functional regions in mouse brain. Reprinted with permission from I Tkac, PG Henry, P Andersen, CD Keene, WC Low, R Gruetter. 2004. Highly resolved in vivo ^1H NMR spectroscopy of the mouse brain at 9.4 T. *Magn Reson Med* 52:478–484. Copyright © 2004, John Wiley & Sons Inc.

4. IN-VIVO ^{13}C NMR SPECTROSCOPY

When considering the sensitivity relative to that of ^1H NMR spectroscopy, natural abundance ^{13}C NMR is certainly not expected to compete in the quantitation of a given compound; however, it has proven invaluable in estimating concentrations, which can aid in quantification of the ^1H NMR spectrum [27,28]. For example, the difficulty in detecting the natural abundance signal of glutathione (GSH) [29–31] indicates a concentration below $3\ \mu\text{mol/g}$, in agreement with ^1H NMR quantification [32], and, similarly, the concentrations of taurine, aspartate, and GABA are expected to be below $2\ \mu\text{mol/g}$ in human brain. The detection of signal from natural abundance compounds in the brain certainly represents a useful complement to in-vivo quantification by ^1H NMR spectroscopy [8,31,33–35], albeit of limited practical value.

When a suitable precursor, such as glucose, is administered with enriched ^{13}C label, the label is transferred to molecules in the metabolic pathway. In this manner not only can the sensitivity be increased, but important information on metabolic pathways can also be obtained. In addition to its importance in assessing metabolism in intact brain, ^{13}C NMR spectroscopy has become an important and useful tool in assessing compartmentation of metabolism in brain cells using extracts [36,37].

There are two principal detection methods available — namely direct and indirect detection of ^{13}C label. For indirect detection via ^1H resonance coupled to ^{13}C , the advantages of high field apply equally well as for regular ^1H NMR spectroscopy (see below).

In addition to its low sensitivity, ^{13}C NMR spectroscopy is methodologically more challenging than ^1H or even ^{31}P NMR spectroscopy. In contrast to the cell culture and suspension studies and related important work, in vivo ^{13}C NMR spectroscopy of intact organs faces a number of problems that make its application more challenging. Complete three-dimensional localization seems necessary in the brain to eliminate the intense triacylglycerol resonances from the scalp and other signals outside the brain, which adds to the challenges of in-vivo ^{13}C NMR. The application of ^{13}C NMR spectroscopy to the brain faces in-vivo some challenges on the technical level that are unique to the ^{13}C nucleus and compounded at high magnetic fields. This section first examines the reverberations of the requirement to decouple the spectrum during acquisition, and then discusses the localization requirements. A more extensive discussion of these issues and technical questions can be found in [30].

4.1. Decoupling: RF Power Considerations

Many ^{13}C nuclei are directly bonded to protons. The resulting magnetic coupling between the ^{13}C nucleus and the ^1H nucleus results in a splitting of the ^{13}C resonance into multiplets separated by J_{CH} Hz. The process of decoupling collapses the multiplets due to heteronuclear coupling into singlets, thereby simplifying the spectra and effectively increasing the sensitivity. Optimization of sensitivity is

critical for successful in-vivo ^{13}C NMR spectroscopy. To maximize the signal-to-noise ratio and spectral resolution in ^{13}C NMR spectra, ^1H decoupling is generally applied during data acquisition, resulting in a simplified spectral pattern. The application of rather intense RF power during acquisition requires that the RF coil be capable of receiving the ^{13}C NMR signal while transmitting ^1H RF power. This places several requirements on the spectrometer console, RF coils, and RF filters.

The need for decoupling results in two requirements for RF coils: First, the ^{13}C coil (operating at a frequency with a wavelength approximately 4 times that of the ^1H frequency) should not interfere with the RF profile of the ^1H coils. Second, the two RF circuits should be sufficiently isolated electrically. For a further discussion of RF coil design for ^{13}C NMR spectroscopy at high fields, see [30].

Most ^{13}C NMR applications have relied on WALTZ decoupling of the protons [38]. Broadband adiabatic ^{13}C decoupling was achieved at 9.4 Tesla using such cycles at a moderate peak $\gamma B_1/2\pi$ of ~ 1 kHz [39] and at 7 Tesla [40].

4.2. Localization Methods for ^{13}C NMR Spectroscopy

The full chemical shift range of most biologically interesting ^{13}C resonances is approximately 160–200 ppm wide. Even when considering the fourfold lower gyromagnetic ratio than ^1H , this is a range that (in Hz) exceeds the range for ^1H resonances of main biological interest (7 ppm) by at least a factor of six (Table 1). Thus, chemical shift displacement error problems are important factors to consider when wishing to localize ^{13}C NMR signals.

Table 1. Chemical Shift Ranges for ^{13}C MRS per Tesla (Expressed in Hz/T), Including the Range of the Corresponding Coupled ^1H Resonances

Compound class	Chemical shift range (ppm)	^{13}C frequency range (Hz/T)	^1H frequency range (Hz/T)
Glycogen/glucose (all)	101–61	430	94
<i>Myo</i> -inositol (all)	76–72	43	34
Amino acids (CH_n)	56–22	363	85
Amino acids (CH)	56–53	32	20
Lipids (CH_n)	131–14	1248	196

Spatial localization does not depend on chemical shift when using the one-dimensional surface-spoiling gradient or spectroscopic imaging [41,42], which is an elegant technique to solve the chemical shift displacement problem when many transients can be acquired [43]. Typically the rather high number of averages acquired for in-vivo ^{13}C NMR spectroscopy bodes well with the use of chemical shift imaging. However, the low spatial resolution may require dedicated solutions to

minimize Gibbs ringing from superficial fat signals, and several approaches have been described [44,45]. In the following we will concentrate on the various methods for full three-dimensional localization of ^{13}C NMR signals using gradient-based methods.

The use of direct localization of ^{13}C is challenging because the large chemical shift requirement leads in general to increased demand on the RF power through the need for an increased RF bandwidth. In some cases, even when the demands on the RF bandwidth can be met, the required gradient strength may very well be limiting, because of the lower gyromagnetic ratio γ . Therefore, for practical reasons, direct localization is typically limited to a given spectral range (Table 1), e.g., the direct measurement of brain glucose C1 in the human brain [9]. In addition, direct localized ^{13}C NMR spectroscopy was used for the first detection of the natural abundance signals of small molecules, as illustrated with *myo*-inositol [8].

4.2.1. Localization on ^1H Magnetization: Polarization Transfer

When using ^{13}C longitudinal magnetization for localization, signal enhancements are commonly achieved using the nuclear Overhauser effect (NOE), which can theoretically provide up to a threefold enhancement of ^{13}C signals. However, for resonances with sufficiently long T_2 , such as those of most brain metabolites as judged from their narrow linewidths of a few Hz [22], it is feasible to use polarization transfer to recover the maximal sensitivity gain of a fourfold enhancement and to localize on the ^1H magnetization, thereby greatly reducing the chemical shift displacement error due to the much smaller chemical shift range (Table 1). Heteronuclear polarization transfer combined with localization on the proton magnetization was shown to minimize the chemical shift displacement error in ^{13}C MRS of the human brain to a level beyond concern even at 4 Tesla [31]. To minimize the number of pulses needed for generating the in-phase ^{13}C signal enhancement and to minimize phase distortions in the spectrum, distortionless enhanced polarization transfer, DEPT [46], was used. The high sensitivity of polarization transfer pulse sequences to variations in B_1 can be ameliorated for the ^{13}C pulses when incorporating adiabatic pulses into the pulsed polarization transfer sequence [11,15,47]. Most polarization methods cannot provide full enhancement over the entire range of J -coupling constants, ^1H spin multiplicities, and chemical shift range. Nonetheless, a high sensitivity was achieved and rich spectral information were obtained at 4 Tesla in human brain and at 9.4 Tesla in rat brain (Figure 4).

4.2.2. Three-Dimensional Localization of the ^{13}C NMR Signals of Glycogen

Clearly, the chemical shift displacement error can be minimized by using ^1H magnetization for localizing the ^{13}C NMR signals in conjunction with polarization transfer. However, methods such as those discussed in the previous paragraph are not applicable in situations where T_2 is very short. For some compounds such as glycogen, it is nearly impossible to realize the full sensitivity gains of the polarization transfer technique. While the SINEPT technique [49] relies on minimizing T_2 -losses by performing polarization transfer on-resonance without refocusing the J

evolution, the method remains in principle susceptible to changes in T_2 , which have been reported to occur depending on the glycogen molecule size and temperature [50]. Unfortunately, the potential fourfold signal gain is reduced by the short T_2 of ^1H and ^{13}C signals — on the order of 5 ms [50,51]. Given the uncertainty of potential changes in transverse relaxation times [50], a robust method relying on outer-volume suppression applied along the six slices parallel to the volume-of-interest was developed. In the brain such localization was crucial to minimize potential contamination of the detected signal with signals from extraneous muscle, especially in the rat [12,14,52].

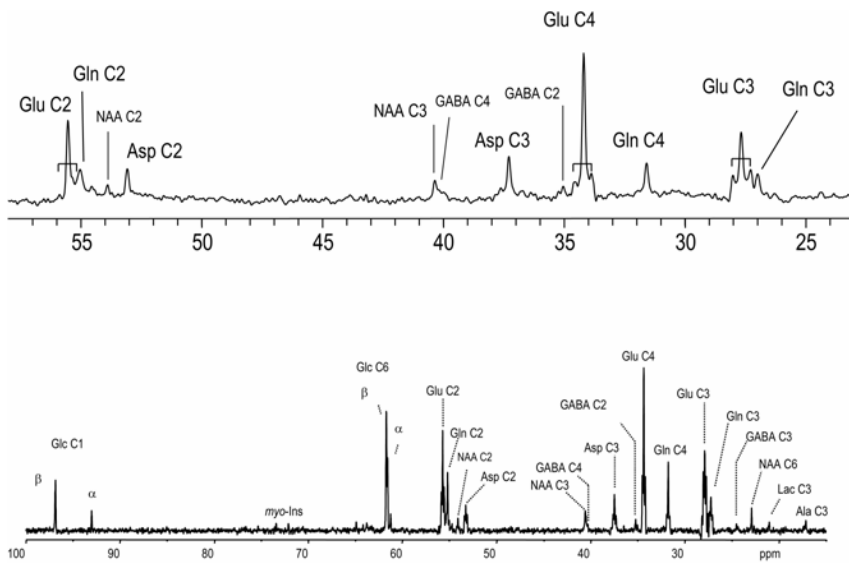


Figure 4. Examples of direct-detected ^{13}C NMR spectroscopy from the brain. (A) ^{13}C NMR detection of label incorporation into mostly cytosolic amino acids at 4 T. Reprinted with permission from R Gruetter, ER Seaquist, K Ugurbil. 2001. A mathematical model of compartmentalized neurotransmitter metabolism in the human brain. *Am J Physiol* **281**:E100–112. Copyright © 2001, American Physiological Society. Shown is a representative spectrum obtained from a 45-ml volume in the human visual cortex during an infusion of 67%-enriched $[1-^{13}\text{C}]$ glucose. In addition, resonances resulting from homonuclear ^{13}C – ^{13}C coupling were readily detected at the positions of all glutamate resonances (indicated by brackets). Processing consisted of a mild Lorentz-Gauss apodization (3 Hz) and the spectrum is shown without baseline correction. (B) In-vivo ^{13}C NMR spectra from a 400- μl volume in the rat brain, acquired at 9.4 T during an infusion of 70%-enriched $[1,6-^{13}\text{C}_2]$ glucose. Reprinted with permission from PG Henry, I Tkac, R Gruetter. 2003. ^1H -localized broadband ^{13}C NMR spectroscopy of the rat brain in vivo at 9.4 T. *Magn Reson Med* **50**:684–692. Copyright © 2003, John Wiley & Sons Inc. Processing consisted of zero-filling, 2 Hz Lorentzian-to-Gaussian resolution enhancement and fast Fourier transform. No baseline correction was applied. Note the complete absence of lipid signals over the entire spectral range. Resonance assignments are as follows: Glu C2 at 55.6 ppm, Gln C2 at 55.0 ppm, NAA C2 at 54.0 ppm, Asp C2 at 53.7 ppm, NAA C3 at 40.5 ppm, GABA C4 at 40.45 ppm, Asp C3 at 37.6 ppm, GABA C2 at 35.3 ppm, Glu C4 at 34.2 ppm, Gln C4 at 31.7 ppm, Glu C3 at 28.0 ppm, Gln C3 at 27.7 ppm.

5. IN-VIVO ^1H NMR SPECTROSCOPY

In contrast to ^{13}C NMR spectroscopy, spectral overlap is a much more pronounced problem with ^1H NMR spectroscopy, and because the ^1H nucleus is much more susceptible to variations in B_0 , shimming (see above) is a critical component in accomplishing the potential gains of higher B_0 . This section deals with the advantages achievable once the problem of shimming can be solved satisfactorily.

5.1. A Word on Localization Methods

Despite its inherent disadvantages for in-vivo ^1H NMR spectroscopy (sensitivity to motion, dynamic range problems when selecting small volumes) ISIS has been successfully used for spatial localization of ^1H NMR in vivo in conjunction with outer volume suppression and mostly with surface coil detection [53].

When using localization based on the more popular stimulated echo (STEAM), the echo time can be minimized to 4–6 ms for human brain and 1–2 ms in rodent brain, effectively minimizing potential T_2 losses and J evolution effects [19,54,55]. However, the method's big disadvantage is the up to twofold sacrifice in sensitivity, which can translate into an up to 26% increased voxel dimension or up to fourfold increased measuring time at equal size of the volume of interest. It may seem unacceptable to sacrifice the sensitivity by twofold while buying a higher magnetic field system. However, sensitivity increases supralinearly with increasing magnetic field.

The sensitivity disadvantage of STEAM is remedied by using the PRESS or double-echo method, which is highly sensitive to those spatial variations in B_1 that are increasingly prevalent at high frequencies. Furthermore, considering traditional (nonadiabatic) RF pulses, the peak RF power has to increase by more than fourfold if one wishes to retain the same chemical shift displacement error as for STEAM. Lastly, for a given RF power and gradient slew rate, the echo time (TE) can be substantially longer.

Some of the aforementioned problems inherent with PRESS can be ameliorated when using adiabatic RF pulses. For example, using offset-independent adiabatic pulses [56], inversion pulses with almost arbitrary bandwidths can be generated for a given peak RF amplitude. This is done, however, at the cost of increased RF pulse duration, as the speed of the adiabatic sweep is reduced. In addition, adiabatic 180° refocusing pulses do not have good slice profiles, unless when applying pulses of the hyperbolic secant type in pairs, which further increases the echo time. One method, LASER [57], takes advantage of adiabatic single-shot localization. LASER addresses the issue of increased echo time by measuring in Carr-Purcell-Meiboom-Gill mode, where the transverse relaxation is increasingly replaced by $T_{1\rho}$ relaxation, which in vivo tends to be longer, thereby minimizing these losses.

Chemical shift imaging [43] will obviously not suffer from chemical shift displacement errors in the dimensions the phase encode gradients are applied. One drawback of the method is that longer acquisition times are necessary to collect the entire data set and that the sensitivity is lower than compared to single-voxel acqui-

sition. Thus, for those biomedical problems, where the region of interest is already known to the investigator or where spatial distribution of the defect is not important, chemical shift imaging may not be the first choice of method. Another issue stems from the fact that the intense lipid signals typically are associated with rather thin skin layers at the surface and the lower resolution of the chemical shift imaging data set results in Gibbs' ringing that may be motion-sensitive [44,45], which must be dealt with [58]. Lastly, effects of motion are not as easily corrected as for single-voxel spectroscopy, which may limit the use of CSI, especially in pediatric applications [59]. At very high magnetic fields, the spatial resolution achievable due to the higher sensitivity may result in a number of phase-encode steps that lead to prohibitively long acquisition times, hence some form of field-of-view restriction or parallel imaging may be necessary.

Given the undisputed sensitivity advantage of PRESS over STEAM, it may seem surprising to see that many pioneering studies at very high field have successfully used STEAM. There are several reasons that make the choice of STEAM quite attractive, all rooted in the use of essentially three 90° slice-selective RF pulses: A well-defined slice profile is easier accomplished with a 90° flip angle, with lower peak RF power and lower average RF power than for 180° pulses. The use of asymmetric RF pulses permits minimization of the effective echo time to 1 ms in rodent scanners [25], and to a few ms in whole-body scanners [54], effectively eliminating the effects of T_2 relaxation and J evolution to spectral appearance, thereby greatly facilitating quantification. Because the sequence relies on detection of a stimulated echo generated by all three 90° pulses, fewer stimulated echoes need to be dephased than in PRESS and spin echoes are easier to dephase in the TM period. Lastly, the sequence is inherently less sensitive to variations in B_1 , a critical issue when considering the spatially inhomogeneous RF field typically encountered in vivo at very high magnetic fields.

5.2. Water Suppression

It has been noted that in general the ^1H linewidths (in ppm) decrease with magnetic field strength in the adult brain, which makes it clear that the spectral resolution increases with magnetic field. This is particularly important for the most intense singlet resonance, namely water, as it implies improved water suppression, as was illustrated with the detection of the glucose signal at 5.23 ppm [34,60]. The sensitivity gains obtained by better and more reliable water suppression are more difficult to quantify, but they can be appreciated when considering, for example, that fewer spurious water signals from outside the VOI may confound the spectral region of interest, that a flatter baseline will yield better confidence intervals for the measurements.

5.3. Spectral Editing: Improved Pulse Selectivity at High Field

The spectral overlap problem inherent in ^1H NMR spectroscopy can be circumvented using spectral editing, which typically exploits the fact that in most metabolites the resonances in a given spin system are magnetically coupled. By specifically manipulating the coherence, the signal of interest can be selectively filtered from the overall background, and it is thus feasible to extract unresolved resonances from underneath much more intense resonances. Examples where this was achieved include GABA, GSH, and lactate [61–63]. Provided the coupling spin system is uniquely excitable, these editing methods are a very powerful tool for the measurement of obscured spin systems. Unfortunately, for one of the most interesting compounds, namely GABA, this uniqueness of spin system does not apply, due to overlap with putative lysine resonances from cytosolic proteins [64]. The traditional editing of the GABA resonance at 3.0 ppm is hampered by the simultaneous excitation of a very similar macromolecule coherence at 1.7 ppm (relative to that of GABA at 1.9 ppm) and alternative editing methods such as editing for the GABA at 2.3 ppm may prove advantageous [65]. Another type of editing that is applied to ^1H spectroscopy is the editing of ^1H resonances with magnetic couplings to ^{13}C nuclei, which are at low field obviously hampered by the limited resolution of the ^1H spectrum. However, at higher fields such as 9.4 Tesla an increased number of resonances can be measured.

Lastly, it is also possible to edit for coherences using total correlation spectroscopy. Using isotropic mixing, such coherence transfer can be used to recover resonance intensity in a spectral region where signal had previously been eliminated, e.g., the water spectral region [66].

In all these experiments, it is important to recognize that the spectral pattern of the resonance for which the editing is performed *in vivo* should be very similar to that predicted for the isolated compound as measured under the same experimental conditions (e.g., ionic strength, temperature and pH) as illustrated for the case of GSH (Figure 5). In addition, editing experiments are intrinsically less sensitive than measurements done directly on the resonance at short echo times (see below), for two reasons — namely the signal loss due to the longer echo time TE, and the potential signal loss from the editing process (in a resonance coupling to CH_2 (e.g., AX_2 spin system) the centerline does not evolve with J and is thus filtered away, leading to at least a twofold reduction in sensitivity). Finally, for many editing experiments, but especially for GABA, changes in B_0 during the experiment can alter the editing efficiency or selectivity, which can result in altered amplitudes and/or contamination, for example, by co-edited macromolecules [67].

5.4. Spectral resolution: The Neurochemical Profile

Provided sufficient spectral resolution is present, as has been shown for numerous compounds at high B_0 [5,19,54,59], it is conceivable that for many compounds spectral editing may not be necessary routinely with increasing sensitivity. As pointed out earlier, the spectral resolution increases in ^1H spectra with high

magnetic field, especially for J -coupled resonances when the macroscopic B_0 inhomogeneities are minimized by shimming. Despite the increased spectral resolution obviously present for coupled ^1H spin systems, even at the highest magnetic field applicable in vivo, substantial spectral overlap remains, unless some form of spectral editing (see above) is used. Hence direct peak integration or simple fitting are likely prone to systematic errors.

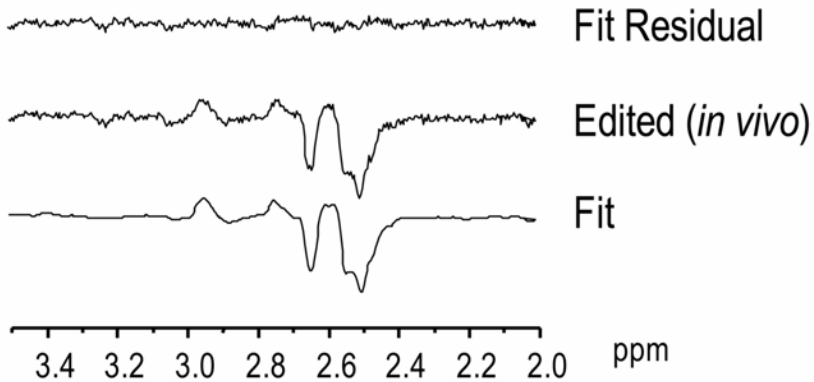


Figure 5. Editing of the spin system of glutathione (GSH) using MEGA-PRESS editing [67,68] at 4 Tesla. The GSH resonance at 2.95 ppm is co-edited with the aspartyl resonance of NAA at 2.6 ppm. The in-vivo spectrum (middle) is almost perfectly matched by the LCModel fit of the respective resonances measured in phantom, as indicated by the fit residual (top trace).

At short echo times, approaches that mimic the in-vivo spectral pattern and that incorporate prior knowledge become increasingly powerful, such as TDFDfit [69], LCModel [5,70], MRUI [71,72], etc. These methods are of increasing importance with decreasing B_0 , as overlap increases. Conversely, the increased spectral dispersion at higher field and increased sensitivity propel the use of short-echo ^1H NMR spectroscopy for measurements in individual patients. For example, incremental changes of various metabolites, such as glutamate and glutamine, can be assessed longitudinally in patients to follow diseases progression and response to treatment [59]. Such noninvasive assessment of pathology over time is expected to eventually aid inpatient management. Sensitivity and reliability are best assessed from the average Cramer-Rao lower bounds, which assess the reliability of the fitted amplitude, as well as from the covariance matrix.

In the determination of metabolite signals, a faithfully determined baseline may prove critical and essential. Baseline determination in vivo is difficult due to the overlap of resonances in the short-echo ^1H spectrum. In addition, a signal background associated with cytosolic proteins (macromolecule background) complicates the shape of the baseline. Fortunately, the T_1 of these macromolecule reso-

nances is much shorter than that of most metabolites, which allows the separate measurement of the macromolecule signals in so-called metabolite-nulled spectra [64]. The such-measured complex signal from macromolecules can be incorporated into the basis set of, e.g., LCMoDel, as reported by Pfeuffer et al. [4,5]. This approach of incorporating the short T_1 background signals (macromolecules) is increasingly being used for in-vivo ^1H NMR spectroscopy of the brain [4,32,73–75]. The information content and deconvolution of the in-vivo spectrum is shown in Figure 6 for human brain at 4 Tesla and for rat brain at 9.4 Tesla.

6. INSIGHTS FROM HIGH FIELD NMR SPECTROSCOPY STUDIES OF THE BRAIN

In-vivo spectroscopy, especially at high fields, provides the investigator with a unique tool. One strength of the method lies in the deterministic nature of the NMR signal: Not only is it in general known at what chemical shift to expect a signal for a given compound, the spectral features, which can be quite complex, can be faithfully reproduced using either model solution and/or simulations. Additionally, the lineshape is subject to certain constraints of similarity between the different metabolites. Finally, some of the concentrations expected should conform to what is reasonably expected from the underlying neurochemistry. These characteristics can serve to allow a faithful measurement of metabolites in vivo. On one hand, the concurrent quantitative measurement by ^1H NMR spectroscopy of many important neurochemicals constituting the neurochemical profile allows for noninvasive insight into the neurochemical consequences of many diseases in human subjects, thereby providing an important translational link. On the other hand, localized NMR spectroscopy of other stable isotopes provides a window on in-vivo brain metabolism, with a unique chemical specificity and diversity of potential measurements not possible by other methods. The metabolism of stable isotopes can be followed noninvasively using NMR, although administration of the “tracer” requires a high isotopic enrichment, for ^{13}C typically above 50% in the precursor pool. Because NMR spectroscopy can be used to detect label in different molecules and different chemical positions, it offers the attractive possibility to follow the metabolism of the precursor, labeled at one or more specific positions. Applications are predominantly focused on nuclei where a stable isotope is present at low natural abundance — examples include ^2H , ^{15}N , ^{19}F , and ^{13}C [76].

Of course, sensitivity for NMR is low when considering the concentrations that are detectable, and the relative sensitivity of ^{13}C NMR is even lower. Nonetheless, despite the sensitivity disadvantage, as shall be discussed in the second half of this review, high field NMR spectroscopy can provide unique insights into brain metabolism. Many consider a low sensitivity and thus low spatial resolution a significant disadvantage. However, it is our belief that the spatial resolution that can be achieved combined with the high specificity of the method allows one to uniquely address a significant number of important biomedical problems/questions.

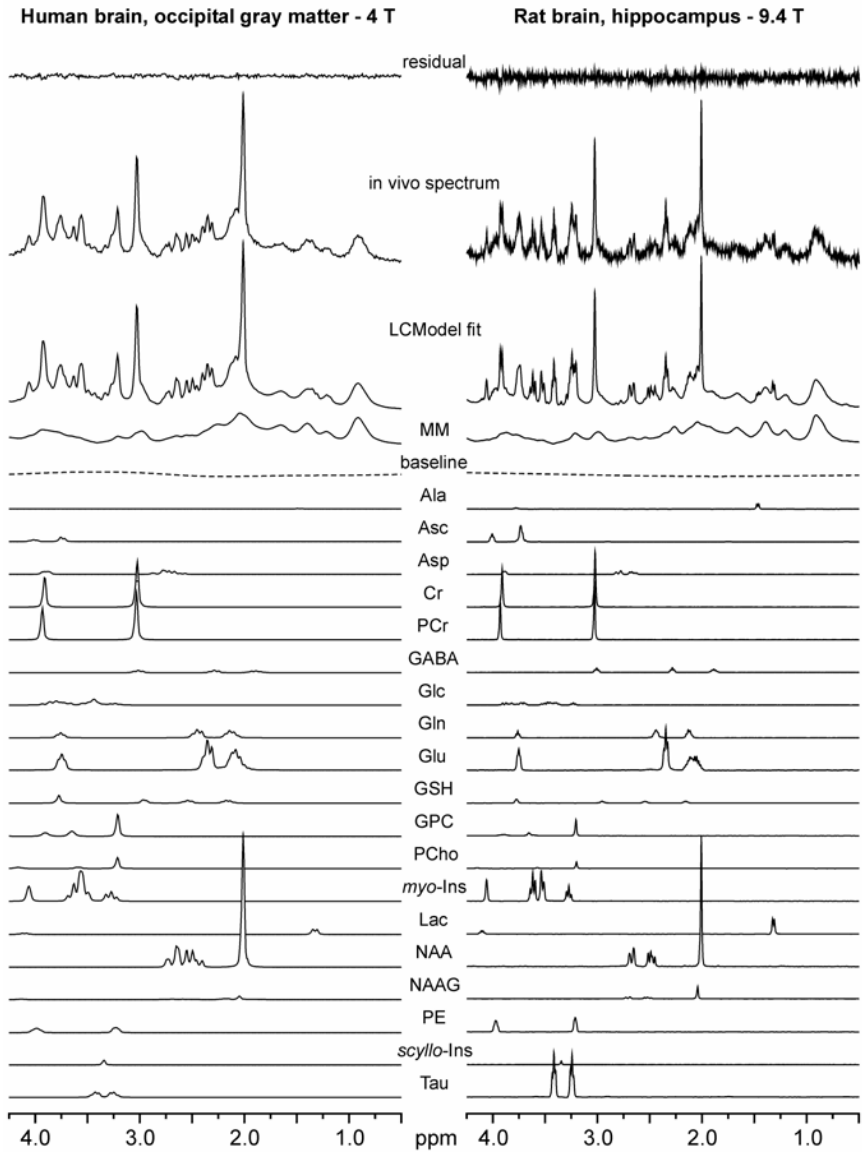


Figure 6. LCMoel analysis of in-vivo ^1H NMR spectra at 4 Tesla (human brain) and 9.4 T (rat brain). Shown is the in-vivo spectrum (top), the LCMoel fit and fit residual, along with the estimated baseline and all contributions from the basis set to the in-vivo spectrum.

6.1. Glucose Concentration, and Distribution in the Brain: Transport Physiology

Glucose is the single most important substrate required for normal brain function, and the brain relies on a continuous import of glucose from the blood, which must occur across the blood–brain barrier. Glucose transport rates into the brain are thus indicative of the maximal sustainable rate of glucose consumption, CMR_{glc} . Aside from lactate and glycogen (12), brain glucose is the only sizable kinetic pool upstream of acetyl-CoA, and the size of the brain glucose pool and its physical distribution space is important for derivation of absolute metabolic fluxes and quantitative positron emission tomography studies [9,77]. It has been shown that steady-state glucose transport kinetics can be derived from the relationship between brain and plasma glucose [9,34,77,78].

Glucose concentrations have been measured using ^1H and ^{13}C NMR spectroscopy [34,79–84]. For a CH group with homonuclear J -coupling, the sensitivity advantage of ^1H compared to ^{13}C is expected to be only 2–3 fold. The proximity of the ^1H resonances of glucose to that of water makes the measurement of brain glucose using ^1H NMR spectroscopy difficult, especially for ^1H resonance [60]. Therefore, in cases where metabolism is followed by ^{13}C NMR, it may be advantageous to measure brain glucose content as well.

When measuring brain glucose transport kinetics, the magnitude of the physical distribution volume, i.e., the volume in the brain into which glucose can diffuse, can affect the interpretation of the derived glucose transport kinetics [85–87]. The physical distribution volume of glucose has been assumed to equal the brain's water phase based on radiotracer and slice diffusion experiments, suggesting that transport of glucose across cell membranes is diffusion-limited [87], although some fraction of the aqueous space might be more accessible on a short time scale [88]. Interestingly, a study concluded that the physical distribution volume of glucose must be large and consistent with that of the brain's water phase from the delayed change in brain glucose following a step function in plasma glucose [89]. In a recent study the diffusion behavior of glucose was measured using diffusion-weighted ^1H NMR spectroscopy [84], and it was found that glucose had a distinctly detectable signal even at very high diffusion weighting (Figure 7), consistent with a predominantly restricted diffusion behavior, reflecting the primarily intracellular origin of the glucose signal. However, the diffusion signal characteristic was different from compounds whose concentration is almost exclusively intracellular, but similar to that of lactate, whose extracellular concentration under normal circumstances is probably similar to whole brain lactate concentrations. From the diffusion behavior of the glucose signal it was concluded that approximately 20% of the NMR signal of glucose originated from the extracellular compartment, which reinforced the notion of a high physical distribution volume for glucose [90].

Traditionally, glucose transport kinetics have been analyzed with a model of brain glucose transport that was based on standard Michaelis-Menten kinetics. However, Michaelis-Menten kinetics is based on the assumption that the initial

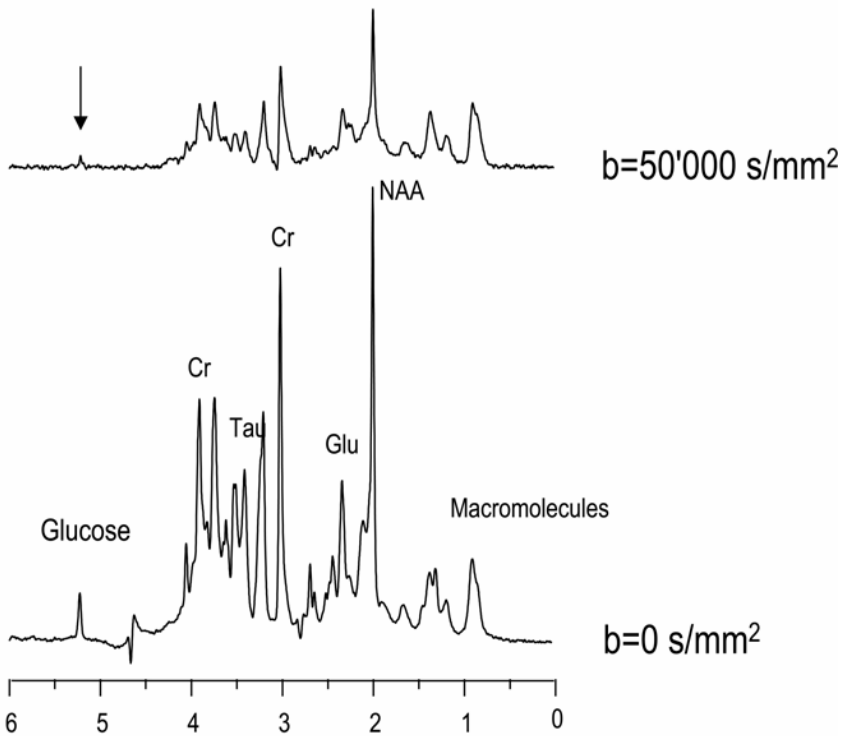


Figure 7. Diffusion-weighted signal of glucose and other metabolites [84]. Signals are strongly reduced at the high b value (diffusion time was 120 ms), more so than the macromolecule signal (at, e.g., 0.9 ppm). The detection of the glucose signal at 5.23 ppm (arrow) indicates that a substantial fraction of the glucose is in intracellular space.

rate of unidirectional product formation is measured, e.g., immediately after substrate and enzyme have been combined. This experimental condition would require elimination of the brain glucose, which is difficult to achieve without interfering with normal brain function. Hence it is reasonable to expect that reversible Michaelis-Menten kinetics is a more appropriate formalism in describing brain glucose transport. Such a model has been proposed [34,91]. It was shown that one implication of the reversible model of brain glucose transport is that the relationship between brain and plasma glucose is linear [34]. Many measurements of brain glucose content as a function of plasma glucose have in the meantime corroborated the observation that brain glucose concentrations are a linear function of plasma glucose [78,81–83], and such a case is illustrated in Figure 8 for two different anesthetic regimes — α -chloralose and pentobarbital. These studies indicated that decreased electrical activity and thus decreased energy metabolism resulted in in-

creased brain glucose concentrations. The increment in brain glucose was consistent with an approximately twofold reduction in brain glucose utilization under pentobarbital anesthesia relative to α -chloralose anesthesia. The presence of a sizeable concentration gradient between brain and plasma glucose implies that net glucose uptake (i.e., glucose consumption at steady state) was appreciable even under conditions close to isoelectricity.

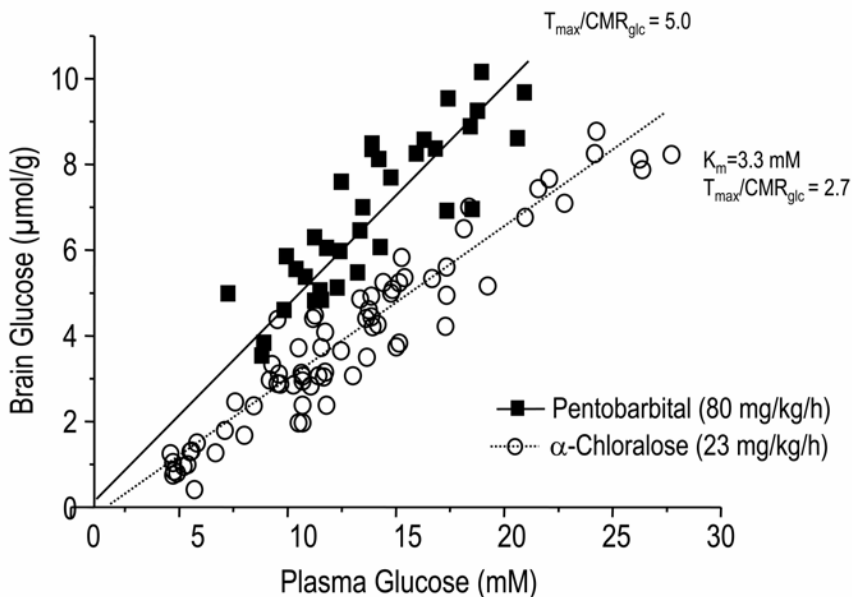


Figure 8. Brain glucose transport kinetics from the measurement of the brain glucose content as a function of plasma glucose concentration. (A) Demonstration of a linear relationship between brain and plasma glucose concentrations, as well as the effect of increased anesthesia (decreased electrical activity) on brain glucose content in vivo. Reprinted with permission from IY Choi, H Lei, R Gruetter. 2002. Effect of deep pentobarbital anesthesia on neurotransmitter metabolism in vivo: on the correlation of total glucose consumption with glutamatergic action. *J Cereb Blood Flow Met* **22**:1343–1351. Copyright © 2002, International Society for Cerebral Blood Flow & Metabolism.

The importance of measuring the brain glucose concentration can be appreciated from its role in regulating brain glucose metabolism: Glucose becomes rate-limiting for metabolism when its concentration approaches that of the K_m of the first step in its metabolism, which is in the brain phosphorylation mostly by hexokinase. Since the K_m of brain hexokinase is very low ($\sim 50 \mu\text{M}$) and NMR sensitivity in vivo generally is too low to detect such small concentrations of glucose, brain glucose concentrations measured by NMR that are close to zero indicate metabolism that is limited by the glucose available to the brain cell. The general con-

sensus is that brain glucose transport is not rate-limiting for metabolism under normal circumstances. We have recently shown in the conscious human and the α -chloralose anesthetized rat that the maximal sustainable rate of glucose consumption is approximately 60–90% above the basal rate of glucose metabolism and brain glucose is therefore not rate-limiting [34,78]. This may, however, not be the case under conditions of extreme metabolic activation or during hypoglycemia [92].

Previously, models of brain glucose transport have been evaluated at normal or hyperglycemic conditions only [34,77,81–83]. A recent study extended the brain glucose concentration measurements to hypoglycemia using ^{13}C NMR spectroscopy [78]. The concentrations measured by ^{13}C NMR were found to be in excellent agreement to those predicted by the reversible Michaelis-Menten model as well as those measured by ^1H NMR spectroscopy [78]. Interestingly, when the brain glucose concentration approached zero, CBF was acutely increased [78] and glycogen degradation started [93], all of which points to brain glucose being important in activating cerebral defenses against a deficiency in fuel supply.

6.2. Brain Glycogen, an Endogenous Energy Store

Additional fuel can be provided to brain cells during, e.g., hypoglycemia, from glycogen, which is present in the brain in measurable quantities and appears to be essential for brain function. Brain glycogen is typically present in quantities that exceed those of tissue glucose in the brain. Similar to glucose, brain glycogen is rapidly eliminated in postmortem tissue [12,94,95]; therefore, its direct biochemical measurement is difficult [96,97]. Localized ^{13}C NMR spectroscopy has the unique capability of following brain glycogen metabolism longitudinally, employing a much smaller number of animals than would be used with biochemical extraction. The rate of brain glycogen degradation during hypoglycemia accounted for the majority of the glucose supply deficit during the hypoglycemic period [93]. Together with the apparent stability of glycogen in the non-stimulated brain at eu- or hyperglycemia [12,98], these data suggest that brain glucose plays an important regulatory role in cerebral glycogenolysis. These studies also showed that brain glycogen increased above the basal level and beyond following a single episode of hypoglycemia [93]. This rebound or super-compensation of brain glycogen may result in increased neuroprotection. It has been proposed that brain glycogen metabolism may be a factor involved in the mechanism of the hypoglycemia unawareness syndrome observed clinically in patients with type I diabetes [93,98], perhaps through the enhanced neuroprotective effect of increased brain glycogen.

Thus glycogen likely is a viable and important store of glucose equivalents in the brain, whose metabolism is affected by hormones, neurotransmitters and second messengers [99].

One obvious investigational power of NMR spectroscopy is its applicability to animal models and humans alike. Because all previous studies measured brain glycogen metabolism in animals, the question remained as to whether brain glycogen

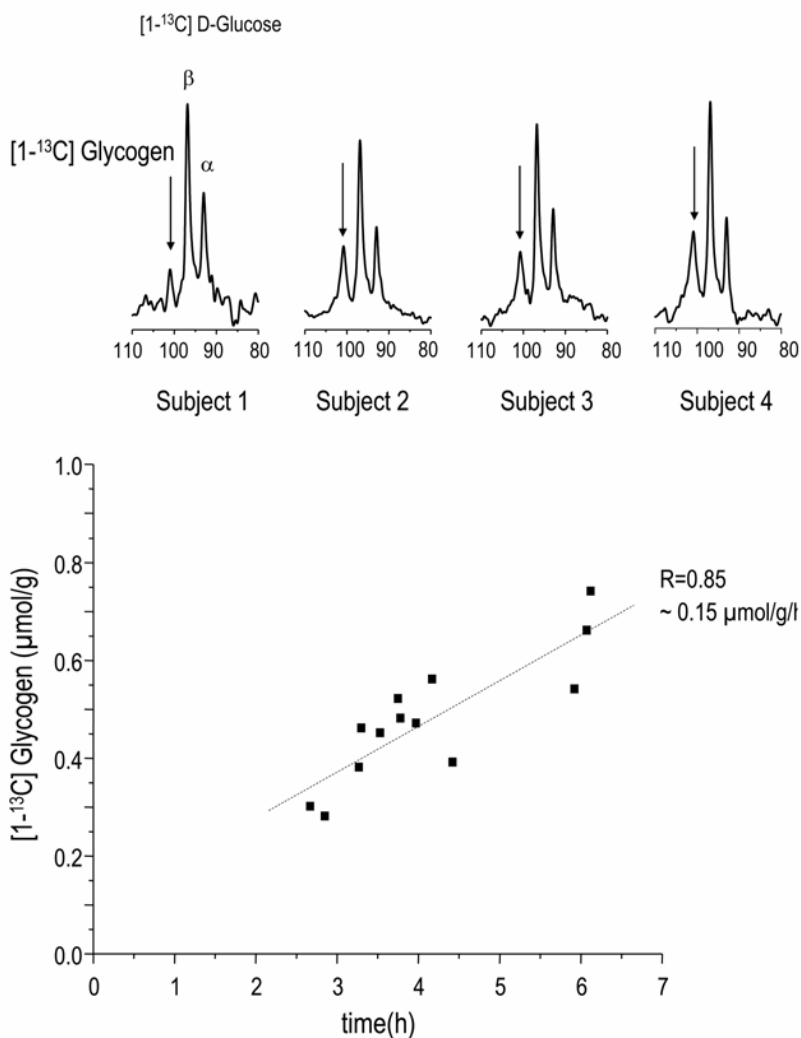


Figure 9. Measurement of glycogen in the human brain. (A) Demonstrates detection of the brain glycogen signal in four different subjects (arrows) along with the glucose C1 resonances. Shown is the spectral region containing the glycogen C1 and glucose C1 resonances. (B) The increase in the quantified glycogen C1 signal represents the accumulation of [1-¹³C] glycogen, which occurred at an extremely slow rate on the order of 0.15 µmol/g/h in the human brain, as illustrated in the graph containing measurements from three different studies. Reprinted with permission from G Oz, PG Henry, ER Sequist, R Gruetter. 2003. Direct, noninvasive measurement of brain glycogen metabolism in humans. *Neurochem Int* 43:323–329. Copyright © 2003, Elsevier.

metabolism may be faster in the conscious human brain. Brain glycogen metabolism had never been measured in the human brain and ^{13}C NMR is the only technique that can provide this insight. We have recently adapted the localization method (see above on localization methods) for measuring brain glycogen in humans and demonstrated that a reproducible measurement of the brain glycogen signal was indeed possible in the human brain [14], illustrated in Figure 9A. These initial results furthermore demonstrated that brain glycogen metabolism was extremely slow in subjects measured in the awake, resting condition (Figure 9B). This observation was in excellent agreement with previous studies showing that under the conditions of this study (plasma glucose at euglycemia or higher with concomitant hyperinsulinemia) the brain glucose concentration is well above the K_m of hexokinase [9,34,83], thereby eliminating the need for appreciable glycogen activation. In fact, the flux through glycogen synthase was estimated at 0.1–0.2 $\mu\text{mol/g/h}$. As a consequence, a brain glycogen pool of a few mM is expected to have a turnover time on the order of several days to a week. These findings suggest that glycogen metabolism is a negligible factor in the energy metabolism of the conscious unstimulated human brain at euglycemia and above.

6.3. Compartmentalized Oxygen Metabolism in Brain

The question of whether there is tight coupling between glucose and oxygen consumption in the brain has become of paramount importance. The landmark study by Fox and Raichle in the late 1980s suggested that there is indeed a large increase in glucose metabolism that exceeds the changes in oxygen metabolism [100]. The concept of uncoupled oxygen metabolism has been supported by studies reporting small increases in brain lactate during focal activation [101,102] that are very difficult to perform [103]. The relatively small magnitude of change in brain lactate [101,102,104] is difficult to reconcile with the reported large uncoupling between oxygen and glucose consumption [105], and explanations linking the lactate increase to brain glycogen [106] at present appear unlikely (see above). To address this question, it is useful to measure the TCA cycle activity in the brain. In intact tissue the transfer of ^{13}C label into the glutamate pool has been linked to TCA cycle flux. The rate of label incorporation indicated a significant difference in the rate of glutamate labeling with activation, but oxygen consumption increased at most by 30%, which is approximately half of the cerebral blood flow increase measured using this stimulation paradigm [107]. This study supported the concept that oxygen consumption increases are less than the associated cerebral blood flow increases, leading to a net decrease in deoxyhemoglobin content during focal activation, which forms the basis of blood-oxygen-level-dependent functional MRI [108].

Measurements of Krebs cycle flux from the flow of label from glucose C1 to glutamate C4 are affected by transport across the highly charged inner mitochondrial membrane. It is likely that such transport is controlled, since rapid transport of acids is unlikely and would interfere with chemiosmosis [109]. Indeed, this ex-

change rate, V_x , was found to be comparable to the flux through pyruvate dehydrogenase, V_{PDH} , in most recent studies of the intact brain [48,81,110], consistent with what has been reported in most other tissues [76,111–113]. Many, but not all, investigators have found that V_x is on the order of V_{PDH} , which implied that the malate–aspartate shuttle may be a major mechanism mediating the exchange of label across the mitochondrial membrane [30,48,81,110,111,114–117].

6.3.1. *Glutamatergic Neurotransmission and Glial Energy Metabolism*

Brain metabolism is exquisitely compartmentalized, with at least two major compartments (attributed to the “neuronal” and “glial” compartment) that are differentiated by the size of the respective glutamate pools associated with the Krebs cycle and that are metabolically linked by the so-called glutamate–glutamine cycle [118,119]. The scheme in Figure 10 summarizes some of the salient features that have been exploited at high field in modeling brain metabolism.

Key to cerebral compartmentation is inactivation of neurotransmitter glutamate by uptake into perisynaptic astrocytes and conversion into electrophysiologically inactive glutamine, which then diffuses back to the neuron [120–123]. Clearly, this mechanism implies a much more active role for astrocytes than is conventionally assumed, since the conversion of neurotransmitter glutamate to glutamine invokes glial energy metabolism [124–126]. The neuron–astrocyte pair thus has to be considered the functional unit (the “tripartite synapse” containing the pre- and postsynaptic neuron and the astrocyte) intimately involved in achieving chemical transmission, as has been proposed in the last decade by Magistretti and others [127–129].

The link between astrocytes and neurons is generally accepted from metabolic and neurophysiological standpoints [130], yet differences exist as to the precise relationship between the metabolic rates and the specific energetics involved [48,81,117,131,132]. The bulk of investigations suggest that non-signaling energy metabolism is approximately a third to half that at resting (non-stimulated) conditions [117,133]. Nonetheless, the controversial hypothesis put forth by Shulman et al. [131,134] linking glucose metabolism with glutamatergic action is intriguing as it emphasizes further the coupling between neurons and glia at the level of energy metabolism as put forward earlier by others (see, e.g., [129]).

Astrocytes have significant oxidative capacity to generate ATP, which can be substantiated with two experimental observations. First, anaplerosis, a mitochondrial reaction confined to the glial compartment, mediated by pyruvate carboxylase, is now generally accepted to have significant activity in vivo [11,13,48,116,117,135,136]. To the extent that anaplerosis leads to net glutamine synthesis (via pyruvate carboxylase) in the glial compartment, a significant net synthesis of ATP occurs oxidatively, thereby generating approximately a third of the ATP per glucose molecule compared to that from complete glucose oxidation [116]. Second, the presence of significant oxidative metabolism in astrocytes stems from the fact that acetate is known to be exclusively metabolized in astrocytes by the TCA cycle [137,138], which can only occur by oxidative metabolism [139].

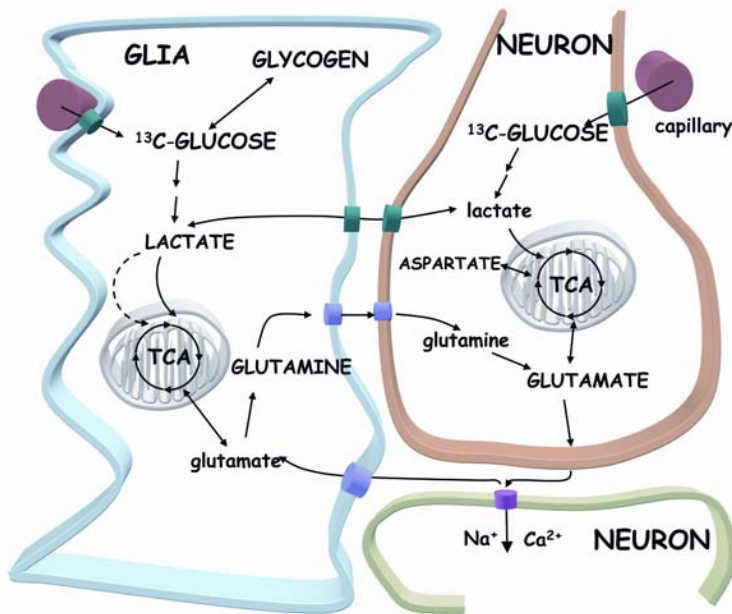


Figure 10. Compartmentation of cerebral neurotransmitter and amino acid metabolism studied via labeling from glucose at, e.g., the C1 position. The glial compartment is on the left and the neuronal on the right. Anaplerosis, mediated by pyruvate carboxylase (dashed arrow), glutamine synthetase, as well as glycogen and its metabolism, are localized to the glial compartment in the adult brain. Most of the glutamine is in the glial compartment and most of the glutamate and aspartate in the neuronal compartment. The metabolites in caps give rise to NMR signals we have measured in vivo. See attached CD for color version.

6.4. Studies of Individual Subjects

The improvements in in-vivo NMR spectroscopy at high fields (highlighted in the first half of the chapter) all translate into increased statistical power, mainly due to sensitivity improvements. Thus smaller volumes can be studied with linear dimensions decreased by the third root of the sensitivity gains, or measurement times can be shortened by the square of the sensitivity improvements.

6.4.1. *Separate Quantification of Glutamate and Glutamine: Hepatic Encephalopathy*

As stated earlier in the chapter, one obvious benefit of higher fields is the clearly increased spectral resolution of especially *J*-coupled resonances, such as glutamate and glutamine. While commonly small changes in brain glutamine are difficult to discern at low fields, such changes in brain glutamine are visually ap-

parent in individual subjects at 4 Tesla [3]. In a study of pediatric patients at 4 Tesla with subclinical hepatic encephalopathy, the increase in brain glutamine was easily detectable (Figure 11). Furthermore, the tight reproducibility of the ^1H NMR spectra allowed to conclude that the increased error in the patient group (Figure 11) was not due to increased quantification errors but rather reflected differences between individual patients. It is of interest to note that while brain glutamine showed distinct and up to a several-fold increase in subclinical HE, the combined Glu and Gln signal (Glx) exhibited only minor variations, as the Gln changes were masked by the much more concentrated Glu signal.

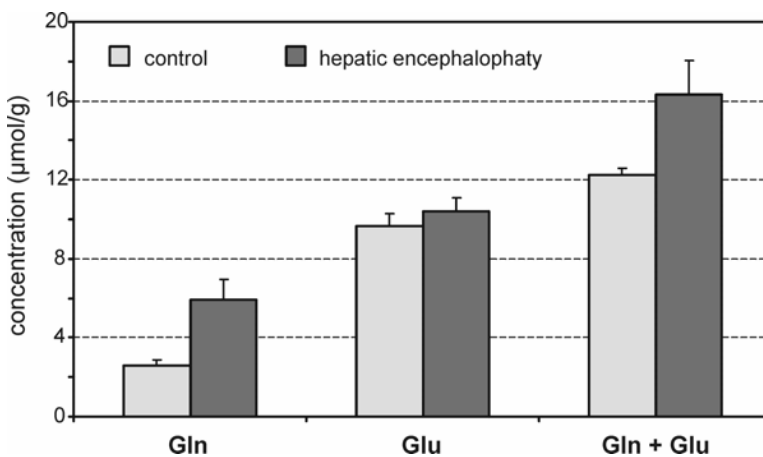


Figure 11. Changes in Glu, Gln, and Glx (Glu + Gln) with HE (bar graph), illustrating the increased statistical power when separating the change in Gln from that of Glu.

6.4.2. Disease Monitoring in Pediatric Patients: Adrenoleukodystrophy

The increases in sensitivity with higher field predispose the method to increased use in especially pediatrics, where subject compliance is difficult to achieve, and hence shorter acquisition times and potential for correction of motion effects can become of paramount importance. Using single-shot acquisition, it was shown that robust and reliable quantification of 12 metabolites was possible in unsedated patients with ALD [59]. Furthermore, in relatively small volumes in white matter (WM), profound changes were observed in the neurochemical profile of lesions (Figure 12). Of special interest was the clear and unambiguous separation of ^1H NMR spectra obtained from lesioned WM, which were unambiguously separated from normal appearing WM, with several-fold differences in some compounds. These observations point to the ability of ^1H NMR spectroscopy to characterize disease onset in prospective lesion sites, long before structural damage is

evident in MRI. In several cases, changes in the neurochemical profile indeed preceded the appearance of hyperintense lesions in T_2 -weighted MRI.

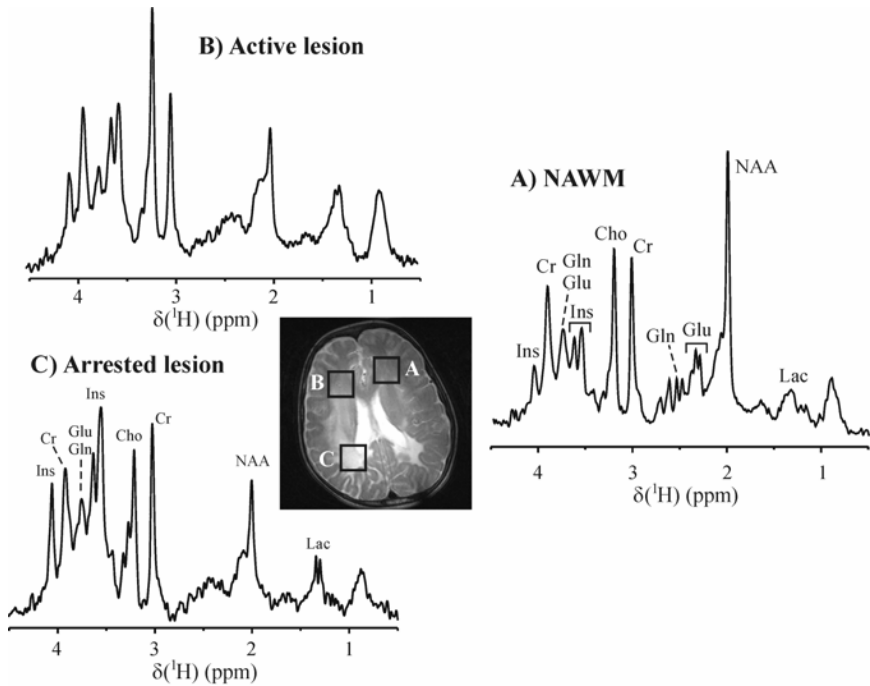


Figure 12. In-vivo NMR spectroscopy at high field can be used for therapy monitoring in individual patients. T_2 -weighted RARE image (TE = 60 ms, echo train length of 8) at 4 Tesla depicting the status of lesions in a patient with the cerebral form of ALD following treatment. Three distinct states of the diseases are discernible in the neurochemical profile: (A) normal-appearing white matter, (B) an active lesion that emerged after treatment, and (C) an arrested lesion.

6.4.3. Detection of Two Important Antioxidants: Glutathione and Vitamin C

Two important antioxidant compounds — glutathione and Vitamin C (ascorbate) — are present in the human brain in sufficient amounts to be detectable in vivo by NMR spectroscopy. The ability to measure glutathione was demonstrated using short-echo spectroscopy at 9.4 Tesla in the rat brain [5]. Changes in glutathione concentration following administration of quinolinic acid in a chemical model of Huntington disease, measured by NMR spectroscopy [26], were in excellent agreement with biochemical studies in the same animal model [140]. The measurement of GSH using short-echo spectroscopy in combination with LCModel analysis is thus likely a robust measurement; however, even at 9.4 Tesla GSH lacks a clearly resolved peak. As pointed out above, spectral editing stands to gain from

the increased spectral specificity of frequency-selective editing pulses at high fields. The ability of spectral editing to measure brain glutathione concentrations was supported by initial results obtained at 1.5 Tesla using multiple-quantum editing [61]. However, since the homonuclear J -coupling is largely independent of field strength, the contribution of the co-edited NAA aspartyl resonance must be taken into account, thereby complicating the analysis of GSH-edited spectra at low fields. In contrast, it was recently shown that using difference editing, it is possible at 4 Tesla to detect a resolved signal from GSH in human brain [32] (Figure 5). Because of its complex spin system, the signal of GSH exhibited a complex spectral pattern that was nevertheless possible to quantify using LCMoDel analysis, yielding a concentration that is in excellent agreement with that obtained by short-echo spectroscopy [32].

The spin system of ascorbate (Vitamin C), on the other hand, is spread over a narrow chemical shift range and more difficult to measure, due to its close proximity to the water resonance. However, the detection of ascorbate is aided at high fields by two factors. First, the increased spectral resolution at higher field does result in improved water suppression and thus a more reliable detection of resonances close to water. Second, the coupled spin system of ascorbate is restricted to a narrow spectral range of 0.8 ppm, making the selective editing by any standard difficult. Nonetheless, with judicious choice of experimental parameters it was shown that the reproducible and reliable detection and quantification of ascorbate was possible at 4 Tesla in the human brain (Figure 13), yielding concentrations on the order of 1.3 mM, in excellent agreement with postmortem analysis [141]. Ascorbate has been mainly ascribed to the neuronal compartment, whereas glutathione appears to have a mainly astrocytic localization, suggesting that the two antioxidant systems act in tandem to protect the brain from oxidative damage. The ability to measure both systems using high field NMR spectroscopy opens the possibility to comprehensively measure cerebral responses to oxidative stress.

7. OUTLOOK

The increased sensitivity at high field is likely to allow the measurement of many neurochemicals in small volumes in individual patients, leading to the potential to follow disease progression and therapy. It is important to recognize in this context that high field alone, without concomitant technical improvements and care, may not allow one to garner these advantages, implying that substantial improvements aside from brute increments in B_0 are likely to enhance the biomedical research power of this investigative tool.

The review presented in this chapter illustrates that with appropriate technical improvements NMR spectroscopy at high fields can and already has made contributions to our understanding of brain metabolism and function, e.g., understanding glucose transport, measuring compartmentalized brain glutamate and glutamine metabolism, brain glycogen metabolism, and the measurement of important antioxidants. In addition, the ability to quantify brain glycogen metabolism has led to the postulation that brain glycogen is an important store of glucose equivalents.

Human In Vivo Detection at 4T

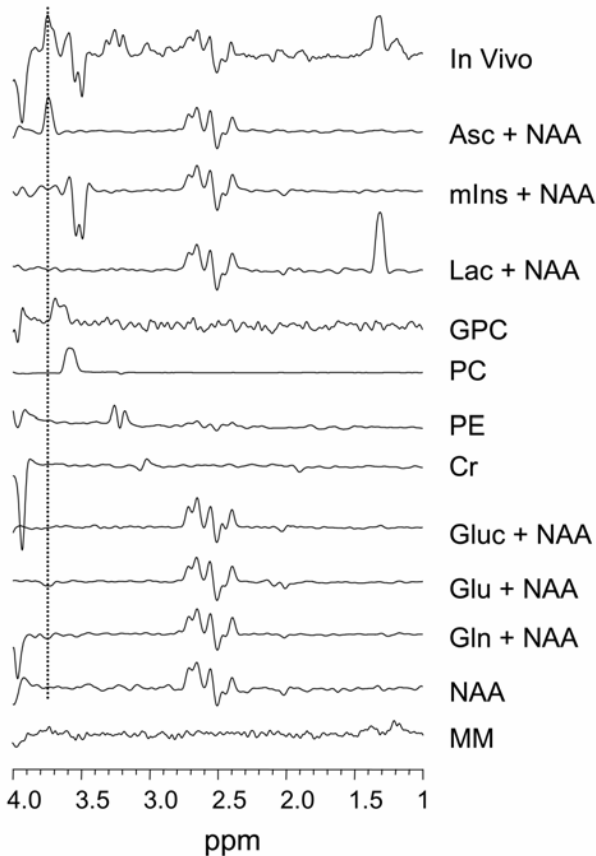


Figure 13. Assignment of in-vivo ^1H NMR signal of Vitamin C in human brain. Reprinted with permission from Terpstra M, Gruetter R. 2004. ^1H NMR detection of vitamin C in human brain in vivo. *Magn Reson Med* **51**:225–229. Copyright © 2004, John Wiley & Sons Inc.

8. ACKNOWLEDGMENTS

The encouragement and support from colleagues at the Center for MR Research is appreciated. Partly supported by the Centre d'Imagerie BioMedicale (CIBM), research partnership in the Lausanne-Geneva region, Switzerland. Supported in part by grants from the U.S. Public Health Service, NIH R21DK58004 (RG), R01NS38672 (RG), R01NS42005 (RG), R21NS45119 (RG), P41RR08079,

M01RR00400, and the Whitaker (RG), Juvenile Diabetes Research (RG), and Keck Foundations.

9. REFERENCES

1. Hoult D, Richards R. 1976. The signal-to-noise ratio of the nuclear magnetic resonance experiment. *J Magn Reson* **24**:71–85.
2. Barker PB, Hearshen DO, Boska MD. 2001. Single-voxel proton MRS of the human brain at 1.5T and 3.0T. *Magn Reson Med* **45**:765–769.
3. Gruetter R, Weisdorf SA, Rajanayagan V, Terpstra M, Merkle H, Truwit CL, Garwood M, Nyberg SL, Ugurbil K. 1998. Resolution improvements in in vivo ^1H NMR spectra with increased magnetic field strength. *J Magn Reson* **135**:260–264.
4. Tkac I, Rao R, Georgieff MK, Gruetter R. 2003. Developmental and regional changes in the neurochemical profile of the rat brain determined by in vivo ^1H NMR spectroscopy. *Magn Reson Med* **50**:24–32.
5. Pfeuffer J, Tkac I, Provencher SW, Gruetter R. 1999. Toward an in vivo neurochemical profile: quantification of 18 metabolites in short-echo-time ^1H NMR spectra of the rat brain. *J Magn Reson* **141**:104–120.
6. Tkac I, Starcuk Z, Choi I-Y, Gruetter R. 1998. Ultra-short Echo-time "Dehydrated" in vivo ^1H NMR Spectroscopy. *Proc Int Soc Magn Reson Med* 1760.
7. Van Cauteren M, Miot F, Segebarth CM, Eisendrath H, Osteaux M, Willem R. 1992. Excitation characteristics of adiabatic half-passage RF pulses used in surface coil MR spectroscopy: application to ^{13}C detection of glycogen in the rat liver. *Phys Med Biol* **37**:1055–1064.
8. Gruetter R, Rothman DL, Novotny EJ, Shulman RG. 1992. Localized ^{13}C NMR spectroscopy of myo-inositol in the human brain in vivo. *Magn Reson Med* **25**:204–210.
9. Gruetter R, Novotny EJ, Boulware SD, Rothman DL, Mason GF, Shulman GI, Shulman RG, Tamborlane WV. 1992. Direct measurement of brain glucose concentrations in humans by ^{13}C NMR spectroscopy. *Proc Natl Acad Sci USA* **89**:1109–1112.
10. deGraaf R, Luo Y, Terpstra M, Garwood M. 1995. Spectral editing with adiabatic pulses. *J Magn Reson B* **109**:184–193.
11. Gruetter R, Seaquist E, Kim S-W, Ugurbil K. 1998. Localized in vivo ^{13}C NMR of glutamate metabolism: initial results at 4 Tesla. *Dev Neurosci* **20**:380–388.
12. Choi IY, Tkac I, Ugurbil K, Gruetter R. 1999. Noninvasive measurements of [$1\text{-}^{13}\text{C}$]glycogen concentrations and metabolism in rat brain in vivo. *J Neurochem* **73**:1300–1308.
13. Shen J, Petersen KF, Behar KL, Brown P, Nixon TW, Mason GF, Petroff OA, Shulman GI, Shulman RG, Rothman DL. 1999. Determination of the rate of the glutamate/glutamine cycle in the human brain by in vivo ^{13}C NMR. *Proc Natl Acad Sci USA* **96**:8235–8240.
14. Oz G, Henry PG, Seaquist ER, Gruetter R. 2003. Direct, noninvasive measurement of brain glycogen metabolism in humans. *Neurochem Int* **43**:323–329.
15. Henry PG, Tkac I, Gruetter R. 2003. ^1H -localized broadband ^{13}C NMR spectroscopy of the rat brain in vivo at 9.4 T. *Magn Reson Med* **50**:684–692.
16. Collins CM, Liu W, Wang J, Gruetter R, Vaughan JT, Ugurbil K, Smith MB. 2004. Temperature and SAR calculations for a human head within volume and surface coils at 64 and 300 MHz. *J Magn Reson Imag* **19**:650–656.

17. van den Bergh AJ, van den Boogert HJ, Heerschap A. 1998. Calibration of the ^1H -decoupling field strength and experimental evaluation of the specific RF absorption rate in ^1H -decoupled human ^{13}C -MRS. *Magn Reson Med* **39**:642–646.
18. Bax A. 1983. A simple method for the calibration of the decoupler radiofrequency field strength. *J Magn Reson* **52**:76–80.
19. Tkac I, Henry PG, Andersen P, Keene CD, Low WC, Gruetter R. 2004. Highly resolved in vivo ^1H NMR spectroscopy of the mouse brain at 9.4 T. *Magn Reson Med* **52**:478–484.
20. Shen J, Rycyna RE, Rothman DL. 1997. Improvements on an in vivo automatic shimming method (FASTERMAP). *Magn Reson Med* **38**:834–839.
21. Manabe A. 1994. Multi-angle projection shim (MAPShim): in vivo shim adjustment up to 2nd order in 0.2 second sequence time. *Proc Soc Magn Reson* 765.
22. Gruetter R. 1993. Automatic, localized in vivo adjustment of all first- and second-order shim coils. *Magn Reson Med* **29**:804–811.
23. Gruetter R, Boesch C. 1992. Fast, non-iterative shimming on spatially localized signals: in vivo analysis of the magnetic field along axes. *J Magn Reson* **96**:323–334.
24. Gruetter R, Tkac I. 2000. Field mapping without reference scan using asymmetric echo-planar techniques. *Magn Reson Med* **43**:319–323.
25. Tkac I, Starcuk Z, Choi I-Y, Gruetter R. 1999. In vivo ^1H NMR spectroscopy of rat brain at 1 ms echo time. *Magn Reson Med* **41**:649–656.
26. Tkac I, Keene CD, Pfeuffer J, Low WC, Gruetter R. 2001. Metabolic changes in quinolinic acid-lesioned rat striatum detected non-invasively by in vivo ^1H NMR spectroscopy. *J Neurosci Res* **66**:891–898.
27. Ross BD, Bluml S, Cowan R, Danielsen E, Farrow N, Gruetter R. 1997. In vivo magnetic resonance spectroscopy of human brain: the biophysical basis of dementia. *Bio-phys Chem* **68**:161–172.
28. Bluml S, Hwang JH, Moreno A, Ross BD. 2000. Novel peak assignments of in vivo ^{13}C MRS in human brain at 1.5 T. *J Magn Reson* **143**:292–298.
29. Choi IY, Gruetter R. 2004. Dynamic or inert metabolism? Turnover of N-acetyl aspartate and glutathione from D-[1- ^{13}C]glucose in the rat brain in vivo. *J Neurochem* **91**:778–787.
30. Gruetter R, Adriany G, Choi IY, Henry PG, Lei H, Oz G. 2003. Localized in vivo ^{13}C NMR spectroscopy of the brain. *NMR Biomed* **16**:313–338.
31. Gruetter R, Adriany G, Merkle H, Andersen PM. 1996. Broadband decoupled, ^1H localized ^{13}C MRS of the human brain at 4 Tesla. *Magn Reson Med* **36**:659–664.
32. Terpstra M, Henry PG, Gruetter R. 2003. Measurement of reduced glutathione (GSH) in human brain using LCModel analysis of difference-edited spectra. *Magn Reson Med* **50**:19–23.
33. Seaquist ER, Gruetter R. 1998. Identification of a high concentration of scyllo-inositol in the brain of a healthy human subject using ^1H and ^{13}C NMR. *Magn Reson Med* **39**:313–316.
34. Gruetter R, Ugurbil K, Seaquist ER. 1998. Steady-state cerebral glucose concentrations and transport in the human brain. *J Neurochem* **70**:397–408.
35. Bluml S. 1999. In vivo quantitation of cerebral metabolite concentrations using natural abundance ^{13}C MRS at 1.5 T. *J Magn Reson* **136**:219–225.
36. Sonnewald U, Gribbestad IS, Westergaard N, Nilsen G, Unsgard G, Schousboe A, Petersen SB. 1994. Nuclear magnetic resonance spectroscopy: biochemical evaluation of brain function in vivo and in vitro. *Neurotoxicology* **15**:579–590.

37. Leibfritz D. 1996. An introduction to the potential of ^1H -, ^{31}P - and ^{13}C -NMR spectroscopy. *Anticancer Res* **16**:1317–1324.
38. Shaka AJ, Keeler J, Freeman R. 1983. Evaluation of a new broadband decoupling sequence: WALTZ-16. *J Magn Reson* **53**:313–340.
39. Pfeuffer J, Tkac I, Choi I-Y, Merkle H, Ugurbil K, Garwood M, Gruetter R. 1999. Localized in vivo ^1H NMR detection of neurotransmitter labeling in rat brain during infusion of $[1-^{13}\text{C}]$ D-glucose. *Magn Reson Med* **41**:1077–1083.
40. De Graaf RA, Mason GF, Patel AB, Rothman DL, Behar KL. 2004. Regional glucose metabolism and glutamatergic neurotransmission in rat brain in vivo. *Proc Natl Acad Sci USA* **101**(34):12700–12705.
41. Muller S, Beckmann N. 1989. ^{13}C spectroscopic imaging. A simple approach to in vivo ^{13}C investigations. *Magn Reson Med* **12**:400–406.
42. van den Bergh AJ, van den Boogert HJ, Heerschap A. 1998. Heteronuclear cross polarization for enhanced sensitivity of in vivo ^{13}C MR spectroscopy on a clinical 1.5 T MR system. *J Magn Reson* **135**:93–98.
43. Brown TR, Kincaid BM, Ugurbil K. 1982. NMR chemical shift imaging in three dimensions. *Proc Natl Acad Sci USA* **79**:3523–3526.
44. Haupt CI, Schuff N, Weiner MW, Maudsley AA. 1996. Removal of lipid artifacts in ^1H spectroscopic imaging by data extrapolation. *Magn Reson Med* **35**:678–687.
45. Hu X, Patel M, Chen W, Ugurbil K. 1995. Reduction of truncation artifacts in CSI by extended sampling using variable TR. *J Magn Reson A* **106**:292–296.
46. Doddrell DM, Pegg DT, Bendall MR. 1982. Distortionless Enhancement of NMR signals by polarization transfer. *J Magn Reson* **48**:323–327.
47. Merkle H, Wei H, Garwood M, Ugurbil K. 1992. B_1 insensitive heteronuclear adiabatic polarization transfer for signal enhancement. *J Magn Reson* **99**:480–494.
48. Gruetter R, Seauquert ER, Ugurbil K. 2001. A mathematical model of compartmentalized neurotransmitter metabolism in the human brain. *Am J Physiol* **281**:E100–E112.
49. Bomsdorf H, Roschmann P, Wieland J. 1991. Sensitivity enhancement in whole-body natural abundance ^{13}C spectroscopy using $^{13}\text{C}/^1\text{H}$ double-resonance techniques at 4 tesla. *Magn Reson Med* **22**:10–22.
50. Overloop K, Vanstapel F, Vanhecke P. 1996. ^{13}C -NMR relaxation in glycogen. *Magn Reson Med* **36**:45–51.
51. Zang LH, Laughlin MR, Rothman DL, Shulman RG. 1990. ^{13}C NMR relaxation times of hepatic glycogen in vitro and in vivo. *Biochemistry* **29**:6815–6820.
52. Choi IY, Tkac I, Gruetter R. 2000. Single-shot, three-dimensional "non-echo" localization method for in vivo NMR spectroscopy. *Magn Reson Med* **44**:387–394.
53. Pan JW, Hetherington HP. 1996. J-refocused coherence transfer spectroscopy to observe GABA at 4.1 T. *Proc Intl Soc Magn Reson Med* 1229.
54. Tkac I, Andersen P, Adriany G, Merkle H, Ugurbil K, Gruetter R. 2001. In vivo ^1H NMR spectroscopy of the human brain at 7 T. *Magn Reson Med* **46**:451–456.
55. Tkac I, Andersen P, Adriany G, Gruetter R, Ugurbil K. 1999. 4-ms echo-time ^1H NMR spectra of human brain measured in a 4 Tesla/90 cm magnet using a body gradient coil. *Proc Int Soc Magn Reson Med*, Poster M1612.
56. Tannus A, Garwood M. 1996. Improved performance of frequency-swept pulses using offset-independent adiabaticity. *J Magn Reson A* **120**:133–137.
57. Garwood M, DelaBarre L. 2001. The return of the frequency sweep: designing adiabatic pulses for contemporary NMR. *J Magn Reson* **153**:155–177.

58. Hetherington HH, Pan JW, Mason GF, Ponder S, Twieg DB, Deutsch G, Mountz J, Pohost GM. 1994. 2D ^1H spectroscopic imaging of the human brain at 4.1T. *Magn Reson Med* **32**:530–534.
59. Oz G, Tkac I, Charnas LR, Choi IY, Bjoraker KJ, Shapiro EG, Gruetter R. 2005. Assessment of adrenoleukodystrophy lesions by high field MRS in non-sedated pediatric patients. *Neurology* **64**:434–441.
60. Gruetter R, Garwood M, Ugurbil K, Seaquist ER. 1996. Observation of resolved glucose signals in ^1H NMR spectra of human brain at 4 Tesla. *Magn Reson Med* **36**:1–6.
61. Trabesinger AH, Weber OM, Duc CO, Boesiger P. 1999. Detection of glutathione in the human brain in vivo by means of double quantum coherence filtering. *Magn Reson Med* **42**:283–289.
62. Rothman DL, Petroff OA, Behar KL, Mattson RH. 1993. Localized ^1H NMR measurements of gamma-aminobutyric acid in human brain in vivo. *Proc Natl Acad Sci USA* **90**:5662–5666.
63. Jouvencal L, Carlier PG, Bloch G. 1996. Practical implementation of single-voxel double-quantum editing on a whole-body NMR spectrometer: localized monitoring of lactate in the human leg during and after exercise. *Magn Reson Med* **36**:487–490.
64. Behar KL, Rothman DL, Spencer DD, Petroff OAC. 1994. Analysis of macromolecule resonances in ^1H MR spectra of human brain. *Magn Reson Med* **32**:294–302.
65. Hanstock CC, Coupland NJ, Allen PS. 2002. GABA X2 multiplet measured pre- and post-administration of vigabatrin in human brain. *Magn Reson Med* **48**:617–623.
66. Marjanska M, Henry PG, Bolan PJ, Vaughan B, Seaquist ER, Gruetter R, Ugurbil K, Garwood M. 2005. Uncovering hidden in vivo resonances using editing based on localized TOCSY. *Magn Reson Med* **53**:783–789.
67. Terpstra M, Ugurbil K, Gruetter R. 2002. Direct in vivo measurement of human cerebral GABA concentration using MEGA-editing at 7 Tesla. *Magn Reson Med* **47**:1009–1012.
68. Mescher M, Merkle H, Kirsch J, Garwood M, Gruetter R. 1998. Simultaneous water suppression and editing in vivo. *NMR Biomed* **11**:266–272.
69. Slotboom J, Boesch C, Kreis R. 1998. Versatile frequency domain fitting using time domain models and prior knowledge. *Magn Reson Med* **39**:899–911.
70. Provencher SW. 1993. Estimation of metabolite concentrations from localized in vivo proton NMR spectra. *Magn Reson Med* **30**:672–679.
71. Naressi A, Couturier C, Devos JM, Janssen M, Mangeat C, de Beer R, Graveron-Demilly D. 2001. Java-based graphical user interface for the MRUI quantitation package. *MAGMA* **12**:141–152.
72. de Beer R, van den Boogaart A, van Ormondt D, Pijnappel WW, den Hollander JA, Marien AJ, Luyten PR. 1992. Application of time-domain fitting in the quantification of in vivo ^1H spectroscopic imaging data sets. *NMR Biomed* **5**:171–178.
73. Provencher SW. 2001. Automatic quantitation of localized in vivo ^1H spectra with LCModel. *NMR Biomed* **14**:260–264.
74. Mader I, Seeger U, Karitzky J, Erb M, Schick F, Klose U. 2002. Proton magnetic resonance spectroscopy with metabolite nulling reveals regional differences of macromolecules in normal human brain. *J Magn Reson Imag* **16**:538–546.
75. Opstad KS, Provencher SW, Bell BA, Griffiths JR, Howe FA. 2003. Detection of elevated glutathione in meningiomas by quantitative in vivo ^1H MRS. *Magn Reson Med* **49**:632–637.

76. Garcia-Martin ML, Garcia-Espinosa MA, Ballesteros P, Bruix M, Cerdan S. 2002. Hydrogen turnover and subcellular compartmentation of hepatic [2-¹³C]glutamate and [3-¹³C]aspartate as detected by ¹³C NMR. *J Biol Chem* **277**:7799–7807.
77. Mason GF, Behar KL, Rothman DL, Shulman RG. 1992. NMR determination of intracerebral glucose concentration and transport kinetics in rat brain. *J Cereb Blood Flow Met* **12**:448–455.
78. Choi IY, Lee SP, Kim SG, Gruetter R. 2001. In vivo measurements of brain glucose transport using the reversible Michaelis-Menten model and simultaneous measurements of cerebral blood flow changes during hypoglycemia. *J Cereb Blood Flow Met* **21**:653–663.
79. Criego AB, Tkac I, Kumar A, Thomas W, Gruetter R, Seaquist ER. 2005. Brain glucose concentrations in patients with type 1 diabetes and hypoglycemia unawareness. *J Neurosci Res* **79**:42–47.
80. Gruetter R, Rothman DL, Novotny EJ, Shulman GI, Prichard JW, Shulman RG. 1992. Detection and assignment of the glucose signal in ¹H NMR spectra of the human brain. *Magn Reson Med* **26**:183–188.
81. Choi IY, Lei H, Gruetter R. 2002. Effect of deep pentobarbital anesthesia on neurotransmitter metabolism in vivo: on the correlation of total glucose consumption with glutamatergic action. *J Cereb Blood Flow Met* **22**:1343–1351.
82. de Graaf RA, Pan JW, Telang F, Lee JH, Brown P, Novotny EJ, Hetherington HP, Rothman DL. 2001. Differentiation of glucose transport in human brain gray and white matter. *J Cereb Blood Flow Met* **21**:483–492.
83. Seaquist ER, Damberg GS, Tkac I, Gruetter R. 2001. The effect of insulin on in vivo cerebral glucose concentrations and rates of glucose transport/metabolism in humans. *Diabetes* **50**:2203–2209.
84. Pfeuffer J, Tkac I, Gruetter R. 2000. Extracellular-intracellular distribution of glucose and lactate in the rat brain assessed noninvasively by diffusion-weighted ¹H nuclear magnetic resonance spectroscopy in vivo. *J Cereb Blood Flow Met* **20**:736–746.
85. Gjedde A, Diemer NH. 1983. Autoradiographic determination of regional brain glucose content. *J Cereb Blood Flow Met* **3**:303–310.
86. Holden JE, Mori K, Dienel GA, Cruz NF, Nelson T, Sokoloff L. 1991. Modeling the dependence of hexose distribution volumes in brain on plasma glucose concentration: implications for estimation of the local 2-deoxyglucose lumped constant. *J Cereb Blood Flow Met* **11**:171–182.
87. Lund-Andersen H. 1979. Transport of glucose from blood to brain. *Physiol Rev* **59**:305–352.
88. Hasselbalch SG, Knudsen GM, Holm S, Hageman LP, Capaldo B, Paulson OB. 1996. Transport of D-glucose and 2-fluorodeoxyglucose across the blood-brain barrier in humans. *J Cereb Blood Flow Met* **16**:659–666.
89. Gruetter R, Novotny EJ, Boulware SD, Rothman DL, Shulman RG. 1996. ¹H NMR studies of glucose transport in the human brain. *J Cereb Blood Flow Met* **16**:427–438.
90. Dienel GA, Cruz NF, Adachi K, Sokoloff L, Holden JE. 1997. Determination of local brain glucose level with [¹⁴C]methylglucose: effects of glucose supply and demand. *Am J Physiol* **273**:E839–849.
91. Cunningham VJ, Hargreaves RJ, Pelling D, Moorhouse SR. 1986. Regional blood-brain glucose transfer in the rat: a novel double-membrane kinetic analysis. *J Cereb Blood Flow Met* **6**:305–314.
92. Gruetter R. 2003. Glycogen: the forgotten cerebral energy store. *J Neurosci Res* **74**:179–183.

93. Choi IY, Seaquist ER, Gruetter R. 2003. Effect of hypoglycemia on brain glycogen metabolism in vivo. *J Neurosci Res* **72**:25–32.
94. Lowry O, Passonneau J, Hasselberger F, Schulz D. 1964. Effect of ischemia on known substrates and cofactors of the glycolytic pathway in brain. *J Biol Chem* **239**:18–30.
95. Swanson RA, Sagar SM, Sharp FR. 1989. Regional brain glycogen stores and metabolism during complete global ischaemia. *Neurol Res* **11**:24–28.
96. Cruz NF, Dienel GA. 2002. High glycogen levels in brains of rats with minimal environmental stimuli: implications for metabolic contributions of working astrocytes. *J Cereb Blood Flow Met* **22**:1476–1489.
97. Kong J, Shepel PN, Holden CP, Mackiewicz M, Pack AI, Geiger JD. 2002. Brain glycogen decreases with increased periods of wakefulness: implications for homeostatic drive to sleep. *J Neurosci* **22**:5581–5587.
98. Choi IY, Gruetter R. 2003. In vivo ^{13}C NMR assessment of brain glycogen concentration and turnover in the awake rat. *Neurochem Int* **43**:317–322.
99. Sorg O, Magistretti PJ. 1992. Vasoactive intestinal peptide and noradrenaline exert long-term control on glycogen levels in astrocytes: blockade by protein synthesis inhibition. *J Neurosci* **12**:4923–4931.
100. Fox PT, Raichle ME, Mintun MA, Dence C. 1988. Nonoxidative glucose consumption during focal physiologic neural activity. *Science* **241**:462–464.
101. Prichard J, Rothman D, Novotny E, Petroff O, Kuwabara T, Avison M, Howseman A, Hanstock C, Shulman R. 1991. Lactate rise detected by ^1H NMR in human visual cortex during physiologic stimulation. *Proc Natl Acad Sci USA* **88**:5829–5831.
102. Sappey-Marinié D, Calabrese G, Fein G, Hugg JW, Biggins C, Weiner MW. 1992. Effect of photic stimulation on human visual cortex lactate and phosphates using ^1H and ^{31}P magnetic resonance spectroscopy. *J Cereb Blood Flow Met* **12**:584–592.
103. Merboldt KD, Bruhn H, Hanicke W, Michaelis T, Frahm J. 1992. Decrease of glucose in the human visual cortex during photic stimulation. *Magn Reson Med* **25**:187–194.
104. Frahm J, Krüger G, Merboldt KD, Kleinschmidt A. 1996. Dynamic uncoupling and recoupling of perfusion and oxidative metabolism during focal brain activation in man. *Magn Reson Med* **35**:143–148.
105. Madsen PL, Cruz NF, Sokoloff L, Dienel GA. 1999. Cerebral oxygen/glucose ratio is low during sensory stimulation and rises above normal during recovery: excess glucose consumption during stimulation is not accounted for by lactate efflux from or accumulation in brain tissue. *J Cereb Blood Flow Met* **19**:393–400.
106. Shulman RG, Hyder F, Rothman DL. 2001. Cerebral energetics and the glycogen shunt: neurochemical basis of functional imaging. *Proc Natl Acad Sci USA* **98**:6417–6422.
107. Chen W, Zhu XH, Gruetter R, Seaquist ER, Adriany G, Ugurbil K. 2001. Study of tricarboxylic acid cycle flux changes in human visual cortex during hemifield visual stimulation using ^1H - ^{13}C MRS and fMRI. *Magn Reson Med* **45**:349–355.
108. Ogawa S, Menon RS, Kim SG, Ugurbil K. 1998. On the characteristics of functional magnetic resonance imaging of the brain. *Ann Rev Biophys Biomol Struct* **27**:447–474.
109. Berkich DA, Xu Y, LaNoue KF, Gruetter R, Hutson SM. 2005. Evaluation of brain mitochondrial glutamate and alpha-ketoglutarate transport under physiologic conditions. *J Neurosci Res* **79**:106–113.
110. Henry PG, Lebon V, Vaufray F, Brouillet E, Hantraye P, Bloch G. 2002. Decreased TCA cycle rate in the rat brain after acute 3-NP treatment measured by in vivo ^1H - ^{13}C NMR spectroscopy. *J Neurochem* **82**:857–866.

111. Yu X, White LT, Alpert NM, Lewandowski ED. 1996. Subcellular metabolite transport and carbon isotope kinetics in the intramyocardial glutamate pool. *Biochemistry* **35**:6963–6968.
112. Jeffrey FM, Reshetov A, Storey CJ, Carvalho RA, Sherry AD, Malloy CR. 1999. Use of a single ^{13}C NMR resonance of glutamate for measuring oxygen consumption in tissue. *Am J Physiol* **277**:E1111–1121.
113. Jucker BM, Ren J, Dufour S, Cao X, Previs SF, Cadman KS, Shulman GI. 2000. $^{13}\text{C}/^{31}\text{P}$ NMR assessment of mitochondrial energy coupling in skeletal muscle of awake fed and fasted rats: relationship with uncoupling protein 3 expression. *J Biol Chem* **275**:39279–39286.
114. LaNoue KF, Tischler ME. 1974. Electrogenic characteristics of the mitochondrial glutamate–aspartate antiporter. *J Biol Chem* **249**:7522–7528.
115. Chatham JC, Forder JR, Glickson JD, Chance EM. 1995. Calculation of absolute metabolic flux and the elucidation of the pathways of glutamate labeling in perfused rat heart by ^{13}C NMR spectroscopy and nonlinear least squares analysis. *J Biol Chem* **270**:7999–8008.
116. Gruetter R. 2002. In vivo ^{13}C NMR studies of compartmentalized cerebral carbohydrate metabolism. *Neurochem Int* **41**:143–154.
117. Oz G, Berkich DA, Henry PG, Xu Y, LaNoue K, Hutson SM, Gruetter R. 2004. Neuroglial metabolism in the awake rat brain: CO₂ fixation increases with brain activity. *J Neurosci* **24**:11273–11279.
118. Yudkoff M, Nissim I, Daikhin Y, Lin Z, Nelson D, Pleasure D, Erecinska M. 1993. Brain glutamate metabolism: neuronal-astroglial relationships. *Dev Neurosci* **15**:343–350.
119. Schousboe A, Westergaard N, Hertz L. 1993. Neuronal-astrocytic interactions in glutamate metabolism. *Biochem Soc Trans* **21**:49–53.
120. McKenna MC, Stevenson JH, Huang X, Hopkins IB. 2000. Differential distribution of the enzymes glutamate dehydrogenase and aspartate aminotransferase in cortical synaptic mitochondria contributes to metabolic compartmentation in cortical synaptic terminals. *Neurochem Int* **37**:229–241.
121. Daikhin Y, Yudkoff M. 2000. Compartmentation of brain glutamate metabolism in neurons and glia. *J Nutr* **130**:1026S–1031S.
122. Schousboe A, Westergaard N, Sonnewald U, Petersen SB, Huang R, Peng L, Hertz L. 1993. Glutamate and glutamine metabolism and compartmentation in astrocytes. *Dev Neurosci* **15**:359–366.
123. Nicklas WJ, Zeevalk G, Hyndman A. 1987. Interactions between neurons and glia in glutamate/glutamine compartmentation. *Biochem Soc Trans* **15**:208–210.
124. Eriksson G, Peterson A, Iverfeldt K, Walum E. 1995. Sodium-dependent glutamate uptake as an activator of oxidative metabolism in primary astrocyte cultures from newborn rat. *Glia* **15**:152–156.
125. Magistretti P, Pellerin L. 1996. Cellular mechanisms of brain energy metabolism: relevance to functional brain imaging and to neurodegenerative disorders. *Ann NY Acad Sci* **777**:380–387.
126. Silver IA, Erecinska M. 1997. Energetic demands of the Na⁺/K⁺ ATPase in mammalian astrocytes. *Glia* **21**:35–45.
127. Tsacopoulos M, Magistretti P. 1996. Metabolic coupling between glia and neurons. *J Neurosci* **16**:877–885.

128. Magistretti PJ, Pellerin L. 1999. Cellular mechanisms of brain energy metabolism and their relevance to functional brain imaging. *Phil Trans Roy Soc London B (Biol Sci)* **354**:1155–1163.
129. Magistretti PJ, Sorg O, Yu N, Martin JL, Pellerin L. 1993. Neurotransmitters regulate energy metabolism in astrocytes: implications for the metabolic trafficking between neural cells. *Dev Neurosci* **15**:306–312.
130. Bergles DE, Dzubay JA, Jahr CE. 1997. Glutamate transporter currents in bergmann glial cells follow the time course of extrasynaptic glutamate. *Proc Natl Acad Sci USA* **94**:14821–14825.
131. Sibson NR, Dhankhar A, Mason GF, Rothman DL, Behar KL, Shulman RG. 1998. Stoichiometric coupling of brain glucose metabolism and glutamatergic neuronal activity. *Proc Natl Acad Sci USA* **95**:316–321.
132. Attwell D, Laughlin SB. 2001. An energy budget for signaling in the grey matter of the brain. *J Cereb Blood Flow Met* **21**:1133–1145.
133. Siegel GJ, Agranoff BW. 1999. *Basic neurochemistry: molecular, cellular and medical aspects*. Philadelphia: Lippincott-Raven Publishers.
134. Rothman DL, Sibson NR, Hyder F, Shen J, Behar KL, Shulman RG. 1999. In vivo nuclear magnetic resonance spectroscopy studies of the relationship between the glutamate-glutamine neurotransmitter cycle and functional neuroenergetics. *Phil Trans Roy Soc London B (Biol Sci)* **354**:1165–1177
135. Lapidot A, Gopher A. 1994. Cerebral metabolic compartmentation: estimation of glucose flux via pyruvate carboxylase/pyruvate dehydrogenase by ^{13}C NMR isotopomer analysis of D-[U- ^{13}C]glucose metabolites. *J Biol Chem* **269**:27198–27208.
136. Merle M, Bouzier-Sore AK, Canioni P. 2002. Time-dependence of the contribution of pyruvate carboxylase versus pyruvate dehydrogenase to rat brain glutamine labelling from [1- ^{13}C]glucose metabolism. *J Neurochem* **82**:47–57.
137. Berl S, Nicklas WJ, Clarke DD. 1970. Compartmentation of citric acid cycle metabolism in brain: labelling of glutamate, glutamine, aspartate and gaba by several radioactive tracer metabolites. *J Neurochem* **17**:1009–1015.
138. Waniewski RA, Martin DL. 1998. Preferential utilization of acetate by astrocytes is attributable to transport. *J Neurosci* **18**:5225–5233.
139. Dienel GA, Liu K, Popp D, Cruz NF. 1999. Enhanced acetate and glucose utilization during graded photic stimulation: neuronal–glial interactions in vivo. *Ann NY Acad Sci* **893**:279–281.
140. Cruz-Aguado R, Francis-Turner L, Diaz CM, Antunez I. 2000. Quinolinic acid lesion induces changes in rat striatal glutathione metabolism. *Neurochem Int* **37**:53–60.
141. Terpstra M, Gruetter R. 2004. ^1H NMR detection of vitamin C in human brain in vivo. *Magn Reson Med* **51**:225–229.

CLINICAL PROMISE: CLINICAL IMAGING AT ULTRA HIGH FIELD

Vera Novak and Gregory Christoforidis*

*Division of Gerontology, Beth Israel Deaconess
Medical Center, Harvard Medical School;*

**Department of Radiology, The Ohio State University*

As the race for increased magnetic field strength continues, ultra high field magnetic resonance systems are entering the clinical arena. Human brain imaging at ultra high field (7, 8, and 9.4 Tesla) offers an unprecedented resolution for anatomical imaging that approaches in-vivo microscopy. Results from healthy volunteers and from stroke and tumor studies have demonstrated that high field MRI can visualize microvasculature, details of pathological conditions, and iron deposits with a resolution not obtainable at lower fields. High-resolution maps of brain function and biochemical markers have been obtained at 7 Tesla. Clinical brain imaging is feasible at ultra high magnetic field, but more studies need to be done to determine its diagnostic potential.

1. INTRODUCTION

The increase of magnetic field strength is among the most significant achievements in in-vivo human brain magnetic resonance imaging (MRI). The signal-to-noise ratio and resolution of the magnetic resonance signal is proportional to the magnetic field strength [1]. The higher image resolution, shortening of acquisition times, and more sensitive functional MRI and MR spectroscopy are potential advantages for clinical imaging at the higher magnetic fields. Commonly used clinical MRI scanners that operate at 0.5–1.5 Tesla (T) provide reasonable images of the brain's anatomy and can delineate certain structural lesions. Routinely obtained resolution, however, does not permit evaluation of subtle abnormalities associated with cerebrovascular small-vessel disease, neurodegenerative disorders such as Alzheimer's disease or Parkinson's disease, tumors, and strokes. In addition, the imaging of the deeper brain structures including the brain stem is of lower quality, allowing imaging of more superficial structures, for a variety of technical reasons. The first human studies at ultra high field showed high-

resolution images of the cortical and subcortical structures approaching the histological level [2–6], an indication that this modality is a viable tool for clinical studies. Although functional MRI (fMRI) and MR spectroscopy at 7 T are still being developed, data so far suggest the potential for high-resolution functional and biochemical evaluations of human brain in vivo [7,8].

2. HIGH-RESOLUTION ANATOMICAL IMAGING

The ultimate goal of anatomical studies is to obtain images with a high tissue contrast that will differentiate structures with similar signal intensity. The initial gradient echo (GE) images at 8 T have shown that high-resolution imaging of brain can be obtained with excellent signal-to-noise ratio, contrast-to-noise ratio, and lower than expected radiofrequency power requirements. The GE images at 8 T were not optimized to evaluate the cerebral cortex anatomy, but in general they have shown excellent differentiation of cerebrospinal fluid and gray and white matter anatomy, revealing details not apparent at the lower fields [2,4,5] (Figure 1).

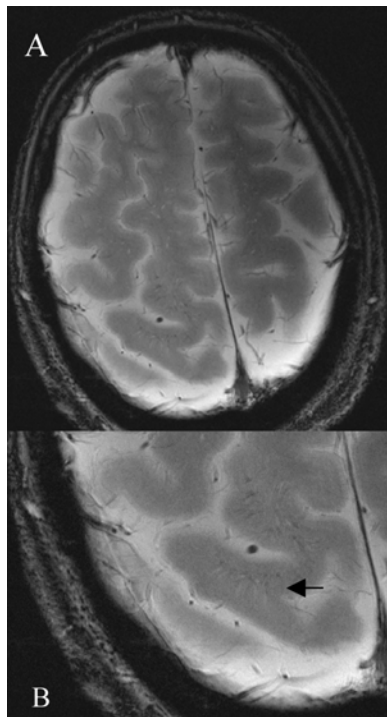


Figure 1. Anaxial image of the cortex from a 61-year-old woman that shows differentiation of gray and white matter (A) and a detail of leptomenigeal vessels (black arrow) as signal voids perpendicular to the sulcus (B). (FOV = 20 x 20 cm; slice thickness = 2.0 mm; TR = 750 msec; TE = 9.2ms; matrix 1024 x 1024).

2.1. Cortex Imaging

Assessments of cortical anatomy and differentiation of gray and white matter boundaries are important for evaluations of neuronal functional decline with aging [9], dementia [10], and neurodegenerative disorders [11]. Although differentiation of the white and gray matter may vary at GE magnitude images, the cortical thickness and microvascular anatomy can be easily estimated with high resolution. It has been reported that the larger superficial cortical arteries and veins (diameter 1–3 mm) were readily visible as signal voids. In addition, the microscopic leptomeningeal vascular anatomy and penetrating vessels (minimally 240 μm) were seen [5]. These small vessels are not regularly visible with the use of routine imaging techniques and surface coils [12]. At high field T_1 tends to increase, and T_2 tends to decrease with increasing magnetic field. As a result, brain images are characterized by the lower contrast and definition of the gray and white matter interface compared with the GE and fast spin-echo (FSE) imaging at lower magnetic field [13]. This is a potential serious limitation for clinical evaluation of brain anatomy and pathology at ultra high fields, particularly using GE techniques. The phase contrast enhancement method [14] that was implemented for post-processing of the GE magnitude images increased differentiation of the white and gray matter boundaries and visualization of the microvasculature. The sensitivity of phase images increased with the strength of the static field as a result of the increased susceptibility-induced phased shifts. Phase images were more homogeneous, provided additional image contrast, and complemented magnitude images. In addition, introduction of FSE [15], FLASH [6], RARE (rapid acquisition with relaxation enhancement), MDEFT (modified driven equilibrium Fourier transform) [16], and other sequences have helped to overcome this limitation.

2.2. Deep Brain Nuclei and Brainstem Imaging

Falls and fall-related injuries are the leading cause of disability in elderly people. Extrapyrmidal findings are surprisingly prevalent among community-dwelling elderly people. Approximately one third of people older than 85 years demonstrate bradykinesia, and more than half show evidence of gait disturbance [11]. This tendency may relate to use of anti-dopaminergic medication, subclinical movement disorders, or small-vessel microangiopathy with basal ganglia lacunae and/or subcortical white matter changes (WMCs). In a study of more than 700 community-dwelling participants from the Cardiovascular Health Study, WMCs were associated with worse performance on balance in clinical and dynamic posturography testing [17]. Among 1077 non-demented elderly men and women participating in the Rotterdam Scan Study [18], those with the most severe diffuse subcortical white matter abnormalities showed psychomotor and gait slowing. While common movement disorders such as Parkinson's disease and falls are routinely diagnosed clinically, MR correlates and diagnostic criteria are yet to be defined. High resolution and magnetic susceptibility to iron and iron-related products at high fields are the desirable features for imaging of deep brain nuclei that may

offer a new avenue for early diagnosis of movement disorders. GE images at high field are sensitive to magnetic field susceptibility, producing distortions at the skull base and in the proximity of sinuses in frontal and temporal regions. However, when these limitations are overcome by optimization of the signal acquisition parameters, high-resolution images of deep brain structures can be obtained. Deep brain nuclei (the caudate, globus pallidus, putamen, substantia nigra, and red nuclei) have been identified on 8T images [13]. The thalamus had the highest signal intensity, followed only by the insular cortex. The posterior and anterior limbs of the internal capsule were seen separating the thalamus, nuclei, and insular cortex. The structures with high iron content have demonstrated a signal loss proportional to increased iron content (notable in the globus pallidus, red nuclei, and the substantia nigra) (Figure 2). The vascular supply to the nuclei followed their margins and has shown the branching patterns from the larger vessels. Preliminary study of Alzheimer's disease has suggested a T_2 signal loss in the CA1 region of the hippocampus, as compared with healthy controls [19].

Brainstem autonomic centers regulating respiration, heart rate, and blood pressure consist of neurons forming a network structure rather than dense nuclei, and this makes them poor candidates for clinical imaging. Routine imaging at 1.5 T delineates only a few important structures. As a result, a significant portion of brainstem strokes and other clinically defined pathologies remains undetected [20]. Brainstem structures were studied from sagittal and axial slices that showed good signal strength and homogeneity with the excellent contours of the upper brainstem, the fourth ventricle, the midbrain, and the pons [21]. Main intra-axial structures were differentiated by higher signal intensities from the predominantly white matter structures such as the corticobulbar, corticopontine, corticospinal tracts, the sensory lemnisci, and the medial longitudinal fasciculus, reticular formation, and the cranial nerves.

Figure 3A shows high-resolution 8T axial slices of the midbrain from a healthy volunteer. The high signal that arises from cerebrospinal fluid (CSF) in the aqueduct also surrounds the midbrain. Multiple vessels, both arteries and veins, are seen traversing midbrain. The profound signal loss reflects a high iron content in the substantia nigra and the red nucleus. While the substantia nigra was easily recognizable, the boundaries appeared larger, extending ventrally. The periaqueductal gray matter surrounding the aqueduct was seen with the higher signal intensity. The medial longitudinal fasciculus was visualized as an area of the lower signal intensity ventrally to the aqueduct. Other myelinated tracts, such as medial and lateral lemniscus, the decussation of the superior cerebellar peduncle, and the pyramidal tracts, were also seen identified as darker areas of lower signal intensity. Figure 3b shows an axial image at 1.5 T with similar parameters. Figure 3C shows a histological slice with Luxol staining for comparison.

2.3. Microvasculature

Visualization of microvasculature within the cerebral cortex and subcortical white matter is limited with standard imaging, even with catheter angiography. At

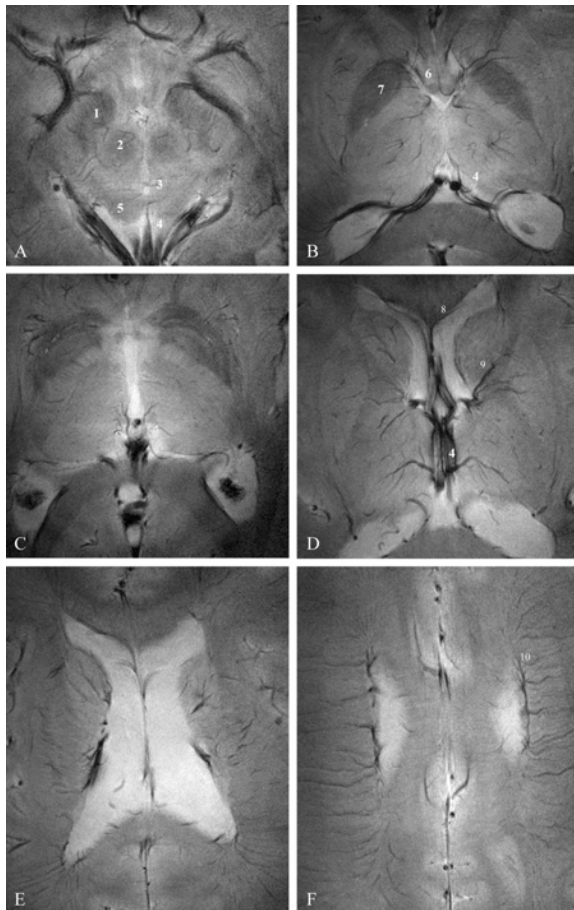


Figure 2. Axial GE images showing details of deep brain structures and microvasculature from a 40-year-old woman. 1 = substantia nigra, 2 = red nucleus, 3 = aqueduct, 4 = internal cerebral veins, 5 = superior colliculus, 6 = mammillary bodies, 7 = globus pallidus, 8 = anterior thalamic vein, 9 = sup. thalamic vein, 10 = transmedullary veins. (GE: FOV = 20 x 20.0 cm, slice thickness = 2.3 mm, TR = 603, TE = 10.0, matrix 1024 x 1024.)

ultra high field in healthy volunteers, essentially all intracranial vessels were seen as signal voids [22]. Most of the larger superficial cortical vessels (1–3 mm wide) were clearly seen without flow or phase artifacts. Many vessels smaller than 1 mm wide are also visible, outlined by higher signal intensity CSF. Cadaver studies, which enabled direct comparisons of unfixed cryotome sections of the whole brain with GE images, have shown microscopic vessels with a resolution of 100 microns [23]. These small leptomeningeal vessels are not visible using routine imaging

techniques at the lower magnetic field, even with surface coils and special image processing. The pattern of these small vessels conforms to the known microscopic leptomeningeal network of arteries and veins supplying the cerebral cortex (Figure 1). These small vessels branch from the more superficial arteries and veins to parallel the surface of the brain before penetrating into it. They are seen outlined by CSF as many small linear branching signal voids within the sulci. The 8T images demonstrated hundreds of these penetrating vessels following the classic pathway, running perpendicular to the gyrus, and then turning to run down along the white matter toward the ventricular margins. However, the intra-cortical arteries and veins could not be differentiated. The ability to directly visualize the microscopic vasculature of the cerebral cortex and subcortical structures is important for clinical studies of cerebral blood flow regulation, offering us new insights into vascular physiology and pathology.

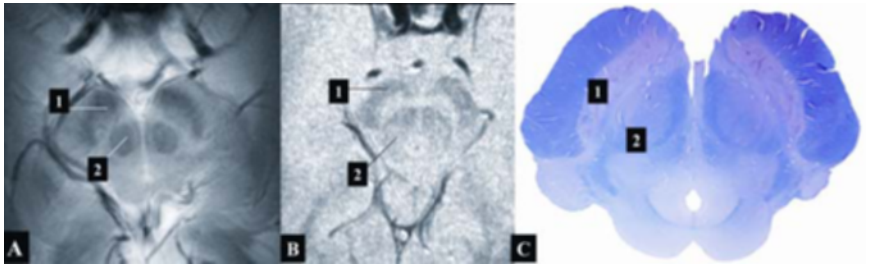


Figure 3. Comparisons of brainstem imaging at 8 (A) and 1.5 T (B) with a histological specimen (C). Panel A shows axial gradient echo 8T image from a healthy volunteer (GE: TR = 1000 msec, TE = 7 msec, FOV = 20 cm, matrix 512 x 512 points, slice thickness = 2mm, receiver bandwidth = 72 kHz). Panel B shows an axial image at 1.5 T with similar parameters (FSE: TR = 750 ms, TE = 8 ms, FOV = 22 cm, slice thickness = 3 mm, receiver bandwidth = 32 kHz). Panel C shows a Lugol-stained histological specimen. See attached CD for color version.

3. CEREBROVASCULAR SMALL-VESEL DISEASE

MR-based techniques have provided evidence that small-vessel subcortical cerebrovascular disease is extremely common among otherwise neurologically normal healthy older adults. T_2 -weighted MR images of older people have repeatedly shown association of silent infarcts and subcortical diffuse periventricular hyperintensities with aging and cardiovascular risk factors [18,24]. Evidence exists that WMCs, arising as a consequence of the longstanding effects of age, hypertension, and other vascular risk factors on cerebral microvasculature [25], reflect the areas of hypoperfusion [26,27]. Supporting this notion are the clinically unrecognized infarctions that were routinely found on brain T_2 -weighted MR images of 28% of elderly people with no history of stroke and 68% of stroke patients [28].

The extent of WMC distribution ranges from narrow rims around the ventricles to the patchy subcortical areas and the involvement of entire white matter. WMCs have not been linked to a single pathophysiological process, and several etiologies — including ischemic, inflammatory, toxic, and metabolic infections or degenerative processes — have been identified. The notion of ischemic process has been supported by the pathological specimens in which periventricular hyperintensities correlate with the severity of demyelination, astrocytic gliosis, and dilatation of perivascular spaces. These findings also support the notion that atherosclerosis is the primary factor in the pathogenesis of white matter changes in the elderly [29,30]. With hypoperfusion as a primary pathogenic mechanism, reduced cerebral blood flow would be found not only in the lesions, but also in the normal-appearing white matter. Hypoperfusion in the normal-appearing white matter would predict lesion development. The strong relationship of WMCs with age [24], cognitive and motor slowing, and other risk factors for stroke suggest that they themselves may be manifestations of clinically important cerebrovascular disease [31]. T_2 -weighted MR images can visualize areas of most prominent tissue damage. The increased signal-to-noise ratio at ultra high field MRI has enhanced resolution for structural and microvascular imaging and enabled visualization of microvasculature within the brain tissue [2,4]. MRI at 8 T has allowed the imaging of the microangiopathy associated with hypertension [32]. The microvascular pattern of signal voids has been demonstrated in healthy volunteers for cortical and subcortical vessels. In a hypertensive patient, these vessels had a hyperintense signal, suggestive of hyalinosis, CSF, or no flow. On sequential sagittal images, hemosiderin and calcium deposits were visible as areas of signal loss within basal ganglia and scattered within the brain [33]. Association between WMCs and patterns of periventricular microvasculature is demonstrated in a series of 8T images obtained from a 45-year-old woman with a small-vessel disease (Figure 4). Rapid acquisition with relaxation enhancement (RARE) images (A, B, C) at the level of ventricles showed confluent WMCs extending from the anterior and posterior horns of the ventricles. Additional focal areas of high signal intensity were seen in the periventricular white matter and basal ganglia. 8T GE images (D, E, F) showed a normal pattern of microvasculature as signal voids. However, some microvessels differed from normal pattern and were seen as high signal intensity lines perpendicular to the ventricle. These microvessels with high signal intensity were seen distally to the normal-appearing vessels. Additional punctuate high signal intensity areas were seen within the basal ganglia. Distribution of microvasculature with hyperintense signal was confined to the periventricular regions and basal ganglia, the areas where white matter lesions were seen on lower-resolution images in other patients with small-vessel disease.

3.1. Iron Deposits, Arterio-Venous Malformations

Microbleeds and iron deposits have higher magnetic susceptibility and therefore can easily be seen as signal void areas that appear larger at high field than with

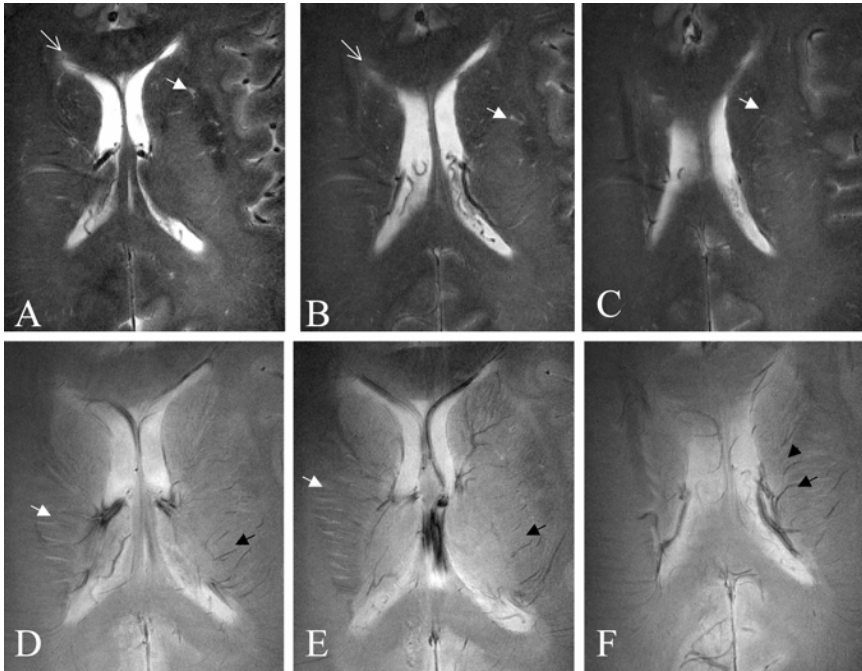


Figure 4. High-resolution axial 8T RARE images at the levels of the ventricles (A, B, C) show high signal intensity confluent white matter changes (white empty arrows) and punctate white matter lesions in basal ganglia and periventricular white matter (white arrows). 8T GE images (D, E, F) at the level of the ventricles show normal-appearing medullary veins as signal voids. Microvessels with high signal intensity are seen distally to the normal vasculature (white arrows). (GE: BW = 69.4 kHz, FOV = 20 x 20 cm, slice thickness = 2.3 mm, TR = 600 ms, TE = 10 ms, matrix 1024 x 1024; RARE: BW = 69.4 kHz, FOV = 20 x 20 cm², slice thickness 2 mm, TR = 3000 ms, TE = 22 ms, matrix 512 x 512, RARE factor 4.)

routine imaging. Incidental findings in ultra high field MRI include iron deposits within brain tissue, fat and calcium deposits within the falx (Figure 5) [32], and vascular pathologies such as angiomas and venous cavernomas [33]. Some angiomas and cavernomas that were not identified at the lower field were more prominent and appeared larger at high field. Cavernous malformations may be clinically silent, or the patient may present with acute neurological deficit, seizures, or hemorrhagic strokes [34]. Cavernomas pose a risk for intralesional rebleeding, as well as extralesional hemorrhage, edema, and in the posterior fossa location increased morbidity and mortality. Visualization of silent vascular abnormalities and tissue iron is clinically relevant because elevated levels of plasma iron, haemorrhages, and intraparenchymal iron deposits are associated with aging, atherosclerosis [35], progression of neurological disorders [36], and adverse outcome after stroke.

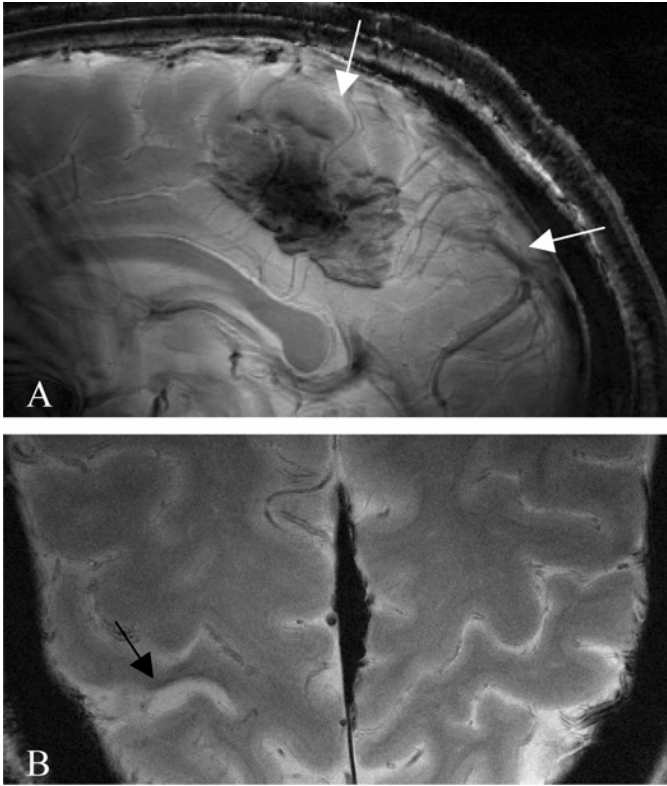


Figure 5. 8T GE sagittal image at midline (A) and axial images of the cortex (B) that show calcium and fat deposits within the falx cerebri (white arrow) as prominent areas of low signal intensity and a prominent venous draining of the posterior sagittal sinus in a 52-year-old man with right parietal stroke (black arrow). (GE: BW = 50.0 kHz, FOV = 20 x 20 cm, slice thickness = 5.0 mm, TR = 504.3 ms, TE = 7.0 ms, matrix = 512 x 512.)

4. STROKE IMAGING

Stroke is a common health problem that affects about 8% of older Americans; 25% of stroke victims die in the acute phase, and 56% or more of those who survive are left with long-term disability. Small-vessel disease accounts for one third of strokes in old age. A cohort of 17 subjects with minor ischemic stroke were studied using T_2 -weighted GE and RARE images with resolution up to 200 μm at 8 Tesla [37]. In 10 subjects, T_1 - and T_2 -weighted FSE and fluid inversion recovery (FLAIR) images were also acquired at 1.5 Tesla MRI. This study was focused on minor stroke or transient ischemic attacks in a younger population (<60 years old).

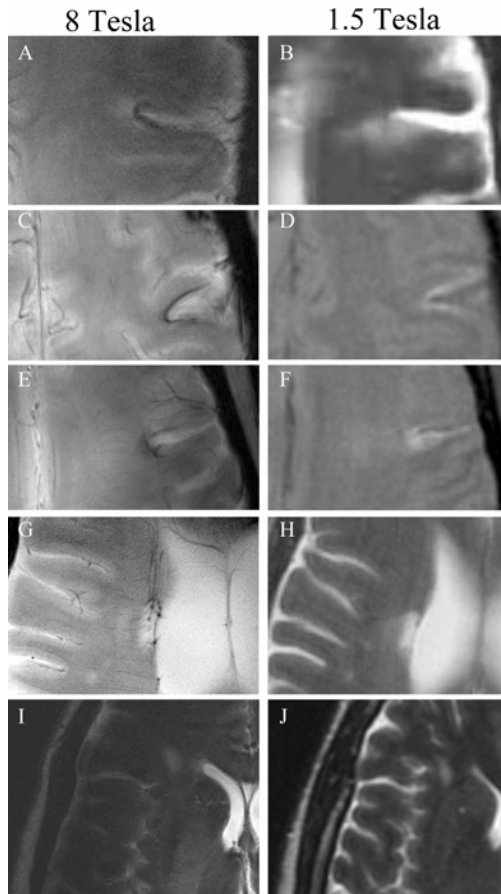


Figure 6. Comparisons of high-resolution axial 8T GE and RARE images and clinical 1.5T FSE and FLAIR images showing small-vessel infarctions. Panels A and B show left posterior frontal cortical hemorrhagic infarction in a 55-year-old man. Panels C, D, E, and F show left temporal cortical infarction in a 40-year-old woman. Panels G and H show right subcortical lacunar infarction in a 51-year-old man. Panel I is an 8T RARE image, and J is a 1.5T FLAIR image in a 57-year-old woman. Panels A,B and G,H were reproduced with permission from Novak V, Kangarlu A, Abduljalil A, Novak P, Slivka A, Chakeres D, et al. 2001. Ultra high field MRI of subacute hemorrhagic stroke at 8 Tesla. *J Comp Assist Tomogr* 25(3):431–435, and Chakeres D, Abduljalil AM, Novak P, Novak V. 2002. Comparison of 1.5 and 8 Tesla high-resolution magnetic resonance imaging of lacunar infarcts. *J Comp Assist Tomogr* 26(4):628–632. (GE: BW = 50.0 kHz, FOV = 20 x 20 cm, slice thickness = 2.3 and 5.0 mm, TE = 12 ms, matrix = 512 x 512 and 1024 x 1024, producing an in-plane pixel size of 390 and 195 microns, respectively. TR = 800ms was selected to maintain a reasonable imaging time of up to 13 minutes with adequate signal-to-noise ratio. To increase the degree of contrast and T_2^* weighting, the nutation angle was set to approximately 20° and the echo time (TE) was set to 12 ms. RARE: slice thickness = 5 mm, number of echoes (N) = 4, TR = 5000 ms, TE = 18 ms, and matrix size 256 x 256. 1.5T parameters: T_1 : slice thickness = 5 mm, TR = 500 ms, TE = 14 ms, FOV = 22 x 22 cm, matrix 256 x 192, N = 16; T_2 : slice thickness 5 mm, TR = 7000 ms, TE = 105 ms, FOV = 22 x 16 cm, matrix 128 x 128, N = 16; FLAIR: slice thickness = 5 mm, TR = 10000 ms, TE = 140 ms, inversion time, TI, = 2200, matrix = 192 x 256, N = 16.)

Subjects were included if they had a minor stroke affecting less than one third of vascular territory and resulting in a minor neurological deficit and if it had been at least 2 months since an acute stroke. Upon admission, 5 subjects had normal 1.5T studies and were diagnosed with transient ischemic attack; 12 subjects were diagnosed with ischemic stroke. The ischemic event etiology was identified as cardioembolism ($N = 4$), small-vessel disease ($N = 7$), and undetermined ($N = 4$). Infarctions were visualized on both 8 and 1.5T images as high signal intensity areas located in the gray matter, white matter, and basal ganglia. The 8T GE images showed a greater number of infarctions ($N = 21$) than did the 1.5T images ($n = 14$) ($p < 0.003$). Figure 6 shows comparisons of high-resolution stroke imaging at 8 T with clinical 1.5T imaging studies. Infarctions appeared better demarcated on 8T than on 1.5T images. Cortical infarctions appeared extended into the white matter, and they were surrounded by the areas of low signal intensity indicative of iron and blood products deposits. Small arteries and veins were seen as dark lines with low, but homogenous, signal intensity at 8T GE images with TE > 4 ms. Figure 6A is a high-resolution 8T GE image that shows a serpentine area of high signal intensity in the posterior left frontal area, suggestive of subacute infarction, of a 55-year-old man. The infarction was surrounded by a low signal intensity area, suggestive of hemorrhagic transformation with hemosiderin deposits, and appeared extended into white matter compared with the T_1 -weighted FSE 1.5T image (B). Figure 6C,E shows high-resolution 8T GE images of the left temporal cortical infarction obtained from a 40-year-old woman, and panels D and F show corresponding T_2 -weighted 1.5T images. Hemosiderin deposits are seen at the infarct borders. A cortical penetrating vessel can be seen within another, higher signal intensity area, anteriorly to the infarction (E) that is not apparent on the 1.5T image. Figure 6G shows high-resolution 8T GE image (matrix 1024 x 1024) of subcortical lacunar infarction in the right basal ganglia of embolic origin in a 51-year-old man with a medical history of patent foramen ovale. A vessel is seen terminating in the infarction with low signal intensity foci, suggestive of hemosiderin deposits. Panel H shows the corresponding 1.5T T_2 -weighted FSE image (matrix 256 x 256). Additional areas of high signal intensity are seen in the area. Panel I is an 8 T RARE image that shows a periventricular lacunar infarction in a 57-year-old woman with a history of right frontal infarct and hypertension and additional white matter hyperintensities. Panel J is the corresponding 1.5T FLAIR image. Additional evidence of periventricular white matter hyperintensities and small-vessel disease is illustrated in Figures 4 and 7. Figure 7 compares high-resolution 8T GE (A) and RARE (C) cortical images with corresponding 1.5T FSE (B) and FLAIR (D) images that show three punctuate lesions in the cortical white matter. Prominent perivascular Virchow-spaces, seen on the 8T RARE image (C), may be suggestive of underlying demyelinating or ischemic processes.

Vascular patterns appeared more prominent in the infarcted than the non-infarcted hemisphere. Small vessels were imaged with infarcts at their termination or supplying the infarcted regions. On some 8T GE images these vessels were seen with high, but inhomogeneous signal intensity. Subcortical hyperintensities were

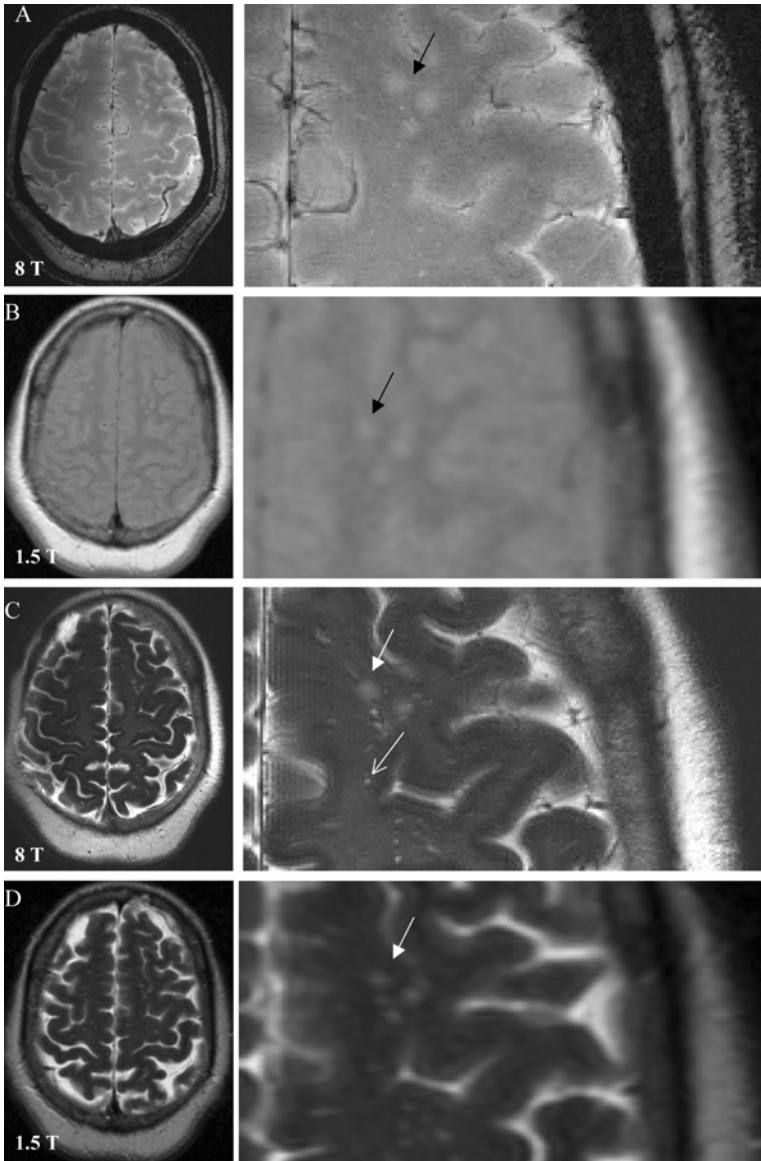


Figure 7. Comparisons of high-resolution axial 8 T GE (A) and RARE (C) cortical images and corresponding 1.5 T FSE (B) and FLAIR (D) images that show three cortical white matter lesions (black and white arrows, respectively). Panel C also shows prominent perivascular Virchow-spaces (white empty arrow). 8T GE: BW = 69.4 kHz, FOV = 20.0 x 20.0 cm, slice thickness = 2.2 mm, TE = 10.8, TR = 600 ms, matrix 512 x 512. 8T RARE: BW = 50.0 kHz, FOV = 20.0 x 20.0 cm, slice thickness = 3.0 mm, TR = 2500 ms, TE = 30 ms, matrix = 512 x 512, $N = 12$, flip angle = 60° , RARE factor = 4.

visible on the 8T images within the periventricular white matter, basal ganglia, and the corona radiata near the gray and white matter junction, but these were not apparent on 1.5T images. These studies illustrate findings on 1.5 and 8T, the relationship of infarcts to microvasculature, the details of infarct site, and incidental vascular lesions.

5. TUMOR IMAGING

Imaging of brain tumors attempts to define the tumor's anatomic location, its extent, the neurologic function that may be affected, and intrinsic characteristics that may predict tumor behavior. Magnetic resonance imaging at higher field strengths has the potential to improve all of these goals. The higher signal-to-noise ratio (SNR) obtained at higher field strengths allows for greater spatial resolution. Greater spatial resolution allows for a more detailed assessment of the relationship of the tumor to adjacent structures such as gray matter, subarachnoid space of vascular structures. Although higher field strength has resulted in greater spatial resolution, the total extent of the brain tumors imaged at 8 and 1.5T has not differed (Figure 8).

The most unique results with brain tumor imaging thus far have been found using high-resolution (<200 μm) proton density/ T_2^* -weighted gradient echo axial images. On these images hundreds of small linear low signal regions correspond to the microvasculature of the brain (Figure 1). As mentioned earlier, the image demonstrates a susceptibility-based signal void for cerebral vasculature with visualization of the cortical penetrating vessels, the transcallosal and transmedullary veins. The expected diameter of some of these vessels is less than 100 microns. This susceptibility-based image contrast is attributed to the presence of deoxyhemoglobin primarily within the venous structures and results in a Blood Oxygen Level dependent (BOLD) contrast. T_2^* in venous blood is very short; the vessels are seen a low-signal regions. Because of their sensitivity to subtle local field variations, gradient echo imaging is most suitable for this purpose. Similar BOLD contrast images have been acquired at lower magnetic field strength [40–42]. Figure 8 depicts the ability of 8T high-resolution imaging to resolve these small structures. Note in Figure 8 that with similar pulse sequences, differences in SNR are clearly visualized. However, practical limitations, most notably RF inhomogeneity, susceptibility artifacts, tissue relaxation times, and suboptimal pulse sequences still hamper ultra high field MRI. The RF coils often used for ultra high field (>7 T) are transverse electromagnetic (TEM) resonators [42,43]. Until recently at this field strength, these volume coils have been unfortunately inhomogeneous in terms of the B_1 fields, not only for the volume, but for various locations on the same image. However, homogeneous excitation is possible, as demonstrated theoretically [44], and most recently experimentally using parallel imaging [45]. Therefore, RF coil inhomogeneity, while present in the early studies, will soon become a thing of the past.

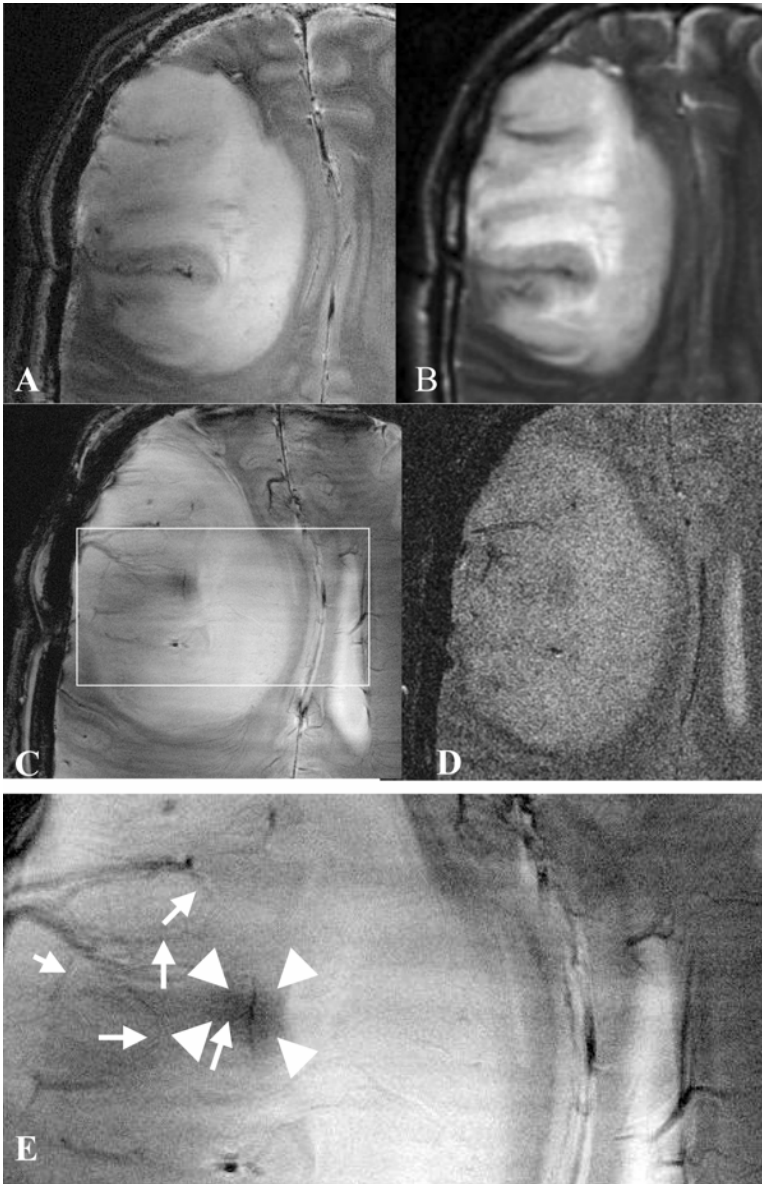
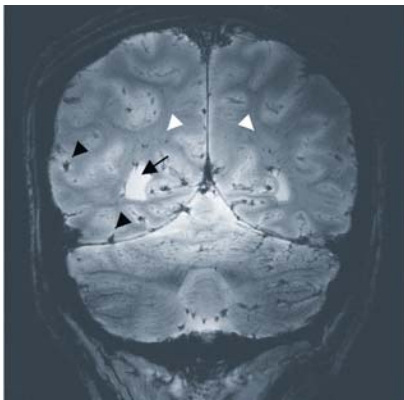


Figure 8. In-vivo MR images through a WHO classification grade III astrocytoma. Panel A: 8T RARE; 512 x 512 matrix; B: 1.5T FSE T_2 , 256 x 256 matrix; C: 8T GRE; 1024 x 1024 matrix; D: 1.5T GRE; 512 x 512 matrix; E: magnification from box depicted on C. No significant differences were identified on extent of signal abnormality between 8 and 1.5 T. E: High-resolution details of tumor site; arrows and arrowheads indicate microvessels and increased vascular density.

The lower signal-to-noise ratio at 1.5 T results in much lower spatial resolution, as noted between Figures 8C and 8D. This improved resolution results in the ability to depict microvascular detail within the tumor bed on Figure 8E. Arrows point to microvessels within the tumor bed, which correlate to greater microvascular density. Arrowheads depict a small region of signal loss suspected to be the result of increased microvascular density beyond the resolution of this image acquisition.



Signal Intensities

Brain = 65-85 (white arrow head)

CSF = 168 +/- 11 (black arrow)

Vessel: 10-13 (black arrow head)

Noise st. dev. = 2-4

SNR = S(0)/SD(noise)

CSF: 42-84 Brain: 16-42 Vessel: 2.5-6.5

CNR = [S0-Sa]/SD(noise)

CSF – vessel: 38-79 Brain-Vessel: 13-37

Figure 9. Coronal in-situ cadaver image acquired (a) at 8 T with a 2D gradient echo sequence using TR/TE 500/9, flip angle <math><20^\circ</math>, FOV = 24cm, 1024 x 1024 matrix size, and 2 mm slice thickness. Not shown are corresponding 1.5T gradient echo images acquired with TR/TE 500/30, flip angle

Increased SNR is the major advantage with ultra high field MRI. Example data comparing 8 and 1.5T images are shown in Figure 9. SNR was computed as the ratio of these signals and the noise in an air-filled region outside the head. CNR is the signal difference divided by the noise. These measurements and histogram analysis showed that there is more than a factor of 2 signal variation due to RF inhomogeneity (see below) across the 8T image; thus, 8T signal measurements are only approximate. For some regions up to a 15-fold SNR improvement is achieved with 8 T.

Tumor growth is believed to depend on angiogenesis. Folkman proposed that without angiogenesis tumor growth is limited to several millimeters in thickness [46]. Furthermore, tumor cells are believed to induce angiogenesis by secreting a number of growth factors (angiogenesis factors) that stimulate endothelial cells [46–49]. Glioblastoma has been shown to be one of the most vascularized tumors for humans [50]. One therapeutic strategy for patients with brain tumors involves the development of agents that modulate angiogenesis [46,49,50]. Validation of

techniques that monitor angiogenesis is key to the development of such strategies. It therefore follows that the imaging identification of angiogenic vessels may serve as a marker for response to anti-angiogenesis treatment. Histopathologic methods grading angiogenesis have been based on number of vessels, degree of glomeruloid vascular structure formation, and endothelial cytology [50]. More recently microvascular density (MVD) counting using panendothelial staining techniques (i.e., factor VIII, CD34) have been used to quantify angiogenesis and have been found to act as an independent prognosticator [51–53]. It should therefore follow that an imaging assessment of vascular density within a tumor bed may act as an indicator for tumoral angiogenesis.

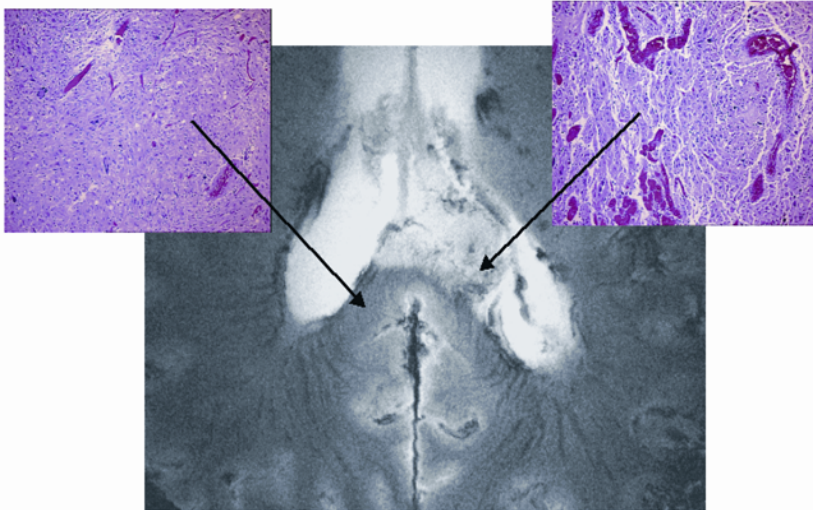
High field MRI at 8 Tesla using a 1024 x 1024 matrix size has been able to visualize vasculature to approximately 100 microns in size [22]. This type of high-resolution imaging has been able to directly identify vascular features within a tumor bed [54]. The MRI findings of distorted vasculature included enlargement of transmedullary veins, increased tortuosity, and increased apparent vessel density [54,55]. Previous studies have demonstrated that apparent vessel density in a nude mice glioma model as identified by 4.7 Tesla gradient echo magnetic resonance images significantly correlates with the histopathologically identified density of blood containing vessels [56]. High-resolution MRI of apparent vascular density has been successfully used as an assay for angiogenesis in this same animal model [56,57]. Using gradient echo 8T imaging, it has been possible to identify microvasculature within brain tumors in humans (see Figures 8 and 10). Figure 10 shows GE 8 Tesla image of a cadaver in situ study of the patient with a known glioblastoma which involves the splenium of the corpus callosum. Note again that there are numerous small vessels visible within the tumor bed. Hematoxylin and eosin (H&E) histologic stains of representative specimens were obtained from the corresponding foci depicted by the arrows. The H&E stain on the left shows tumor infiltration without increase in microvascular density. The H&E stain on the right shows larger and more tortuous vessels in a dense concentration. Note that the vessels in the region of the exophytic tumor are also severely deformed on the 8T image with loss of the normal organization. The vessels can be seen crossing from the corpus callosum into the exophytic part of the tumor.

The tumor bed can be analyzed for foci with vascular distortion. These foci of microvasculature can then be assessed for microvessel size and concentration compared with that found in gray and white matter. Semiquantitative determination of the number of foci with areas of abnormal vasculature, as well as the size and density of the abnormal microvascular structures relative to gray and white matter, has been noted to correlate with tumoral grade [58]. In addition, foci of vascular distortion within the tumor bed on gradient echo 8T MRI correspond to areas of increased cerebral blood volume on dynamic contrast enhanced 1.5T MRI [59] (see Figure 11). Finally, in our experience, directed brain tumor biopsies derived from foci corresponding to microvascular distortion on gradient echo 8T MRI have corresponded to areas of increased microvasculature and neovasculature on histopathology. Note that the general appearance of this tumor could suggest a differential diagnosis, which at that time included metastasis, meningioma, or primary brain

tumor based on the 1.5T images. The 8T images clearly delineate microvasculature clearly outside the enhancing region (arrows), which would not be expected with either meningioma or metastasis, thus suggesting that this is likely primary brain tumor. Further improvement in spatial resolution would be possible with larger matrix size (Figure 12); however, the acquisition times may be prohibitively long for routine in-vivo work.

Tumor infiltrated white matter,
more normal microvasculature

Tumor with severely distorted
microvasculature



8T 1024x1024 GE in situ image, known cadaver glioblastoma multiforme

Figure 10. 8T GE axial image, 1024 x 1024, 20-cm FOV, TR = 600 msec, TE = 12 msec, approximately 20° flip angle. GE 8T image of a cadaver in-situ study of patient with a known glioblastoma that involves the splenium of the corpus callosum. Hematoxylin and eosin (H&E) histologic stains of representative specimens were obtained from the corresponding foci depicted by the arrows. See attached CD for color version.

More recently the use of ultra-small particle iron oxide (USPIO) contrast agents has been shown to increase the visibility of these microvascular structures in a rodent model. The total volume of increased microvasculature within the tumor bed identified on 8T MRI following intravenous administration of USPIO (Figure 13) is substantial [60]. It is interesting that foci exist within the tumor bed that show microvasculature prior to USPIO injection and other foci that do not. Since visualization of microvasculature prior to USPIO injection depends on the BOLD

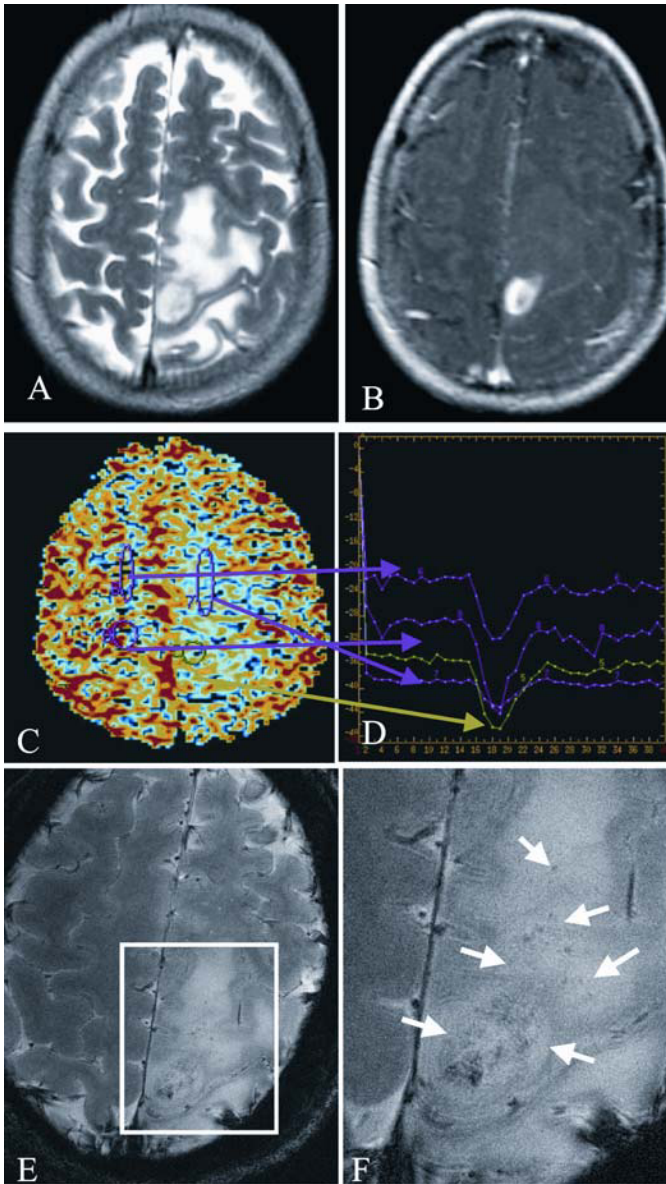


Figure 11. Corresponding FSE T_2 1.5T images (A), post-gadolinium T_1 1.5T (B), cerebral volume map obtained at 1.5T (C), time-intensity curves (D), and GE 8T (E) with magnification (F) of region within white square on 11E. Arrows indicate microvasculature. See attached CD for color version.

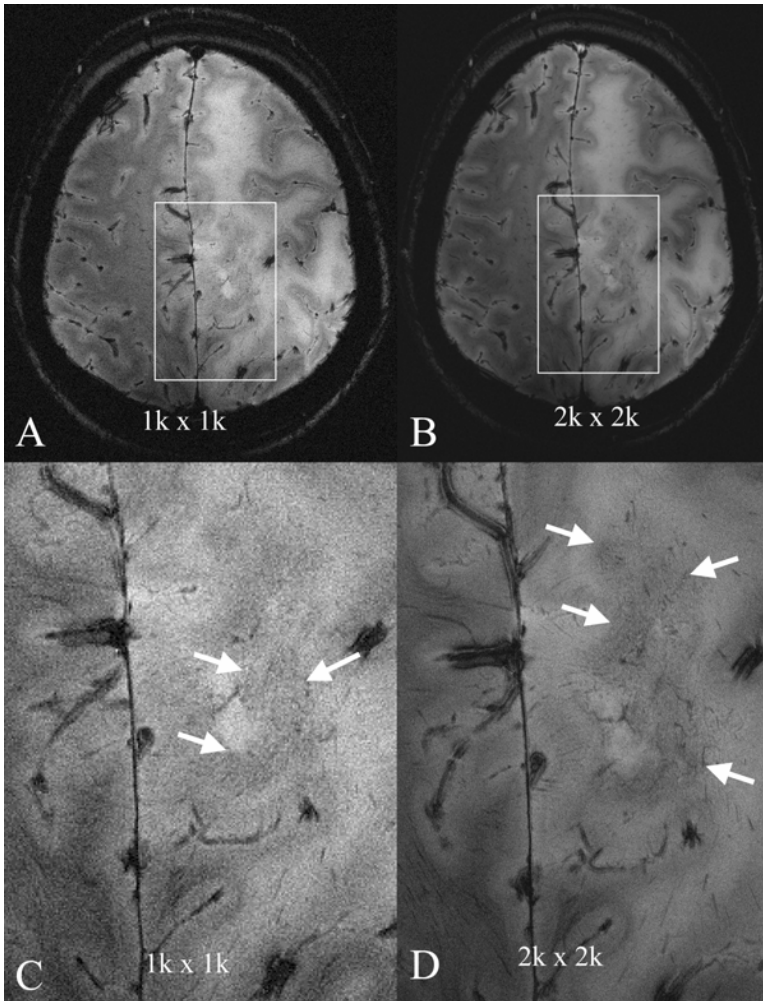


Figure 12. 8 Tesla GE images from the same patient depicted in Fig. 11 obtained 3 months later postmortem with a 1024 x 1024 matrix size (A) and a 2048 x 2048 matrix size (B) with corresponding magnification from boxed regions (C and D). Note the improved delineation of the microvasculature (arrows) with the higher matrix size. Additionally, notice that the area surrounding the visualized microvasculature has a lower signal than the adjacent tumor bed. This loss of signal may be attributed to deoxyhemoglobin within microvessels beyond the resolution of these exams.

effect, these difference may relate to differences in deoxyhemoglobin concentration between different regions within the tumor bed. As such it would lend support to the hypothesis that this type of imaging may be useful in identifying foci of hy-

poxia within the tumor bed. It has been shown that tumor perfusion and vessel reactivity can vary between tumor types [61,62]. A decrease in vessel reactivity can result in inefficient oxygen delivery. On the other hand, this difference may result from vessel tortuosity, which in turn may limit erythrocyte access in certain parts of the tumor bed, resulting in lower deoxyhemoglobin concentration and thereby less BOLD effect with lesser visualization of these vascular structures. Exogenous contrast agents would, however, have the opportunity to visualize the total perfused vascular volume [62]. Because tumoral oxygenation is critical in influencing tumor response to radiation and some chemotherapeutic agents, imaging of hypoxic regions could provide an in-vivo marker for potential treatment response [63].

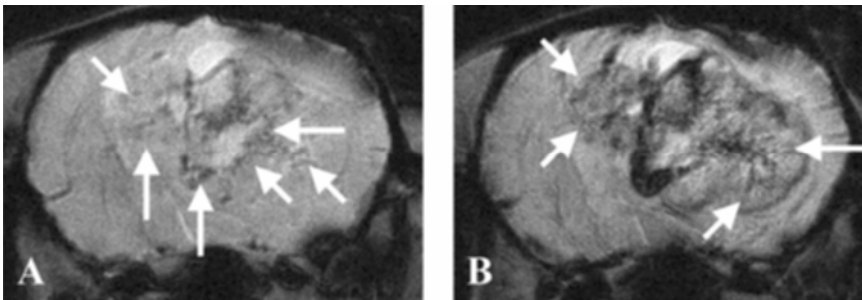


Figure 13. Pre- (A) and post- (B) intravenous USPIO administration GE 8T MRI of a Fisher rat bearing an F98 glioma. Note the improved delineation of microvasculature (arrows) in the post-contrast images compared with the non-contrast study.

The capabilities of UHF MRI as they apply to brain tumor imaging have yet to be fully explored. It is expected that with time the higher signal-to-noise ratios derived from higher field strengths will result in improved spatial resolution not only of microvasculature but also functional imaging, dynamic contrast enhancement, spectroscopic imaging and MRI derived from protons other than water such as phosphorus, sodium or fluorine. These methods have yet to be applied to brain tumor imaging at ultra high field strengths.

6. FUNCTIONAL MRI AND SPECTROSCOPY

Functional brain mapping is a new MRI dimension that allows assessment of neuronal activity, regional blood flow, and biochemical properties in the human brain by means of nuclear spins of water molecules without using contrast agents. Functional MRI (fMRI) has rapidly developed over the past decade, has become available for clinical evaluations at 1.5 T, and has been recently implemented at ultra high MRI at 7 T [7,8]. The most commonly used fMRI technique is based on blood oxygenation level-dependent (BOLD) contrast [64], which is derived from the fact that deoxyhemoglobin is paramagnetic and changes in deoxyhemoglobin

concentrations affect MRI signal locally. The regional blood flow increases in response to greater neuronal activity, leading to an increase of oxyhemoglobin and a relative reduction of deoxyhemoglobin. Consequent to a reduction of deoxyhemoglobin, the signal-to-noise ratio on T_2^* - and T_2 -weighted MR images increases. The functional maps are derived from the comparisons between the baseline and experimental conditions associated with functional stimulation of anatomical area of interest. The ability to map the areas of brain function with unprecedented resolution was demonstrated through a series of functional studies of the visual cortex [65]. The spatial accuracy of the high-field, high-resolution images [66], however, may be affected by magnetic field and image-to-image fluctuations. Functional mapping at 7 T demonstrated resolution at the level of orientation and ocular dominance columns in visual cortex. At 7 T, the maps of functional activation were reproducible and larger than 4T maps [8]. The Hahn spin-echo-based BOLD imaging at ultra high field improved sensitivity to capillary blood flow changes, thereby offering a new way for evaluating cerebral autoregulation in responses to neuronal activity with a voxel size of <1 mm [3,67], and it can be used to map individual functional columns of visual cortex [7]. Functional tonotopic maps of the human auditory cortex have recently been generated using 7T fMRI [68].

MR spectroscopy (MRS) benefits from higher spatial resolution, an increased signal-to-noise ratio, and a large chemical shift at ultra high magnetic fields [69]. In addition to the proton, other nuclei of biological interest — such as ^{13}C , ^{31}P , ^{23}Na , and ^{19}F — have been explored. High spatial resolution enables localization of brain function and bioenergetic processes using ^{13}C MRS. In the human brain, ^{13}C spectra that were obtained at 4 T allowed investigation of glutaminergic neurotransmission [70] and GABA neurotransmission at 7 T [71] in relatively small sections of visual cortex that were in excellent agreement with previous ^{13}C labeling experiments. Through calculation of the rate of glutaminergic neurotransmission, these studies enabled investigation of major excitatory processes. In-vivo ^{31}P spectra acquired from the human primary visual cortex at 7 T reflected the effect of magnetization transfer on γ -ATP resonance mediated by ATP synthesis [72]. The relaxation times of cerebral metabolites, intracellular pH, and rate constant of the creatine kinase reaction were measured from normal subjects [73]. Functional imaging at high field thus has potential for studying brain function and chemistry by providing high-resolution maps of neuronal activation and biochemical markers.

7. SAFETY AND LIMITATIONS

The clinical experience with imaging at ultra high field has been limited to healthy subjects and patients with stable medical conditions such as hypertension, chronic stroke, and tumors. Only recently, a few patients with acute stroke have been studied. At this time, there are clinical limitations associated with ultra high field MRI: (1) a longer scanning time is required to obtain high-resolution images; (2) patients with bioimplants have been excluded from ultra high field studies, and

more work needs to be done to determine the safety of aneurysm clips, arterial stents, and other implants; (3) the experience with contrast agents at ultra high field is limited; and (4) image distortion is associated with magnetic field inhomogeneity and magnetic susceptibility artifacts. Magnetic susceptibility artifacts-induced field distortion could give rise to both image distortion and signal loss, two major problems in high field strength, particularly when using gradient-echo methods [15].

Safety studies to date have not demonstrated adverse effects beyond transient phenomena known to be expected with higher magnetic field strength. These include vertigo, balance difficulty after leaving the magnet, nausea, vomiting, headache, and a metallic taste in the mouth [74].

Animal and human studies so far have not demonstrated significant changes in physiological parameters (heart rate, blood pressure, body temperature) after exposure for 1 hour to high magnetic field [75]. An average increase of 3.6 mm Hg in systolic blood pressure was seen with 8T exposure in normal volunteers, with no significant change in diastolic blood pressure. The cognitive testing at 0 and 8 T did not reveal clinically significant differences [76]. Transient ECG changes, e.g., a known T-wave swell phenomenon, can be expected during exposure at high fields. While ECG interpretation of ECG tracings during 8T exposure was precluded by artifacts, ECG rhythm analysis after exposure demonstrated no significant changes [77]. However, more studies are needed to determine the feasibility and limitations of ultra high magnetic field for routine diagnostic imaging.

8. CONCLUSIONS

Ultra high field MRI is a new emerging tool that has been changing clinical magnetic resonance imaging in many ways. Although technical challenges have increased significantly with the ultra high field, many of which are still to be overcome, this approach has already demonstrated a potential for clinical imaging in health and disease. High-resolution anatomical imaging has shown an ability to reveal pathologies not apparent at the lower magnetic fields. Functional imaging and spectroscopy has permitted evaluation of brain neuronal and biochemical activity with unprecedented resolution. As the development of new sequences and analytical methods at high field continues, the goal of in-vivo microscopic examinations of brain anatomy, function, and chemistry in human subjects is on the horizon.

9. REFERENCES

1. Chen CN, Sank VJ, Cohen SM, Hoult DI. 1986. The field dependence of NMR imaging, I: laboratory assessment of signal-to-noise ratio and power deposition. *Magn Reson Med* 3:722–729.
2. Robitaille PML, Abduljalil AM, Kangarlu A, Zhang X, Yu Y, Burgess RE, et al. 1998. Human magnetic resonance imaging at 8T. *NMR Biomed* 11:263–265.

3. Robitaille PM, Kangarlu A, Abduljalil AM. 1999. RF penetration in ultra high field MRI: challenges in visualizing details within the center of the human brain. *J Comput Assist Tomogr* **23**:845–849.
4. Abduljalil AM, Kangarlu A, Zhang X, Burgess RE, Robitaille PML. 1999. Acquisition of human multislice images at 8T. *J Comput Assist Tomogr* **23**:335–340.
5. Burgess RE, Yu Y, Christoforidis GA, Kangarlu A, Abduljalil AM, Robitaille PML. 1999. Human leptomeningeal and cortical vascular anatomy of the cerebral cortex at 8 T. *J Comput Assist Tomogr* **23**:850–856.
6. Burgess RE, Yu Y, Abduljalil AM, Kangarlu A, Robitaille PML. 1999. High signal to noise FLASH imaging at 8 Tesla. *Magn Reson Imag* **17**:1099–1103.
7. Duong TQ, Kim DS, Ugurbil K, Kim SG. 2001. Localized cerebral blood flow response at submillimeter columnar resolution. *Proc Natl Acad Sci USA* **98**:10904–10909.
8. Yacoub E, Shmuel A, Pfeuffer J, Van de Moortele PF, Adriany G, Andersen P, et al. 2001. Imaging brain function in humans at 7 Tesla. *Magn Reson Med* **45**:588–594.
9. Park DC, Polk TA, Park R, Minear M, Sacage A, Smith MR. 2004. Aging reduces neural specialization in ventral visual cortex. *Proc Natl Acad Sci USA* **101**:1309–1315.
10. Meyer JS, Rogers RL, Judd BW, Mortel KF, Sims P. 2003. Cognition and cerebral blood flow fluctuate together in multi-infarct dementia. *Stroke* **19**:163–169.
11. Bennett DA, Beckett LA, Murray A, Shannon KM, Goetz CG, Pilgrim DM, et al. 1996. Prevalence of parkinsonian signs and associated mortality in a community population of older people. *New Engl J Med* **334**:71–76.
12. Rivera M, Vaquero JJ, Santos A, Ruiz-Cabello J, del Pozo F. 1998. MRI visualization of small structures using improved surface coils. *Magn Reson Imag* **16**:157–166.
13. Bourekas E, Christoforidis G, Abduljalil AM, Kangarlu A, Chakeres DM, Spigos D, Robitaille PML. 1999. High resolution MRI of deep gray nuclei at 8 Tesla. *J Comput Assist Tomogr* **23**:867–866.
14. Abduljalil A, Schmalbrock P, Novak V, Chakeres DW. 2003. Enhanced gray and white matter contrast of phase susceptibility-weighted images in ultra-high field magnetic resonance imaging. *J Magn Reson Imag* **18**:284–290.
15. Abduljalil AM, Kangarlu A, Yu Y, Robitaille PML. 1999. Macroscopic susceptibility in ultra high field MRI, II: acquisition of spin echo images from human head. *J Comput Assist Tomogr* **23**:842–844.
16. Norris DG, Kangarlu A, Schwarzbauer C, Abduljalil AM, Christoforidis G, Robitaille PML. 1999. MDEFT imaging of the human brain at 8 T. *MAGMA* **9**:92–96.
17. Tell GS, Lefkowitz DS, Diehr P, Elster AD. 1998. Relationship between balance and abnormalities in cerebral magnetic resonance imaging in older adults. *Arch Neurol* **55**:73–9.
18. deGroot JC, de Leeuw FE, Ouderkerk M, Hofman A, Jolles J, Breteler MM. 2001. Cerebral white matter lesions and subjective cognitive dysfunction: the Rotterdam Scan Study. *Neurology* **56**(1):1539–1541.
19. Whitaker CDS, Schmalbrock P, Dansher RA, Beversdorf DQ, Santi MS, Abduljalil AM, et al. 2001. Ultra-high field magnetic resonance imaging signal intensity change in Alzheimer's disease [Abstract]. *Soc Neurosci* **27**:323.15.
20. Ay H, Buonanno FS, Rordorf G, Schaefer PW, Schwamm LH, Wu O, et al. 1999. Normal diffusion-weighted MRI during stroke-like deficits. *Neurology* **52**:1784–1792.
21. Novak P, Novak V, Kangarlu A, Abduljalil AM, Chakeres D, Robitaille PML. 2001. High resolution MRI of the brainstem at 8 Tesla. *J Comput Assist Tomogr* **25**:242–246.

22. Christoforidis GA, Bourekas E, Baujan M, Abduljalil AM, Kangarlu A, Spigos D, Robitaille PML. 1999. High resolution MRI of the deep brain vascular anatomy at 8 Tesla: susceptibility-based enhancement of the venous structures. *J Comput Assist Tomogr* **23**:857–866.
23. Dashner RA, Kangarlu A, Clark DL, Ray-Chaudhuri A, Chakeres DW. 2004. Limits of 8-Tesla magnetic resonance imaging spatial resolution of the deoxygenated cerebral microvasculature. *J Magn Reson Imag* **19**:303–307.
24. Wahlund LO, Barkhof F, Fazekas F, Bronge L, Augustin M, Sjogren M, et al. 2001. A new rating scale for age-related white matter changes applicable to MRI and CT. *Stroke* **32**:1318–1322.
25. Marstrand JR, Garde E, Rostrup E, Ring P, Rosenbaum S, Mortensen EL, et al. 2002. Cerebral perfusion and cerebrovascular reactivity are reduced in white matter hyperintensities. *Stroke* **34**(4):972–976.
26. Pantoni L, Garcia JH. 1997. Pathogenesis of leukoaraiosis: a review. *Stroke* **28**:652–659.
27. Inzitari D. 2003. Leukoaraiosis: an independent risk factor for stroke? *Stroke* **34**(8):2067–2071.
28. Price TR, Manolio TA, Kronmal RA, Kittner SJ, Yue NC, Robbins J, et al. 1997. Silent brain infarction on magnetic resonance imaging and neurological abnormalities in community-dwelling older adults. *Stroke* **28**:1158–1164.
29. van Swieten JC, van den Hout JH, van Ketel BA, Hijdra A, van Gijn J. 1991. Periventricular lesions in the white matter on magnetic resonance imaging in the elderly: a morphometric correlation with arteriosclerosis and dilated perivascular spaces. *Brain* **114**:761–774.
30. Roob G, Schmidt R, Kappeller P, Lechner A, Hartung HP, Fazekas F. 1999. MRI evidence of past cerebral microbleeds in a healthy elderly population. *Neurology* **52**:991–994.
31. Desmond DW, Tatemichi TK, Myunghee P, Stern Y. 1993. Risk factors for cerebrovascular disease as correlate of cognitive function in a stroke-free cohort. *Arch Neurol* **50**:162–166.
32. Novak V, Abduljalil AM, Kangarlu A, Slivka AP, Bourekas E, Novak P, et al. 2001. Intracranial ossifications and micronagiopathy at 8 Tesla MRI. *Magn Reson Imag* **19**:1133–1137.
33. Novak V, Chowdhary A, Abduljalil A, Novak P, Chakeres D. 2003. Venous cavernoma at 8 Tesla MRI. *Magn Reson Imag* **21**:1087–1089.
34. Kupersmith MJ, Kalish H, Epstein F, Yu G, Berenstein A, Woo H, et al. 2001. Natural history of brainstem cavernous malformations. *Neurosurgery* **48**(1):47–54.
35. Ong WY, Halliwell B. 2004. Iron, atherosclerosis, and neurodegeneration: a key role for cholesterol in promoting iron-dependent oxidative damage? *Ann NY Acad Sci* **1012**:51–64.
36. Dobson J. 2004. Magnetic iron compounds in neurological disorders. *Ann NY Acad Sci* **1012**:183–192.
37. Novak V, Abduljalil AM, Novak P, Robitaille PML. 2005. High resolution ultra high field MRI of stroke. *Magn Reson Imag*. In press.
38. Novak V, Kangarlu A, Abduljalil A, Novak P, Slivka A, Chakeres D, et al. 2001. Ultra high field MRI of subacute hemorrhagic stroke at 8 Tesla. *J Comput Assist Tomogr* **25**(3):431–435.

39. Chakeres D, Abduljalil AM, Novak P, Novak V. 2002. Comparison of 1.5 and 8 Tesla high-resolution magnetic resonance imaging of lacunar infarcts. *J Comput Assist Tomogr* **26**(4):628–632.
40. Reichenbach JR, Barth M, Haacke EM, Klarhofer M, Kaiser WA, Moser E. 2000. High-resolution MR venography at 3.0 Tesla. *J Comput Assist Tomogr* **24**:949–957.
41. Reichenbach JR, Essig M, Haacke EM, Lee BC, Przetak C, Kaiser WA, et al. 2004. High-resolution venography of the brain using magnetic resonance imaging. *MAGMA* **6**:62–69.
42. Haacke EM, Tkach JA, Parrish TB. 2004. Reducing T*, dephasing in gradient field-echo imaging. *Radiology* **170**:457–462.
43. Ibrahim TS, Lee R, Baertlein BA, Abduljalil AM, Zhu H, Robitaille PML. 2001. Effect of RF coil excitation on field inhomogeneity at ultra high fields: a field optimized TEM resonator. *Magn Reson Imag* **19**:1339–1347.
44. Ibrahim TS, Abduljalil AM, Baertlein BA, Lee R, Robitaille PML. 2004. Analysis of B₁ field profiles and SAR values for multi-strut transverse electromagnetic RF coils in high field MRI applications. *Phys Med Biol* **46**:2545–2555.
45. Adriany G, Van de Morrtele PF, Wiesinger F, Moeller S, Strupp JP, Andersen P, et al. 2005. Transmit and receive transmission line arrays for 7 Tesla parallel imaging. *Magn Reson Med* **53**:434–445.
46. Folkman J. 1995. Angiogenesis in cancer, vascular, reumatoid and other disease. *Nat Med* **1**:27–31.
47. Plate KH, Risau W. 1995. Angiogenesis in malignant gliomas. *Glia* **15**:339–347.
48. Weller RO, Foy M, Cox S. 1977. The development and ultrastructure of the microvasculature in malignant gliomas. *Appl Neurobiol* **3**:300–322.
49. Haddad SF, Moore SA, Schlefer RL, Goeken JA. 1992. Vascular smooth muscle hyperplasia underlies the formation of glomeruloid vascular structures in glioblastoma multiforme. *J Neuropath Exp Neurol* **51**:488–492.
50. Brem S, Cotran R, Folkman J. 1972. Tumor angiogenesis: A quantitative method for histologic grading. *J Natl Cancer Inst* **48**:347–356.
51. Weidner N. 1998. Tumoral vascularity as a prognostic factor in cancer patients: the evidence continues to grow. *J Pathol* **184**:119–122.
52. Fox SB. 1997. Tumor angiogenesis and prognosis. *Histopathology* **30**:294–301.
53. Eberhard A, Kahlert S, Goede V, Hemmerlein B, Plate KH, Augustin HG. 2004. Heterogeneity of angiogenesis and blood vessel maturation in human tumors: implications for antiangiogenic tumor therapies. *Cancer Res* **60**:1388–1393.
54. Christoforidis GA, Grecula JC, Newton HB, Kangarlu A, Abduljalil AM, Schmalbrock P, et al. 2002. Visualization of microvasculature in glioblastoma multiforme with 8-T high-spatial-resolution MR imaging. *Am J Neuroradiol* **23**:1553–1556.
55. Christoforidis GA, Kangarlu A, Abduljalil AM, Schmalbrock P, Chaudhry A, Yates A, et al. 2004. Susceptibility-based imaging of glioblastoma microvasculature at 8 T: correlation of MR imaging and postmortem pathology. *Am J Neuroradiol* **25**:756–760.
56. Abramovitch R, Frenkiel D, Neeman M. 1998. Analysis of subcutaneous angiogenesis by gradient echo magnetic resonance imaging. *Magn Reson Med* **38**:813–824.
57. Abramovitch R, Meir G, Neeman M. 1995. Neovascularization induced growth of implanted C6 glioma multicellular spheroids: magnetic resonance microimaging. *Cancer Res* **55**:1956–1962.

58. Christoforidis G, Yang M, Figueredo T, Chakeres D, Abduljalil A. 2004. Microvasculature within human gliomas identified at 8T High resolution MRI and histopathology [Abstract]. *Proc ASNR*.
59. Christoforidis G, Varakis K, Newton HB, Kangarlu A, Abduljalil AM, Schmalbrock P, et al. 2002. Comparison of brain tumor microvasculature identified on gradient echo 8T MRI with perfusion MRI at 1.5 T [Abstract]. *Proc Int Soc Magn Reson Med*.
60. Christoforidis G, Yang M, Barth W, Chaudhury RF, Chakeres DW, Heverhagen D, et al. 2002. Imaging of microvasculature within the F98 glioma model using intravascular contrast agent on high-resolution ultra-high field MRI with histopathologic correlation [Abstract]. *Proc ASNR*.
61. Neeman M, Dafni H, Bukhari O, Braun RD, Dewhirst MW. 2001. In vivo BOLD contrast MRI mapping of subcutaneous vascular function and maturation: validation by intravital microscopy. *Magn Reson Med* **45**:887–898.
62. Robinson SP, Rijken PF, Howe FA, McSheehy PM, van der Sanden BP, Heerschap A, et al. 2003. Tumor vascular architecture and function evaluated by non-invasive susceptibility MRI methods and immunohistochemistry. *J Magn Reson Imag* **17**:445–454.
63. Yetkin FZ, Mendelson D. 2002. Hypoxia imaging in brain tumors. *Neuroimag Clin N Am* **12**:537–542.
64. Ogawa S, Lee TM, Kay AR, Tank DW. 1990. Brain magnetic resonance imaging with contrast dependent on blood oxygenation. *Proc Natl Acad Sci USA* **87**:9868–9872.
65. Pfeuffer J, Adriany G, Shmuel A, Yacoub E, Van de Moortele PF, Hu X, et al. 2002. Perfusion-based high-resolution functional imaging in the human brain at 7 Tesla. *Magn Reson Med* **47**:903–911.
66. Pfeuffer J, McCullough JC, Van de Moortele PF, Ugurbil K, Hu X. 2003. Spatial dependence of the nonlinear BOLD response at short stimulus duration. *NeuroImage* **18**:990–1000.
67. Yacoub E, Duong TQ, Van de Moortele PF, Lindquist M, Adriany G, Kim SG, et al. 2003. Spin-echo fMRI in humans using high spatial resolutions and high magnetic fields. *Magn Reson Med* **49**:655–664.
68. Formisano E, Kim DS, Di Salle F, Van de Moortele PF, Ugurbil K, Goebel R. 2003. Mirror-symmetric tonotopic maps in human primary auditory cortex. *Br J Radiol* **76**:631–637.
69. Ugurbil K, Adriany G, Andersen P, Chen W, Garwood M, Gruetter R, et al. 2003. Ultrahigh field magnetic resonance imaging and spectroscopy. *Magn Reson Imag* **21**:1263–1281.
70. Gruetter R, Seaquist ER, Kim S, Ugurbil K. 1998. Localized in vivo ¹³C-NMR of glutamate metabolism in the human brain: initial results at 4 tesla. *Dev Neurosci* **20**:380–388.
71. Terpstra M, Ugurbil K, Gruetter R. 2002. Direct in vivo measurement of human cerebral GABA concentration using MEGA-editing at 7 Tesla. *Magn Reson Med* **47**:1009–1012.
72. Lei H, Ugurbil K, Chen W. 2003. Measurement of unidirectional Pi to ATP flux in human visual cortex at 7 T by using in vivo ³¹P magnetic resonance spectroscopy. *Proc Natl Acad Sci USA* **100**:14409–14414.
73. Lei H, Zhu XH, Zhang XL, Ugurbil K, Chen W. 2004. In vivo ³¹P magnetic resonance spectroscopy of human brain at 7 T: an initial experience. *Magn Reson Med* **49**:199–205.
74. Hu X, Norris DG. 2004. Advances in high-field magnetic resonance imaging. *Annu Rev Biomed Eng* **6**:157–184.

75. Kangarlu A, Burgess RE, Zhu H, Nakayama T, Hamlin RL, Abduljalil A, et al. 1999. Cognitive, cardiac, and physiological safety studies in ultra high field magnetic resonance imaging. *Magn Reson Imag* **17**:1407–1416.
76. Chakeres DW, Bornstein R, Kangarlu A. 2003. Randomized comparison of cognitive function in humans at 0 and 8 Tesla. *J Magn Reson Imag* **18**:342–345.
77. Chakeres DW, Kangarlu A, Boudoulas H, Young DC. 2003. Effect of static magnetic field exposure of up to 8 Tesla on sequential human vital sign measurements. *J Magn Reson Imag* **18**:346–352.

CONTENTS OF PREVIOUS VOLUMES

VOLUME 1

Chapter 1

NMR of Sodium-23 and Potassium-39 in Biological Systems

Mortimer M. Civan and Mordechai Shporer

Chapter 2

High-Resolution NMR Studies of Histones

C. Crane-Robinson

Chapter 3

PMR Studies of Secondary and Tertiary Structure of Transfer RNA in Solution

Philip H. Bolton and David R. Kearns

Chapter 4

Fluorine Magnetic Resonance in Biochemistry

J. T. Gerig

Chapter 5

ESR of Free Radicals in Enzymatic Systems

Dale E. Edmondson

Chapter 6

Paramagnetic Intermediates in Photosynthetic Systems

Joseph T. Warden

Chapter 7

ESR of Copper in Biological Systems

John F. Boas, John R. Pilbrow, and Thomas D. Smith

VOLUME 2

Chapter 1

Phosphorus NMR of Cells, Tissues, and Organelles

Donald P. Hollis

*Chapter 2***EPR of Molybdenum-Containing Enzymes***Robert C. Bray**Chapter 3***ESR of Iron Proteins***Thomas D. Smith and John R. Pilbrow**Chapter 4***Stable Imidazoline Nitroxides***Leonid B. Volodarsky, Igor A. Grigor'ev, and Renad Z. Sagdeev**Chapter 5***The Multinuclear NMR Approach to Peptides: Structures, Conformation, and Dynamics***Roxanne Deslauriers and Ian C. P. Smith***VOLUME 3***Chapter 1***Multiple Irradiation ^1H NMR Experiments with Hemoproteins***Regula M. Keller and Kurt Wüthrich**Chapter 2***Vanadyl(IV) EPR Spin Probes: Inorganic and Biochemical Aspects***N. Dennis Chasteen**Chapter 3***ESR Studies of Calcium- and Protein-Induced Photon Separations in Phosphatidylserine–Phosphatidylcholine Mixed Membranes***Shun-ichi Ohnishi and Satoru Tokutomi**Chapter 4***EPR Crystallography of Metalloproteins and Spin-Labeled Enzymes***James C. W. Chien and L. Charles Dickinson**Chapter 5***Electron Spin Echo Spectroscopy and the Study of Metalloproteins***W. B. Mims and J. Peisach*

VOLUME 4

Chapter 1

Spin Labeling in Disease

D. Allan Butterfield

Chapter 2

Principles and Applications of ^{113}Cd NMR to Biological Systems

Ian M. Armitage and James D. Otvos

Chapter 3

Photo-CIDNP Studies of Proteins

Robert Kaptein

Chapter 4

Application of Ring Current Calculations to the Proton NMR of Proteins and Transfer RNA

Stephen J. Perkins

VOLUME 5

Chapter 1

CMR as a Probe for Metabolic Pathways *in Vivo*

R. L. Baxter, N. E. Mackenzie, and A. L. Scott

Chapter 2

Nitrogen-15 NMR in Biological Systems

Felix Blomberg and Heinz Rüterjans

Chapter 3

Phosphorus-31 Nuclear Magnetic Resonance Investigations of Enzyme Systems

B. D. Nageswara Rao

Chapter 4

NMR Methods Involving Oxygen Isotopes in Biophosphates

Ming-Daw Tsai and Larol Bruzik

Chapter 5

ESR and NMR Studies of Lipid-Protein Interactions in Membranes

Philippe F. Devaux

VOLUME 6*Chapter 1***Two-Dimensional Spectroscopy as a Conformational Probe of Cellular Phosphates***Philip H. Bolton**Chapter 2***Lanthanide Complexes of Peptides and Proteins***Robert E. Lenkinski**Chapter 3***EPR of Mn(II) Complexes with Enzymes and Other Proteins***George H. Reed and George D. Markham**Chapter 4***Biological Applications of Time Domain ESR***Hans Thomann, Larry R. Dalton, and Lauraine A. Dalton**Chapter 5***Techniques, Theory, and Biological Applications of Optically Detected Magnetic Resonance (ODMR)***August H. Maki***VOLUME 7***Chapter 1***NMR Spectroscopy of the Intact Heart***Gabriel A. Elgavish**Chapter 2***NMR Methods for Studying Enzyme Kinetics in Cells and Tissue***K. M. Brindle, I. D. Campbell, and R. J. Simpson**Chapter 3***Endor Spectroscopy in Photobiology and Biochemistry***Klaus Möbius and Wolfgang Lubitz**Chapter 4***NMR Studies of Calcium-Binding Proteins***Hans J. Vogel and Sture Forsén*

VOLUME 8*Chapter 1***Calculating Slow Motional Magnetic Resonance Spectra:
A User's Guide***David J. Schneider and Jack H. Freed**Chapter 2***Inhomogeneously Broadened Spin-Label Spectra***Barney Bales***Chapter 3****Saturation Transfer Spectroscopy of Spin-Labels: Techniques and
Interpretation of Spectra***M. A. Hemminga and P. A. de Jager**Chapter 4***Nitrogen-15 and Deuterium Substituted Spin Labels for Studies of
Very Slow Rotational Motion***Albert H. Beth and Bruce H. Robinson**Chapter 5***Experimental Methods in Spin-Label Spectral Analysis***Derek Marsh**Chapter 6***Electron–Electron Double Resonance***James S. Hyde and Jim B. Feix**Chapter 7***Resolved Electron–Electron Spin–Spin Splittings in EPR Spectra***Gareth R. Eaton and Sandra S. Eaton**Chapter 8***Spin-Label Oximetry***James S. Hyde and Witold S. Subczynski**Chapter 9***Chemistry of Spin-Labeled Amino Acids and Peptides: Some New Mono-
and Bifunctionalized Nitroxide Free Radicals***Kálmán Hideg and Olga H. Hankovsky**Chapter 10***Nitroxide Radical Adducts in Biology: Chemistry, Applications, and Pitfalls***Carolyn Mottley and Ronald P. Mason*

*Chapter 11***Advantages of ^{15}N and Deuterium Spin Probes for Biomedical Electron Paramagnetic Resonance Investigations***Jane H. Park and Wolfgang E. Trommer**Chapter 12***Magnetic Resonance Study of the Combining Site Structure of a Monoclonal Anti-Spin-Label Antibody***Jacob Anglister**Appendix***Approaches to the Chemical Synthesis of ^{15}N and Deuterium Substituted Spin Labels***Jane H. Park and Wolfgang E. Trommer***VOLUME 9***Chapter 1***Phosphorus NMR of Membranes***Philip L. Yeagle**Chapter 2***Investigation of Ribosomal 5S Ribonucleotide Acid Solution Structure and Dynamics by Means of High-Resolution Nuclear Magnetic Resonance Spectroscopy***Alan G. Marshall and Jiejun Wu**Chapter 3***Structure Determination via Complete Relaxation Matrix Analysis (CORMA) of Two-Dimensional Nuclear Overhauser Effect Spectra: DNA Fragments***Brandan A. Borgias and Thomas L. James**Chapter 4***Methods of Proton Resonance Assignment for Proteins***Andrew D. Robertson and John L. Markley**Chapter 5***Solid-State NMR Spectroscopy of Proteins***Stanley J. Opella**Chapter 6***Methods for Suppression of the H_2O Signal in Proton FT/NMR Spectroscopy: A Review***Joseph E. Meier and Alan G. Marshall*

VOLUME 10

*Chapter 1***High-Resolution ^1H -Nuclear Magnetic Resonance Spectroscopy of Oligosaccharide-Alditols Released from Mucin-Type O-Glycoproteins***Johannis P. Kamerling and Johannes F. G. Wiegenthart**Chapter 2***NMR Studies of Nucleic Acids and Their Complexes***David E. Wemmer*

VOLUME 11

*Chapter 1***Localization of Clinical NMR Spectroscopy***Lizann Bolinger and Robert E. Lenkinski**Chapter 2***Off-Resonance Rotating Frame Spin-Lattice Relaxation: Theory, and *in Vivo* MRS and MRI Applications***Thomas Schleich, G. Herbert Caines, and Jan M. Ryzdzewski**Chapter 3***NMR Methods in Studies of Brain Ischemia***Lee-Hong Chang and Thomas L. James**Chapter 4***Shift-Reagent-Aided ^{23}Na NMR Spectroscopy in Cellular, Tissue, and Whole-Organ Systems***Sandra K. Miller and Gabriel A. Elgavish**Chapter 5****In Vivo* ^{19}F NMR***Barry S. Selinski and C. Tyler Burt**Chapter 6****In Vivo* ^2H NMR Studies of Cellular Metabolism***Robert E. London**Chapter 7***Some Applications of ESR to *in Vivo* Animals Studies and EPR Imaging***Lawrence J. Berliner and Hirotada Fujii*

VOLUME 12*Chapter 1***NMR Methodology for Paramagnetic Proteins***Gerd N. La Mar and Jeffrey S. de Ropp**Chapter 2***Nuclear Relaxation in Paramagnetic Metalloproteins***Lucia Banci**Chapter 3***Paramagnetic Relaxation of Water Protons***Cathy Coolbaugh Lester and Robert G. Bryant**Chapter 4***Proton NMR Spectroscopy of Model Hemes***F. Ann Walker and Ursula Simonis**Chapter 5***Proton NMR Studies of Selected Paramagnetic Heme Proteins***J. D. Satterlee, S. Alam, Q. Yi, J. E. Erman, I. Constantinidis,
D. J. Russell, and S. J. Moench**Chapter 6***Heteronuclear Magnetic Resonance: Applications to Biological and Related Paramagnetic Molecules***Joël Mispelter, Michel Momenteau, and Jean-Marc Lhoste**Chapter 7***NMR of Polymetallic Systems in Proteins***Claudio Luchinat and Stefano Ciurli***VOLUME 13***Chapter 1***Simulation of the EMR Spectra of High-Spin Iron in Proteins***Betty J. Gaffney and Harris J. Silverstone**Chapter 2***Mössbauer Spectroscopy of Iron Proteins***Peter G. Debrunner*

*Chapter 3***Multifrequency ESR of Copper: Biophysical Applications***Riccardo Basosi, William E. Antholine, and James S. Hyde**Chapter 4***Metalloenzyme Active-Site Structure and Function through Multifrequency CW and Pulsed ENDOR***Brian M. Hoffman, Victoria J. DeRose, Peter E. Doan, Ryszard J. Gurbiel, Andrew L. P. Houseman, and Joshua Telser**Chapter 5***ENDOR of Randomly Oriented Mononuclear Metalloproteins: Toward Structural Determinations of the Prosthetic Group***Jürgen Hüttermann**Chapter 6***High-Field EPR and ENDOR in Bioorganic Systems***Klaus Möbius**Chapter 7***Pulsed Electron Nuclear Double and Multiple Resonance Spectroscopy of Metals in Proteins and Enzymes***Hans Thomann and Marcelino Bernardo**Chapter 8***Transient EPR of Spin-Labeled Proteins***David D. Thomas, E. Michael Ostap, Christopher L. Berger, Scott M. Lewis, Piotr G. Fajer and James E. Mahaney**Chapter 9***ESR Spin-Trapping Artifacts in Biological Model Systems***Aldo Tomasi and Anna Iannone***VOLUME 14****Introduction: Reflections on the Beginning of the Spin Labeling Technique***Lawrence J. Berliner**Chapter 1***Analysis of Spin Label Line Shapes with Novel Inhomogeneous Broadening from Different Component Widths: Application to Spatially Disconnected Domains in Membranes***M. B. Sankaram and Derek Marsh*

*Chapter 2***Progressive Saturation and Saturation Transfer EPR for Measuring Exchange Processes and Proximity Relations in Membranes***Derek Marsh, Tibor Páli, and László Horváth**Chapter 3***Comparative Spin Label Spectra at X-band and W-band***Alex I. Smirnov, R. L. Belford, and R. B. Clarkson**Chapter 4***Use of Imidazoline Nitroxides in Studies of Chemical Reactions: ESR Measurements of the Concentration and Reactivity of Protons, Thiols, and Nitric Oxide***Valery V. Khrantsov and Leonid B. Volodarsky**Chapter 5***ENDOR of Spin Labels for Structure Determination: From Small Molecules to Enzyme Reaction Intermediates***Marvin W. Makinen, Devkumar Mustafi, and Seppo Kasa**Chapter 6***Site-Directed Spin Labeling of Membrane Proteins and Peptide–Membrane Interactions***Jimmy B. Feix and Candice S. Klug**Chapter 7***Spin-Labeled Nucleic Acids***Robert S. Keyes and Albert M. Bobst**Chapter 8***Spin Label Applications to Food Science***Marcus A. Hemminga and Ivon J. van den Dries**Chapter 9***EPR Studies of Living Animals and Related Model Systems (*In-Vivo* EPR)***Harold M. Swartz and Howard Halpern***Appendix***Derek Marsh and Karl Schorn*

VOLUME 15*Chapter 1***Tracery Theory and ^{13}C NMR***Maren R. Laughlin and Joanne K. Kelleher**Chapter 2* **^{13}C Isotopomer Analysis of Glutamate: An NMR Method to Probe Metabolic Pathways Intersecting in the Citric Acid Cycle***A. Dean Sherry and Craig R. Malloy**Chapter 3***Determination of Metabolic Fluxes by Mathematical Analysis of ^{13}C Labeling Kinetics***John C. Chatham and Edwin M. Chance**Chapter 4***Metabolic Flux and Subcellular Transport of Metabolites***E. Douglas Lewandowski**Chapter 5***Assessing Cardiac Metabolic Rates During Pathologic Conditions with Dynamic ^{13}C NMR Spectra***Robert G. Weiss and Gary Gerstenblith**Chapter 6***Applications of ^{13}C Labeling to Studies of Human Brain Metabolism *in Vivo****Graeme F. Mason**Chapter 7****In-Vivo* ^{13}C NMR Spectroscopy: A Unique Approach in the Dynamic Analysis of Tricarboxylic Acid Cycle Flux and Substrate Selection***Pierre-Marie Luc Robitaille***VOLUME 16***Chapter 1***Determining Structures of Large Proteins and Protein Complexes by NMR***G. Marius Clore and Angela M. Gronenborn*

*Chapter 2***Multidimensional ^2H -Based NMR Methods for Resonance Assignment, Structure Determination, and the Study of Protein Dynamics***Kevin H. Gardner and Lewis E. Kay**Chapter 3***NMR of Perdeuterated Large Proteins***Bennett T. Farmer II and Ronald A. Venters**Chapter 4***Recent Developments in Multidimensional NMR Methods for Structural Studies of Membrane Proteins***Francesca M. Marassi, Jennifer J. Gesell, and Stanley J. Opella**Chapter 5***Homonuclear Decoupling to Proteins***Eriks Kupce, Hiroshi Matsuo, and Gerhard Wagner**Chapter 6***Pulse Sequences for Measuring Coupling Constants***Geerten W. Vuister, Marco Tessari, Yasmin Karimi-Nejad, and Brian Whitehead**Chapter 7***Methods for the Determination of Torsion Angle Restraints in Biomacromolecules***C. Griesinger, M. Hennig, J. P. Marino, B. Reif, C. Richter, and H. Schwalbe***VOLUME 17***Chapter 1***Aspects of Modeling Biomolecular Structure on the Basis of Spectroscopic or Diffraction Data***Wilfred F. van Gunsteren, Alexandre M. J. J. Bonvin, Xavier Daura, and Lorna J. Smith**Chapter 2***Combined Automated Assignment of NMR Spectra and Calculation of Three-Dimensional Protein Structures***Yuan Xu, Catherine H. Schein, and Werner Braun*

*Chapter 3***NMR Pulse Sequences and Computational Approaches for Automated Analysis of Sequence-Specific Backbone Resonance Assignments of Proteins**

*Gaetano T. Montelione, Carlos B. Rios, G. V. T. Swapna,
and Diane E. Zimmerman*

*Chapter 4***Calculation of Symmetric Oligomer Structures from NMR Data**

Seán I. O'Donoghue and Michael Nilges

*Chapter 5***Hybrid–Hybrid Matrix Method for 3D NOESY–NOESY Data Refinements**

*Elliott K. Gozansky, Varatharasa Thiviyanathan, Nishantha Illangasekare,
Bruce A. Luxon, and David G. Gorenstein*

*Chapter 6***Conformational Ensemble Calculations: Analysis of Protein and Nucleic Acid NMR Data**

*Anwer Mujeeb, Nikolai B. Ulyanov, Todd M. Billeci,
Shauna Farr-Jones, and Thomas L. James*

*Chapter 7***Complete Relaxation and Conformational Exchange Matrix (CORCEMA) Analysis of NOESY Spectra of Reversibly Forming Ligand–Receptor Complexes: Application to Transferred NOESY**

N. Rama Krishna and Hunter N. B. Moseley

*Chapter 8***Protein Structure and Dynamics from Field-Induced Residual Dipolar Couplings**

James K. Prestegard, Joel R. Tolman, Hashim M. Al-Hashimi, and Michael Andrec

*Chapter 9***Recent Developments in Studying the Dynamics of Protein Structures from ¹⁵N and ¹³C Relaxation Time Measurements**

Jan Engelke and Heinz Rüterjans

*Chapter 10***Multinuclear Relaxation Dispersion Studies of Protein Hydration**

Bertil Halle, Vladimir P. Denisov, and Kandadai Venu

*Chapter 11***Hydration Studies of Biological Macromolecules by Intermolecular Water–Solute NOEs**

Gottfried Otting

VOLUME 18*Chapter 1***Introduction to *in Vivo* EPR**

Harold M. Swartz and Lawrence J. Berliner

*Chapter 2***Principles of *in Vivo* EPR**

Sankaran Subramanian, James B. Mitchell, and Murali C. Krishna

*Chapter 3***Frequency and Power Considerations for *in Vivo* EPR and Related Techniques**

James M. S. Hutchison

*Chapter 4***CW EPR Signal Detection Bridges**

Janusz Koscielniak

*Chapter 5***Resonators for Low Field *in Vivo* EPR**

Kenneth A. Rubinson

*Chapter 6***Principles of Imaging: Theory and Instrumentation**

Periannan Kuppasamy, Michael Chzhan, and Jay L. Zweier

*Chapter 7***Time-Domain Radio Frequency EPR Imaging**

Sankaran Subramanian, James B. Mitchell, and Murali C. Krishna

*Chapter 8***Stable Soluble Paramagnetic Compounds**

Howard J. Halpern

*Chapter 9***Stable Particulate Paramagnetic Materials as Oxygen Sensors in EPR Oximetry**

*R. B. Clarkson, Paul Peroke, Shong-Wan Norby,
and B. M. Odintsov*

*Chapter 10***Packaging of Stable Paramagnetic Materials in Oximetry and Other Applications**

Bernard Gallez

*Chapter 11***Spin Trapping *in Vivo*: Facts and Artifacts***Graham S. Timmins and Ke Jian Liu**Chapter 12****Ex Vivo* Detection of Free Radical Metabolites of Toxic Chemicals and Drugs by Spin Trapping***Ronald P. Mason and Maria B. Kadiiska**Chapter 13***Chemistry and Biology of Nitric Oxide***Andrei M. Komarov**Chapter 14****In Vivo* and *in Vitro* Detection of NO by EPR***Hirotaada Fujii and Lawrence J. Berliner**Chapter 15***The Measurement of Oxygen *in Vivo* Using *in-Vivo* EPR Techniques***Harold M. Swartz**Chapter 16***Cardiac Applications of *in-Vivo* EPR Spectroscopy and Imaging***Jay L. Zweier, Alexandre Samouilov, and Periannan Kuppusamy**Chapter 17***Applications of *in-Vivo* EPR Spectroscopy and Imaging in Cancer Research***Howard J. Halpern**Chapter 18***Applications of *in-Vivo* EPR Spectroscopy and Imaging to Skin***Jürgen Fuchs, Norbert Groth, and Thomas Herrling**Chapter 19***Pharmaceutical Applications of *in-Vivo* EPR***Karsten Mäder and Bernard Gallez**Chapter 20***Proton–Electron Double-Resonance Imaging (PEDRI)***David J. Lurie**Chapter 21***Combining NMR and EPR/ESR for *in-Vivo* Experiments***Jeff F. Dunn and Harold M. Swartz*

*Chapter 22***Potential Medical (Clinical) Applications of EPR: Overview and Perspectives***Harold M. Swartz***VOLUME 19***Chapter 1***Distance Measurements by CW and Pulsed EPR***Sandra S. Eaton and Gareth R. Eaton**Chapter 2***Relaxation Times of Organic Radicals and Transition Metal Ions***Sandra S. Eaton and Gareth R. Eaton**Chapter 3***Structural Information from CW-EPR Spectra of Dipolar Coupled Nitroxide Spin Labels***Eric J. Hustedt and Albert H. Beth**Chapter 4***Determination of Protein Folds and Conformational Dynamics Using Spin-Labeling EPR Spectroscopy***Hassane S. Mchaourab and Eduardo Perozo**Chapter 5***EPR Spectroscopic Ruler: The Deconvolution Method and Its Applications***Wenzhong Xiao and Yeon-Kyun Shin**Chapter 6***TOAC: The Rigid Nitroxide Side Chain***Joseph C. McNulty and Glenn L. Millhauser**Chapter 7***Depth of Immersion of Paramagnetic Centers in Biological Systems***Gertz I. Likhtenshtein**Chapter 8***Determination of Distances Based on T_1 and T_m Effects***Sandra S. Eaton and Gareth R. Eaton*

*Chapter 9***Double-Quantum ESR and Distance Measurements***Petr P. Borbat and Jack H. Freed**Chapter 10***"2+1" Pulse Sequence as Applied for Distance and Spatial Distribution Measurements of Paramagnetic Centers***A. Raitsimring**Chapter 11***Double Electron–Electron Resonance***Gunnar Jeschke, Martin Pannier, and Hans W. Spiess**Chapter 12***Electron Paramagnetic Resonance Distance Measurements in Photosynthetic Reaction Centers***K. V. Lakshmi and Gary W. Brudvig**Chapter 13***Photo-Induced Radical Pairs Investigated using Out-of-Phase Electron Spin Echo***Sergei A. Dzuba and Arnold J. Hoff***VOLUME 20***Chapter 1***Transverse Relaxation Optimized Spectroscopy***Konstantin V. Pervushin**Chapter 2***Segmental Isotopic Labeling: Prospects for a New Tool to Study the Structure-Function Relationships in Multi-Domain Proteins***Jennifer J. Ottesen, Ulrich K. Blaschke, David Cowburn, and Tom W. Muir**Chapter 3***Characterization of Inter-Domain Orientations in Solution Using the NMR Relaxation Approach***David Fushman and David Cowburn**Chapter 4***Global Fold Determination of Large Proteins using Site-Directed Spin Labeling***John Battiste, John D. Gross, and Gerhard Wagner*

*Chapter 5***Solid State NMR Studies of Uniformly Isotopically Enriched Proteins***Ann McDermott**Chapter 6***NMR Spectroscopy of Encapsulated Proteins Dissolved in Low Viscosity Fluids***A. Joshua Wand, Charles R. Babu, Peter F. Flynn,
and Mark J. Milton**Chapter 7***Angular Restraints from Residual Dipolar Couplings for Structure Refinement***Christian Griesinger, Jens Meiler, and Wolfgang Peti**Chapter 8***Protein Structure Refinement using Residual Dipolar Couplings***Angela M. Gronenborn**Chapter 9***Hydrogen Bond Scalar Couplings — A New Tool in Biomolecular NMR***Stephan Grzesiek, Florence Cordier, and Andrew Dingley**Chapter 10***NMR Methods for Screening the Binding of Ligands to Proteins: Identification and Characterization of Bioactive Ligands***Thomas Peters, Thorsten Biet, and Lars Herfurth***VOLUME 21***Chapter 1***Microwave Engineering Fundamentals and Spectrometer Design***C. J. Bender**Chapter 2***EPR Spectrometers at Frequencies below X-Band***G. R. Eaton and S. S. Eaton**Chapter 3***Frequency Dependence of EPR Sensitivity***G. A. Rinard, R. W. Quine, S. S. Eaton, and G. R. Eaton*

*Chapter 4***ENDOR Coils and Related Radiofrequency Circuits***C. J. Bender**Chapter 5***The Generation and Detection of Electron Spin Echoes***C. J. Bender**Chapter 6***Convolution-Based Algorithm: From Analysis of Rotational Dynamics to EPR Oximetry and Protein Distance Measurements***A. L. Smirnov and T. I. Smirnova**Chapter 7***1d and 2d Electron Spin Resonance Imaging (ESRI) of Transport and Degradation Processes in Polymers***M. V. Motyakin and S. Schlick**Chapter 8***Peptide Aggregation and Conformation Properties as Studied by Pulsed Electron–Electron Double Resonance***Y. D. Tsvetkov***VOLUME 22***Chapter 1***The Early Years***Oleg Y. Grinberg and Alexander A. Dubinskii**Chapter 2***The Development of High-Field/High-Frequency ESR***Jack H. Freed**Chapter 3***Primary Processes in Photosynthesis: What Do We Learn from High-Field EPR Spectroscopy?***Klaus Möbius, Anton Savitsky, and Martin Fuchs**Chapter 4***High Field ESR: Applications to Protein Structure and Dynamics, HF-ESR Protein Structure and Dynamics***Keith A. Earle and Alex I. Smirnov*

*Chapter 5***The Use of Very High Frequency EPR (VHF-EPR) in Studies of Radicals and Metal Sites in Proteins and Small Inorganic Models***Anne-Laure Barra, Astrid Gräslund, and K. Kristoffer Andersson**Chapter 6***Time-Resolved High-Frequency and Multifrequency EPR Studies of Spin-Correlated Radical Pairs in Photosynthetic Reaction Center Proteins***Marion C. Thurnauer, Oleg G. Poluektov, and Gerd Kothe**Chapter 7***Molecular Dynamics of Gd(III) Complexes in Aqueous Solution by HF-EPR***Alain Borel, Lothar Helm, and André E. Merbach**Chapter 8***Pulse High-Frequency EPR***Thomas F. Prisner**Chapter 9***High-Frequency EPR, ESEEM and ENDOR Studies of Paramagnetic Centers in Single-Crystalline Materials***Edgar J. J. Groenen and Jan Schmidt**Chapter 10***W-Band Pulse ENDOR of Transition Metal Centers in Orientationally Disordered Systems and Single Crystals***Daniella Goldfarb and Vladimir Krymov**Chapter 11***Sample Resonators for Quasioptical EPR***David E. Budil and Keith A. Earle**Chapter 12***The Bruker ELEXSYS E600/680 94 Ghz Spectrometer Series***P. Höfer, A. Kamlowskil, G. G. Maresch, D. Schmalbein, and R. T. Weber**Chapter 13***HF-EPR Spectra of Spin Labels in Membranes***V. A. Livshits and D. Marsh*

*Chapter 14***Modern Developments and Prospects in Multi-Frequency High Field EMR**

Louis-Claude Brunel, Anna Lisa Maniero, Alexander Angerhofer Stephen Hill, and J. (Hans) van Tol

VOLUME 23**SECTION I: JAMES S. HYDE AND BIOMEDICAL EPR***Chapter 1***Helmut Beinert***Chapter 2***An Incomplete History of Jim Hyde and the EPR Center at MCW**

Harold M. Swartz

SECTION II: BIOLOGICAL FREE RADICALS AND MEDICINE*Chapter 3***Free Radicals and Medicine**

Harold M. Swartz, Ronald P. Mason, Neil Hogg, Balaraman Kalyanaraman, Tadeusz Sarna, Przemyslaw M. Plonka, Mariusz Zareba, P. L. Gutierrez, and Lawrence J. Berliner

*Chapter 4***Superoxide Generation from Nitric Oxide Synthase: Role of Cofactors and Protein Interaction**

Jeannette Vásquez-Vivar, Pavel Martísek, and B. Kalyanaraman

*Chapter 5****In Vivo* Spin Trapping of Free Radical Metabolites of Drugs and Toxic Chemicals Utilizing *Ex Vivo* Detection**

Ronald P. Mason and Maria B. Kadiiska

*Chapter 6***Post Processing Strategies in EPR Spin-Trapping Studies**

Agnes Keszler and Neil Hogg

*Chapter 7***Biophysical Studies of Melanin: Paramagnetic, Ion-Exchange and Redox Properties of Melanin Pigments and Their Photoreactivity**

Tadeusz Sarna and Przemyslaw M. Plonka

*Chapter 8***Application of Spin Labels To Membrane Bioenergetics: Photosynthetic Systems of Higher Plants***Alexander N. Tikhonov and Witold K. Subczynski***SECTION III: *IN VIVO* EPR AND PHYSIOLOGY***Chapter 9***EPR Spectroscopy of Function *in Vivo*: Origins, Achievements, and Future Possibilities***Harold M. Swartz and Nadeem Khan**Chapter 10***EPR Oximetry in Biological and Model Samples***Witold K. Subczynski and Harold M. Swartz**Chapter 11****In Vivo* EPR Imaging***Benjamin B. Williams and Howard J. Halpern**Chapter 12***Time-Domain Radio Frequency EPR Imaging***Sankaran Subramanian and Murali C. Krishna***SECTION IV: METALS***Chapter 13***Copper Biomolecules in Solution***Riccardo Basosi, Giovanni Della Lunga, and Rebecca Pogni**Chapter 14***Low-Frequency EPR of Cu^{2+} in Proteins***William E. Antholine**Chapter 15***Electron Spin-Echo Envelope Modulation Studies of ^{14}N in Biological Systems***Michael J. Colaneri and Jack Peisach*

VOLUME 24

SECTION I: INSTRUMENTATION AND METHODOLOGY

Chapter 1

Saturation Recovery EPR

Sandra S. Eaton and Gareth R. Eaton

Chapter 2

Loop-Gap Resonators

George A. Rinard and Gareth R. Eaton

Chapter 3

EPR Interfaced To Rapid Mixing

Charles P. Scholes

Chapter 4

Application of Angle-Selected Electron Nuclear Double Resonance to Characterize Structured Solvent in Small Molecules and Macromolecules

Devkumar Mustafi and Marvin W. Makinen

Chapter 5

Solution-ENDOR of Some Biologically Interesting Radical Ions

Fabian Gerson and Georg Gescheidt

Chapter 6

Electron–Electron Double Resonance

Lowell D. Kispert

Chapter 7

Digital Detection by Time-Locked Sampling in EPR

James S. Hyde, Theodore G. Camenisch, Joseph J. Ratke, Robert A. Strangeway, and Wojciech Froncisz

Chapter 8

Measurement of Distances Between Electron Spins Using Pulsed EPR

Sandra S. Eaton and Gareth R. Eaton

SECTION II: MOTION, PROTEINS, AND MEMBRANES

Chapter 9

ESR and Molecular Dynamics

Jack H. Freed

*Chapter 10***SDSL: A Survey of Biological Applications***Candice S. Klug and Jimmy B. Feix**Chapter 11***Saturation Transfer Spectroscopy of Biological Membranes***Derek Marsh, László I. Horváth, Tibor Páli, and
Vsevolod A. Livshits**Chapter 12***Saturation Transfer EPR: Rotational Dynamics of Membrane Proteins***Albert H. Beth and Eric J. Hustedt**Chapter 13***Trends in EPR Technology***James S. Hyde**Chapter 14***Prognosis***Sandra S. Eaton and Gareth R. Eaton***VOLUME 25***Chapter 1***Microwave Amplitude Modulation Technique to Measure Spin–Lattice (T_1) and Spin–Spin (T_2) Relaxation Times***Sushil K. Misra**Chapter 2***Improvement in the Measurement of Spin–Lattice Relaxation Time in Electron Paramagnetic Resonance***Robert Lopez — translated by Sushil K. Misra**Chapter 3***Quantitative Measurement of Magnetic Hyperfine Parameters and the Physical Organic Chemistry of Supramolecular Systems***Christopher J. Bender**Chapter 4***New Methods of Simulation of Mn(II) EPR Spectra: Single Crystals, Polycrystalline and Amorphous (Biological) Materials***Sushil K. Misra**Chapter 5***Density Matrix Formalism of Angular Momentum in Multi-Quantum Magnetic Resonance***H. Watari and Y. Shimoyama*

INDEX

- Acoustic noise, 50–51, 61, 74, 113.
 See also Noise
 and gradients, 35–37
 and Lorentz force, 75
 reduction of, 75–78, 114
- Activation-induced signal changes, 315
- Active shielded magnets, 30
- Active shielding, 48, 107
- Actively detuned coils, 153–154
- Adiabatic inversion pulse, 89–91
- Adiabatic RF pulses, 384
- Adrenoleukodystrophy, 398–399
- Alderman Grant coil, 142
- Algorithm in RF coil simulation, 168–169
- Alzheimer's disease
 and brain imaging, 298–299
 ex-vivo imaging in, 362–365
- Amplifier cooling, 117
- Amyloid plaques, detection of, 298–299
- Anaplerosis, 396–397
- Anatomical imaging, 412–416
- Angiogenesis, imaging of, 425–426
- Angiomas, 418
- Antenna-array excitation, 198–202
- Antenna reaction theory, 189–190
- Antioxidants, detection of, 399–400
- Application software in ultra high field MRI, 55
- Array coils, 136–137, 345
 for human microimaging, 348–350
 and SNR, 289–291
- Array receiver coil, 154
- Arterial spin labeling (ASL), 91, 320
- Arterial spin tagging, 320
- Arterio-venous malformations, 417–418
- Artifactual edge ringing, 358
- Ascorbate, detection of, 400
- Astrocytes, 396
- Astrocytoma, 424
- Atherosclerosis, 417
- ATP synthesis, 327–328
- Auditory cortex, 359
- Axial images, 199–202
 and excitation, 192–195
- Axial stress, 25
- B_0 field, 95
 characterization of distortion, 254–258
 gradients, 75–76, 268
 and NMR sensitivity, 374
 noise as function of, 226–227
 signal as function of, 223–226
 and SNR, 223–229, 239
- B_0^2 behavior, 5
- B_1 field, 66, 87–88, 169
 frequency and electromagnetic properties of tissue, 210–211
 inhomogeneity, 67, 68, 89–90, 97
 magnitude, 148–150
 nonuniformities at high magnetic fields, 291–295
 shimming, 6, 67–68, 97
 and SNR, 240, 287–291
- B_1^- field, 224–226
- B_1^+ field, 175–178, 189–190, 191–195, 224, 226
 distribution of, 180–181, 201–202
 homogeneity of, 229–230
 and SNR, 228–229
 in TEM resonator, 182–184
- Backfolding, 78
- Band of Baillarger, 353–354
- Bandpass birdcage, 142–143
- Basal ganglia, 417
- Bioenergetics and neuronal activity, 327–328
- Birdcage coil, 142–143, 178–182
 modeling, 168–170, 222
- Birdcage shield, 142–143
- Blood
 flow and spatial specificity, 302–303
 and gradient echo BOLD functional imaging, 311
 and Hahn spin echo-based BOLD images, 307–310
 imaging of, 298

- large vessels and CNR, 302
 - and magnetic fields during neuronal activity, 306–307
 - size in fMRI, 305
- Blood oxygen level dependent contrast.
 - See* BOLD-based contrast
- Blood signal, 91
- Blood spins, 91
- Blurring artifact in EPI, 272–274
- Body coils, 153, 154–156
- BOLD-based contrast, 21, 61, 300–301, 423, 430
 - Hahn spin echo-based, 307–310
 - and magnetic field, 304–307
- Boltzmann's equation, 2
- Boltzmann's constant, 223
- Bore diameter, 45–46
- Bound surface current, 250
- Boundary conditions, 219–220
- Brain
 - deep brain nuclei imaging, 413–414
 - function and T_2^* contrast, 251–252
 - functional and physiological imaging in, 300–321
 - and glucose transport kinetics, 390–393
 - and glycogen metabolism, 393–395
 - and high field NMR spectroscopy, 388–400
 - imaging, 411–432
 - microimaging of cortex, 347, 353–360, 413
 - microimaging, ex-vivo, 360–365
 - morphological imaging of, 295–300
 - and oxygen metabolism, 395–397
- Brain glycogen
 - and localization of ^{13}C NMR signals, 382–383
 - metabolism, 393–395
- Brain iron concentration, 253
- Brain lactate, 395
- Brain tumor imaging, 423–430
- Brainstem imaging, 413–414
- Broadband noise, 47
- Bruker supervisor system, 117
- Bulk magnetization, 223–224
- Bulk vibration, 50–51
- ^{13}C NMR spectroscopy, 373
 - and brain glycogen metabolism, 393
 - and glucose transport, 327–330, 390
 - in-vivo, 380–383
 - localization methods for, 381–383
 - localization of signals, 382–383
 - sensitivity of, 388
- ^{13}C nucleus, 380
- Cabling, 118
 - in scanner room, 115
- Capacitors, 142
 - in coil modeling, 222
 - loss, 129, 143
 - lumped, 180–181
- Cardiac array coil, 70
- Center brightening effect, 69, 85, 233–235, 294–295
- Cerebral blood flow, 300, 324, 330–331
- Cerebral glycogenolysis, 393
- Cerebral metabolic oxygen consumption (CMRO₂)
 - and functional mapping, 313–314
 - and oxygen 17 mapping, 324–325, 330–331
- Cerebral spinal fluid space and intensity changes, 312–313
- Cerebrovascular small-vessel disease, 416–419
- Chemical shift, 50
 - in ^{13}C NMR, 381–382
 - imaging, 384–385
- α -chloralose, 391–392
- CINE, 346
- Circularly polarized (CP) transmit/receive (TX/RX) coil, 69
- Climate control of scanner, 108–109
- Clinical imaging, 411–432
 - on 7T, 87–95
 - at ultra high field MRI, 59–61
- Closed cycle coolers, 29–30
- Closed-cycle low-temperature refrigeration, 41
- CNR, 254
 - in fMRI, 302, 314–316
 - in Hahn spin echo-based BOLD images, 310
- Coaxial line, 138, 141
- Cobalt in shims, 33
- Coil formers, 29
- Coil inductance, 35
- Coil interfaces, 51–53
- Coil noise dominance, 228
- Coil receptivity, 224–226
- Coils. *See also* Specific types of coils
 - cardiac array, 70
 - circuits, 138–142
 - compensation, 24
 - conductor resistance, 129–130
 - copper, 24–25
 - design, 54–55, 148–150
 - magnet, 23–24
 - multi-nuclear, 152–153
 - receive, 70
 - size of, 52
 - solenoidal, 24–25
 - superconductor, 38–39

- and tissue heating, 132
 - and tissue losses, 131–132
 - use of multiple, 241–242
 - and voltage impedance, 52
- Coil strut, 175–176
- Coil volume and microimaging, 345
- Coil windings, 49
- Columnar level mapping, 303–304, 310
- Compensated solenoid, 23
- Compensation coils, 24
- Compensation gradient, 258
- Conduction currents, 210
- Conductive strip lines, 141
- Conductivity of the body, 84–86
- Conductors, 25–26, 142, 173
 - in low-field frequency, 227
 - vibrating, 50–51
- Continuous ASL (CASL), 91
- Contrast-to-noise ratio. *See* CNR
- Cool-down shrinkage in magnets, 24–25
- Coolant, 117
- Cooling of gradient and power amplifier, 116–117
- Copper coil, 24–25
- Cortex
 - imaging, 413
 - microimaging of, 347, 353–360
- Cortical arteries and veins, 413
- Cortical dysplasia, 360
- Cortical lamina, myelin-based microimaging of, 352–360
- Cortical ribbon, 355
- Coupling
 - of current, 179–180, 197
 - in neuronal activity and functional imaging, 303
- Critical field in superconductivity, 37–38
- Cryocoolers, 41, 112
- Cryogenics in UHFMRI, 48
- Cryogens, loss of, 121
- Cryorefrigerators, 29, 48–49
- Cryostats, 27–30
- Curl equations, 212–217
- Currents
 - affecting gradient coil, 50
 - bound surface, 250
 - on coil elements, 178–182
 - conduction, 210
 - displacement, 34, 131
 - distribution in low-field frequency, 227
 - eddy, 37, 83, 131, 134
 - induced electrical and SAR, 235–237
 - shim, 82, 83
- Cytoskeleton changes due to ultra high field MRI, 7
- 2D localized imaging, 94, 200–202
- 2D-FT image, 259–260, 262
- 3D FLASH imaging, 89
- 3D-FT image set, 259–260
- 3D imaging, 94, 200–202
 - and GESEPI, 263
- Decoupling and RF power, 380–381
- Deep brain nuclei imaging, 413–414
- Degrees of freedom in coil control, 154
- Deoxyhemoglobin, 429–431
 - and BOLD-based imaging signals, 304–305
 - and cerebral oxygen consumption, 314
 - and magnetic fields during neuronal activity, 306–307, 310–311
 - and neuronal activity changes, 300, 303
- Depth penetration of small array coils, 350–352
- Diamagnetic materials, 250
 - and magnetic forces, 87
- Dielectric center brightening, 65
- Dielectric constant, 148–150
- Dielectric effects, 61, 83
 - of the body, 84–86
- Dielectric focusing, 196
- Dielectric losses, 129
- Dielectric resonances, 2–3, 5, 195–198, 233, 292
- Dielectric space, 149–150
- Differential mapping, 304
- Diffusion behavior of glucose, 390
- Diffusion tensor imaging (DTI), 60, 72, 320–321
- Diffusion weighing gradients, 307–310
- Displacement current density, 132
- Displacement currents, 131, 134
- Door in scanner room, 113, 114
- Double-echo method, 384
- Draining vessel and functional imaging, 303
- Drive ports, 179–180, 199–200
- Driving voltage, 232
 - calculation of, 230–231
- Dry dual-action fire protection sprinkler system, 109, 112
- Dynamic averaging, 305, 306
- Dynamic shimming, 83
- ECG changes in imaging, 432
- Echo peak, 265–266
- Echo Planar Imaging (EPI), 20, 37, 61, 72, 95–96, 270, 321
 - and geometric distortion in, 274–276
 - and reduction of blurring artifact, 272–274

- Echo shift, 262
 Echo time, 384
 Eddy currents, 37, 83, 131, 134
 Eigenmode frequencies, 75
 Electric field displacement, 131
 Electric field reference points, 216
 Electrical circuits, 112
 Electrical conductivity in tissue, 210–211
 Electrical currents. *See* Currents; *See also*
 Specific types of currents
 Electrical isolation, 111–112
 Electrical leakage, 111
 Electrical permittivity in tissue, 210–211
 Electrical properties of tissue, 220–221
 Electrical supply of scanner, 110–112
 Electromagnetic field, 80
 Electromagnetic wavelength and B_1 field
 frequency, 210–211
 Electromotive force, 51
 Embedded passive shims, design characteristics
 of, 54
 Embedded resistive shim coils, design
 characteristics of, 53
 Emergency response personnel and fringe field
 containment, 108
 Encapsulation of noise, 76
 Energy storage in magnets, 27
 Entorhinal cortex, 77, 362
 EPISTAR, 91
 Euler's Law, 131
 Ex-vivo imaging, 360–365
 Excitation
 and B_1 inhomogeneity, 97
 in RF coils, 173, 175
 of spins, 186–187
 Excitation ports, 192–195
 and image homogeneity, 195–198
 Excitation profile, 262
 Excitation sources of RF coils, 180–181
 Extravascular BOLD effect and SNR, 316
 Extravascular space in fMRI, 304–306
 Extravascular spin-echo BOLD effects, 307
 Faraday shield, 143
 FASTMAP, 378
 FDTD method. *See* Finite-difference time-
 domain (FDTD) method
 Ferromagnetic objects and fringe field
 containment, 108
 Ferroshimming, 81
 Fiberglass rods, 29
 Fiberoptic lighting, 114–115
 FID amplitude, 230–231
 and SNR, 240
 Field drift, 32, 34
 Field gradients, 253–254
 Field inhomogeneity artifacts with reversed
 spiral imaging, 276–279
 Field of view (FOV), 127, 136, 137
 restriction of, 321
 Field strength and signal-to-noise ratio,
 46–47
 Filters for electrical supply, 110–111
 Finite-difference (FD) method of B_0 field
 distortion, 257–258
 Finite-difference time-domain (FDTD) method,
 51, 68, 165, 166, 212–222
 accuracy of, 218–219
 code, 173–174
 and modeling RF coils, 221–222
 outer boundary conditions for, 219–220
 and RF coil stimulator, 167–174
 and specific absorption rate (SAR), 84
 stability of, 217–218
 Finite-element analysis method of B_0 field
 distortion, 255–256
 Finite-Element Method (FEM), 24, 133,
 165, 166
 Fire protection system, 109, 112
 FLASH imaging, 151, 152, 361
 Flexing of cables, 115
 Flip angle, 87–88, 175, 230
 and excitation source, 194–195
 and SAR, 232, 236
 and SNR, 240
 Flip angle gradient echo image, 195–198
 Floor drainage system, 109
 Flooring and vibration control, 109–110
 Flux shielding, 134
 fMRI, 3, 60, 72, 91, 92, 430–431
 at 4 T, 286
 clinical applications of, 105
 and mapping of neuronal activity alterations,
 300–321
 noise in, 314–316
 and T_2^* contrast, 251–253
 Fold-over artifact, 74–75
 Fourier encoding, 358
 Fourier transform, 261
 FOV. *See* Field of view (FOV)
 Frahm's compensation gradient
 method, 259
 Free Induction Decay (FID), 20
 Frequency switching, 152–153
 Frequency tuning, 170–172
 Fringe field of magnet, 63–64
 containment of, 107–108
 safety aspects of, 87

- Full-wave modeling
 - of RF coils, 164–166
 - of RF power requirements, 177–178
- Functional magnetic resonance imaging. *See* fMRI
- Functional mapping with initial "dip," 313–314
- Functional MRI. *See* fMRI

- GABA, 386
 - neurotransmission, 431
- Garolite bars, 115
- Gaussian pulse, 222, 232
- G_z , 263, 272
- Geometric distortion artifact, 274–276
- GESEPI, 259
 - and conventional 3D imaging, 263
 - at high magnetic field, 266–270
 - and reversed spiral imaging, 279
 - with SENSE imaging, 275–276
 - theory of, 261–263
- Gibbs artifact, 358–359
- Gibbs ringing, 358–359
- Glial energy metabolism, 396–397
- Glioblastoma, 425
 - and ultra high field MRI, 7
- Global shim coils, 81
- Glucose
 - and oxygen metabolism, 395
 - resonance of, 326–327
 - transport kinetics in the brain, 390–393
- Glutamate, 396
 - quantification of, 397–398
- Glutamate–glutamine cycle, 329–330, 396–397
- Glutamatergic neurotransmission, 396–397
- Glutamine, 396
 - quantification of, 397–398
- Glutamnergic neurotransmission, 431
- Glutathione, detection of, 399–400
- Glycogen. *See* Brain glycogen
- Glycol–water mixture as coolant, 117
- Gradient area per unit time, 50
- Gradient cables, 115
- Gradient coils, 35–37, 50–51, 72–73
 - in B_0 , 75
 - design characteristics of, 53
 - head insert, 73–74
 - impedance of, 61, 79
 - in microimaging, 345
 - small-bore, 73, 74
 - whole-body, 73–74
- Gradient conductor, 50
- Gradient cooling, 116–117
- Gradient drivers, design characteristics of, 54
- Gradient-echo condition, 258
- Gradient Echo Slice Excitation Profile Imaging. *See* GESEPI
- Gradient echo (T_2^*) BOLD functional imaging, 310–313
- Gradient echoes, 301
- Gradient efficiency, 35
- Gradient linearity, 74
- Gradient magnetic field, 80
- Gradient power amplifier cooling, 117
- Gradient power amplifier (GPA), 80
- Gradient recalled echo imaging, 61, 89, 238–239, 266–269, 412–413, 421
 - for brain tumor, 423
 - and CNR, 316
 - and tissue contrast, 251
- Gradient set of scanner, 123, 124
- Gradient strength, 345
 - and image distortion, 81
- Gradients, 72–80
 - atomic/molecular, 268
 - in B_0 , 75–78
 - and bore diameter, 45–46
 - field, 253–254
 - interaction with magnet, 79–80
 - rise time of, 7
- Gray/white contrast, 89
- G_z^1 , 263, 272

- H_1^- field, 190, 191–195
- ^1H NMR spectroscopy, 375, 380, 382, 388, 389
 - and disease monitoring, 398–399
 - and glucose transport, 390
 - in-vivo, 384–388
 - localization methods of, 384
- ^1H nucleus, 380
- Hahn spin echo (HSE), 301
- HSE-based imaging, 307–310, 431
 - and CNR, 317
- Harmonic magnetic field density, 187
- Harmonics and shimming, 35
- Head coils, 137–138, 142, 153–154
- Head insert coil, 73–74
 - and acoustic noise, 76–77
- Head insert gradient coils, 78–79
- Head model for RF coil simulation, 167–168
- Head-only gradients, 345
- Head-only magnet, 63–64
- Head volume coils, 184
- Hearing protection, 114

- Helium
 - boil-off, 27, 29–30, 112
 - in cryostat, 27
 - and refrigeration, 41–42
 - reservoir in magnet, 27, 29, 40
 - in superconductors, 48
- Hematoxylin and eosin (H&E) stain, 426
- Hepatic encephalopathy, 397–398
- Heschel's gyrus, 359
- High field NMR spectroscopy and the brain, 388–400
- High field spectroscopy, 4
- High-frequency coils. *See* RF coils
- High-pass birdcage, 142–143
- High-performance insert-gradient coils, 77
- High-power chain, 65–66
- Higher-order shims, 82, 83
- Hippocampus, 363–364
- Homogeneity of magnetic field, 122
- Hoop stress, 25
- Humans
 - imaging, safety of, 147
 - laminar imaging of, 359–360
 - microimaging in, 347–352
 - array coils for, 348–350
- Huntington disease, 399
- Hyper-Echo technique, 84, 94, 97
- Hypoglycemia, 393
- Hypoperfusion, 416–417

- Image acquisition, 3
 - speed, 254
- Image artifacts, 154–156
- Image blurring artifact in rapid imaging, 270–272
- Image brightening, 69
- Image contrast, 254
- Image distortion and gradient strength, 81
- Image homogeneity, 148, 195–198, 199–202
- Image intensity, 291–295
- Image optimization, 148–152
- Image quality and shimming, 35
- Image-space bandwidth, 265–266
- Image-to-image fluctuations, 314–316
- Imaging
 - safety of, 431–432
 - using low-gyromagnetic nuclei, 322–325
- Imaging time, 60
- Impedance
 - adjustment of, 148
 - of gradient coil, 61, 79
- Impedance transformer, 52
- In-flow effects, 309
- In-vivo shimming, 34–35, 61

- Inductance, 27, 136–137
- Inductive coupling, 52
- Inductively decoupled loops, 137
- Infarctions, 416, 420–421
- Inorganic phosphate, 327–328
- Input impedance, 139–140
- Interfering wave phenomena, 132
- Intra-oral diamagnetic passive shim, 81
- Intracranial calcification, 253
- Intracranial hemorrhage, 253
- Intravascular BOLD effects in functional images, 307–308, 310–311
- Intravascular space in fMRI, 306–307
- Intravoxel phase dispersion, 263
- Intrinsic noise, 47
- Iron deposits, 417–418
- Iron room, 109
 - electrical isolation of, 111–112
- Ischemic stroke, 421
- Iso-orientation columns, 304
- Isotopes, NMR spectroscopy of, 388
- Isotopomer analysis, 373

- J*-coupling, 375

- k*-space, 261
 - sampling, 274
- Krebs cycle flux, 395–396

- Laminar imaging
 - of humans, 359–360
 - of primates, 355–359
- Large blood vessels
 - and gradient echo BOLD functional imaging, 311–313
 - and SNR, 316
- Large-bore magnet technology, 106
- Large phantom, 179–180
- Larmor frequency, 174
- LASER, 384
- Lattice plane in FDTD method, 217–218
- LC circuit loop, 132–133
- Leptomeningeal vessels, 415–416
- Light flashing, 124
- Lighting in scanner room, 114–115
- Line-element array, 144
- Line of Gennari, 359
- Linear-element coil, 141
- Linear-element TEM volume coil, 145–146
- Linear excitation, 180–182, 190–192
- Linear polarization, 182
- Linear shims, 81
- Liquid helium. *See* Helium
- Load geometry and excitation port, 194–195

- Load resistance, 51
- Local field maximum, 234
- Local field minimum, 234
- Localization
 - of ^{13}C NMR signals, 382–383
 - on ^1H magnetization, 382
- Long-term drift, 32
- Loop coils, 141, 186
- Loop-element TEM volume coil, 145–146
- Lorentz forces, 50, 75
- Lossless approximation, 140
- Low-gyromagnetic nuclei, and imaging, 322–325
- Low-input impedance preamplifiers, 52
- Low-noise preamplifiers, 65
- Low-SAR T_2 -weighted imaging, 94–95, 97
- Low-temperature superconductors, 41
- Lumped-element loop, 138
- Lumped-element surface coil, 133

- Macaque, microimaging of, 355–359
- Macroscopic gradient, 268
- Magnet coils, 23–24
- Magnet formers, 23–24
- Magnet homogeneity, 31, 49
 - and fold-over artifact, 74
 - and increasing field strength, 81
- Magnet room and grounding, 111
- Magnet windings, 23–24, 29
- Magnetic current density, 188
- Magnetic field
 - choice of, 106–107
 - frequency, 209
 - homogeneity of, 122
 - increasing strength of, 40–41
 - inhomogeneities, 253–254, 270, 321
 - inhomogeneity artifacts, 258–270
 - perturbations, 250
 - reference points, 216
 - and signal loss, 258–261
 - strength, 19, 128, 209
- Magnetic flux B_0 , 81
- Magnetic flux density, 187, 188
- Magnetic forces and safety, 86–87
- Magnetic permeability, 250–251
- Magnetic resonance imaging. *See* MRI
- Magnetic susceptibility effect, 81, 249–280
- Magnetic vector potential, 131
- Magnetization-Prepared Rapid Gradient-Echo Imaging (MPRAGE), 89–91
- Magnets
 - active shielded, 30
 - conductors and, 25–26
 - cooling of, 121–122
 - design strategies, 22–27, 53
 - energy management of, 27
 - geometrical issues, 22–23
 - head-only, 63–64
 - homogeneity of, 22–23
 - interaction with gradients, 79–80
 - mechanical issues, 23–25
 - in microimaging, 344–345
 - mode of operation, 27
 - in 9.4T system, 120–123
 - parameters of, 120
 - passive shielded, 30
 - pumping of, 39–40
 - shielding stray field, 30–31
 - for UHFMRI, 47–50
 - ultra high field, 20–22
 - in ultra high field MRI, 19–22
 - vibration control of, 109–110
 - whole-body, 63
- Maximum background field, 37
- Maximum current-carrying capacity, 37
- Maximum intensity projection (MIP) technique, 93
- Maxwell-Ampere Law, 131
- Maxwell's curl equations, 212–217
 - discretizing, 213–217
- Maxwell's divergence relations, 212–213
- Maxwell's equations, 187
- MC₂, 188–189
- Medial longitudinal fasciculus, 414
- Medial temporal lobe imaging, 363–365
- Mesh element in Yee cell cube, 221
- Mesoscopic gradient, 268
- Metabolic pathways, 329–330
- Metabolite-nulled spectra, 388
- Method of moments (MM), 166
- Mice and microimaging, 346
- Michaelis-Menten kinetics, 390–391
- Microangiopathy, 417
- Microbleeds, 417–418
- Microimaging
 - in ex-vivo brain, 360–365
 - in humans, 347–352
 - instrumentation for, 344–355
 - of medial temporal lobe, 363–365
 - myelin-based, 352–360
 - in small animals, 345–346
- Microvascular density (MVD) counting, 426
- Microvasculature, 414–416
 - and CNR, 302
 - imaging of, 423–424, 426–429
 - and SNR, 316
- Missile effect, 108
- Movement disorders, diagnosis, 413–414

- MRI
 future of, 40–42
 historical perspective, 1–2
 and increasing magnetic field strength, 163–164
 relating RF field calculations to, 222–233
 RF power requirements in, 174–178
- MTL, 363, 365
- Multi-array RF coils, 376
- Multi-coil arrays, 321
- Multi-nuclear coils, 152–153
- Multi-tissue models and B_0 field distortion, 257–258
- Multichannel array coils and SNR, 288–291
- Multichannel coil interface, 144–145
- Mutual decoupling, 136–137
- Myelin-based microimaging, 352–360
- $N/2$ ghosting, 80
- Nb_3Sn superconducting alloy, 38–39, 41
- Nb_3Sn wire, 41
- $NbTi$ superconducting alloy, 38–39, 41
- $NbTi$ wire, 26
- Neuronal activity alterations, mapping of, 300–321
- Neurons and astrocytes, 396–397
- Neurotransmission rate, 329–330
- NMR spectroscopy
 and brain glycogen metabolism, 393–395
 of glutamate and glutamine, 325–326
 and oxygen 17 imaging, 323–325
 and RF component, 185–190
 and RF power, 376–379
 sensitivity of, 374–376
 and shimming, 377–379
 and SNR losses, 128
- Noise. *See also* Acoustic noise
 as function of B_0 field strength, 226–227
 generation in magnets, 35–37
 insulation, 76
 power, 6
- Normalization in clinical imaging, 93–94
- Nyquist's equation for thermal noise, 226–227
- Ohmic losses, 129
- Ohmic resistance, 128, 129
- Ohm's Law, 131
- Optimal sensitivity, 47
- Oscillating magnetic fields, 210
- Outer boundary conditions for FDTD method, 219–220
- Over-sampling, 265–266
- Oxygen 17 imaging, 323–325
- Oxygen consumption rates, 324
- Oxygen metabolism in the brain, 395–397
- ^{31}P spectra, 327
- Parallel array coil, 136
- Parallel imaging, 37, 84, 144, 241–242, 321–322
- Parallel lumped-element circuits, 138
- Parallel reception, 128
- Parallel transmit arrays, 67–68
- Paramagnetic materials, 250
 and magnetic forces, 87
- Passive shielding, 30, 63, 107
- Passive shims, 32–35
- Patient bed, 117–118
- Patient handling, 117–118
 in ultra high field MRI, 55
- Patient safety, 86–87
- Patient transporter, 117–119
- Peak amplitude, 50
- Peak slew rate, 50
- Penetrating vessels, 413
- Penetration depth and B_1 field frequency, 210–211
- Penetration effects, 235
- Penetration panel in scanner room, 113
- Perfect electrically conducting (PEC) boundary, 220
- Perfectly matched layer (PML) boundary condition, 219
- Perforant pathway, 365
- Perfusion imaging, 303–304, 320
 and large vessels, 311–313
- Peripheral nerve stimulation (PNS), 73, 78
- Periventricular microvasculature, 417
- Periventricular white matter, 417
- Permeability tensor, 187
- Permittivity of the body, 84–86
- Persistent mode of magnets, 27
- Phantoms
 and polarization, 192–194
 in RF coils, 179
- Phase and gain control, 151–152
- Phase contrast enhancement method, 413
- Phase dispersion factor, 261–262
- Phase velocity, 139
- Phased array of coils, 6, 52, 136, 348–350
 excitation, 198–202
- Phosphocreatine, 327–328
- Physiological noise, 317
- PICORE, 91
- PIN diodes, 137
- Piping connections, 117
- Plane wave excitation, 195–197

- Plaques
 - detection of, 298–299
 - imaging of, 363
 - and tangle disposition, 362
- Plasma glucose, 391
- Point spread function (PSF), 272
- Polarization
 - in RF coils, 188–189, 192
 - in TEM resonator, 182
 - in tissue, 210
- Polarization transfer, 382
- Power amplifiers, 106
- Power conditioning, 110
- Power deposition rate in tissue, 52
- Power loss, 135
- Preamplifiers, 137
 - low-input impedance, 52
- Prescribed signal evolution (PSE), 84, 94, 97
- PRESS, 384–385
- Pressure and the cryostat, 29
- Primate laminar imaging, 355–359
- Propagation constant, 139
- Proton density, 296
- Pulse duration and SAR, 232
- Pulse selectivity, 386
- Pulse Tube Refrigerators (PTR), 41
- Pumping station on magnets, 39–40
- Pyrolytic graphite, 50

- Q factor, 129
- Quadrature excitation, 181–182, 197–198
- Quadrature splitter-combiner, 225
- Quasi point source, 261
- Quasistatic field approximations, 164
- Quasistatic model of RF power requirements, 175–176
- Quench, 27
 - protection, 63
- Quenching, 121
- QUIPSS, 91

- R_2^* map, 269
- Radiation effects in cryostat, 29
- Radiation resistance, 128, 129, 130–131
- Radiation shields, 48–49
- Radiative losses, 128, 130–131, 133
- Radiofrequency isolation of scanner, 112–113
- Ramping scanner, 121–122
- Rapid imaging and image blurring artifact, 270–272
- Receive and transmit fields
 - patterns, 293–295
 - theory of, 190–192
- Receive channels, 64, 65, 70
- Receive-only coils, 137–138, 142
- Receiver channels, 52
- Receiver coils, 70, 153–154, 186–188
 - multiple, 241–242
 - size of, 348
- Receiver interface, design characteristics of, 55
- Receiver system, 349–350
- Reception sensitivity, 290
- Reciprocity, 224–226, 227
 - in MRI, 186
- Reduction factor, 274
- Refrigeration and liquid helium, 41–42
- Region of interest (ROI), 137
- Region of uniformity, 35
- Regional cerebral blood flow (rCBV), 253
- Relaxation properties of the brain, 361
- Relaxation times, 47, 373
- Resistance values for coil and sample, 227
- Resistive losses, 128, 129–130
- Resistive shim drivers, design characteristics of, 54
- Resistor-diode network, 27
- Resonance frequency, 138, 143, 174
- Retinal stimulation, 124
- Reversed spiral imaging, 276–279
- RF, penetration, 5
- RF coil stimulator, 167–174
- RF coils, 3, 6, 68–72, 118–119, 127–157
 - and coil interfaces, 51–53
 - current distributions, 182–184
 - design of, 54, 164–166, 240–242
 - efficiency of, 127, 132–142
 - and FDTD method, 221–222
 - full-wave modeling, 164–166
 - and head interaction, 6
 - homogeneity, 74
 - implanted, 324
 - interface, 54
 - leaks of, 112–113
 - length of, 132–133
 - loading of, 182–184
 - losses, 128–132
 - modeling, 178–185
 - sensitivity, 47
 - surface, 127, 132–138
 - in tumor imaging, 423
 - volume, 127–128
- RF field, 84
 - calculations of, 209–242
 - FDTD method, 212–222
 - results of, 233–242
 - patterns, 233–235
- RF heating potential, 135

- RF power, 2–4, 376–379
 - and decoupling, 380–381
 - and flip angle, 87–88
 - requirement, 5–6, 66–67
 - in MRI, 174–178
 - and SAR, 84
- RF power amplifier, 65–66, 151
- RF power-frequency dependence, 174–178
- RF receiver, design characteristics of, 54
- RF rooms, 112–115
- RF small-signal components, 64–65
- RF supervisor, 110–120
- RF system, 64–72
- RF transmitter, design characteristics
 - of, 54
- Rise time of gradient, 37
- Room temperature bore tube, 29
- Room-temperature (RT) shims,
 - 34–35, 106
- Rotation matrix, 187, 189
- Safety of imaging, 431–432
- Sagittal images, 199–202
- SAR, 87–88, 135
 - calculations of, 231–233
 - and coupling of current, 179–180
 - estimation of, 165
 - and excitation sources, 180–182
 - IEC limits, 232
 - and induced electrical currents, 235–237
 - monitoring, 68
 - and RF coil and tissue interactions, 199
 - and RF power, 376–377
 - supervision of, 119–120
 - in T_2 -weighted imaging, 93–95, 97
- Scanner for human brain imaging, 105–125
- Second-order accurate in FDTD method,
 - 218–219
- Second-order shims, 81, 83
- Self-shielded shim coils, 83
- Self-shielding magnet, 63
- SENSitivity Encoding (SENSE) imaging, 37,
 - 144, 322
 - and geometric distortion artifact reduction,
 - 274–276
- Sensitivity in UHFMRI, 46–47
- Series capacitance, 133
- Shield windings, 48
- Shielding of magnets, 30–31
 - active, 48
- Shim coils, 377–379
- Shim currents, 82, 83
- Shim fields, 82
- Shimming, 32–37, 62, 81–83, 122, 148,
 - 377–379
 - B_1 , 67–68
 - in-vivo, 34–35, 61
- Shims, 23
 - design characteristics of, 53–54
 - passive, 32–35
 - room-temperature, 34–35
 - sensitivity, 82
 - superconducting, 32
- Signal amplification, 65
- Signal amplitude, 231
- Signal as function of B_0 field strength, 223–226
- Signal intensity
 - and neuronal activity alterations, 300–301
 - patterns, 237, 238
 - in rapid imaging, 270–272
- Signal-loss artifact, 258–261, 275–276
 - mathematic analysis of, 261–270
 - reduction, 259–261
 - and reverse spiral imaging, 278–279
- Signal strength, 226
- Signal to Noise Ratio. *See* SNR
- Signal voids, 81
- Sinc-function modulation, 271–272
- Sine pulse, 232
- Single-condition mapping, 304, 313
- Single-strut coil, 190–191
- Siting of scanner, 107
- Skin depth, 129–130
- Slew rate, 345
- Slice excitation profile, 263
- Small animal imaging, 345–346
- Small array coils, depth penetration of, 350–352
- Small-bore gradient coil, 73, 74
- Small phantom, 179–181
- SNR, 3–4, 37, 46–47, 60, 70, 72, 237,
 - 239–240, 254
 - and B_0 field, 223–229
 - and B_1 field, 287–291
 - and brain imaging, 423, 425
 - and coupling between coils, 137–138
 - gains with increasing magnetic field, 291
 - in GESEPI images, 264–266
 - and gradients, 72
 - in high field MRI, 228–229
 - isolation of in scanner room, 112–113
 - in loop array, 146
 - at low field, 227–228
 - and magnetic field strength, 19
 - and microimaging, 344
 - in mid-field, 228
 - in parallel imaging, 322
 - in the periphery, 287–291

- and phased array of coils, 349–350
 - in primate laminar imaging, 357
 - reduction of, 128
 - in T_2 -weighted imaging, 94
- Solenoid magnets, 23, 47–48
- Solenoidal coils, 24–25
- Solid-state amplifier, 65
- Sound pressure level (SPL), 51, 75
- Spatial resolution, 388, 423
- Spatial specificity, 307, 313
 - in functional images, 302–303
- Specific absorption rate (SAR), 61
 - limits, 52
 - at 7T imaging, 84
- Spectral editing, 386
- Spectral overlap, 374–375
 - in ^1H NMR, 384
- Spectral resolution, 3–4, 386–388
- Spectrometer, design characteristics of, 55
- Spectroscopy at high magnetic fields, 325–331
- Spin echo images, 238
- Spin echo T_1 -weighted imaging, 88–89
- Spin excitation, 290
- SPIRAL, 321
- Spiral images, 270
- Square dependence, 175–176
- Static averaging, 305, 306
- STEAM, 384
- Steel
 - and shielding, 48
 - in shims, 34
- Stejskal and Tanner gradient pair, 307–310
- Strain gauges, 31
- Stray field of magnet, 30–31
- Stress patterns in magnets, 24
- Stroke imaging, 419–423
- Substantia nigra, 414
- Sumitomo RGD408D cryocooler, 41
- Superconducting magnets, 47–50
- Superconducting shims, 32
- Superconducting wire, 37
- Superconductors, 25–26, 38–39
 - low-temperature, 41
- Superinsulation, 29
- Surface coils, 127, 132–138, 376
 - and arrays, 136
 - integration of receive-only coils with transmit coils, 137–138
 - safety, 135–136
 - thermal properties of, 135
 - tissue losses, 133–135
- Susceptibility effects on image, 35
- Susceptibility variations, 50
- Switch heater, 27
- Switch in magnets, 27
- System integration, 45–46
- 3T Echospeed system, 20
- 3T imaging, 60, 105
 - magnet system, 20, 21
- 4T imaging, 3–4, 19
 - and B_1 nonuniformities, 292–295
- 7T imaging, 21, 60, 62–83
 - of brain, 347
 - challenges of, 83–87
 - clinical scanning, 87–95
 - safety aspects of, 86–87
 - specific absorption rate (SAR), 84
- 9.4T scanner, 37, 105–125
 - acoustical dampening, 114
 - cabling, 115
 - choice of magnetic field strength, 106–107
 - climate control of, 108–109
 - cooling of, 121–122
 - electrical supply and, 110–112
 - fringe field containment, 107–109
 - gradient set of, 123, 124
 - as human delivery system, 117–118
 - lighting, 114–115
 - magnet, 120–123
 - radiofrequency isolation of, 112–113
 - and site planning, 107–123
 - supervision of SAR, 119–120
 - vibration control, 109–110
- 3T Sigma™, 21
- T_1 , 361
 - and brain tissue imaging, 296–298
 - contrast, 89
 - and oxygen 17 imaging, 323
 - weighted imaging, 88–91
- T_2
 - and brain tissue imaging, 298–300
 - and oxygen 17 imaging, 323
- T_2^*
 - and brain tissue imaging, 298, 300
 - contrast at high magnetic field, 251–253
 - contrast images, 266–270
 - relaxation, 271–272
 - and reversed spiral imaging, 277
- T_2^* -weighted imaging, 91, 93–95, 97
 - limitations of, 253–254
- Tailored RF pulse (TRFP), 259–260
- Tangles, imaging of, 363
- TE
 - and blood contributions to BOLD effects, 309–310
 - in BOLD-based imaging signals, 305
- Teflon, 137

- TEM arrays, 145–146
- TEM coils, 143–147
 - independent tuning of, 152–153
 - safety of, 147
- TEM resonator, 3, 191, 423
 - model of, 170–173
- TEM theory, 130–131, 138, 143, 178
- Temperature
 - change in head imaging, 147
 - and critical field variation, 39–40
 - of shims, 33
 - in winding of magnet, 24–25
- Temporal signal fluctuations, 319–320
- Tensor, 187
- Thermal energy, 232–233
- Thermal hotspots, 135
- Thermal isolation of magnets, 27–29
- Thermal modeling, 166
- Thermal noise, 318
- Thermal radiation, 48
- Third-arm artifacts, 74, 78
- Three-dimensional gradient-echo (3D-GE) image, 259
- Through-plane local gradient, 270
- Time of Flight (TOF) MR angiography, 91–93
- Time step procedure in RF coil simulations, 173–174
- Tissue
 - and B_1 field frequency, 210–211
 - and coil losses, 131–132
 - electrical properties of, 220–221
 - heating, 132
 - losses in surface coils, 133–135
- Tissue signal weighting factor, 226, 229
- Tractography, 320, 321
- Transmission line (TEM) coil circuits, 138–142
 - examples of, 141–142
- Transmission line theory. *See* TEM theory
- Transmit and receive fields, 156
 - theory of, 190–192
- Transmit coils, 137–138
 - design characteristics of, 55
- Transmit-receive (TR) switches, 144–145
- Transmit SENSE, 68, 97
- Transmit signal, splitting of, 144–145
- Transmit (TX) channel, 64–65
- Transmit volume coil, 153–154
- Transverse electromagnetic theory. *See* TEM theory
- Transverse magnetization, 186–187
- Tube amplifier, 65
- Tumor imaging, 423–430
- Tumoral angiogenesis, 425–426
- Tune-and-match network, 137
- Tuning of coil model, 222
- Turbo Spin Echo (TSE) imaging, 93–94
- Twisted projection imaging (TPI), 124, 125
- UHFMRI. *See* Ultra high field MRI
- Ultra high field MRI, 1–2
 - clinical imaging, 7, 411–432
 - design characteristics of, 53–55
 - early results, 4–6
 - evolution of, 19–22
 - experimental results, 3–4
 - magnetic susceptibility effects in, 249–280
 - magnets for, 47–50
 - motivation for, 46–47
 - safety of, 6–7
 - theoretical arguments against, 2–3
- Ultra-small particle iron oxide (USPIO), 427
- Veins and CNR, 320
- Venous cavernomas, 418
- Vertigo, 117–118, 124
- Vessel density, 426
- Vessel reactivity, 430
- Vibration
 - and acoustic noise, 61
 - of coils, 74
 - control of scanner, 109–110
 - and magnetic field distortion, 80
 - and noise of gradient coils, 75–76
- Visual cortex, microimaging of, 362
- Vitamin C, detection of, 400
- Voltage
 - calculation of necessary driving, 230–231
 - in gradient coil, 50–51
- Volume coil mode, 293–295
- Volume coils, 127–128, 142–156, 376
 - actively detuned, 153–154
 - birdcages, 142–143
 - body coils, 153–154
 - control of, 150–152
 - multi-nuclear coils, 152–153
 - TEM, 143–147
- Volume of interest (VOI), 68, 229
- Volume resonators, 51
- Volume TEM coil and SNR, 289–291
- Voxel, 231
 - and magnetic moments, 311
 - and signal decay, 305–306
 - signal intensities, 262, 264–266
 - and small array coils, 351
 - volume
 - and CNR, 317–319
 - and image resolution, 344

- Water cooling in magnets, 50
- Water suppression, 385
- White matter changes (WMCs), 413, 416–417
- White matter lesions, 398–399
- Whole-body gradient coils, 73–74
 - and acoustic noise, 76
- Whole-body gradients, 73
- Whole-body imaging, 65–66
- Whole-body magnet, 63
- Winding structures, 63
- Windings
 - gradient, 50
 - in magnets, 23–24
- Window in scanner room, 113
- Wire
 - critical field of, 37
 - grading, 26
 - in magnets, 25–26
- Wire-in-channel (WIC) wire, 26
- Wraparound artifacts, 78
- Yee cell cube, 215–216, 220–221
- Z-shim method, 259